

## Article

# A Deep Learning Approach for Diabetic Foot Ulcer Classification and Recognition

Mehnoor Ahsan <sup>1</sup>, Saeeda Naz <sup>1,\*</sup>, Riaz Ahmad <sup>2</sup>, Haleema Ehsan <sup>1</sup> and Aisha Sikandar <sup>1</sup>

<sup>1</sup> Computer Science Department, GGPGC No.1, Abbottabad 22020, Pakistan

<sup>2</sup> Computer Science Department, Shaheed Benazir Bhutto University, Upper Dir 00384, Pakistan

\* Correspondence: saeedanaz292@gmail.com

**Abstract:** Diabetic foot ulcer (DFU) is one of the major complications of diabetes and results in the amputation of lower limb if not treated timely and properly. Despite the traditional clinical approaches used in DFU classification, automatic methods based on a deep learning framework show promising results. In this paper, we present several end-to-end CNN-based deep learning architectures, i.e., AlexNet, VGG16/19, GoogLeNet, ResNet50.101, MobileNet, SqueezeNet, and DenseNet, for infection and ischaemia categorization using the benchmark dataset DFU2020. We fine-tune the weight to overcome a lack of data and reduce the computational cost. Affine transform techniques are used for the augmentation of input data. The results indicate that the ResNet50 achieves the highest accuracy of 99.49% and 84.76% for Ischaemia and infection, respectively.

**Keywords:** DFU; AlexNet; VGG16/19; GoogLeNet; ResNet50/101; MobileNet; SqueezeNet; DenseNet

## 1. Introduction

Diabetes is a chronic disease that has a huge negative influence on people's lives, families, and society all over the world [1,2]. A serious consequence of diabetes can lead to the amputation of the foot or leg from diabetic foot ulcers (DFUs). Recognizing infection and ischaemia is critical for determining factors that predict DFU healing progress and amputation risk. A good grasp of the vascular architecture of the leg, particularly ischaemia, enables medical professionals to make better decisions when predicting the potential of DFU healing based on available blood supply [3]. According to the International Diabetes Federation [4], in 2019 roughly 463 million adults globally had diabetes. By 2045, this value is predicted to rise to 700 million.

Lower limb amputation may occur as a result of insufficient microvascular and macrovascular tissue perfusion, and infection. A diabetic patient with a "high-risk" foot needs routine doctor visits, ongoing pricey medication, and sanitary personal care to prevent further complications [5]. This places a heavy financial burden on the patients and their families, particularly in underdeveloped nations where the expense of treating this illness can be as high as 5.7 years of annual income [6]. The ability to quickly intervene and receive adequate therapy to either heal foot ulcers or stop the development of amputation may be made possible by the early detection and better classification of foot problems. Early surveillance through self-diagnosis at home may be helpful in stopping the onset and progression of DFU.

The simplest monitoring method, eye inspection, has certain drawbacks, such as the inability of those with obesity or visual impairment to accurately identify subtle changes. Recent studies show that a home-temperature monitoring system could identify 97% of DFUs in early stages [7]. Patients who have their feet temperatures monitored continuously are at a lower risk of developing foot problems. The evaluation of DFU in current clinical practices includes a variety of significant responsibilities in early diagnosis and in monitoring progress, and a number of time-consuming steps need to be completed to



**Citation:** Ahsan, M.; Naz, S.; Ahmad, R.; Ehsan, H.; Sikandar, A. A Deep Learning Approach for Diabetic Foot Ulcer Classification and Recognition. *Information* **2023**, *14*, 36. <https://doi.org/10.3390/info14010036>

Academic Editor: Andrej Kastrin

Received: 9 October 2022

Revised: 31 December 2022

Accepted: 3 January 2023

Published: 6 January 2023



**Copyright:** © 2023 by the authors. Licensee MDPI, Basel, Switzerland. This article is an open access article distributed under the terms and conditions of the Creative Commons Attribution (CC BY) license (<https://creativecommons.org/licenses/by/4.0/>).

ensure the treatment and care of DFU for each individual case. Firstly, the patient's medical background is examined, then diabetic foot experts extensively analyze the DFU [8]; further testing such as CT scans, MRIs, and X-rays can also be helpful for doctors to analyze DFUs. The DFU typically has fluctuating formations and uncertainty outside borders. The visual characteristics of DFU and the skin around it depend on the different stages, such as redness, substantial callus development, and blisters.

The DFU has recently drawn the attention of many researchers because it is a major and global issue for diabetic patients. In severe cases, the patient's survival rate is reduced due to the removal of all or a portion of a limb. Since 2020, the DFU challenge has attracted researchers to work on the identification and detection of DFU using some machine learning and deep learning approaches. To detect infection and ischaemia in DFU, a new dataset and a computer vision approach were introduced in [9] using the super pixel color descriptor, along with the customized machine learning approach. Then, the authors applied the ensemble convolutional neural network model to more accurately identify ischaemia and infection. Their ensemble CNN deep learning algorithms outperformed handcrafted machine learning algorithms for classification tasks, achieving 90% accuracy in ischaemia classification and 73% accuracy in infection classification.

It was found that deformable convolution, a faster R-CNN variation, performed the best, with an F1-Score of 0.7434 and a mean average precision of 0.6940, when comparing the results in DFUC2020 (deep learning-based algorithms proposed by the winning teams, including Faster R-CNN, three variations of Faster R-CNN, an ensemble approach, YOLOv3, and YOLOv5 [10]). In addition, a fresh deep convolutional neural network called DFU QUTNet was created in order to automatically distinguish between the classes of normal skin (healthy skin) and abnormal skin (DFU) [11]. The F1-score on their DFU QUTNet network was 94.5%. In order to classify DFU images, ref. [12] suggests an ensemble strategy made up of five modified convolutional neural networks, i.e., VGG-16, VGG-19, Resnet-50, InceptionV3, and Densenet-201. It is found that the combination of the five CNNs greatly improved the classification rates. After five-fold cross-validation, the average accuracy of 95.04% and a Kappa index of over 91.85% were achieved.

Xie et al. [13] developed a reliable model to predict the probability of in-hospital amputation in DFU patients. A multi-class classification model was created using the light gradient boosting machine (LightGBM) and to forecast the three outcomes. In addition, they utilized the SHapley Additive exPlanations 72 (SHAP) method to evaluate the model's predictions and obtained AUCs of 85%, 90%, and 73.86% for minor amputation, non-amputation, and major amputation outcomes, respectively. On foot thermogram images, ref. [14] compared numerous state-of-the-art convolutional neural networks (CNNs) to a machine learning-based scoring technique using feature selection and optimization techniques, as well as learning classifiers, and provided a reliable solution to diagnose the diabetic foot. They conclude that the AdaBoost Classifier used 10 features and obtained an F1 score of 97%, and MobilenetV2 only produced an F1 score of 95% percent for a two-foot thermogram image-based classification.

To help medical professionals make an early diagnosis, deep learning algorithms are becoming more and more popular and achieving promising performance in different fields of bio-informatics, medial imaging, and biomedical [9,15–20]. Deep learning models would be based on the precise evaluation of these visual cues as texture and color descriptors for DFU classification. This paper presented the performance of a number of CNNs architectures using pre-trained weights, outcome evaluation utilizing various matrices, and a comparison of the top deep learning model and cutting-edge methods.

The major contributions of this study include:

- To use several end-to-end CNN-based deep learning architectures to transfer the learnt knowledge and update and analyze visual features for infection and ischemia categorization using the DFU202 dataset.
- To use fine-tune weight to overcome a lack of data and avoid computational costs.

- To investigate whether Affine transform techniques for the augmentation of input data affect the performance of transfer learning based on a fine tuned approach or not.
- To investigate and select the best CNN model for DFU classification.

The remainder of the paper is organized as follows. Section 2 covers the materials and methods utilized in the study; Section 3 contains the results; and Section 4 has the conclusion.

## 2. Materials and Methods

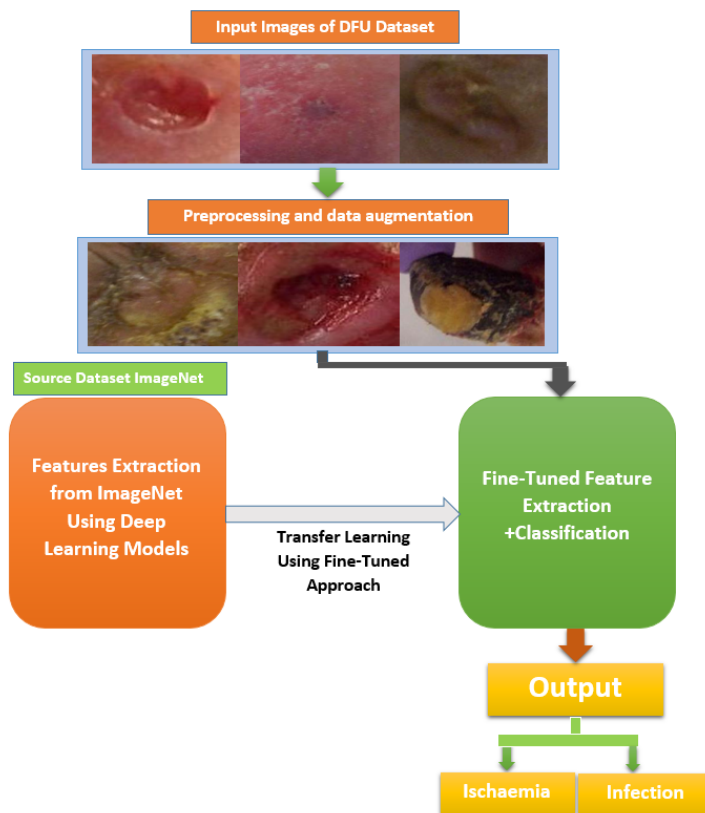
Diabetic Foot Ulcer 2020 (DFU2020) dataset <https://www.touchendocrinology.com/diabetes/journal-articles/the-dfuc-2020-dataset-analysis-towards-diabetic-foot-ulcer-detection/> (accessed on 13 June 2020), is subjected to an augmentation process in the first step of the pre-processing stage of this study. The proposed methods for DFU classification and recognition consist of the technique of transfer learning using fine-tuned weights using source and target domains. ImageNet is a big benchmark image dataset that can be used for image categorization in the source domain. There are 1000 classes, 1.28 million training pictures, and 50,000 validation pictures in total. The dataset was created with the intention of serving as a research and development tool for better computer vision systems. We retrained a number of pretrained models, including AlexNet, VGG16/19, ResNet 50/101, GoogLeNet, MobileNet, SqueezeNet, and DenseNet, and we used the DFU2020 dataset to assess the efficacy of the proposed approaches.

Figure 1 depicts the proposed framework of this study. It can be seen that images are pre-processed using different data-augmentation strategies, including rotation, flipping, scaling, translation, mirror, and shearing, applied to patches to increase the input size of target domain. The sample images of the augmented dataset are fed into the number of CNNs architectures, separately. Then, the feature vector of the ImageNet dataset of the source domain is fine-tuned and retrained using the CNN models on the destination DFU2020 dataset of the target domain. Fine-tuned features are extracted, and classification is carried out for two cases of ischaemia and infection. Details of dataset, data augmentation, and classification models are illustrated in subsections.

### 2.1. Dfu Dataset and Preprocessing

The diabetic foot ulcer (DFU) dataset 2020 [9] contains two cases of ischemia vs. all and infection vs. all. This is two binary classification tasks, one for ischaemia and the other for infection. The infection-denoting microorganisms in the wound and ischaemia denote insufficient blood flow.

This dataset's initial release included 1459 photos with sizes ranging from  $1600 \times 1200$  and  $3648 \times 2736$ . The ischaemia "positive" and "negative" classes had 1431 and 235 cases, respectively, indicating an imbalance in the dataset. Similarly, the infection "negative" and "positive" groups have 628 and 831 cases, respectively, and the dataset was roughly balanced. Different data-augmentation strategies (rotation, flipping, scaling, translation, mirror, pepper and salt noise, Gaussian noise, and shearing) were then applied to balance the dataset. The augmented dataset contains 4935 patches for ischaemia and 2945 patches for infection. Figure 2 illustrated sample images of all cases.



**Figure 1.** Proposed framework of transfer learning using fine-tuning approach for classification of ischemia and infection classes of DFU .

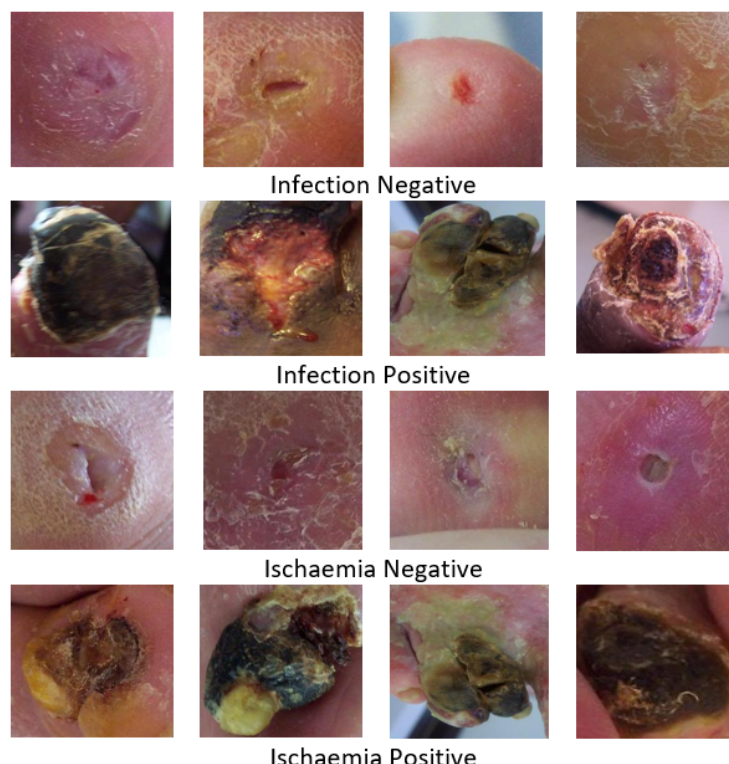


**Figure 2.** DFU2020 dataset: Sample images of infection (negative and positive) and ischaemia (negative and positive).

## 2.2. Features Learning and Classification

In the field of medicine and medical imaging, there is always a scarcity of data and the problem of the verification of ground truth or the labelling of data by medical experts. The convolution neural network requires a huge number of data for feature extraction and classification, and high computational resources. The transfer learning with the fine-tune approach has been deployed to overcome the above limitations and drawbacks. In this section, we utilized a number of pre-trained fine-tuned-based deep learning models such as AlexNet, VGG16/19, GoogLeNet, ResNet50.101, MobileNet, SqueezeNet, and DenseNet. These convolutional neural networks (CNNs) have been pretrained on ImageNet [21]. In general, a pretrained model is a model created by someone else to tackle a similar problem. We do not have to develop pretraind models from scratch when we use them. The only change that is required in a pretrained model is to change the last three layers according to the ones that are needed. For automatic feature extraction, we employed nine deep learning models, i.e., AlexNet, GoogLeNet, VGG 16, VGG 19, MobileNet, ResNet 50, ResNet 101, SqueezeNet, and DenseNet.

Alex Krizhevsky proposed *AlexNet* in 2012 [21]. The imangenet large-scale visual recognition challenge (ILVRC) was awarded its first place in 2012. It has eight layers, three of which are compeletely linked layers and five of which are convolutional layers. Maxpooling layers are placed after the first two convolutional layers. The third, fourth, and fifth convolution layers are directly related. Following the fifth convolution layer is the maxpooling layer, and the output of the maxpooling layer is passed to the fully connected layer. The softmax classifier is used in the final fully connected layer for classification.

In 2014, Simonyan and Zisserman proposed *VGG* [22]. A variation of VGG called VGG 16 indicates that it has 16 convolutional layers with a  $3 \times 3$  dimension, and a version of VGG called VGG 19 indicates that it has 19 such layers. Three completely connected layers follow the convolutional layer.

*GoogLeNet* was created in a research project at Google in 2014 [23]. In contrast to other models, the GoogLeNet architecture contains inception blocks instead of a basic sequential structure. It includes nine inception modules, along with convolution and maxpooling layers. Additionally, many layers are concatenated to boost the model's capacity for learning.

*ResNet* first appeared in 2015. With encouraging outcomes, it supports hundreds or thousands of layers. Skipping connections was a notion first offered by ResNet. Skip connections address the vanishing gradient issue. Both ResNet 50 and 101 will be used in this study. Resent 50 contains 50 layers. It has five residual blocks, each of which has an identity block and a convolution block. There are 101 levels in ResNet 101. It includes three convolution and identity blocks, in addition to three residual blocks.

In 2016, *SqueezeNet* was released [24]. Convolution and maxpooling layers are used as the foundation. Following the initial layers, there are five modules, and convolutional and average pooling layers complete the process.

In a model's learning phase, *DenseNet* [25] can also accommodate hundreds or even thousands of layers. However, it differs from ResNet in that it uses concatenation rather than addition. Each layer in a dense block is linked to all of the blocks before it.

A key component of *MobineNet* [26] is a structure known as depth-wise separable convolutions. Linear bottlenecks between the layers and skip connections between the bottlenecks are two characteristics of this approach.

## 3. Experimental Results, Analysis, and Comparison

This section presents the experimental setups and results analysis for identifying DFU disease using the convolutional neural-network-based architectures. Using the pre-learnt knowledge on ImageNet dataset, we retrain and assess the CNN networks on various patterns of ischemia and infection using a transfer-learning approach in order to obtain the best parameter values for our system.

### 3.1. Results and Analysis

For the experimental analysis and performance of our proposed systems for ischemia and infection classification, we split the data into training, test, and validation sets with a 80:10:10 split. Prior to training, we configure the learning parameters to maximize accuracy while preserving learning stability. We decided to use a momentum of around 0.8. A learning rate of 0.001 was initially specified. With a batch size of 32, we used 30 epochs to train each model.

The evaluation measures employed in this study are sensitivity, specificity, precision, F-measure, accuracy, area under the curve, and Mathew correlation coefficient, to assess the model's effectiveness. Precision or positive predictive value (PPV) is derived as in Equation (1);

$$P = \frac{TP}{TP + FP} \quad (1)$$

where,  $P$  denotes precision,  $FP$  denotes false positive, and  $FN$  denotes false negative.

The ratio of accurately predicted positive observations to all observations in the actual class is known as recall and is also known as the true positive rate or sensitivity. The formula for recall is shown in Equation (2);

$$R = \frac{TP}{TP + FN} \quad (2)$$

The F1 score (Equation (3)), which weighs the average of the recall and precision, accounts for both false positives and false negatives. This is necessary to strike a balance between recall and precision.

$$F1 = \frac{2PR}{P + R} \quad (3)$$

The percentage of actual TNs that the model properly predicted can be calculated as specificity and sensitivity, respectively, and can be written as shown in Equations (4) and (5).

$$Specificity = \frac{TN}{TN + FP} \quad (4)$$

$$Sensitivity = \frac{TP}{TP + FN} \quad (5)$$

AUC is defined as area under ROC. Machine learning measures the effectiveness of binary classifications using the matthews correlation coefficient (MCC), sometimes known as the phi coefficient. The formula used to compute MCC is shown in Equation (6).

$$MMC = \frac{(TP * TN - FP * FN)}{\sqrt{(TP + FP)(TP + FN)(TN + FP)(TN + FN)}} \quad (6)$$

Table 1 shows the test results of nine architectures of seven models, i.e., AlexNet, VGG16/19, GoogLeNet, ResNet50/101, MobileNet, SqueezeNet, and DenseNet.

It can be seen from Table 1 that ResNet50 outperforms AlexNet, VGG16/19, GoogLeNet, ResNet101, MobileNet, SqueezeNet, and DenseNet models and achieved 99.49% accuracy, 99.59% sensitivity, 99.39% specificity, 99.39% precision, 99.49% F-Score, 99.96% AUC, and 98.99% MCC. Similarly, in case of infection, ResNet50 outperforms other models and produces 84.76% accuracy, 89.80% sensitivity, 85.71% specificity, 83.27% precision, 85.00% F-Score, 94.16 AUC, and 75.57% MCC, respectively.

**Table 1.** Performance comparison of pre-trained AlexNet, VGG16/19, GoogleNet, ResNet 50/101, MobileNet, SqueezeNet, and DenseNet on test set of DFU2020 Part-B dataset.

Model	Accuracy	Sensitivity	Specificity	Precision	F-Score	AUC	MCC
DFU Ischaemia							
AlexNet	83.56	84.41	82.71	83.00	83.70	91.42	67.14
VGG16	98.58	98.07	99.09	99.08	98.57	99.87	97.17
VGG19	98.48	98.28	98.68	98.68	98.48	99.87	96.96
GoogleNet	99.65	99.80	99.49	99.49	99.65	99.59	99.29
<b>ResNet50</b>	<b>99.49</b>	99.59	99.39	99.39	<b>99.49</b>	99.96	98.99
ResNet101	99.39	99.39	99.80	99.80	99.39	99.59	99.19
MobileNet	99.08	99.70	99.90	99.90	99.40	99.91	99.59
SqueezeNet	99.04	99.09	99.90	99.90	99.44	99.92	99.09
DenseNet	99.30	99.49	99.80	99.80	99.34	99.93	99.29
DFU Infection							
AlexNet	83.22	91.19	75.25	78.65	84.46	90.43	67.30
VGG16	79.32	76.61	82.03	81.00	78.75	86.87	58.73
VGG19	80.17	76.61	83.73	82.48	79.44	87.05	60.49
GoogleNet	79.66	92.54	66.78	73.58	81.98	91.09	61.39
<b>ResNet50</b>	<b>84.76</b>	89.80	85.71	83.27	<b>85.00</b>	<b>94.16</b>	<b>75.57</b>
ResNet101	84.12	92.20	82.03	83.69	84.74	93.05	74.62
MobileNet	82.48	85.07	77.89	79.75	83.25	90.30	65.24
SqueezeNet	82.88	72.20	93.56	91.81	80.83	93.34	67.32
DenseNet	83.20	89.80	80.61	81.24	83.85	92.13	70.71

The biggest obstacles in the field of DFU detection are asymmetrical forms of skin lesions, diverse types of colors for skin, and locating the area of interest on each dermoscopy image. To define minute changes in skin, you must be an expert in this field. However, these minor variations may be overlooked during a human-eye test. Deep learning approaches can assist doctors in this respect, potentially saving countless lives [27]. With the goal of saving lives, we attempted to classify ischaemia and infection and identify malignant instances. Detecting DFU is a difficult task, and providing the data to the model also involves some pre-processing.

It is evident from the results that performance is promising on DFU ischaemia as compared to DFU infection using ResNet50. As DFU infection contains much fewer samples than DFU ischaemia, we can deduce that a larger data set may allow deep learning models to perform better as the classifier could be trained on more representative class distributions. The small number of data that are currently available to the scientific community is a significant obstacle to DFU detection studies.

Dermatologists may take photos of skin lesions, but they are only allowed to be used inside the clinic, maybe due to privacy or commercial considerations. Much larger data sets must be gathered for training and testing these decision-support systems to achieve strong models and statistical validity.

### 3.2. Comparison

In the past, a variety of conventional approaches for the identification and classification of various diseases, including DFU, were used, but the results were not promising. With the advent of deep learning, various researchers implemented deep learning methods for identification, recognition, detection, and semantic segmentation in different fields. Deep learning proved its significance over machine learning techniques. For classifying DFU, numerous strategies have been put forwarded by various researchers. We contrast our suggested research with recently published articles in this area. The results are compared on the basis of accuracy, AUC, and MCC.

Ischaemia AlexNet achieved 83.56% accuracy, 91.42% AUC, and 67.14% MCC. VGG16 achieved 98.58% accuracy, 99.87% AUC, and 97.17% MCC. VGG19 achieved 98.48% ac-

curacy, 99.87% AUC, and 96.96% MCC. GoogLeNet achieved 99.65% accuracy, 99.59% AUC, and 99.29% MCC. ResNet50 achieved 99.49% accuracy, 99.96% AUC, and 98.99% MCC. ResNet101 achieved 99.39% accuracy, 99.59% AUC, and 99.19% MCC. MobileNet achieved 99.09% accuracy, 99.91% AUC, and 99.59% MCC. SqueezeNet achieved 99.04% accuracy, 99.92% AUC, and 99.09% MCC. DenseNet achieved 99.30% accuracy, 99.93% AUC, and 99.29% MCC. We can deduce that ResNet50 outperforms all models in the case of ischaemia.

Similarly, Infection AlexNet achieved 83.22% accuracy, 90.43% AUC, and 67.30% MCC. VGG16 achieved 79.32% accuracy, 86.87% AUC, and 58.73.17% MCC. VGG19 achieved 80.17% accuracy, 87.05% AUC, and 60.49% MCC. GoogLeNet achieved 79.66% accuracy, 91.09% AUC, and 61.39% MCC. ResNet50 achieved 84.76% accuracy, 94.16% AUC, and 75.57% MCC. ResNet101 achieved 84.12% accuracy, 93.05% AUC, and 74.62% MCC. MobileNet achieved 82.48% accuracy, 90.30% AUC, and 65.24% MCC. SqueezeNet achieved 82.88% accuracy, 93.34% AUC, and 67.32% MCC. DenseNet achieved 83.20% accuracy, 92.13% AUC, and 70.71% MCC. Ischaemia ResNet50 outperformed all models in cases of infection as well.

After comparing the performance of all of the pre-trained fine-tuned models, we compared the performance of ResNet50 with [9,28]. From Table 2, it can be seen that [28] achieved 90.3% accuracy for ischaemia, 90.2% F1-Score, 80.7% MCC, and 90.4% AUC, and [28] achieved 99% accuracy, 99% F1-Score, and 99.5% AUC. ResNet50 achieved 99.49% accuracy, 99.49% F1-Score, 99.80% MCC, and 99.5% AUC, which shows that the proposed strategy performed better than other techniques. Similarly, for infection cases, [28] achieved 72.7% accuracy, 72.2% F1-Score, 45.4% MCC, and 73.1% AUC, while [28] achieved 74.4% accuracy, 74.4% F1-Score, and 82.0% AUC. Our ResNet50 outperformed both the studies with 99.49% accuracy, 99.49% F1-Score, 99.80 MCC, and 99.5% AUC.

**Table 2.** Comparative analysis of the proposed system with other systems for DFU identification.

Study	Model	Class	Evaluation Metrics (%)			
			Accuracy	F1-Score	MCC	AUC
Goyal et al. [9]	Ensemble of CNNs	ischaemia	90.3	90.2	80.7	90.4
		Infection	72.7	72.2	45.4	73.1
Al-Garaawi et al. [28]	CNNs	ischaemia	99	99	—	99.5
		Infection	74.4	74.4	—	82.0
Proposed Systems	ResNet50	ischaemia	99.49	99.49	99.80	99.99
		infection	84.76	85.00	94.16	75.57

#### 4. Conclusions and Future Work

DFU is becoming more common and is affecting an increasing number of people every day. If detected in its early stages, it can be properly treated. Early detection and treatment will result in a higher survival rate and, ultimately, a lower mortality rate. However, existing clinical approaches for the diagnosis of skin malignancy are sensitive to human error due to subjectivity and inexperienced clinicians. As a result, there is a need for more dependable and precise solutions that may benefit both experienced and inexperienced physicians. The goal of our deep learning approaches was to detect DFU. The effectiveness of pre-trained fine-tuned models such as AlexNet, VGG16/19, GoogLeNet, ResNet 50/101, MobileNetv2, SqueezeNet, and Densenet201 has been examined. ResNet outperformed all of the other models, scoring 99.49 for the DFU ischemia dataset and 84.76 for the DFU infection dataset. However, only 84% of DFU infections were detected, but we believe the true percentage may be higher. We may attempt to increase the classification rates of infection in the future.

**Author Contributions:** Conceptualization, S.N.; methodology, S.N., M.A. and H.E.; software, M.A. and H.E.; validation, M.A., H.E. and S.N.; formal analysis, S.N. and A.S.; investigation, S.N. and R.A.; resources, S.N. and A.S.; data curation, S.N., A.S. and R.A.; writing—original draft preparation, M.A. and S.N.; writing—review and editing, S.N. and R.A.; visualization, A.S., M.A. and H.E.; supervision, S.N.; and project administration, S.N. All authors have read and agreed to the published version of the manuscript.

**Funding:** This research received no external funding.

**Institutional Review Board Statement:** The study is approved by research committee of Government Girls Postgraduate College No.1, Abbottabad, Khyber Pakhtunkhwa, Pakistan.

**Informed Consent Statement:** Informed consent was obtained from all subjects involved in the study.

**Data Availability Statement:** <https://www.touchendocrinology.com/diabetes/journal-articles/the-dfuc-2020-dataset-analysis-towards-diabetic-foot-ulcer-detection/> (accessed on 13 June 2020).

**Conflicts of Interest:** The authors declare no conflict of interest.

## Abbreviations

The following abbreviations are used in this manuscript:

ML	Machine
DFU	Diabetic Foot Ulcer
CNN	Convolutional Neural Network
MRI	Magnetic resonance imaging
CT	Computed Tomography

## References

1. Crocker, R.M.; Palmer, K.N.; Marrero, D.G.; Tan, T.W. Patient perspectives on the physical, psycho-social, and financial impacts of diabetic foot ulceration and amputation. *J. Diabetes Its Complicat.* **2021**, *35*, 107960. [[CrossRef](#)] [[PubMed](#)]
2. Navarro-Flores, E.; Cauli, O. Quality of life in individuals with diabetic foot syndrome. *Endocr. Metab. Immune-Disord.-Drug Targets (Former. Curr. Drug-Targets-Immune Endocr. Metab. Disord.)* **2020**, *20*, 1365–1372. [[CrossRef](#)] [[PubMed](#)]
3. Bus, S.; Van Netten, S.; Lavery, L.; Monteiro-Soares, M.; Rasmussen, A.; Jubiz, Y.; Price, P. IWGDF guidance on the prevention of foot ulcers in at-risk patients with diabetes. *Diabetes/Metab. Res. Rev.* **2016**, *32*, 16–24. [[CrossRef](#)] [[PubMed](#)]
4. Saeedi, P.; Petersohn, I.; Salpea, P.; Malanda, B.; Karuranga, S.; Unwin, N.; Colagiuri, S.; Guariguata, L.; Motala, A.A.; Ogurtsova, K.; et al. Global and regional diabetes prevalence estimates for 2019 and projections for 2030 and 2045: Results from the International Diabetes Federation Diabetes Atlas. *Diabetes Res. Clin. Pract.* **2019**, *157*, 107843. [[CrossRef](#)] [[PubMed](#)]
5. Iraj, B.; Khorvash, F.; Ebneshahidi, A.; Askari, G. Prevention of diabetic foot ulcer. *Int. J. Prev. Med.* **2013**, *4*, 373.
6. Cavanagh, P.; Attinger, C.; Abbas, Z.; Bal, A.; Rojas, N.; Xu, Z.R. Cost of treating diabetic foot ulcers in five different countries. *Diabetes/Metab. Res. Rev.* **2012**, *28*, 107–111. [[CrossRef](#)]
7. Reyzelman, A.M.; Koelewijn, K.; Murphy, M.; Shen, X.; Yu, E.; Pillai, R.; Fu, J.; Scholten, H.J.; Ma, R. Continuous temperature-monitoring socks for home use in patients with diabetes: Observational study. *J. Med. Internet Res.* **2018**, *20*, e12460. [[CrossRef](#)]
8. Sumpio, B.E. Foot ulcers. *N. Engl. J. Med.* **2000**, *343*, 787–793. [[CrossRef](#)]
9. Goyal, M.; Reeves, N.D.; Rajbhandari, S.; Ahmad, N.; Wang, C.; Yap, M.H. Recognition of ischaemia and infection in diabetic foot ulcers: Dataset and techniques. *Comput. Biol. Med.* **2020**, *117*, 103616. [[CrossRef](#)]
10. Yap, M.H.; Hachiuma, R.; Alavi, A.; Brüngel, R.; Cassidy, B.; Goyal, M.; Zhu, H.; Rückert, J.; Olshansky, M.; Huang, X.; et al. Deep learning in diabetic foot ulcers detection: A comprehensive evaluation. *Comput. Biol. Med.* **2021**, *135*, 104596. [[CrossRef](#)]
11. Alzubaidi, L.; Fadhel, M.A.; Olewi, S.R.; Al-Shamma, O.; Zhang, J. DFU\_QUTNet: Diabetic foot ulcer classification using novel deep convolutional neural network. *Multimed. Tools Appl.* **2020**, *79*, 15655–15677. [[CrossRef](#)]
12. Santos, E.; Santos, F.; Dallyson, J.; Aires, K.; Tavares, J.M.R.; Veras, R. Diabetic Foot Ulcers Classification using a fine-tuned CNNs Ensemble. In Proceedings of the 2022 IEEE 35th International Symposium on Computer-Based Medical Systems (CBMS), Shenzhen, China, 21–23 July 2022; pp. 282–287.
13. Xie, P.; Li, Y.; Deng, B.; Du, C.; Rui, S.; Deng, W.; Wang, M.; Boey, J.; Armstrong, D.G.; Ma, Y.; et al. An explainable machine learning model for predicting in-hospital amputation rate of patients with diabetic foot ulcer. *Int. Wound J.* **2022**, *19*, 910–918. [[CrossRef](#)]
14. Khandakar, A.; Chowdhury, M.E.; Reaz, M.B.I.; Ali, S.H.M.; Hasan, M.A.; Kiranyaz, S.; Rahman, T.; Alfkey, R.; Bakar, A.A.A.; Malik, R.A. A machine learning model for early detection of diabetic foot using thermogram images. *Comput. Biol. Med.* **2021**, *137*, 104838. [[CrossRef](#)]
15. Goyal, M.; Reeves, N.D.; Davison, A.K.; Rajbhandari, S.; Spragg, J.; Yap, M.H. Dfunet: Convolutional neural networks for diabetic foot ulcer classification. *IEEE Trans. Emerg. Top. Comput. Intell.* **2018**, *4*, 728–739. [[CrossRef](#)]

16. Ayaz, Z.; Naz, S.; Khan, N.H.; Razzak, I.; Imran, M. Automated methods for diagnosis of Parkinson's disease and predicting severity level. *Neural Comput. Appl.* **2022**, *1*–36. [[CrossRef](#)]
17. Naseer, A.; Rani, M.; Naz, S.; Razzak, M.I.; Imran, M.; Xu, G. Refining Parkinson's neurological disorder identification through deep transfer learning. *Neural Comput. Appl.* **2020**, *32*, 839–854. [[CrossRef](#)]
18. Ashraf, A.; Naz, S.; Shirazi, S.H.; Razzak, I.; Parsad, M. Deep transfer learning for alzheimer neurological disorder detection. *Multimed. Tools Appl.* **2021**, *80*, 30117–30142. [[CrossRef](#)]
19. Naz, S.; Ashraf, A.; Zaib, A. Transfer learning using freeze features for Alzheimer neurological disorder detection using ADNI dataset. *Multimed. Syst.* **2022**, *28*, 85–94. [[CrossRef](#)]
20. Kamran, I.; Naz, S.; Razzak, I.; Imran, M. Handwritten Dynamics Assessment for Early Identification of Parkinson's Patient. *Future Genration* **2020**, *117*, 234–244.
21. Krizhevsky, A.; Sutskever, I.; Hinton, G.E. Imagenet classification with deep convolutional neural networks. *Commun. ACM* **2017**, *60*, 84–90. [[CrossRef](#)]
22. Simonyan, K.; Zisserman, A. Very deep convolutional networks for large-scale image recognition. *arXiv* **2014**, arXiv:1409.1556.
23. Szegedy, C.; Liu, W.; Jia, Y.; Sermanet, P.; Reed, S.; Anguelov, D.; Erhan, D.; Vanhoucke, V.; Rabinovich, A. Going deeper with convolutions. In Proceedings of the IEEE Conference on Computer Vision and Pattern Recognition, Boston, MA, USA, 7–12 July 2015; pp. 1–9.
24. Iandola, F.N.; Han, S.; Moskewicz, M.W.; Ashraf, K.; Dally, W.J.; Keutzer, K. SqueezeNet: AlexNet-level accuracy with 50x fewer parameters and <0.5 MB model size. *arXiv* **2016**, arXiv:1602.07360.
25. Huang, G.; Liu, Z.; Van Der Maaten, L.; Weinberger, K.Q. Densely connected convolutional networks. In Proceedings of the IEEE Conference on Computer Vision and Pattern Recognition, Honolulu, HI, USA, 21–26 July 2017; pp. 4700–4708.
26. Sandler, M.; Howard, A.; Zhu, M.; Zhmoginov, A.; Chen, L.C. Mobilenetv2: Inverted residuals and linear bottlenecks. In Proceedings of the IEEE Conference on Computer Vision and Pattern Recognition, 18–23 June 2018, Salt Lake City, UT, USA; pp. 4510–4520.
27. Pham, T.C.; Luong, C.M.; Hoang, V.D.; Doucet, A. AI outperformed every dermatologist in dermoscopic melanoma diagnosis, using an optimized deep-CNN architecture with custom mini-batch logic and loss function. *Sci. Rep.* **2021**, *11*, 17485. [[CrossRef](#)] [[PubMed](#)]
28. Al-Garaawi, N.; Ebsim, R.; Alharan, A.F.; Yap, M.H. Diabetic foot ulcer classification using mapped binary patterns and convolutional neural networks. *Comput. Biol. Med.* **2022**, *140*, 105055. [[CrossRef](#)] [[PubMed](#)]

**Disclaimer/Publisher's Note:** The statements, opinions and data contained in all publications are solely those of the individual author(s) and contributor(s) and not of MDPI and/or the editor(s). MDPI and/or the editor(s) disclaim responsibility for any injury to people or property resulting from any ideas, methods, instructions or products referred to in the content.

# A Machine Learning Model for Early Detection of Diabetic Foot using Thermogram Images

**Amith Khandakar<sup>1,2</sup> Muhammad E. H. Chowdhury<sup>1\*</sup>, Mamun Bin Ibne Reaz<sup>2\*</sup>, Sawal Hamid Md Ali<sup>2</sup>, Md Anwarul Hasan<sup>3</sup>, Serkan Kiranyaz<sup>1</sup>, Tawsifur Rahman<sup>1</sup>, Rashad Alfkey<sup>4</sup>, Ahmad Ashrif A. Bakar<sup>2</sup>, Rayaz A. Malik<sup>5</sup>**

<sup>1</sup>Department of Electrical Engineering, Qatar University, Doha-2713, Qatar

<sup>2</sup>Dept. of Electrical, Electronics and Systems Engineering, Universiti Kebangsaan Malaysia, Bangi, Selangor 43600, Malaysia

<sup>3</sup>Department of Industrial and Mechanical Engineering, Qatar University, Doha-2713, Qatar

<sup>4</sup>Acute Care Surgery and General Surgery, Hamad Medical Corporation, Qatar

<sup>5</sup>Weill Cornell Medicine-Qatar, Ar-Rayyan, Qatar

\*Correspondence: Muhammad E.H. Chowdhury ([mchowdhury@qu.edu.qa](mailto:mchowdhury@qu.edu.qa)); Mamun Bin Ibne Reaz ([mamun@ukm.edu.my](mailto:mamun@ukm.edu.my))

## Abstract

Diabetes foot ulceration (DFU) and amputation are a cause of significant morbidity. The prevention of DFU may be achieved by the identification of patients at risk of DFU and the institution of preventative measures through education and offloading. Several studies have reported that thermogram images may help to detect an increase in plantar temperature prior to DFU. However, the distribution of plantar temperature may be heterogeneous, making it difficult to quantify and utilize to predict outcomes. We have compared a machine learning-based scoring technique with feature selection and optimization techniques and learning classifiers to several state-of-the-art Convolutional Neural Networks (CNNs) on foot thermogram images and propose a robust solution to identify the diabetic foot. A comparatively shallow CNN model, MobilenetV2 achieved an F1 score of ~95% for a two-feet thermogram image-based classification and the AdaBoost Classifier used 10 features and achieved an F1 score of 97 %. A comparison of the inference time for the best-performing networks confirmed that the proposed algorithm can be deployed as a smartphone application to allow the user to monitor the progression of the DFU in a home setting.

**INDEX TERMS** Thermogram, Diabetes Mellitus, Diabetic Foot, Convolutional Neural Network, Machine learning algorithms, Image enhancement techniques, Diagnostic utility

## **1. Introduction**

Diabetes Mellitus (DM) leads to major complications such as heart disease, stroke, renal failure, blindness, and diabetic foot ulceration (DFU) with lower limb amputation [1]. Healing of DFU can be difficult or delayed [2] with an increased risk of infection and amputation [3]. DFU recurs in approximately 40% of patients after the first year and in 60% after three years [4, 5] and leads to amputation in over 1 million diabetic patients annually in the USA [6]. In Europe, 250,000 diabetic patients undergo lower limb amputation with an associated mortality of 30% at one month and 50% at 1 year [7]. Diabetic foot ulceration is associated with markedly increased healthcare costs, decreased quality of life, infection, amputation, and death. The detection of patients at risk of DFU may enable timely intervention to prevent foot ulceration, amputation, and death.

Self-care via monitoring without medical assistance, for early signs of DFU, may allow timely offloading to prevent skin breakdown and development of a wound. Visual inspection has its limitations as people with obesity or visual impairment cannot see their site of ulceration. However, recent studies utilizing temperature monitoring have shown that they can predict the development of DFU in 97% of patients [4, 8-10]. Indeed, patients undergoing continuous foot temperature monitoring had a lower risk of DFU [11]. Skin temperature monitoring emerged during the 1970s, with “asymmetry analysis” proving to be very effective in identifying ulcers at an early stage [12]. A temperature difference of  $2.22^{\circ}\text{C}$  ( $4^{\circ}\text{F}$ ) over at least two consecutive days could be used as a threshold for therapy to prevent DFU [8]. The system correctly identified the development of DFU in 97% of participants, with an average lead time of 37 days [13].

Thermography is a rapid non-invasive imaging technique to quantify thermal changes in the diabetic foot [13]. Several studies have proposed thermogram-based techniques for identifying those at risk of DFU [2, 3, 14] by identifying a characteristic thermal distribution in the infrared image. The control group had a specific butterfly pattern [15] compared to a large variety of spatial patterns in the patients with diabetes [16, 17]. Whilst it is possible to assess thermal changes in one foot compared to the contralateral foot [18-21] if both feet have thermal changes without a butterfly pattern, then one foot cannot act as a reference. Asymmetry cannot be measured despite a large temperature difference and identical spatial distributions in both feet. An alternative approach is to calculate the temperature change with respect to the butterfly pattern of a control group [22-24].

Machine learning (ML) techniques have been widely used for automatic image classification using feature extraction, feature ranking, and using different ML models, such as Artificial Neural Networks (ANN), k-nearest neighbors (KNN), and Support Vector Machines (SVM) [25-27]. The change of focus

from traditional paradigms in machine learning to Deep Learning (DL) is the product of the high accuracy achieved through its large learning structures, enabling DL to obtain deeper data traits. The need for large data size and high computational complexity can be addressed using transfer learning on pre-trained networks. Whilst it is reasonably straightforward to distinguish the foot thermogram of a control subject with a specific spatial pattern, the distribution in a diabetic foot without a specific spatial pattern is more challenging, especially as the spatial distribution may change and the detection of a temperature rise in the plantar region is important for diabetic patients.

Several studies [22, 23, 28-35] have attempted to extract features to identify the hot region in the plantar thermogram, to identify tissue damage or inflammation. Etehadtavakol et al. [35] proposed a method called lazy snapping to extract the extreme temperature areas in the thermogram images which can easily differentiate the coarse and fine-scale change. A thresholding method was used to identify the highest temperature areas from the plantar region [22], while Gururaj Rao et al. [34] used an active contour model of plantar segmentation and a thresholding method to extract the highest temperature points. Adam et al. [33] used Discrete Wavelet Transformation (DWT) and higher-order spectra (HOS) to derive several coefficients from the characteristics of texture and entropy. A double density-dual tree-complex wavelet transform (DD-DT-CWT) was used to decompose the image and extract several key features [32]. Saminathan et al. [31] segmented the plantar area into 11 regions using region-raising and extracted texture characteristics to classify it into a normal or ulcer group. Most of these works were reported on a small private dataset and utilized post-processing techniques, which might not be able to generalize on a different dataset and the real-time applicability and inference time were not reported. Moreover, the performance of these methods were not comparable to the machine learning based techniques.

Very few studies have applied the deep learning (DL) technique to classify thermogram images from controls and diabetic patients. Maldonado et al. [30] utilized the DL technique to segment the thermogram of the plantar area to classify ulceration or necrosis. Hernandez et al. [23] proposed a quantitative thermal change index (TCI) to measure the thermal change in the plantar region of diabetic patients to classify patients from controls. Hernandez et al. [23, 29] utilized the “Plantar Thermogram Database” of 334-foot thermogram images and used TCI to classify subjects into Class 1 to 5 based on the spatial temperature distribution and temperature range. Cruz-Vega et al. [28] also proposed a DL technique to classify the images of the ‘Plantar Thermogram Database’ into two classes at a time, but the technique is questionable as it cannot be used for clinical decision making and the applicability of such a solution for a smartphone application is not discussed.

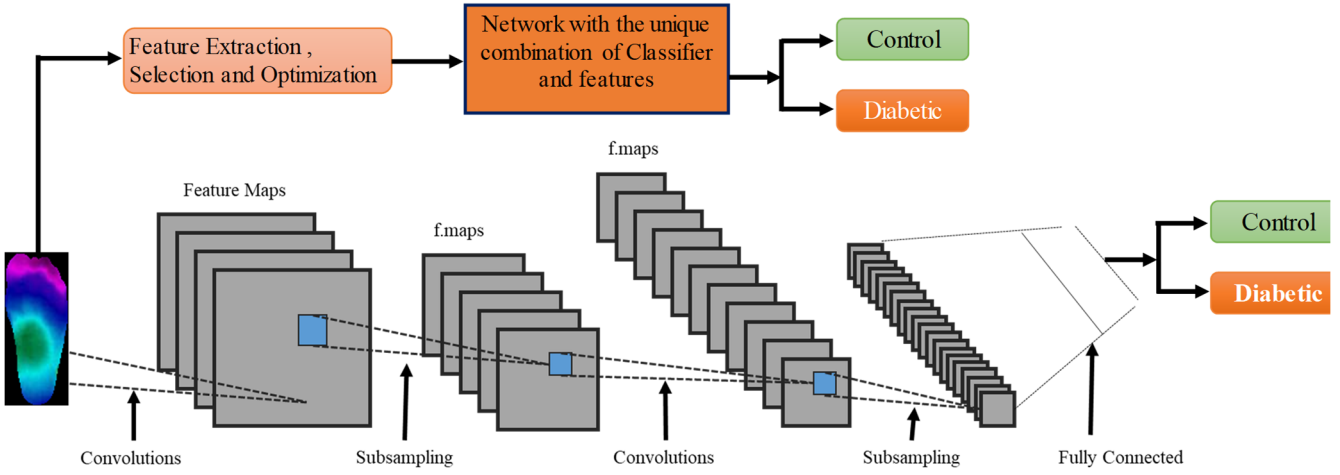


**Figure 1.** Proposed classification pipeline using one-dimensional (1D) machine learning classifiers and 2-dimensional (2D) thermogram image.

We have utilized an available dataset to classify control and diabetic groups and developed a novel technique to automatically classify the thermogram images and compared the outcome to a 2D deep learning technique. Moreover, the light architecture and machine learning model are deployable in smartphones.

The major contributions of this paper are:

- Comparative evaluation over the state-of-the-art 2D CNN models and image enhancement techniques for the detection of diabetic foot with high accuracy.
- A detailed investigation of the relevant features to improve the detection performance when used as input to traditional classifiers.
- An investigation of feature selection and optimization techniques and classification models to maximize detection performance utilizing light classifiers.

Section II discusses the methodology, section III presents the results and discussion and section IV presents the conclusions and proposes topics for future research.

## 2. Methodology

Figure 1 shows the complete system block diagram. The thermogram is used as an input to extract important features, feature optimization, and ranking by different ranking techniques. The best combination of the top-ranked features was used as input to the classifier to stratify the thermogram images into diabetic and control groups. The performance of the proposed technique was compared with a 2D CNN-based image classification model for comparative evaluation. Various image enhancement techniques were utilized to enhance the 2D thermogram images and improve the performance of 2D CNN [36].

## DATASET DESCRIPTION

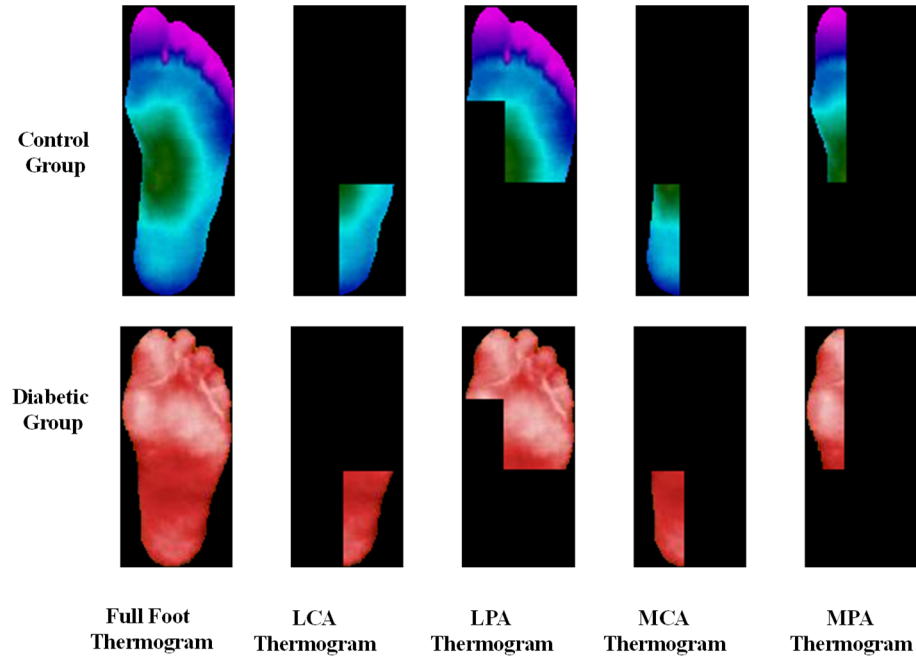


**Figure 2:** Sample of MPA, LPA, MCA, and LCA angiosomes for control and diabetic foot thermogram.

A database of age, gender, height, and weight and 167-foot pair thermograms from 122 participants with diabetes mellitus and 45 controls was made public by Hernandez-Contreras et al. [29]. Continuous variables were reported with the number of missing data, median, mean, and quartiles (Q1, Q3) for diabetic and control groups (Table I). The chi-square test was conducted for gender while the rank-sum test was conducted on other features. A p-value  $<0.05$  was used as the cut-off for statistical significance. The foot thermogram images were segmented to remove the background and were also segmented into four angiosomes for the medial plantar artery (MPA), lateral plantar artery (LPA), medial calcaneal artery (MCA), and lateral calcaneal artery (LCA) [37] (Figure 2). The angiosome related information is not only useful to identify the arteries associated with ulceration risk but also shows the local temperature of each angiosome. Pixelated temperature readings for the full foot and the four angiosomes for both feet were available in the dataset, to encounter the problem in two dimensions: pixelated temperature and the 2D thermogram image.

### 2.1 Feature extraction from temperature map

Different features have been extracted by different research groups from foot thermograms over the last decade. Cajacuri et al. [38] highlighted the importance of age, gender and body mass index. Contreras et al. [29] developed the thermal change index (TCI), the mean temperature difference between the corresponding angiosomes from a diabetic patient and a control group as shown in Equation (1).

$$TCI = \frac{CG_{ang} - DG_{ang}}{4} \quad (1)$$

where  $CG_{ang}$  and  $DG_{ang}$  are the temperature values of the angiosome for the control and diabetic groups, respectively. Barreto et al. [39] proposed features, such as Estimate temperature (ET), estimated temperature difference (ETD), and hot spot estimator (HSE) for analyzing thermograms, as shown in Equation (2)-(4).

$$ET = \frac{a_{j-1}C_{j-1} + a_jC_j + a_{j+1}C_{j+1}}{a_{j-1} + a_j + a_{j+1}} \quad (2)$$

$$ETD = | ET_{left\ Angiosome} - ET_{right\ angiosome} | \quad (3)$$

$$HSE = | C_l - ET | \quad (4)$$

To calculate these features, the temperature map in the thermogram image is categorized into temperature classes:  $C_0$  to  $C_7$ . A histogram is generated for the percentage of pixels in the thermogram image, which lies in different temperature classes, where  $C_0=26.5^{\circ}\text{C}$ ,  $C_1=28.5^{\circ}\text{C}$ ,  $C_2=29.5^{\circ}\text{C}$ ,  $C_3=30.5^{\circ}\text{C}$ ,  $C_4=31^{\circ}\text{C}$ ,  $C_5=32.5^{\circ}\text{C}$ ,  $C_6=33.5^{\circ}\text{C}$ , and  $C_7=34.5^{\circ}\text{C}$ . The highest frequency of a temperature class is denoted by  $C_j$  and the percentage of pixels in that region is  $a_j$ . The values  $a_{j-1}$  and  $a_{j+1}$  are the percentages of pixels in the neighboring temperature classes  $C_{j-1}$  and  $C_{j+1}$ , respectively. The  $a_j$  and  $C_j$  values are used to calculate the ET of the thermogram for each angiosome which is used to calculate the ETD values. Finally, the HSE is calculated using ET and  $C_l$  values, where  $C_l$  is the highest temperature present in the angiosome regardless of its percentage in the histogram. HSE can identify severe DFU. Saminathan et al. [31] have stressed the importance of standard statistical parameters such as mean, standard deviation, and median used in various biomedical applications [40-42].

In addition to the above-mentioned features, features which are visually important to distinguish the variation in the plantar temperature distribution were formulated. Five distinct temperature ranges were found in the dataset and verified with the TCI parameters [29].

TABLE I. STATISTICAL ANALYSIS OF 1D FEATURES FOR BINARY CLASSIFICATION.

	Item	Control	Diabetic	Total	Method	Statistic	P value
1	Gender				Chi-square test	39.3886	P <.0001
	• Male (%)	58(64%)	66(28%)	124(37%)			
	• Female (%)	32(36%)	178(72%)	210(63%)			
2	Age (Years)				Rank-sum test	12.6108	P <.0001
	• N (missing)	90(0)	244(0)	334(0)			
	• Mean $\pm$ SD	28 $\pm$ 8	55.98 $\pm$ 10.6	48.4 $\pm$ 16			
	• Median	25	55	52			
	• Q1, Q3	23,30	50,63	34, 60			
	• Min, Max	21,52	23,84	21,84			
3	Full-Foot Temperature ( $^{\circ}\text{C}$ )	90(0)	244(0)	334(0)	Rank-sum test	7.6913	P <.0001
	• N (missing)	26.7 $\pm$ 1.6	29.7 $\pm$ 2.9	28.9 $\pm$ 2.9			

	<ul style="list-style-type: none"> <li>• Mean <math>\pm</math> SD</li> <li>• Median</li> <li>• Q1, Q3</li> <li>• Min, Max</li> </ul>	26.8 25.9, 27.7 22, 29.6	30 27.9, 32 20.4, 35.6	28.8 26.6, 31.2 20.4, 35.6				
4	LCA Temperature ( $^{\circ}$ C)	<ul style="list-style-type: none"> <li>• N (missing)</li> <li>• Mean <math>\pm</math> SD</li> <li>• Median</li> <li>• Q1, Q3</li> <li>• Min, Max</li> </ul>	90(0) 26.6 $\pm$ 1.5 26.5 25.9, 27.6 22.8, 30.1	244(0) 29.3 $\pm$ 2.7 29.4 27.4, 31.2 20.9, 35.9	334(0) 28.5 $\pm$ 2.7 28.4 26.5, 30.6 20.9, 35.3	Rank-sum test	7.3563	P <.0001
5	LPA Temperature ( $^{\circ}$ C)	<ul style="list-style-type: none"> <li>• N (missing)</li> <li>• Mean <math>\pm</math> SD</li> <li>• Median</li> <li>• Q1, Q3</li> <li>• Min, Max</li> </ul>	90(0) 26.4 $\pm$ 1.8 26.3 25.4, 27.6 21.4, 30	244(0) 29.9 $\pm$ 3.2 30.3 27.6, 32.4 19.8, 35.9	334(0) 28.9 $\pm$ 3.3 28.9 26.3, 31.8 19.8, 35.9	Rank-sum test	7.8004	P <.0001
6	MCA Temperature ( $^{\circ}$ C)	<ul style="list-style-type: none"> <li>• N (missing)</li> <li>• Mean <math>\pm</math> SD</li> <li>• Median</li> <li>• Q1, Q3</li> <li>• Min, Max</li> </ul>	90(0) 27 $\pm$ 1.5 27.2 26.1, 28 23, 30.2	244(0) 29.5 $\pm$ 2.6 29.6 27.8, 31.4 21.3, 35.1	334(0) 28.8 $\pm$ 2.6 28.8 27, 30.8 21.3, 35.1	Rank-sum test	7.2299	P <.0001
7	MPA Temperature ( $^{\circ}$ C)	<ul style="list-style-type: none"> <li>• N (missing)</li> <li>• Mean <math>\pm</math> SD</li> <li>• Median</li> <li>• Q1, Q3</li> <li>• Min, Max</li> </ul>	90(0) 26.7 $\pm$ 1.9 26.7 25.7, 27.9 21.3, 30.5	244(0) 30.1 $\pm$ 3.1 30.6 28, 32.3 20.3, 36.1	334(0) 29.2 $\pm$ 3.2 29.2 26.7, 31.8 20.3, 36.1	Rank-sum test	7.8193	P <.0001
8	TCI Temperature ( $^{\circ}$ C)	<ul style="list-style-type: none"> <li>• N (missing)</li> <li>• Mean <math>\pm</math> SD</li> <li>• Median</li> <li>• Q1, Q3</li> <li>• Min, Max</li> </ul>	90(0) 14 $\pm$ 12.7 13 1.2, 26.8 0.12, 29.6	244(0) 29.7 $\pm$ 2.9 30 27.8, 31.8 20.6, 35.5	334(0) 25.5 $\pm$ 9.9 28.7 25.8, 31.1 0.12, 35.5	Rank-sum test	10.6670	P <.0001
9	Outcome (%)	90(27%)	244(73%)	334				

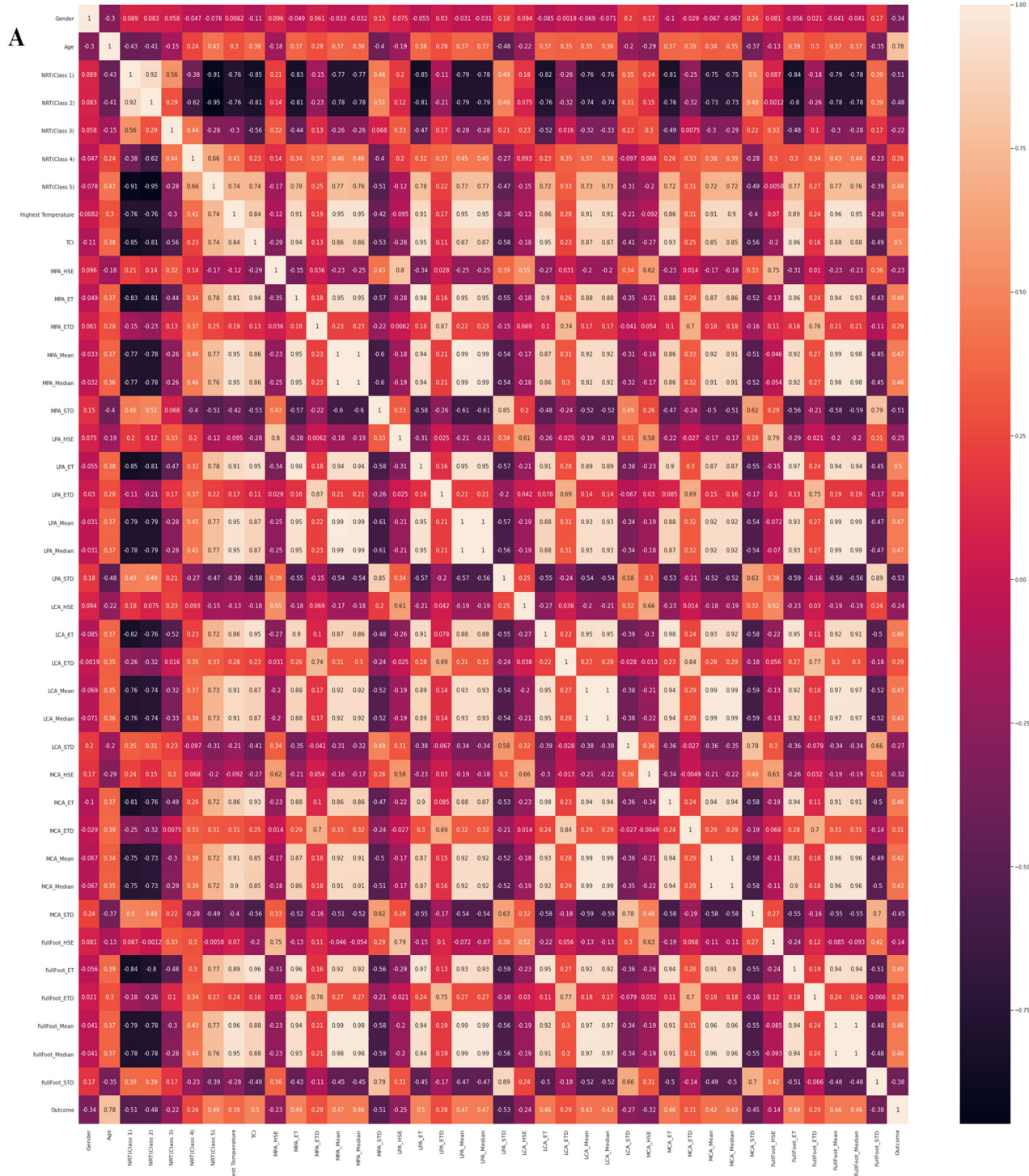
Five distinct temperature ranges were classified into normalized temperature ranges (NTR). We have computed the variable  $NRT_{class\ j}$  which is the number of pixels in  $class\ j$  temperature range over the total number of non-zero pixels, where  $class\ j$  can be class 1 to 5. For the temperature ranges in the class, we have used the same temperature range as reported in [29].

39 features were extracted for the early detection of diabetic foot, which are age, gender, TCI, highest temperature value, NTR (Class 1-5), HSE, ET, ETD, mean, median, SD of temperature for the different angiosomes: LPA, LCA, MPA, MCA, and the full foot.

The final list of features was optimized to remove redundant features by finding the correlation between the different features. Features with more than 95 % correlation were removed, which improves the overall performance by reducing the number of redundant features, avoiding overfitting [40-43].

## 2.2. Classification using thermogram features

Five-fold cross-validation was used in this study, where each fold was divided into a 80 % training and 20 % testing set. 20% of the training data was spared as the validation set. To avoid the issue of an imbalanced training dataset and biased estimates [44], Synthetic Minority Oversampling Technique (SMOTE) [45] was used for training data augmentation.





different angiosomes, Full Foot, and ET, mean of LPA and LCA.

The shortlisted parameters of the dataset, after optimization, were assessed to take decisions and identify the top features for binary classification. Three different sets of feature ranking were identified using the Multi-Tree Extreme Gradient Boost (XGBoost) [46], Random Forest [47], and Extra Tree [48] techniques. Default parameters were used for the feature ranking techniques to avoid overfitting, a common problem with a large number of features and a limited sample size [49, 50]. The best performing top-ranked features from the different feature ranking techniques are used to identify the best combination of features using a rigorous investigation to identify the best combination of features that gave the best performance.

*Classifiers:* For a detailed investigation, different classifiers such as multilayer perceptron (MLP) [51], Logistic regression [52], K-Nearest Neighbor (KNN) [53], Adaboost [54], Support Vector Machine (SVM) [55], Random Forest [56], Extra Tree [57], Gradient Boosting [58], Extreme Gradient Boost (XGBoost) [59], Linear Discriminant Analysis (LDA) [60] were used. An MLP is characterized by several layers of neurons connected between the input and the output layers. MLP uses backpropagation for training the network. Logistic regression is a variant of regression function which uses a logistic function to model a binary dependent variable. While typical linear regression uses a linear relation between predictors and output, logistic regression uses a sigmoid function to relate output with linear prediction and linear prediction works like multivariate linear regression. KNN starts by determining “k”, i.e., the number of neighbors to be compared. Once the parameter “k” is determined, the object’s distance is computed with every object available in the dataset and the k-least distances were identified. XGBoost is the streamlined group calculation dependent on GBDT (Gradient Boosting Decision Tree). The principle concept of the boosting calculation is that numerous decision trees perform superior to a single one. LDA is a multi-class classification model, which can be used for dimensionality reduction. Random Forest is an ensemble of Decision Trees that combine the qualities of filter and wrapper methods. Extra Tree is a type of ensemble learning technique which aggregates the results of multiple de-correlated decision trees collected in a “forest” to output its classification result. It is similar to a Random Forest and only differs from it in the manner of construction of the decision trees in the forest. AdaBoost classifier is a meta-estimator that begins by fitting a classifier on the original dataset and then fits additional copies of the classifier on the same dataset and adjusted focusing more on difficult cases.

In this experiment, 3 feature selection techniques with 10 machine learning models were investigated with 28 optimized features to identify the best-combined results in 840 investigations.

### 2.3. Thermogram Image Classification by 2D CNNs

The application of 2D CNNs in biomedical applications is popular for automatic and early detection of abnormalities such as COVID-19 pneumonia [61-63], Tuberculosis [64], community acquired pneumonia [65], and many others [66]. As before, five-fold cross-validation is applied, i.e. the dataset is divided into five-folds, and performance metrics were reported for cumulative folds. Overall accuracy and weighted average of Precision, Sensitivity, Specificity, and F1-Score are reported. Since the binary class dataset is not balanced and the number of images in 80% of the dataset (training set per fold) was small. The training dataset was augmented using image rotation and translation [61-65]. The details of the training, validation and testing dataset for 2D binary classification are presented in Table II.

Table II  
Details of the dataset used for training, validation, and testing.

Dataset	Class	Training Dataset Details			
		Training Data/ Fold	Augmented Training Data/ Fold	Validation Data/ Fold	Test Data/ Fold
Contreras et al. [29]	DM	190	1330	8	46
	CG	64	1664	4	22

*Transfer Learning:* Since the dataset size is small, pre-trained models, originally trained on the ImageNet database [67] were used in this study. Based on an extensive literature review and previous work [61-65], six well-known pre-trained deep learning CNNs were used in this study: ResNet18, ResNet50 [68], DenseNet201[68], InceptionV3 [69], VGG19 [70] and MobileNetV2 [71]

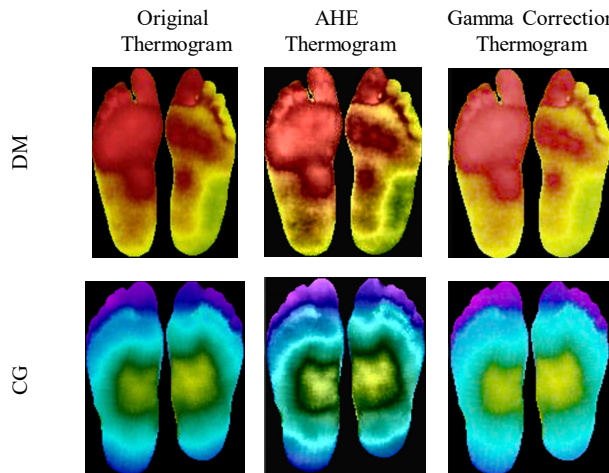


**Figure 4.** Original versus enhanced thermogram images using adaptive histogram equalization (AHE) and Gamma Correction for control and diabetic foot thermograms.

*Image Enhancement:* Image enhancement techniques such as Histogram Equalization (HE) [72], and Adaptive Histogram Equalization (AHE), and Gamma correction [73] can help 2D CNN in classification performances [36]. We have used the AHE technique (Figure 3) which performs histogram equalization over small regions (i.e., patches) in the image to enhance the contrast of each region individually. It improves local contrast and edges adaptively in each region of the image to the local distribution of pixel intensities instead of the global information of the image. Gamma correction was also applied to enhance the thermogram images. It performs a non-linear operation on the source image pixels, which alternates the pixel value to improve the image using the projection relationship between the value of the pixel and the value of the gamma according to the internal map. Sample thermogram image for DM and CG patients and the enhanced images with AHE and gamma correction are shown in Figure 4.

#### 2.4 Performance metrics

Six performance metrics: Sensitivity, Specificity, Precision, Accuracy, F1-Score, and Area under the curve (AUC) were used as evaluation metrics where TP, FP, TN and FN are True Positive, False Positive, True Negative, and False Negative, respectively.

$$Sensitivity = \frac{(TP)}{(TP + FN)} \quad (5)$$

$$Specificity = \frac{(TN)}{(TN + FP)} \quad (6)$$

$$Precision = \frac{(TP)}{(TP + FP)} \quad (7)$$

$$Accuracy = \frac{TP + TN}{(TP + FN) + (FP + TN)} \quad (8)$$

$$F1\ Score = \frac{(2 * Precision * Sensitivity)}{(Precision + Sensitivity)} \quad (9)$$

TP is the number of thermograms correctly identified as DM, FP is the number of incorrectly identified thermograms as DM, TN is the number of thermograms correctly classified as CG, and FN is the number of thermograms incorrectly identified as CG. We report the overall accuracy and weighted performance metric, with a 95 % confidence interval (CI), for Sensitivity, Specificity, Precision, and F1 Score. In addition, to compare the computational complexity of the different machine learning techniques, the

inference time was calculated for the best performing 2D CNN models and 1D classifiers. The models that can be deployed in a smartphone were also identified.

All the experiments were performed by a computer with the following configuration: CPU Intel i7–10750H @2.6 GHz, GPU NVIDIA GeForce RTX 2070 Super, RAM 32 GB. Matlab 2020a was used for initial pre-processing and scikit-learn and PyTorch were used for classical machine learning and deep learning models, respectively.

### 3. Results and Discussion

The experimental results are divided into two sections: The first section presents the foot ulcer detection results by deep CNN models with transfer learning over the pre-trained networks while exploring the effects of different image enhancement techniques on thermogram image classification. Moreover, the effect of single and dual-foot as input was investigated for binary classification. In the second section, comparative evaluations among the best-performing machine learning models on the optimized thermogram features are presented.

Table III

Performance metrics for the binary classification using a single foot thermogram using 2D CNN. The best-performing network is highlighted in bold.

Network	Class	Accuracy (%)	Precision (%)	Sensitivity (%)	F1-score (%)	Specificity (%)	Inference time (msec)
MobilenetV2	DM	$92.51 \pm 5.44$	$94.69 \pm 4.63$	$95.08 \pm 4.47$	$94.88 \pm 4.55$	$85.56 \pm 7.26$	5.252
	CG	$92.51 \pm 3.30$	$86.52 \pm 4.29$	$85.56 \pm 4.41$	$86.04 \pm 4.35$	$95.08 \pm 2.71$	
	Overall	$92.51 \pm 2.82$	$92.49 \pm 2.83$	$92.51 \pm 2.82$	$92.50 \pm 2.82$	$88.13 \pm 3.47$	
Resnet18	DM	$90.42 \pm 6.08$	$91.41 \pm 5.79$	$95.90 \pm 4.10$	$93.60 \pm 5.06$	$75.56 \pm 8.88$	2.545
	CG	$90.42 \pm 3.69$	$87.18 \pm 4.19$	$75.56 \pm 5.39$	$80.96 \pm 4.93$	$95.90 \pm 2.49$	
	Overall	$90.42 \pm 3.16$	$90.27 \pm 3.18$	$90.42 \pm 3.16$	$90.19 \pm 3.19$	$81.04 \pm 4.20$	
Resnet50	DM	$93.41 \pm 5.13$	$94.05 \pm 4.89$	$97.13 \pm 3.45$	$95.57 \pm 4.25$	$83.33 \pm 7.70$	6.164
	CG	$93.41 \pm 3.11$	$91.46 \pm 3.51$	$83.33 \pm 4.68$	$87.21 \pm 4.19$	$97.13 \pm 2.09$	
	Overall	$93.41 \pm 2.66$	$93.35 \pm 2.67$	$93.41 \pm 2.66$	$93.32 \pm 2.68$	$87.05 \pm 3.60$	
DenseNet201	DM	<b><math>94.01 \pm 4.91</math></b>	<b><math>95.91 \pm 4.11</math></b>	<b><math>95.91 \pm 4.11</math></b>	<b><math>95.91 \pm 4.11</math></b>	<b><math>88.89 \pm 6.49</math></b>	26.138
	CG	<b><math>94.01 \pm 2.98</math></b>	<b><math>88.89 \pm 3.94</math></b>	<b><math>88.89 \pm 3.94</math></b>	<b><math>88.89 \pm 3.94</math></b>	<b><math>95.91 \pm 2.49</math></b>	
	Overall	<b><math>94.01 \pm 2.54</math></b>	<b><math>94.01 \pm 2.54</math></b>	<b><math>94.01 \pm 2.54</math></b>	<b><math>94.01 \pm 2.54</math></b>	<b><math>90.78 \pm 3.11</math></b>	
InceptionV3	DM	$93.71 \pm 5.02$	$93.73 \pm 5.01$	$97.95 \pm 2.93$	$95.79 \pm 4.15$	$82.22 \pm 7.90$	15.353
	CG	$93.71 \pm 3.05$	$93.67 \pm 3.06$	$82.22 \pm 4.80$	$87.57 \pm 4.14$	$97.95 \pm 1.78$	
	Overall	$93.71 \pm 2.60$	$93.71 \pm 2.60$	$93.71 \pm 2.60$	$93.58 \pm 2.63$	$86.46 \pm 3.67$	
VGG19	DM	$92.22 \pm 5.53$	$93.60 \pm 5.06$	$95.90 \pm 4.10$	$94.74 \pm 4.61$	$82.22 \pm 7.90$	6.284
	CG	$92.22 \pm 3.36$	$88.10 \pm 4.06$	$82.22 \pm 4.80$	$85.06 \pm 4.47$	$95.90 \pm 2.49$	
	Overall	$92.22 \pm 2.87$	$92.12 \pm 2.89$	$92.21 \pm 2.87$	$92.13 \pm 2.89$	$85.91 \pm 3.73$	

#### 3.1 Detection results by deep CNN models

The detection results of six deep CNN models for classifying the thermograms into control and diabetic groups from a single foot thermogram without and with image enhancement are presented in Table III

and IV; while the data for both feet are shown in Table V and VI, respectively. It can be seen that the original thermograms perform better than the image enhancement techniques (AHE and Gamma), (Table IV) using the single foot thermogram. Among the six different deep CNN models investigated, DenseNet201 outperforms other networks with overall 94.01% sensitivity for the detection of DF and the class-wise sensitivities are 95.9% and 88.89% for DM and CG, respectively.

Table IV

Performance metrics for the best performing networks using 2D CNN on different image enhancement techniques using single foot thermograms. The best-performing network is highlighted in bold.

Enhancement Technique	Best Network	Class	Accuracy (%)	Precision (%)	Sensitivity (%)	F1-score (%)	Specificity (%)	Inference time (msec)
Original	<b>DenseNet201</b>	DM	<b>94.01 ± 4.91</b>	<b>95.91 ± 4.11</b>	<b>95.91 ± 4.11</b>	<b>95.91 ± 4.11</b>	<b>88.89 ± 6.49</b>	26.138
		CG	<b>94.01 ± 2.98</b>	<b>88.89 ± 3.94</b>	<b>88.89 ± 3.94</b>	<b>88.89 ± 3.94</b>	<b>95.91 ± 2.49</b>	
		Overall	<b>94.01 ± 2.54</b>	<b>94.01 ± 2.54</b>	<b>94.01 ± 2.54</b>	<b>94.01 ± 2.54</b>	<b>90.78 ± 3.11</b>	
AHE	InceptionV3	DM	92.22 ± 5.53	94.67 ± 4.64	94.67 ± 4.64	94.67 ± 4.64	85.56 ± 7.26	15.450
		CG	92.22 ± 3.36	85.56 ± 4.41	85.56 ± 4.41	85.56 ± 4.41	94.67 ± 2.82	
		Overall	92.22 ± 2.87	92.22 ± 2.87	92.22 ± 2.87	92.22 ± 2.87	88.01 ± 3.48	
Gamma Correction	InceptionV3	DM	93.41 ± 6.44	93.70 ± 6.30	97.54 ± 6.30	95.58 ± 6.30	82.22 ± 9.92	15.422
		CG	93.41 ± 6.12	92.51 ± 5.30	82.22 ± 5.30	87.06 ± 5.30	97.54 ± 3.30	
		Overall	93.41 ± 3.11	93.38 ± 3.12	93.41 ± 3.12	93.28 ± 3.12	86.35 ± 4.30	

Table V

Performance metrics for the binary classification using Gamma enhanced dual-foot thermogram using deep CNNs. The best-performing network is highlighted in bold.

Network	Class	Accuracy (%)	Precision (%)	Sensitivity (%)	F1-score (%)	Specificity (%)	Inference time (msec)
<b>MobilenetV2</b>	DM	<b>95.81 ± 4.14</b>	<b>97.52 ± 3.21</b>	<b>96.72 ± 3.68</b>	<b>97.12 ± 3.46</b>	<b>93.33 ± 5.15</b>	5.188
	CG	<b>95.81 ± 2.51</b>	<b>91.30 ± 3.54</b>	<b>93.33 ± 3.13</b>	<b>92.30 ± 3.35</b>	<b>96.72 ± 2.23</b>	
	Overall	<b>95.81 ± 2.15</b>	<b>95.84 ± 2.14</b>	<b>95.81 ± 2.15</b>	<b>95.82 ± 2.15</b>	<b>94.24 ± 2.50</b>	
Resnet18	DM	93.41 ± 5.13	94.40 ± 4.75	96.72 ± 3.68	95.55 ± 4.26	84.44 ± 7.49	2.430
	CG	93.41 ± 3.11	90.48 ± 3.68	84.44 ± 4.55	87.36 ± 4.17	96.72 ± 2.23	
	Overall	93.41 ± 2.66	93.34 ± 2.67	93.41 ± 2.66	93.34 ± 2.67	87.75 ± 3.52	
Resnet50	DM	90.42 ± 6.08	92.74 ± 5.36	94.26 ± 4.81	93.49 ± 5.1	80.00 ± 8.26	6.164
	CG	90.42 ± 3.69	83.72 ± 4.63	80.00 ± 5.02	81.82 ± 4.84	94.26 ± 2.92	
	Overall	90.42 ± 3.16	90.31 ± 3.17	90.42 ± 3.16	90.35 ± 3.17	83.84 ± 3.95	
DenseNet201	DM	91.62 ± 5.72	92.86 ± 5.32	95.90 ± 4.10	94.36 ± 4.77	80.00 ± 8.26	25.732
	CG	91.62 ± 3.48	87.80 ± 4.11	80.00 ± 5.02	83.72 ± 4.63	95.90 ± 2.49	
	Overall	91.62 ± 2.97	91.50 ± 2.99	91.62 ± 2.97	91.49 ± 2.99	84.28 ± 3.90	
InceptionV3	DM	93.41 ± 5.13	93.70 ± 5.02	97.54 ± 3.20	95.58 ± 4.25	82.22 ± 7.90	16.701
	CG	93.41 ± 3.11	92.50 ± 3.30	82.22 ± 4.80	87.06 ± 4.21	97.54 ± 1.94	
	Overall	93.41 ± 2.66	93.38 ± 2.67	93.41 ± 2.66	93.28 ± 2.69	86.35 ± 3.68	
VGG19	DM	92.22 ± 5.53	92.91 ± 5.30	96.72 ± 3.68	94.78 ± 4.60	80.00 ± 8.26	6.292
	CG	92.22 ± 3.36	90.00 ± 3.76	80.00 ± 5.02	84.71 ± 4.52	96.72 ± 2.23	
	Overall	92.22 ± 2.87	92.13 ± 2.89	92.21 ± 2.87	92.07 ± 2.90	84.51 ± 3.88	

Table VI

Performance metrics for the best-performing networks using 2D CNN on different image enhancement techniques of combined foot thermograms.

Enhancement Technique	Network	Class	Accuracy	Precision	Sensitivity	F1-score	Specificity	Inference time (msec)
Original	DenseNet201	DM	$90.72 \pm 5.99$	$93.47 \pm 5.10$	$93.85 \pm 4.96$	$93.66 \pm 5.03$	$82.22 \pm 7.90$	24.362
		CG	$90.72 \pm 3.64$	$83.15 \pm 4.70$	$82.22 \pm 4.80$	$82.68 \pm 4.75$	$93.85 \pm 3.01$	
		Overall	$90.72 \pm 3.11$	$90.69 \pm 3.12$	$90.72 \pm 3.11$	$90.70 \pm 3.11$	$85.35 \pm 3.79$	
AHE	MobilenetV2	DM	$92.22 \pm 5.53$	$94.67 \pm 4.64$	$94.67 \pm 4.64$	$94.67 \pm 4.64$	$85.56 \pm 7.26$	5.363
		CG	$92.22 \pm 3.36$	$85.56 \pm 4.41$	$85.56 \pm 4.41$	$85.56 \pm 4.41$	$94.67 \pm 2.82$	
		Overall	$92.22 \pm 2.87$	$92.22 \pm 2.87$	$92.22 \pm 2.87$	$92.22 \pm 2.87$	$88.01 \pm 3.48$	
Gamma Correction	MobilenetV2	DM	$95.81 \pm 5.20$	$97.52 \pm 4.04$	$96.72 \pm 4.62$	$97.12 \pm 4.34$	$93.33 \pm 6.48$	<b>5.188</b>
		CG	$95.81 \pm 4.95$	$91.30 \pm 6.96$	$93.33 \pm 6.16$	$92.30 \pm 6.58$	$96.72 \pm 4.40$	
		Overall	<b><math>95.81 \pm 2.51</math></b>	<b><math>95.84 \pm 2.51</math></b>	<b><math>95.81 \pm 2.51</math></b>	<b><math>95.82 \pm 2.51</math></b>	<b><math>94.24 \pm 2.92</math></b>	

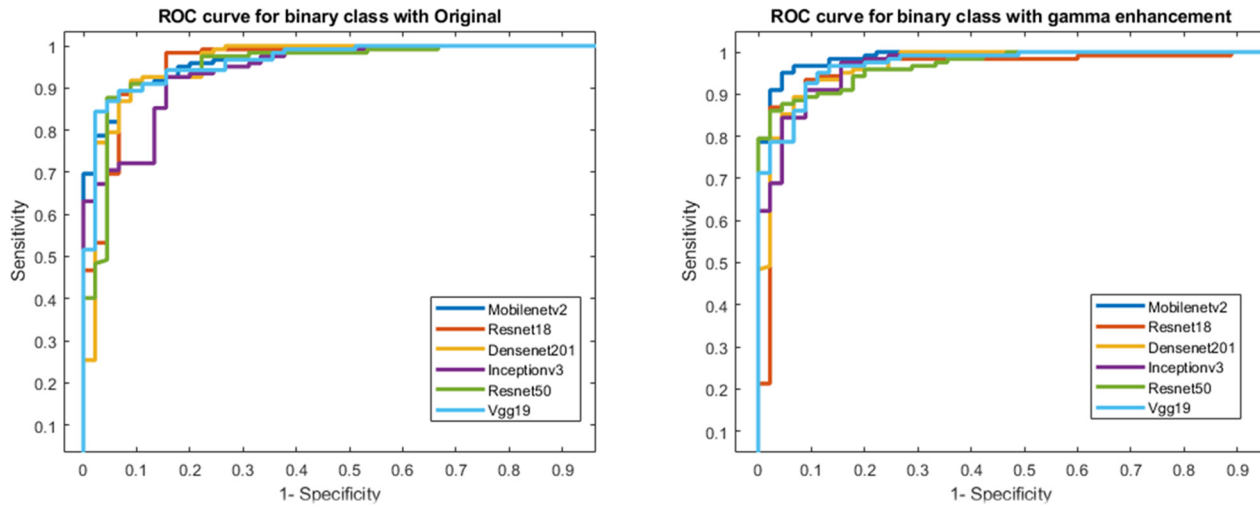


**Figure 5.** ROC for the Original and Gamma Correction Enhanced thermogram using Combined Foot Thermograms.

We have further investigated whether or not using a combination of foot images improves the detection performance. It was found that the Gamma enhanced dual-foot thermogram has outperformed the other methods (Table V). Interestingly, shallow network MobilenetV2 provides the best performance with an overall 95.81% sensitivity for diabetic foot detection and the class-wise sensitivities are 96.72% and 93.33% for DM and CG, respectively.

The outperformance using a combination of foot images is explained by the fact that combined foot thermograms provide more distinguishable features which are further enhanced by the image enhancement techniques.

Figure 5 clearly shows that the utilization of Gamma enhanced thermograms improved the classification performance compared to the original thermogram images for dual-foot investigation.

### 3.2 Feature-based detection results

We have investigated the performance of the 10 traditional classifiers with the three feature selection techniques and different combinations of optimized features. The summary of the top-performing five combinations is presented in Table VII. It can be seen that the AdaBoost Classifier with Random Forest Feature selection technique and the top 10 features shows the best performance of 96.71% sensitivity for diabetic foot detection and the class-wise sensitivities are 97.75% and 93.85% for DM and CG, respectively which is better than the top performance achieved by the deep CNN models.

TABLE VII  
Performance metrics for the best-performing combinations.

Classififer	Feature Selection	# of Feature	Class	Accuracy	Precision	Sensitivity	F1-score	Specificity	Inference time (ms)
AdaBoost	Random Forest	10	DM	96.71 ± 3.69	97.55 ± 3.19	97.95 ± 2.93	97.75 ± 3.06	93.33 ± 5.15	
			CG	96.71 ± 2.24	94.38 ± 2.89	93.33 ± 3.13	93.85 ± 3.01	97.95 ± 1.78	
			Overall	96.71 ± 1.91	96.70 ± 1.92	96.71 ± 1.91	96.70 ± 1.92	94.58 ± 2.43	
AdaBoost	Extra Tree	12	DM	96.41 ± 3.85	98.33 ± 2.64	96.72 ± 3.68	97.52 ± 3.21	95.56 ± 4.26	
			CG	96.41 ± 2.34	91.49 ± 3.50	95.56 ± 2.59	93.48 ± 3.10	96.72 ± 2.23	0.441
			Overall	96.41 ± 2.00	96.49 ± 1.97	96.41 ± 2.00	96.43 ± 1.99	95.87 ± 2.13	
AdaBoost	Random Forest	17	DM	96.41 ± 3.85	97.93 ± 2.94	97.13 ± 3.45	97.53 ± 3.21	94.44 ± 4.73	
			CG	96.41 ± 2.34	92.39 ± 3.33	94.44 ± 2.87	93.41 ± 3.11	97.13 ± 2.09	0.519
			Overall	96.41 ± 2.00	96.44 ± 1.99	96.41 ± 2.00	96.42 ± 1.99	95.17 ± 2.30	
AdaBoost	Random Forest	19	DM	96.41 ± 3.85	97.93 ± 2.94	97.13 ± 3.45	97.53 ± 3.21	94.44 ± 4.73	
			CG	96.41 ± 2.34	92.39 ± 3.33	94.44 ± 2.87	93.41 ± 3.11	97.13 ± 2.09	0.420
			Overall	96.41 ± 2.00	96.44 ± 1.99	96.41 ± 2.00	96.42 ± 1.99	95.17 ± 2.3	
Extra Tree	Extra Tree	8	DM	96.11 ± 4.00	97.93 ± 2.94	96.72 ± 3.68	97.32 ± 3.34	94.44 ± 4.73	
			CG	96.11 ± 2.43	91.40 ± 3.52	94.44 ± 2.87	92.90 ± 3.22	96.72 ± 2.23	0.299
			Overall	96.11 ± 2.07	96.17 ± 2.06	96.11 ± 2.07	96.13 ± 2.07	95.06 ± 2.32	

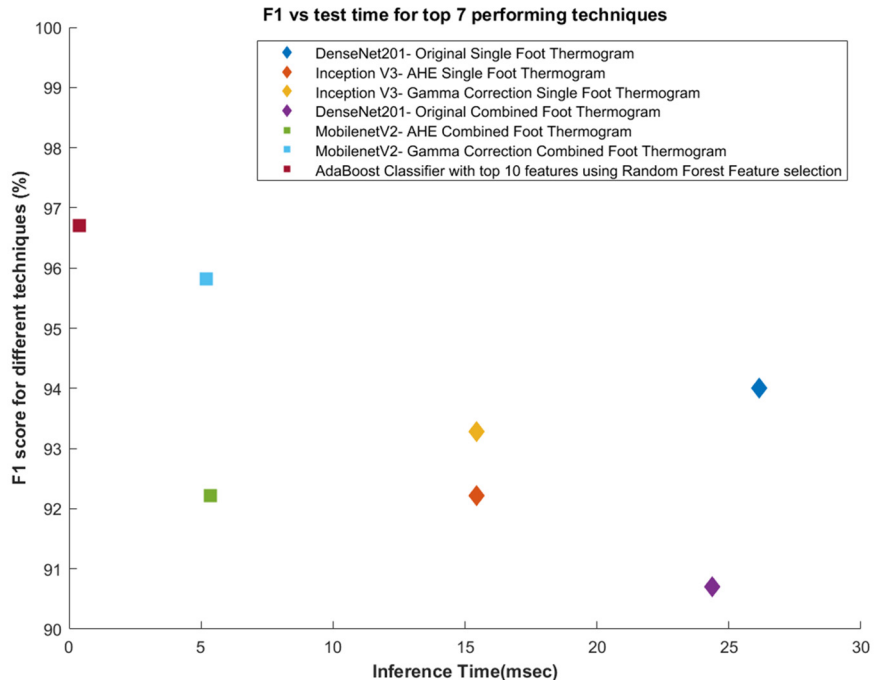
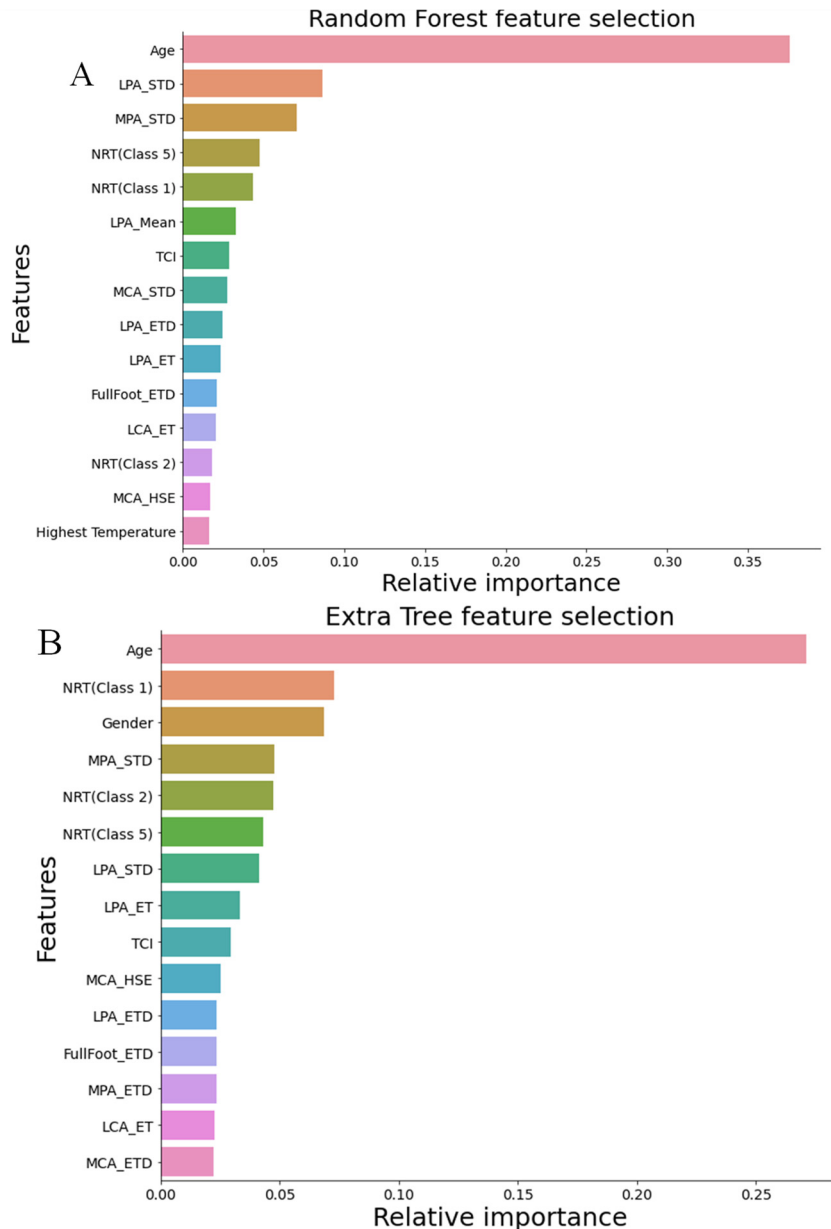


Figure 6. Comparison of F1-score versus Inference time for the top 7 performing techniques. Note:

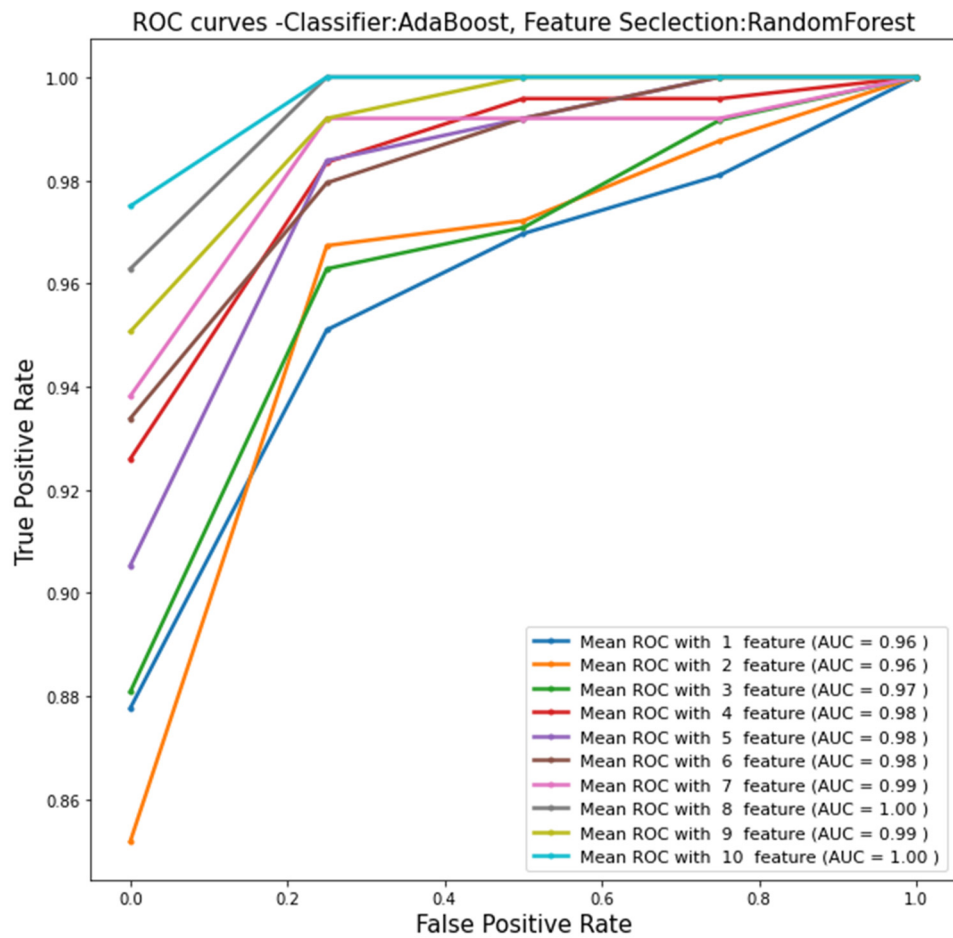
The top-performing networks that can be deployed on smart portable devices are shown as Square blocks while Diamond blocks represent non-deployable models.

Figure 6 shows the comparison of the F1-score and inference time for the top 7 performing machine learning techniques from each category- i) different image enhancement on single foot thermogram, ii) different image enhancement on combined foot thermogram, and iii) the best performing 1D classifier, respectively. Only MobileNetv2 among the CNN models and AdaBoost classifier are deployable in the mobile platform.



**Figure 7.** Top 15 features using A) Random Forest and B) Extra Tree feature selection techniques.

To the best of the author's knowledge, this is the first detailed investigation for diabetic foot detection using deep CNN models versus traditional machine learning approaches. All possible combinations in terms of classifier and feature selection techniques, along with the ranked features were investigated. As can be seen from Table VII, the Adaboost classifier outperforms other classifiers and the random forest feature ranking technique provides the best feature combination. The top 15 features among 28 features using Random Forest and Extra Tree feature selection techniques, after removing the highly correlated features from the initial 39 features, are shown in Figure 7. It is evident from Table VII that AdaBoost with the top 10 features (Age, LPA\_STD, MPD\_STD, NRT (Class 1), NRT (Class 5), LPA\_mean, TCI, MCA\_STD, LPA\_ETD, and LPA\_ET) has achieved the best classification performance.



**Figure 8.** ROC curves for the top 10 feature combinations.

It should be noted that the feature-based classification was done using single foot thermogram features which outperform the dual-foot approach of enhanced image thermogram using deep CNNs. However, in the feature-based approach, demographic information such as age helps to improve its performance as reported in previous work [38]. Peregrine et al. [39] have identified 11 regions of interest (ROI), which can be used to identify the diabetic foot with the help of ET, ETD, and HSE. Figure 8 demonstrating the

ROC curves for the top 1 to 10 feature combinations also confirm that the top 10 feature combinations provided the best AUC.

As the hallux/big toe is a prominent region of interest and is in the LPA section of the foot, its contribution in the classification of the foot into diabetic and control is vital in the classification and it is natural to be included in the top 10 features. Age is a strong predictor of the diabetic foot as observed in this study [38]. Minor temperature variation is typically expected in the feet, but less variation, indicated by a lower standard deviation of temperature in LPA and MCA angiosomes, can also be an indicator of the diabetic foot. TCI is also an important indicator as it is a summary of the temperature variation in all angiosomes.

To the best of our knowledge, no previous study has reported an image enhancement effect for the detection of the diabetic foot using thermogram images. Different pre-trained networks with and without image enhancement techniques were investigated and it was found that the image enhancement techniques helped in the classification performance. The best performing Adaboost classifier can be deployed in a smartphone and can be used in the foot clinic and by users in the home setting for the early detection of DFU.

The following interesting observations can be summarized from this study:

- Gamma Correction due to its special feature enhancement has helped the network to distinguish the diabetic and control group using the dual-foot thermogram.
- A single-foot thermogram in any CNN-based classification does not improve the classification performance compared with the dual-foot approach.
- Of the various machine learning algorithms tested on the optimized feature sets the Adaboost classifier with random forest feature ranking technique outperforms all other classifiers and the 2D image-based deep learning approach.

## V. CONCLUSION

Diabetic foot ulceration has a major impact on morbidity and mortality in patients with diabetes [5]. Early detection may help to limit DFU progression and eventually amputation. The application of artificial intelligence for early detection may have considerable utility for health care professionals, especially in primary care, and for caregivers and patients to keep track of their disease. Such online solutions become more important particularly during pandemic situations where healthcare support is drastically affected due to the burden on the healthcare system. In this study, we propose a classical machine learning-based framework for the early detection of the diabetic foot from thermogram images captured using Infra-Red

(IR) cameras with a smartphone. Optimization of the thermogram features from a single foot thermogram has enabled the development of a diagnostic system that outperforms 2D image-based deep learning techniques. The proposed network can be easily deployed on a smartphone-based application and validate in a clinical trial.

## ACKNOWLEDGEMENT

This work was made possible by Qatar National Research Fund (QNRF) NRP12S-0227-190164 and International Research Collaboration Co-Fund (IRCC) grant: IRCC-2021-001 and Universiti Kebangsaan Malaysia under Grant DPK-2021-001. The statements made herein are solely the responsibility of the authors. Open Access publication of this article is supported by Qatar National Library.

## REFERENCES

- [1] N. Cho, J. Kirigia, J. Mbanya, K. Ogurstova, L. Guariguata, and W. Rathmann, "IDF Diabetes Atlas-8th," *Int. Diabetes Federation*, p. 160(2015)
- [2] D. S. Sims Jr, P. R. Cavanagh, and J. S. Ulbrecht, "Risk factors in the diabetic foot: recognition and management," *Physical therapy*, vol. 68 (12), pp. 1887-1902(1988)
- [3] M. M. Iversen, G. S. Tell, T. Riise, B. R. Hanestad, T. Østbye, M. Graue, *et al.*, "History of foot ulcer increases mortality among individuals with diabetes: ten-year follow-up of the Nord-Trøndelag Health Study, Norway," *Diabetes care*, vol. 32 (12), pp. 2193-2199(2009)
- [4] A. M. Reyzelman, K. Koelewijn, M. Murphy, X. Shen, E. Yu, R. Pillai, *et al.*, "Continuous temperature-monitoring socks for home use in patients with diabetes: observational study," *Journal of medical Internet research*, vol. 20 (12), p. e12460(2018)
- [5] D. G. Armstrong, A. J. Boulton, and S. A. Bus, "Diabetic foot ulcers and their recurrence," *New England Journal of Medicine*, vol. 376 (24), pp. 2367-2375(2017)
- [6] C. E. Ananian, Y. S. Dhillon, C. C. Van Gils, D. C. Lindsey, R. J. Otto, C. R. Dove, *et al.*, "A multicenter, randomized, single-blind trial comparing the efficacy of viable cryopreserved placental membrane to human fibroblast-derived dermal substitute for the treatment of chronic diabetic foot ulcers," *Wound Repair and Regeneration*, vol. 26 (3), pp. 274-283(2018)
- [7] B. Peter-Riesch, "The diabetic foot: the never-ending challenge," *Novelties in Diabetes*, vol. 31 pp. 108-134(2016)
- [8] R. G. Frykberg, I. L. Gordon, A. M. Reyzelman, S. M. Cazzell, R. H. Fitzgerald, G. M. Rothenberg, *et al.*, "Feasibility and efficacy of a smart mat technology to predict development of diabetic plantar ulcers," *Diabetes Care*, vol. 40 (7), pp. 973-980(2017)
- [9] F. N. Inagaki Nagase, "The impact of diabetic foot problems on health-related quality of life of people with diabetes," 2017)
- [10] R. F. van Doremalen, J. J. van Netten, J. G. van Baal, M. M. Vollenbroek-Hutten, and F. van der Heijden, "Infrared 3D thermography for inflammation detection in diabetic foot disease: a proof of concept," *Journal of diabetes science and technology*, vol. 14 (1), pp. 46-54(2020)
- [11] P. A. Crisologo and L. A. Lavery, "Remote home monitoring to identify and prevent diabetic foot ulceration," *Annals of translational medicine*, vol. 5 (21), 2017)
- [12] J. W. Albers and R. Jacobson, "Decompression nerve surgery for diabetic neuropathy: a structured review of published clinical trials," *Diabetes, metabolic syndrome and obesity: targets and therapy*, vol. 11 p. 493(2018)
- [13] D. Hernandez-Contreras, H. Peregrina-Barreto, J. Rangel-Magdaleno, and J. Gonzalez-Bernal, "Narrative review: Diabetic foot and infrared thermography," *Infrared Physics & Technology*, vol. 78 pp. 105-117(2016)
- [14] F. Ring, "Thermal imaging today and its relevance to diabetes," *Journal of diabetes science and technology*, vol. 4 (4), pp. 857-862(2010)
- [15] A. W. Chan, I. A. MacFarlane, and D. R. Bowsher, "Contact thermography of painful diabetic neuropathic foot," *Diabetes Care*, vol. 14 (10), pp. 918-922(1991)

- [16] T. Nagase, H. Sanada, K. Takehara, M. Oe, S. Iizaka, Y. Ohashi, *et al.*, "Variations of plantar thermographic patterns in normal controls and non-ulcer diabetic patients: novel classification using angiosome concept," *Journal of Plastic, reconstructive & aesthetic Surgery*, vol. 64 (7), pp. 860-866(2011)
- [17] T. Mori, T. Nagase, K. Takehara, M. Oe, Y. Ohashi, A. Amemiya, *et al.*, "Morphological pattern classification system for plantar thermography of patients with diabetes," ed: SAGE Publications Sage CA: Los Angeles, CA, 2013.
- [18] B. F. Jones, "A reappraisal of the use of infrared thermal image analysis in medicine," *IEEE transactions on medical imaging*, vol. 17 (6), pp. 1019-1027(1998)
- [19] N. Kaabouch, Y. Chen, J. Anderson, F. Ames, and R. Paulson, "Asymmetry analysis based on genetic algorithms for the prediction of foot ulcers," in *Visualization and Data Analysis 2009*, 2009, p. 724304.
- [20] N. Kaabouch, Y. Chen, W.-C. Hu, J. W. Anderson, F. Ames, and R. Paulson, "Enhancement of the asymmetry-based overlapping analysis through features extraction," *Journal of Electronic Imaging*, vol. 20 (1), p. 013012(2011)
- [21] C. Liu, J. J. van Netten, J. G. Van Baal, S. A. Bus, and F. van Der Heijden, "Automatic detection of diabetic foot complications with infrared thermography by asymmetric analysis," *Journal of biomedical optics*, vol. 20 (2), p. 026003(2015)
- [22] D. Hernandez-Contreras, H. Peregrina-Barreto, J. Rangel-Magdaleno, J. Ramirez-Cortes, and F. Renero-Carrillo, "Automatic classification of thermal patterns in diabetic foot based on morphological pattern spectrum," *Infrared Physics & Technology*, vol. 73 pp. 149-157(2015)
- [23] D. Hernandez-Contreras, H. Peregrina-Barreto, J. Rangel-Magdaleno, J. Gonzalez-Bernal, and L. Altamirano-Robles, "A quantitative index for classification of plantar thermal changes in the diabetic foot," *Infrared Physics & Technology*, vol. 81 pp. 242-249(2017)
- [24] D. A. Hernandez-Contreras, H. Peregrina-Barreto, J. D. J. Rangel-Magdaleno, and F. Orihuela-Espina, "Statistical approximation of plantar temperature distribution on diabetic subjects based on beta mixture model," *IEEE Access*, vol. 7 pp. 28383-28391(2019)
- [25] P. Kamavisdar, S. Saluja, and S. Agrawal, "A survey on image classification approaches and techniques," *International Journal of Advanced Research in Computer and Communication Engineering*, vol. 2 (1), pp. 1005-1009(2013)
- [26] J. Ren, "ANN vs. SVM: Which one performs better in classification of MCCs in mammogram imaging," *Knowledge-Based Systems*, vol. 26 pp. 144-153(2012)
- [27] D. Lu and Q. Weng, "A survey of image classification methods and techniques for improving classification performance," *International journal of Remote sensing*, vol. 28 (5), pp. 823-870(2007)
- [28] I. Cruz-Vega, D. Hernandez-Contreras, H. Peregrina-Barreto, J. d. J. Rangel-Magdaleno, and J. M. Ramirez-Cortes, "Deep Learning Classification for Diabetic Foot Thermograms," *Sensors*, vol. 20 (6), p. 1762(2020)
- [29] D. A. Hernandez-Contreras, H. Peregrina-Barreto, J. de Jesus Rangel-Magdaleno, and F. J. Renero-Carrillo, "Plantar thermogram database for the study of diabetic foot complications," *IEEE Access*, vol. 7 pp. 161296-161307(2019)
- [30] H. Maldonado, R. Bayareh, I. Torres, A. Vera, J. Gutiérrez, and L. Leija, "Automatic detection of risk zones in diabetic foot soles by processing thermographic images taken in an uncontrolled environment," *Infrared Physics & Technology*, vol. 105 p. 103187(2020)
- [31] J. Saminathan, M. Sasikala, V. Narayananmurthy, K. Rajesh, and R. Arvind, "Computer aided detection of diabetic foot ulcer using asymmetry analysis of texture and temperature features," *Infrared Physics & Technology*, vol. 105 p. 103219(2020)
- [32] M. Adam, E. Y. Ng, S. L. Oh, M. L. Heng, Y. Hagiwara, J. H. Tan, *et al.*, "Automated detection of diabetic foot with and without neuropathy using double density-dual tree-complex wavelet transform on foot thermograms," *Infrared Physics & Technology*, vol. 92 pp. 270-279(2018)
- [33] M. Adam, E. Y. Ng, S. L. Oh, M. L. Heng, Y. Hagiwara, J. H. Tan, *et al.*, "Automated characterization of diabetic foot using nonlinear features extracted from thermograms," *Infrared Physics & Technology*, vol. 89 pp. 325-337(2018)
- [34] S. B. Gururajarao, U. Venkatappa, J. M. Shivaram, M. Y. Sikkandar, and A. Al Amoudi, "Infrared thermography and soft computing for diabetic foot assessment," in *Machine Learning in Bio-Signal Analysis and Diagnostic Imaging*, ed: Elsevier, 2019, pp. 73-97.
- [35] M. Etehad tavakol, Z. Emrani, and E. Y. K. Ng, "Rapid extraction of the hottest or coldest regions of medical thermographic images," *Medical & biological engineering & computing*, vol. 57 (2), pp. 379-388(2019)
- [36] A. K. Tawsifur Rahman, Yazan Qiblawey, Anas Tahir, Serkan Kiranyaz, Saad, M. T. I. Bin Abul Kashem, Somaya Al Maadeed, Susu M Zughraier,, and M. E. H. C. Muhammad Salman Khan, "Exploring the Effect of Image Enhancement Techniques on COVID-19 Detection using Chest X-rays Images" *arxiv preprint arXiv:2012.02238*, 2020, 2020)
- [37] G. I. Taylor and J. H. Palmer, "Angiosome theory," *British journal of plastic surgery*, vol. 45 (4), pp. 327-328(1992)
- [38] L. A. V. Cajacuri, "Early diagnostic of diabetic foot using thermal images," 2013.

- [39] H. Peregrina-Barreto, L. A. Morales-Hernandez, J. Rangel-Magdaleno, J. G. Avina-Cervantes, J. M. Ramirez-Cortes, and R. Morales-Caporal, "Quantitative estimation of temperature variations in plantar angiosomes: a study case for diabetic foot," *Computational and mathematical methods in medicine*, vol. 2014 2014
- [40] M. E. Chowdhury, K. Alzoubi, A. Khandakar, R. Khallifa, R. Abouhasera, S. Koubaa, *et al.*, "Wearable real-time heart attack detection and warning system to reduce road accidents," *Sensors*, vol. 19 (12), p. 2780(2019)
- [41] M. E. Chowdhury, A. Khandakar, K. Alzoubi, S. Mansoor, A. M Tahir, M. B. I. Reaz, *et al.*, "Real-time smart-digital stethoscope system for heart diseases monitoring," *Sensors*, vol. 19 (12), p. 2781(2019)
- [42] M. H. Chowdhury, M. N. I. Shuzan, M. E. Chowdhury, Z. B. Mahbub, M. M. Uddin, A. Khandakar, *et al.*, "Estimating Blood Pressure from the Photoplethysmogram Signal and Demographic Features Using Machine Learning Techniques," *Sensors*, vol. 20 (11), p. 3127(2020)
- [43] M. A. Hall, "Correlation-based feature selection for machine learning," 1999
- [44] H. Han, W.-Y. Wang, and B.-H. Mao, "Borderline-SMOTE: a new over-sampling method in imbalanced data sets learning," in *International conference on intelligent computing*, 2005, pp. 878-887.
- [45] N. V. Chawla, K. W. Bowyer, L. O. Hall, and W. P. Kegelmeyer, "SMOTE: synthetic minority over-sampling technique," *Journal of artificial intelligence research*, vol. 16 pp. 321-357(2002)
- [46] T. Chen, T. He, M. Benesty, V. Khotilovich, and Y. Tang, "Xgboost: extreme gradient boosting," *R package version 0.4-2*, pp. 1-4(2015)
- [47] Y. Saeys, T. Abeel, and Y. Van de Peer, "Robust feature selection using ensemble feature selection techniques," in *Joint European Conference on Machine Learning and Knowledge Discovery in Databases*, 2008, pp. 313-325.
- [48] M. Petković, D. Kocev, and S. Džeroski, "Feature ranking for multi-target regression," *Machine Learning*, vol. 109 (6), pp. 1179-1204(2020)
- [49] L. Yan, H.-T. Zhang, J. Goncalves, Y. Xiao, M. Wang, Y. Guo, *et al.*, "An interpretable mortality prediction model for COVID-19 patients," *Nature Machine Intelligence*, pp. 1-6(2020)
- [50] W. Li, Y. Yin, X. Quan, and H. Zhang, "Gene Expression Value Prediction Based on XGBoost Algorithm," *Frontiers in genetics*, vol. 10 p. 1077(2019)
- [51] (2021). *Multilayer perceptron* [Online]. Available: [https://en.wikipedia.org/wiki/Multilayer\\_perceptron](https://en.wikipedia.org/wiki/Multilayer_perceptron). [2nd March]
- [52] (2021). *Logistic regression*. Available: [https://en.wikipedia.org/wiki/Logistic\\_regression](https://en.wikipedia.org/wiki/Logistic_regression). [2nd March]
- [53] G. Guo, H. Wang, D. Bell, Y. Bi, and K. Greer, "KNN model-based approach in classification," in *OTM Confederated International Conferences" On the Move to Meaningful Internet Systems"*, 2003, pp. 986-996.
- [54] T.-K. An and M.-H. Kim, "A new diverse AdaBoost classifier," in *2010 International conference on artificial intelligence and computational intelligence*, 2010, pp. 359-363.
- [55] S. S. Keerthi, S. K. Shevade, C. Bhattacharyya, and K. R. K. Murthy, "Improvements to Platt's SMO algorithm for SVM classifier design," *Neural computation*, vol. 13 (3), pp. 637-649(2001)
- [56] M. Pal, "Random forest classifier for remote sensing classification," *International journal of remote sensing*, vol. 26 (1), pp. 217-222(2005)
- [57] A. Sharaff and H. Gupta, "Extra-tree classifier with metaheuristics approach for email classification," in *Advances in Computer Communication and Computational Sciences*, ed: Springer, 2019, pp. 189-197.
- [58] N. Chakrabarty, T. Kundu, S. Dandapat, A. Sarkar, and D. K. Kole, "Flight arrival delay prediction using gradient boosting classifier," in *Emerging Technologies in Data Mining and Information Security*, ed: Springer, 2019, pp. 651-659.
- [59] V. Bobkov, A. Bobkova, S. Porshnev, and V. Zuzin, "The application of ensemble learning for delineation of the left ventricle on echocardiographic records," in *2016 Dynamics of Systems, Mechanisms and Machines (Dynamics)*, 2016, pp. 1-5.
- [60] Q. Gu, Z. Li, and J. Han, "Linear discriminant dimensionality reduction," in *Joint European conference on machine learning and knowledge discovery in databases*, 2011, pp. 549-564.
- [61] M. E. Chowdhury, T. Rahman, A. Khandakar, R. Mazhar, M. A. Kadir, Z. B. Mahbub, *et al.*, "Can AI help in screening viral and COVID-19 pneumonia?," *arXiv preprint arXiv:2003.13145*, 2020
- [62] T. Rahman, A. Khandakar, Y. Qiblawey, A. Tahir, S. Kiranyaz, S. B. A. Kashem, *et al.*, "Exploring the Effect of Image Enhancement Techniques on COVID-19 Detection using Chest X-rays Images," *arXiv preprint arXiv:2012.02238*, 2020
- [63] A. Tahir, Y. Qiblawey, A. Khandakar, T. Rahman, U. Khurshid, F. Musharavati, *et al.*, "Coronavirus: Comparing COVID-19, SARS and MERS in the eyes of AI," *arXiv preprint arXiv:2005.11524*, 2020
- [64] T. Rahman, A. Khandakar, M. A. Kadir, K. R. Islam, K. F. Islam, R. Mazhar, *et al.*, "Reliable Tuberculosis Detection using Chest X-ray with Deep Learning, Segmentation and Visualization," *IEEE Access*, vol. 8 pp. 191586-191601(2020)

- [65] T. Rahman, M. E. Chowdhury, A. Khandakar, K. R. Islam, K. F. Islam, Z. B. Mahbub, *et al.*, "Transfer Learning with Deep Convolutional Neural Network (CNN) for Pneumonia Detection using Chest X-ray," *Applied Sciences*, vol. 10 (9), p. 3233(2020)
- [66] S. M. Anwar, M. Majid, A. Qayyum, M. Awais, M. Alnowami, and M. K. Khan, "Medical image analysis using convolutional neural networks: a review," *Journal of medical systems*, vol. 42 (11), p. 226(2018)
- [67] J. Deng, W. Dong, R. Socher, L.-J. Li, K. Li, and L. Fei-Fei, "Imagenet: A large-scale hierarchical image database," in *2009 IEEE conference on computer vision and pattern recognition*, 2009, pp. 248-255.
- [68] M. Mishra, H. Menon, and A. Mukherjee, "Characterization of \$ S\_1 \$ and \$ S\_2 \$ Heart Sounds Using Stacked Autoencoder and Convolutional Neural Network," *IEEE Transactions on Instrumentation and Measurement*, vol. 68 (9), pp. 3211-3220(2018)
- [69] C. Szegedy, V. Vanhoucke, S. Ioffe, J. Shlens, and Z. Wojna, "Rethinking the inception architecture for computer vision," in *Proceedings of the IEEE conference on computer vision and pattern recognition*, 2016, pp. 2818-2826.
- [70] K. Simonyan and A. Zisserman, "Very deep convolutional networks for large-scale image recognition," *arXiv preprint arXiv:1409.1556*, 2014)
- [71] M. Sandler, A. Howard, M. Zhu, A. Zhmoginov, and L.-C. Chen, "Mobilenetv2: Inverted residuals and linear bottlenecks," in *Proceedings of the IEEE conference on computer vision and pattern recognition*, 2018, pp. 4510-4520.
- [72] M. Veluchamy and B. Subramani, "Image contrast and color enhancement using adaptive gamma correction and histogram equalization," *Optik*, vol. 183 pp. 329-337(2019)
- [73] J. B. Zimmerman, S. M. Pizer, E. V. Staab, J. R. Perry, W. McCartney, and B. C. Brenton, "An evaluation of the effectiveness of adaptive histogram equalization for contrast enhancement," *IEEE Transactions on Medical Imaging*, vol. 7 (4), pp. 304-312(1988)

Received 27 October 2023, accepted 7 November 2023, date of publication 13 November 2023,  
date of current version 17 November 2023.

Digital Object Identifier 10.1109/ACCESS.2023.3332292



## RESEARCH ARTICLE

# Automated Diabetic Foot Ulcer Detection and Classification Using Deep Learning

SUNNAM NAGARAJU<sup>1</sup>, KOLLATI VIJAYA KUMAR<sup>ID 2</sup>, B. PRAMEELA RANI<sup>3</sup>, E. LAXMI LYDIA<sup>ID 4</sup>, MOHAMAD KHAIRI ISHAK<sup>5,6</sup>, IMEN FILALI<sup>7</sup>, FATEH KHALID KARIM<sup>ID 7</sup>, AND SAMIH M. MOSTAFA<sup>ID 8</sup>

<sup>1</sup>Department of Mechanical Engineering, MLR Institute of Technology, Hyderabad 500043, India

<sup>2</sup>Department of Computer Science and Engineering, GITAM School of Technology, Vishakhapatnam Campus, GITAM (Deemed to be a University), Visakhapatnam 530045, India

<sup>3</sup>Department of CSE-AIML, Aditya College of Engineering, Surampalem, Andhra Pradesh 533437, India

<sup>4</sup>Department of Computer Science and Engineering, Vignan's Institute of Information Technology, Visakhapatnam 530049, India

<sup>5</sup>Department of Electrical and Computer Engineering, College of Engineering and Information Technology, Ajman University, Ajman, United Arab Emirates

<sup>6</sup>School of Electrical and Electronic Engineering, Universiti Sains Malaysia, Engineering Campus, Nibong Tebal, Pulau Pinang 14300, Malaysia

<sup>7</sup>Department of Computer Sciences, College of Computer and Information Sciences, Princess Nourah Bint Abdulrahman University, Riyadh 11671, Saudi Arabia

<sup>8</sup>Computer Science Department, Faculty of Computers and Information, South Valley University, Qena 83523, Egypt

Corresponding author: Samih M. Mostafa (samih\_montser@sci.svu.edu.eg)

This work was supported by Princess Nourah bint Abdulrahman University Researchers Supporting Project number (PNURSP2023R300), Princess Nourah bint Abdulrahman University, Riyadh, Saudi Arabia.

**ABSTRACT** Diabetic foot ulcers (DFU) are a common and serious complication in individuals with diabetes, and early detection plays a crucial role in effective treatment and prevention of further complications. Automated DFU Detection and Classification using Deep learning (DL) refers to the application of deep learning techniques to automatically detect and classify diabetic foot ulcers from medical images. DL, a subfield of machine learning, has shown promising results in medical imaging analysis, including diabetic foot ulcer detection. The use of deep learning in DFU detection provides various benefits, including the ability to learn complex features, adaptability to different image modalities, and the potential for high accuracy in detection and classification tasks. Therefore, this article introduces a novel sparrow search optimization (SSO) with deep learning enabled diabetic foot ulcer detection and classification (SSODL-DFUDC) technique. The presented SSODL-DFUDC technique's goal lies in identifying and classifying DFU. The proposed technique employs the Inception-ResNet-v2 model for feature vector generation to accomplish this. Since the trial and error manual hyperparameter tuning of the Inception-ResNet-v2 model is a tedious and erroneous process, the SSO algorithm can be used for the optimal hyperparameter selection of the Inception-ResNet-v2 model which in turn enhances the overall DFU classification results. Moreover, the classification of DFU takes place using the stacked sparse autoencoder (SSAE) model. The comprehensive experimental outcomes demonstrate the improved performance of the SSODL-DFUDC system related to existing DL techniques.

**INDEX TERMS** Medical image analysis, deep learning, diabetic foot ulcer, sparrow search optimization, computer-aided diagnosis.

## I. INTRODUCTION

Amputation of the limb or foot may be caused by a diabetic foot ulcer (DFU) infection. The probability of survival can be lesser for patients having amputated limbs [1]. It damages the

The associate editor coordinating the review of this manuscript and approving it for publication was Bijoy Chand Chatterjee<sup>ID</sup>.

livelihood of quality and distresses social participation and the outcome of these causes and tissue death because of diseases. The DFU is increasing rapidly. Because of the scarcity of specialists and lack of resources in the medication for diabetic foot ulcers, over a million diabetic patients at higher risk of diabetic Mellitus will lose out foot (partly) every year [2]. Notably, for every 20 seconds, one diabetic foot functioned.

A complete study of medical data was essential for specialists to accomplish a precise outcome [3]. Conventional diagnostic techniques were labour-intensive and vulnerable to human errors. The computer-based diagnostic process's utility includes minimal performance enhancement [4]. Current advancements in wearable and mobile health gadgets help in controlling diabetes and its limitations, improving the standards of life and extending remission for patients by controlling harmful sensing and foot pressure and inflammation [5]. The development of novel-generation medical sensors recommends expanding such devices' utility in the medical field [6]. In the contemporary healthcare mechanism, medical images are used for diagnosing several patient difficulties [7].

Conventional approaches for analysis of DFU use hand-crafted rendered technique [8]. However, research activities in the publication have displayed that learned attributes by deep neural networks (DNN) have high potential compared to classical hand-crafted features [9]. Wide research was conducted to enhance the outcome of computerized are very popular in this sector since they were superior to other techniques [10]. The common method that is utilized in the DL technique in medical image classification is convolutional neural networks (CNNs). The CNNs can efficiently derive valuable attributes for image segmentation, image classification, other vision tasks, and object detection [11]. With the obtainability of large-scale trained data and high-performing modern application specific integrated circuit (ASICs) and graphics processing units (GPUs) and techniques related to CNNs have enhanced the precision of image classification. Renowned CNNs for general image classifier tasks involve ResNet, AlexNet, EfficientNet, and VGG [12]. Such networks generally serve as the pillar of medical image classifier networks or directly enforce medical image classifications by transfer learning (TL) with pre-trained variables on large-scale datasets (e.g., ImageNet). Practically, labelling and collecting medical images were costly [13]. TL was a potential way to overcome the need for medicinal trained data.

This article introduces a novel sparrow search optimization with deep learning enabled diabetic foot ulcer detection and classification (SSODL-DFUDC) technique. The goal of this technique lies in the identification and classification of DFU. To perform this task, the SSODL-DFUDC technique employs the Inception-ResNet-v2 model for feature vector generation and utilizes the SSO algorithm for hyperparameter tuning. The SSAE model is used for DFU data set classification.

The rest of the paper is organized as follows. Section II provides the related works and section III offers the proposed model. Then, section IV gives the result analysis and section V concludes the paper.

## II. LITERATURE REVIEW

Cassidy et al. [14] present a mobile and cloud-based structure for the automatic recognition of DFUs and perform an anal-

ysis of its efficiency. This method utilizes a cross-platform mobile structure which allows the utilization of mobile applications for several environments utilizing a single TypeScript code base. A DCNN has been used in a cloud-based environment, but the mobile application sends photographs of patients' feet to inference for detecting the occurrence of DFUs. Munadi et al. [15] present a new structure for the DFU classifier dependent upon thermal imaging utilizing DNNs and decision fusion. At this point, decision fusion integrates the classifier outcome in a parallel classification. The author utilized the CNN technique of MobileNetV2 and ShuffleNet as the baseline classification. In evolving the classification process, initially, the ShuffleNet and MobileNetV2 can be trained to utilize plantar thermogram databases.

Alshayeqi and Sindhu's [16] investigation is new since, without any prior analysis utilized typical ML techniques for the analysis of DFU in the thermal image and also did not utilize SURF, BOF, or SIFT approaches. Also, the authors utilize direct temperature files of all feet and then map them on images to obtain the correct temperature distribution. Typical ML techniques are chosen in the last step to binary classifier betwixt normal and DFU. D'Angelo et al. [17] examine a method dependent upon Genetic Programming (GP) for creating an easy global explainable classifier termed X-GPC that different present tools, like SHAP and LIME, offer a global analysis of DFU with the mathematical process. Moreover, the medicinal clinical staff was offered a simple consultable 3D graph that is utilised to understand the patient's condition and make decisions for patient recovery. In [18], a new Deep CNN, DFU\_QUTNet, is also presented for the automatic classifier of normal skin (healthy skin) towards abnormal skin (DFU) classes. Stacking further layers to a classic CNN to arrive very deep could not cause optimum efficacy, resulting in worse execution because of the gradient.

Goyal [19] progressed automatic computer vision (CV) schemes which recognize the DFU of distinct grades and steps. Primarily, the authors utilized ML techniques for classifying the DFU spots against normal skin spots of the foot area to determine the feasible misclassified reasons for both classes. Secondarily, the authors utilized FCN for the segmentation of DFU and neighbouring skin from entire foot images. Lastly, the authors utilized robust and lightweight deep localization schemes from mobile devices for detecting the DFU on foot image to a remote monitor. In [20], a novel image processing system was presented for effectual calculation and classifier of DFU images. Primarily, pre-processed was completed by cascaded fuzzy filter and then non-linear partial differential equation (NPDE) based segmentation which segmented the foot ulcer areas. Accordingly, the LBP was utilized for extracting the valuable features. Afterwards, the presented hybrid GWO-CNN technique utilizes these features for identifying the DFU areas. In [21], a unique stacked parallel convolutional layer-based network (DFU\_SPNet) was presented for performing DFU versus normal skin classification.

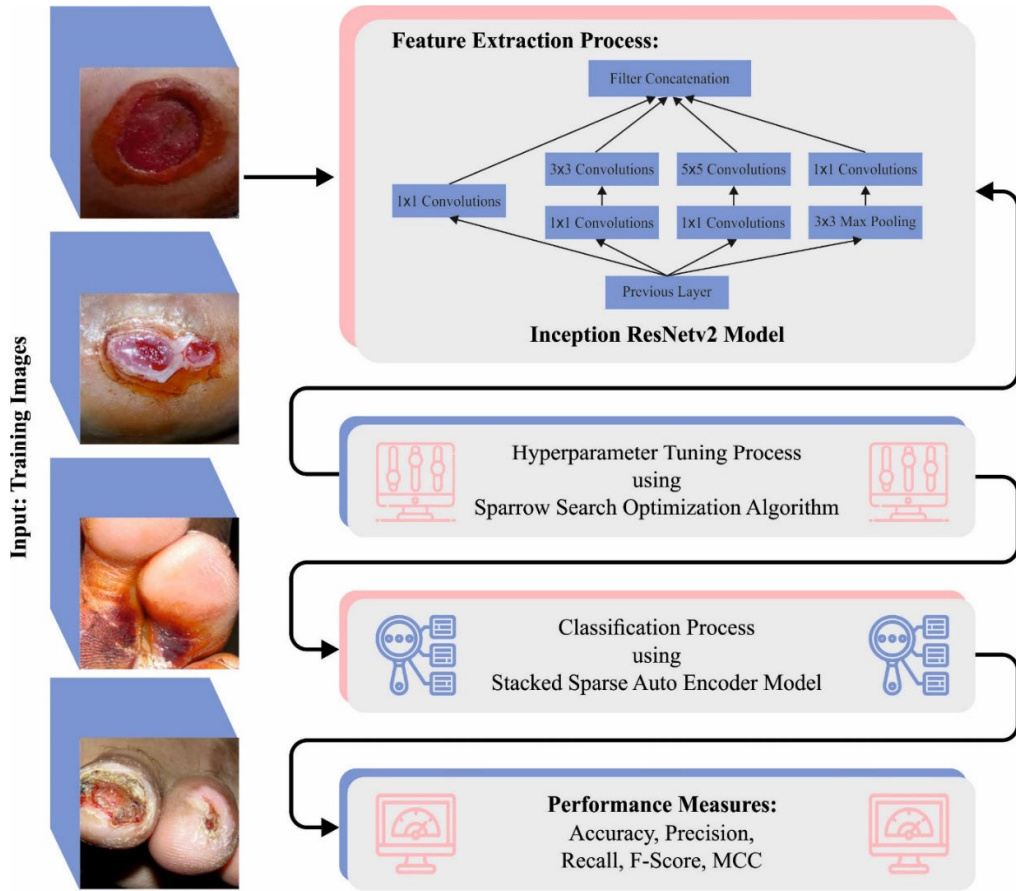


**FIGURE 1.** Workflow of SSODL-DFUDC approach.

In [22], a pre-training ResNet-50 approach and altered classical-quantum approach can be employed for DFU classification as equivalent class labels like ischaemia/non-ischaemia and normal/abnormal. Al-Garaawi et al. [23] examine a CNN-based DFU classification approach where it can be demonstrated that feeding a suitable feature to the CNN technique offers a complementary efficiency to typical RGB-based deep approaches of DFU classification tasks and the optimum solution was attained when either RGB images or their texture features can be integrated and utilized as input to CNN. da Costa Oliveira et al. [24] present the utilisation of DL approaches to help in the cure of DFUs. In detail, the recognition of ulcers by photos taken in the patient feet. The authors present a development of Faster R-CNN utilizing data augmentation approaches and modifications in parameter settings. Venkatesan et al. [25] aimed to develop and design a novel lightweight CNN approach to analyse NFU termed as NFU-Net.

Huang et al. [26] present an endwise ViT-AMC network (ViT-AMCNet) with adaptive model fusion and multi-objective optimizer which combines and fuses the ViT and AMC blocks. Zhou et al. [27] examine an adaptive sparse interaction ResNet-ViT dual-branch network (ASI-DBNet). Initially, the authors plan the ResNet-ViT parallel infrastruc-

ture for simultaneously capturing and retaining the local and global data of pathology images. Huang et al. [28] introduce an endwise depth domain adaptive network (DDANet) with a combination gradient CAM and priori experience-guided attention for improving the tumour grading solution and interpretability by presenting the pathologist's previous experience in high-magnification as depth model. Zhou et al. [29] developed a laryngeal cancer classification network (LPCANet) that relies on a CNN and attention mechanisms. Primary, the original histopathological images can be sequentially cropped as patches. Huang et al. [30] introduce a novel fusion attention block network (FABNet) for addressing these issues.

### III. THE PROPOSED MODEL

In this article, we have developed a new SSODL-DFUDC technique to detect and classify DFU. The presented SSODL-DFUDC technique's goal lies in identifying and classifying DFU. Fig. 1 represents the workflow of the SSODL-DFUDC algorithm. The figure indicates that the presented SSODL-DFUDC technique follows three major processes: Inception-ResNet-v2 feature extraction, SSO-based hyperparameter tuning, and SSAE classification.

#### A. FEATURE EXTRACTION USING OPTIMAL DL MODEL

The presented SSODL-DFUDC technique employed the Inception-ResNet-v2 model for feature vector generation. CNN is the algorithm of the DL algorithm. CNN is a progression of MLP developed for processing the dataset in grid form [31]. CNN is exploited on the image dataset. The objective of the training model is to train the ANN module to reduce the error of predictive results of the model with the original dataset. The convolutional layer is a convolutional operation betwixt 2 vectors. In Eq. (1), it is convolutional of two functions where  $g(x)$  is named the convolutional kernel (filter) that is functioned in shifts on the vector  $F(x)$ .

$$h(x) = F(x) \cdot g(x) = \int F(a) \cdot g(x-a) \quad (1)$$

CNN comprises two phases. Initially, group images with feedforward. Then, use the backpropagation algorithm. Currently, the wrapping and cropping systems are performed to emphasize the categorised object before doing the classification. Next, training can be done by backpropagation and feed-forward techniques. The structure of CNN is split into two most important parts, such as the Fully-Connected Layer and Feature Extraction Layer. Inception-ResNetV2 is a CNN architecture trained originally on the ImageNet datasets, comprising 164 layers. The model has learned feature representation and is stronger for a large number of image types. This model accepts the input of  $299 \times 299$  and the hybridization of two currently established networks, the modern architectural version, and residual links. There are sequences of filters, namely  $1 \times 1$ ,  $3 \times 3$ ,  $5 \times 5$ , and so on, merged with all the branch concatenation. The split-transformation-mixing architecture of the initiation model is perceived in its thick layer as a stronger representation. The residual connection enables the training of progressively DNN, leading to remarkable performance. This model was trained and fine-tuned through TL in this work.

**TABLE 1. Details of dataset.**

Class	No. of Images
Abnormal	410
Normal	434
Total Number of Images	844

In this work, the SSODL-DFUDC technique utilizes the SSO algorithm for hyperparameter tuning. The SSO is a recent heuristic approach inspired by the behaviours of sparrows foraging and avoiding predators and characteristics of group socialization [32]. The SSO benefits from strong optimization ability, simple architecture, easier implementation, few control parameters, and so on. The SSO to converge to the present optimum solution is to jump towards the existing ideal solution's locality directly. Hence the SSO technique is better than the particle swarm optimization, grey wolf optimization, and gravity search algorithms with respect to robustness, accuracy, convergence speed, and stability.



**FIGURE 2. Sample images a) Normal (Healthy) b) Abnormal (Ulcer).**

In this work, sparrows are alienated into vigilant and discoverer followers. The location of every sparrow corresponds to the solution. The position of each sparrow in the sparrow groups is characterized as  $X$  matrix:

$$X = \begin{pmatrix} x_{1,1} & \dots & x_{1,d} \\ \vdots & \dots & \vdots \\ x_{m,1} & \dots & x_{m,d} \end{pmatrix} \quad (2)$$

In Eq. (10),  $m$  indicates the count of sparrows, and  $d$  denotes the dimension of the variable that is enhanced. The fitness function (FF) corresponds to all the sparrows are characterized as an  $F$  matrix:

$$F = \begin{pmatrix} f([x_{1,1} \dots x_{1,d}]) \\ \vdots \\ f([x_{m,1} \dots x_{m,d}]) \end{pmatrix} \quad (3)$$

where  $f([x_{i,1}, \dots, x_{i,d}])$  signifies the fitness value of  $i - th$  sparrows. In all the iterations, the position of discoverer will be upgraded, as follows:

$$X_{ij}^{t+1} = \begin{cases} x_{ij}^t \cdot \exp\left(\frac{-i}{\alpha \cdot N}\right), & \text{if } R_2 < ST \\ x_{ij}^t + Q \cdot L, & \text{if } R_2 \geq ST \end{cases} \quad (4)$$

where  $t$  signifies the existing amount of iterations, and  $N$  signifies the maximum amount.  $\alpha$  indicates a random integer, and  $\alpha \in (0, 1]$ .  $R_2$  characterizes the alarm value that is an arbitrary integer, and  $R_2 \in [0, 1][0, 1]$ .  $ST$  signifies the safety threshold and  $ST \in [0.5, 1.0]$ .  $Q$  shows the random number subjected to the standard distribution, and  $L$  represents the row vector whose element is equivalent to 1. The updating rules of the follower are shown below:

$$X_{ij}^{t+1} = \begin{cases} Q \cdot \exp\left(\frac{X_W^t - X_{ij}^t}{i^2}\right), & \text{if } i > \frac{n}{2} \\ x_{DB}^{t+1} + |X_{ij}^t - x_{DB}^{t+1}| \cdot M' \cdot L, & \text{if } i \leq \frac{n}{2} \end{cases} \quad (5)$$

In Eq. (5)  $X_W^t$  signifies the worst location of the  $t - th$  iteration, and  $x_{DB}^{t+1}$  signifies the location of finders with maximum fitness value at the  $t + 1$  iteration.  $M$  signifies the  $1 \times d$

**TABLE 2.** Classifier outcome of SSODL-DFUDC approach with distinct measures and folds.

Class	Accuracy <sub>bal</sub>	Precision	Recall	F-Score	AUC Score	MCC
<b>Fold - 1</b>						
Abnormal	99.02	99.27	99.02	99.15	99.17	98.34
Normal	99.31	99.08	99.31	99.19	99.17	98.34
Average	<b>99.17</b>	<b>99.17</b>	<b>99.17</b>	<b>99.17</b>	<b>99.17</b>	<b>98.34</b>
<b>Fold - 2</b>						
Abnormal	98.78	99.26	98.78	99.02	99.04	98.10
Normal	99.31	98.85	99.31	99.08	99.04	98.10
Average	<b>99.04</b>	<b>99.06</b>	<b>99.04</b>	<b>99.05</b>	<b>99.04</b>	<b>98.10</b>
<b>Fold - 3</b>						
Abnormal	98.78	99.26	98.78	99.02	99.04	98.10
Normal	99.31	98.85	99.31	99.08	99.04	98.10
Average	<b>99.04</b>	<b>99.06</b>	<b>99.04</b>	<b>99.05</b>	<b>99.04</b>	<b>98.10</b>
<b>Fold - 4</b>						
Abnormal	99.02	99.27	99.02	99.15	99.17	98.34
Normal	99.31	99.08	99.31	99.19	99.17	98.34
Average	<b>99.17</b>	<b>99.17</b>	<b>99.17</b>	<b>99.17</b>	<b>99.17</b>	<b>98.34</b>
<b>Fold - 5</b>						
Abnormal	99.02	99.27	99.02	99.15	99.17	98.34
Normal	99.31	99.08	99.31	99.19	99.17	98.34
Average	<b>99.17</b>	<b>99.17</b>	<b>99.17</b>	<b>99.17</b>	<b>99.17</b>	<b>98.34</b>
<b>Fold - 6</b>						
Abnormal	99.02	99.27	99.02	99.15	99.17	98.34
Normal	99.31	99.08	99.31	99.19	99.17	98.34
Average	<b>99.17</b>	<b>99.17</b>	<b>99.17</b>	<b>99.17</b>	<b>99.17</b>	<b>98.34</b>
<b>Fold - 7</b>						
Abnormal	98.78	99.26	98.78	99.02	99.04	98.10
Normal	99.31	98.85	99.31	99.08	99.04	98.10
Average	<b>99.04</b>	<b>99.06</b>	<b>99.04</b>	<b>99.05</b>	<b>99.04</b>	<b>98.10</b>
<b>Fold - 8</b>						
Abnormal	99.27	99.27	99.27	99.27	99.29	98.58
Normal	99.31	99.31	99.31	99.31	99.29	98.58
Average	<b>99.29</b>	<b>99.29</b>	<b>99.29</b>	<b>99.29</b>	<b>99.29</b>	<b>98.58</b>
<b>Fold - 9</b>						
Abnormal	99.02	99.27	99.02	99.15	99.17	98.34
Normal	99.31	99.08	99.31	99.19	99.17	98.34
Average	<b>99.17</b>	<b>99.17</b>	<b>99.17</b>	<b>99.17</b>	<b>99.17</b>	<b>98.34</b>
<b>Fold - 10</b>						
Abnormal	98.78	96.20	98.78	97.47	97.55	95.06
Normal	96.31	98.82	96.31	97.55	97.55	95.06
Average	<b>97.55</b>	<b>97.51</b>	<b>97.55</b>	<b>97.51</b>	<b>97.55</b>	<b>95.06</b>

matrix where the element is randomly fixed to 1 or—1,  $M' = M^T(M \cdot M^T)^{-1}$ , and  $M^T$  implies the matrix was transposed. The position updating of vigilant is:

$$X_{i,j}^{t+1} = \begin{cases} x_{GB}^t + \gamma \cdot |X_{ij}^t - x_{GB}^t|, & \text{if } f_i \neq f_B \\ x_{GB}^t + k \cdot \left( \frac{X_{ij}^t - x_{GB}^t}{|f_i - f_w| + \epsilon} \right), & \text{if } f_i = f_B \end{cases} \quad (6)$$

In Eq. (6),  $x_{GB}^t$  signifies the global optimum position at  $t$  the  $t$ th iteration,  $\gamma$  indicates the control step size, and  $\gamma \sim N(O, 1)$ .  $k$  shows the random value and  $k \in [-1, 1]$ , while  $\epsilon$  indicates the constant that rises to avoid the denominator from being.  $f_i$  indicates the fitness value of  $i - t$ th sparrows, whereas  $f_B$  and  $f_w$  signify the fitness values of global optimum and worst sparrows, correspondingly. The superparameters that the SSO could alter include the safety value ST, the maximal amount of iterations  $N$ , and  $n$ , the number of sparrows. Furthermore, there are upper and lower bounds of the independent parameter  $DL$ , several discoveries  $PD$ , and the number of vigilantes  $SD$ . The independent parameter's d dimension is determined by the number of network layers and the input vector.

The fitness selection can be a vital element in the SSO method. Solution encoding can be used to evaluate the goodness of the candidate solution. The accuracy value was the main condition used to devise an FF.

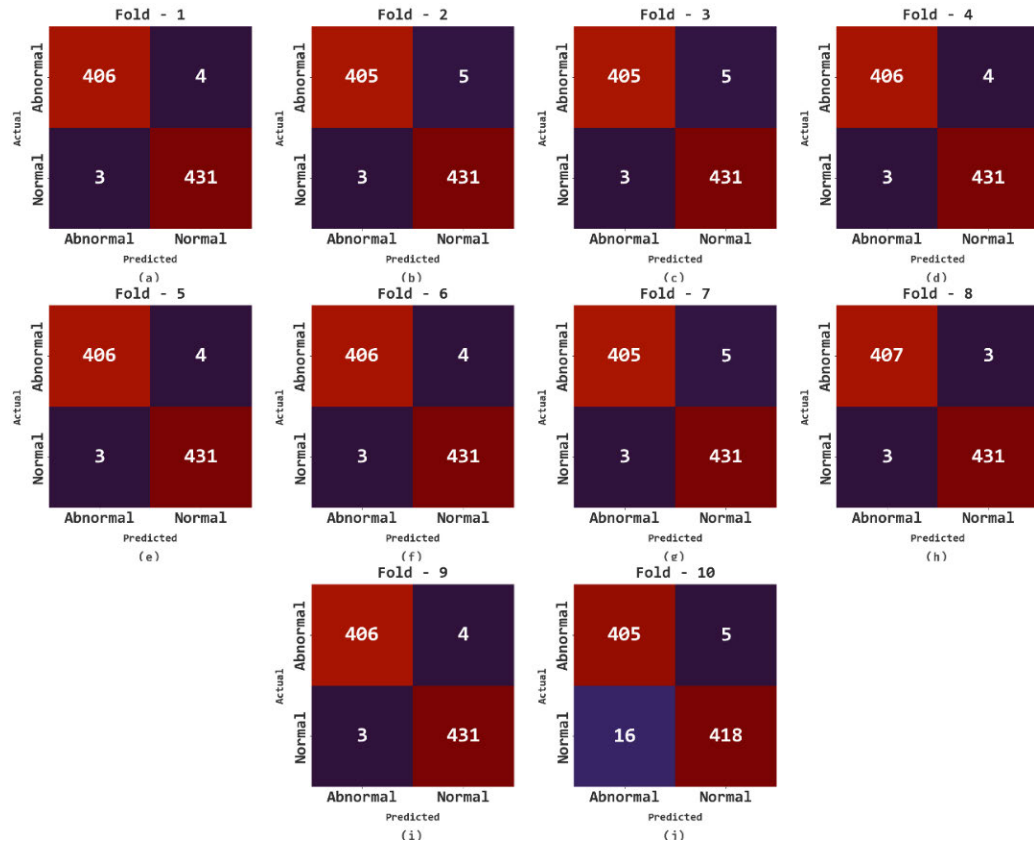
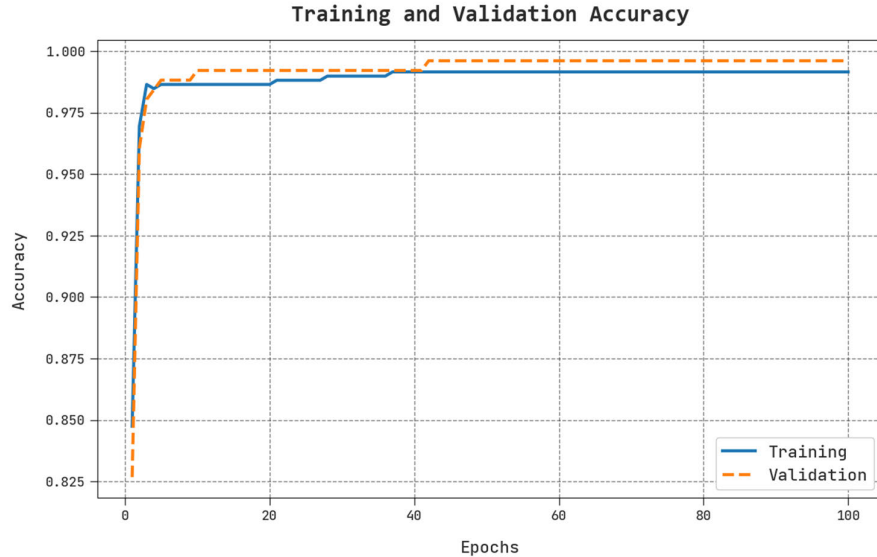
$$\text{Fitness} = \max(P) \quad (7)$$

$$P = \frac{TP}{TP + FP} \quad (8)$$

From the expression, TP represents the true positive, and FP denotes the false positive value.

## B. DFU CLASSIFICATION USING THE SSAE MODEL

In this study, the classification of DFU takes place using the SSAE model. Hinton, in 2006, proposed an Autoencoder (AE) paradigm of ANN, and it is extensively used in reduction dimensionality [33]. The primary objective is to train the model with a similar input and output dataset. The architecture of the AE network contains a hidden layer (HL) with  $m$  neurons, an input layer with  $n$  neurons, and an output layer with  $n$  neurons. Firstly, the  $n$ -dimension sample is mapped from the input to the hidden layers that characterize an encoding method of  $h_{w1,b1}(x) \in R^m$ . Following,

**FIGURE 3.** Confusion matrices of SSODL-DFUDC approach (a-j) Fold 1-10.**FIGURE 4.** TACC and VACC analysis of the SSODL-DFUDC system.

$h_{w1,b1}(x)$  is decoded from the HL and mapped back to the  $n$ -dimensional space  $R^n$  to recreate the input. The training process of the AE network is to perform the backpropagation of error and continuously upgrade the network parameter for making the  $\tilde{x}$  output to the  $x$  input, where  $\tilde{x} = h_{w,b}(x)$ . The

loss function of the AE network can be determined by:

$$J_{AE}(W, b) = \frac{1}{N} \sum_{i=1}^m \left( \frac{1}{2} \|\tilde{x}_i - x_i\|_2^2 \right) + \frac{\lambda}{2} \sum_{j=1}^2 \|W_j\|_2^2 \quad (9)$$

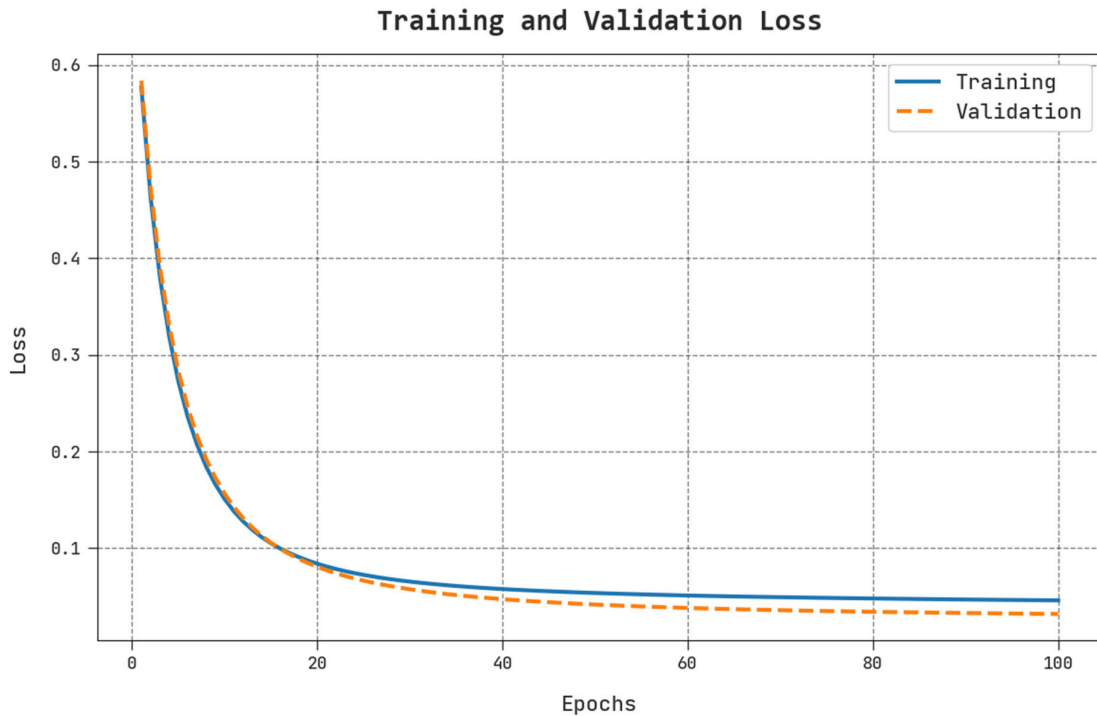


**FIGURE 5.** TLS and VLS analysis of SSODL-DFUDC system.

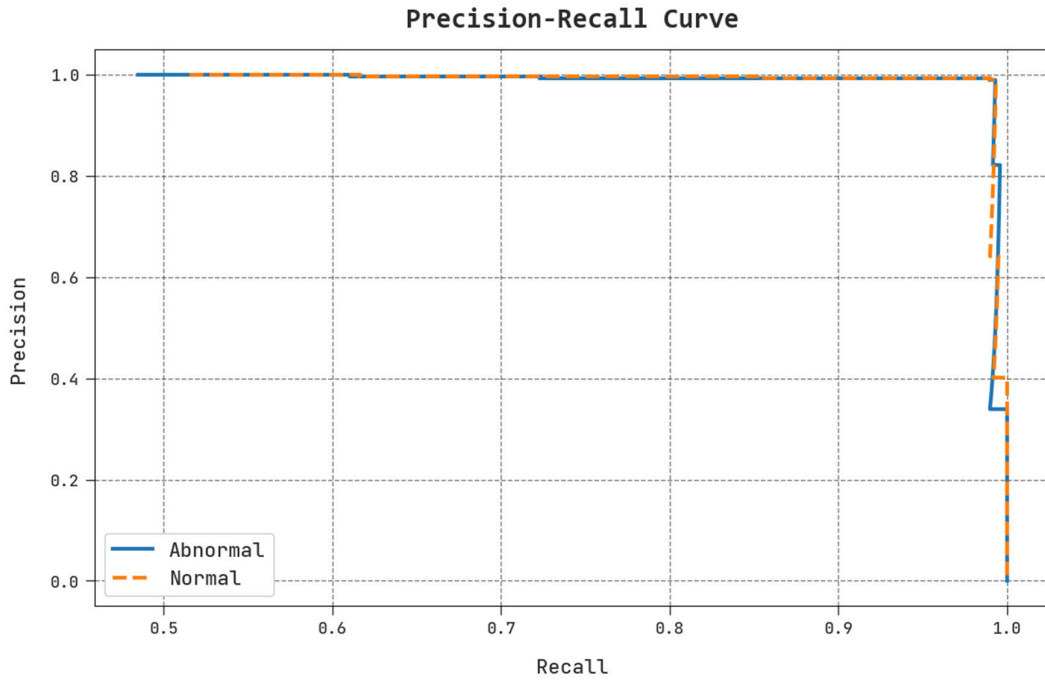


**FIGURE 6.** Precision-recall analysis of SSODL-DFUDC system.

where  $J_{AE}(W, b)$  indicates the loss function of the AE network,  $x$  denotes the input of the network,  $\tilde{x}$  shows the output of the network,  $N$  represents the overall amount of input samples,  $\|W_j\|_2^2$  shows the regularization,  $W_j$  indicates the

weight matrices between  $j^{th}$  layers and the next layer, and  $\lambda$  denotes the weight of regularization. Once the amount of HL nodes is lesser than the input layer, the output of HL is regarded as a new feature extracted to accomplish

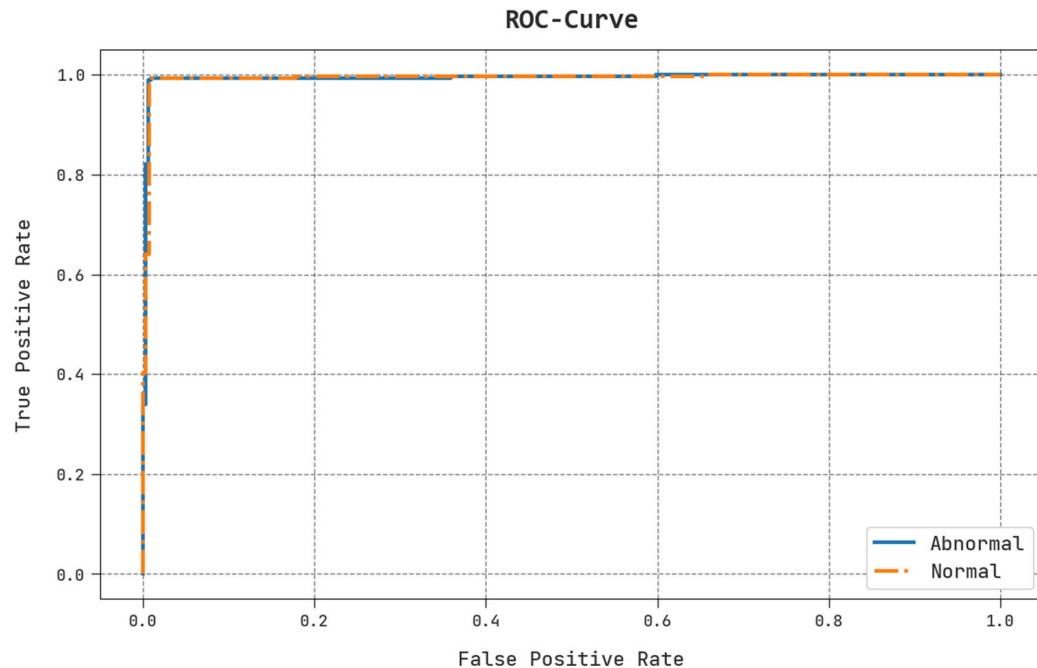


**FIGURE 7.** ROC analysis of the SSODL-DFUDC system.

reduction dimensionality. Once the amount of HL nodes is larger, a sparse autoencoder (SAE) is adopted. To avoid overfitting, SAE added sparsity limitation to the AE network and exploited the sigmoid function as an activation function that inhibits the neuron in the hidden layer. The suppressed state implies that the neuron output is closer to zero. For the input  $x$ , the activation degree of  $j^{th}$  neurons in the HL is  $h_j(x)$ , then the average activation degree of these neurons in the entire training samples  $S = \{x_{(i)}\}_{i=1}^N$  is  $\hat{\rho}_j = \frac{1}{N} \sum_{i=1}^N h_j(x_{(i)})$ . To guarantee that the neuron is suppressed, we must make the average activation degree closer to the sparse variable  $\rho$ , which is generally closer to zero. A penalty factor is added to the loss function of AE to accomplish the sparsity. The loss function of the SAE network is formulated by:

$$J_{\text{sparse}}(W, b) = J_{AE}(W, b) + \beta \sum_{j=1}^J \text{KL}(\rho \parallel \hat{\rho}_j) \quad (10)$$

In Eq. (10),  $\hat{\rho}_j$  indicates the average activation degree of each neuron with every training sample,  $\rho$  denotes the sparse variable to be set.  $\text{KL}(\rho \parallel \hat{\rho}_j)$  represents the relative entropy between  $\rho$  and  $\hat{\rho}_j$ , viz., the KL divergence that value increases monotonically as the difference between  $\rho$  and  $\hat{\rho}_j$ .  $\beta$  denotes the weight of KL divergence. Once  $\rho$  and  $\hat{\rho}_j$  are equivalent, then  $\text{KL}(\rho \parallel \hat{\rho}_j)$  is equivalent to for getting its minimal value. Since  $\rho$  is generally closer to zero,  $\hat{\rho}_j$  of each neuron in the HL would be controlled to be within a smaller range afterwards training, and the sparse representation of the input signal is lastly attained. The SSAE is encompassed by a single-layer SAE network, with the output of SAE of the preceding layer, which acts as an input of SAE of the following adjacent layer. By training the SAE network layer-wise, the SSAE network

could eventually extract the feature concealed in the input for realizing reduction dimensionality.

#### IV. EXPERIMENTAL VALIDATION

In this section, the DFU results of the SSODL-DFUDC technique are tested using a dataset from the Kaggle repository [34]. The dataset includes 844 samples, with 410 abnormal and 434 standard samples, as demonstrated in Table 1. Fig. 2 showcases the sample images of normal and abnormal.

Table 2 represents the overall DFU detection results of the SSODL-DFUDC technique under different folds. The results showed that the SSODL-DFUDC technique has enhanced results under all folds. For instance, with fold-1, the SSODL-DFUDC technique reaches average  $accu_{bal}$ ,  $prec_n$ , and  $recal$  of 99.17%, 99.17%, and 99.17%, respectively. Meanwhile, with fold-5, the SSODL-DFUDC system gains average  $accu_{bal}$ ,  $prec_n$ , and  $recal$  of 99.17%, 99.17%, and 99.17%, correspondingly. Eventually, with fold-10, the SSODL-DFUDC approach attains average  $accu_{bal}$ ,  $prec_n$ , and  $recal$  of 99.55%, 97.51%, and 97.55%, correspondingly.

The TACC and VACC of the SSODL-DFUDC approach are investigated on DFU performance in Fig. 4. The figure pointed out that the SSODL-DFUDC system has shown improved performance with improved values of TACC and VACC. It is perceptible that the SSODL-DFUDC system has reached maximal TACC outcomes.

The classification results of the SSODL-DFUDC technique are inspected in the form of a confusion matrix in Fig. 3. The results implied that the SSODL-DFUDC technique has successfully recognized the presence of normal and abnormal samples.

**TABLE 3.** Comparative analysis of SSODL-DFUDC system with existing algorithms [35].

Methods	Accuracy	Precision	Recall	F1-Score
SSODL-DFUDC	99.29	99.29	99.29	99.29
Inception-ResNet-v2	98.98	98.71	98.68	98.94
AlexNet	92.01	90.93	87.22	88.94
VGG16	97.87	92.21	90.18	90.67
DFUNet-KNN	95.63	93.75	92.39	93.00
DFUNet	96.97	94.17	92.11	92.75
DFUNet-SVM	96.23	95.17	92.86	94.09
GoogleNet	97.12	95.17	90.22	92.85
EfficientNet	98.89	98.64	98.54	99.11

The TLS and VLS of the SSODL-DFUDC method are tested on DFU performance in Fig. 5. The figure states that the SSODL-DFUDC technique has exposed improved performance with the lowest values of TLS and VLS. It is observable that the SSODL-DFUDC model has resulted in reduced VLS outcomes.

An evident precision-recall study of the SSODL-DFUDC methodology in the test database is described in Fig. 6. The figure implied that the SSODL-DFUDC system has led to superior values of precision-recall values in two classes.

A detailed ROC study of the SSODL-DFUDC algorithm in the test database is exposed in Fig. 7. The outcome stated the SSODL-DFUDC system has displayed its capability to classify two class labels.

To illustrate the enhanced performance of the SSODL-DFUDC technique, a widespread comparison study is made in Table 3 and Fig. 8 [35]. The experimental values indicated that the AlexNet model reaches poor performance. At the same time, the DFUNet-KNN, DFUNet, and DFUNet-SVM models have attained slightly enhanced outcomes. Along with that, the VGG16 and GoogleNet models have obtained moderately improved performance. Although the EfficientNet model results in reasonable performance, the SSODL-DFUDC technique outperforms the existing ones with an increased  $acc_y$  of 99.29%,  $prec_n$  of 99.29%,  $recal$  of 99.29%, and  $F1_{score}$  of 99.29%. These results assured the improved performance of the SSODL-DFUDC technique in the classification process.

## V. CONCLUSION

In this article, we have developed a novel SSODL-DFUDC system to detect and classify DFU. The presented SSODL-DFUDC technique's goal lies in identifying and classifying DFU. To accomplish this, the presented SSODL-DFUDC technique has applied the Inception-ResNet-v2 model for feature vector generation. In addition, the SSODL-DFUDC technique utilizes the SSO algorithm for hyperparameter tuning purposes. Moreover, the classification of DFU takes place using the SSAE model. The experimental results of the SSODL-DFUDC technique take place using the DFU dataset. The comprehensive experimental outcomes demonstrate

the improved efficiency of the SSODL-DFUDC approach compared to existing DL techniques. In the future, the SSODL-DFUDC algorithm's performance can be improved by advanced DL classification models. In addition, weakly supervised learning techniques can be explored to reduce the dependency on precise pixel-level annotations. Instead of relying solely on expert-labeled ulcer regions, weakly supervised learning can utilize weak labels, such as image-level or bounding box annotations, making it more scalable and easier to collect data.

## ACKNOWLEDGEMENT

Princess Nourah bint Abdulrahman University Researchers Supporting Project number (PNURSP2023R300), Princess Nourah bint Abdulrahman University, Riyadh, Saudi Arabia.

## REFERENCES

- [1] S. Wang, J. Wang, M. X. Zhu, and Q. Tan, "Machine learning for the prediction of minor amputation in university of Texas grade 3 diabetic foot ulcers," *PLoS ONE*, vol. 17, no. 12, Dec. 2022, Art. no. e0278445.
- [2] M. Swerdlow, L. Shin, K. D'Huyvetter, W. J. Mack, and D. G. Armstrong, "Initial clinical experience with a simple, home system for early detection and monitoring of diabetic foot ulcers: The foot selfie," *J. Diabetes Sci. Technol.*, vol. 17, no. 1, pp. 79–88, Jan. 2023.
- [3] M. Goyal, N. D. Reeves, S. Rajbhandari, N. Ahmad, C. Wang, and M. H. Yap, "Recognition of ischaemia and infection in diabetic foot ulcers: Dataset and techniques," *Comput. Biol. Med.*, vol. 117, Feb. 2020, Art. no. 103616.
- [4] J. Yogapriya, V. Chandran, M. G. Sumithra, B. Elakkiya, A. S. Ebenezer, and C. S. G. Dhas, "Automated detection of infection in diabetic foot ulcer images using convolutional neural network," *J. Healthcare Eng.*, vol. 2022, pp. 1–12, Apr. 2022.
- [5] K. S. Chan and Z. J. Lo, "Wound assessment, imaging and monitoring systems in diabetic foot ulcers: A systematic review," *Int. Wound J.*, vol. 17, no. 6, pp. 1909–1923, Dec. 2020.
- [6] B. Cassidy, C. Kendrick, N. D. Reeves, J. M. Pappachan, C. O'Shea, D. G. Armstrong, and M. H. Yap, "Diabetic foot ulcer grand challenge 2021: Evaluation and summary," in *Diabetic Foot Ulcers Grand Challenge*. Cham, Switzerland: Springer, Sep. 2021, pp. 90–105.
- [7] H. Pan, H. Peng, Y. Xing, L. Jiayang, X. Hualiang, T. Sukun, and F. Peng, "Breast tumour grading network based on adaptive fusion and microscopic imaging," *Opto-Electron. Eng.*, vol. 50, no. 1, 2023, Art. no. 220158.
- [8] Y. Wang, F. Luo, X. Yang, Q. Wang, Y. Sun, S. Tian, P. Feng, P. Huang, and H. Xiao, "The Swin-transformer network based on focal loss is used to identify images of pathological subtypes of lung adenocarcinoma with high similarity and class imbalance," *J. Cancer Res. Clin. Oncol.*, vol. 149, no. 11, pp. 8581–8592, Sep. 2023.

- [9] P. Huang, X. Tan, C. Chen, X. Lv, and Y. Li, "AF-SENet: Classification of cancer in cervical tissue pathological images based on fusing deep convolution features," *Sensors*, vol. 21, no. 1, p. 122, 2020.
- [10] C. Du, Y. Li, P. Xie, X. Zhang, B. Deng, G. Wang, Y. Hu, M. Wang, W. Deng, D. G. Armstrong, Y. Ma, and W. Deng, "The amputation and mortality of inpatients with diabetic foot ulceration in the COVID-19 pandemic and postpandemic era: A machine learning study," *Int. Wound J.*, vol. 19, no. 6, pp. 1289–1297, Oct. 2022.
- [11] O. Güley, S. Pati, and S. Bakas, "Classification of infection and ischemia in diabetic foot ulcers using VGG architectures," in *Diabetic Foot Ulcers Grand Challenge*. Cham, Switzerland: Springer, Sep. 2021, pp. 76–89.
- [12] J. Tulloch, R. Zamani, and M. Akrami, "Machine learning in the prevention, diagnosis and management of diabetic foot ulcers: A systematic review," *IEEE Access*, vol. 8, pp. 198977–199000, 2020.
- [13] W. Ren, A. H. Bashkandi, J. A. Jahanshahi, A. Q. M. AlHamad, D. Javaheri, and M. Mohammadi, "Brain tumor diagnosis using a step-by-step methodology based on courtship learning-based water strider algorithm," *Biomed. Signal Process. Control*, vol. 83, May 2023, Art. no. 104614.
- [14] B. Cassidy, N. D. Reeves, J. M. Pappachan, N. Ahmad, S. Haycocks, D. Gillespie, and M. H. Yap, "A cloud-based deep learning framework for remote detection of diabetic foot ulcers," *IEEE Pervasive Comput.*, vol. 21, no. 2, pp. 78–86, Apr. 2022.
- [15] K. Munadi, K. Saddami, M. Oktiana, R. Roslidar, K. Muchtar, M. Melinda, R. Muharar, M. Syukri, T. F. Abidin, and F. Arnia, "A deep learning method for early detection of diabetic foot using decision fusion and thermal images," *Appl. Sci.*, vol. 12, no. 15, p. 7524, Jul. 2022.
- [16] M. H. Alshayeqi, S. C. Sindhu, and S. Abed, "Early detection of diabetic foot ulcers from thermal images using the bag of features technique," *Biomed. Signal Process. Control*, vol. 79, Jan. 2023, Art. no. 104143.
- [17] G. D'Angelo, D. Della-Morte, D. Pastore, G. Donadel, A. De Stefanico, and F. Palmieri, "Identifying patterns in multiple biomarkers to diagnose diabetic foot using an explainable genetic programming-based approach," *Future Gener. Comput. Syst.*, vol. 140, pp. 138–150, Mar. 2023.
- [18] L. Alzubaidi, M. A. Fadhel, S. R. Oleiwi, O. Al-Shamma, and J. Zhang, "DFU\_QUTNet: Diabetic foot ulcer classification using novel deep convolutional neural network," *Multimedia Tools Appl.*, vol. 79, nos. 21–22, pp. 15655–15677, Jun. 2020.
- [19] M. Goyal, "Novel computerised techniques for recognition and analysis of diabetic foot ulcers," Ph.D. thesis, Manchester Metropolitan Univ., 2019. [Online]. Available: [https://e-space.mmu.ac.uk/625105/1/Thesis\\_Manu\\_Revised.pdf](https://e-space.mmu.ac.uk/625105/1/Thesis_Manu_Revised.pdf)
- [20] T. Arumuga Maria Devi and R. Hepzibai, "Clinical assessment of diabetic foot ulcers using GWO-CNN based hyperspectral image processing approach," *IETE J. Res.*, 2022, doi: 10.1080/03772063.2022.2099469.
- [21] S. K. Das, P. Roy, and A. K. Mishra, "DFU\_SPNet: A stacked parallel convolution layers based CNN to improve diabetic foot ulcer classification," *ICT Exp.*, vol. 8, no. 2, pp. 271–275, Jun. 2022.
- [22] J. Amin, M. A. Anjum, A. Sharif, and M. I. Sharif, "A modified classical-quantum model for diabetic foot ulcer classification," *Intell. Decis. Technol.*, vol. 16, no. 1, pp. 23–28, Apr. 2022.
- [23] N. Al-Garaawi, R. Ebsim, A. F. H. Alharan, and M. H. Yap, "Diabetic foot ulcer classification using mapped binary patterns and convolutional neural networks," *Comput. Biol. Med.*, vol. 140, Jan. 2022, Art. no. 105055.
- [24] A. Oliveira, A. B. de Carvalho, and D. Dantas, "Faster R-CNN approach for diabetic foot ulcer detection," in *Proc. 16th Int. Joint Conf. Comput. Vis., Imag. Comput. Graph. Theory Appl.*, 2021, pp. 677–684.
- [25] C. Venkatesan, M. G. Sumithra, and M. Murugappan, "NFU-Net: An automated framework for the detection of neurotrophic foot ulcer using deep convolutional neural network," *Neural Process. Lett.*, vol. 54, no. 5, pp. 3705–3726, Oct. 2022.
- [26] C. A. Ferreira, T. Melo, P. Sousa, M. I. Meyer, E. Shakibapour, P. Costa, and A. Campilho, "Classification of breast cancer histology images through transfer learning using a pre-trained inception resnet v2," in *Proc. Int. Conf. Image Anal. Recognit.* Cham, Switzerland: Springer, May 2018, pp. 763–770.
- [27] P. Huang, P. He, S. Tian, M. Ma, P. Feng, H. Xiao, F. Mercaldo, A. Santone, and J. Qin, "A ViT-AMC network with adaptive model fusion and multiobjective optimization for interpretable laryngeal tumor grading from histopathological images," *IEEE Trans. Med. Imag.*, vol. 42, no. 1, pp. 15–28, Jan. 2023.
- [28] X. Zhou, C. Tang, P. Huang, S. Tian, F. Mercaldo, and A. Santone, "ASI-DBNet: An adaptive sparse interactive ResNet-vision transformer dual-branch network for the grading of brain cancer histopathological images," *Interdiscipl. Sci., Comput. Life Sci.*, vol. 15, no. 1, pp. 15–31, 2023, doi: 10.1007/s12539-022-00532-0.
- [29] P. Huang, X. Zhou, P. He, P. Feng, S. Tian, Y. Sun, F. Mercaldo, A. Santone, J. Qin, and H. Xiao, "Interpretable laryngeal tumor grading of histopathological images via depth domain adaptive network with integration gradient CAM and priori experience-guided attention," *Comput. Biol. Med.*, vol. 154, Mar. 2023, Art. no. 106447.
- [30] X. Zhou, C. Tang, P. Huang, F. Mercaldo, A. Santone, and Y. Shao, "LPCANet: Classification of laryngeal cancer histopathological images using a CNN with position attention and channel attention mechanisms," *Interdiscipl. Sci., Comput. Life Sci.*, vol. 13, no. 4, pp. 666–682, Dec. 2021.
- [31] P. Huang, X. Tan, X. Zhou, S. Liu, F. Mercaldo, and A. Santone, "FABNet: Fusion attention block and transfer learning for laryngeal cancer tumor grading in P63 IHC histopathology images," *IEEE J. Biomed. Health Informat.*, vol. 26, no. 4, pp. 1696–1707, Apr. 2022.
- [32] Y. Guo, D. Yang, Y. Zhang, L. Wang, and K. Wang, "Online estimation of SOH for lithium-ion battery based on SSA-elman neural network," *Protection Control Mod. Power Syst.*, vol. 7, no. 1, pp. 1–17, Dec. 2022.
- [33] B. Li, S. Liang, D. Chen, and X. Li, "A decision-making method for air combat maneuver based on hybrid deep learning network," *Chin. J. Electron.*, vol. 31, no. 1, pp. 107–115, Jan. 2022.
- [34] *Diabetic Foot Ulcer (DFU)*. Accessed: Jul. 14, 2023. [Online]. Available: <https://www.kaggle.com/datasets/laithjj/diabetic-foot-ulcer-dfu>
- [35] P. N. Thotad, G. R. Bharamagoudar, and B. S. Anami, "Diabetic foot ulcer detection using deep learning approaches," *Sensors Int.*, vol. 4, Jan. 2023, Art. no. 100210.



**SUNNAM NAGARAJU** received the B.Tech. degree from JNTUH, Hyderabad, in 2007, and the M.Tech. degree from NIT, Trichy, Tamil Nadu. He was an Assistant Professor with Lovely Professional University, Jalandhar, Punjab, India, from 2010 to 2016. He was also a Plant Engineer with OCTL, Hyderabad. He is currently an Associate Professor with MLRIT, Hyderabad, in 2010.



**KOLLATI VIJAYA KUMAR** received the Ph.D. degree in computer science and engineering from Karpagam University, Coimbatore. He has 15 years of teaching experience. He is currently an Associate Professor with the Department of CSE, GITAM School of Technology, GITAM University, Visakhapatnam, Andhra Pradesh, India. He has published 24 articles in international journals. His research interests include wireless networking, big data, data analytics, network security, cloud computing, and information security.

**B. PRAMEELA RANI** received the B.Tech. degree from the Aditya College of Engineering and Technology (ACET), Surampalem, in 2014, and the M.Tech. degree from the Aditya College of Engineering (Autonomous), Surampalem. She is currently an Assistant Professor with the Aditya College of Engineering. She was an Instructor in engineering colleges, from 2014 to 2021, on various technologies. Her current research interests include machine learning models and deep learning mechanisms.



**E. LAXMI LYDIA** is currently a Professor in computer science engineering with GMRIT. She is also a Big Data Analytics Online Trainer with the International Training Organization. She has presented various webinars on big data analytics. She is also with the Government DST Funded Project. She is also certified by the Microsoft Certified Solution Developer (MCSD). She is the author of the *Big Data Analytics* book. She holds a patent. She has published ten research papers in international conference proceedings. She has published more than 100 research articles in international journals in *Big Data Analytics* and *Data Science Journal*.



**MOHAMAD KHAIRI ISHAK** received the B.Eng. degree in electrical and electronics engineering from International Islamic University Malaysia (IIUM), Malaysia, the M.Sc. degree in embedded system from the University of Essex, U.K., and the Ph.D. degree from the University of Bristol, U.K. He is currently a Registered Graduate Engineer with the Board of Engineers Malaysia (BEM). He is also a Senior Lecturer in mechatronics engineering with the School of Electrical and Electronic Engineering, Universiti Sains Malaysia (USM). His background includes outstanding teaching experience with Universiti Sains Malaysia, instructing students to stimulate engineering information interest and retention while invigorating classes through the use of new technologies and models. His research interests include embedded systems, real-time control communications, and Internet of Things (IoT). Emphasis is given toward the development of theoretical and practical methods which can be practically validated. Recently, significant research effort has been directed toward important industrial issues of embedded networked control systems and IoT.

**IMEN FILALI** received the master's degree in networks and distributed systems and the Ph.D. degree from the University of Nice Sophia-Antipolis, France, in 2007 and 2011, respectively. She has been an Assistant Professor with the National Engineering School of Gabes, Tunisia, since 2011. From December 2014 to September 2015, she was a Postdoctoral Researcher with the Swiss Federal Institute of Technology of Lausanne (EPFL) working within the Distributed Information Systems Laboratory (LSIR). Since January 2018, she has been with the Department of Computer Science, College of Computer and Information Sciences, Princess Nourah Bint Abdulrahman University, as an Assistant Professor. Her main research interests include cloud computing, big data analytics, artificial intelligence, and computer vision.

**FATEN KHALID KARIM** received the Ph.D. degree in computing and information technology from Flinders University, SA, Australia. She is currently an Assistant Professor with the Department of Computer Sciences, College of Computer and Information Sciences, Princess Nourah Bint Abdulrahman University, Riyadh, Saudi Arabia. Her research interests include cloud computing and information technology. She has published several research articles in her field.



**SAMIH M. MOSTAFA** received the bachelor's and M.Sc. degrees in computer science from the Computer Science-Mathematics Department, Faculty of Science, South Valley University, in 2004 and 2010, respectively, and the Ph.D. degree in computer science from the Advanced Information Technology Department, Graduate School of Information Technology, Kyushu University, Japan, in 2017. His research interests include machine learning and CPU scheduling. He is currently a fellow of the Academy of Scientific Research and Technology (ASRT), Egypt.

• • •

# Journal of Biomedical Optics

BiomedicalOptics.SPIEDigitalLibrary.org

## Automatic detection of diabetic foot complications with infrared thermography by asymmetric analysis

Chanjuan Liu  
Jaap J. van Netten  
Jeff G. van Baal  
Sicco A. Bus  
Ferdi van der Heijden

# Automatic detection of diabetic foot complications with infrared thermography by asymmetric analysis

Chanjuan Liu,<sup>a</sup> Jaap J. van Netten,<sup>b</sup> Jeff G. van Baal,<sup>b</sup> Sicco A. Bus,<sup>b,c</sup> and Ferdi van der Heijden<sup>a,\*</sup>

<sup>a</sup>University of Twente, Faculty of Electrical Engineering, Mathematics and Computer Science, P.O. Box 217, 7500AE Enschede, The Netherlands

<sup>b</sup>Ziekenhuisgroep Twente, Department of Surgery, Diabetic Foot Unit, P.O. Box 7600, 7600SZ Almelo, The Netherlands

<sup>c</sup>University of Amsterdam, Academic Medical Center, Department of Rehabilitation, Meibergdreef 9, 1105AZ Amsterdam, The Netherlands

**Abstract.** Early identification of diabetic foot complications and their precursors is essential in preventing their devastating consequences, such as foot infection and amputation. Frequent, automatic risk assessment by an intelligent telemedicine system might be feasible and cost effective. Infrared thermography is a promising modality for such a system. The temperature differences between corresponding areas on contralateral feet are the clinically significant parameters. This asymmetric analysis is hindered by (1) foot segmentation errors, especially when the foot temperature and the ambient temperature are comparable, and by (2) different shapes and sizes between contralateral feet due to deformities or minor amputations. To circumvent the first problem, we used a color image and a thermal image acquired synchronously. Foot regions, detected in the color image, were rigidly registered to the thermal image. This resulted in  $97.8\% \pm 1.1\%$  sensitivity and  $98.4\% \pm 0.5\%$  specificity over 76 high-risk diabetic patients with manual annotation as a reference. Nonrigid landmark-based registration with B-splines solved the second problem. Corresponding points in the two feet could be found regardless of the shapes and sizes of the feet. With that, the temperature difference of the left and right feet could be obtained. © 2015 Society of Photo-Optical Instrumentation Engineers (SPIE) [DOI: 10.1117/1.JBO.20.2.026003]

**Keywords:** diabetic foot complications; prevention; infrared imaging; inflammation; thermal image segmentation; asymmetric analysis; telemedicine.

Paper 140467PR received Jul. 21, 2014; accepted for publication Jan. 12, 2015; published online Feb. 11, 2015.

## 1 Introduction

Diabetes mellitus (DM) is one of the major health care problems worldwide and continues to increase in population and significance.<sup>1</sup> Foot diseases are common and costly complications of DM. Approximately 15% to 25% of patients with DM eventually develop a foot ulcer.<sup>2</sup> This is one of the key complications of DM: if not adequately treated, the risk of amputations and mortality is increased.<sup>3</sup> Early identification and subsequent treatment of diabetic foot complications and its presigns, such as ulceration, inflammation, callus formation, and blisters, are fundamental in the prevention of these devastating consequences. Timing is essential for early identification. However, frequent risk assessment by health care professionals is costly and impractical. Manual examination of patients has its limitations because of various health impairments caused by DM such as peripheral neuropathy, visual impairment, limited joint mobility, and cognitive impairments.<sup>4</sup> Automatic assessment and detection of diabetic foot complications in a noninvasive, noninteractive, and easy to use manner may be a major benefit for foot care. The objective of our project is to develop technology that enables automated foot assessment in order to detect diabetic foot complications. Such a technology could then be applied in an intelligent (tele)medicine system to be deployed at the patients' homes, at health centers, or perhaps at hospitals. We investigate three possible imaging modalities: hyperspectral imaging, photometric stereo imaging, and thermal imaging. Within the context of the project, the current paper only addresses the

image processing and pattern analysis needed for the detection of complications in infrared (IR) thermographic images. The engineering of the telemedicine apparatus, suitable for use in, for instance, a home environment and the exploration of its usability and cost effectiveness are outside the scope of this paper.

### 1.1 Related Work

#### 1.1.1 Telemedicine using digital photography

Frequent foot screening for risk assessment is possible by means of telemedicine systems based on digital photography.<sup>5,6</sup> However, inflammation and infection, which are the vicarious markers of diabetic foot complications, are difficult to assess using digital photography.<sup>5</sup> Furthermore, such systems are not yet capable of automatic detection of diabetic foot complications. This limits their application and implementation.

#### 1.1.2 Thermography

Associations have been found between increased plantar foot temperature and the occurrence of diabetic foot complications.<sup>7</sup> Clinical studies on the home monitoring of plantar foot temperature have shown that frequent temperature assessment and treatment in the case of temperature differences  $>2.2^\circ\text{C}$ , between a foot region and the same region on the contralateral foot, can prevent diabetic foot complications.<sup>8,9</sup> Thus, thermography is a promising modality for an intelligent telemedicine monitoring system.

\*Address all correspondence to: Ferdi van der Heijden, E-mail: f.vanderheijden@utwente.nl

The technologies for temperature measurement of the plantar foot fall in three categories: handheld dermal IR thermometers,<sup>8,9</sup> IR camera systems,<sup>10–12</sup> and liquid crystal thermography (LCT).<sup>13,14</sup> The use of handheld dermal IR thermometers in the home environment has been validated by randomized controlled trials for the prevention of recurrent diabetic foot ulceration.<sup>8,9</sup> The shortcoming of this technology is that the temperature is measured manually on specific spots on the foot. This makes it subjective, and it is impossible to obtain the temperature distribution of the whole foot. Furthermore, this technology misses the opportunity for automatic detection of diabetic foot complications. Compared with LCT, IR camera systems have the advantage of being noncontact, which prevents unwanted pressures and the transmission of pathological organisms.<sup>15</sup> The temperatures of noncontact foot regions, such as the medial arch, can be easily measured with IR camera systems. Additionally, it is capable of measuring the dorsal side of the foot as well. As such, IR camera systems show a greater potential for telemedical applications and they will be the focus of this article.

### 1.1.3 Asymmetric analysis

The methodology for attaining temperature differences between corresponding areas on the left and right feet, can be referred to as “asymmetric analysis.”<sup>11,12</sup> Generally, three steps are involved:

1. Foot segmentation: Extract the left and the right feet from the background.
2. Feet registration: Register the two feet to associate areas of one foot with the corresponding areas of the contralateral foot.
3. Detection: Compare the temperature of the associated areas: if the difference between the temperatures of two associated areas is larger than a certain threshold, then one of these two areas is assumed to be at risk.

Kaabouch et al. conducted studies using thermal images to detect neuropathic ulceration, combining a genetic automatic thresholding algorithm with “asymmetric analysis”<sup>11</sup> and “line scanning.”<sup>12</sup> The authors noted that the asymmetric analysis tended to find false abnormal areas when the left and right

feet had different sizes and shapes. In these cases, noncorresponding areas were compared. The “line scanning” algorithm was proposed to overcome this limitation, but this algorithm was not targeted for strong foot deformations such as the one caused by minor amputations. The method was correspondingly validated: diabetic feet with strong deformations were not included. However, foot deformations and/or minor amputations frequently cause morphological differences between the left and right feet in patients at high risk for developing diabetic foot complications.<sup>3</sup> In these cases, the association between left and right parts of the feet is nontrivial. Another problem is in the segmentation of the feet in the thermal image. It cannot be prevented that sometimes the temperature of a part of the foot is similar to the ambient temperature of the setup.<sup>16</sup> The genetic automatic thresholding techniques cannot accurately detect these foot boundaries.<sup>17</sup> For instance, in the case in Fig. 1(a), due to poor blood perfusion the temperature of the top of the toes is almost equal to the room temperature. A stabilization of the temperature of the setup below the ambient temperature is not desirable because of the discomfort for the patient and for technical reasons.

This article aims to overcome the shortcomings mentioned above. The improvements are as follows:

- More accurate foot segmentations in the thermal images even when there was no clear thermal contrast between foot and background. This was due to the accompanying color images that guided the segmentation.
- A better association between corresponding areas in the left and right feet regardless of the foot poses, positions, shapes, or sizes, and even with amputated parts. This was obtained by using nonrigid landmark-based registration B-splines.<sup>18,19</sup>
- The validation of the image analysis was applied to a group of high-risk diabetic patients that showed significant asymmetries between left and right feet, rather than to subjects with healthy feet.

### 1.2 Outline of the Article

In Sec. 2, the experimental setup for acquiring thermal images and color images from patients with DM, the measurement

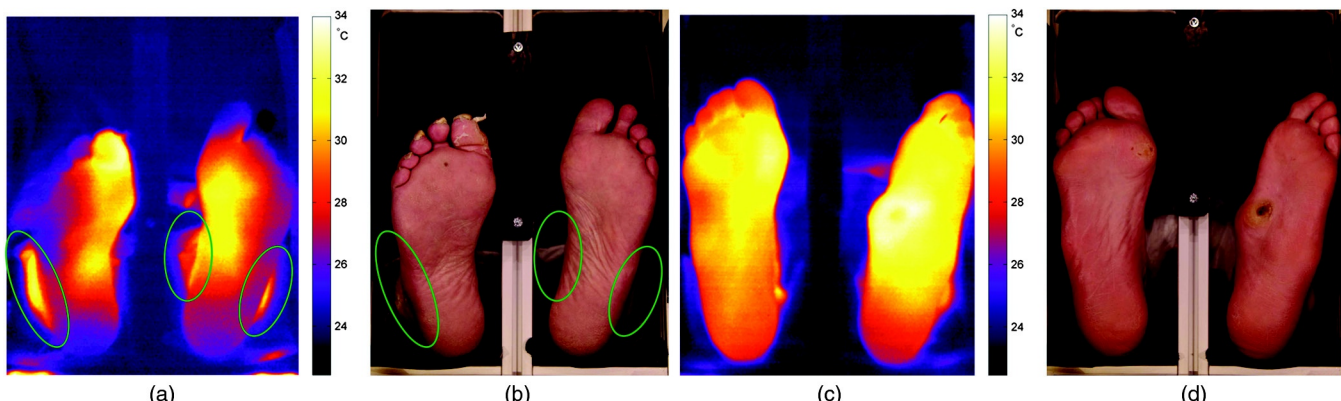


**Fig. 1** Examples of acquired thermal images with their RGB images. In example 1, the patient has cold toes, which have temperatures comparable with the background. Ankles have temperatures comparable with the feet (green ellipses). The ankles are also visible in the RGB image (green ellipses). In this modality, segmentation is difficult but not impossible, as shown in Fig. 7. (a) Example 1; (b) RGB image for example 1; (c) example 2; and (d) RGB image for example 2.

procedure, patient recruitment, and data collection are described. The methodology of conducting asymmetric analysis to detect foot complications using the assistance of color images and non-rigid landmark-based registration with B-splines is introduced in Sec. 3. Analysis, results, and discussion follow in Sec. 4. Finally, conclusions and future plans are presented in Sec. 5.

## 2 Materials and Measurements

Figure 2 presents an experimental setup that housed the acquisition devices for thermal imaging and RGB imaging. As the setup also housed hyperspectral imaging and photometric stereo imaging, thereby offering a versatile platform for experimentation, it was rather large. In a later stage of development, a user friendly, cheaper, and down-scaled version can be engineered for further clinical evaluation and effectiveness studies. The equipment for the thermal imaging modality consisted of an IR camera, FLIR SC305, and a commercial digital RGB camera, Canon EOS 40D. A separate RGB camera was chosen instead of an IR camera with a built-in visual camera to have full freedom in selecting the two cameras with their desired specifications. The IR camera was placed at a distance of 860 mm from the object plane. The camera's specification is as follows. It has a resolution of  $320 \times 240$  pixels and covers a field of view of  $400 \times 350 \text{ mm}^2$ . The pixel distance on the foot soles is about 1.25 mm. The spectral range is 7.5 to 13  $\mu\text{m}$ . The temperature range is from  $-20^\circ\text{C}$  to  $+120^\circ\text{C}$ . The accuracy is  $\pm 2^\circ\text{C}$ . With external thermal references in the range from  $+20^\circ\text{C}$  to  $+38^\circ\text{C}$ , we were able to reduce this to  $\pm 0.25^\circ\text{C}$ . Before deployment, we tested the nonuniformity error over the image plane (it was not specified), and this appeared to be less than  $0.25^\circ\text{C}$ . The digital camera, placed at the same distance as the IR camera, covered the same field of view and acquired images of 1936  $\times$  1288 pixels (pixel distance: 0.2 mm). The two cameras were mounted in such a way that they had the same field of view, but from slightly different view points.

Patients were recruited from the multidisciplinary diabetic foot clinic of the Hospital Group Twente, Almelo, The Netherlands. The patients included in this study were all diagnosed with DM and showed diabetic foot complications, e.g., callus, blisters, redness, ulceration, or had a history of ulceration. The average age of the 76 included patients, 64 male and 12 female, was 66 years ( $SD = 12$ ). Among them, there were 7 patients with type I DM and 69 patients with type II DM.

All patients were asked to remain in a seated position with bare feet for 5 to 10 min before the measurements. This was to achieve the equilibrium of the foot temperature. The feet were

then placed on the foot support of the experimental setup. A hospital cloth was placed over the legs of the patients for hygiene reasons and one piece of black cloth was draped over the shield of the setup to block external light entering the setup and to provide a homogeneous background. During thermal imaging, all illumination sources inside the experimental setup were turned off and turned on back during the acquisition of color images with the digital camera. A 30-min interval was assured between measurements of different patients to eliminate heat residue from the illumination or from the body of the previous patient.

For each patient, a live assessment form of the plantar surface of both feet was completed by wound care specialists. This live assessment was used as a reference for the validation of the automatic detection. Examples of the acquired thermal and RGB images are given in Fig. 1.

## 3 Methodology for Automatic Detection of Diabetic Foot Complications

### 3.1 Overview of the Proposed Methodology

The proposed methodology for patient-specific image analysis to automatically detect diabetic foot complications is illustrated in Fig. 3.

The first step after image acquisition was the segmentation of the feet. As explained in Sec. 1, the temperature difference between some foot parts and the ambient temperature can be so small that accurate segmentation is difficult to perform directly in the thermal image. Thus, foot segmentation in the color images was preceded to assist the segmentation in the thermal images. Details about foot segmentation in the color images can be found in Sec. 3.2.

The next step is the alignment of the RGB images and thermal images. If the object was situated in a single plane, a projective transform would suffice. Since we intended to acquire a thermal image without any additional pressure on the feet, no sidelong support bars were mounted that would force the feet to a standard position and orientation in the imaging system. As a result, the surfaces of the foot soles only approximately coincided with the plane that was used for the projective registration. If the object's depth varies with a deviation of  $\Delta Z$  around a mean plane depth of  $Z$ , and the distance between the view points is  $t$ , then, despite the projective transform, the parallax error could be as high as  $(t\Delta Z)/Z$ . Thus, if the object distances are large compared with  $t$ , the parallax error is negligible. This condition is usually met in commercial handheld IR

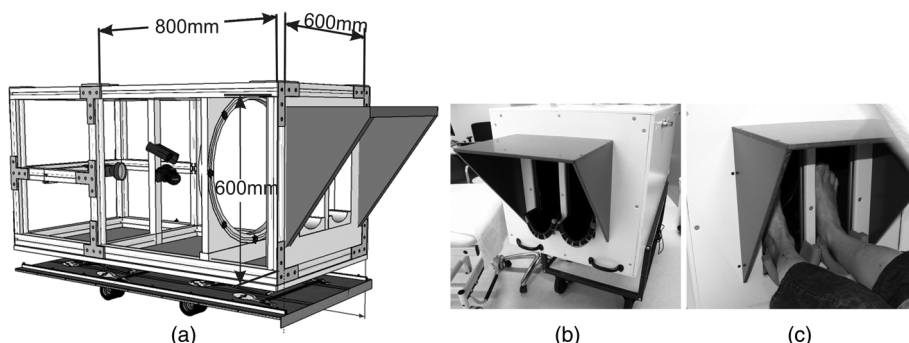


**Fig. 2** The experimental setup for foot scanning: (a) the schematic of the experimental setup with two cameras installed, which are the thermal camera (upper) and the RGB camera (lower). (b) The appearance of the experimental set and (c) positioning of patients' feet during measurement.

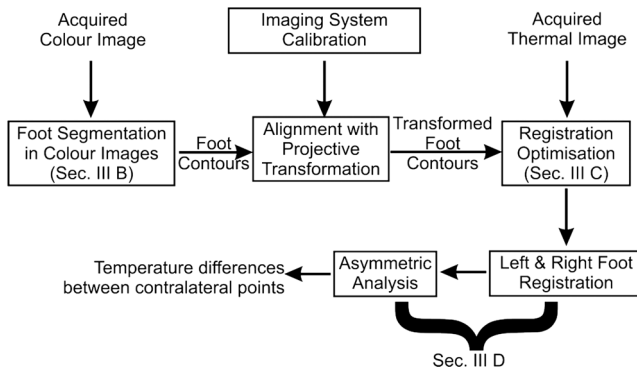


**Fig. 3** Schematic flowchart of the proposed methodology for automatic detection of diabetic foot complications.

cameras with a built-in visual camera, e.g., the FLUKE TiR27. In our case, the object distances were in the range from 80 to 90 cm, and the distance between the view points is about 15 cm, yielding a parallax error on the order of 1 cm. In a down-scaled version of the device, the view point distance could be reduced to about 5 cm (like in the FLUKE TiR27), but if the object distance were reduced proportionally, the parallax problem would remain.

The alignment was done in two steps. Before the actual deployment of the device, the parameters of a two-dimensional (2-D) projective transformation that maps the RGB images onto the thermal images were determined from 12 control points. These points were all located in a single plane in front of the cameras at a distance that matched the mean object distance. Details of the fine optimization can be found in Sec. 3.3.

The performance evaluation of the segmentation in the color images and that in the thermal images was achieved through comparison with manually segmented references provided by one of the researchers. The method for manual segmentation with custom-made software has been described elsewhere.<sup>20</sup>

The last step was to conduct asymmetric analysis to detect the temperature differences of contralateral regions on the left and right feet. To facilitate this, a good registration between left and right feet, irrespective of feet positions, poses, shapes, or sizes, was essential. Nonrigid landmark-based registration was performed for this purpose. Details of this part can be found in Sec. 3.4.

### 3.2 Foot Segmentation in Color Images

The aim of the foot segmentation with acquired color images is to determine whether a color pixel is on a foot or on the background.

#### 3.2.1 Machine learning for color image segmentation

RGB is the most common color representation for storing images. Other color representations can be obtained by a linear or a nonlinear transformation of RGB space. Although many studies have been done on the use of different color representations in segmentation, it is hard to come to a conclusion about which color space is best.<sup>21</sup> It has been observed that the skin colors differ more in intensity than in chrominance.<sup>22</sup> Thus, it is a common practice to ignore the luminance in skin color detection. In this study, we performed segmentation on the six color representations that are commonly used in human skin

detection: RGB, normalized RGB (rgb), RGB-ratio, HSV, CIE L\*a\*b\*, and YCbCr.<sup>22</sup>

Machine learning techniques play an important role in image segmentation. The goal is to partition the image plane into  $K$  disjoint regions. Suppose that the three-color channels of the  $\ell$ 'th pixel in the image are represented by a three-dimensional (3-D) vector  $\mathbf{x}_\ell \in \mathbb{R}^3$  and that the image contains  $L$  pixels, so that  $\ell = 1, 2, \dots, L$ . The segmentation is accomplished by assigning to each pixel  $\mathbf{x}_\ell$  a class label  $k_\ell$ . The set of possible class labels is  $k_\ell \in \{1, \dots, K\}$ . Each class corresponds to a region.

The techniques for machine learning can be divided into two groups: supervised and unsupervised learning.<sup>23</sup> In supervised learning, the segmentation parameters are obtained during the design stage of the segmentation by means of preselected, fixed training data. In contrast, in unsupervised learning, the segmentation parameters are calculated during the utilization of the segmentation by means of the actual data. As such, unsupervised learning has the ability to adapt itself to the statistics of this actual data.<sup>23</sup>

In this study, all patients had a wide variety in skin health status and accordingly in colors of the skin. It is difficult to cover all the possible variations in a training set. As unsupervised learning adapts itself to the data from each individual image, unsupervised learning was selected. Two common techniques in this category were chosen,  $K$ -means clustering and expectation-maximization (EM) clustering.

$K$ -means clustering is one of the simplest unsupervised learning algorithms, aiming to define  $K$  centroids for  $K$  clusters.  $K$  is predefined. At the initialization step, the  $K$  centroids are randomly picked. A binding step follows to associate each object in the training set to the nearest centroid. When no point is pending, the  $K$  centroids are recalculated. With the new  $K$  centroids, a new binding step is done. This procedure iterates until the  $K$  centroids do not move any more.  $K$ -means minimizes the sum of the distances over all objects in  $\mathbf{X}$  to the nearest center  $\mathbf{m}_k$ , and the algorithm converges to a (local) minimum.<sup>23</sup>

The EM algorithm is a popular technique in unsupervised learning.<sup>23</sup> We used the EM algorithm (as defined in Algorithm 1) for the case where the model is a mixture of Gaussian probability densities. Each class is represented by a Gaussian density  $N(\mathbf{x}|\mathbf{m}_k, \mathbf{C}_k)$  with mean  $\mathbf{m}_k$  and covariance matrix  $\mathbf{C}_k$ . The prior probabilities of the classes are denoted by  $\pi_k$ . We implemented two versions of the EM algorithm; one with class independent covariance matrices, i.e.,  $\forall k: \mathbf{C}_k = \mathbf{C}_0$ , and the other with class-dependent matrices. The first one is referred to as EM-LDC (linear discriminant classifier), and the second one as EM-QDC (quadratic discriminant classifier):

#### Algorithm 1 EM for image segmentation.

- **Inputs:** Data set with  $L$  pixels (3-D vectors)  $\mathbf{x}_\ell$ . Desired number of clusters  $K$ .
- **Output:**
  - A model consisting of the parameters of the mixture of Gaussians, i.e., for  $k = 1, \dots, K: \mathbf{m}_k, \mathbf{C}_k, \pi_k$ .
  - For each pixel  $\ell$  and each class  $k$ , an ownership variable  $y_{\ell,k}$  such that  $\sum_k y_{\ell,k} = 1$ . The ownership indicates to what degree pixel  $\mathbf{x}_\ell$  is attributed to cluster  $k$ .

- **Initialization:**

- Determine  $K$  centers  $\mathbf{m}_k$  from the  $L$  pixels using the  $K$ -means algorithm.<sup>23</sup>
- Initialize the ownerships  $y_{\ell,k}$  as the distance of pixel  $\ell$  to the class center  $\mathbf{m}_k$  relative to the sum of distances to all class centers.

- **Loop while the model improves:**

- For all  $k$ : (re-)estimate the prior probabilities:

$$\pi_k = \frac{1}{L} \sum_{\ell=1}^L y_{\ell,k}. \quad (1)$$

- For all  $k$ : (re-)estimate the means:

$$\mathbf{m}_k = \frac{1}{\pi_k L} \sum_{\ell=1}^L y_{\ell,k} \mathbf{x}_{\ell}. \quad (2)$$

- For all  $k$ : (re-)estimate the covariance matrices:

$$\mathbf{C}_k = \frac{1}{\pi_k L} \sum_{\ell=1}^L y_{\ell,k} (\mathbf{x}_{\ell} - \mu_k)(\mathbf{x}_{\ell} - \mu_k)^T. \quad (3)$$

- Equalize the covariance matrices (EM-LDC only):

$$\mathbf{C}_0 = \sum_{k=1}^K \pi_k \mathbf{C}_k \quad \mathbf{C}_k := \mathbf{C}_0. \quad (4)$$

- For all  $k$  and all  $\ell$ : re-estimate the ownerships:

$$y_{\ell,k} = \frac{\pi_k N(\mathbf{x}_{\ell}, \mathbf{m}_k, \mathbf{C}_k)}{\sum_{m=1}^K \pi_m N(\mathbf{x}_{\ell}, \mathbf{m}_m, \mathbf{C}_m)}. \quad (5)$$

There are two different regions in this application, foreground (foot regions) and background. Consequently, the number  $K$  of clusters should also be set to 2. However, since the background was made up of different parts, it could be advantageous to increase this number. It was set to 2, 3, and 4, respectively. In the case of more than two clusters, only one of them was identified as foreground (foot region). Postprocessing of the segmentation was performed by morphological operations. Small objects either in the foreground (foot area) or in the background were removed.

All the image processing and pattern classification were performed on the MATLAB R2012b platform with an additional toolbox PRtools V5<sup>23</sup> in 64 bits Windows 7.

### 3.2.2 Segmentation evaluation

To select the number  $K$  of desired clusters, and the most suitable algorithm ( $K$ -means, EM-LDC, or EM-QDC), a quantitative measure of the segmentation performance is necessary. Two measures were included in the evaluation step for the segmentation:

*Sensitivity and specificity.* Sensitivity and specificity are the measures of the performance of a two-class classification algorithm. Sensitivity, in our case, measures the ratio of the

pixels inside the feet regions that are correctly labeled. Sensitivity represents the ability of the segmentation method in finding the feet. Specificity, on the other hand, measures the portion of negatives (the background, in our case) that are correctly identified:

$$\text{Sensitivity} = \frac{|F_R \cap F_S|}{|F_R|}, \quad (6)$$

$$\text{Specificity} = \frac{|B_R \cap B_S|}{|B_R|}, \quad (7)$$

where  $B_R$  and  $F_R$  represent the background and foreground of the reference image, while  $B_S$  and  $F_S$  denote the background and foreground according to the algorithm under test, respectively.  $|\cdot|$  is the set cardinality.

*Mean distance error of wrongly classified area  $\mathbf{D}_{EA}$ .*

This reflects the cost of wrong segmentation. For each pixel on the image, the Euclidean distance was calculated to the nearest foot contours resulting in a distance map  $\mathbf{D}_{\text{map}}$  as shown in Fig. 4. The distance of each pixel that was wrongly assigned was summed up and averaged to get the mean distance error ( $\bar{D}_{EA}$ ):

$$\bar{D}_{EA} = \frac{\sum_{Nwb} \mathbf{D}_{\text{map}} \mathbf{W}_B + \sum_{Nwf} \mathbf{D}_{\text{map}} \mathbf{W}_F}{Nwb + Nwf}, \quad (8)$$

where  $\mathbf{W}_B$  represents a binary map containing the foot pixels that are wrongly assigned to the background, i.e.,  $F_R \cap B_S$  with  $Nwb = |F_R \cap B_S|$ , and  $\mathbf{W}_F$  represents a binary map containing the background pixels that are wrongly assigned to the foot, i.e.,  $B_R \cap F_S$  with  $Nwf = |B_R \cap F_S|$ .

### 3.3 Registration Optimization

As explained in Sec. 3.1, deviations from the registration plane caused misalignments between color and thermal images. The main disagreement was located at the toes area. This is explained by the fact that when the patient's feet were well positioned onto the foot supporters underneath the heels, the heels were near the projective plane. Examples of the misalignments can be found in Fig. 5(a).

A patient-specific fine registration was needed to correct this possible misalignment. A rigid transformation consisting of translation, rotation, and vertical scaling was assumed to suffice. Four parameters are needed to define this transformation. Horizontal scaling was not needed as the deviations between foot soles and projective plane were mainly slants in the longitudinal direction of the foot soles.

To optimize the four parameters, a quantitative criterion was needed. We selected a criterion based on the observation that the statistics of the temperatures in a region inside the foot will differ the most when compared with statistics of a region entirely outside the foot. We defined pairs of small regions positioned at both sides of the hypothesized foot contour. The difference between histograms of the temperatures in these opposite regions should be maximized. By the aggregation of a measure of this difference, calculated along different points on the hypothesized foot contour, a global optimization criterion was found. Although parts of the foot, such as the toes, had low contrast against the background, the contour points at

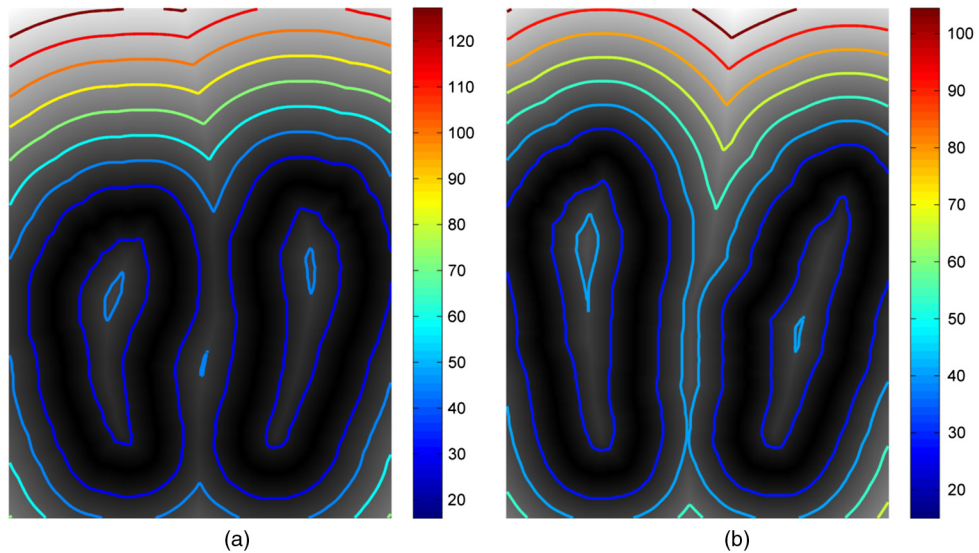


**Fig. 4** Examples of Euclidean distance map of the reference foot contours (Unit: pixel): (a)  $D_{\text{map}}$  of example 1; and (b)  $D_{\text{map}}$  of example 2.

these regions had low importance in driving the registration optimization.

The regions were defined as a set of foot contour points  $\{(x_c, y_c) | c = 1, \dots\}$  resulting from the color segmentation. A polygonal perpendicular was placed at each contour point as shown in Fig. 5. The polygon was split into two parts,  $R_{\text{in}}(x_c, y_c)$  and  $R_{\text{out}}(x_c, y_c)$ , representing the parts inside and outside the foot area. The measure of difference between  $R_{\text{in}}$  and  $R_{\text{out}}$  at each point  $(x_c, y_c)$  was defined as the  $\chi^2$  distance between the histograms  $h^{\text{in}}$  and  $h^{\text{out}}$  in the polygons:

$$\chi^2(x_c, y_c) = \frac{1}{2} \sum_i \frac{[h^{\text{in}}(i) - h^{\text{out}}(i)]^2}{h^{\text{in}}(i) + h^{\text{out}}(i)}. \quad (9)$$

Aggregation of all these distances along the contour yields:

$$D = \sum_c \chi^2(x_c, y_c). \quad (10)$$

Fine registration was done by changing the four transformation parameters so as to minimize  $D$ . The optimization was implemented with the optimization toolbox in MATLAB with the sequential quadratic programming algorithm searching for the local maximum of  $D$  within a bounded region of four parameters.

### 3.4 Asymmetric Analysis of Diabetic Foot Complications

The temperature difference of the corresponding points on the left and right feet is an indicator for diabetic foot complications.<sup>8,9</sup> However, the two feet in the thermal images were hardly at symmetric positions in the image, and they often showed asymmetric deformations due to DM or due to amputations. Therefore, the left and right feet needed to be registered with each other.

The goal of the left and right feet registrations was to find the optimal transformation  $\mathbf{T}: (x, y) \mapsto (x', y')$ , which maps any point  $(x, y)$  in the segmented left foot onto the corresponding point  $(x', y')$  in the segmented right foot. Due to local foot deformations (caused by DM), amputations, and projection distortions, a rigid left to right foot registration did not suffice and a nonrigid registration was needed. We employed a landmark-based deformation model with B-splines.<sup>18,19</sup> This model consists of an orthogonal  $n_x \times n_y$  mesh that covers the image plane. The shifts of the mesh points form the parameters  $\Phi$  of the registration. The shifts of pixels between grid points are obtained by the B-spline interpolation. To find  $\Phi$ , a number of corresponding landmarks on the left and right feet are needed. Due to deformities and amputations, points at the lower half (near the heel) are more stable than the one near the toes. The procedure to obtain these corresponding points is defined in Algorithm 2.

To find the best parameters  $\Phi$ , the sum of the squared differences between the transformed left landmarks and the corresponding right landmarks was minimized with the steepest descent algorithm. The gradient vector, which is needed for this optimization, was obtained numerically.

After estimation of the parameters of registration, the associated geometric transformation was applied to the left foot to

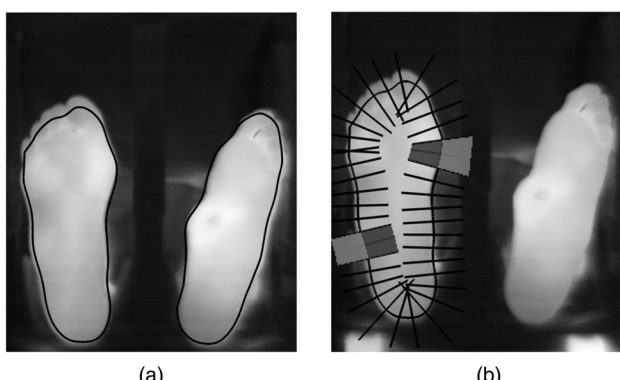


**Fig. 5** (a) Examples of ill-positioned feet contours, mapping directly from color image segmentation. (b) Illustration of the perpendicular line profiles of the foot contour, which defined the polygonal mask in and out of the foot contour. Note, for illustrative purposes, the left panel displays the longer profile lines (length = 51 pixels) and larger polygonal window than actually used.

**Algorithm 2** Selection of corresponding points in the left and right feet.

• **Inputs:** Contours  $(x_n^l, y_n^l)$  and  $(x_n^r, y_n^r)$  with  $n = 1, \dots$ . These are the sequences of 2-D coordinates in the thermal image denoting the boundaries of the left and right feet regions in the thermal image.

- Selection in the left foot and in the right foot (see Fig. 6):
  - Determine the centroid  $(x_c^l, y_c^l)$  of the contour points.
  - Determine the midline of the lower half of the foot: (a) Determine segments for each horizontal line that connect the left boundary point to a right boundary point and that are below the centroid, the midpoint. (b) Determine the least squares linear fit of these midpoints.
  - Rotate the contour around the centroid such that the midline stands vertical.
  - Shift the contour vertical such that the lowest point (the heel) is at the  $x$ -axis.
  - Define the horizontal lines on either foot with normalization with respect to the foot lengths. The vertical spacing of these lines below the centroid is smaller than above the centroid.
  - The intersection points of these horizontal lines with the foot contours are the landmarks (together with the heel points). Detect whether a part is missing on either foot. If so, delete these points from the list.

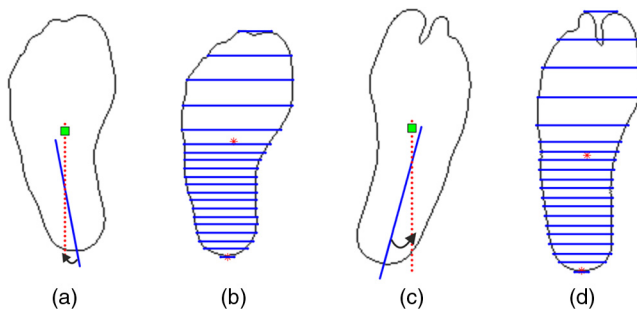


**Fig. 6** Selection of corresponding landmarks in the left and right foot contours for left/right foot registration: (a) and (c) The midlines of the lower halves of the foot regions were used to align the feet vertically; and (b) and (d) horizontal line scanning with two different step sizes.

make the pixels correspond with the pixels on the right foot. The likelihood of a foot complication of a spot was calculated simply by subtraction of the temperatures of corresponding pixels. The threshold we used for complications detection is  $2.2^\circ\text{C}$ .<sup>8,9</sup> This criterion is the only one that has been clinically validated for determining diabetic foot complications with temperature measurements.

To evaluate the registration results, four corresponding regions on the left and the right feet of each patient were manually labeled. These regions were located near the border of the foot at top, bottom, medial, and lateral positions. If any region of either foot had been amputated, no region was selected. Examples of the annotation can be found in Fig. 9. Comparison between the labeled regions on the right foot and the regions on the registered left foot was done to obtain a rough measure of the registration quality. This evaluation is limited by the subjectiveness of the manual labeling.

## 4 Results and Discussion

### 4.1 Feet Segmentation Results in Color Images

Initially, six color representations were considered: RGB, normalized RGB (rgb), RGB-ratio, HSV, CIE L\*a\*b\*, and YCbCr. All have three color channels. For two of them, CIE L\*a\*b\* and

YCbCr, it might make sense to skip the luminance channel yielding the a\*b\* and CbCr representations. This left us with eight possible representations. A representation can be processed by the K-means, the EM-LDC, or by EM-QDC. The considered numbers of classes were:  $K = 1, 2$ , and  $3$ . These numbers were determined based on the visual inspection of the number of objects (i.e., feet, ankle, black foot side supporting bars, black cloth, aluminium bars, and the white hospital cloth) in the acquired RGB images. Thus, in full, 72 combinations of representations, algorithms, and number of classes could possibly lead to a viable method.

A preselection of combinations/methods was made based on the following criterions:

- Visual inspection of the segmentation results. If a method clearly showed inferior results, then it was deleted from the list.
- Near resemblance of performance. All methods based on the RGB space and on the YCbCr space had nearly identical performances. This might be explained by the way that YCbCr encodes RGB. This resemblance motivated us to delete the YCbCr-based methods.
- Assessed performance measures. If the sensitivity, averaged over the population of patients, was less than 95%, then the method was deleted from the list. Likewise, if the specificity was less than 95%, or the mean distance error  $\bar{D}_{\text{EA}}$  (averaged over the population) was larger than 10 mm, then the method was also excluded from consideration.
- Instability. If the standard deviation of the sensitivity or specificity, calculated over the population, was larger than 15%, then the method was crossed out for it was not capable of segmenting the feet with a stable performance.

Only nine methods out 72 survived these elimination rules. The quantitative assessment of the remaining methods can be found in Table 1. The difference between the performance of these nine methods is not very statistically significant except for a\*b\* with EM-LDC or EM-QDC and  $K = 3$ . This method presented relatively lower mean sensitivities, just above 95%,

**Table 1** Assessment of foot segmentation in color image over 76 patients.

		Four clusters	Three clusters		Two clusters	
		CIE L*a*b*	CIE L*a*b*	a*b*a	CbCr <sup>b</sup>	a*b*
Sensitivity (%)	K-means				96.8 ± 1.2	97.3 ± 1.0
	EM-LDC	96.7 ± 1.8	97.9 ± 0.7	95.1 ± 2.6	96.5 ± 1.3	97.2 ± 1.2
	EM-QDC	97.1 ± 2.6		95.8 ± 1.4		
Specificity (%)	K-means				98.4 ± 2.8	99.0 ± 1.0
	EM-LDC	98.9 ± 3.3	98.9 ± 0.7	99.5 ± 0.86	98.3 ± 3.1	98.9 ± 1.0
	EM-QDC	99.0 ± 0.81		99.3 ± 0.69		
$\bar{D}_{EA}$ (mm)	K-means				2.86 ± 5.32	1.51 ± 2.22
	EM-LDC	1.35 ± 1.61	1.61 ± 1.72	1.61 ± 0.98	3.55 ± 7.00	1.90 ± 5.19
	EM-QDC	1.53 ± 1.90		1.65 ± 1.22		

<sup>a</sup>The two color components in CIE L\*a\*b\* color representation.

<sup>b</sup>The two color components in YcbCr color representation.

but the mean specificities were the highest. This indicates an increased risk for assigning the foot area to the background. CbCr with all the methods and  $K = 2$  obtained relatively higher  $\bar{D}_{EA}$  and relatively lower sensitivity. Thus, the segmentations with CbCr for two clusters and those with a\*b\* for three clusters for all methods were excluded as well.

To conclude, the foot segmentation from the color images can be achieved in CIE L\*a\*b\*, either using all the three color channels with EM-QDC for four clusters or EM-LDC for three or four clusters or using only the two color components through K-means, EM-LDC, and EM-QDC for two clusters. Two examples of the segmentation results are illustrated in Fig. 7. The sensitivities and specificities of these combinations were all around 98% ± 1% and 99% ± 1%, respectively, and  $\bar{D}_{EA} = 2 \pm 2$  mm. In the following sections, results are presented based on the foot segmentations obtained using all the three color channels in CIE L\*a\*b\* with EM-LDC for three clusters.

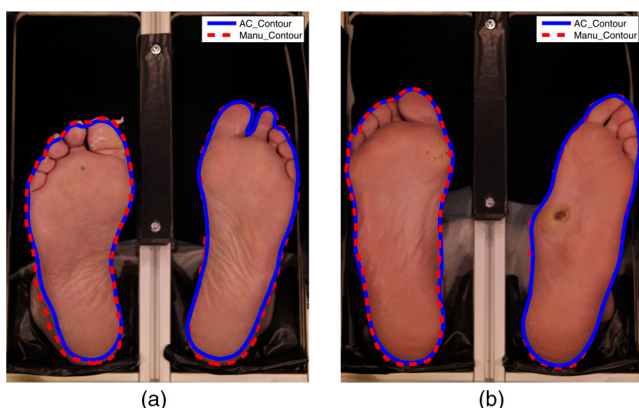


**Fig. 7** Examples of foot segmentation done with EM-QDC using three color channels in CIE L\*a\*b\* (blue solid line) and the manual segmentation (red dashed line): (a) example 1; and (b) example 2.

## 4.2 Registration Optimization in the Thermal Images

The parameters of the fine registrations are the shift ( $x_t, y_t$ ), the rotation angle  $r$ , and the vertical scale  $s$ . Since the pivot of the rotation was near the heel, the foot contour was not rotated around its centroid point, but around the heel point (the furthest point on the foot contour when the foot was rotated to stand vertically).

The length of the perpendicular profile line (shown in Fig. 5), which is equivalent to the window size, was set to 11 pixels with 5 pixels inside and 5 pixels outside the foot region. To bound the search area, the ranges of the parameters were limited; for shift:

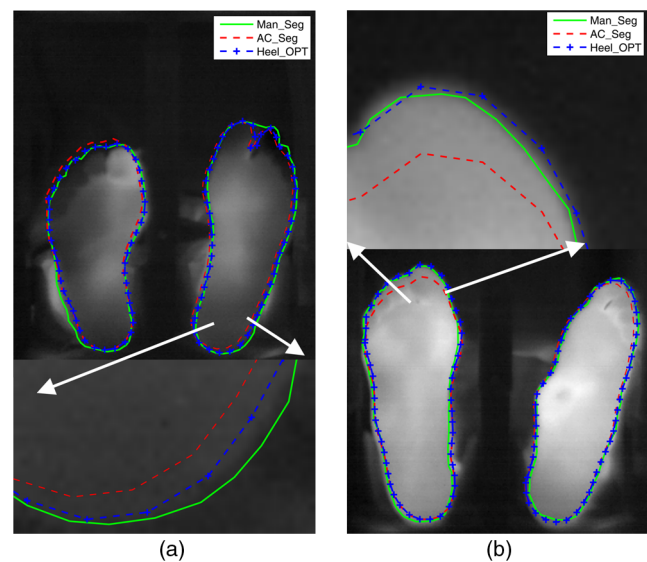


**Fig. 8** Examples of results from optimized registration. The green solid lines represent the foot contours obtained from manual segmentation done by experienced clinicians. The red dashed lines correspond to the foot contours obtained from projective transformation of the contours from the color images. The blue dashed lines come from the optimized registration: (a) example 1 and (b) example 2.

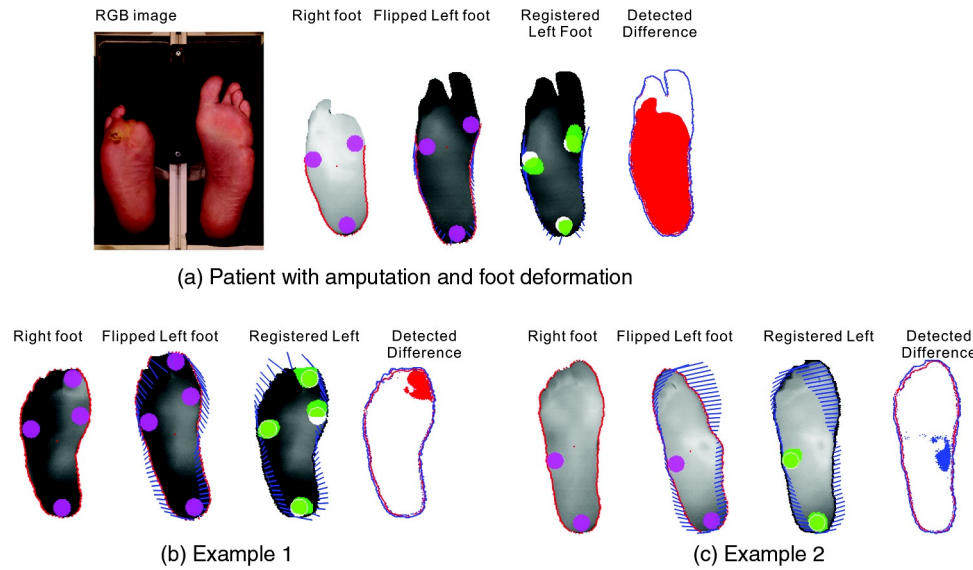


**Fig. 9** Examples of registration and risk identification with  $2.2^{\circ}\text{C}$  as criterion. Magenta regions on the right foot and the flipped left foot show the contralateral region selection. The blue lines represent the shifts due to the B-spline registration. The green regions represent the regions on the right foot after transformation while the white region underneath is the one selected manually on the right foot. The detected differences: in red/blue regions the temperature of the right/left foot exceeds the one of the left/right foot by more than  $2.2^{\circ}\text{C}$ : (a) results of a patient with an infected ulcer and an amputated hallux on the right foot; (b) Results of a patient [see Fig. 1(a)] who had callus and an ulcer on the hallux of the right foot (red area); (c) results of a patient [see Fig. 1(c)] who had callus and an ulcer on the arch of the left foot (blue area).

$x_t, y_t \in [-20, 20]$  (pixel), for rotation:  $r \in [-3, 3]$  (deg), and for vertical scaling:  $s \in [0.95, 1.05]$ . Examples of the optimization results can be found in Fig. 8.

Compared with manual segmentation in the thermal images, the sensitivity and specificity of feet segmentation in the thermal images with transformation parameter optimization, before fine registration, are  $96.0\% \pm 2.0\%$  and  $98.1\% \pm 0.7\%$  with  $\bar{D}_{\text{EA}} = 2.7 \pm 1.0$  mm; and after fine registration:  $97.9\% \pm 1.1\%$  and  $98.3\% \pm 0.5\%$  with  $\bar{D}_{\text{EA}} = 1.9 \pm 0.6$  mm.

#### 4.3 Left and Right Feet Registrations and Detection of Diabetic Foot Complications

For each patient, the right foot was chosen as the static object and the left foot was mapped on the right foot. Examples of the registration between left and right feet, and the regions with more than  $2.2^{\circ}\text{C}$  temperature difference, are given in Fig. 9.

To get a quantitative assessment of the registration results, a comparison between manual association of some regions on the right and left foot and automated association (by our right/left registration algorithm) was performed: the sensitivity and specificity are  $85\% \pm 1\%$  and  $98.4\% \pm 0.4\%$ , respectively, and  $\bar{D}_{\text{EA}} = 4 \pm 1$  mm. The error may come partly from the subjectiveness of the manual association and partly from the asymmetric deformations of the feet (which can locally make the association difficult or even impossible). Taking this into account, the registration results are considered to be accurate.

Taking  $2.2^{\circ}\text{C}$  as the cut-off point for risk identification, 35 out of 37 diabetic foot ulcers were successfully detected (95%). The two missed ulcers were small ( $\sim 5 \times 5$  mm $^2$ ), one of which was only found after debridement of abundant callus. The database also contained three Charcot feet, which were all detected. This suggests that the clinical assessment of Charcot neuro-osteoarthropathy may benefit from the monitoring

system, as it provides a full temperature map of the foot instead of only local temperature changes.

#### 4.4 Limitations of the Study

A limitation of the proposed asymmetric analysis was that it could only detect diabetic foot complications by comparing the two feet of the patient. This means that when one foot is amputated, any complication in the other foot cannot be detected. Additionally, in case that the both feet have similar complications in corresponding regions, the complications will also be missed. In addition, in finding the asymmetry between left and right feet, registration was always done from left and right feet. This registration itself may introduce artificial asymmetry, which has not been investigated in this article.

Another limitation of the study is that we did not have a “gold standard” to evaluate the segmentation and registration of the feet. We used manually segmented references that were labeled by one clinical investigator. This may be subjected to some bias since another observer may come to different observations. However, we expect that this interobserver variability will not significantly affect the found sensitivity and specificity.

### 5 Conclusion

In this contribution, an experimental setup with an IR camera system and an RGB camera was developed. With the data collected from diabetic patients with foot complications or patients who are at high risk of foot complications, a methodology was proposed for automatic detection of these foot complications with the acquired thermal images. The method is based on a simple asymmetric analysis combined with foot segmentation from color images and nonrigid landmark-based registration between left and right feet.

Foot segmentation with unsupervised machine learning in different color spaces was investigated. The foot segmentation in CIE L\*a\*b\* color space achieved a sensitivity and specificity of  $98\% \pm 1\%$  and  $99\% \pm 1\%$ , respectively. With registration optimization to map the foot segments onto the thermal image, the final sensitivity and specificity of the foot segmentation in the thermal images were  $97.9\% \pm 1.1\%$  and  $98.3\% \pm 0.5\%$ , respectively. The registration between the left and right feet, based on foot contours, presented fairly good results regardless of the shapes, sizes, poses, or positions of the two feet. In this paper, we provide the proof-of-principle that the thermal images acquired through our experimental setup can detect diabetic foot complications.

These promising outcomes of thermal image analysis of the foot may prove to be promising in the early detection of foot complications in patients with DM and patients who are at high risk for these complications. Future research objectives are: (a) Both the left and right feet may be restored to a general and unbiased foot contour template to reduce the asymmetry in the foot registration. (b) Thermal image analysis of the ipsilateral foot to detect diabetic foot complications without the need to image the contralateral foot. (c) Combining the thermography technology with other modalities, such as photometric stereo imaging<sup>24</sup> and multispectral imaging,<sup>25</sup> in the experimental setup to predict the development or healing of diabetic foot complications. (d) Comparing the effectiveness and efficiency of predicting diabetic foot complications using different modalities. (e) Developing and investigating an intelligent telemedicine system with the most cost-effective modality or modalities to monitor diabetic foot status, thereby also adapting the usability and the operational conditions required in daily clinical practice.

### Acknowledgments

This project is supported by public funding from ZonMw, The Netherlands Organisation for Health Research and Development (project ID: 40-00812-98-09031). The authors are grateful to the patients who participated in the data collection and the clinicians in the Diabetic Foot Unit, Department of Surgery, Hospital Group Twente, Almelo, The Netherlands. We also appreciate the contribution of Geert-Jan Laanstra of the Signals and Systems Group, Faculty of EEMCS, University of Twente, who gave us plenty of support in building the experimental setup. We also appreciate the efforts of Tim J.P.M Op't Root and Marvin E. Klein from DEMCON Advanced Mechatronics BV, Enschede, The Netherlands, who developed the thermal reference elements and calibrated the camera for the purpose of these measurements.

### References

- J. E. Shaw, R. A. Sicree, and P. Z. Zimmet, "Global estimates of the prevalence of diabetes for 2010 and 2030," *Diabetes Res. Clin. Pract.* **87**, 4–14 (2010).
- A. J. Boulton et al., "The global burden of diabetic foot disease," *Lancet* **366**, 12–18 (2005).
- J. Apelqvist et al., "Practical guidelines on the management and prevention of the diabetic foot," *Diabetes/Metab. Res. Rev.* **24**, S181–S187 (2008).
- E. J. Boyko et al., "Prediction of diabetic foot ulcer occurrence using commonly available clinical information: the Seattle diabetic foot study," *Diabetes Care* **29**(6), 1202–1207 (2006).
- C. E. Hazenberg et al., "Telemedical home-monitoring of diabetic foot disease using photographic foot imaging—a feasibility study," *J. Telemed. Telecare* **18**, 32–36 (2012).
- S. Franc et al., "Telemedicine: what more is needed for its integration in everyday life?" *Diabetes Metab.* **37**(4), S71–S77 (2011).
- D. G. Armstrong et al., "Skin temperature monitoring reduces the risk for diabetic foot ulceration in high-risk patients," *Am. J. Med.* **120**, 1042–1046 (2007).
- L. A. Lavery et al., "Home monitoring of foot skin temperatures to prevent ulceration," *Diabetes Care* **27**, 2642–2647 (2004).
- L. A. Lavery et al., "Preventing diabetic foot ulcer recurrence in high-risk patients: use of temperature monitoring as a self-assessment tool," *Diabetes Care* **30**, 14–20 (2007).
- P. Sun et al., "Relationship of skin temperature to sympathetic dysfunction in diabetic at-risk feet," *Diabetes Res. Clin. Pract.* **73**, 41–46 (2006).
- N. Kaabouch et al., "Enhancement of the asymmetry-based overlapping analysis through features extraction," *J. Electron. Imaging* **20**(1), 013012 (2011).
- N. Kaabouch, W.-C. Hu, and Y. Chen, "Alternative technique to asymmetry analysis-based overlapping for foot ulceration examination: scalable scanning," *J. Diabetes Metab.* **S5**, 003 (2011).
- K. Roback, M. Johansson, and A. Starkhammar, "Feasibility of a thermographic method for early detection of foot disorders in diabetes," *Diabetes Technol. Ther.* **11**, 663–337 (2009).
- R. G. Frykberg, A. Tallis, and E. Tierney, "Diabetic foot self examination with the tempstat as an integral component of a comprehensive prevention program," *J. Diabetic Foot Complications* **1**(1), 13–18 (2009).
- T. Nagase et al., "Variations of plantar thermographic patterns in normal controls and non-ulcer diabetic patients: novel classification using angiosome concept," *J. Plast. Reconstr. Aesthetic Surg.* **64**, 860–866 (2011).
- T. Delchar, "From thermometry to thermography: physics and its applications," Chapter 1 in *Physics in Medical Diagnosis*, Springer, London (1997).
- C. Liu et al., "Infrared dermal thermography on diabetic feet soles to predict ulcerations: a case study," *Proc. SPIE* **8572**, 85720N (2013).
- D. J. Kroon, "Segmentation of the mandibular canal in cone-beam CT data," PhD Dissertation, University of Twente, MIRA Institute for Biomedical Technology and Technical Medicine, Enschede, The Netherlands (2011).
- D. J. Kroon, "B-spline grid, image and point based registration," MATLAB Central File Exchange, 2008 <http://www.mathworks.com/matlabcentral/fileexchange/20057-b-spline-grid--image-and-point-based-registration> (26 January 2015).
- J. J. van Netten et al., "Infrared thermal imaging for automated detection of diabetic foot complications," *J. Diabetes Sci. Technol.* **7**(5), 1122–1129 (2013).
- N. Vandenbroucke, L. Macaire, and J.-G. Postaire, "Color image segmentation by pixel classification in an adapted hybrid color space. application to soccer image analysis," *Comput. Vision Image Understanding* **90**(2), 190–216 (2003).
- P. Kakumanu, S. Makrigiannis, and N. Bourbakis, "A survey of skin-color modeling and detection methods," *Pattern Recognit.* **40**, 1106–1122 (2007).
- F. van der Heijden et al., *Classification, Parameter Estimation and State Estimation An Engineering Approach Using MATLAB*, John Wiley & Sons, Chichester (2004).
- C. Liu, F. van der Heijden, and J. J. van Netten, "Towards surface analysis on diabetic feet soles to predict ulcerations using photometric stereo," *Proc. SPIE* **8214**, 82141D (2012).
- C. Liu et al., "Statistical analysis of spectral data: a methodology for designing an intelligent monitoring system for the diabetic foot," *J. Biomed. Opt.* **18**(12), 126004 (2013).

**Chanjuan Liu** received her BSc degree from the Beijing Jiaotong University in 2006. She received her MSc and PhD degrees from the Faculty EEMCS at the University of Twente in 2010 and 2014, respectively. Her PhD degree research focuses on techniques to build an intelligent telemedicine monitoring system that can be deployed at the patients' home environment for frequent examination of patients' feet, to detect precursors of ulceration.

Biographies of the other authors are not available.

## Article

# Automatic Diabetic Foot Ulcer Recognition Using Multi-Level Thermographic Image Data

Ikramullah Khosa <sup>1,\*</sup>, Awais Raza <sup>1</sup>, Mohd Anjum <sup>2</sup>, Waseem Ahmad <sup>3</sup> and Sana Shahab <sup>4,\*</sup>

<sup>1</sup> Department of Electrical and Computer Engineering, COMSATS University Islamabad, Lahore Campus, Lahore 54000, Pakistan

<sup>2</sup> Department of Computer Engineering, Aligarh Muslim University, Aligarh 202002, India

<sup>3</sup> Department of Computer Science and Engineering, Meerut Institute of Engineering and Technology, Meerut 250005, India

<sup>4</sup> Department of Business Administration, College of Business Administration, Princess Nourah Bint Abdulrahman University, P.O. Box 84428, Riyadh 11671, Saudi Arabia

\* Correspondence: ikramullahkhosa@cuilahore.edu.pk (I.K.); sshahab@pnu.edu.sa (S.S.)

**Abstract:** Lower extremity diabetic foot ulcers (DFUs) are a severe consequence of diabetes mellitus (DM). It has been estimated that people with diabetes have a 15% to 25% lifetime risk of acquiring DFUs which leads to the risk of lower limb amputations up to 85% due to poor diagnosis and treatment. Diabetic foot develops planter ulcers where thermography is used to detect the changes in the planter temperature. In this study, publicly available thermographic image data including both control group and diabetic group patients are used. Thermograms at image level as well as patch level are utilized for DFU detection. For DFU recognition, several machine-learning-based classification approaches are employed with hand-crafted features. Moreover, a couple of convolutional neural network models including ResNet50 and DenseNet121 are evaluated for DFU recognition. Finally, a CNN-based custom-developed model is proposed for the recognition task. The results are produced using image-level data, patch-level data, and image–patch combination data. The proposed CNN-based model outperformed the utilized models as well as the state-of-the-art models in terms of the AUC and accuracy. Moreover, the recognition accuracy for both the machine-learning and deep-learning approaches was higher for the image-level thermogram data in comparison to the patch-level or combination of image–patch thermograms.

**Keywords:** diabetes mellitus; diabetic foot ulcer; thermograms; deep learning; machine learning



**Citation:** Khosa, I.; Raza, A.; Anjum, M.; Ahmad, W.; Shahab, S. Automatic Diabetic Foot Ulcer Recognition Using Multi-Level Thermographic Image Data. *Diagnostics* **2023**, *13*, 2637. <https://doi.org/10.3390/diagnostics13162637>

Academic Editor: Marijn Speeckaert

Received: 27 June 2023

Revised: 29 July 2023

Accepted: 6 August 2023

Published: 10 August 2023



**Copyright:** © 2023 by the authors. Licensee MDPI, Basel, Switzerland. This article is an open access article distributed under the terms and conditions of the Creative Commons Attribution (CC BY) license (<https://creativecommons.org/licenses/by/4.0/>).

## 1. Introduction

Insulin insufficiency in the body causes diabetes mellitus (DM), which results in high blood glucose (hyperglycemia) for an extended period. Uncontrolled diabetes for a long period of time can lead to complications such as nephropathy, retinopathy, Charcot foot development, amputation, or even death [1]. Uncontrolled DM damages the nerves; if the nerves in the legs or feet are damaged, it causes a lack of feeling called sensory diabetic neuropathy. When a patient does not feel a sore or cut in his foot due to neuropathy, that cut causes infection and worsens the foot condition. The other situation is the low flow of blood. Peripheral vascular disease causes low blood flow in the arms and legs. If the cut is not healing due to low blood flow, there is a risk of developing ulcers. DFU (diabetic foot ulcer) is most common in diabetic patients; more than 15% of patients face this problem [2]. An illustration of DFU is shown in Figure 1.

Diabetic foot issues are expensive and have a negative impact on one's quality of life. This may be prevented or considerably delayed in many situations by undertaking a risk assessment and inspection of diabetes patients' foot health at an early stage. For that purpose, temperature may have an impact. Diabetics' plantar foot temperature may fluctuate due to neuropathy, ischemia, or infection. Temperature differences of more

than  $2.2^{\circ}\text{C}$  ( $4^{\circ}\text{F}$ ) between the right and left foot are considered abnormal, where the normal difference is typically less than  $1^{\circ}\text{C}$  [3–5]. With the use of a thermal-imaging camera, problems may be identified early, saving time and money in the long run. Infrared thermography may be utilized to produce a clear image of the thermal energy released by the site being monitored in real time if the temperature is above absolute zero [6–8]. Thermography is a non-invasive, non-contact, cost-effective, rapid, and painless means of screening the patient's skin temperature. This imaging technique can detect temperature changes on human skin.

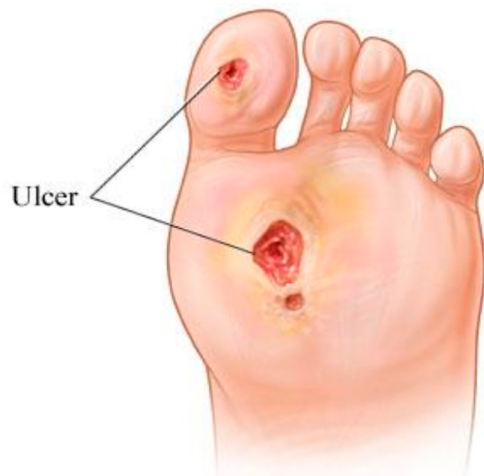


**Figure 1.** An illustration of foot ulcers.

To detect the ulcer, the thermogram needs to be assessed by a professional expert. The availability of such experts is a challenge, particularly in remote areas. Therefore, several research studies have targeted the provision of an automatic DFU recognition system. Few among them utilized foot thermograms [9,10] while many considered visible-band (RGB camera) images [11–18]. In this study, the thermogram images of diabetic foot are considered for DFU detection. For the recognition of DFU, the experiments are carried out at three levels of thermogram data: image-level, patch-level, and a combination of image–patch thermogram data. To detect the DFU foot, pre-trained deep-learning models are employed using transfer learning. Moreover, a problem-oriented, custom, CNN-based, computationally light model is developed to compare with the state-of-the-art results. For a comprehensive and comparative analysis, classical feature-based recognition using machine-learning techniques is also carried out. The details of the rest of the paper are as follows: Section 2 presents the background work and related studies; Section 3 includes the dataset and augmentation details. The methodology is discussed in Section 4. The results and discussions are presented in Section 5. The conclusion is added in Section 6.

## 2. Background

Machine-learning and deep-learning techniques have gained a lot of interest in recent years for diabetic foot ulcer monitoring and diagnosis in patients with neuropathic diabetes. Much research has been carried out recently for DFU recognition and classification [12,13,15,16,18,19]. However, those studies considered the visible-band images of diabetic feet. Most of these studies employed deep-learning approaches for DFU diagnosis. In contrast, fewer studies judged the thermographic image data. Since this study is focused on the thermographic image data, the literature related to DFU classification in thermograms is discussed.

In the study [9], the researchers compared different machine-learning and deep-learning models. Automatic segmentation and ROI with feature extraction were represented by a fuzzy entropy set with a histogram-based segmentation method for optimization. After augmentation, the data were trained and tested. The SVM produced the lowest

AUC (area under the curve), sensitivity, and accuracy. The proposed network model DFT-Net and the common ANN had the best performances, using AUC values of 0.8533 and 0.8333%, respectively. In a study by [20], the quantity of pixels with a temperature exceeding 2.2 °C was measured to compute the region of interest. The produced segmentation masks were 99.25% accurate in detecting the absence of a foot sole, 98.83% accurate in constructing a bounding box, and 94.95% accurate in detecting the presence of a foot sole. In another study [14], the authors collected the IRT (infrared thermograph) images and made a dataset with 39 ischemic DFU patients, of which 14 had active ischemic wounds and the remainder had healing wounds. The image ROI abstract was classified by ANN, kNN (k-nearest neighbor), and SVM (support vector machines), while the image was decomposed using DST (discrete wavelength transform) and HOS (higher-order spectra). The best achieved accuracy reported was 98.39% using the SVM classifier. Researchers in study [21] took thermograms in controlled environments with a homogeneous background and used k-means clustering, and a further approach on every foot for foot segmentation. The identification of ulceration on the image was different pixel to pixel and a thresholding technique was used. They successfully differentiated between ulcer and non-ulcer wounds with the help of a classifier and segmented based on a machine-learning model with 91.8% sensitivity, 98.4% specificity, and 91.1% accuracy. In another study [22], the authors used a controlled environment with a room temperature of 20 °C for thermogram images and foot segmentation. A temperature threshold matrix was created, as well as an additional method established to label each foot. A pattern spectrum with thresholding techniques was used to identify the ulceration in the image. They claimed results between the risk and non-risk zones with the help of a classifier and performed segmentation based on a machine-learning model with a sensitivity of 97.33% and specificity of 91.33%. In another study [23], analysis of DFU thermograms with machine learning was performed where the researcher used controlled environments at a room temperature of 20 °C and humidity of 55% for thermogram and foot segmentation. The health-care expert identified the ulceration in the image. The SVM classifier and wavelet characteristics vector were used. They produced results between DF and non-DF with the help of a classifier with an accuracy of 89.39%, sensitivity of 81.81%, and specificity of 96.97%. The detection of DFU thermograms with machine learning has been presented in [24], in an uncontrolled environment with respect to room temperature, illumination, and close-ups for the image of the thermogram. With the temperature filter, the average temperature and threshold were used for diagnostic purposes with the help of a machine-learning-based classifier. They claimed results between DF and non-DF based on a machine-learning model with a non-risk class sensitivity of 91.32% and specificity of 91.84% and ulcer class sensitivity of 90.29%, accuracy of 90.28, and specificity of 90.28%. The authors in study [10] used infrared imaging to detect abnormalities in foot segmentation and registration. They concluded that the ACWE (active contour without edges) method produced quite good results. Automatic pre-symptomatic ulcer detection was performed to determine the clinically relevant difference in temperature between the feet, which was 2.2 °C. The researchers in [7] used infrared imaging and for image decomposition, they examined the ROI of complete feet and mean temperatures. In individuals with localized difficulties, the ipsilateral and contralateral foot and mean temperatures are the same. When compared to a similar area in the contralateral foot and the mean of the entire ipsilateral foot, the ROI temperature was greater than 2 °C. The average temperature difference between both ipsilateral and contralateral feet was greater than 3 °C in patients with widespread problems. In study [25], infrared imaging and clinical foot assessments were presented. For image decomposition, they examined the ROC curve. With a 76% sensitivity and 40% specificity, the contralateral locations had a difference of 2.2 °C between each other, which showed the best cut-off value for diagnosing diabetic foot. The variation of 3.5 °C between the mean temperature of the right and left foot was shown to be the best cut-off value for determining the urgency for treatment, with an 89% sensitivity. In this study [26], the authors employed infrared imaging to detect anomalies, followed by grayscale characterization and temperature pattern foot

segmentation. Then, to pattern the spectrum, mathematical morphology was used as well as a multi-layer perceptron with k-fold validation. The subjects had a butterfly pattern, and the pattern spectrum was like that of ovals and rounds. Quadrant 4 had the greatest mean percentage of pixels for the control group, at 88.05%. Due to the different patterns, the pattern spectrum was abnormal. In quadrant 3, the mean proportion of pixels for the diabetic group was 28.87%, while the authors achieved an average classification rate of 94.33 percent. In this paper [27], they examined a database of dynamic IRT plantar diagnostic images with 39 current diabetic foot ulcer patients. The mean temperature of the region of interest, which corresponds to the important change places of diabetic foot ulcer, was assessed and the images were examined by assessing the mean temperature of the region of interest, which relates to some of the important change places of diabetic foot ulcer. The statistics found no evidence of a significant difference between the thermal asymmetry values and thermal recovery differences in any region of interest, except the one at the medial forefoot. The regions of interest were assessed on both feet, with the value of the thermal asymmetry factored into each one. A decision support system was constructed using the database and analytical results to classify the data and examine the accurate identification of the DFU using machine-learning methods such as ANN, kNN, and SVM. The best overall results were achieved with a kNN of 5 neighbors.

### 3. Data and Augmentation

A public dataset of thermograms is used in this study [3]. These data comprise 334 plantar thermograms obtained from 122 individuals diagnosed with diabetes mellitus (DM) and 45 individuals not diagnosed with diabetes (control group). In the DM group, there were 16 female and 29 male subjects aged between 20 and 35 years. Moreover, there were 89 females and 33 males with their age ranging from 45–65 years in the control group. The subjects were recruited as volunteers from the city of Puebla, Mexico, and thermogram acquisition was carried out over a period of three years (2012–2014). A sample pair of feet from each group is shown in Figure 2.

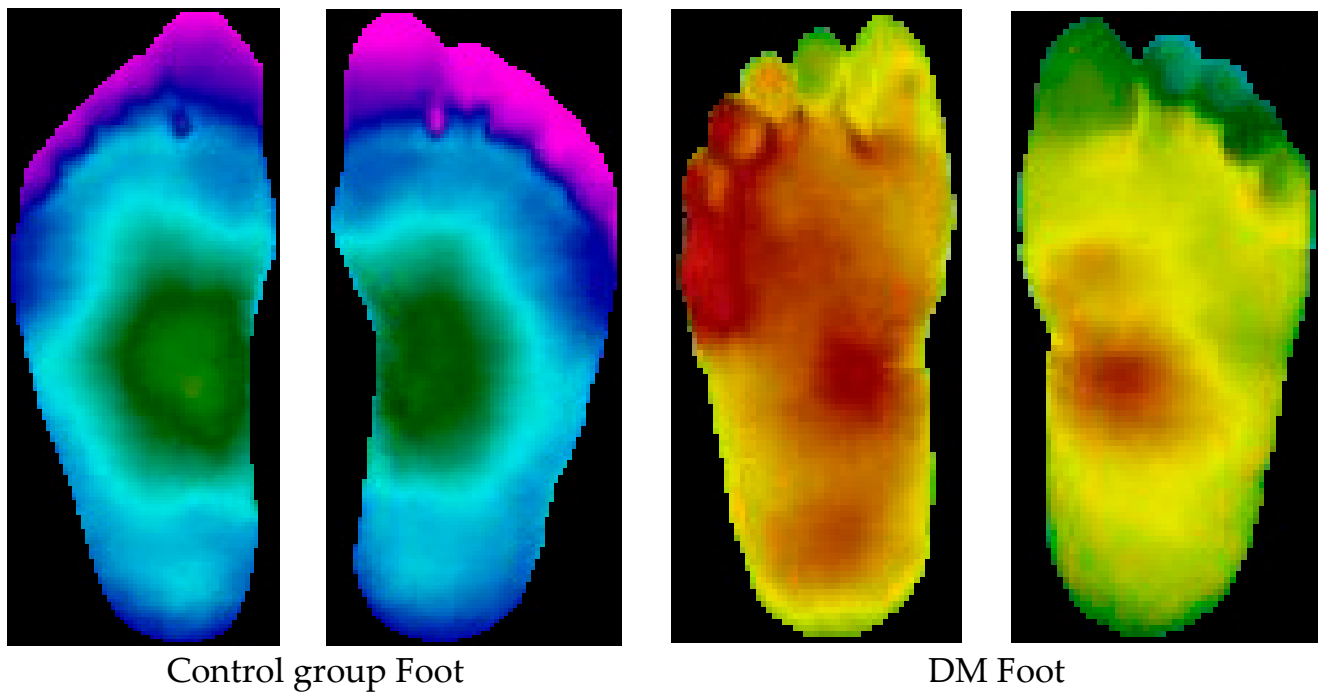


**Figure 2.** Sample images of healthy foot and DM foot.

Each thermogram includes four more images representing plantar angiosomes. Those are considered as patches in this study. A sample of full images and corresponding patch images (plantar angiosomes) from both categories are shown in Figure 3. For infrared (IR) image acquisition, the subject was laid on a bed with an IR camera at a distance of one meter from the feet [3]. To avoid sensing the temperature from the rest of the body, an IR obstructive material was placed. Two IR camera FLIR E60 and FLIR E6 were used at a room temperature of  $20 \pm 1$  C [3]. Since the database includes the segmented foot and patch RGB images, those are used as they are without any pre-processing. However, data augmentation is utilized to increase the dataset size as well as to balance the classes. Augmentation is carried out by rotating the images at  $90^\circ$ ,  $180^\circ$ , and  $270^\circ$ , as well as by horizontal flip, vertical flip, and both horizontal and vertical flip simultaneously. Image-level augmentation is performed by making 500 samples for each class and patch-level augmentation is performed to prepare 1500 samples per class. The class-wise detail of the thermograms is summarized in Table 1.

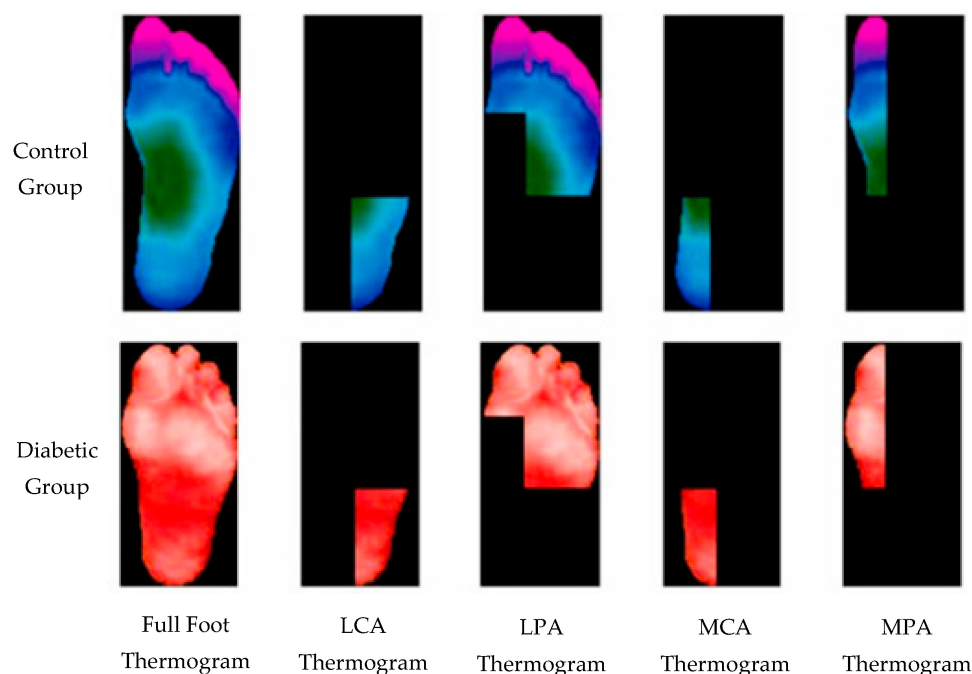


**Figure 3.** A sample of thermograms from diabetic and control group and corresponding patch images (plantar angiosomes). MPA: medial plantar artery, LPA: lateral plantar artery, MCA: medial calcaneal artery, LCA: lateral calcaneal artery.

**Table 1.** Thermogram image data detail: original and after augmentation.

Category	Diabetic Group	Control Group	Total
No. of cases	122	45	167
Original full images	244	90	334
Images after augmentation	500	500	1000
Original patches	976	360	1336
Patches after augmentation	1500	1500	3000

#### 4. Methodology

Computer-aided diagnostic techniques assist medical practitioners in being able to diagnose with a higher confidence. Machine-learning and deep-learning techniques have been of interest for utilization as a decision support system.

#### 4.1. Machine-Learning Approaches

Traditional machine-learning techniques have been considered for the classification of thermograms in the literature. Based on their proven performance in the literature, including medical diagnosis, several of them were considered for this study for comprehensive comparative analysis including SVM, random forest (RF), multi-layer perceptron (MLP), naive Bayes, kNN, XGBoost, AdaBoost, and bagging.

**Support Vector Machines:** Support vector machine may be utilized both for regression and classification problems [28]. For classification, it is a classifier with a goal to locate a hyperplane separating the two classes with a large margin.

**Random Forest:** It is a classifier with several decision trees on various subsets of the provided dataset that takes the average to enhance the predicted accuracy of that dataset [29]. To anticipate the ultimate output, the random forest collects guesses from all of its trees and combines them into a single prediction. Overfitting can be avoided by having a larger number of trees to choose from when making a model.

**kNN:** k-nearest neighbor algorithm assigns the class to the test sample based on the nearest neighbors with the largest majority [30]. Being nearest depends on the distance metric which is normally the Euclidean distance or absolute distance.

**Naive Bayes:** To categorize the data, a naive Bayes classifier applies concepts from probability theory [31]. The theorem developed by Bayes is utilized by the naive Bayes classification algorithms. The most important takeaway from Bayes' theorem is that the probability of an event can be recalculated whenever new evidence is added to the mix.

**XGBoost:** Extreme gradient boosting is built on supervised machine learning, decision trees, ensemble learning, and gradient boosting [32].

**AdaBoost:** As part of an ensemble method in machine learning, adaptive boosting is a technique known as AdaBoost [33]. AdaBoost's most frequent algorithm is a decision tree with only one split, known as a decision tree with only one level. Decision stumps are another name for these trees. This algorithm creates a model and equally weighs all the input data points in that model.

**Bagging:** An ensemble meta-estimator, bagging classifiers fit base classifiers on random subsets of the original dataset and then aggregate their individual predictions (either by voting or average) to generate a final forecast [34].

#### 4.2. Feature Extraction

The machine-learning classifiers discussed above require feature extraction. There are many features in the literature that have been used for computer vision and pattern recognition tasks; a few of the popular ones among them are used in this study including local binary pattern, gray level cooccurrence matrix, histogram of oriented gradients, and Gabor features to be used with machine-learning classifiers.

**Local Binary Patterns (LBP):** Each pixel in a picture is labelled using the local binary patterns operator by thresholding a 3x3 neighborhood surrounding each pixel with the center value [35]. These classes are used to label pixels. Each result is assigned a binary value, which is either a 1 or a 0, depending on whether the surrounding pixels are equal or greater than the center pixels.

**Histogram of Oriented Gradients (HOG):** The purpose of HOG is to detect the presence of a particular object oriented at a specified direction [36]. The magnitude of pixel orientation data is weighted to establish the criteria for characterizing an item in these attributes.

**Gabor Filters:** They are linear Gabor filters that detect if an image has a certain frequency content within a given region of interest for texture research [37]. Many current vision experts believe that the frequency and orientation representations of Gabor filters are like those perceived in the human eye.

**Gray Level Cooccurrence Matrix (GLCM):** A GLCM is a matrix representing the frequency of cooccurrence of a pair of pixel intensities at a specified distance and angle [38]. The GLCM is computed to extract the texture features from images. Cluster prominence, cluster

shade, dissimilarity, energy, entropy, homogeneity, and maximum probability are the GLCM features used in this study.

#### 4.3. Deep-Learning Approaches

Currently, deep-learning approaches, particularly convolutional neural networks, have been extensively employed in computer-aided medical diagnostics. In this study, two deep-learning models are employed via transfer learning including ResNet50 and DenseNet. Moreover, a custom-developed CNN model is proposed.

**ResNet50:** This model [39] was originally trained for 1000 classes using the ImageNet database [40]. The ResNet50 CNN model is adequately efficient on vision tasks, and particularly fits well considering the efficiency as well as complexity. Moreover, this has been widely used as the default choice for deep transfer learning in computer vision tasks. It has 48 convolutional layers, one max-pool, and one average-pool layer. For diabetic foot ulcer recognition, the last three layers' parameters were updated via transfer learning by network training using thermogram image data. The input image was resized as  $224 \times 224$  to match the ResNet input image resolution requirement. The output was restricted to one neuron, providing the probability for the sample to be recognized as a diabetic group.

**DenseNet121:** DenseNet was developed with the aim to obtain benefit from a deep network while keeping fewer parameters [41]. It improves the accuracy by minimizing the problem of a vanishing gradient. It has 120 convolutional layers and 4 average-pool layers. To use it with diabetic foot thermogram data, the last two layers were used for the parameter update via training. The input image was resized at  $224 \times 224$  for this network also.

**Proposed CNN Model:** In addition to pre-trained networks, a custom CNN model was developed specifically for DF classification. For this purpose, the DFTNet model was adopted as the base model [9]; however, there were major differences. This study utilized the input volume size  $180 \times 80 \times 3$ ; however, the DFTNet used an input volume of  $227 \times 227 \times 3$ . The learning rate was chosen as 0.001 with the Adam optimizer. The batch size was set to 64. The network architecture diagram is shown in Figure 4. The detailed working of the proposed model is shown in Figure 5.

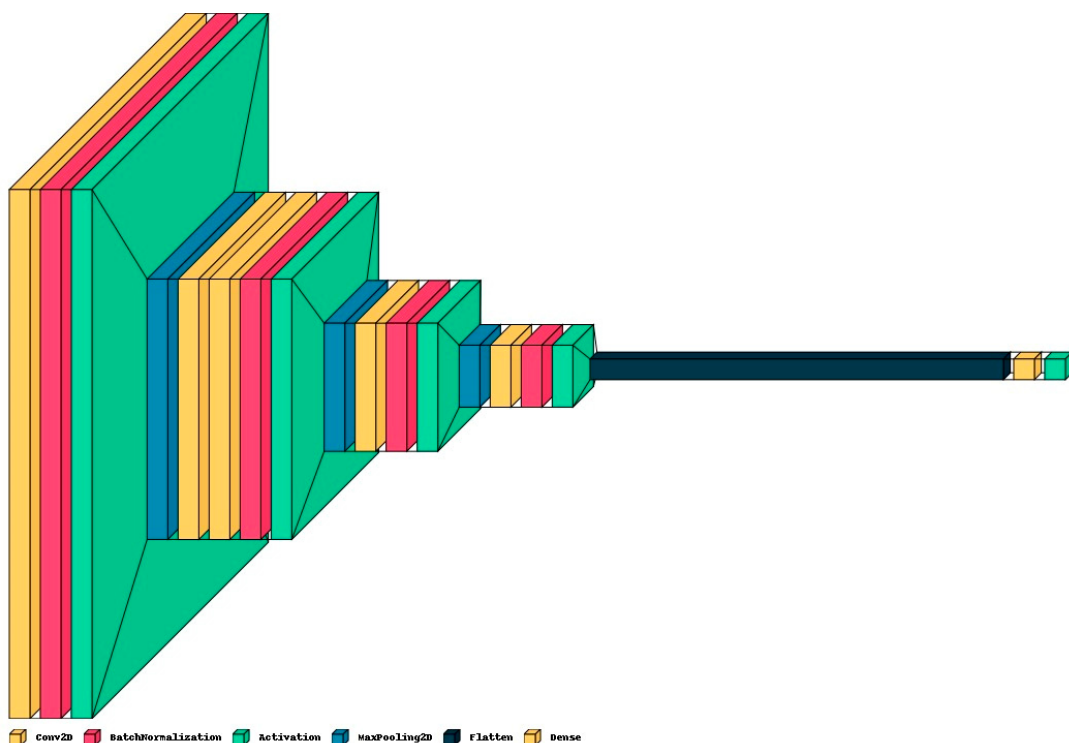


**Figure 4.** The architecture diagram of proposed model for DFU classification.

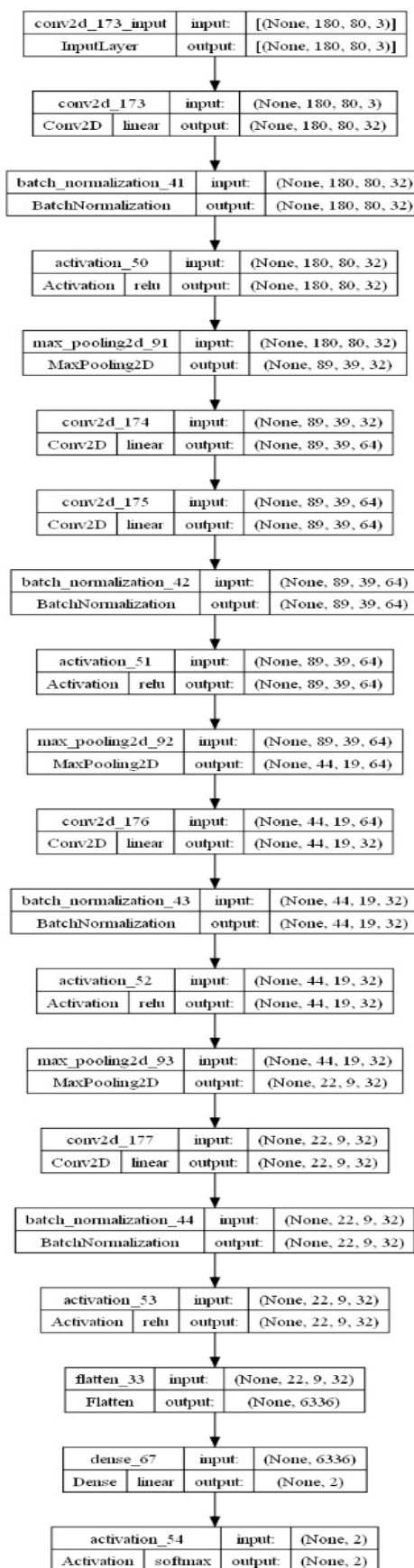


**Figure 5.** The complete architecture working map of the proposed model for DFU classification.

## 5. Results and Discussion

For training the classifiers, 80% of the data were used for training and the remaining 20% for test purposes. For performance evaluation, classification measures such as the sensitivity, specificity, precision, accuracy, and F1-score were considered. The mathematical expressions of these measures are as follows:

$$\text{Sensitivity} = \frac{\text{TP}}{\text{TP} + \text{FN}} \quad (1)$$

$$\text{Specificity} = \frac{\text{TN}}{\text{TN} + \text{FP}} \quad (2)$$

$$\text{Accuracy} = \frac{\text{TP} + \text{TN}}{\text{TP} + \text{TN} + \text{FP} + \text{FN}} \quad (3)$$

$$\text{F1 Score} = \frac{2\text{TP}}{2\text{TP} + \text{FP} + \text{FN}} \quad (4)$$

where TP: true positive, TN: true negative, FP: false positive, FN: false negative.

### 5.1. Results of Machine-Learning Approaches

As discussed in the methodology section, the machine-learning approaches used for the classification of thermogram data include SVM, RF, XGBoost, naive Bayes, AdaBoost, kNN, and bagging. To compute the results for each of these algorithms, all individual features including HOG, Gabor, GLCM, and LBP were employed. Moreover, a combination of all features was also used.

#### 5.1.1. Classification of Combined Data (Image+Patch)

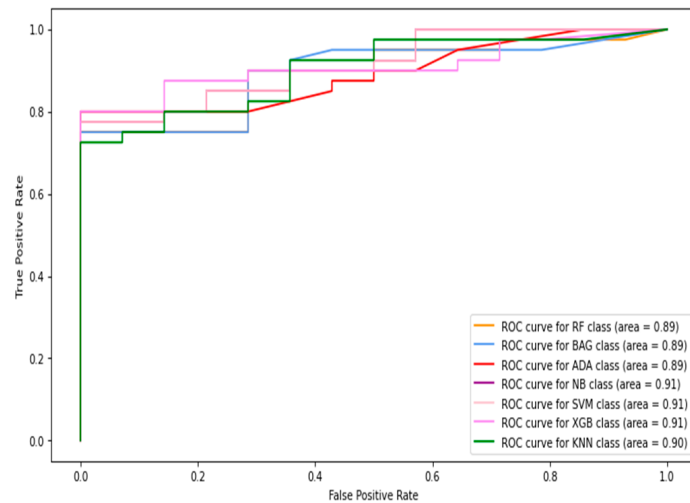
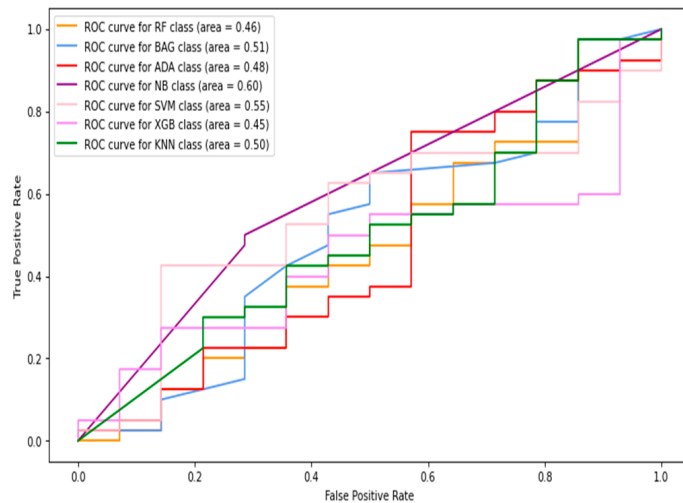
In this section, the images and patches are combined to form the total data. Then, the features are extracted from these data and used for classification. The receiver operative characteristic (ROC) curve and AUC (area under the curve) results of the machine-learning classifiers are shown in Figures 6–10, using individual as well as combined features. Table 2 shows the results in terms of the evaluation metrics for the individual and combined features. It can be observed that a sensitivity score of 0.71 was recorded using the SVM, RF, XGBoost, and bagging classifiers with HOG features. The SVM and bagging produced the best results using both the HOG features and Gabor features. In the case of specificity, again, the SVM produced 0.95 using the GLCM features. The overall best accuracy of 78% was achieved by the SVM classifier while combining all four kinds of features. The highest F1-score was recorded by both the RF and XGBoost classifiers of 0.71. By comparing the ROC curves of classifiers employing different features, it can be observed that the HOG features produced the best results among the other individual features. The overall best AUC of 0.93 was recorded by employing combined features from multiple classifiers including RF, bagging, and naive Bayes. Concretely, the SVM happened to be the best machine-learning classifier regarding recognizing the diabetes class (with the highest sensitivity value observation), while the combined features gave the best accuracy as well as AUC.

**Table 2.** Machine-learning classifier results using different features for combined image+patch data.

Evaluation Metric	Features	SVM	RF	XGBoost	Naive Bayes	AdaBoost	kNN	Bagging
Sensitivity	HOG	<b>0.71</b>	<b>0.71</b>	<b>0.71</b>	0.64	0.57	0.67	<b>0.71</b>
	Gabor	<b>0.71</b>	0.14	0.16	<b>0.71</b>	0.28	0.14	<b>0.71</b>
	GLCM	0.26	0.28	0.36	0.14	0.14	0.36	0.4
	LBP	0.07	0.14	0.14	0.07	0.07	0.14	0.19
	Combined	0.53	0.51	0.51	0.46	0.64	0.57	0.55

**Table 2.** Cont.

Evaluation Metric	Features	SVM	RF	XGBoost	Naive Bayes	AdaBoost	kNN	Bagging
Specificity	<b>HoG</b>	0.85	0.9	0.9	0.85	0.87	0.7	0.87
	<b>Gabor</b>	0.9	0.77	0.87	0.47	0.8	0.9	0.87
	<b>GLCM</b>	<b>0.95</b>	0.75	0.75	0.85	0.9	0.75	0.77
	<b>LBP</b>	0.9	0.78	0.78	0.8	0.85	0.73	0.88
	<b>Combined</b>	0.89	0.83	0.82	0.94	0.79	0.81	0.83
Accuracy	<b>HoG</b>	0.71	0.65	0.69	0.66	0.59	0.7	0.73
	<b>Gabor</b>	0.68	0.61	0.65	0.54	0.67	0.7	0.73
	<b>GLCM</b>	0.7	0.63	0.65	0.67	0.6	0.65	0.67
	<b>LBP</b>	0.69	0.59	0.6	0.61	0.65	0.57	0.59
	<b>Combined</b>	<b>0.78</b>	0.73	0.72	0.79	0.75	0.73	0.74
F1-score	<b>HoG</b>	0.67	<b>0.71</b>	<b>0.71</b>	0.62	0.59	0.6	0.69
	<b>Gabor</b>	0.7	0.16	0.1	0.44	0.3	0.2	0.69
	<b>GLCM</b>	0.34	0.29	0.34	0.18	0.2	0.34	0.36
	<b>LBP</b>	0.1	0.16	0.19	0.08	0.09	0.15	0.17
	<b>Combined</b>	0.59	0.54	0.53	0.57	0.61	0.57	0.57

**Figure 6.** The ROC curves of classifiers using HOG feature (image + patch).**Figure 7.** The ROC curves of classifiers using Gabor feature (image + patch).

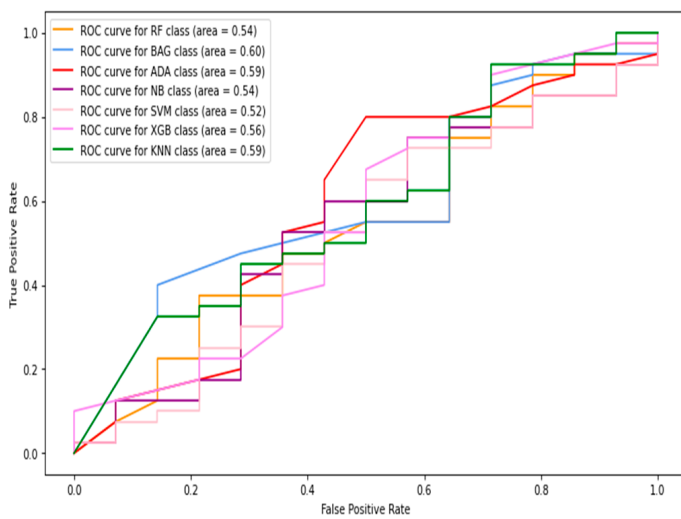


**Figure 8.** The ROC curves of classifiers using GLCM feature (image + patch).

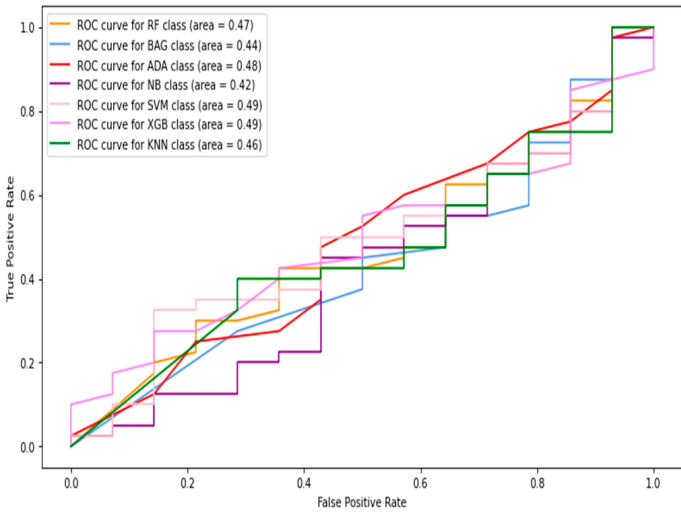


**Figure 9.** The ROC curves of classifiers using LBP feature (image + patch).

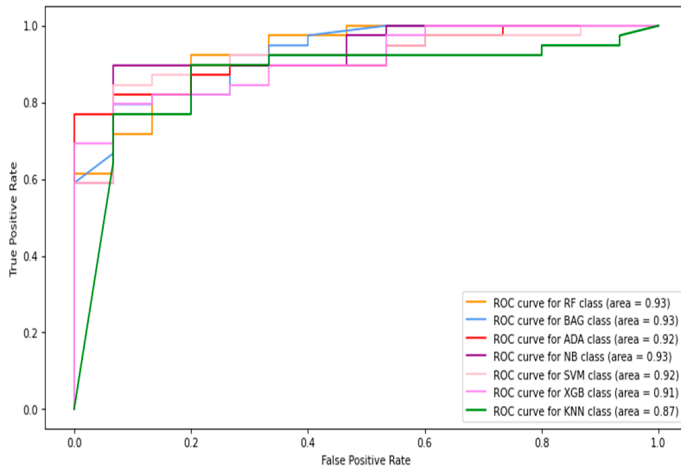


**Figure 10.** The ROC curves of classifiers using HOG + Gabor + GLCM + LBP feature (image + patch).

### 5.1.2. Full-Image Thermogram-Based Classification Results

In this section, thermogram image-level data are considered to record the classification results. Considering the results presented in the previous section, further experiments with machine-learning classifiers were restricted to using combined features only. Therefore, the HOG, Gabor, GLCM, and LBP features were extracted from the images and combined to be fed into the classifiers. Table 3 shows the image-level classification results using the combined features. The ROC curves are shown in Figure 11. The best sensitivity 0.642 was recorded using the kNN classifier while the SVM produced the best specificity value of 0.968. The XGBoost classifier achieved the best results for image-level classification with an 85.6% accuracy and F1-score of 0.688. The highest AUC of 0.84 was recorded with the naive Bayes classifier.

**Table 3.** Machine-learning classifier results using different features for full-image-level data.

Models	Sensitivity	Specificity	Accuracy	F1-Score
<b>SVM</b>	0.345	<b>0.968</b>	0.811	0.479
<b>RF</b>	0.559	0.948	0.850	0.652
<b>XGB</b>	0.630	0.932	<b>0.856</b>	<b>0.688</b>
<b>NB</b>	0.392	0.9	0.772	0.464
<b>ADA</b>	0.630	0.896	0.829	0.650
<b>kNN</b>	<b>0.642</b>	0.916	0.847	0.679
<b>BAG</b>	0.619	0.908	0.835	0.654

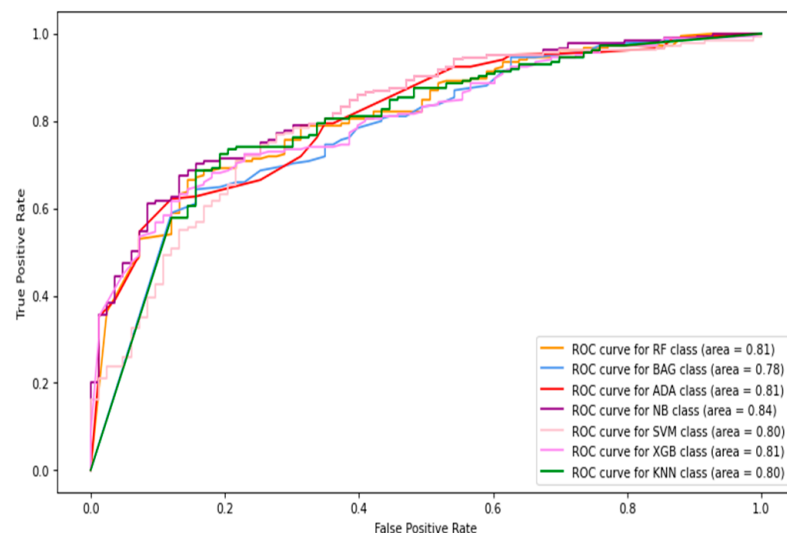


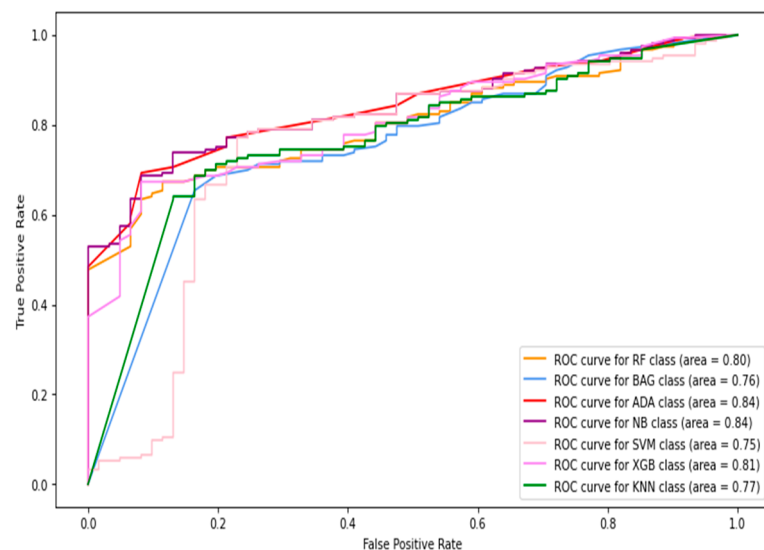
**Figure 11.** The ROC curves of classifiers using HOG + Gabor + GLCM + LBP feature (full images only).

### 5.1.3. Thermogram Patch-Based Classification Results

In this section, only thermogram patch-level data are considered to compute the results. The HOG, Gabor, GLCM, and LBP features were extracted from the image patches and combined to be fed into the classifiers. Table 4 shows the image-level classification results using the combined features. The AdaBoost classifier produced the best sensitivity score and F1-score of 0.638 and 0.609. In contrast, the naive Bayes classifier achieved the highest specificity and accuracy of 0.935 and 78.7%, respectively. The ROC curves of the patch-level results are shown in Figure 12. The highest AUC of 0.84 was observed by the naive Bayes classifier.

**Table 4.** Machine-learning classifier results using different features for patch-level data.

Models	Sensitivity	Specificity	Accuracy	F1-Score
<b>SVM</b>	0.530	0.886	0.776	0.594
<b>RF</b>	0.506	0.827	0.727	0.535
<b>XGB</b>	0.506	0.821	0.723	0.531
<b>NB</b>	0.457	<b>0.935</b>	<b>0.787</b>	0.571
<b>ADA</b>	<b>0.638</b>	0.794	0.746	<b>0.609</b>
kNN	0.566	0.805	0.731	0.566
BAG	0.554	0.827	0.742	0.571

**Figure 12.** The ROC curves of classifiers using HOG + Gabor + GLCM + LBP feature (patches only).

### 5.2. Results of Deep-Learning Approaches

In this section, the results of the CNN-based models are presented. As discussed earlier in the methodology section, the ResNet50 and DesnseNet121 models are used via transfer learning to classify the thermogram data. Moreover, the customized CNN model was developed for DFU classification. For the deep-learning approaches, the results are recorded at image level, at patch level, and by combining the images and patches. The results of both pre-trained models as well as the customized model are shown in Table 5. It can be observed that the proposed CNN model outperformed the pre-trained models in terms of sensitivity at each data representation level while achieving a best value of 0.97 at image level. The ResNet50 model produced the best specificity at patch level and at image-patch level of 0.913 and 0.902, respectively. However, the highest specificity of 0.958 was achieved by the proposed model again. The proposed model achieved the best accuracy among the three deep-learning models with a value of 97.1%, 93%, and 93.3% at image level, patch level, and image-patch level, respectively. The best F1-score of 0.891 was again recorded for the proposed model for all data representation levels. In medical diagnosis, it is critical to reduce false negatives so that the potential patient may be treated on time and the risk of amputation may be reduced. Table 5 presents the sensitivity and specificity analysis of the pre-trained models as well as the custom model. It can be observed that the custom model achieved the highest sensitivity rate and ensured the minimization of false negatives at all three levels. The graphical representation of the results using deep-learning-based models are shown in Figure 13. The accuracy and loss observations for the proposed CNN model are illustrated in Figures 14–16 at image level, patch level, and image-patch level, respectively. The proposed custom-developed CNN model was trained on the original foot thermogram data from scratch. In comparison, the pre-trained model was utilized with pre-trained weights originally tuned on ImageNet data; only the weights

of the last couple of layers were tuned based on the thermogram data. Therefore, the accuracy of the custom-developed model was better than the pre-trained models.

**Table 5.** Deep-learning classifier results using data at different levels.

	Models	Sensitivity	Specificity	Accuracy	F1-Score	AUC
Image Level	ResNet50	0.778	0.571	0.627	0.875	0.623
	DenseNet121	0.5	0.542	0.521	0.511	0.52
	Custom Model	<b>0.97</b>	<b>0.958</b>	<b>0.97</b>	<b>0.891</b>	<b>0.976</b>
Patch Level	ResNet50	0.565	<b>0.913</b>	0.832	0.874	0.834
	DenseNet121	0.661	0.822	0.791	0.8	0.788
	Custom Model	<b>0.839</b>	0.889	<b>0.93</b>	<b>0.891</b>	<b>0.932</b>
Image + Patch Level	ResNet50	0.697	<b>0.902</b>	0.881	0.75	0.879
	DenseNet121	0.75	0.875	0.843	0.8	0.841
	Custom Model	<b>0.839</b>	0.889	<b>0.933</b>	<b>0.891</b>	<b>0.938</b>

## Deep Learning DFU Classification Results

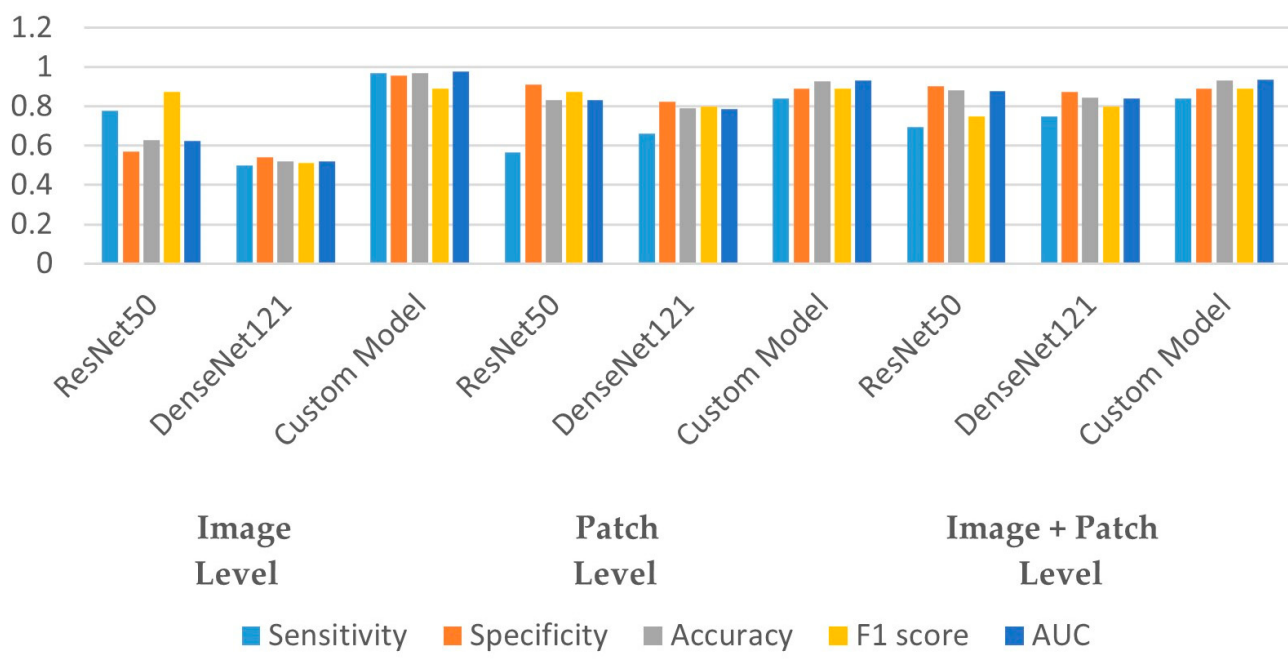


**Figure 13.** DFU classification results using deep-learning approaches.

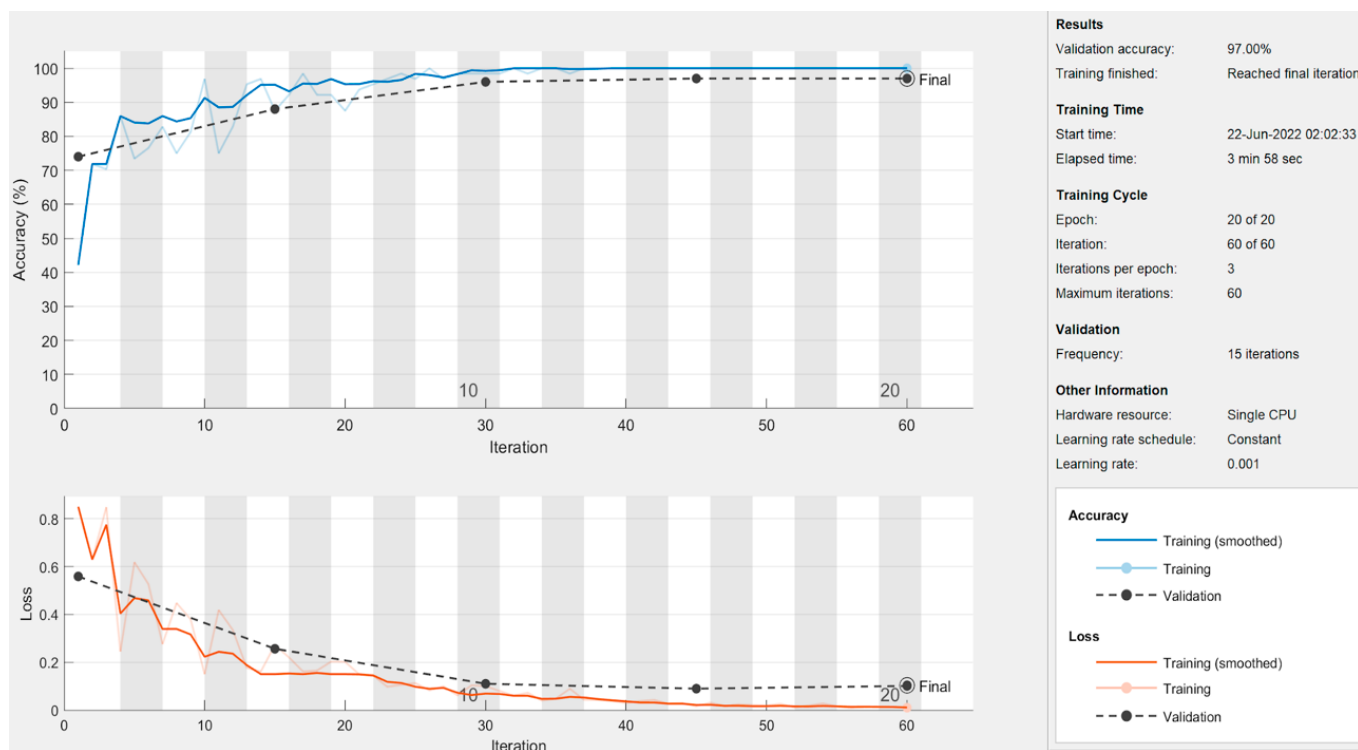


Figure 14. Full-image-level results of the proposed model.

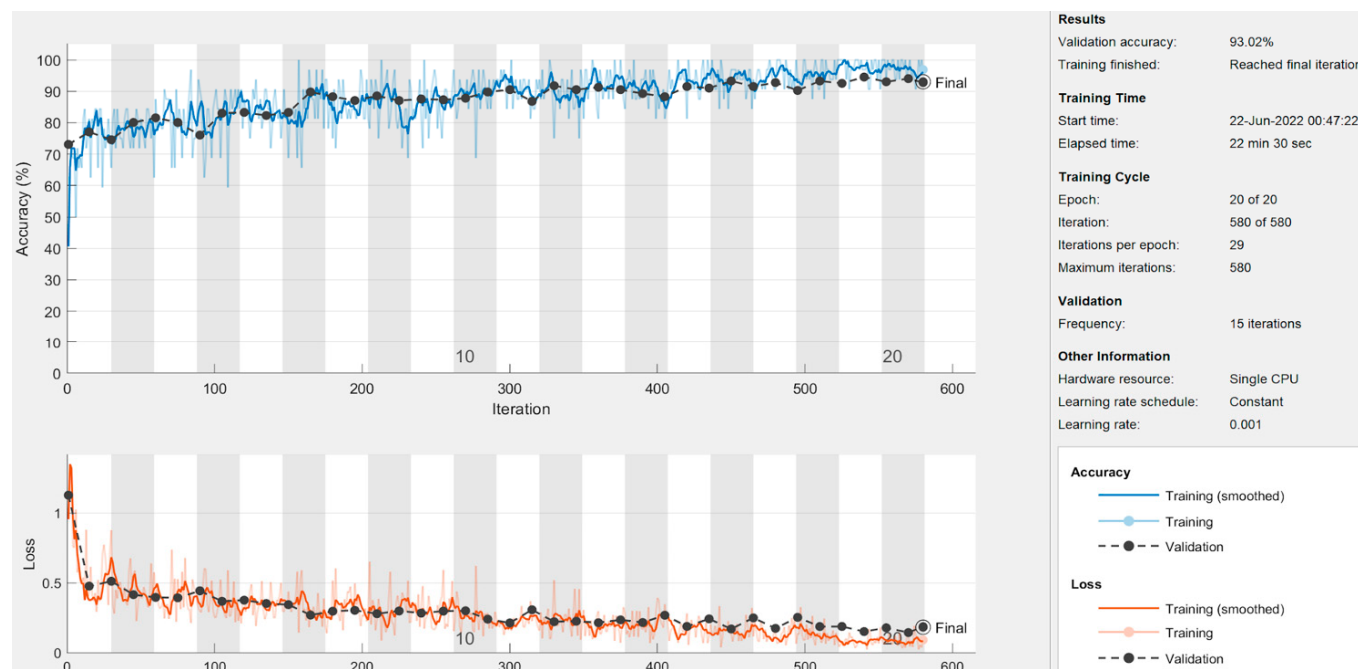
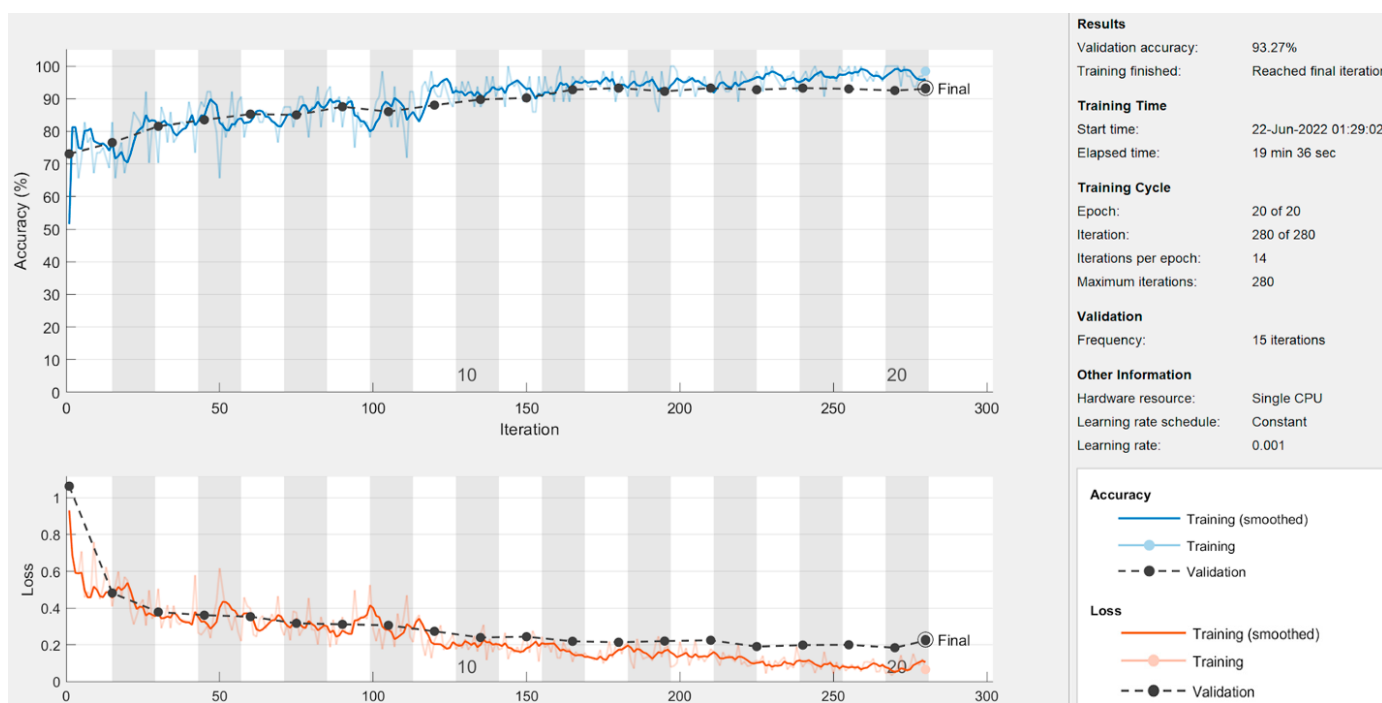


Figure 15. Patch-level results of the proposed model.



**Figure 16.** Image-patch level results of the proposed model.

When comparing the results of the proposed model with the state-of-the-art existing solution [9], the comparison is not straight forward. Firstly, the number of samples used after augmentation with the DFTNet were  $10\times$  than the original samples; however, the samples after augmentation were almost  $3\times$  which means that only  $1/3$  of data were used in this study in comparison to [9]. Next, only the patch-level thermogram data were considered in the study [9]. However, this study used data representation and result computation at image level, patch level, and image-patch level. Moreover, this study presents a binary classification between the diabetic foot and control group foot. However, the study [9] segregated the data as five distinct classes, and performed binary classification by taking two classes at a time randomly. Yet, they [9] achieved the best AUC score of 0.8533 and 0.8333 using the DFTNet and ANN, respectively. In comparison, we achieved an AUC score of 0.976, 0.932, and 0.938 for the image-level, patch-level, and image-patch level data, respectively. The DFTNet [9] achieved the best accuracy of 0.853 while the proposed model produced a 0.97 accuracy. Concretely, the comparison with the study [9] is not simple and there are many differences with respect to data selection, data quantity, data representation, and class representation. However, the proposed model outperforms by looking at several possible simpler comparisons.

Regarding the limitations of this study, it is worth mentioning that in all the experiments, including machine-learning and deep-learning classification, the thermogram images of the database and the augmented samples were utilized without any pre-processing. However, since the augmentation was performed only by rotation and flipping, the content of the image was retained. Speaking about the practical applicability of the proposed model, it cannot replace a human expert completely; however, it can provide a reliable second opinion while diagnosing the diabetic foot ulcer diagnosis. In contrast, in remote areas where a medical expert is not available, such a system can play a significant role in decision-making for DFU diagnosis.

## 6. Conclusions

In this study, the classification of DFU foot is presented via the comprehensive and comparative analysis of machine-learning as well as deep-learning approaches. The thermogram data of DFU and non-DFU feet are used at image level, patch level, and combined image-patch levels. The results of the machine-learning approaches are presented by employing several features extracted from thermograms. The SVM classifier among the machine-learning techniques proved to be the best. The classification results of the machine-learning models were best when the data at the full-image level were used. Among the pre-trained and the proposed deep-learning models, the proposed model produced the best results. The comparison of the proposed model with an existing solution based on the used thermogram data was not straight forward. However, while comparing at an abstract level, the proposed model performed better given the constraints.

**Author Contributions:** Conceptualization, I.K.; methodology, I.K. and A.R.; software, W.A. and A.R.; validation, M.A., S.S. and W.A.; formal analysis, I.K., A.R., M.A., S.S. and W.A.; investigation, I.K., M.A. and S.S.; resources, I.K. and A.R.; writing—original draft preparation, I.K. and A.R.; writing—review and editing, M.A., S.S. and W.A.; supervision, I.K. All authors have read and agreed to the published version of the manuscript.

**Funding:** This research was supported by the Princess Nourah bint Abdulrahman University Researchers Supporting Project number (PNURSP2023R259), Princess Nourah bint Abdulrahman University, Saudi Arabia.

**Institutional Review Board Statement:** The study only used a public dataset which was originally collected in another study. No human was involved in this study.

**Informed Consent Statement:** Informed consent was obtained from all subjects involved in the study.

**Data Availability Statement:** The data presented in this study are openly available online: <https://ieee-dataport.org/open-access/plantar-thermogram-database-study-diabetic-foot-complications>, accessed on 13 February 2022.

**Conflicts of Interest:** The authors declare no conflict of interest.

## References

- Wang, S.; Zhang, K.; Chao, L.; Li, D.; Tian, X.; Bao, H.; Chen, G.; Xia, Y. Exploring the Utility of Radar and Satellite-Sensed Precipitation and Their Dynamic Bias Correction for Integrated Prediction of Flood and Landslide Hazards. *J. Hydrol.* **2021**, *603*, 126964. [[CrossRef](#)]
- Iversen, M.M.; Tell, G.S.; Riise, T.; Hanestad, B.R.; Østbye, T.; Graue, M.; Midthjell, K. History of Foot Ulcer Increases Mortality Among Individuals with DiabetesTen-Year Follow-up of the Nord-Trøndelag Health Study, Norway. *Diabetes Care* **2009**, *32*, 2193–2199. [[CrossRef](#)] [[PubMed](#)]
- Hernandez-Contreras, D.A.; Peregrina-Barreto, H.; Rangel-Magdaleno, J.D.J.; Renero-Carrillo, F.J. Plantar Thermogram Database for the Study of Diabetic Foot Complications. *IEEE Access* **2019**, *7*, 161296–161307. [[CrossRef](#)]
- Ring, F. Thermal Imaging Today and Its Relevance to Diabetes. *J. Diabetes Sci. Technol.* **2010**, *4*, 857–862. [[CrossRef](#)]
- Bagavathiappan, S.; Philip, J.; Jayakumar, T.; Raj, B.; Rao, P.N.S.; Varalakshmi, M.; Mohan, V. Correlation between Plantar Foot Temperature and Diabetic Neuropathy: A Case Study by Using an Infrared Thermal Imaging Technique. *J. Diabetes Sci. Technol.* **2010**, *4*, 1386–1392. [[CrossRef](#)]
- Hernandez-Contreras, D.; Peregrina-Barreto, H.; Rangel-Magdaleno, J.; Gonzalez-Bernal, J. Narrative Review: Diabetic Foot and Infrared Thermography. *Infrared Phys. Technol.* **2016**, *78*, 105–117. [[CrossRef](#)]
- Liu, C.; van der Heijden, F.; Klein, M.E.; van Baal, J.G.; Bus, S.A.; van Netten, J.J. Infrared Dermal Thermography on Diabetic Feet Soles to Predict Ulcerations: A Case Study. *Adv. Biomed. Clin. Diagn. Syst. XI* **2013**, *8572*, 102–110. [[CrossRef](#)]
- Faust, O.; Rajendra Acharya, U.; Ng, E.Y.K.; Hong, T.J.; Yu, W. Application of Infrared Thermography in Computer Aided Diagnosis. *Infrared Phys. Technol.* **2014**, *66*, 160–175. [[CrossRef](#)]
- Cruz-Vega, I.; Hernandez-Contreras, D.; Peregrina-Barreto, H.; Rangel-Magdaleno, J.d.J.; Ramirez-Cortes, J.M. Deep Learning Classification for Diabetic Foot Thermograms. *Sensors* **2020**, *20*, 1762. [[CrossRef](#)]

10. Adam, M.; Ng, E.Y.K.; Oh, S.L.; Heng, M.L.; Hagiwara, Y.; Tan, J.H.; Tong, J.W.K.; Acharya, U.R. Automated Detection of Diabetic Foot with and without Neuropathy Using Double Density-Dual Tree-Complex Wavelet Transform on Foot Thermograms. *Infrared Phys. Technol.* **2018**, *92*, 270–279. [[CrossRef](#)]
11. Goyal, M.; Reeves, N.D.; Davison, A.K.; Rajbhandari, S.; Spragg, J.; Yap, M.H. DFUNet: Convolutional Neural Networks for Diabetic Foot Ulcer Classification. *IEEE Trans. Emerg. Top. Comput. Intell.* **2018**, *4*, 728–739. [[CrossRef](#)]
12. Nanda, R.; Nath, A.; Patel, S.; Mohapatra, E. Machine Learning Algorithm to Evaluate Risk Factors of Diabetic Foot Ulcers and Its Severity. *Med. Biol. Eng. Comput.* **2022**, *60*, 2349–2357. [[CrossRef](#)] [[PubMed](#)]
13. Cao, C.; Qiu, Y.; Wang, Z.; Ou, J.; Wang, J.; Hounye, A.H.; Hou, M.; Zhou, Q.; Zhang, J. Nested Segmentation and Multi-Level Classification of Diabetic Foot Ulcer Based on Mask R-CNN. *Multimed. Tools Appl.* **2022**, *82*, 18887–18906. [[CrossRef](#)]
14. Fraiwan, L.; AlKhodari, M.; Ninan, J.; Mustafa, B.; Saleh, A.; Ghazal, M. Diabetic Foot Ulcer Mobile Detection System Using Smart Phone Thermal Camera: A Feasibility Study. *Biomed. Eng. Online* **2017**, *16*, 117. [[CrossRef](#)] [[PubMed](#)]
15. Xu, Y.; Han, K.; Zhou, Y.; Wu, J.; Xie, X.; Xiang, W. Classification of Diabetic Foot Ulcers Using Class Knowledge Banks. *Front. Bioeng. Biotechnol.* **2022**, *9*, 811028. [[CrossRef](#)]
16. Ai, L.; Yang, M.; Xie, Z. ACTNet: Asymmetric Convolutional Transformer Network for Diabetic Foot Ulcers Classification. *Phys. Eng. Sci. Med.* **2022**, *45*, 1175–1181. [[CrossRef](#)]
17. Goyal, M.; Reeves, N.D.; Rajbhandari, S.; Yap, M.H. Robust Methods for Real-Time Diabetic Foot Ulcer Detection and Localization on Mobile Devices. *IEEE J. Biomed. Health Inform.* **2019**, *23*, 1730–1741. [[CrossRef](#)]
18. Santos, F.; Santos, E.; Vogado, L.H.; Ito, M.; Bianchi, A.; Tavares, J.M.; Veras, R. DFU-VGG, a Novel and Improved VGG-19 Network for Diabetic Foot Ulcer Classification. In Proceedings of the 2022 29th International Conference on Systems, Signals and Image Processing (IWSSIP), Sofia, Bulgaria, 1–3 June 2022. [[CrossRef](#)]
19. Al-Garaawi, N.; Ebsim, R.; Alharan, A.F.H.; Yap, M.H. Diabetic Foot Ulcer Classification Using Mapped Binary Patterns and Convolutional Neural Networks. *Comput. Biol. Med.* **2022**, *140*, 105055. [[CrossRef](#)]
20. Tulloch, J.; Zamani, R.; Akrami, M. Machine Learning in the Prevention, Diagnosis and Management of Diabetic Foot Ulcers: A Systematic Review. *IEEE Access* **2020**, *8*, 198977–199000. [[CrossRef](#)]
21. Niri, R.; Lucas, Y.; Treuillet, S.; Douzi, H. Smartphone-Based Thermal Imaging System for Diabetic Foot Ulcer Assessment. In *Journées d'Etude sur la TéléSanté*; Sorbonne Universités: Paris, France, 2019.
22. Liu, C.; van Netten, J.J.; van Baal, J.G.; Bus, S.A.; van der Heijden, F. Automatic Detection of Diabetic Foot Complications with Infrared Thermography by Asymmetric Analysis. *J. Biomed. Opt.* **2015**, *20*, 026003. [[CrossRef](#)]
23. Vardasca, R.; Magalhaes, C.; Seixas, A.; Carvalho, R.; Mendes, J. Diabetic Foot Monitoring Using Dynamic Thermography and AI Classifiers. In Proceedings of the 3rd Quantitative InfraRed Thermography Asia Conference (QIRT), Tokyo, Japan, 1–5 July 2019. [[CrossRef](#)]
24. Adam, M.; Ng, E.Y.K.; Oh, S.L.; Heng, M.L.; Hagiwara, Y.; Tan, J.H.; Tong, J.W.K.; Acharya, U.R. Automated Characterization of Diabetic Foot Using Nonlinear Features Extracted from Thermograms. *Infrared Phys. Technol.* **2018**, *89*, 325–337. [[CrossRef](#)]
25. Van Netten, J.J.; Van Baal, J.G.; Liu, C.; Van Der Heijden, F.; Bus, S.A. Infrared Thermal Imaging for Automated Detection of Diabetic Foot Complications. *J. Diabetes Sci. Technol.* **2013**, *7*, 1122–1129. [[CrossRef](#)]
26. Van Netten, J.J.; Prijs, M.; Van Baal, J.G.; Liu, C.; Van Der Heijden, F.; Bus, S.A. Diagnostic Values for Skin Temperature Assessment to Detect Diabetes-Related Foot Complications. *Diabetes Technol. Ther.* **2014**, *16*, 714–721. [[CrossRef](#)]
27. Khosa, I.; Pasero, E. *Defect Detection in Food Ingredients Using Multilayer Perceptron Neural Network*; IEEE: Piscataway, NJ, USA, 2014. ISBN 9781479928057.
28. Schölkopf, B. SVMs—A Practical Consequence of Learning Theory. *IEEE Intell. Syst. Their Appl.* **1998**, *13*, 18–21. [[CrossRef](#)]
29. Breiman, L. Random Forests. *Mach. Learn.* **2001**, *45*, 5–32. [[CrossRef](#)]
30. Baskett, F.; Shustek, L.J. An Algorithm for Finding Nearest Neighbors. *IEEE Trans. Comput.* **1975**, *C-24*, 1000–1006. [[CrossRef](#)]
31. Cichosz, P. Naïve Bayes Classifier. In *Data Min. Algorithms*; Wiley Data and Cybersecurity: Hoboken, NJ, USA, 2015; pp. 118–133. [[CrossRef](#)]
32. Chen, T.; Guestrin, C. XGBoost: A Scalable Tree Boosting System. In Proceedings of the 22nd ACM SIGKDD International Conference on Knowledge Discovery and Data Mining, New York, NY, USA, 13–17 August 2016. [[CrossRef](#)]
33. Rätsch, G.; Onoda, T.; Müller, K.R. Soft Margins for AdaBoost. *Mach. Learn.* **2001**, *42*, 287–320. [[CrossRef](#)]
34. Breiman, L. Bagging Predictors. *Mach. Learn.* **1996**, *24*, 123–140. [[CrossRef](#)]
35. Pietikäinen, M. Image Analysis with Local Binary Patterns. *Lect. Notes Comput. Sci.* **2005**, *3540*, 115–118. [[CrossRef](#)]
36. Dalal, N.; Triggs, B. Histograms of Oriented Gradients for Human Detection. In Proceedings of the 2005 IEEE Computer Society Conference on Computer Vision and Pattern Recognition (CVPR’05), San Diego, CA, USA, 20–25 June 2005; Volume I, pp. 886–893. [[CrossRef](#)]
37. Fogel, I.; Sagi, D. Gabor Filters as Texture Discriminator. *Biol. Cybern.* **1989**, *61*, 103–113. [[CrossRef](#)]
38. Haralick, R.M.; Dinstein, I.; Shanmugam, K. Textural Features for Image Classification. *IEEE Trans. Syst. Man Cybern.* **1973**, *SMC-3*, 610–621. [[CrossRef](#)]
39. He, K.; Zhang, X.; Ren, S.; Sun, J. Deep Residual Learning for Image Recognition. In Proceedings of the IEEE Conference on Computer Vision and Pattern Recognition (CVPR), Las Vegas, NV, USA, 26 June–1 July 2016.

40. Deng, J.; Dong, W.; Socher, R.; Li, L.-J.; Li, K.; Fei-Fei, L. ImageNet: A Large-Scale Hierarchical Image Database. In Proceedings of the 2009 IEEE Conference on Computer Vision and Pattern Recognition, Miami, FL, USA, 20–25 June 2009; Institute of Electrical and Electronics Engineers (IEEE): Piscataway, NJ, USA, 2010; pp. 248–255.
41. Huang, G.; Liu, Z.; van der Maaten, L.; Weinberger, K.Q. Densely Connected Convolutional Networks. In Proceedings of the IEEE Conference on Computer Vision and Pattern Recognition, Honolulu, HI, USA, 21–26 July 2017; pp. 4700–4708.

**Disclaimer/Publisher’s Note:** The statements, opinions and data contained in all publications are solely those of the individual author(s) and contributor(s) and not of MDPI and/or the editor(s). MDPI and/or the editor(s) disclaim responsibility for any injury to people or property resulting from any ideas, methods, instructions or products referred to in the content.



## Computer aided detection of diabetic foot ulcer using asymmetry analysis of texture and temperature features

J. Saminathan<sup>a,\*</sup>, M. Sasikala<sup>a</sup>, VB. Narayananmurthy<sup>b</sup>, K. Rajesh<sup>b</sup>, R. Arvind<sup>b</sup>

<sup>a</sup> Department of Electronics and Communication Engineering, CEG Campus, Anna University, Chennai, Tamil Nadu, India

<sup>b</sup> Hycare for Wounds, Chennai, Tamil Nadu, India



### ARTICLE INFO

#### Keywords:

Diabetic foot  
Asymmetry analysis  
Foot ulcer  
Thermal Image  
Temperature  
Texture  
Support vector machine

### ABSTRACT

Diabetic foot ulcer is a foremost complication of poorly controlled diabetes mellitus leading to lower extremity amputation. Early identification depends on repeated risk assessment, preferably on a day-to-day basis especially for high-risk patients. The temperature variations in the areas prone to ulcer are higher than non-ulcerous regions of the foot. The ultimate aim of this study was to develop an efficient algorithm for early detection of diabetic foot with infrared thermal images using asymmetry analysis. The left and right foot regions are segmented using region growing method. In normal plantar thermograms, symmetric temperature distributions are observed, whereas, in the case of the diabetic foot, asymmetry was observed between ipsilateral and contralateral regions of the foot. The texture and temperature features are extracted from the 11 regions of interest from the foot and asymmetric analysis was performed for the features extracted from the ipsilateral and contralateral regions of the foot. Support vector machine was used to classify the region of interest into normal and ulcer. The proposed method achieved maximum accuracy of 95.61%, sensitivity of 96.5% and specificity of 92.41%. The performance of the proposed technique shows that it is trustworthy and effective for early identification of pre-signs of ulceration and aids the clinicians in the treatment of the diabetic foot.

### 1. Introduction

Diabetes is a chronic disease characterized by hyperglycemia resulting from defects in insulin secretion, insulin action, or both. The chronic hyperglycemia of diabetes is associated with long-term damage, dysfunction, and failure of different organs, especially the eyes, kidneys, nerves, heart, and blood vessels [1]. The International Diabetes Federation (IDF) reports that currently there are 382 million people with diabetes worldwide and by 2035 this number is expected to increase up to 592 million people [2,3]. People with chronic diabetes and people with poor circulation are prone to diabetic foot ulcer that occurs due to the destruction of deep tissue in the lower limb. Foot ulcers are especially common in people who have one or more of the health complications such as peripheral neuropathy, circulatory problems, and abnormalities in the bones or muscles of the feet [4]. A vascular and neurological disorder in lower extremities is one of the common complications with Diabetes Mellitus (DM). Critical foot complications arise at the future stage of DM and are in about 15%–25% of diabetic patients and among them, 6% of the people will be hospitalized. These foot problems arise as a consequence of foot ulceration, infection and also due to peripheral ischemia. Peripheral neuropathy and lower extremity

ischemia due to peripheral artery disease are the principal causes of diabetic foot ulcers, which affects the capability of the foot to feel and sense. Common signs and symptoms of a diabetic foot ulcer include numbness, the appearance of drainage on the person's socks, redness, unusual swelling, and regions with increased temperature [5,6].

Infrared (IR) thermal imaging cameras have been increasingly used in clinical situations for accurate and objective thermal mapping of the human body, particularly as a complementary, noninvasive, non-radioactive diagnostic method [5,7–12,35,36,38]. A blackbody or a full radiator is defined as a radiator of uniform surface temperature whose radiant exitance in all parts of the spectrum is the maximum obtainable. The emissivity of a full radiator is unity for all wavelengths. Since the human skin has an emissivity value of 0.98, thus making it more competent for the measurement of temperature distribution using infrared thermal imaging system [9]. The thermal image of the foot gives a complete representation of the distribution of temperatures in the plantar region [10]. Several studies report that the ulceration caused by inflammation that has occurred at the site of measurement is indicated in terms of temperature increase greater than 2.2 °C between right and left foot. [3,13–17,35]. Comparison of temperature distributions of both the feet from the same subject is made and this information is

\* Corresponding author.

E-mail address: [saminathan23@yahoo.in](mailto:saminathan23@yahoo.in) (J. Saminathan).

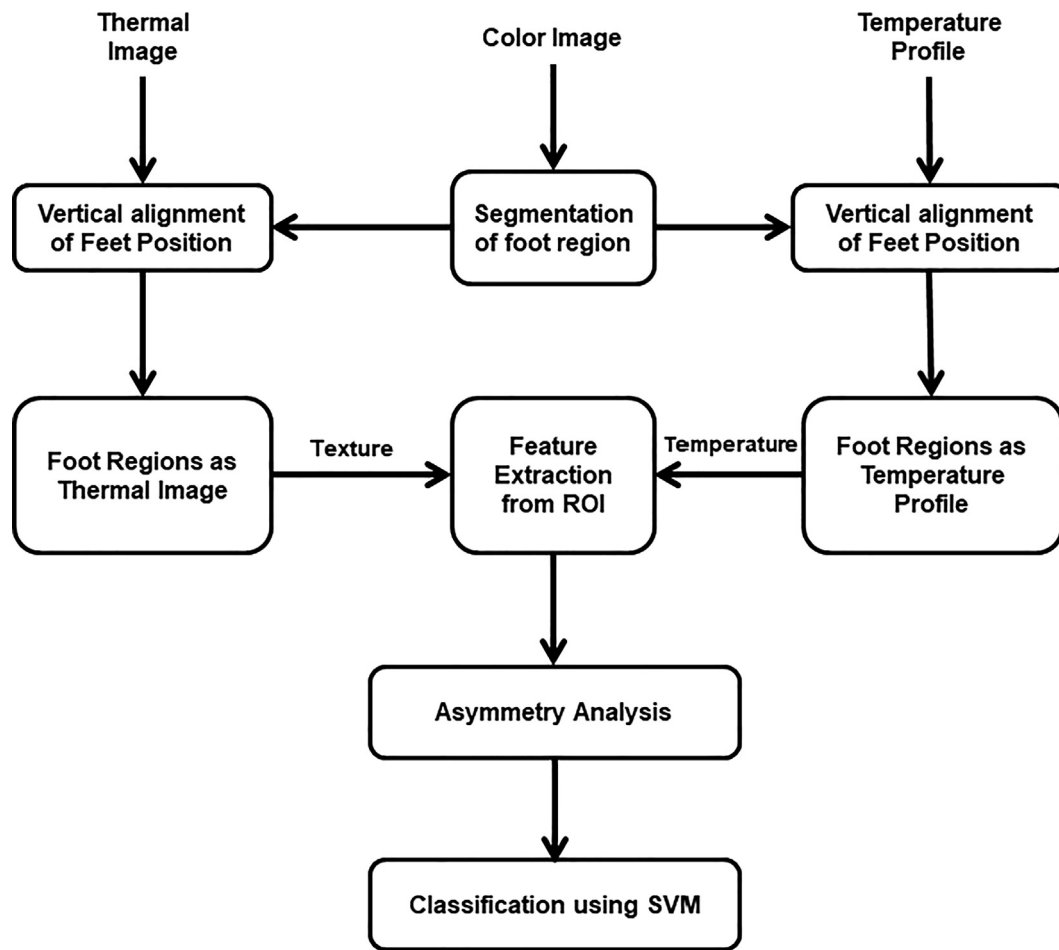


Fig. 1. Schematic flowchart of the proposed methodology.

combined to predict the ulcers using a thresholding technique [18]. The texture and temperature distributions are different for control and for patients who have diabetic foot complications. Symmetric texture and temperature distributions are observed in foot thermogram of control foot whereas asymmetry is observed when there is foot complication in one of the foot regions. From the literature, it is inferred that asymmetric analysis in temperature distribution and external stress analysis have been the most common analyses for identifying diabetic foot complications, while the distribution of texture analysis has been least used so far.

The main objective of this study is to develop an efficient algorithm for early detection of diabetic foot with infrared thermal images using asymmetry analysis of both texture and temperature features. Texture and temperature features are extracted from the plantar foot thermal images. A support vector machine (SVM) is trained to classify the features into normal or prone to an ulcer.

## 2. Materials and methods

The proposed schematic flow for early detection of diabetic foot ulcer is shown in Fig. 1. The thermal image and color image of the foot are acquired using the FLIR E60 thermal imaging camera. The left and right foot regions are segmented from the color image of the foot using region growing algorithm. These foot regions are used to segment the foot regions from the thermal image and temperature profile of the foot. Textural and temperature features are extracted and asymmetric analysis is performed for most prone areas which can develop diabetic foot ulcer. These features are used to train the support vector machine and classify the region of interest as normal or prone to an ulcer.

### 2.1. Thermal imaging camera

Most of the work in the plantar foot thermography has been done on thermograms acquired using infrared thermal imaging camera. Thermal imaging cameras with a finer resolution made for medical applications are able to measure subtle changes in temperature and hence are capable of improved detection of diabetic foot complications. A FLIR E60 thermal imaging camera is used for the present study to acquire plantar foot thermal images. It has a resolution of  $320 \times 240$  pixels and covers a field of view (FOV) of  $25^\circ \times 19^\circ$ . The range of operation of the camera is in the region of the infrared spectrum from  $7.5 \mu\text{m}$  to  $13 \mu\text{m}$  wavelength. It has the ability to detect the temperature in the range of  $-20^\circ\text{C}$  to  $650^\circ\text{C}$  with thermal sensitivity of less than  $0.07^\circ\text{C}$  at  $30^\circ\text{C}$  and has an onboard digital camera with a resolution of 3.1 megapixels (MP). The onboard digital camera covers the same FOV as that of thermal imaging camera and acquired images are of size  $2048 \times 1536$  pixels. The temperature values are associated with a color palette (Rainbow Color Scheme palette) in order to represent and distinguish them graphically. It is ensured that the thermal imaging camera is calibrated against a black body reference as per the manufacturer's recommendations [20].

### 2.2. Image acquisition protocol

Thermal image and color image of the plantar foot are acquired from sixty subjects in the present work, out of which 24 are non-diabetic subjects that form the control group and 36 with diagnosed diabetes that forms the DM group. Both control and DM groups include male and female participants, aged between 30 and 65 years. Ethical



**Fig. 2a.** Color image of the foot – control.



**Fig. 3a.** Color image of the foot – diabetes mellitus.

approval was sought and granted by the Institution Ethics Committee of Hycare for Wounds, Chennai. All the participants provided their written informed consent to take part in this study. The experimental room is shielded from any other available infrared (IR) radiation source. Thermal imaging camera is positioned perpendicular to the plane of acquisition at a distance of 1.1 m. The thermal images are obtained in a closed room with a controlled temperature of  $20 \pm 2^\circ\text{C}$ . During the examination, the participants are seated fairly equidistant and adequately spaced from each wall. The subjects are instructed to remove the footwear to clean their foot by wiping them thoroughly using a damp towel. Subsequently, the participants remained barefooted for 10–15 min before the acquisition of thermal images to achieve equilibrium with the contrast ambient temperature [5,6,9,10,21–24,32–34,37].

A uniform backdrop is placed to ensure a homogenous background. The regions prone to ulcer, determined by wound care specialists, was considered as ulcer regions for the classification of the region of interests. The acquired images of the plantar foot of a participant from the control group and DM group with the onboard digital camera and thermal imaging camera, are shown in Figs. 2(a), 2(b) and Figs. 3(a), 3(b) respectively. The temperature profile ( $320 \times 240$ ) for all the pixel of the acquired thermal image, are exported to comma-separated values (CSV) format with the help of FLIR research and development software.

### 2.3. Segmentation of foot region

Color images (images acquired through the onboard digital camera) of the plantar foot are converted to grayscale and divided into two sub-images of size  $240 \times 160$ , in which first sub-image represents the left



**Fig. 3b.** Thermal image of the foot – diabetes mellitus.

foot and second sub-image represents the right foot. The left and right foot regions are segmented without background using region growing algorithm [25]. The initial seed pixel was fixed at the midpoint of the foot region. The region is grown from the initialized seed pixel by adding in adjacent pixels that are similar, increasing the size of the region. An initial set of small areas are iteratively appended according to the similarity constraints until there are no modifications in two successive iterative stages. The segmented foot regions are in the form of a binary image (foreground or foot region as 1 and background as 0).

### 2.4. Vertical alignment of feet position

A participant's left foot and right foot does not persist vertical position in resting position during the image acquisition of plantar foot. Instead, they are laterally displaced. The feet position is corrected by drawing a segment from the centroid of the foot to the center of the calcaneal base (the heel). The orientation angle is calculated between the center of the calcaneal base with respect to a perpendicular line from the centroid of the segmented foot region. Then the right and left foot regions are rotated around the centroid for the orientation angle to make the vertical alignment of the foot region, which is depicted in Figs. 4a and 4b. The thermal image of the foot region and temperature profile are also rotated in the same manner for both the left and right foot. The binary image of the segmented foot regions is multiplied with the red, green and blue planes of the respective foot image and concatenated together to get the segmented foot regions from the thermal image. The segmented left and right foot regions of the control group and DM group are illustrated in Figs. 5a and 5b, respectively. The binary image of the segmented foot regions is multiplied with the

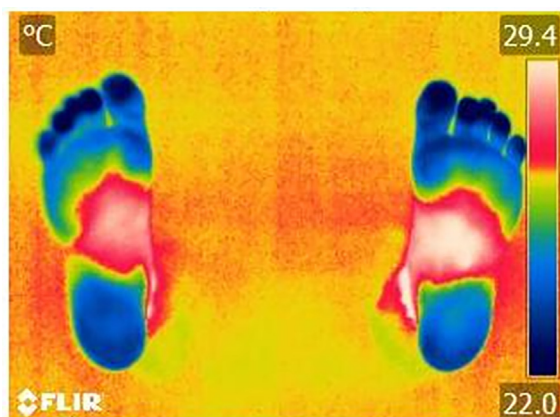


**Fig. 2b.** Thermal image of the foot – control.

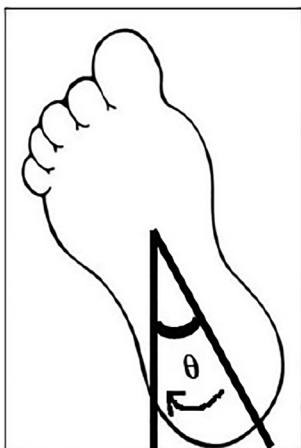


Fig. 4a. Vertical alignment of right foot.



Fig. 4b. Vertical alignment of left foot.

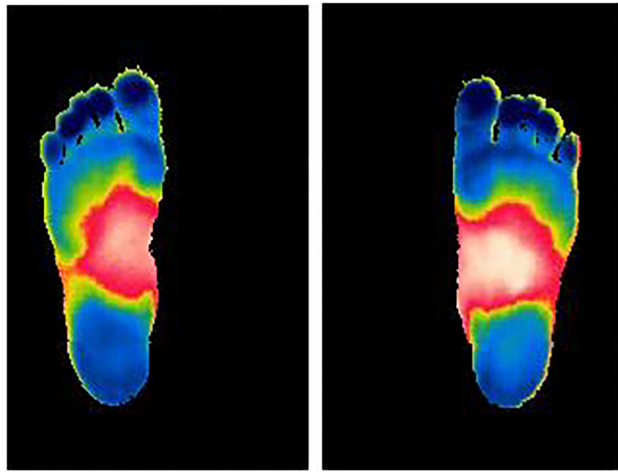


Fig. 5a. Segmented left and right foot regions of the Control Group.

temperature profile of the corresponding foot regions to acquire the temperature distribution for foot regions.

## 2.5. Feature extraction

The toe apices (great toe, index toe, middle toe, fourth toe, little toe), 5 metatarsal heads behind the phalanges of the toe apices and

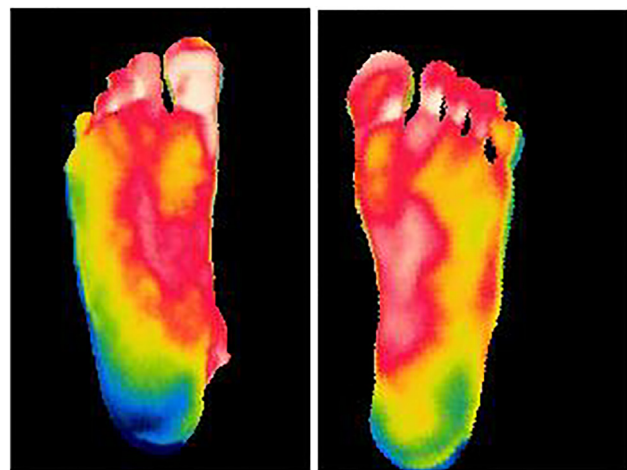


Fig. 5b. Segmented left and right foot regions of the DM Group.

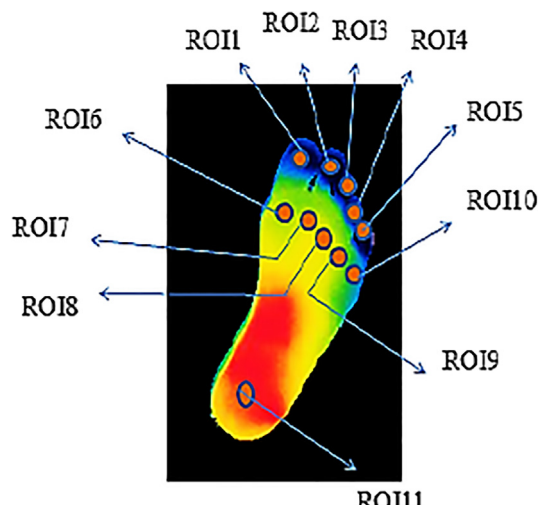


Fig. 6. Primary regions 'at risk' for developing diabetic foot complications.

calcaneal heel are considered as primary regions of interest (ROI) 'at risk' for developing diabetic foot ulcer [26,27]. These regions are selected in both the foot regions as shown in Fig. 6. These eleven ROIs (ROI1 – ROI11) are selected from segmented left and right foot regions manually and converted to grayscale. Similarly, the same eleven ROIs are selected from the temperature distribution of both the foot regions. The mean and standard deviation (SD) of temperature is found for all ROIs and stored as feature vectors for further processing. The following equations define these features

(1) Mean temperature

$$f_1 = \frac{1}{N} \sum_{i=1}^N T_i \quad (1)$$

(2) Standard deviation of temperature

$$f_2 = \sqrt{\frac{1}{N-1} \sum_{i=1}^N |T_i - f_1|^2} \quad (2)$$

The gray level co-occurrence matrix (GLCM), a renowned statistical technique based on joint probability distribution of pair of pixels is used for extracting second order texture features from ROIs in this study.

An image with the size of  $M \times N$  pixels and  $L$  gray levels could illustrate the frequency of pixel (i.e.) at the position  $[x + d_x, y + d_y]$  that occur with gray level  $j$  and in accordance with a distance  $d$  from a certain pixel at the position  $(x, y)$  with gray level  $i$ . The frequency is

denoted by  $P$  and its mathematical expression is given as

$$p_{(i,j,d,\theta)} = \sum_{x=1}^K \sum_{y=1}^K \begin{cases} 1, & \text{if } I(x, y) = i \text{ and } I(x + d_x, y + d_y) = j \\ 0, & \text{Otherwise} \end{cases} \quad (3)$$

where  $(x, y)$  denotes the coordinates of the image  $I$ , pixel  $i$  and  $j$  are the gray values.  $d_x$  and  $d_y$  denote the position offsets  $d$  is the step,  $\theta$  is the direction. Once the GLCM in a certain direction is constructed,  $p_{(i,j,d,\theta)}$  needs to be normalized to ensure that its feature is not influenced by the regions limitations. The normalized  $p_{(i,j,d,\theta)}$  is

$$p_{(i,j,d,\theta)} = \frac{p_{(i,j,d,\theta)}}{R} \quad (4)$$

If  $\theta = 0^\circ$ ,  $R$  is taken as  $2M \times (N - 1)$

If  $\theta = 90^\circ$ ,  $R$  is taken as  $2N \times (M - 1)$

If  $\theta = 45^\circ = 135^\circ$ ,  $R$  is taken as  $2(M - 1) \times (N - 1)$ .

For a given offset distance, co-occurrence matrices are calculated for offset angle of  $0^\circ$  and 12 GLCM texture features are derived in this study. The features are defined in equation numbers 9–20. Let  $p(i, j)$  be the  $(i, j)$ th entry in the normalized GLCM [28–31]. The mean and standard deviation for rows and columns of the matrix are

$$\mu_x = \sum_i \sum_j i \cdot p(i, j) \quad (5)$$

$$\mu_y = \sum_i \sum_j j \cdot p(i, j) \quad (6)$$

$$\sigma_x = \sum_i \sum_j (i - \mu_x)^2 \cdot p(i, j) \quad (7)$$

$$\sigma_y = \sum_i \sum_j (j - \mu_y)^2 \cdot p(i, j) \quad (8)$$

The texture features are as follows.

(3) Autocorrelation

$$f_3 = \sum_i \sum_j (ij) p(i, j) \quad (9)$$

(4) Contrast

$$f_4 = \sum_{n=0}^{N_g-1} n^2 \left\{ \sum_{i=1}^{N_g} \sum_{j=1}^{N_g} p(i, j) \mid |i - j| = n \right\} \quad (10)$$

(5) Correlation

$$f_5 = \frac{\sum_i \sum_j (ij) p(i, j) - \mu_x \mu_y}{\sigma_x \sigma_y} \quad (11)$$

(6) Dissimilarity

$$f_6 = \sum_i \sum_j |i - j| p(i, j) \quad (12)$$

(7) Energy

$$f_7 = \sum_i \sum_j p(i, j)^2 \quad (13)$$

(8) Entropy

$$f_8 = - \sum_i \sum_j p(i, j) \log(p(i, j)) \quad (14)$$

(9) Homogeneity

$$f_9 = \sum_i \sum_j \frac{1}{1 + (i - j)^2} p(i, j) \quad (15)$$

(10) Maximum Probability

$$f_{10} = \max_{(i,j)} p(i, j) \quad (16)$$

(11) Sum of Squares: Variance

$$f_{11} = \sum_i \sum_j (i - \mu)^2 p(i, j) \quad (17)$$

(12) Sum Average

$$f_{12} = \sum_{i=2}^{2N_g} i p_{x+y}(i) \quad (18)$$

(13) Sum Entropy

$$f_{13} = - \sum_{i=2}^{2N_g} p_{x+y}(i) \log(p_{x+y}(i)) \quad (19)$$

(14) Sum Variance

$$f_{14} = \sum_{i=2}^{2N_g} (i - f_{11})^2 p_{x+y}(i) \quad (20)$$

The above twelve texture features are extracted from the GLCM of the all eleven ROIs for both left and right foot region and stored as feature vectors in the database for training the network.

## 2.6. Asymmetry analysis

Asymmetry analysis is an indicator used to determine the difference in the extracted texture and temperature features between ipsilateral and contralateral foot regions (ROIs) [18,19,33,34]. The GLCM texture features and temperature features are extracted from all the 11 ROIs in left and right foot regions. The ROI-1 of temperature features and texture features of right foot region is subtracted from the ROI-1 of temperature features and texture features of left foot region to get the asymmetric analysis between the left foot and right foot. This process is performed in the similar method for the remaining ROIs (ROI-2 to ROI-11). In the foot thermograms of the control group, symmetric temperature distributions are habitually observed in both foot region and, hence, texture and temperature features extracted from ipsilateral and contralateral regions of the foot (ROIs) are almost the same. Thus, the difference in feature values between them will be negligible. However, this difference will be noteworthy in the case of diabetic foot complications, due to the inherent thermal asymmetry between the ipsilateral and contralateral region of foot regions.

## 2.7. Classification using SVM

Support Vector Machine (SVM) is a discriminative classifier algorithm, in regard to the patterns represented by the subset  $d_i = +1$  and the patterns represented by the subset  $d_i = -1$  are linearly separable. The decision surface that is in the form of a hyperplane that does the separation is given as follows.

$$w^T x = \sum_i w_i x_i \quad (21)$$

$$w^T x + b = 0 \quad (22)$$

where  $x$  is an input vector,  $w$  is an adjustable weight vector and  $b$  is bias. The point closest to hyperplane is called the ‘support vector’. The SVM classifier maximizes the margin of separation ( $\rho$ ) between the classes and minimizes the classification errors [32]. SVM classifies the input feature vectors by finding the best hyperplane that separates all data points of one class (control group) from those of the other class (DM group). The best hyperplane for SVM is the one with the largest margin between the two classes as illustrated in Fig. 7. The classification performance of SVM classifier is evaluated by the following metrics.

$$\text{Accuracy} = \frac{TP + TN}{TP + TN + FP + FN} \times 100\% \quad (23)$$

$$\text{Sensitivity} = \frac{TP}{TP + FN} \times 100\% \quad (24)$$

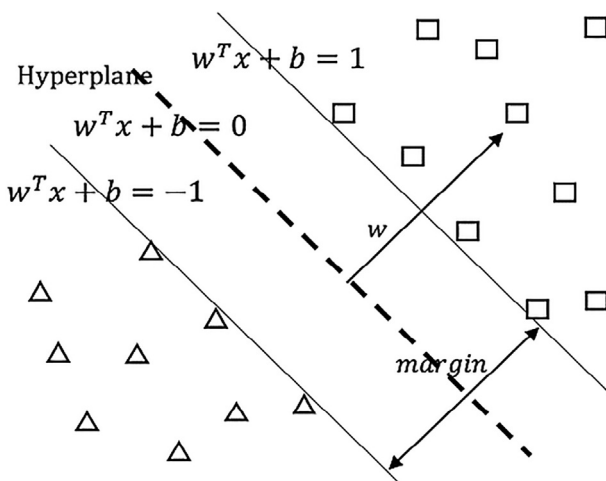


Fig. 7. Linear support vector machine.

$$\text{Specificity} = \frac{TN}{TN + FP} \times 100\% \quad (25)$$

where TP, FP, TN, FN are abbreviations for true positive, false positive, true negative and false negative, respectively [30].

### 3. Results and discussion

The main goal of this study was to develop an efficient algorithm for early detection of diabetic foot with infrared thermal images using asymmetry analysis of temperature and texture features. Sixty subjects participated voluntarily in the present work out of which 24 are from the control group and 36 from the DM group. The left and right foot regions are segmented using region growing algorithm from color images. The binary image of the segmented foot regions was multiplied with the red, green and blue planes of the respective foot thermal images and concatenated together to get the segmented foot regions from the thermal image. Similarly, the binary image of the segmented foot regions was multiplied with the temperature profile of the corresponding foot regions to obtain the temperature distribution for foot regions. 11 ROIs which are prone to ulcer were selected from segmented left and right foot of thermal images and temperature profiles. 12 texture features which are represented as co-occurrence features and 2 temperature features were extracted from all the ROIs for left and right foot regions.

Asymmetry analysis was used to find the difference in the extracted texture and temperature features between ipsilateral and contralateral foot regions (ROIs). All the regions (ROIs) were taken as separate input for finding the asymmetry in extracted features, which results in 11 ROIs for a single subject and 660 regions for 60 subjects. In the control group, the asymmetry in texture features was found to be small due to the symmetric nature of foot thermogram but was not so in patients with diabetic foot complications. The mean value and standard deviation of the asymmetry in the extracted temperature and texture features were computed for both the control group and the DM group, which are tabulated in Table 1. The methodology adopted in this work can be used as a baseline for further comparison and early identification of diabetic foot complications to avoid the amputation of the lower extremity. The SVM classifier is trained with asymmetry features of 140 regions (70 from the control group and 70 from the DM group) and tested with the remaining 520 regions. The performance of the SVM classifier to classify the test data into normal and prone to the ulcer is tabulated in Table 2.

**Table 1**  
Asymmetry in extracted features.

Features	Mean $\pm$ Standard deviation	
	Control group	Diabetic group
Mean Temperature	0.48 $\pm$ 0.36	3.18 $\pm$ 0.86
SD of Temperature	0.05 $\pm$ 0.04	0.11 $\pm$ 0.17
Auto Correlation	5.10 $\pm$ 5.54	16.15 $\pm$ 11.30
Contrast	0.17 $\pm$ 0.22	0.17 $\pm$ 0.20
Correlation	0.19 $\pm$ 0.23	0.19 $\pm$ 0.21
Dissimilarity	0.11 $\pm$ 0.10	0.11 $\pm$ 0.08
Energy	0.17 $\pm$ 0.16	0.25 $\pm$ 0.20
Entropy	0.48 $\pm$ 0.37	0.66 $\pm$ 0.47
Homogeneity	0.05 $\pm$ 0.04	0.05 $\pm$ 0.04
Maximum Probability	0.18 $\pm$ 0.14	0.24 $\pm$ 0.18
Sum of Squares: Variance	5.06 $\pm$ 5.59	16.08 $\pm$ 11.20
Sum Average	1.36 $\pm$ 1.25	3.19 $\pm$ 2.45
Sum Variance	18.22 $\pm$ 21.60	61.88 $\pm$ 40.05
Sum Entropy	0.44 $\pm$ 0.36	0.61 $\pm$ 0.43

**Table 2**  
Performance of the SVM classifier.

Performance measures	Value (in %)
Accuracy	95.61
Sensitivity	96.50
Specificity	92.41

### 4. Conclusion

A computer-assisted diagnostic system for the early detection of diabetic foot ulcer is developed. In this study, the texture features are extracted along with temperature features. The 11 ROIs which are prone to get ulceration in both left and right foot regions are selected from thermal images and temperature profiles. The 2 temperature features and 12 GLCM texture features were extracted and the asymmetry analysis was performed between the ipsilateral and contralateral regions of the foot. The features are classified into normal and ulcer using SVM classifier with an accuracy of 95.61%, sensitivity of 96.5% and specificity of 92.41%. The performance achieved by the proposed method was significantly better than the other methods reported in the literature. The study concludes that asymmetry analysis of texture and temperature features extracted from acquired plantar foot thermal images and temperature profiles were able to detect the diabetic foot ulceration. In future studies, the texture features extracted from color images which are essential for early identification of diabetic foot complications can be combined to extend the promising early findings obtained in the study.

### Funding

This research did not receive any specific grant from funding agencies in the public, commercial, or not-for-profit sectors in the subject matter or materials discussed in this manuscript.

### Acknowledgement

The authors are thankful to the patients and healthy volunteers who actively participated in the data collection and the clinicians in the Hycare for Wounds, Chennai.

### Declaration of Competing Interest

The authors declare that there is no conflict of interests regarding the publication of this paper.

## Appendix A. Supplementary material

Supplementary data to this article can be found online at <https://doi.org/10.1016/j.infrared.2020.103219>.

## References

- [1] American Diabetes Association, Diagnosis and classification of diabetes mellitus, *Diabetes Care* 37 (Supplement 1) (2014) S81–S90.
- [2] Paula Sousa, Virginie Felizardo, Daniel Oliveira, Rafael Couto and Nuno M Garcia, *Expert Review of Medical Devices*, A review of thermal methods and technologies for diabetic foot assessment, 2015, pp. 1–10.
- [3] Y. Liu, A. Polo, M. Zequera, R. Harba, R. Canals, Vilcahuaman L and Bello Y, Detection of Diabetic Foot Hyperthermia by using a regionalization method, based, on the plantar angiosomes, on Infrared Images, Proceedings 38th Annual International Conference of the IEEE Engineering in Medicine and Biology Society (EMBC), 2016, pp. 1389–1392.
- [4] Makoto Oe, Rie Roselyne Yotsu, Hiromi Sanada, Takashi Nagase, Takeshi Tamaki, Screening for osteomyelitis using thermography in patients with diabetic foot, *Ulcers 2013* (2013) 1–6.
- [5] Luay Fraiwan, Mohanad AlKhodari, Jolu Ninan, Basil Mustafa, Adel Saleh, Mohammed Ghazal, Diabetic foot ulcer mobile detection system using smart phone thermal camera: a feasibility study, *Biomed. Eng. Online* 16 (117) (2016) 1–19.
- [6] Chanjuan Liu, Ferdi van der Heijden, Marvin E. Klein, Jeff G. van Baal, Sicco A. Bus, Jaap J. van Netten, Infrared dermal thermography on diabetic feet soles to predict ulcerations: a case study, *Adv. Biomed. Clin. Diagnostic Syst. XI*, 2013, vol. 8572; pp. 87520N-1 – 9.
- [7] Luciane Fachin, Balbinot Caroline, Cabral Robinson, Matilde Achaval, Milton Antônio Zaroand, Marcos Leal Brioschi, Repeatability of infrared plantar thermography in diabetes patients: a pilot study, *J. Diabet. Sci. Technol.* 7 (5) (2013) 1130–1137.
- [8] L. Vilcahuaman, R. Harba, R. Canals, M. Zequera, C. Wilches, M.T. Arista, L. Torres, H. Arbañil, Detection of Diabetic Foot Hyperthermia by Infrared Imaging, Proceedings 36th Annual International Conference of the IEEE Engineering in Medicine and Biology Society (EMBC), 2014, pp. 4831–4834.
- [9] Alfred Gatt, Cynthia Formosa, Kevin Cassar, Kenneth P. Camilleri, Clifford De Raffaele, Anabelle Mizzi, Carl Azzopardi, Stephen Mizzi, Owen Falzon, Stefania Cristina, Nachiappan Chockalingam, Thermographic patterns of the upper and lower limbs: baseline data, *Int. J. Vascular Med.* 2015 (2014) 1–9.
- [10] D. Hernandez-Contreras, H. Peregrina-Barreto, J. Rangel-Magdaleno, J. Ramirez-Cortes, F. Renero-Carrillo, and G. Avina-Cervantes, Evaluation of thermal patterns and distribution applied to the study of diabetic foot, Proceedings IEEE International Instrumentation and Measurement Technology Conference (I2MTC), 2015; pp.1–6.
- [11] E.F.J. Ring, K. Ammer, Infrared thermal imaging in medicine, *Physiol. Meas.* (2012) R33–R46.
- [12] Ruben Usamentiaga, Pablo Venegas, Jon Guerediaga, Laura Vega, Julio Molleda, Francisco G. Bulnes, Infrared thermography for temperature measurement and non-destructive testing, *Sensors* 14 (2014) 12305–12348.
- [13] Lawrence A. Laverty, Kevin R. Higgins, Dan R. Lancet, George P. Constantinides, Ruben G. Zamorano, David G. Armstrong, A. Kyriacos, C. Athanasiou, Mauli Agrawal, Home monitoring of foot skin temperatures to prevent ulceration, *J. Diabetes Care* 27 (11) (2004) 2642–2647.
- [14] Jaap J. van Netten, Jeff G. van Baal, Chanjuan Liu, Ferdi van der Heijden, Sicco A. Bus, Infrared thermal imaging for automated detection of diabetic foot complications, *J. Diabetes Sci. Technol.* 7 (5) (2013) 1122–1129.
- [15] Constantijn E.V.B. Hazenberg, Jaap J. van Netten, G. van Sjef Baal, Sicco A. Bus, Assessment of signs of foot infection in diabetes patients using photographic foot imaging and infrared thermography, *Diabetes Technol. Ther.* 16 (6) (2014) 1–8.
- [16] H. Peregrina-Barreto, L.A. Morales-Hernandez, J.J. Rangel-Magdaleno, J.G. Avina-Cervantes, J.M. Ramirez-Cortes, R. Morales-Caporal, Quantitative estimation of temperature variations in plantar angiosomes: a study case for diabetic foot, *Comput. Math. Methods Med.* 2014 (2014) 1–10.
- [17] N. Pappanas, K. Papatheodorou, D. Papazoglou, C. Monastiriotis, E. Maltezou, Foot temperature in type 2 diabetic patients with or without peripheral neuropathy, *Exp. Clin. Endocrinol. Diabetes* 117 (1) (2009) 44–47.
- [18] Naima Kaabouch, Yi Chen, Wen-Chen Hu, Julie Anderson, Forrest Ames, and Rolf Paulson, Early Detection of Foot Ulcers through Asymmetry Analysis, *Medical Imaging 2009: Biomedical Applications in Molecular, Structural, and Functional Imaging*, 2009, vol.7262; pp.72621L-1 – 9.
- [19] Chanjuan Liu, Jaap J. van Netten, Jeff G. van Baal, Sicco A. Bus, Ferdi van der Heijden, Automatic detection of diabetic foot complications with infrared thermography by asymmetric analysis, *J. Biomed. Opt.* 20 (2) (2015) pp. 026003 (1–10).
- [20] F.L.I.R. Systems, Thermal Imaging Camera-Model E60, Technical data (2016).
- [21] Institute for Advanced Computer Technology, Technical Report, Standards, and Protocols in Clinical Thermographic Imaging, Thermography guidelines, 2002.
- [22] V. Sheeja Francis, M. Sasikala, Automatic detection of abnormal breast thermograms using asymmetry analysis of texture features, *J. Med. Eng. Technol.* 37 (1) (2013) 17–21.
- [23] Mahnaz Etehadavakol, Eddie Y.K. Ng, Assessment of foot complications in diabetic patients using thermography: a review, *Appl. Infrared Biomed. Sci.* 1 (1) (2017) 33–43.
- [24] Jean Gauci, Owen Falzon, Cynthia Formosa, Alfred Gatt, Christian Ellul, Stephen Mizzi, AnabelleMizzi Cassandra, Sturgeon Delia, Kevin Cassar, Nachiappan Chockalingam, Kenneth P. Camilleri, Automated region extraction from thermal images for peripheral vascular disease monitoring, *J. Healthcare Eng.* 2018 (2018) 1–15.
- [25] Patrick Nigri Happ, Raul Queiroz Feitosa, Cristiana Bentos, Ricardo Farias, A region-growing segmentation algorithm for GPUs, *IEEE Geosci. Remote Sens. Lett.* 10 (6) (2013) 1612–1616.
- [26] A.J.M. Boulton, F.A. Gries, J.A. Jervell, Guidelines for the diagnosis and outpatient management of diabetic peripheral neuropathy, *Diabet. Med.* 15 (6) (1998) 508–514.
- [27] Audrey Macdonald, Nina Petrova, Suhail Ainarkar, John Allen, Peter Plassmann, Aaron Whittam, John Bevans, Francis Ring, Ben Kluwe, Rob Simpson, Leon Rogers, Graham Machin, Mike Edmonds, Thermal symmetry of healthy feet: a precursor to a thermal study of diabetic feet prior to skin breakdown, *Physiol. Measur. Inst. Phys. Eng. Med.* 38 (2017) 33–44.
- [28] Robert M. Haralick, K. Shanmugam, Its'hak Dinstein, Textural features for image classification, *IEEE Trans. Syst. Man Cybernet.* 3 (6) (1973) 610–621.
- [29] Leen-Kiat Soh, Costas Tsatsoulis, Texture analysis of SAR sea ice imagery using gray level co-occurrence matrices, *IEEE Trans. Geosci. Remote Sens.* 37 (2) (1999) 780–795.
- [30] M. Sasikala, N. Kumaravel, A wavelet-based optimal texture feature set for classification of brain tumours, *J. Med. Eng. Technol.* 32 (3) (2008) 198–205.
- [31] P. Manika, K.M. Patit, Balasubramanian, V.B. Narayananamurthy, R. Parivalavan, Foot sole soft tissue characterization in diabetic neuropathy using texture analysis, in: Proceedings of the Biomechanics Conference, I.I.T, Delhi, Dec.2004, pp 26–33.
- [32] Zhuping Zhou, Jiwei Yang, Yong Qi, Yifei Cai, Support vector machine and back propagation neural network approaches for trip mode prediction using mobile phone data, *IET Intel. Transport Syst.* 12 (10) (2018) 1220–1226.
- [33] Naima Kaabouch, Yi Chen, Julie Anderson, Forrest Ames, Rolf Paulson, Asymmetry analysis based on genetic algorithms for the prediction of foot ulcers, visualization and data, *Analysis* 7243 (2009) pp. 724304–1 – 6.
- [34] Audrey Macdonald, Nina Petrova, Suhail Ainarkar, John Allen, Peter Plassmann, Aaron Whittam, John Bevans, Francis Ring, Ben Kluwe, Rob Simpson, Leon Rogers, Graham Machin, Mike Edmonds, Thermal symmetry of healthy feet: a precursor to a thermal study of diabetic feet prior to skin breakdown, *Physiol. Measur.* 2017 (38) (2017) 33–44.
- [35] S. Madhava Prabhu, Seema Verma, A Systematic Literature Review for Early Detection of Type, II Diabetes, Proceedings IEEE International Conference on Advanced Computing & Communication Systems (ICACCS), 2019, pp. 1–5.
- [36] S. Madhava Prabhu, Seema Verma, Comparative analysis of segmentation techniques for progressive evaluation and risk identification of diabetic foot ulcers, in: Proceedings IEEE 4th MEC International Conference on Big Data and Smart City (ICBDSC), 2019; pp.1–6.
- [37] Daniel Alejandro Hernandez-Contreras, Hayde Peregrina-Barreto, Jose De Jesus Rangel-Magdaleno, Francisco Javier Renero-Carrillo, Plantar thermogram database for the study of diabetic foot complications, *IEEE Access* 7 (2019) 161296–161307.
- [38] Arjaleena Ilo, Pekka Roms, Jussi Mäkelä, Infrared thermography and vascular disorders in diabetic feet, *J. Diabetes Sci. Technol.* 14 (1) (2019) 28–36.

# Accepted Manuscript

Computer aided diagnosis of diabetic foot using infrared thermography: A review

Muhammad Adam, Eddie Y.K. Ng, Jen Hong Tan, Marabelle L. Heng, Jasper W.K. Tong, U. Rajendra Acharya



PII: S0010-4825(17)30356-6

DOI: [10.1016/j.combiomed.2017.10.030](https://doi.org/10.1016/j.combiomed.2017.10.030)

Reference: CBM 2823

To appear in: *Computers in Biology and Medicine*

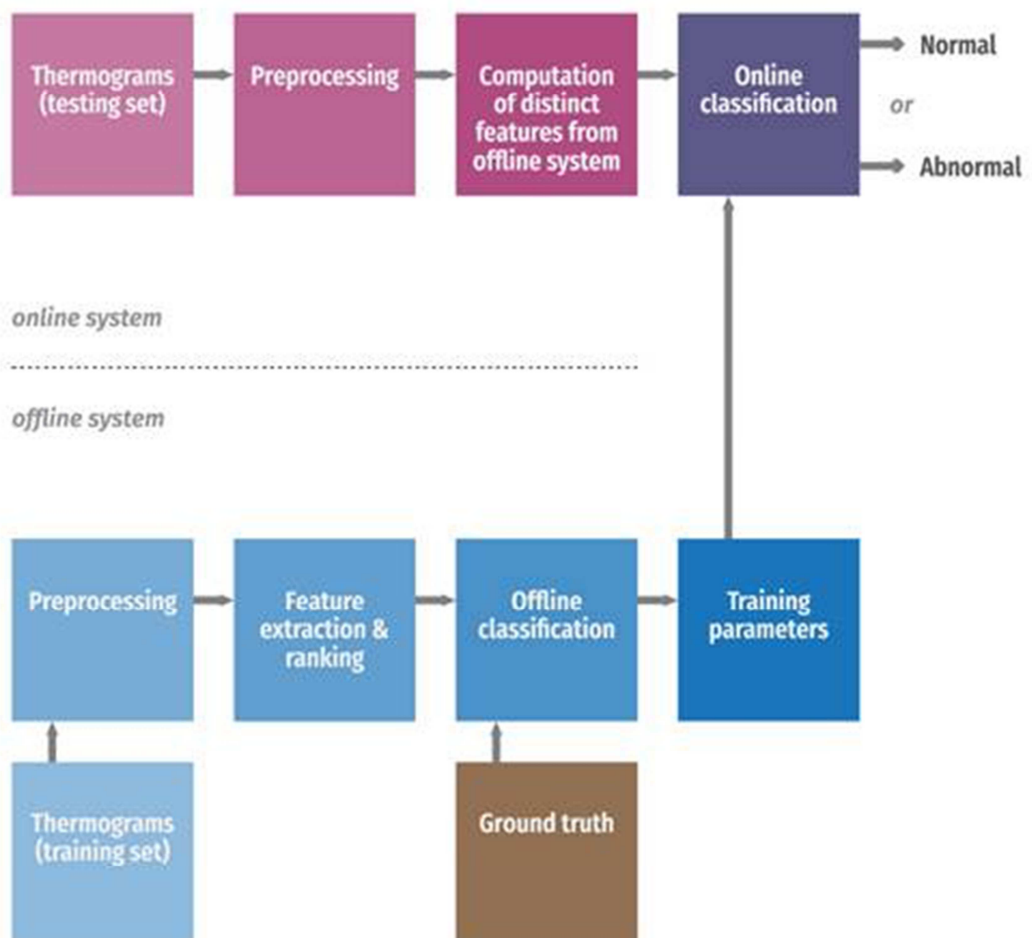
Received Date: 8 August 2017

Revised Date: 24 October 2017

Accepted Date: 25 October 2017

Please cite this article as: M. Adam, E.Y.K. Ng, J.H. Tan, M.L. Heng, J.W.K. Tong, U.R. Acharya, Computer aided diagnosis of diabetic foot using infrared thermography: A review, *Computers in Biology and Medicine* (2017), doi: [10.1016/j.combiomed.2017.10.030](https://doi.org/10.1016/j.combiomed.2017.10.030).

This is a PDF file of an unedited manuscript that has been accepted for publication. As a service to our customers we are providing this early version of the manuscript. The manuscript will undergo copyediting, typesetting, and review of the resulting proof before it is published in its final form. Please note that during the production process errors may be discovered which could affect the content, and all legal disclaimers that apply to the journal pertain.



# Computer Aided Diagnosis of Diabetic Foot

## Using Infrared Thermography: A Review

Muhammad Adam<sup>1\*</sup>, Eddie Y K Ng<sup>2</sup>, Jen Hong Tan<sup>1</sup>, Marabelle L. Heng<sup>5</sup>, Jasper W.K. Tong<sup>6</sup>, U Rajendra Acharya<sup>1,3,4</sup>

<sup>1</sup>Department of Electronics and Computer Engineering, Ngee Ann Polytechnic, Singapore.

<sup>2</sup>School of Mechanical and Aerospace Engineering, Nanyang Technological University, Singapore.

<sup>3</sup>Department of Biomedical Engineering, School of Science and Technology, SIM University, Singapore.

<sup>4</sup>Department of Biomedical Engineering, Faculty of Engineering, University of Malaya, Malaysia.

<sup>5</sup>Podiatry Department, Singapore General Hospital.

<sup>6</sup>Allied Health Office, KK Women's and Children Hospital.

\*Corresponding Author

Postal Address: <sup>1</sup>Department of Electronics and Computer Engineering, Ngee Ann Polytechnic, Singapore 599489

Telephone: +65-64607887; Email Address: [muhdadam@hotmail.com](mailto:muhdadam@hotmail.com)

### ABSTRACT

Diabetes mellitus (DM) is a chronic metabolic disorder that requires regular medical care to prevent severe complications. The elevated blood glucose level affects the eyes, blood vessels, nerves, heart, and kidneys after the onset. The affected blood vessels (usually due to atherosclerosis) may lead to insufficient blood circulation particularly in the lower extremities and nerve damage (neuropathy), which can result in serious foot complications. Hence, an early detection and treatment can prevent foot complications such as ulcerations and amputations. Clinicians often assess the diabetic foot for sensory deficits with clinical tools, and the resulting foot severity is often manually evaluated. In recent years, various infrared thermography-based computer aided diagnosis (CAD) systems for diabetic foot have been proposed. Infrared thermography is a fast, nonintrusive and non-contact method that allows the visualization of foot plantar temperature distribution. In this paper, the diabetic foot, its pathophysiology, conventional assessments methods, infrared

thermography and the different infrared thermography-based CAD analysis methods are reviewed.

**Keywords:** foot, diabetes, neuropathy, atherosclerosis, plantar, infrared image

## 1. Introduction

Diabetes mellitus (DM) is a serious endocrine disorder characterized by chronic high blood glucose (hyperglycemia) caused by deficiency in the secretion of insulin, or ineffective use of insulin by the body (1). In general, insulin is produced by beta cells of the pancreas to maintain normal blood glucose level in the body. The characteristic symptoms of DM are weight loss, blurred vision, dehydration and frequent urination. Prolonged uncontrolled DM may lead to specific complications such as nephropathy leading to kidney failure, retinopathy resulting in blindness, and neuropathy with increased risk of ulceration, Charcot foot development and amputation (1). These complications may affect the quality of life, cause disability and even early death.

According to the World Health Organization (WHO), an estimated 3.7 million deaths were reported in 2012 due to high blood glucose levels (2). In this, 1.5 million deaths were directly caused by diabetes and remaining 2.2 million deaths were due to heart diseases, renal disease and tuberculosis in relation to high blood glucose. Further, majority of these deaths (43%) happen prior to the age of 70, which are considered as premature and accounting for 1.6 million global deaths (2). In any case, diabetic foot ulcers (DFUs) are among the most common foot complication that critically affect about 15% of the diabetic population (3). Moreover, diabetic patients are 12% to 25% more likely to develop foot ulcers in their lifetime (4, 5) with nearly 85% of the lower limb amputations due to non-healing and infected foot ulcers (6). The risk factors leading to the development of foot ulcers are primarily neuropathy and arterial disease in the lower limb (7). It is approximated that 50% of the diabetes patients with foot ulcer will have neuropathy, nearly 20% of them will have lack of arterial blood perfusion as illustrated in Figure 1, and almost 80% of them will have both conditions (8, 9).

The diabetic foot wounds are many times develop in patient who at least have two risk factors simultaneously, with peripheral neuropathy as the major one (10). Nearly 66% of the diabetic patients are at risk of developing peripheral neuropathy (11). Because of this neuropathy, the foot sensation is impaired and may leads to foot deformity which causes gait abnormalities (10). For diabetic patients with neuropathy, foot ulcerations may develop due to a minor wound. This minor wound can be caused by bruise, blister, improper footwear or even barefoot walking. Equally important, the foot may also experience unnatural biomechanical loading as result of insensitive and deformed foot, and limited joint movement. This yields large pressure on certain regions which in turn results in the formation of callus (dense skin) (10). Generally, the further increase in loading results in bleeding into the skin and ultimately ulcerations. Consequently, the wound healing process on the insensitive foot will be impaired if patients continue to walk.

Typically, diabetic patients will have their feet screen at least once annually to determine patients with at risk foot and to search for signs of peripheral arterial disease or peripheral neuropathy. Minimally, the examination and inspection of the feet comprised of foot and medical history examination and, neuropathy assessment (10). The foot and medical history examinations includes health conditions of the vascular, skin, bone and joint, and the previous history of ulceration or amputation (10). For neuropathy assessment, the following methods are being conducted: enquiring on pain or tingling symptoms in the lower extremities; pressure perception using Semmes-Weinstein monofilaments; vibration perception using 128 Hz tuning fork; discrimination using pin prick on dorsum of foot superficial; tactile sensation using cotton wool or by lightly touching the toes tips with index fingers; and assessing the Achilles tendon reflexes (10).

The advancement in infrared (IR) camera technology, in terms of resolution and response time, has transformed the field of measuring temperature and is now being extensively used for medical purposes (12). The IR techniques allow rapid capturing of large number of pixels, or picture elements (13). The individual pixels at the respective points denote the temperature. Collectively, these pixels create an image illustrating the surface temperature distribution. Essentially, temperature changes are linked to certain diseases

detected by viewing the temperature distribution on the body using IR thermography. The IR thermography has been employed in various medical studies, namely vascular disorders (14-17), rheumatoid arthritis (18), breast cancer (19-23), muscular pain (24, 25) and dry eye (26, 27). Also, infrared thermography has been widely used for diabetes detection such as to analyze body temperature variations (28) and metabolic parameters (29), estimate blood glucose (30), detect temperature variations in hypoglycemia (31), and compare infrared thermography with biochemical assay methods (32). Also, IR thermography is used in many diabetic foot studies as tabulated in Table 1, 2,3, and 4. These diabetic foot studies are based on the temperature distribution of the plantar foot that rely on blood perfusion. In conditions, when blood circulation is significantly reduced (ischemic), especially at the peripheral limbs, the temperature pattern will change (33).

In this review, the aim is to highlight the potential of infrared thermography in the medical field as a temperature measurement method. The IR thermogram based CAD system for diabetic foot and provide an overview on the various proposed diabetic foot studies using different analysis methods on the foot plantar thermograms. These analysis methods are categorized into four types of analysis: separate lower limb, asymmetric temperature, temperature distribution and, independent thermal and physical stress.

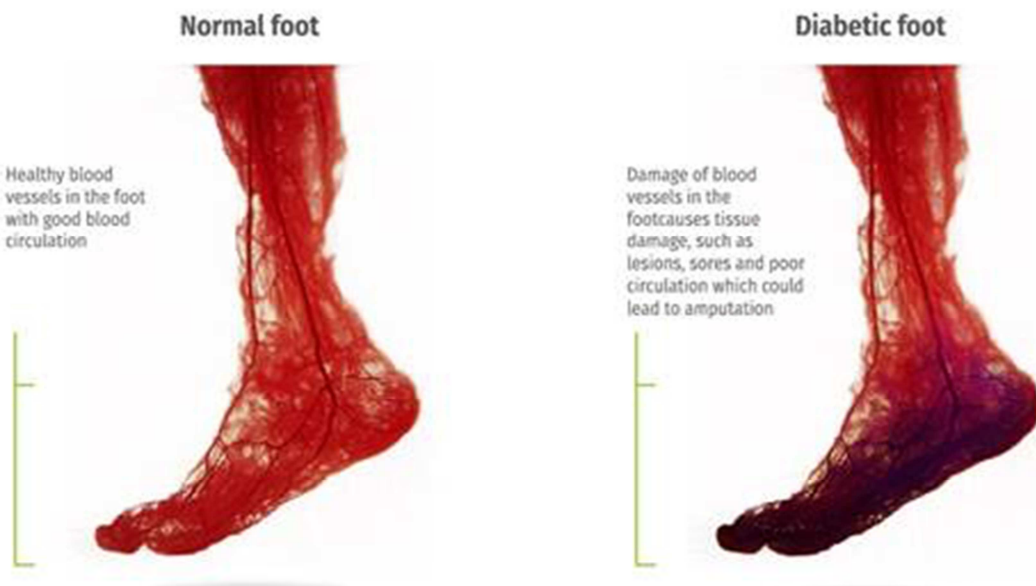


Figure 1: Illustrations of blood circulation in normal and diabetic foot.

## 2. Infrared thermography

The human beings are homeotherms with the capability to sustain inner body temperature regardless of the variations in the surrounding temperature by altering heat loss and heat production rates (34-36). Indeed, this is achieved by the thermoregulatory mechanism of the human body, namely behavioral adjustments to the surrounding temperature and autonomic nervous responses. The autonomic nervous responses include the cutaneous vasomotor and sweating responses for heat loss (34). Therefore, any unusual changes to the body temperature can be an indication of a disease.

The first use of thermobiological diagnostic began around 480 BC, discovered in the writings of Hippocrates (37). Basically, color changes of the mud placed on the abdomen of a patient is studied while drying. The regions, where the mud is observed to have dried first are considered to indicate underlying pathology in that body part.

Many physical achievements have elucidated the reasons for this phenomena throughout history. The discovery and acquisition of thermal radiation from the human body by William Herschel in the early 1800s was a huge stepping stone (38). Based on the physical laws, any object which includes the human body, with a temperature higher than absolute zero (-273 K) emit the electromagnetic radiation, called infrared radiation (39). In addition, the human skin has an emissivity within the wavelength range of 2-20  $\mu m$  and an average peak of 9-10  $\mu m$ .

Despite this knowledge, it was in 1934 that Hardy et al. (40) explained the physiological characteristics of infrared emitted from the body surface. They further found that the skin thermal properties and physiological activities are affected by numerous factors. This is because the skin helps to regulate the core body temperature. Nonetheless, the presence of disease will cause these factors to change. Thus, infrared measurement can be utilized for diagnostic reasons. With this fundamental knowledge, infrared thermography was introduced to the medical sciences as a potential imaging modality (41). The infrared thermography was first present to the modern medicine by Lawson in 1956, later discovered the relationship between breast carcinoma and increasing skin temperature

(42). The potential and feasibility of infrared (IR) thermography are explored as an instrument for breast lesions study (43). The IR thermography measures the temperature distribution using IR radiation emitted from the body surface, that creates an image known as thermogram. The acquired 2D thermogram is a distinct representation of temperature distribution by capturing the reflected IR radiation from the body in the presence of external IR energy origins (44). The IR thermography is a non-contact, non-invasive and fast approach of measuring temperature. Further, IR thermography offers the real time visualization of temperature distribution on the body surface without affecting the surface temperature (44).

A black body is defined as one that absorbs all the energy reaching it but does not reflect anything back (45). Based on the Planck's law, the spectral intensity  $I$  of thermal radiation at temperature  $T$  and at all wavelengths  $\lambda$  from black body in relation to wavelength is defined as:

$$I_{\lambda b} (\lambda, T) = \frac{2\pi hc^2}{\lambda^5 (e^{\frac{hc}{\lambda kT}} - 1)} W cm^{-2} \mu m^{-1} \quad (1)$$

where  $h$  is the Planck constant ( $6.626 \times 10^{-34} J s$ ),  $k$  is the Boltzmann constant ( $1.381 \times 10^{-23} J K^{-1}$ ),  $c$  is the speed of light in vacuum ( $2.998 \times 10^8 m s^{-1}$ ),  $\lambda$  is the wavelength ( $m$ ) and  $T$  is the absolute temperature ( $K$ ).

The spectral emissivity power of black body as a diffuse emitter is given by:

$$E_{\lambda b} (\lambda, T) = I_{\lambda b} (\lambda, T) = \frac{A_1}{\lambda^5 (e^{\frac{A_2}{\lambda T}} - 1)} \quad (2)$$

where  $A_1 = 2\pi hc^2 = 3.742 \times 10^8 W \mu m^4 / m^2$  and  $A_2 = hc/k = 1.439 \times 10^4 \mu m K$ .

The integration of Planck function with respect to all the frequencies results in attaining the Stefan-Boltzmann's law relating to the overall emissivity of black body (46):

$$E_b = \int_0^{\infty} \frac{A_1}{\lambda^5 (e^{\frac{A_2}{\lambda T}} - 1)} d\lambda = \sigma T^4 \quad (3)$$

where  $\sigma$  is the Stefan-Boltzmann constant ( $5.67 \times 10^{-8} \text{ W/m}^2 \text{ K}^4$ ).

For a black body, the overall energy emitted per unit area is directly proportional to the fourth power of its absolute temperature. The radiation emitted by most real objects are often partial to that emitted by black body of the same wavelength and temperature. The emissivity is defined as ratio of radiation emitted by real object  $E_\lambda$  to the radiation emitted by black body  $E_{b,\lambda}$  at same temperature (T) (46):

$$\varepsilon(T) = \frac{E_\lambda(T)}{E_{b,\lambda}(T)} \quad (4)$$

From Eq. (4), the Stefan-Boltzmann's law can be rewritten for real object in relation to emissivity as:

$$E = \varepsilon \sigma T^4 \quad (5)$$

As shown in Eq. (5), the energy radiated by real object is proportional to the surface temperature, which is then captured by the infrared detectors. Nevertheless, the detected energy relies on the surface emissivity coefficient. This coefficient ranges from 0 (non-emitting) to 1 (fully emitting) depending on the material (47). In this case, the human skin has an emissivity coefficient of about  $0.98 \pm 0.01$  at normal angles (13). This is a crucial factor as it allows the true plantar foot temperature to be determined. Hence, infrared imaging method is highly effective in studying the skin temperature distribution (48).

### 3. Computer Aided Diagnosis (CAD) system

The computer aided diagnosis (CAD) system assists in providing the accurate diagnosis for clinicians. The assessment of medical images by human are prone to errors due to negligence, fatigue and sensory overwhelm by huge amount of information (49). Moreover, the limitations due to human visual perception, and optical illusions may affect the diagnosis accuracy (50). Besides, few healthcare institutions may not have sufficient clinicians for the diagnosis task. Therefore, the development of CAD system is necessary to overcome these drawbacks. Recent studies have proposed image processing algorithms with enhanced detection accuracy based on automated segmentation, image improvement and restoration and, feature extraction and classification approaches (21, 51-53).

The general layout of typical CAD system is shown in Figure 2. In general, the block diagram is separated into online and offline systems. For an offline system, the images are first preprocessed and subsequently the features are extracted using different feature extraction methods. The extracted features are then analyzed using statistical techniques to determine the highly significant features for the subsequent classification process. In the online system, the same distinct features are obtained and then classified to get the unknown class.

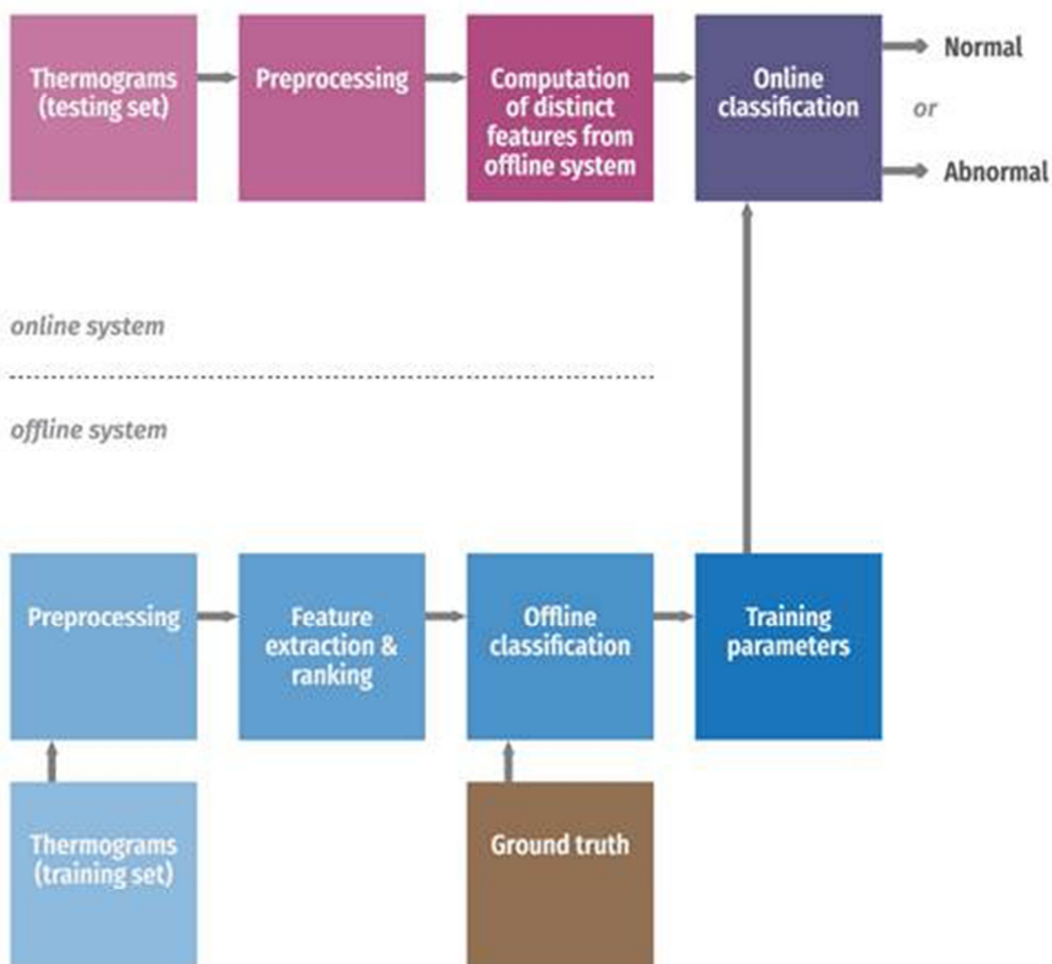


Figure 2: Block diagram of CAD system based on foot plantar thermogram.

#### 4. Infrared thermography (temperature) analysis

IR thermography is widely used in many studies to detect the diabetic foot problems based on the temperature distribution of plantar foot. The examples of segmented feet thermograms ( $^{\circ}\text{C}$ ) of normal and diabetes patient without neuropathy are shown in Figure 3(a)-(b) respectively. The diabetic foot study using IR thermography is categorized into four types. They are separate lower limb temperature, asymmetric temperature, temperature distribution and, independent thermal and physical stress analysis. The individual analysis is briefly described below.

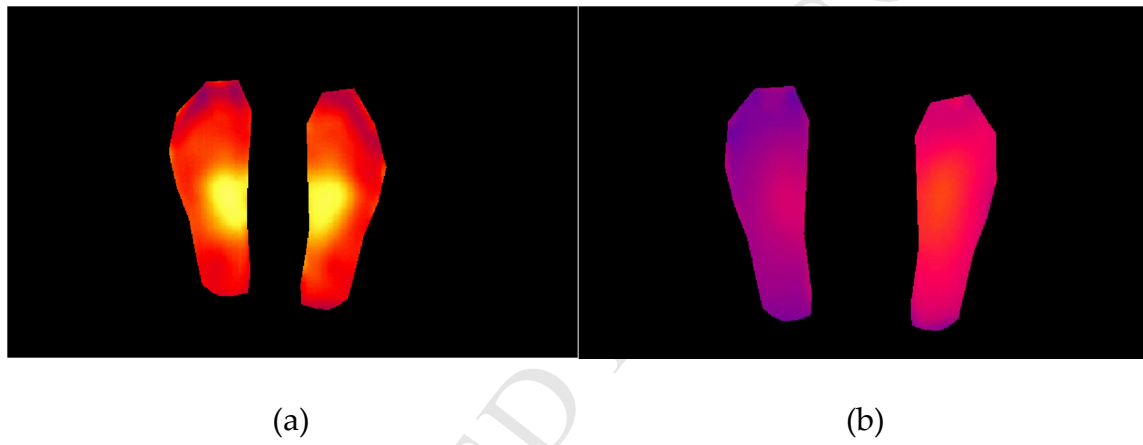


Figure 3(a) - (b): The cropped feet thermograms ( $^{\circ}\text{C}$ ) of (a) normal and (b) diabetes patient without neuropathy.

##### 4.1. Separate lower limb temperature analysis

The summary of studies performing temperature analysis on the lower limb separately using IR thermography is presented in Table 1. Ammer et al. (54) studied the statistical relationship between the hotspots on the plantar and development of callus, toe nail onychomycosis and foot deformities. However, there is no relationship between the skin changes and areas of elevated skin temperature. The thermal imaging not useful in detecting skin changes normally present in the diabetic foot. Melnizky et al. (55) analyzed the development of thermal gradient inversion among the type 2 diabetic patients and then correlated the temperature gradient with blood glucose level, foot deformation, limited range of motion and nerve conductivity measurements. Their study confirmed that almost half of the diabetic patients have inverted temperature gradient on the leg but could not

clearly explain the phenomenon. Nishide et al (56) employed ultrasonography and thermography to determine the latent inflammation around the foot callus and studied the correlation between inflammation observed in callus and, with or without diabetes. The proposed methods may be useful to detect early ulcerations in diabetic patients with callouses. Bharara et al. (57) presented a quantitative thermography method using thermal index on a single case report of diabetic foot ulcer assessment and correlated with the standard wound measurement method. Nevertheless, the index analysis requires more patients. Bagavathiappan et al. (58) explored the relationship between type 2 diabetic patients with neuropathy and foot temperature using IR thermography. Their study revealed that IR thermography may be applicable as an additional screening device to evaluate high risk diabetic feet.

Table 1: Separate lower limb temperature analysis using IR thermography.

Reference (Year)	Methodology	Findings
Ammer et al, 2001. (54)	<ul style="list-style-type: none"> <li>• Physical examination of feet</li> <li>• Neurological assessment</li> <li>• Thermal imaging</li> <li>• Single Measure Intraclass Correlation</li> <li>• Mann-Whitney U-test</li> </ul>	<ul style="list-style-type: none"> <li>• No relationship between skin changes and increased skin temperature</li> </ul>
Melnizky et al, 2002. (55)	<ul style="list-style-type: none"> <li>• Physical examination of feet</li> <li>• Nerve conduction test</li> <li>• Thermal imaging</li> <li>• SPSS 10.0 for statistical analysis</li> </ul>	<ul style="list-style-type: none"> <li>• A pathological temperature gradient was detected on the right limb of 36 diabetes patients (mean pathological gradient: <math>-0.27\pm0.68K</math> vs <math>-1.84\pm0.81K</math>) whereas 39 patients on the left limb (<math>-0.77\pm1.15K</math> vs <math>-1.49\pm1.21K</math>)</li> <li>• No correlation between temperature measurements and nerve conduction</li> </ul>
Sun et al, 2005. (59)	<ul style="list-style-type: none"> <li>• Electromyography for sympathetic skin response (SSR) test</li> <li>• Thermal imaging</li> <li>• Compute average temperature of six sub regions on each healthy sole</li> <li>• Analyze sole temperature normalization relative to forehead temperature of diabetes patients</li> <li>• SPSS for statistical analysis</li> </ul>	<ul style="list-style-type: none"> <li>• Highest temperature (<math>29.3\pm0.9^\circ C</math>) in the arc areas and lowest for the toes (<math>26.2\pm1.2^\circ C</math>).</li> <li>• Diabetes patients without sympathetic skin response (SSR) had higher mean plantar temperature (<math>27.6\pm1.8^\circ C</math>) compared to those with SSR (<math>26.8\pm2.2^\circ C</math>)</li> <li>• Equilibrium temperature is</li> </ul>

		achieved at mean plantar temperature ( $27.8 \pm 1.0^\circ\text{C}$ ) after 15 minutes
Sun et al, 2006. <a href="#">(60)</a>	<ul style="list-style-type: none"> <li>Seattle Wound Classification system</li> <li>Thermal imaging</li> <li>Electromyography for sympathetic skin response (SSR) test</li> <li>Neurological assessment</li> <li>SPSS for statistical analysis</li> </ul>	<ul style="list-style-type: none"> <li>At risk diabetes patients with pre-ulcerative skin and without SSR had highest mean foot temperature (<math>30.2 \pm 1.3^\circ\text{C}</math>) compared to diabetes patients without SSR (<math>27.9 \pm 1.7^\circ\text{C}</math>), diabetes patients with SSR (<math>27.1 \pm 2.0^\circ\text{C}</math>), and normal subjects (<math>26.8 \pm 1.8^\circ\text{C}</math>)</li> </ul>
Sun et al, 2008. <a href="#">(61)</a>	<ul style="list-style-type: none"> <li>Seattle Wound Classification system</li> <li>Thermal imaging</li> <li>Electromyography for sympathetic skin response (SSR) test</li> <li>Neurological assessment</li> <li>Nerve conduction test</li> <li>SPSS for statistical analysis</li> </ul>	<ul style="list-style-type: none"> <li>At-risk class is 13.4 times more likely to develop plantar ulcerations than the diabetes patients with and without SSR during the 4-year period</li> </ul>
Nishide et al, 2009. <a href="#">(56)</a>	<ul style="list-style-type: none"> <li>Ankle Brachial Index (ABI)</li> <li>Toe Brachial Index (TBI)</li> <li>Achilles tendon reflex and vibratory perception</li> <li>Semmes-Weinstein monofilament test</li> <li>Thermography</li> <li>Ultrasonography</li> <li>Fisher's exact probability test</li> <li>Mann-Whitney U-test</li> <li>SPSS for statistical analysis</li> </ul>	<ul style="list-style-type: none"> <li>Ultrasonography and thermography detect inflammation symptoms in 10% of the calli in diabetes class whereas no inflammation detected in the normal class.</li> </ul>
Bharara et al, 2010. <a href="#">(57)</a>	<ul style="list-style-type: none"> <li>Thermal imaging</li> <li>Thermal index</li> <li>Image J Software</li> </ul>	<ul style="list-style-type: none"> <li>Thermal index/ wound inflammatory index moved from negative to positive (<math>p &lt; 0.05</math>) prior to reaching zero</li> </ul>
Bagavathiappan et al, 2010. <a href="#">(58)</a>	<ul style="list-style-type: none"> <li>Anthropometric measurements</li> <li>Glycated hemoglobin (HbA1c)</li> <li>Neuropathy assessment</li> <li>Vascular sufficiency assessment</li> <li>Thermal imaging</li> <li>SPSS for statistical analysis</li> </ul>	<ul style="list-style-type: none"> <li>Diabetes neuropathy patients recorded highest foot temperature (<math>32 - 35^\circ\text{C}</math>) than non-neuropathy diabetes patients (<math>27 - 30^\circ\text{C}</math>)</li> <li>Higher mean foot temperature (MFT) for Diabetes neuropathy patients</li> <li>No relationship between MFT and glycated hemoglobin</li> </ul>

#### 4.2. Asymmetric temperature analysis

The studies on asymmetric analysis of diabetic foot thermograms are summarized in Table 2. Kaabouch et al in (62-65) proposed an asymmetric analysis method for the detection of inflammation and predicting foot ulcerations risk using IR thermography. All the proposed methods can detect the inflammation and ulcers accurately. Kaabouch et al. (66) proposed an asymmetry analysis-based scalable scanning technique which provided a valid comparison of both feet, particularly of different sizes and shapes. The implemented scalable scanning method yielded fewer false abnormal regions and, the genetic algorithms effectively cropped the feet from background and eliminated most of the noise. Liu et al. (67) studied the effectiveness of proposed dermal thermography as a screening instrument for the early detection of ulcers. The segmentation of the feet from the background remains challenging because the foot, especially the toes have lower temperature compared to other body parts. Peregrina-Barreto et al. (68) proposed a technique that provides quantitative details with regard to the temperature difference and distribution, and the divided four regions (angiosomes) on the plantar. The proposed method can provide a reliable complimentary information to assist the clinicians in early identification of foot ulcers risk. van Netten et al. (69) studied various cut-off values of skin temperatures for the identification and treatment of diabetic foot problems. The proposed method yielded low specificity, which may result in over diagnosis. Nevertheless, the *mean* temperature difference between the left and right foot may be a good marker to determine the need for treatment. Liu et al. (70) initiated an asymmetric analysis technique that include the color image segmentation and non-rigid landmark based registration B-splines of the right and left foot. The proposed method can significantly detect diabetic foot ulcers with high accuracy including all the Charcot foot.

Table 2: Asymmetric temperature analysis using IR thermography.

Reference (Year)	Methodology	Findings
Harding et al, 1998. (71)	<ul style="list-style-type: none"> <li>Infrared imaging</li> <li>Radiography</li> </ul>	<ul style="list-style-type: none"> <li>Out of the 26 diabetes patients with positive thermograms, 21 of whom are confirmed with osteomyelitis by radiological evidence</li> <li>Positive thermogram is described as at least <math>0.5^{\circ}\text{C}</math> rise in temperature of the affected foot skin with respect to the contralateral foot sole</li> </ul>
Kaabouch et al, 2009. (62)	<ul style="list-style-type: none"> <li>Infrared imaging</li> <li>Segmentation</li> <li>Geometric transformation</li> <li>Asymmetry analysis</li> </ul>	<ul style="list-style-type: none"> <li>Able to detect and determine inflammation and ulcers accurately and rapidly</li> </ul>
Kaabouch et al, 2009. (63)	<ul style="list-style-type: none"> <li>Infrared imaging</li> <li>Automatic thresholding</li> <li>Geometric transformation</li> <li>Asymmetry analysis</li> <li>Features extraction</li> </ul>	<ul style="list-style-type: none"> <li>Genetic algorithm yields superior thresholding results</li> <li>Low and high order statistics effectively enhance the asymmetry analysis in detecting foot abnormalities</li> </ul>
Kaabouch et al, 2010. (65)	<ul style="list-style-type: none"> <li>Infrared imaging</li> <li>Segmentation</li> <li>Geometric transformation</li> <li>Asymmetry analysis</li> </ul>	<ul style="list-style-type: none"> <li>Genetic algorithm produces superior thresholding results</li> </ul>
Kaabouch et al, 2011. (64)	<ul style="list-style-type: none"> <li>Infrared imaging</li> <li>Segmentation</li> <li>Geometric transformation</li> <li>Asymmetry analysis and abnormality identification</li> <li>Features extraction</li> </ul>	<ul style="list-style-type: none"> <li>Genetic algorithm produces superior thresholding results</li> <li>Low and high order statistics effectively enhance the asymmetry analysis in detecting foot abnormalities</li> </ul>
Kaabouch et al, 2011. (66)	<ul style="list-style-type: none"> <li>Infrared imaging</li> <li>Genetic algorithms</li> <li>Asymmetry analysis-based scalable scanning</li> </ul>	<ul style="list-style-type: none"> <li>Genetic algorithms effectively crop the feet from background and eliminate most noise</li> <li>Scalable scanning method yield fewer false abnormal regions</li> </ul>
Liu et al, 2013. (67)	<ul style="list-style-type: none"> <li>Infrared imaging</li> <li>Foot segmentation</li> <li>Feet registration</li> <li>Abnormal detection</li> </ul>	<ul style="list-style-type: none"> <li>Active contours without edges method acquire reasonable result</li> <li>Automated detection of pre-symptoms ulceration by computing temperature difference of the feet</li> <li><math>2.2^{\circ}\text{C}</math> as the clinical relevant difference</li> </ul>
Peregrina- Barreto et al,	<ul style="list-style-type: none"> <li>Infrared imaging</li> <li>Color characterization</li> </ul>	<ul style="list-style-type: none"> <li>The temperature estimate difference between corresponding angiosomes can</li> </ul>

2013. (72)	<ul style="list-style-type: none"> <li>• Foot angiosomes and color classification</li> </ul>	be used to screen for abnormality
van Netten et al, 2013. (73)	<ul style="list-style-type: none"> <li>• Infrared imaging</li> <li>• Mean temperature of whole foot and regions of interest</li> </ul>	<ul style="list-style-type: none"> <li>• Mean temperature of contralateral and ipsilateral foot is the same in patients with localized problems</li> <li>• Temperature at ROI was more than <math>2^{\circ}\text{C}</math> compared to the similar area in contralateral foot and to the mean of the entire ipsilateral foot</li> <li>• Mean temperature differences between the contralateral and ipsilateral foot was more than <math>3^{\circ}\text{C}</math> in patients with diffuse problems</li> </ul>
Peregrina-Barreto et al, 2014. (68)	<ul style="list-style-type: none"> <li>• Infrared imaging</li> <li>• Color characterization</li> <li>• Temperature estimated difference</li> <li>• Hot spots detection</li> </ul>	<ul style="list-style-type: none"> <li>• HSE capable of detecting abnormal small areas in the early phase that were not detected by ETD estimator</li> </ul>
van Netten et al, 2014. (69)	<ul style="list-style-type: none"> <li>• Infrared imaging</li> <li>• Clinical foot assessments</li> <li>• Kruskal-Wallis test</li> <li>• Receiver operating characteristic (ROC) curve and area using SPSS</li> </ul>	<ul style="list-style-type: none"> <li>• Optimal cut-off value for skin temperature in identifying diabetes foot problems was difference of <math>2.2^{\circ}\text{C}</math> between contralateral spots, with 76% sensitivity and 40% specificity</li> <li>• Optimal cut-off values for skin temperature to decide the urgency for treatment was difference of <math>3.5^{\circ}\text{C}</math> between left and right foot mean temperature, with 89% sensitivity and 78% specificity</li> </ul>
Vilcahuaman et al, 2014. (74)	<ul style="list-style-type: none"> <li>• Infrared imaging</li> <li>• Image processing</li> </ul>	<ul style="list-style-type: none"> <li>• In the clinical study, 10% of the diabetes patients had signs of significant hyperthermia on the foot plantar with temperature difference of more than <math>2.2^{\circ}\text{C}</math></li> </ul>
Vilcahuaman et al, 2015. (75)	<ul style="list-style-type: none"> <li>• Infrared imaging</li> <li>• Image processing</li> </ul>	<ul style="list-style-type: none"> <li>• High risk group had significantly higher temperature (<math>32\pm2^{\circ}\text{C}</math>) than medium risk group (<math>31\pm2^{\circ}\text{C}</math>)</li> <li>• In the study, 9 out of 82 diabetes patients had significant hyperthermia</li> </ul>
Liu et al, 2015. (70)	<ul style="list-style-type: none"> <li>• Infrared imaging</li> <li>• Foot segmentation</li> <li>• Registration optimization</li> <li>• Asymmetric analysis</li> </ul>	<ul style="list-style-type: none"> <li>• The study yielded an accuracy of 95% with 35 out of the 37 diabetic foot ulcers identified</li> <li>• All three Charcot feet are successfully detected.</li> </ul>

#### **4.3. Temperature distribution analysis**

Many studies have observed similar skin temperature distribution on the feet of healthy individuals compared to varying temperature distribution in diabetic patients. In 1991, Chan et al. (76) described the temperature distribution on the feet of healthy individuals as symmetric butterfly pattern in which the highest temperature is at the arch and lowest at the toes.

The summary of studies on temperature distribution analysis is shown in Table 3. Nagase et al. (77) and Bharara et al. (78) proposed a characterization method of plantar thermography patterns based on plantar angiosomes concept. The disadvantages in their studies may be bias of variations in the control group due to smaller number of participants. The unmatched gender and age in the control group may lead to confounding factors during data interpretation. Besides, the proposed manual classification method of 20 categories may be complicated for clinical purposes. Oe et al. (79) studied the thermography data of patients with osteomyelitis and the diabetic foot. The limitations are that the morphology analysis of thermography patterns are subjective and possibly affected by the surrounding environment, expertise of the researcher and patients' information biasness. Furthermore, the diagnosis of osteomyelitis is based on MRI without performing biopsy of the tissues or bone. Thus, the pathophysiology condition that underlie the ankle pattern cannot be fully understood. Mori et al. (80) proposed a system that characterized plantar thermal patterns with image segmentation technique based on mode seeking technique. The drawbacks are that variables biasness may be present in the control group because of smaller number of participants. Again, the unmatched gender and age in the control group may lead to difficulties in data interpretation. Moreover, the proposed method only focused on the forefoot region of the thermographic patterns. Hernandez-Contreras et al. (81) proposed a characterization technique to distinguish the thermal patterns of normal and diabetic patients. The proposed technique analyzed the regions of high temperature, localization and distribution. The analysis using pattern spectrum yielded reasonable results. Nonetheless,

the technique is unable to offer details relating to the position of these regions. Again, Hernandez-Contreras et al. (82) proposed a characterization technique to distinguish the thermal patterns of normal and diabetic patients. The technique comprised of plantar area and hotspot segmentations, characterization and pattern classification, which yielded an average classification rate of 94.33% with the extracted features.

Table 3: Temperature distribution analysis.

Reference (Year)	Methodology	Findings
Branemark et al, 1967. (83)	<ul style="list-style-type: none"> <li>Infrared imaging</li> <li>Clinical assessment</li> </ul>	<ul style="list-style-type: none"> <li>Abnormal emission patterns from hand and feet of all diabetes patients</li> <li>Reduced emission on the metatarsal and toes areas</li> </ul>
Nagase et al, 2011. (77)	<ul style="list-style-type: none"> <li>Infrared imaging</li> <li>Conceptual classification comprising of 20 categories of plantar thermography patterns</li> </ul>	<p><b>Normal</b></p> <ul style="list-style-type: none"> <li>48 feet (or 75%) are characterized to the seven categories and the remaining 16 feet characterized as atypical</li> <li>The Id category (butterfly pattern) is mostly identified with 30 feet (or 46.9%)</li> </ul> <p><b>Diabetes</b></p> <ul style="list-style-type: none"> <li>225 (or 87.2%) diabetes feet are characterized to 18 categories and the remaining 33 feet (or 12.8%) as atypical</li> <li>The IIa category (medial and lateral plantar arteries undamaged) is mostly identified with 101 feet (or 39.1%)</li> </ul>
Oe et al, 2013. (79)	<ul style="list-style-type: none"> <li>MRI scans</li> <li>Infrared imaging</li> <li>Ankle-brachial index (ABI)</li> <li>Toe-brachial index (TBI)</li> <li>Nerve conduction velocity</li> <li>SPSS for statistical analysis</li> </ul>	<ul style="list-style-type: none"> <li>Ankle pattern is mostly common in patients with osteomyelitis</li> <li>Sensitivity = 60%</li> <li>Specificity = 100%</li> <li>PPV = 100%</li> <li>NPV = 71.4%</li> </ul>
Mori et al, 2013. (80)	<ul style="list-style-type: none"> <li>Ankle-brachial index (ABI)</li> <li>Toe-brachial index (TBI)</li> <li>Achilles tendon reflex</li> <li>Semmes-Weinstein monofilament test</li> <li>Vibratory sensation test</li> <li>Infrared imaging</li> <li>Image partitioning algorithm</li> <li>T test or chi square test</li> </ul>	<p><b>Normal</b></p> <ul style="list-style-type: none"> <li>47 feet are characterized to the four categories and the remaining 17 feet characterized as anomalous</li> <li>The type 1 (butterfly pattern) (44%) is mostly identified</li> </ul> <p><b>Diabetes</b></p> <ul style="list-style-type: none"> <li>198 diabetes feet are characterized to six categories and the remaining 60</li> </ul>

		feet as atypical
Bharara et al, 2014. (78)	<ul style="list-style-type: none"> <li>• Clinical assessment</li> <li>• Semmes Weinstein monofilament</li> <li>• Vibratory perception threshold</li> <li>• Infrared imaging</li> </ul>	<p><b>Normal</b></p> <ul style="list-style-type: none"> <li>• Subjects are mostly represented by IId category (Butterfly Pattern) during measurements with 47.2% at rest, 13.8% at post stress and 27.8% at recovery</li> </ul>
Hernandez-Contreras et al, 2015. (81)	<ul style="list-style-type: none"> <li>• Infrared imaging</li> <li>• Grayscale characterization</li> <li>• Arch segmentation based on histogram distribution</li> <li>• Mathematical morphology</li> </ul>	<p><b>Normal</b></p> <ul style="list-style-type: none"> <li>• Butterfly pattern is presented in the subjects and pattern spectrum is same as oval</li> <li>• Mean percentage of pixels for control group is highest in quadrant 4 with 88.05%</li> </ul>
Hernandez-Contreras et al, 2015. (82)	<ul style="list-style-type: none"> <li>• Infrared imaging</li> <li>• Grayscale characterization</li> <li>• Foot segmentation</li> <li>• Temperature pattern</li> <li>• Mathematical morphology</li> <li>• Pattern spectrum</li> <li>• Multilayer perceptron</li> <li>• K-fold cross validation</li> </ul>	<p><b>Diabetes</b></p> <ul style="list-style-type: none"> <li>• Pattern spectrum is irregular due to the dissimilar pattern</li> <li>• Mean percentage of pixels is 28.87% for diabetes group in quadrant 3.</li> </ul> <p><b>Normal</b></p> <ul style="list-style-type: none"> <li>• Proposed technique achieved average classification rate of 94.33%</li> </ul>

#### 4.4. Independent thermal and physical stress analysis

The goal of independent thermal and physical stress analysis is to study the reaction of body thermoregulation system under applied thermal and/or physical stress. The stress may include soaking the body part into cold or hot water, or mechanical stress like running or walking.

The summary of studies based on independent thermal and physical stress analysis prior to thermogram acquisition is presented in Table 4. Fushimi et al. (84) studied the

vasoreactions of peripheral arteries by subjecting the hands of normal and diabetic subjects to cold stimuli and then record the temperature changes in the toes using IR thermography. The pattern for abnormal temperature changes is classified into 3 types, namely increasing, decreasing and flat. The atherosclerosis of peripheral arteries is highly related to the abnormal vasoreaction of toe arteries following the application of cold stimulus on both hands. The advantage of this study is that cold stimulated IR thermography helps to assess the peripheral atherosclerosis condition. Fujiwara et al. (85) evaluated the blood flow in the skin of diabetic patients using IR thermography before and after soaking the lower limb into cold water. The study confirmed that lower skin temperature recovery rate in diabetic patients is attributed to peripheral arterial sclerosis, abnormal blood coagulation fibrinolysis and sympathetic nerve dysfunction. Hosaki et al. (86) proposed a novel and nonintrusive diagnosis method for peripheral circulation in diabetic patients. The study found that the results for peripheral circulation in these patients obtained using laser-Doppler blood flowmetry and thermography are correlated. The study showed that these methods can determine diabetic patients with poor peripheral perfusion. Balbinot et al. (87) assessed the specificity and sensitivity of plantar thermography in diagnosing diabetes patients with polyneuropathy by utilizing heart rate variability (HRV) as a reference. Evidently, the plantar thermography is applicable in diagnosing diabetic neuropathy early, especially the autonomic and small fibers that are related to sub clinical condition. Nonetheless, this is a cross sectional study that includes sensitive test. Barriga et al. (88) proposed a CAD system for pre-clinical stages of peripheral neuropathy based on thermogram analysis. The study confirmed that cold stimuli and IR thermography can successfully identify patients with microvascular abnormalities. Najafi et al. (89) studied the dynamic fluctuation in plantar temperature with respect to the pre-defined steps taken by the diabetic and peripheral neuropathic patients with and without Charcot neuroarthropathy. There are several disadvantages in this study. The development stage of Charcot foot is not controlled in this study whereby few patients may be in the coalescence phase. Moreover, the offloading foot wear is not standardized and hence, unable to sufficiently perform stratified analysis by stage and type of offloading foot wear. Lastly, due to the technology drawbacks, a short hold-up is needed to analyze the plantar temperature after each gait. Balbinot et al. (90) compared the plantar temperatures and analyzed the plantar re-warming index

repeatability after cold stress on two separate days and groups (diabetes and normal). The proposed study observed good repeatability between two days presented by the rewarming index after the cold stimuli. However, the drawback is that, small sample size is used as it is a pilot study and neurophysiological study is not done to assess the existence of diabetic peripheral neuropathy. Further, the clinical assessment performed has not identified diabetic patients with neuropathy. Yavuz et al. (91) studied the statistical correlation between the plantar stresses and increase in foot plantar temperature after exercise using IR thermography. The disadvantages are that small number of participants without diabetic patients are involved. Also, there are more female subjects in this study and the size of the customized pressure shear instrument restrict the shear measurements of the whole foot. Agurto et al. (92) proposed a technique for the classification of diabetic peripheral neuropathy patients using IR thermography and independent component analysis (ICA). The limitations of this study are that few initial frames are not considered for the analysis and some areas, particularly the toes, present artifacts which require stabilizing the toes to avoid significant movements.

Table 4: Independent thermal and physical stress analysis.

Reference (Year)	Methodology	Findings
Fushimi et al, 1996. (84)	<ul style="list-style-type: none"> <li>• ECG</li> <li>• Ankle pressure index</li> <li>• Infrared imaging</li> <li>• Ultrasonic imaging</li> </ul>	<p><b>Normal</b></p> <ul style="list-style-type: none"> <li>• All subjects had normal pattern</li> </ul> <p><b>Diabetes</b></p> <ul style="list-style-type: none"> <li>• 43 had normal, 19 increasing and 26 decreasing and 24 flat patterns</li> </ul>
Fujiwara et al, 2000. (85)	<ul style="list-style-type: none"> <li>• Infrared imaging</li> <li>• Ankle-brachial index</li> <li>• Doppler meter</li> <li>• Motor nerve conduction velocity</li> <li>• Sensory nerve conduction velocity</li> <li>• ECG</li> <li>• Schellong's test</li> <li>• Photo-dispersion method</li> <li>• ANOVA with Neuman-Keuls multiple comparison test</li> </ul>	<ul style="list-style-type: none"> <li>• Smaller skin temperature drop in diabetes patients compared to normal subjects after immersing into cold water</li> <li>• Diabetes patients had lower skin temperature recovery rate due to causal factors such as peripheral arterial sclerosis, abnormal blood coagulation fibrinolysis and sympathetic nerve dysfunction</li> </ul>
Hosaki et al, 2002. (86)	<ul style="list-style-type: none"> <li>• Infrared imaging</li> <li>• Laser Doppler blood flowmeter</li> </ul>	<ul style="list-style-type: none"> <li>• Recovery ratios for the 27 diabetes patients were in the range of 0-93.5%</li> </ul>

	<ul style="list-style-type: none"> <li>Hot loading at 36 °C</li> <li>Cold loading at 20 °C</li> <li>Compute recovery ratio</li> </ul>	<p>and the average was 34%</p> <ul style="list-style-type: none"> <li>Blood flow and recovery ratio were correlated (<math>r = 0.634</math>, <math>p &lt; 0.0001</math>)</li> <li>Ratio of blood flow after cold loading over the blood flow after hot loading was in the range of 38.1% - 122% and average of 80.6%.</li> <li>This ratio and recovery ratio is correlated (<math>r = 0.502</math>, <math>p &lt; 0.0001</math>)</li> </ul>
Balbinot et al, 2012. (87)	<ul style="list-style-type: none"> <li>Clinical assessments</li> <li>Heart rate variability</li> <li>Infrared imaging</li> <li>Electromyography</li> <li>Statistical analysis</li> </ul>	<p><b>Diabetes</b></p> <ul style="list-style-type: none"> <li>Interdigital anisothermal method performed better than thermal recovery index with 46.2% specificity and 81.3% sensitivity</li> </ul> <p><b>Prediabetes</b></p> <ul style="list-style-type: none"> <li>All three tests achieved 25% specificity and 80% sensitivity equally</li> </ul>
Barriga et al, 2012. (88)	<ul style="list-style-type: none"> <li>Infrared imaging</li> <li>Motion tracking of thermal features</li> <li>Exponential curve fitting</li> </ul>	<ul style="list-style-type: none"> <li>Diabetes neuropathy patient recorded recovery rate of 2% at the two toes and approximately 0.4% at the heel</li> <li>Normal subject recorded high recovery of 4% at the medial arch as compared to less than 1.5% in the diabetes neuropathy patient</li> </ul>
Najafi et al, 2012. (89)	<ul style="list-style-type: none"> <li>Two pre-defined paths of 50 and 150 steps</li> <li>Infrared imaging</li> <li>Image processing</li> <li>Student t test</li> <li>ANOVA</li> </ul>	<ul style="list-style-type: none"> <li>In Charcot neuroarthropathy group, the decreased in temperature for non-affected foot is 1.9 folds more than the affected foot</li> <li>Plantar temperature for both foot in Charcot neuroarthropathy group significantly increased beyond 50 steps and remain higher on the affected foot at 200 steps</li> </ul>
Balbinot et al, 2013. (90)	<ul style="list-style-type: none"> <li>Clinical assessments</li> <li>Infrared imaging</li> <li>Data analysis</li> <li>Statistical analysis</li> </ul>	<ul style="list-style-type: none"> <li>Significant difference in the average temperatures of normal subjects between the two days before and after cold stress test compared to no difference in the average temperatures for diabetes patients</li> <li>Rewarming index of both groups did not differ between the two days</li> </ul>
Yavuz et al, 2014. (91)	<ul style="list-style-type: none"> <li>Walking on pressure shear plate</li> <li>Treadmill walking</li> <li>Infrared imaging</li> <li>Peak shear stress and peak resultant stress</li> <li>Statistical analysis</li> </ul>	<ul style="list-style-type: none"> <li>Significant correlation between temperature rises and peak shear stress (<math>r = 0.78</math>)</li> <li>Increased in plantar temperature can predict the site of peak resultant stress and peak shear stress in 39% and 23% of the subjects</li> </ul>
Aguro et al, 2015. (92)	<ul style="list-style-type: none"> <li>Cold stimulus</li> <li>Infrared imaging</li> <li>Independent component</li> </ul>	<ul style="list-style-type: none"> <li>Components 2, 6 and 8 significantly differentiate the normal and diabetes peripheral neuropathy patients</li> </ul>

---

analysis (ICA)

- Higher recovery rate in normal subjects for component 6
  - Diabetes peripheral neuropathy patients have lower temperature recovery rate in most parts of the foot plantar
- 

## 5. DISCUSSION

An early detection of diabetic foot problems and the subsequent medical treatment can prevent the occurrence of foot ulcerations and lower limb amputation. Undeniably, the complications of the diabetic foot are costly and it reduces the quality of life in most of the patients. In this case, neuropathic foot ulcers are the leading cause of morbidity and prolonged hospitalizations (93).

The conventional clinical techniques are not able to identify changes in the integrity of the skin until occurrence of ulcerations (64). Moreover, the seriousness of neuropathy may be diagnosed with electrophysiological analysis and quantitative examinations using sensory modalities. However, these assessments are unable to specifically determine the cause of neuropathy, either due to diabetes or other reasons (94). Nonetheless, not all classification/scoring systems available are robustly verified within and among the healthcare centers (95). It is notably less assuring that a particular system is robust, meaningful and possible for populations in other countries. This is crucial because the etiological factors may vary among countries. For instance, arterial disease is particularly common in United States and Europe as compared to developing countries. Furthermore, bacterial infection may have significant impact in countries where the antibiotics availability is less. Hence, external verification is essential when the results of the system are taken into consideration as management plan (95). In the case of bone infection management, surgical intervention by bone amputation or debridement is needed based on protocols. A system in one center may give a high score for bone visibility as poor predictor of healing without surgery. However, this may not be applicable elsewhere where bone infection may be first treated with antibiotics.

The peripheral neuropathy and vascular disease are the main risk factors of the diabetic foot. These risk factors generate superficial temperature fluctuations that can be detected using temperature measurement methods (96). Many studies have indicated the temperature fluctuations on the plantar foot areas due to diabetic foot complications (76, 97-102). The IR thermometry (97, 98, 100, 101), liquid crystal thermography (LCT) (76, 99, 102, 103) and IR thermography (14, 59, 77, 104, 105) have been used to measure the plantar temperature. The IR thermometry is a temperature monitoring method that measures the temperature at various points on the feet (100). Nevertheless, it becomes difficult to measure the temperature at many points on the foot. Next, the LCT method produces a color reaction relative to the temperature of the skin surface, which touches the thermochromic liquid crystals. Despite being cheap and providing visualization of plantar thermal distribution, LCT is a contact method which produces slow responses and thus, may not be useful for certain applications (12).

Lastly, the infrared thermography is a fast, nonintrusive and non-contact method that allows the visualization of plantar temperature distribution. Further, it is passive whereby no harmful radiation passes through the body but only capturing of the body heat radiation (12). Infrared thermography is a non-contact method and has the advantage over the other assessment tools such as the monofilament and vibration sensation tests. It limits the unnecessary contact and pressure that may affect the temperature readings and mitigate the spread of infection through the apparatus (77). Moreover, IR thermography permits the measurement of temperature distribution of the whole foot regardless of the shapes or surfaces, particularly the medial arch which is a non-contact surface of the foot. Finally, IR thermography can be administered (picture taken) by a non-clinician and passed on to clinician for assessment and correlating clinically. For this purpose, the applications of IR thermography have significantly increased over the years especially in the study of diabetic foot related complications (33).

The infrared thermography is used to observe the morphology of the skin temperature pattern, which is influenced by blood perfusion. In conditions where blood circulation at the peripheral limbs are reduced (ischemic), there will be a change in the temperature patterns

(33). The various analysis methods performed with diabetic foot problems are presented in Table 1, 2, 3 and 4. Table 1 presents a separate lower limb temperature analysis representing the range of temperatures for the respective study groups. However, this analysis is not able to determine the specific risk regions associated to diabetic foot complications. In contrast, the temperature distribution analysis in Table 3 does not compare the plantar temperature between feet but instead, studied each foot independently. Despite studies showing same plantar temperature distribution in normal subjects, there has been no representative pattern for this group thus far. In addition, the plantar temperature distribution in diabetic patients are irregular in patterns. Hence, classification of the temperature distribution may be difficult. The independent thermal and physical stress analysis in Table 4 analyzed the plantar temperature reaction to the applied external stimulus. The temperature is evaluated by analyzing separately before and after the application of external stress. Nevertheless, the external stress that consist of walking or immersing the limb into cold or hot water for a period may result in subjects feeling uncomfortable and inconvenient.

Comparatively, asymmetric temperature analysis is the most commonly used method in analyzing the foot plantar thermograms. Several studies in Table 2 have achieved satisfactory results in detecting diabetic foot risk regions. The asymmetric temperature analysis performed temperature comparison between one foot and the contralateral foot. The foot plantar temperature distribution of healthy individuals is contralateral symmetric whereas asymmetric temperature distributions on the foot plantar indicate abnormality (35). Evidently, Gatt et al. (106) observed that the healthy skin temperature of similar areas in contralateral limbs is generally symmetrical in terms of pattern and magnitude using IR thermography. Hence, pre-established thermal pattern atlas is not required for healthy individuals, which are normally used as a control group. The diagnosis process involved the application of image processing and feature extraction techniques that extract details from the temperature pattern differences among the feet. Nevertheless, the application of feature extraction and machine learning algorithms are inconsistent among the studies. In fact, no classification techniques were implemented for classification performance evaluation. In addition, asymmetric temperature analysis may not be able to identify the risk regions if the same complications are present on both feet.

The association between diabetic foot and heat pattern on the plantar foot is subtle and often nonlinear (49). Therefore, the development of computer aided system is essential in helping to interpret the plantar thermograms. The knowledge discovery and data mining algorithms may provide improvement to the thermogram based CAD system in various main areas. First, screening clinicians may experience possible visual overloading. With thermogram based CAD system, diagnosis workload can be reduced and more attention can be given on complicated cases. Thus, enhancing the level of medical care. Second is the inter observer variability. Thermogram diagnosis based on human can be subjective and the qualities may vary extensively. Thus, objective technique based on mathematics and computer science can help in objectifying the diagnosis and decrease the inter observer variability. The last part is the quality of diagnosis. To a large extent, the progress of thermogram diagnosis based on human depends on training level and experience of the screening clinicians. Meanwhile, the progress of CAD system is based on the software and hardware in which computing machinery is increasingly becoming more potent. Moreover, the software domain progresses by integrating and developing better image processing algorithms. Hence, CAD system may be able to outperform the clinicians based on cost, accuracy and speed.

## 6. CONCLUSION

Diabetes mellitus is a long term metabolic disorder affecting various parts of the human body. The high blood glucose level causes reduction in the blood perfusion, which may often result in diabetic foot complications. The diabetic foot is the most critical and expensive complication causing disability and impairing the quality of life. The burden of diabetic foot diseases is expected to rise in future due to the growing number of diabetic patients. Thus, an early detection of diabetic foot complication is important for effective medical treatments. In this paper, conventional foot assessment methods, infrared thermography and, CAD system analysis for the diabetic foot using infrared thermography are discussed. Indeed, the IR thermography application has been growing over the years particularly in the field of medicine due to its advantages over other methods. Various techniques for thermal image analysis are presented in this paper. Among them, asymmetric

temperature analysis is commonly used technique as it is simple to implement and yielded satisfactory results in previous studies. Also, new algorithms need to be developed to overcome the drawbacks of this analysis. The continuous advances in the image processing and data mining algorithms may help to overcome the existing limitations. This may help in the early detection of diabetic foot complications, and hence, assist the clinicians to intervene early. The accuracy of the CAD system can be improved further using better nonlinear features and deep learning techniques. The developed CAD system can be introduced in clinics and healthcare institutions to assess the severity of diabetic foot complications.

#### **REFERENCES:**

1. Organization WH. Definition, diagnosis and classification of diabetes mellitus and its complications: report of a WHO consultation. Part 1, Diagnosis and classification of diabetes mellitus. 1999.
2. Organization WH. Global report on diabetes: World Health Organization; 2016.
3. Boulton AJ, Vileikyte L, Ragnarson-Tennvall G, Apelqvist J. The global burden of diabetic foot disease. *The Lancet*. 2005;366(9498):1719-24.
4. Abbott CA, Garrow AP, Carrington AL, Morris J, Van Ross ER, Boulton AJ. Foot ulcer risk is lower in South-Asian and African-Caribbean compared with European diabetic patients in the UK. *Diabetes care*. 2005;28(8):1869-75.
5. Ramsey SD, Newton K, Blough D, McCulloch DK, Sandhu N, Reiber GE, et al. Incidence, outcomes, and cost of foot ulcers in patients with diabetes. *Diabetes care*. 1999;22(3):382-7.
6. Pecoraro RE, Reiber GE, Burgess EM. Pathways to diabetic limb amputation: basis for prevention. *Diabetes care*. 1990;13(5):513-21.
7. Glaudemans A, Uçkay I, Lipsky B. Challenges in diagnosing infection in the diabetic foot. *Diabetic Medicine*. 2015;32(6):748-59.
8. McNeely MJ, Boyko EJ, Ahroni JH, Stensel VL, Reiber GE, Smith DG, et al. The Independent Contributions of Diabetic Neuropathy and Yasculopathy in Foot Ulceration: How great are the risks? *Diabetes care*. 1995;18(2):216-9.
9. Group NDD, Diabetes NIo, Digestive, Diseases K. Diabetes in America: National Institutes of Health, National Institute of Diabetes and Digestive and Kidney Diseases; 1995.
10. Schaper N, Van Netten J, Apelqvist J, Lipsky B, Bakker K. Prevention and management of foot problems in diabetes: a Summary Guidance for Daily Practice 2015, based on the IWGDF Guidance Documents. *Diabetes/metabolism research and reviews*. 2016;32(S1):7-15.

11. Zubair M, Malik A, Ahmad J. Clinico-microbiological study and antimicrobial drug resistance profile of diabetic foot infections in North India. *The Foot*. 2011;21(1):6-14.
12. Lahiri B, Bagavathiappan S, Jayakumar T, Philip J. Medical applications of infrared thermography: a review. *Infrared Physics & Technology*. 2012;55(4):221-35.
13. Bouzida N, Bendada A, Maldague XP. Visualization of body thermoregulation by infrared imaging. *Journal of Thermal Biology*. 2009;34(3):120-6.
14. Bagavathiappan S, Saravanan T, Philip J, Jayakumar T, Raj B, Karunanihi R, et al. Investigation of peripheral vascular disorders using thermal imaging. *The British Journal of Diabetes & Vascular Disease*. 2008;8(2):102-4.
15. Bagavathiappan S, Saravanan T, Philip J, Jayakumar T, Raj B, Karunanihi R, et al. Infrared thermal imaging for detection of peripheral vascular disorders. *Journal of medical physics/Association of Medical Physicists of India*. 2009;34(1):43.
16. Henderson H, Hackett M. The value of thermography in peripheral vascular disease. *Angiology*. 1978;29(1):65-75.
17. Huang C-L, Wu Y-W, Hwang C-L, Jong Y-S, Chao C-L, Chen W-J, et al. The application of infrared thermography in evaluation of patients at high risk for lower extremity peripheral arterial disease. *Journal of vascular surgery*. 2011;54(4):1074-80.
18. Snehalatha U, Anburajan M, Teena T, Venkatraman B, Menaka M, Raj B, editors. Thermal image analysis and segmentation of hand in evaluation of rheumatoid arthritis. *Computer Communication and Informatics (ICCCI), 2012 International Conference on*; 2012: IEEE.
19. Acharya UR, Ng EY-K, Tan J-H, Sree SV. Thermography based breast cancer detection using texture features and support vector machine. *Journal of medical systems*. 2012;36(3):1503-10.
20. Boquete L, Ortega S, Miguel-Jiménez JM, Rodríguez-Ascariz JM, Blanco R. Automated detection of breast cancer in thermal infrared images, based on independent component analysis. *Journal of medical systems*. 2012;36(1):103-11.
21. Ng E-K. A review of thermography as promising non-invasive detection modality for breast tumor. *International Journal of Thermal Sciences*. 2009;48(5):849-59.
22. Schaefer G, Závišek M, Nakashima T. Thermography based breast cancer analysis using statistical features and fuzzy classification. *Pattern Recognition*. 2009;42(6):1133-7.
23. Tan TZ, Quek C, Ng GS, Ng E. A novel cognitive interpretation of breast cancer thermography with complementary learning fuzzy neural memory structure. *Expert Systems with Applications*. 2007;33(3):652-66.
24. Dibai Filho AV, Packer AC, de Souza Costa AC, dos Santos Berni-Schwarzenbeck KC, Rodrigues-Bigaton D. Assessment of the upper trapezius muscle temperature in women with and without neck pain. *Journal of manipulative and physiological therapeutics*. 2012;35(5):413-7.

25. Zaproudina N, Ming Z, Hänninen OO. Plantar infrared thermography measurements and low back pain intensity. *Journal of manipulative and physiological therapeutics.* 2006;29(3):219-23.
26. Acharya UR, Tan JH, Koh JE, Sudarshan VK, Yeo S, Too CL, et al. Automated diagnosis of dry eye using infrared thermography images. *Infrared Physics & Technology.* 2015;71:263-71.
27. Acharya UR, Tan JH, Vidya S, Yeo S, Too CL, Lim WJE, et al. Diagnosis of response and non-response to dry eye treatment using infrared thermography images. *Infrared Physics & Technology.* 2014;67:497-503.
28. Anburajan M, Sivanandam S, Bidyarasmi S, Venkatraman B, Menaka M, Raj B, editors. Changes of skin temperature of parts of the body and serum asymmetric dimethylarginine (ADMA) in type-2 diabetes mellitus Indian patients. *Engineering in Medicine and Biology Society, EMBC, 2011 Annual International Conference of the IEEE;* 2011: IEEE.
29. Jiang G, Shang Z, Zhang M, editors. Metabolism parameter analysis of diabetics based on the thermography. *Engineering in Medicine and Biology, 2002 24th Annual Conference and the Annual Fall Meeting of the Biomedical Engineering Society EMBS/BMES Conference, 2002 Proceedings of the Second Joint;* 2002: IEEE.
30. Sivanandam S, Anburajan M, Venkatraman B, Menaka M, Sharath D. Estimation of blood glucose by non-invasive infrared thermography for diagnosis of type 2 diabetes: an alternative for blood sample extraction. *Molecular and cellular endocrinology.* 2013;367(1):57-63.
31. Sejling A-S, Lange KH, Frandsen CS, Diemar SS, Tarnow L, Faber J, et al. Infrared thermographic assessment of changes in skin temperature during hypoglycaemia in patients with type 1 diabetes. *Diabetologia.* 2015;58(8):1898-906.
32. Sivanandam S, Anburajan M, Venkatraman B, Menaka M, Sharath D. Medical thermography: a diagnostic approach for type 2 diabetes based on non-contact infrared thermal imaging. *Endocrine.* 2012;42(2):343-51.
33. Ring F. Thermal imaging today and its relevance to diabetes. *SAGE Publications;* 2010.
34. Gilman S. *Neurobiology of disease:* Academic Press; 2011.
35. Jones BF. A reappraisal of the use of infrared thermal image analysis in medicine. *IEEE transactions on medical imaging.* 1998;17(6):1019-27.
36. Biederman-Thorson MA, Schmidt RF, Thews G. *Human Physiology:* Springer Science & Business Media; 2013.
37. Adams F. The genuine works of Hippocrates. *Southern Medical Journal.* 1922;15(6):519.
38. Ring E. The historical development of temperature measurement in medicine. *Infrared physics & technology.* 2007;49(3):297-301.
39. Diakides NA, Bronzino JD. *Medical Infrared Imaging.* 2007. CRC Press, Boca Raton, Florida, USA.

40. Hardy JD. The radiation of heat from the human body: I. An instrument for measuring the radiation and surface temperature of the skin. *Journal of Clinical Investigation.* 1934;13(4):593.
41. Ng EY, EtehadTavakol M. Application of Infrared to Biomedical Sciences: Springer; 2017.
42. Lawson R. Implications of surface temperatures in the diagnosis of breast cancer. *Canadian Medical Association Journal.* 1956;75(4):309.
43. Lawson R. Thermography a new tool in the investigation of breast lesions. *Can Med Assoc J.* 1957;13:517-24.
44. Tan J-H, Ng E, Acharya UR, Chee C. Infrared thermography on ocular surface temperature: a review. *Infrared physics & technology.* 2009;52(4):97-108.
45. Lienhard JH. A heat transfer textbook: Courier Corporation; 2013.
46. Bergman TL, Incropera FP. Fundamentals of heat and mass transfer: John Wiley & Sons; 2011.
47. Meola C, Carlomagno GM. Recent advances in the use of infrared thermography. *Measurement science and technology.* 2004;15(9):R27.
48. Ring FJ, editor Criteria for thermal imaging in medicine. Engineering in Medicine and Biology Society, 1995, IEEE 17th Annual Conference; 1995: IEEE.
49. Faust O, Acharya UR, Ng E, Hong TJ, Yu W. Application of infrared thermography in computer aided diagnosis. *Infrared Physics & Technology.* 2014;66:160-75.
50. Suissa S, Ernst P. Optical illusions from visual data analysis: example of the New Zealand asthma mortality epidemic. *Journal of clinical epidemiology.* 1997;50(10):1079-88.
51. Etehad Tavakol M, Lucas C, Sadri S, Ng E. Analysis of breast thermography using fractal dimension to establish possible difference between malignant and benign patterns. *Journal of Healthcare Engineering.* 2010;1(1):27-43.
52. Ng EY-K, Chen Y. Segmentation of breast thermogram: improved boundary detection with modified snake algorithm. *Journal of mechanics in medicine and biology.* 2006;6(02):123-36.
53. Ng EY, Sudharsan N. Computer simulation in conjunction with medical thermography as an adjunct tool for early detection of breast cancer. *BMC cancer.* 2004;4(1):17.
54. Ammer K, Melnizky P, Rathkolb O, Ring EF, editors. Thermal imaging of skin changes on the feet of type II diabetics. 2001 Conference Proceedings of the 23rd Annual International Conference of the IEEE Engineering in Medicine and Biology Society; 2001 2001.
55. Melnizky P, Ammer K, Rathkolb O. Thermographic findings of the lower extremity in Patients with Type II diabetes. *Thermol int.* 2002;12:107-14.
56. Nishide K, Nagase T, Oba M, Oe M, Ohashi Y, Iizaka S, et al. Ultrasonographic and thermographic screening for latent inflammation in diabetic foot callus. *Diabetes Res Clin Pract.* 2009;85(3):304-9.

57. Bharara M, Schoess J, Nouvong A, Armstrong DG. Wound Inflammatory Index: A "Proof of Concept" Study to Assess Wound Healing Trajectory. *Journal of Diabetes Science and Technology*. 2010;4(4):773-9.
58. Bagavathiappan S, Philip J, Jayakumar T, Raj B, Rao PNS, Varalakshmi M, et al. Correlation between Plantar Foot Temperature and Diabetic Neuropathy: A Case Study by Using an Infrared Thermal Imaging Technique. *Journal of Diabetes Science and Technology*. 2010;4(6):1386-92.
59. Sun P-C, Jao S-HE, Cheng C-K. Assessing foot temperature using infrared thermography. *Foot & ankle international*. 2005;26(10):847-53.
60. Sun PC, Lin HD, Jao SH, Ku YC, Chan RC, Cheng CK. Relationship of skin temperature to sympathetic dysfunction in diabetic at-risk feet. *Diabetes Res Clin Pract*. 2006;73(1):41-6.
61. Sun PC, Lin HD, Jao SH, Chan RC, Kao MJ, Cheng CK. Thermoregulatory sudomotor dysfunction and diabetic neuropathy develop in parallel in at-risk feet. *Diabet Med*. 2008;25(4):413-8.
62. Kaabouch N, Chen Y, Anderson JW, Ames F, Paulson R, editors. Asymmetry analysis based on genetic algorithms for the prediction of foot ulcers. VDA; 2009.
63. Kaabouch N, Chen Y, Hu W-C, Anderson J, Ames F, Paulson R, editors. Early detection of foot ulcers through asymmetry analysis. Proc SPIE; 2009.
64. Kaabouch N, Chen Y, Hu W-C, Anderson JW, Ames F, Paulson R. Enhancement of the asymmetry-based overlapping analysis through features extraction. *Journal of Electronic Imaging*. 2011;20(1):013012-7.
65. Kaabouch N, Hu W-C, Chen Y, Anderson JW, Ames F, Paulson R. Predicting neuropathic ulceration: analysis of static temperature distributions in thermal images. *Journal of biomedical optics*. 2010;15(6):061715--6.
66. Kaabouch N, Hu W-C, Chen Y. Alternative technique to asymmetry analysis-based overlapping for foot ulcer examination: Scalable scanning. arXiv preprint arXiv:160603578. 2016.
67. Liu C, van der Heijden F, Klein ME, van Baal JG, Bus SA, van Netten JJ. Infrared dermal thermography on diabetic feet soles to predict ulcerations: a case study. 2013.
68. Peregrina-Barreto H, Morales-Hernandez LA, Rangel-Magdaleno J, Avina-Cervantes JG, Ramirez-Cortes JM, Morales-Caporal R. Quantitative estimation of temperature variations in plantar angiosomes: a study case for diabetic foot. *Computational and mathematical methods in medicine*. 2014;2014.
69. van Netten JJ, Prijs M, van Baal JG, Liu C, van Der Heijden F, Bus SA. Diagnostic values for skin temperature assessment to detect diabetes-related foot complications. *Diabetes technology & therapeutics*. 2014;16(11):714-21.
70. Liu C, van Netten JJ, Van Baal JG, Bus SA, van Der Heijden F. Automatic detection of diabetic foot complications with infrared thermography by asymmetric analysis. *Journal of biomedical optics*. 2015;20(2):026003-.
71. Harding J, Wertheim D, Williams R, Melhuish J, Banerjee D, Harding K, editors. Infrared imaging in diabetic foot ulceration. *Engineering in Medicine and*

Biology Society, 1998 Proceedings of the 20th Annual International Conference of the IEEE; 1998: IEEE.

72. Peregrina-Barreto H, Morales-Hernández L, Rangel-Magdaleno J, Vázquez-Rodríguez P, editors. Thermal image processing for quantitative determination of temperature variations in plantar angiosomes. Instrumentation and Measurement Technology Conference (I2MTC), 2013 IEEE International; 2013: IEEE.
73. van Netten JJ, van Baal JG, Liu C, van Der Heijden F, Bus SA. Infrared thermal imaging for automated detection of diabetic foot complications. SAGE Publications Sage CA: Los Angeles, CA; 2013.
74. Vilcahuaman L, Harba R, Canals R, Zequera M, Wilches C, Arista M, et al., editors. Detection of diabetic foot hyperthermia by infrared imaging. Engineering in Medicine and Biology Society (EMBC), 2014 36th Annual International Conference of the IEEE; 2014: IEEE.
75. Vilcahuaman L, Harba R, Canals R, Zequera M, Wilches C, Arista M, et al., editors. Automatic Analysis of Plantar Foot Thermal Images in at-Risk Type II Diabetes by Using an Infrared Camera. World Congress on Medical Physics and Biomedical Engineering, June 7-12, 2015, Toronto, Canada; 2015: Springer.
76. Chan AW, MacFarlane IA, Bowsher DR. Contact thermography of painful diabetic neuropathic foot. *Diabetes Care*. 1991;14(10):918-22.
77. Nagase T, Sanada H, Takehara K, Oe M, Iizaka S, Ohashi Y, et al. Variations of plantar thermographic patterns in normal controls and non-ulcer diabetic patients: novel classification using angiosome concept. *Journal of Plastic, reconstructive & aesthetic Surgery*. 2011;64(7):860-6.
78. Bharara M, Boulger E, Grewal GS, Schoess JN, Armstrong DG, editors. Applications of angiosome classification model for monitoring disease progression in the diabetic feet. Proceedings of the 2014 Summer Simulation Multiconference; 2014: Society for Computer Simulation International.
79. Oe M, Yotsu R, Sanada H, Nagase T, Tamaki T. Screening for osteomyelitis using thermography in patients with diabetic foot. *Ulcers*. 2013;2013.
80. Mori T, Nagase T, Takehara K, Oe M, Ohashi Y, Amemiya A, et al. Morphological pattern classification system for plantar thermography of patients with diabetes. SAGE Publications Sage CA: Los Angeles, CA; 2013.
81. Hernandez-Contreras D, Peregrina-Barreto H, Rangel-Magdaleno J, Ramirez-Cortes J, Renero-Carrillo F, Avina-Cervantes G, editors. Evaluation of thermal patterns and distribution applied to the study of diabetic foot. 2015 IEEE International Instrumentation and Measurement Technology Conference (I2MTC) Proceedings; 2015
- .
82. Hernandez-Contreras D, Peregrina-Barreto H, Rangel-Magdaleno J, Ramirez-Cortes J, Renero-Carrillo F. Automatic classification of thermal patterns in diabetic foot based on morphological pattern spectrum. *Infrared Physics & Technology*. 2015;73:149-57.

83. Bränemark P-I, Fagerberg S-E, Langer L, Säve-Söderbergh J. Infrared thermography in diabetes mellitus a preliminary study. *Diabetologia*. 1967;3(6):529-32.
84. Fushimi H, Inoue T, Yamada Y, Matsuyama Y, Kubo M, Kameyama M. Abnormal vasoreaction of peripheral arteries to cold stimulus of both hands in diabetics. *Diabetes research and clinical practice*. 1996;32(1-2):55-9.
85. Fujiwara Y, Inukai T, Aso Y, Takemura Y. Thermographic measurement of skin temperature recovery time of extremities in patients with type 2 diabetes mellitus. *Experimental and clinical endocrinology & diabetes*. 2000;108(07):463-9.
86. Hosaki Y, Mitsunobu F, Ashida K, Tsugeno H, Okamoto M, Nishida N, et al. Non-invasive study for peripheral circulation in patients with diabetes mellitus. *岡大三朝分院研究報告*. 2002;72:31-7.
87. Balbinot LF, Canani LH, Robinson CC, Achaval M, Zaro MA. Plantar thermography is useful in the early diagnosis of diabetic neuropathy. *Clinics*. 2012;67(12):1419-25.
88. Barriga ES, Chekh V, Carranza C, Burge MR, Edwards A, McGrew E, et al., editors. Computational basis for risk stratification of peripheral neuropathy from thermal imaging. Engineering in Medicine and Biology Society (EMBC), 2012 Annual International Conference of the IEEE; 2012: IEEE.
89. Najafi B, Wrobel JS, Grewal G, Menzies RA, Talal TK, Zirie M, et al. Plantar temperature response to walking in diabetes with and without acute Charcot: the Charcot Activity Response Test. *Journal of aging research*. 2012;2012.
90. Balbinot LF, Robinson CC, Achaval M, Zaro MA, Brioschi ML. Repeatability of infrared plantar thermography in diabetes patients: a pilot study. *SAGE Publications Sage CA: Los Angeles, CA*; 2013.
91. Yavuz M, Brem RW, Davis BL, Patel J, Osbourne A, Matassini MR, et al. Temperature as a predictive tool for plantar triaxial loading. *Journal of biomechanics*. 2014;47(15):3767-70.
92. Agurto C, Barriga S, Burge M, Soliz P, editors. Characterization of diabetic peripheral neuropathy in infrared video sequences using independent component analysis. *Machine Learning for Signal Processing (MLSP)*, 2015 IEEE 25th International Workshop on; 2015: IEEE.
93. Jeffcoate WJ, Harding KG. Diabetic foot ulcers. *The lancet*. 2003;361(9368):1545-51.
94. Ahmad J. The diabetic foot. *Diabetes & Metabolic Syndrome: Clinical Research & Reviews*. 2016;10(1):48-60.
95. Game F. Classification of diabetic foot ulcers. *Diabetes/metabolism research and reviews*. 2016;32(S1):186-94.
96. Etehad tavakol M, Ng EY. Assessment of Foot Complications in Diabetic Patients Using Thermography: A Review. *Application of Infrared to Biomedical Sciences*: Springer; 2017. p. 33-43.

97. Armstrong DG, Holtz-Neiderer K, Wendel C, Mohler MJ, Kimbriel HR, Lavery LA. Skin temperature monitoring reduces the risk for diabetic foot ulceration in high-risk patients. *The American journal of medicine.* 2007;120(12):1042-6.
98. Armstrong DG, Lavery LA, Liswood PJ, Todd WF, Tredwell JA. Infrared dermal thermometry for the high-risk diabetic foot. *Physical Therapy.* 1997;77(2):169-75.
99. Benbow SJ, Chan AW, Bowsher DR, Williams G, Macfarlane IA. The prediction of diabetic neuropathic plantar foot ulceration by liquid-crystal contact thermography. *Diabetes care.* 1994;17(8):835-9.
100. Lavery LA, Higgins KR, Lanctot DR, Constantinides GP, Zamorano RG, Armstrong DG, et al. Home monitoring of foot skin temperatures to prevent ulceration. *Diabetes care.* 2004;27(11):2642-7.
101. Lavery LA, Higgins KR, Lanctot DR, Constantinides GP, Zamorano RG, Athanasiou KA, et al. Preventing diabetic foot ulcer recurrence in high-risk patients. *Diabetes care.* 2007;30(1):14-20.
102. Stess RM, Sisney PC, Moss KM, Graf PM, Louie KS, Gooding GA, et al. Use of liquid crystal thermography in the evaluation of the diabetic foot. *Diabetes care.* 1986;9(3):267-72.
103. Roback K, Johansson M, Starkhammar A. Feasibility of a thermographic method for early detection of foot disorders in diabetes. *Diabetes technology & therapeutics.* 2009;11(10):663-7.
104. Medina A, Scott PG, Ghahary A, Tredget EE. Pathophysiology of chronic nonhealing wounds. *Journal of burn care & research.* 2005;26(4):306-19.
105. Mendes R, Sousa N, Almeida A, Vilaça-Alves J, Reis VM, Neves EB. Thermography: a technique for assessing the risk of developing diabetic foot disorders. *Postgraduate medical journal.* 2015;91(1079):538-.
106. Gatt A, Formosa C, Cassar K, Camilleri KP, De Raffaele C, Mizzi A, et al. Thermographic patterns of the upper and lower limbs: baseline data. *International journal of vascular medicine.* 2015;2015.

## Highlights

- Pathogenesis and burden of diabetic foot is reviewed
- Automated diagnosis methods of diabetic foot are studied
- Various infrared thermography methods are discussed
- Asymmetric temperature analysis has yielded better results

### Conflict of Interest Statement

Muhammad Adam Bin Abdul Rahim  
Department of Electronics and Computer Engineering, Ngee Ann Polytechnic, Singapore.  
Singapore 599489  
**Email:** muhdadam@hotmail.com  
**Home:** <https://scholar.google.com.sg/citations?user=zXBM-D4AAAAJ&hl=en&oi=ao>

Journal Manager  
Computers in Biology and Medicine

**Sub:** Submission of revised manuscript for the Computers in Biology and Medicine

Dear Sir,

We are submitting the manuscript entitled "*Computer Aided Diagnosis of Diabetic Foot Using Infrared Thermography: A review*" to the Computers in Biology and Medicine journal for possible publication. **There is no conflict of interest in this work.**

Best Regards,  
Muhammad Adam Bin Abdul Rahim



# DFU\_QUTNet: diabetic foot ulcer classification using novel deep convolutional neural network

Laith Alzubaidi<sup>1,2</sup> · Mohammed A. Fadhel<sup>2</sup> · Sameer R. Olewi<sup>3</sup> ·  
Omran Al-Shamma<sup>2</sup> · Jinglan Zhang<sup>1</sup>

Received: 16 March 2019 / Revised: 9 May 2019 / Accepted: 21 May 2019

Published online: 27 June 2019

© Springer Science+Business Media, LLC, part of Springer Nature 2019

## Abstract

Diabetic Foot Ulcer (DFU) is the main complication of Diabetes, which, if not properly treated, may lead to amputation. One of the approaches of DFU treatment depends on the attentiveness of clinicians and patients. This treatment approach has drawbacks such as the high cost of the diagnosis as well as the length of treatment. Although this approach gives powerful results, the need for a remote, cost-effective, and convenient DFU diagnosis approach is urgent. In this paper, we introduce a new dataset of 754-ft images which contain healthy skin and skin with a diabetic ulcer from different patients. A novel Deep Convolutional Neural Network, DFU\_QUTNet, is also proposed for the automatic classification of normal skin (healthy skin) class versus abnormal skin (DFU) class. Stacking more layers to a traditional Convolutional Neural Network to make it very deep does not lead to better performance, instead leading to worse performance due to the gradient. Therefore, our proposed DFU\_QUTNet network is designed based on the idea of increasing the width of the network while keeping the depth compared to the state-of-the-art networks. Our network has been proven to be very beneficial for gradient propagation, as the error can be back-propagated through multiple paths. It also helps to combine different levels of features at each step of the network. Features extracted by DFU\_QUTNet network are used to train Support Vector Machine (SVM) and K-Nearest Neighbors (KNN) classifiers. For the sake of comparison, we have fine-tuned then re-trained and tested three pre-trained deep learning networks (GoogleNet, VGG16, and AlexNet) for the same task. The proposed DFU\_QUTNet network outperformed the state-of-the-art CNN networks by achieving the F1-score of 94.5%.

**Keywords** Diabetic foot ulcers · Convolutional neural networks · Deep learning · Classification · Transfer learning

---

✉ Laith Alzubaidi  
laith.alzubaidi@hdr.qut.edu.au

Extended author information available on the last page of the article

## 1 Introduction

Diabetes can lead to serious complications like lower limb amputation, blindness, kidney failure, and cardiovascular diseases. These complications are commonly preceded by Diabetic Foot Ulcers (DFUs) [55]. DFUs, generally known as sores, are open wounds that can develop on the feet of people with diabetes. Based on global reporting, there were only 108 million people suffering from diabetes in 1980, while this number increased to more than 422 million people in 2014. For instance, looking at the adults over 18 years old, the overall prevalence increased from 4.7% to 8.5% during the period 1980–2014 [56]. Furthermore, the number of people living with diabetes is expected to increase up to 600 million by the end of 2035. It is also important to mention that about 80% of these people are from developing countries due to the lack of health care facilities and poor awareness [5]. Moreover, around 15% to 25% of diabetic patients will develop DFU at an advanced stage of the disease, which may lead to lower limb amputation if proper care is unavailable [34]. Due to failure to recognize and improper DFU treatment, over one million diabetic people with a ‘high-risk foot’ will lose part of their leg each year [3]. Hygienic personal care, continuous medication, and periodic checkup with doctors are required for people with diabetes to prevent additional consequences. Therefore, diabetes will cause a huge financial burden for people with this disease and their families, mainly in developing countries, since the treatment cost is about 5.7 times the annual income [7].

Nowadays, the assessment of the early diagnosis of DFU in clinical systems involves several significant tasks, which represent continuous tracking of numerous lengthy actions enclosed in handling and managing of DFU for every individual case. These actions include; evaluation of patient’s medical history, examination of the DFU carefully by a diabetic foot specialist, and extra tests for assessment in developing the treatment plan, such as x-ray, MRI, and CT scans. In general, DFU patients have an inflated leg problem which may be itchy and aching depending on each case. Additionally, the DFU usually has uncertain external boundaries and asymmetrical structure. Several factors affect the DFU surrounding skin and its visual appearance, which include; scaly skin, bleeding, slough, important tissues (e.g. Granulation), blisters, callus formation, and redness. Therefore, the exact evaluation of these visual symptoms like texture features and color descriptors is the base of generating powerful computer vision algorithms for ulcer assessment [21].

However, the task of classifying DFU has many challenges. Firstly, the collection and professional labeling of DFU images require large time. Secondly, the similarity between DFU and healthy skin has high inter-class and intra-class variations depending on the patient’s ethnicity, lighting conditions, and the DFU classification [31]. Lastly, it is hard to differentiate between healthy skin and DFU in some cases, for instance, when there are small sizes of DFU, skin wrinkles, and images with a toe.

Our contributions reveal many interesting observations are summarized below:

- (1) We have introduced a new dataset of total 754-ft images which consist of healthy skin and skin with a diabetic ulcer from different patients. The dataset has been manually labeled by a DFU expert.
- (2) We have designed and implemented a novel and robust Deep Convolutional Neural Network, DFU\_QUTNet, from scratch based on the idea of increasing in the network’s width along with the global average pooling. Our network’s structure has proven to be helpful since it has different levels of features at each step of the network. It has also

- proved to be very beneficial for gradient propagation, as the error can be back-propagated through multiple paths.
- (3) Our model used to classify feet skin images into two classes: normal and abnormal (DFU). We improved the performance of DFU classification in term of the F1-score. Our model achieved a F1-score of 94.5% in classifying unseen images of our dataset, which outperforms the state-of-the-art CNN networks.
  - (4) We have trained the multi-classifiers of K-Nearest Neighbor and Support Vector Machine (SVM) classifiers with the features extracted by our proposed DFU\_QUTNet network.
  - (5) We have fine-tuned and re-trained three pre-trained deep learning networks (GoogleNet, VGG16, and AlexNet) for DFU classification task to be compared with our model. DFU\_QUTNet outperforms these three state-of-the-art CNN networks.
  - (6) We have re-implemented DFUNet which was designed by Goyal, et al. [19] and trained it with our dataset. As far as we know, this is the only paper that employed CNNs to classify normal skin against abnormal skin (DFU). Our proposed DFU\_QUTNet network outperforms DFUNet network.
  - (7) As described in Section2, we have reviewed some of the state-of-the-art methods for deep learning and the traditional methods used to classify DFU.

The rest of the paper is organized as follows: Section 2 reviews the related work. Section 3 explains the proposed methodology. Section 4 presents the results. Lastly, section5 draws conclusions.

## 2 Related work

Numerous medical-telecommunication systems, including diabetes monitoring systems, have been developed in recent years [12, 52]. The objectives of these systems are: to offer automated solutions for the lack in the specialists, to enhance the access of medical facilities, to enhance the available health care systems, and to reduce the cost of medical facilities [16]. However, a small number of expert systems related to the evaluation of diabetic foot pathologies which can be classified as automated and non- automated systems have been developed.

### 2.1 DFU telemedicine systems

New technology devices, such as laptops smart-phones and Internet media, have been developed which offer the possibility of remote communications. With the sophisticated mobile Internet (e.g. 5G), these devices have the ability to capture and send very high-quality pictures, audio and video [14, 15]. Medical-telecommunication systems of the non-automated type, which are frequently set-up in a distant location, offer facilities for patients' evaluation such as optical scanner [13], digital photography [21], 3D wound imaging [6], and video conferencing [9]. However, the availability of professional medical experts is still required to complete the patient's evaluation on the other side. Although these systems give powerful results, the need for automated DFU pathology detection is urgent.

The employment of automated DFU detection systems is still in the earlier development stages and has extremely limited applications. Notably, in 2015, C. Liu et al. [34] and O. Jegede et al. [27] presented a smart system for DFU detection based on 3D surface

reconstruction, infrared thermal images, and spectral imaging. However, the implementation of the system requires much expert training and expensive devices in order to work properly. Another system by Wang, et al. [53] is based on capturing an image using a capture box and determines the DFU area by utilizing the two-stage classification of Support Vector Machine. The first step of this system is segmentation which is executed by a super-pixel methodology. The extraction of features represents the second step which is used to implement two staged classification. In spite of the fact that the system presented powerful results, it has some drawbacks including its invalidity on a big dataset and the impracticality of the captured image box for data collection due to the need for patient's foot to be in contact with box surface which in turn does not allow by the health care setting due to worries concerning infection control. Other important research by Manu, et al. [20] has implemented the DFU segmentation on whole foot images.

Furthermore, computerized methodologies based on image processing or manually engineered-feature methods were applied for related skin cut segmentation (such as a wound) and tissue classification. In general, the conventional machine learning technique was applied through extracting several features like color descriptors and texture descriptors on small defined patches of injury images. Then, the classification task takes place to categorize skin patches into normal and abnormal by utilizing machine learning algorithms [11, 28, 48, 49]. The hand\_crafting features methods are influenced by lighting conditions as in several computer vision systems, whereas skin color relying upon the patient ethnicity group. Generally, all the skin cuts connected to an ulcer and wound are labeled as a wound. From the medical viewpoint, the ulcer is due to an internal problem, while the wound is due to an external problem. There are more differences between ulcers and wounds in the skin cut such as the appearance of skin in case of wound or ulcer, pathology (disease processes), physiology (the method the body responds), and aetiology (the cause) [23, 38]. Therefore, DFU takes into consideration the work of finding the difference between normal and abnormal skin at the same place of appearance.

## 2.2 Deep learning

In recent years, deep learning has powered and solved many pattern recognition and computer vision tasks such as image classification [60], age classification [24], sketch recognition [43] and nuclei detection [1]. It is considered the main factor for such improvements in medical image analysis [4, 33]. It has been successfully employed in many biomedical image analysis challenges, such as malaria detection [51], skin biopsy histopathological image annotation [59] and retinal ailment detection [36]. Classical image analysis and Classical machine learning include a series of steps, which are preprocessing, feature extraction, and careful selection of features, learning, and classification. The performance of these methods is strongly dependent on the chosen features and the accuracy of the preceding steps while deep learning enables automated learning of the feature sets for particular problems instead of hand-crafting features [32]. Figure 1 shows the difference between deep learning and machine learning.

Deep learning has been used in different tasks such as detection, counting, and classification. In spite of the fact that each of these tasks has its own specificities, there is essential overlap in pipeline implementation of these applications as shown in Fig. 2. Classification is one of the most significant tasks in the medical field [33]. Several approaches of this task have been proposed in recent years, but still, remain challenging problems. There are numerous factors affect the performance of this task's algorithms such as noise, overlapping, complex

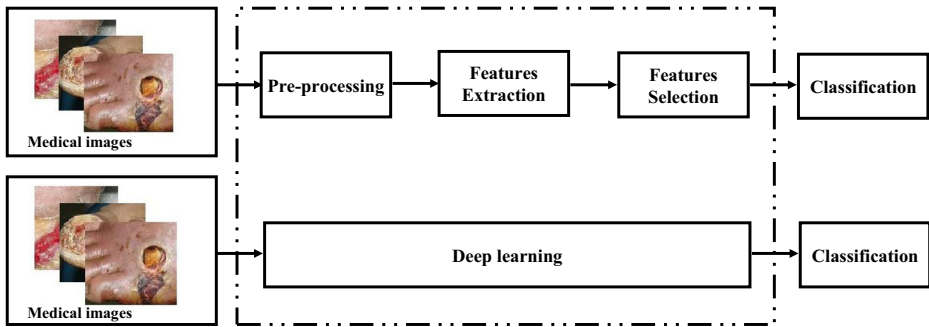


**Fig. 1** The difference between deep learning and machine learning

shapes, as well as low-resolution of images, and there exists no single method that successfully handles all these factors. However, deep learning has overcame most of these challenges and has shown great improvements in the field of medical image classification as well as in different computer vision areas, especially towards the hard and important issues such as understanding images of different scopes such as spectral, marine organism classification, Sickle Cell Anemia classification and hatching eggs classification [2, 17, 35, 58].

Machine learning algorithms and conventional computer vision have many limitations including the need of countless manual tuning for each image, the difficulties in data representation with multi-level abstraction, and the processing ability of a large image data. The solution is a newly developed machine-learning algorithm, termed as Deep Convolutional Neural Networks [32]. This solution has the ability to obtain multi-level representation methods using non-linear simple modules first. Then, the simple feature representations are transformed into extra advanced abstract representations by these modules. In other words, the deep convolutional networks employ images as input for learning features, like locations from the pixel array values and edges at certain directions. Then, a combination of these edges has performed at a higher level in learning additional significant abstract features like desirable object components. The final stage is the connection of these components together to form the final objects [46].

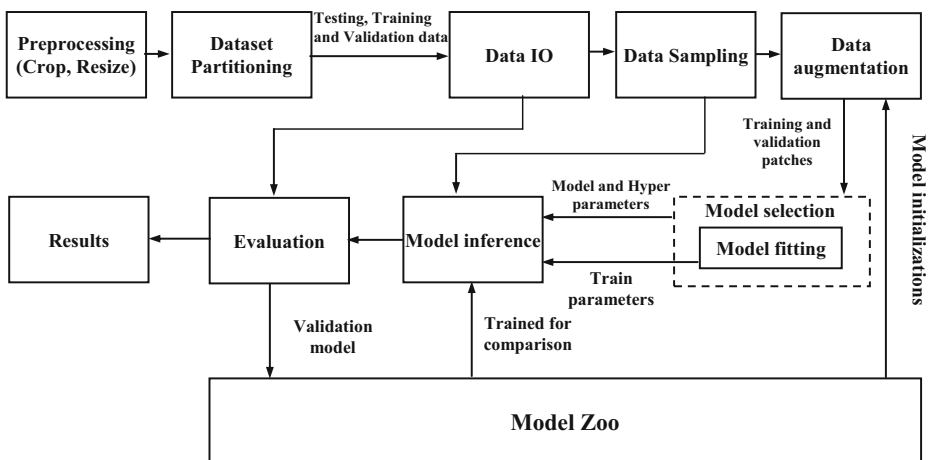


**Fig. 2** Workflow of deep learning tasks

Convolutional Neural Networks (CNNs) are one of the reasons that make deep learning popular today [41]. They have shown record-breaking performance in different image classification tasks [60]. CNN was first proposed for image classification tasks [30]. CNN is a feed-forward neural network consisting of one or more convolutional layers followed by pooling layers as shown in Fig. 3. Additionally, the high performance and classification accuracy of CNN has made it popular for almost all classification tasks specifically for image classification. Convolutional Neural Networks (CNNs) play the core role in medical image classification [33].

One of these CNNs is AlexNet. It was the first significant development in 2012 [30]. These significant developments have included several improvements. Firstly, it introduced better non-linearity in the network with ReLU activation. ReLU helps to avoid demising gradient problems. Secondly, it presents the dropout concept identical to regularization. In the dropout concept, the neurons are arbitrarily activated and deactivated in all layers for avoiding overfitting problem. Accordingly, the data is compelled to come across different routes. Hence, the network is capable of better generalization. Thirdly, introducing data augmentation indicates that the images are displayed with an arbitrary crop, rotation, and translation when supplied to the network. Consequently, it enforces the network since it has extra awareness of the image attributes, instead of the image itself. Last, but not least, for improving the classification accuracy, extra convolutional layers are stacked in advance the pooling layers. Afterward, the VGGNet network was introduced [44]. It inserted additional layers of convolutions and pooling for boosting the accuracy [44]. After VGGNet, GoogleNet was introduced [46], where convolution layers with different filter sizes are processed on the same input and then concatenated together. This type of structure assists in having multi-level feature extraction at each step. The ResNet network was introduced after the GoogleNet network. ResNet presented the concept of residual connection which is every two layers; there is an identity mapping via an element-wise addition [22]. An extra complicated structure was developed by the DenseNet network by connecting the entire blocks of layers to each other [25]. These networks have been fine-tuned to classify different tasks of medical image classification [19, 37, 50]. Stacking extra layers to traditional CNN will not always improve the performance, but it may be the inverse because of the gradient. Therefore, we present a convolutional neural network model based on the Directed acyclic graph (DAG) concept where we increased the width of the network. Our proposed model will help to have different levels of features at each step of the network and will be very beneficial for gradient propagation.

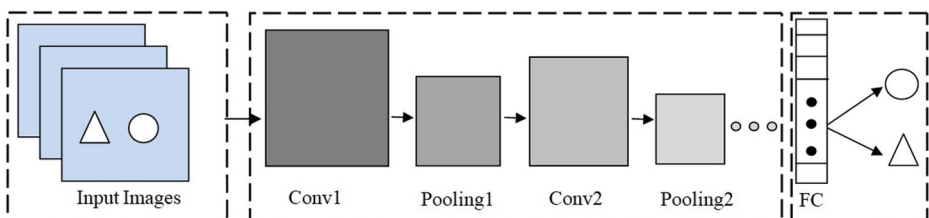


**Fig. 3** Basic structure of CNN. Conv refers to Convolution layer, Pooling refers to Pooling layer, FC refers to a fully connected layer

### 3 Methodology

This section consists of five parts: (i) our dataset with examples of diabetic foot ulcer for different patients (ii) labeling process of our dataset as normal and abnormal patched skin (iii) pre-processing of Training patches (data augmentation) (iv) fine-tuned CNNs architectures of pre-trained models (ALEXNET [30], GoogleNet [46], and VGG16 [44]) (v) our proposed model (DFU\_QUTNet) which is our own CNN architecture, DFU\_QUTNet, to enhance the DFU classification performance.

#### 3.1 Our dataset

We first collected a standardized dataset of color images of diabetic foot ulceration from different patients. Our comprehensive dataset consists of 754 images of patient's feet with DFU and healthy skin from the Nasiriyah Hospital's diabetic center which is located in the south of Iraq, with ethical approval and written consent from all relevant persons and patients. These images are captured by Samsung galaxy note 8 and iPad with different brightness and angles. All collected images have been de-identified and will be managed following related policies. The collected images were then pre-processed to create patches with standard sizes in order to be used to train and test the proposed model and pre-trained deep-learning models (GoogleNet, VGG16, and AlexNet) for DFU classification.

#### 3.2 Expert labeling of images

We first cropped the Region of Interest (ROI) with a size of  $224 \times 224$ . This region is a significant region around the ulcer which includes important tissues of both skin classes (normal and abnormal), then the specialist labeled the cropped patches. The ground-truth labels are marked by a medical specialist in two forms of normal and abnormal skin patches. We collected a total of 1609 skin patches with 542 normal and 1067 abnormal (DFU). Finally, we divided the data-set into 80% of patches for training, and 20% of patches for a testing set of images. Figure 4 shows samples of normal and abnormal patches before the cropping process. Figure 5 shows some samples from our dataset.

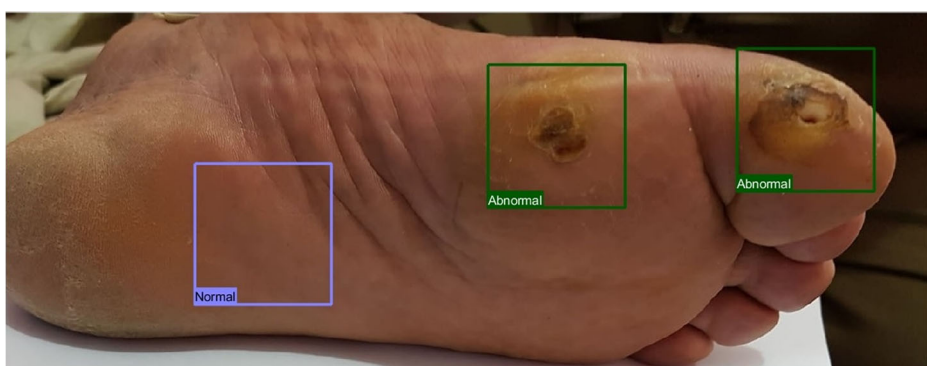


**Fig. 4** Samples of Normal and Abnormal patches



**Fig. 5** Samples of patches with labels in our dataset

### 3.3 Augmentation of training patches

CNN requires a large volume of the labeled training set to perform well. If the training set is small, the parameters of CNN will not be well tuned and results in considerable overfitting. The data augmentation process generally improves the performance of different tasks with deep learning [42, 54]. Furthermore, collecting a large amount of medical data is costly and difficult. Thus, we applied data augmentation techniques to enhance the performance of the deep learning models and avoiding the overfitting problem. We utilized a set of different image processing methods like flipping, rotation, contrast improvement, using various color models, and random scaling to complete the data augmentation. The rotation is achieved by rotating the image by an angle of 45, 90, 145, 180, 245, 280, 345. Then, two types of flipping (horizontal flip, vertical flip) with contrast and brightness of 70 and 90 degrees were applied to the original patches. The size of the patches is  $224 \times 224$ . With data augmentation techniques, these patches are duplicated 13 times for training. Figure 6 illustrates all types of image processing methods.

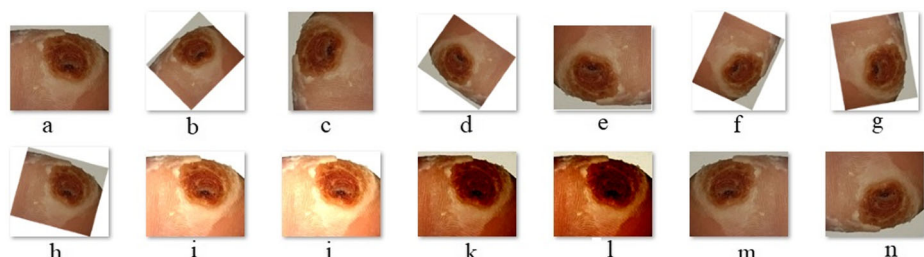


**Fig. 6** Data augmentation samples **a** original image **b** rotation of 45 **c** rotation of 90 **d** rotation of 145 **e** rotation of 180 **f** rotation of 245 **g** rotation of 280 **h** rotation of 345 **i** brightness of 70 **j** brightness of 90 **k** contrast of 70 **l** contrast of 90 **m** horizontal flip **n** vertical flip

### 3.4 Pre-trained CNN architectures

The state-of-the-art CNNs networks have been trained and tested on enormous image datasets such as ImageNet dataset which is approximately 1.28 million natural images of various domains for several classification tasks [40]. Pre-trained CNNs can be fine-tuned on medical image data sets, enabling the large networks for learning specific features of the interesting task. A large number of studies have shown that transfer learning of pre-trained models is effective and efficient for medical image classification [8, 39, 57]. Using the transfer learning approach of pre-trained models enhances performance. We have used three CNNs models which are (GoogleNet [46], AlexNet [30], and VGG16 [44]). These CNNs models have achieved high accuracy in different domains and we fine-tuned them for classification of abnormal (DFU) and normal (healthy skin) classes. Figure 7 explains the steps of our process of transfer learning:

- (1) VGGNet 16: This network was proposed by Simonyan, et al., [44] and was one of the winners of ILSVRC 2014. VGG-16 has 13 convolutional layers, 5 layers of max-pooling, and 3 fully connected layers [44]. The inputs image size is 224x224x3 with  $3 \times 3$  filters size for convolutional layers. VGGNet was used for the classification of different 1000 classes.
- (2) AlexNet: Alex Krizhevsky, et al., [30], introduced the AlexNet and won the ILSVRC 2012. It is comprised of five convolutional layers with max-pooling layers which follows some of them plus three full-connected layers with an ending of softmax layer. The first convolutional layer has 96 kernels of  $11 \times 11 \times 3$  pixel pace size for filtering the input image of size  $227 \times 227 \times 3$  while the second convolutional layer has 256 kernels of size  $5 \times 5 \times 48$  for filtering the first convolutional layer output. The pooled/normalized outputs of the second layer are connected to the third convolutional layer, which consists of 384 kernels of size  $3 \times 3 \times 256$ . The next convolutional layer (fourth) contains 384 kernels of size  $3 \times 3 \times 192$  while the last convolutional layer (the fifth) comprises 256 kernels of size  $3 \times 3 \times 192$ . Note that the last three convolutional layers (third, fourth, and fifth) do not have any normalization or pooling layers connected between each other. Finally, there are 4096 neurons in the fully-connected layers. AlexNet was used to classify 1000 classes of images. We resized the images of our dataset to fit with the input size of AlexNet.
- (3) GoogLeNet: This model was originally trained on ImageNet dataset and introduced by Szegedi, et al., [46] at 2015. It is composed of 22 convolutional layers involving nine Inception modules. Each Inception module has three dissimilar kernel sizes, which are  $1 \times 1$ ,  $3 \times 3$ , and  $5 \times 5$  for convolutional, as well as,  $3 \times 3$  for pooling. The input size is 224x224x3 of the color image. In a similar manner to the other CNNs, the training stage of the convolutional filter entries is based on the stochastic gradient descent algorithm (SGD). GoogLeNet structure helps to have multi-level feature extraction at each step.

All these pre-trained Networks have been fine-tuned to classify feet's skin into two classes namely normal and abnormal (DFU) and re-trained with our dataset. GoogLeNet, AlexNet, and VGG16 Networks are commonly employed for classification with transfer learning. GoogLeNet utilizes multi-size convolution kernels, in addition to pooling, inside a single layer. AlexNet is considered the first improvement of CNNs. Finally, the VGG network follows the common arrangement of the basic CNN, i.e., a sequence of convolutional, max pooling, activation, and full-connected layers. (Figure 6 and 7)

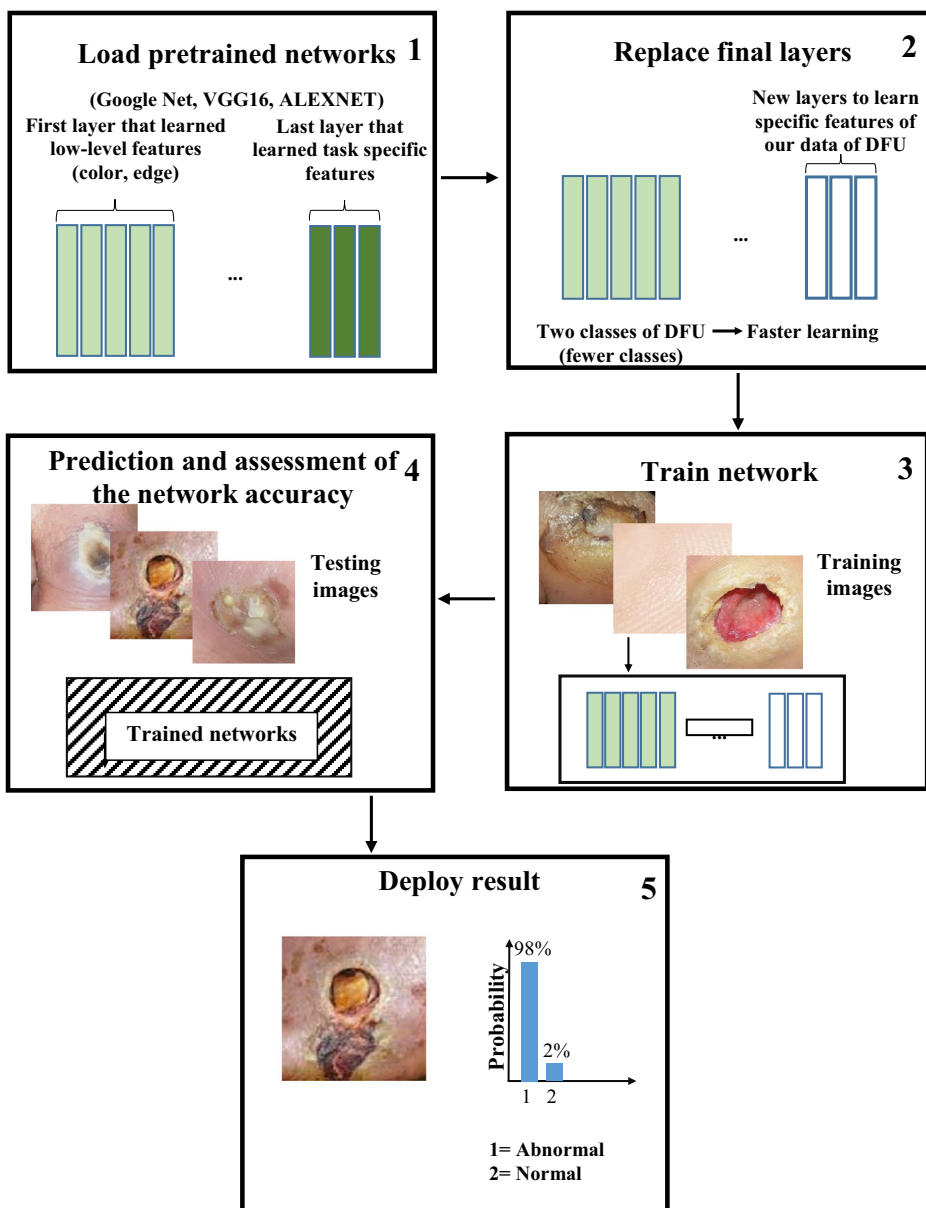


**Fig. 7** Transfer Learning Steps

### 3.5 Proposed approach-DFU\_QUTNet model

An innovative architecture of a deep convolutional neural network called DFU\_QUTNet is proposed for improving the extraction of major features related to the classification of DFU. It is designed based on the idea of the Directed Acyclic Graph (DAG) concept. Two significant issues are considered for using this type of networks. The first issue is that increasing the number of convolutional layers to a traditional CNN model in order to enhance the accuracy is

good at a limited number of layers then increasing more layers which may lead to a decline in performance (ii) A network with a small number of layers and simple structure is sufficient for some applications. However, DFU Classification requires a network with a more complicated structure to extract more features in order to discriminate between normal and abnormal classes. Our proposed model has an excellent benefit of increasing its width without significantly increasing its computing cost. This is also helping not only to boost the details possible to learn but also its accuracy. The general workflow of our classification illustrated in Fig. 8.

The DFU\_QUTNet structure consists of several layers, which are:

- (1) Input layer: it consists of three channels. Each channel has a size of  $224 \times 224$  pixels. Initially, the input image is cropped into  $224 \times 224$  patches of two classes of normal class and abnormal class as shown in Fig. 5, then these patches are used to train the DFU\_QUTNet network.
- (2) Convolutional layer: This layer convolves the outcome of the previous layer through learnable filter set [47] since the weights identify the convolution filter. All filters are slid throughout the height and width of the input volume to produce two-dimensional activation maps of the corresponding filters. Note that each filter has an identical depth as the input [18]. In addition, the output size can be manipulated through three hyper-parameters, which are the zero-padding (i.e., padding zeros around the input borders for preserving its

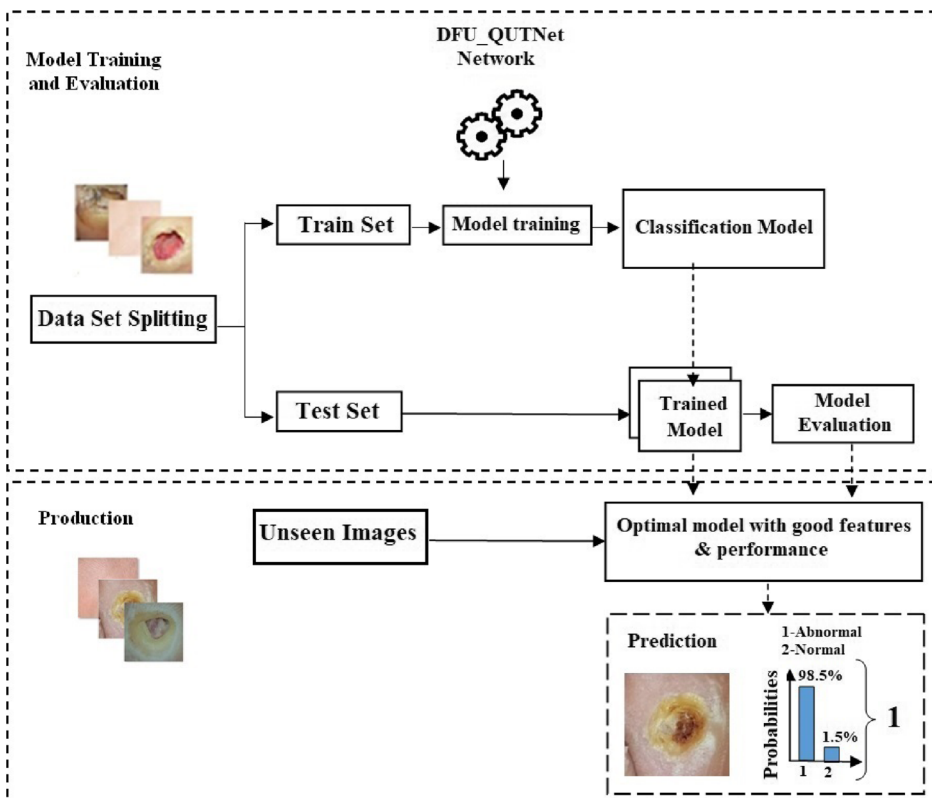


**Fig. 8** Illustration of our classification pipeline

size), stride (i.e., number of pixels that the filter skips whereas sliding across the image), and depth (i.e., it represents the number of filters operated to the input image). These filters identify structures, for example, blobs, corners, edges, etc.). In this work, the model consists of 17 convolutional layers with filters of the size of  $3 \times 3$ . Each convolutional layer is followed by layers of batch normalization and the Rectified Linear Unit.

- (3) Batch normalization (BN) layer: This layer normalizes each input channel through a mini-batch. It is utilized for speeding up CNN's training process, as well as, diminishing the sensitivity of the network initialization [26]. In this work, the batch normalization layer is placed between the convolution and ReLU layers. There are 17 batch normalization layers used in this work. The batch normalization layer mechanism starts by normalizing the activations of each channel via subtracting the mini-batch average and dividing by the standard deviation of the mini-batch. Then, the input is moved the BN layer with a learnable offset  $\beta$  and scaled it via a learnable scale factor  $\gamma$ .
- (4) Rectified Linear Unit (ReLU): This layer performs data filtering by employing the function  $\max(0, x)$  [10], where  $x$  is the input to the neuron.
- (5) Addition Layer: This layer adds inputs from two or multiple neural network layers. In order to use this layer, all inputs to this layer should have the same dimension.
- (6) Average pooling layer: This layer reduces its input size by partitioning it into rectangular pooling areas with different sizes such as  $2 \times 2$ ,  $3 \times 3$ , etc., then computing the average values of small spatial block [29]. Average pooling gives normalized feature information from a block which may contain significant as well as less significant pixel information. Even a block may contain only significant pixel information which may denote sharpening features or the block which may contain only pixels having less significant characteristics other than sharpening features. Max polling derives sharpening features which may include sharp edges, corners, and lines. In order to avoid losing some features which can be eliminated by the max pooling layer, we have applied global average pooling in the last part of the network instead of max pooling. All these features both significant and less significant are important to discriminate between classes.
- (7) Dropout Layer: This layer is used to avoid overfitting and improve performance [45]. In this layer, neurons are randomly turned on and off in each layer to prevent overfitting problem. One dropout layer has been employed in the proposed method between the fully connected layers with probability  $p = 0.5$ .
- (8) Fully Connected (FC) layer: this layer connects to all the neurons of the previous layer [29]. This layer combines the features for classifying the patches of the feet's skin into two categories: normal, and abnormal. Two FC layers are utilized in our proposed DFU\_QUTNet network.

As shown in Fig. 10, the output layer is located on the top of the last fully connected layer. In this layer, the Softmax function is employed for classification as shown in Fig. 9. The overall number of DFU\_QUTNet layers is 58 as described in Table 1. The output extracted features by DFU\_QUTNet network are utilized for training the KNN classifier (DFU\_QUTNet+KNN) and the SVM (DFU\_QUTNet+SVM) as shown in Fig. 9. Note that the KNN classifier categorizes the objects according to the nearest training samples in the space of feature. An object is categorized via its neighbor's majority. Support vector machine (SVM) is a margin-based classifier. The idea of this algorithm is to discover the optimal linear partition between two classes so that objects are in the maximum distance of that line. Different types of kernels which are linear, polynomial, and radial basis function (RBF) that can be employed in SVM.

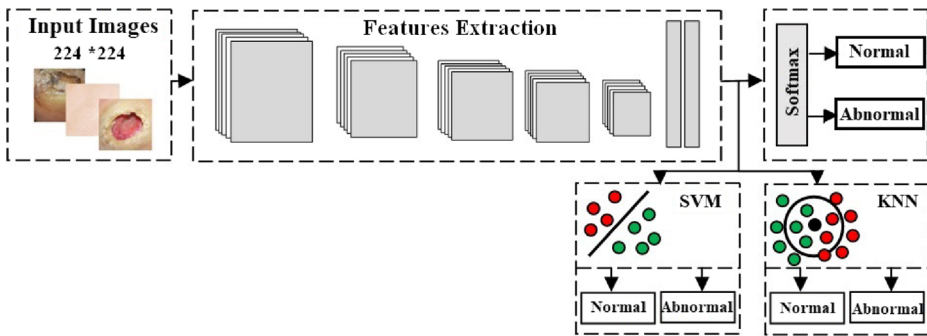


**Fig. 9** Overview of the network training steps

The DFU\_QUTNet structure is new which helps to have multi-level feature extraction at each step.

With each convolution layer, there are more discriminative features. Healthy skin has lower activations because of the lack of skin abnormalities as shown in Fig. 11. On the other hand, skin with an ulcer has higher activations because of skin abnormality as shown in Figs. 12 and

**Table 1** DFU\_QUTNet architecture, Conv refers to convolutional layers, BN refers Batch Normalization layer, ReLU refers Rectified Linear Unit, drop refers dropout layer, FC refers fully connected layer

Name of layer	Kernel size and stride	Activations
Input layer	—	224 × 224 × 3
Conv1, BN1, ReLU1	Conv1: Kernel size = 3 × 3, stride = 1	224 × 224 × 32
Conv2, BN2, ReLU2	Conv2: Kernel size = 3 × 3, stride = 2	112 × 112 × 32
Conv3, BN3	Conv3: Kernel size = 3 × 3, stride = 1	112 × 112 × 32
Conv4, BN4, ReLU4	Conv4: Kernel size = 3 × 3, stride = 2	112 × 112 × 32
Conv5, BN5	Conv5: Kernel size = 3 × 3, stride = 1	112 × 112 × 32
Add1	Addition of two inputs	112 × 112 × 32
ReLU3	Activation Function	112 × 112 × 32
Conv6, BN6, ReLU6	Conv6: Kernel size = 3 × 3, stride = 2	56 × 56 × 64
Conv7, BN7	Conv7: Kernel size = 3 × 3, stride = 1	56 × 56 × 64
Conv8, BN8, ReLU8	Conv8: Kernel size = 3 × 3, stride = 2	56 × 56 × 64
Conv9, BN9	Conv9: Kernel size = 3 × 3, stride = 1	56 × 56 × 64
Add2	Addition of two inputs	56 × 56 × 64
ReLU7	Activation Function	56 × 56 × 64
Conv10, BN10, ReLU10	Conv10: Kernel size = 3 × 3, stride = 2	28 × 28 × 128
Conv11, BN11	Conv11: Kernel size = 3 × 3, stride = 1	28 × 28 × 128
Conv12, BN12, ReLU12	Conv12: Kernel size = 3 × 3, stride = 2	28 × 28 × 128
Conv13, BN13	Conv13: Kernel size = 3 × 3, stride = 1	28 × 28 × 128
Add3	Addition of two inputs	28 × 28 × 128
ReLU11	Activation Function	28 × 28 × 128
Conv14, BN14, ReLU14	Conv14: Kernel size = 3 × 3, stride = 2	14 × 14 × 256
Conv15, BN15	Conv15: Kernel size = 3 × 3, stride = 1	14 × 14 × 256
Conv16, BN16, ReLU16	Conv16: Kernel size = 3 × 3, stride = 2	14 × 14 × 256
Conv17, BN17	Conv17: Kernel size = 3 × 3, stride = 1	14 × 14 × 256
Add4	Addition of two inputs	14 × 14 × 256
ReLU15	Activation Function	14 × 14 × 256
Average Pooling Layer	Kernel size = 8 × 8, stride = 1,	7 × 7 × 256
FC1	100 fully connected	1 × 1 × 100
Drop1	Dropout layer with learning rate:0.5	1 × 1 × 100
FC2	2 fully connected	1 × 1 × 2
Softmax layer	0 = Normal, 1 = Abnormal (DFU)	1 × 1 × 2

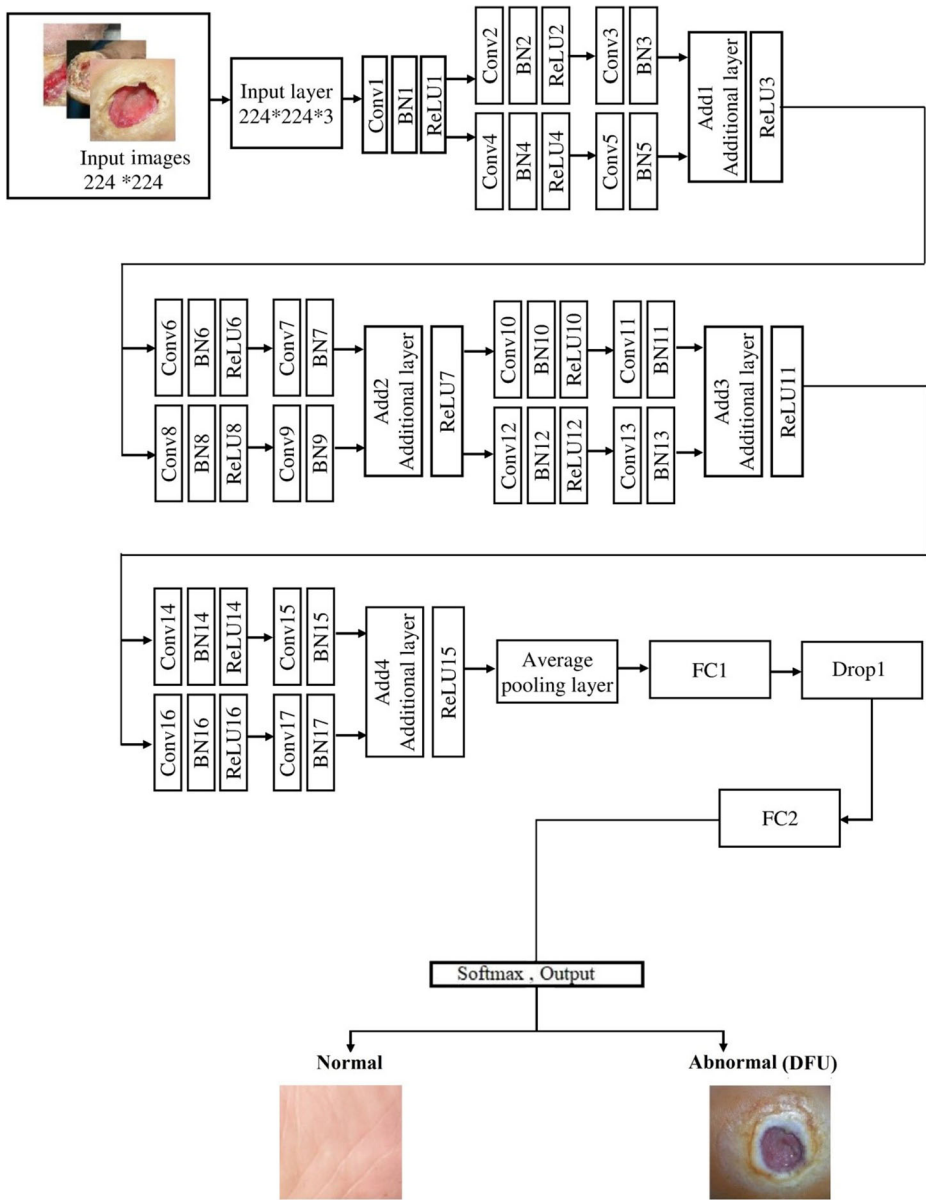


**Fig. 10** DFU\_QUTNet architecture

13. Our model and pre-trained models have been trained on our dataset for 100 epochs until the learning stopped.

By using same training parameters that were used to train our network and pre-trained networks (GoogleNet [46], AlexNet [30], and VGG-16 [44]), we trained DFUNet described in [19]. DFUNet is the state-of-the-art network in the task of DFU classification. We wrote the code for the DFUNet network structure from scratch. The permission to use the DFUNet network has been approved by the author of the paper.

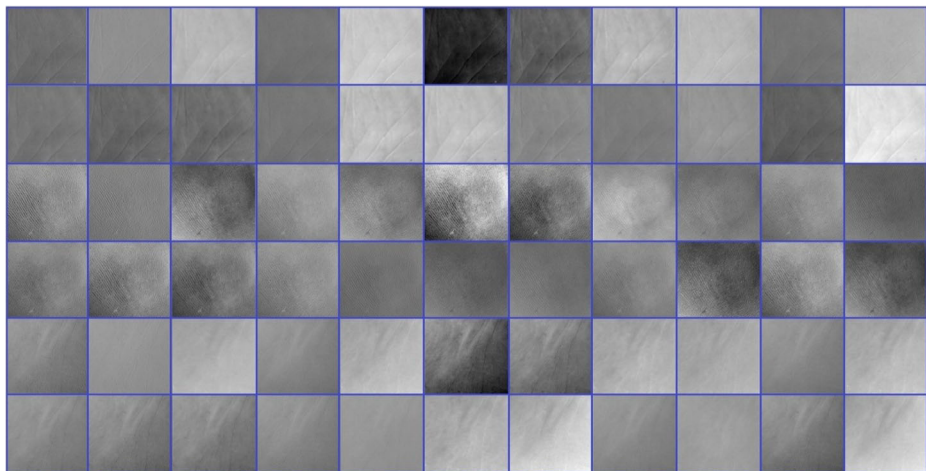


**Fig. 11** Some learnable filters from the first convolutional layer for normal skin

Lastly, the processor properties used in this experiment are Intel (R) Core TM i7-5829K CPU @ 3.30 GHz, the RAM was 16 GB and the GPU was 8 GB. Matlab2018 was used to implement the experiments.

## 4 Experimental results

As mentioned above, we divided our dataset to the training phase and test phase. We implemented several experiments on our challenging dataset to evaluate the classification performance of our network and fine-tuned networks that we have used. Our model and fine-tuned models effectiveness are measured by a F1-score. F1- scores convey the balance between the precision (P) and the recall(R) (Eq. 3). Recall and Precision are

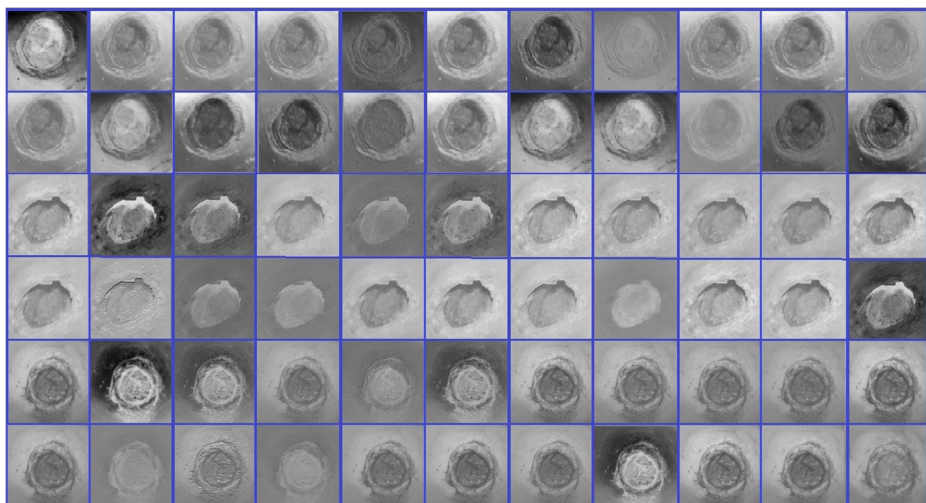


**Fig. 12** Some learnable filters from the first convolutional layer for abnormal skin

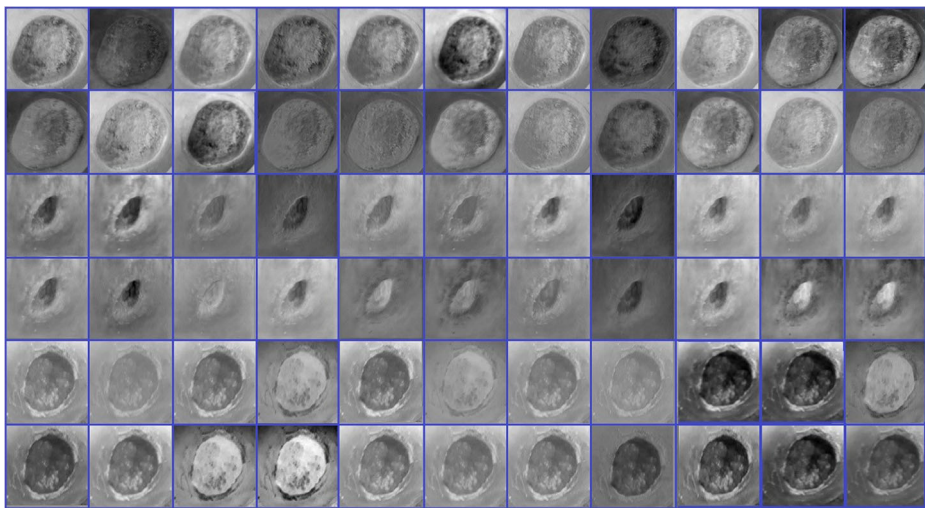


**Fig. 13** Some learnable filters from the second convolutional layer for abnormal skin

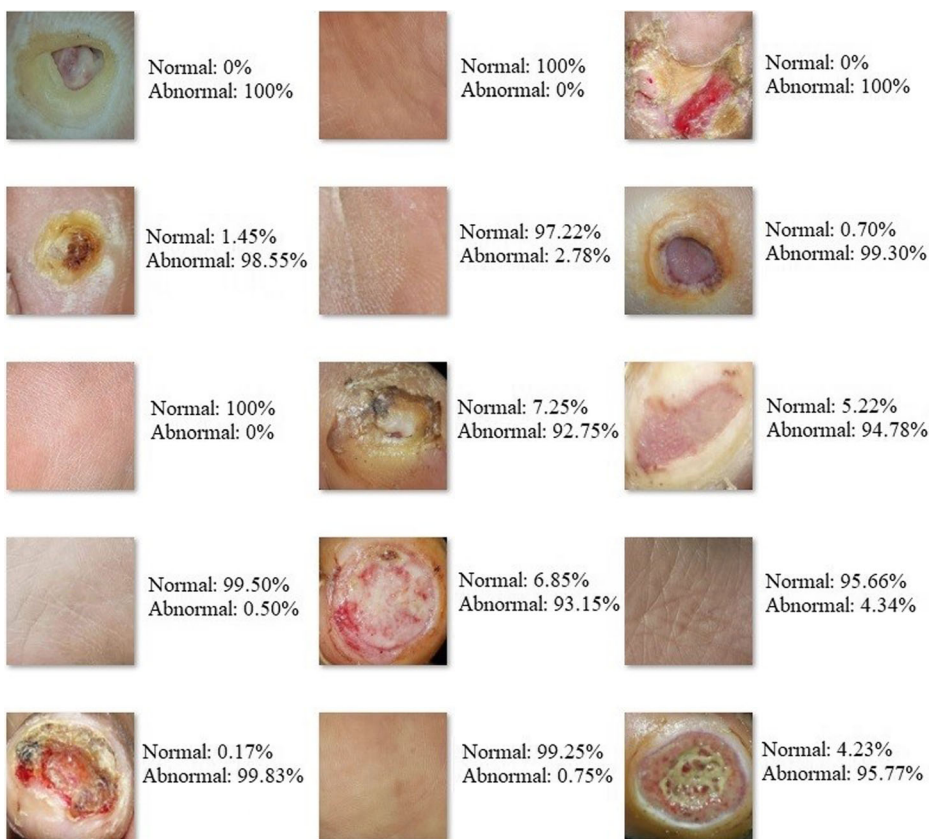


**Fig. 14** Prediction of some test patches for both abnormal and normal classes

**Table 2** DFU\_QUTNet with different classifiers

classifier	Precision (%)	Recall (%)	F1-Score (%)
DFU_QUTNet	94.2	92.6	93.4
DFU_QUTNet+KNN	93.8	92.7	93.2
DFU_QUTNet+SVM	95.4	93.6	94.5

two basic parameters for the assessment of the proposed approach, which are calculated (Eq. 1 and 2):

$$Precision = \frac{TP}{TP + FP} \quad (1)$$

$$Recall = \frac{TP}{TP + FN} \quad (2)$$

$$F1-Score = 2 \times \frac{Precision \times Recall}{Precision + Recall} \quad (3)$$

Where TP (True Positive) is the number of images that the Network correctly identifies as relevant. TN (True Negative) is the number of images the Network correctly identifies as irrelevant. FP (False Positive) is the number of images the Network falsely identifies as relevant. FN (False Negative) is the number of relevant images that the Network fails to identify.

Table 2 reported the measurements of our proposed DFU\_QUTNet with different classifiers. DFU\_QUTNet with SVM has the highest measures in precision, recall, and F1-score with 95.4%, 93.6%, and 94.5% respectively. DFU\_QUTNet with KNN achieved the lowest scores of 93.8% for precision and 93.2% for the F1-score while the recall score is 92.7% which is higher than the recall score of DFU\_QUTNet using softmax. DFU\_QUTNet using softmax achieved 94.2%, 92.6%, 93.4% for precision, recall, and F1-score respectively. Prediction of some test patches with DFU\_QUTNet is shown in Fig. 14.

For the sake of comparison, we have trained and tested three state-of-the-art networks on our dataset and compared them to our proposed DFU\_QUTNet as reported in Table 3. AlexNet achieved the lowest scores with 91.1% for precision, 87.2% for recall and 89.1 for F1-score. Our proposed DFU\_QUTNet with SVM has the highest evaluation performance in the recall, with a score of 93.6% and F1-score with 94.5%, whereas, GoogleNet has the highest score in precision with 95.6%. We also compared our proposed model to DFUNet as reported in Table 4. Our proposed model outperformed DFUNet network in all evaluation

**Table 3** Comparison of DFU\_QUTNet with state-of-the-art Networks for classification

Network	Precision (%)	Recall (%)	F1-Score (%)
AlexNet [30]	91.1	87.2	89.1
VGG16 [44]	92.3	89.7	90.9
GoogleNet [46]	95.6	90.5	92.9
Proposed DFU_QUTNet+SVM	95.4	93.6	94.5

**Table 4** Competitive results of DFU\_QUTNet+SVM classification with DFUNet Network

Network	Precision (%)	Recall (%)	F1-Score (%)
DFUNet [19]	93.8	92.5	93.1
Proposed DFU_QUTNet+SVM	95.4	93.6	94.5

measurements. DFU\_QUTNet without any other classifiers is still superior to the state-of-the-art Networks.

Due to the type of structure that our model is designed for, it has the ability to find more subtle changes and discriminate between two classes of normal and abnormal. It also handled many hard cases such as small sizes of DFU, skin wrinkles and patches with a toe.

## 5 Conclusions and future work

A novel CNN model, DFU\_QUTNet, for automated classification of DFU into two classes: normal (healthy skin) and abnormal (DFU) is proposed in this paper. The architecture of DFU\_QUTNet is designed based on the idea of increasing the width. It has the great advantage of boosting its width without drastically boosting its computational cost. We collected a large dataset of total 754-ft of patients with DFU and healthy skin. The dataset has been labeled into two classes normal and abnormal by an expert. Our proposed DFU\_QUTNet model has been trained on our dataset. Features extracted by our proposed model were used to train the SVM and KNN classifiers. We compared the performance of our network with state-of-the-art CNN networks (GoogleNet, AlexNet, and VGG16). These CNN networks were trained on a large dataset of the ImageNet dataset. After the fine-tuning process, we re-trained them on our dataset with transferring the previous learning of these deep learning networks. The comparison shows that the proposed framework, DFU\_QUTNet with SVM, has higher F1-Score of 94.5% than the state-of-the-practice methods. The proposed DFU\_QUTNet network is not limited to the DFU classification task only. For instance, we aim to fine-tune DFU\_QUTNet model to classify seven classes of skin cancer. Since DFU\_QUTNet network extracted significant features to differentiate between classes of normal and abnormal, we also aim to employ DFU\_QUTNet network in the task of DFU detection.

## Compliance with ethical standards

**Conflict of interest** The authors declare that they have no conflict of interest.

**Ethical approval** This article does not contain any studies with human participants or animals performed by any of the authors.

## References

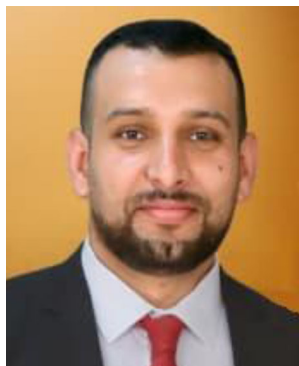
1. Al-Zubaidi L (2016) Deep learning based nuclei detection for quantitative histopathology image analysis (Doctoral dissertation, University of Missouri–Columbia)
2. Alzubaidi L., Al-Shamma O., FadhelM.A., Farhan L., Zhang J. (2020) Classification of Red Blood Cells in Sickle Cell Anemia Using Deep Convolutionalrk. In: Abraham A., Cherukuri A., Melin P., Gandhi N. (eds)

- Intelligent Systems Design and Applications. ISDA 2018 2018. Advances in IntelligentSystems and Computing, vol 940. Springer, Cham
- 3. Armstrong DG, Lavery LA, Harkless LB (1998) Validation of a diabetic wound classification system: the contribution of depth, infection, and ischemia to risk of amputation. *Diabetes Care* 21(5):855–859
  - 4. Bakator M, Radosav D (2018) Deep learning and medical diagnosis: a review of literature. *Multimodal Technologies and Interaction* 2(3):47
  - 5. Boulton AJ, Vileikyte L, Ragnarsson-Tennvall G, Apelqvist J (2005) The global burden of diabetic foot disease. *Lancet* 366(9498):1719–1724
  - 6. Bowling FL, King L, Paterson JA, Hu J, Lipsky BA, Matthews DR, Boulton AJ (2011) Remote assessment of diabetic foot ulcers 11 using a novel wound imaging system. *Wound Repair Regen* 19(1):25–30
  - 7. Cavanagh P, Attinger C, Abbas Z, Bal A, Rojas N, Xu Z-R (2012) Cost of treating diabetic foot ulcers in five different countries. *Diabetes / Metabolism Research and Reviews* 28(S1):107–111
  - 8. Cheng PM, Malhi HS (2017) Transfer learning with convolutional neural networks for classification of abdominal ultrasound images. *J Digit Imaging*:234–243
  - 9. Clemensen J, Larsen SB, Kirkevold M, Ejskjaer N (2008) Treatment of diabetic foot ulcers in the home: video consultations as an alternative to outpatient hospital care. *Int J Telemed Appl* 2008:1
  - 10. Dahl GE, Sainath TN, Hinton GE (2013) Improving deep neural networks for LVCSR using rectified linear units and dropout. In: 2013 IEEE international conference on acoustics, speech and signal processing (pp. 8609–8613). IEEE
  - 11. Deng Y, Manjunath BS (2001) Unsupervised segmentation of colortexture regions in images and video. *IEEE Trans Pattern Anal Mach Intell* 23(8):800–810
  - 12. El-Gayar O, Timsina P, Nawar N, Eid W (2013) A systematic review of it for diabetes self-management: are we there yet? *Int J Med Inform* 82(8):637–652
  - 13. Foltynski P, Wojcicki JM, Ladyzynski P, Migalska-Musial K, Rosinski G, Krzymien J, Karmelat W (2011) Monitoring of diabetic foot syndrome treatment: some new perspectives. *Artif Organs* 35(2):176–182
  - 14. Fraiwan L, AlKhodari M, Ninan J, Mustafa B, Saleh A, Ghazal M (2017) Diabetic foot ulcer mobile detection system using smart phone thermal camera: a feasibility study. *Biomed Eng Online* 16(1):117
  - 15. Fraiwan L, Ninan J, Al-Khodari M (2018) Mobile application for ulcer detection. *The Open Biomedical Engineering Journal* 12:16
  - 16. Franc S, Daoudi A, Mounier S, Bou cherie B, Laroye H, Peschard C, Dardari D, Juy O, Requeda E, Canipel L et al (2011) Telemedicine: what more is needed for its integration in everyday life? *Diabetes Metab* 37:S71–S77
  - 17. Geng L, Yan T, Xiao Z, Xi J, Li Y (2017) Hatching eggs classification based on deep learning. *Multimed Tools Appl*:1–12
  - 18. Gibiansky A (2018) Convolutional neural networks. <http://andrew.gibiansky.com/blog/machine-learning/> Accessed 26 December 2018
  - 19. Goyal M, Reeves ND, Davison AK, Rajbhandari S, Spragg J, Yap MH (2018) Dfunet: convolutional neural networks for diabetic foot ulcer classification. *IEEE Transactions on Emerging Topics in Computational Intelligence*
  - 20. Goyal M, Yap MH, Reeves ND, Rajbhandari S, Spragg J (2017) Fully convolutional networks for diabetic foot ulcer segmentation. In: 2017 IEEE international conference on systems, man, and cybernetics (SMC) (pp. 618–623). IEEE
  - 21. Hazenberg CE, van Netten JJ, van Baal SG, Bus SA, Bus S (2014) Assessment of signs of foot infection in diabetes patients using photographic foot imaging and infrared thermography. *Diabetes Technol Ther* 16(6):370–377
  - 22. He K, Zhang X, Ren S, Sun J (2016) Deep residual learning for image recognition. In: Proceedings of the IEEE conference on computer vision and pattern recognition (pp. 770–778)
  - 23. Hermans MH (2010) Wounds and ulcers: back to the old nomenclature. *Wounds* 22(11):289–293
  - 24. Huang J, Li B, Zhu J, Chen J (2017) Age classification with deep learning face representation. *Multimed Tools Appl*:20231–20247
  - 25. Huang G, Liu Z, Van Der Maaten L, Weinberger KQ (2017) Densely connected convolutional networks. In: Proceedings of the IEEE conference on computer vision and pattern recognition (pp. 4700–4708)
  - 26. Ioffe S, Szegedy C (2015) Batch normalization: accelerating deep network training by reducing internal covariate shift. arXiv preprint arXiv:1502.03167
  - 27. Jegede O, Ferens K, Griffith B, Podaima B (2015) A smart shoe to prevent and manage diabetic foot diseases. In: Int'l Conf. Health informatics and medical systems (pp. 47–54)
  - 28. Kolesnik M, Fexa A (2006) How robust is the SVM wound segmentation? In: Proceedings of the 7th Nordic Signal Processing Symposium-NORSIG 2006 (pp. 50–53). IEEE.
  - 29. Koushik J (2016) Understanding convolutional neural networks. arXiv preprint arXiv:1605.09081
  - 30. Krizhevsky A, Sutskever I, Hinton GE (2012) Imagenet classification with deep convolutional neural networks. In: Advances in neural information processing systems (pp. 1097–1105)

31. Lavery LA, Armstrong DG, Harkless LB (1996) Classification of diabetic foot wounds. *J Foot Ankle Surg* 35(6):528–531
32. LeCun Y, Bengio Y, Hinton G (2015) Deep learning. *Nature* 521(7553):436
33. Litjens G, Kooi T, Bejnordi BE, Setio AAA, Ciompi F, Ghafoorian M, Sánchez CI (2017) A survey on deep learning in medical image analysis. *Med Image Anal* 42:60–88
34. Liu C, van Netten JJ, van Baal JG, Bus SA, van der Heijden F (2015) Automatic detection of diabetic foot complications with infrared thermography by asymmetric analysis. *J Biomed Opt* 20(2):26003
35. Lu H, Li Y, Uemura T, Ge Z, Xu X, He L, Kim H (2018) FDCNet: filtering deep convolutional network for marine organism classification. *Multimed Tools Appl* 77(17):21847–21860
36. Nair LR (2019) RetoNet: a deep learning architecture for automated retinal ailment detection. *Multimed Tools Appl*:1–10
37. Nawaz W, Ahmed S, Tahir A, Khan HA (2018) Classification of breast Cancer histology images using ALEXNET. In: International conference image analysis and recognition. Springer, Cham, pp 869–876
38. Ram Avrahami MD, Jonathan Rosenblum DPM, Michael Gazes DPM, Sean Rosenblum DPM (2015) The effect of combined ultrasound and electric field stimulation on wound healing in chronic ulcerations. *Wounds* 27(7):199–208
39. Ravishankar H, Sudhakar P, Venkataramani R, Thiruvenkadam S, Annangi P, Babu N, Vaidya V (2016) Understanding the mechanisms of deep transfer learning for medical images. In: Deep learning and data labeling for medical applications. Springer, Cham, pp 188–196
40. Russakovsky O, Deng J, Su H, Krause J, Satheesh S, Ma S, Berg AC (2015) Imagenet large scale visual recognition challenge. *Int J Comput Vis* 115(3):211–252
41. Sainath TN, Mohamed AR, Kingsbury B, Ramabhadran B (2013) Deep convolutional neural networks for LVCSR. In: 2013 IEEE international conference on acoustics, speech and signal processing (pp. 8614–8618). IEEE
42. Salamon J, Bello JP (2017) Deep convolutional neural networks and data augmentation for environmental sound classification. *IEEE Signal Processing Letters* 24(3):279–283
43. Sert M, Boyaci E (2019) Sketch recognition using transfer learning. *Multimedia Tools and Applications*. <https://doi.org/10.1007/s11042-018-7067-1>
44. Simonyan K, Zisserman A (2014) Very deep convolutional networks for large-scale image recognition. *arXiv preprint arXiv:1409.1556*
45. Srivastava N, Hinton G, Krizhevsky A, Sutskever I, Salakhutdinov R (2014) Dropout: a simple way to prevent neural networks from overfitting. *The Journal of Machine Learning Research* 15(1):1929–1958
46. Szegedy C, Liu W, Jia Y, Sermanet P, Reed S, Anguelov D, Rabinovich A (2015) Going deeper with convolutions. In: Proceedings of the IEEE conference on computer vision and pattern recognition (pp. 1–9)
47. Vedaldi A, Lenc K (2015) Matconvnet: convolutional neural networks for matlab. In: Proceedings of the 23rd ACM international conference on multimedia (pp. 689–692). ACM
48. Veredas FJ, Luque-Baena RM, Martín-Santos FJ, Morilla-Herrera JC, Morente L (2015) Wound image evaluation with machine learning. *Neurocomputing* 164:1–11
49. Veredas F, Mesa H, Morente L (2010) Binary tissue classification on wound images with neural networks and bayesian classifiers. *IEEE Trans Med Imaging* 29(2):410–427
50. Vesal S, Ravikumar N, Davari A, Ellmann S, Maier A (2018) Classification of breast cancer histology images using transfer learning. In: International conference image analysis and recognition. Springer, Cham, pp 812–819
51. Vijayalakshmi A, Rajesh Kanna B (2019) Deep learning approach to detect malaria from microscopic images. *Multimedia Tools Application*:1–21
52. Vilcahuaman L, Harba R, Canals R, Zequera M, Wilches C, Arista M, Torres L, Arbanil H (2015) Automatic analysis of plantar foot thermal images in at-risk type II diabetes by using an infrared camera. *IFMBE Proc* 51:228–231
53. Wang L, Pedersen PC, Agu E, Strong DM, Tulu B (2017) Area determination of diabetic foot ulcer images using a cascaded two-stage SVM-based classification. *IEEE Trans Biomed Eng* 64(9):2098–2109
54. Wang J, Perez L (2017) The effectiveness of data augmentation in image classification using deep learning. *Convolutional Neural Networks Vis. Recognit.*
55. Wild S, Roglic G, Green A, Sicree R, King H (2004) Global prevalence of diabetes estimates for the year 2000 and projections for 2030. *Diabetes Care* 27(5):1047–1053
56. World Health Organization (2016) Global report on diabetes. <http://www.who.int/diabetes/global-report/en> Accessed 6 Feb. 2009
57. Yu Y, Lin H, Meng J, Wei X, Guo H, Zhao Z (2017) Deep transfer learning for modality classification of medical images. *Information* 8(3):91
58. Zeiler MD, Fergus R (2014) Visualizing and understanding convolutional networks. In: European conference on computer vision. Springer, pp 818–833

59. Zhang G, Hsu C-HR, Lai H, Zheng X (2018) Deep learning based feature representation for automated skin histopathological image annotation. *Multimed Tools Appl* 77(8):9849–9869
60. Zhu X, Li Z, Zhang X-Y, Li P, Xue Z, Wang L (2018) Deep convolutional representations and kernel extreme learning machines for image classification. *Multimed Tools Appl*:1–20

**Publisher's note** Springer Nature remains neutral with regard to jurisdictional claims in published maps and institutional affiliations.



**Laith Alzubaidi** is currently a Ph.D. student at Queensland University of Technology / Faculty of Science and Engineering, Brisbane, Australia. He received his Master's degree in computer science from the university of Missouri/USA in 2016. In his Master's thesis he worked on the detection and classification of breast cancer with deep learning. Laith broad research area falls in artificial intelligence and Internet of Things (IoT). In particular, his research interests include Deep Learning for medical applications and IoT.



**Mohammed A. Fadhel** received the Master degree from University of technology/Computer engineering /Iraq in 2015. He is currently assistant lecturer in the Business Informatics Collage, in University of Information Technology and Communications /Baghdad/ Iraq. His research interests include embedded system, image and acoustic processing, artificial intelligence, deep learning, and medical imaging analysis.



**Sameer R. Oleiwi** received the BSc, Sciences of Nursing, University of Baghdad, Iraq, 1989, MSc, Adult Nursing, University of Baghdad, Iraq, 2006 and PhD, Adult Nursing, University of Baghdad, Iraq, 2012 and California School of health and sciences. He is currently a lecturer in the University of Muthanna/Collage of nursing / Muthanna / Iraq. His research interests include Medical surgical nursing, nursing education, Health education, nursing research. He supervised up to 6 theses for PhD and MSc students. In his PhD dissertation, he worked on Diabetic Foot Ulcer (DFU) treatment.



**Omran Al-Shamma** received the BSc, Control and Systems Eng., University of Technology, Iraq, 1980, MSc, Computer Engineering, University of Technology, Iraq, 1984 and PhD, Computer Engineering, University of Hertfordshire, UK, 2013. He is currently a senior lecturer in the University of Information Technology and Communications /Baghdad/ Iraq. His research interests include interactive computer design software, embedded system, image and acoustic processing, artificial intelligence, Deep learning, and medical imaging analysis.



**Jinglan Zhang** is a senior lecturer in Queensland University of Technology. She received her PhD in information technology in 2003 from Queensland University of Technology. Dr. Jinglan Zhang's broad research area falls in artificial intelligence and information systems. In particular, her research interests include visual and acoustic information (graphics, images, and sound) processing and retrieval, big data analysis and visualization, computer human interaction, e-science, software engineering, and mobile and web applications.

## Affiliations

**Laith Alzubaidi<sup>1,2</sup> • Mohammed A. Fadhel<sup>2</sup> • Sameer R. Olewi<sup>3</sup> • Omran Al-Shamma<sup>2</sup> • Jinglan Zhang<sup>1</sup>**

<sup>1</sup> Faculty of Science & Engineering, Queensland University of Technology, Brisbane, Australia

<sup>2</sup> University of Information Technology and Communications, Baghdad, Iraq

<sup>3</sup> Muthanna University, Muthanna, Iraq

Received 23 August 2023, accepted 2 September 2023, date of publication 6 September 2023,  
date of current version 13 September 2023.

Digital Object Identifier 10.1109/ACCESS.2023.3312531



## RESEARCH ARTICLE

# DFU-SIAM a Novel Diabetic Foot Ulcer Classification With Deep Learning

MOHAMMUD SHAAD ALLY TOOFANEE<sup>ID1,2</sup>, SABEENA DOWLUT<sup>ID2</sup>,  
MOHAMED HAMROUN<sup>ID1,4</sup>, KARIM TAMINE<sup>1</sup>, VINCENT PETIT<sup>ID2</sup>, ANH KIET DUONG<sup>3</sup>,  
AND DAMIEN SAUVERON<sup>ID1</sup>

<sup>1</sup>Department of Computer Science, XLIM, UMR CNRS 7252, University of Limoges, 87060 Limoges, France

<sup>2</sup>Applied Computer Science Department, Université des Mascareignes, Roches Brunes, Beau Bassin-Rose Hill, Mauritius

<sup>3</sup>Faculty of Science and Technology, University of Limoges, 87060 Limoges, France

<sup>4</sup>3iL Ingénieurs, 87015 Limoges, France

Corresponding author: Mohammad Shaad Ally Toofanee (stoofanee@udm.ac.mu)

This work was supported by the XLIM Laboratory of University of Limoges.

**ABSTRACT** Diabetes affects roughly 537 million people in the world, and it is predicted to reach 783 million by 2045. Diabetic Foot Ulcer (DFU) is a major issue with diabetes that may lead to lower limb amputation. The rapid evolution of DFU demands immediate intervention to prevent the terrible consequences of amputation and related complications. This research introduces a novel approach utilizing deep neural networks and machine learning for the accurate classification of diabetic foot ulcer (DFU) images. The proposed method harnesses the cutting-edge capabilities of Convolutional Neural Networks (CNN) and Vision Image Transformers (ViT) within a Siamese Neural Network (SNN) Architecture. By employing similarity learning, the model efficiently categorizes DFU images into four distinct classes: None, Infection, Ischemia, or Both. The training process involves the use of the DFU2021 dataset, with all ethical clearances duly obtained. Notably, the model exhibits remarkable performance on both the validation and test data, indicating a significant breakthrough in the field of DFU disease image classification. The potential of this innovative model extends beyond classification; it holds promise as an integral component of a comprehensive detection tool and longitudinal treatment protocol validation for DFU disease.

**INDEX TERMS** DFU, deep learning, CNN, vision transformers, Siamese network, similarity detection, DFU classification.

## I. INTRODUCTION

Diabetes is one of the major diseases that affect roughly 537 million people, with a prediction to reach 783 million by 2045 [1]. Diabetic Foot Ulcer (DFU) is a prevalent complication among individuals with diabetes mellitus. In a recent research, it was found that mortality from DFU was high, with global mortality from diabetic foot ulcers standing at approximate 50% within 5 years [2]. This condition increases the risk of lower limb amputations in individuals with diabetes. When treating DFUs, promptness and assertiveness can make a significant difference in slowing the wound's course and preventing the need for an amputation [3].

Healing DFU can become a challenging and daunting task. Hence, to reduce the risk of DFU, certain preventive

The associate editor coordinating the review of this manuscript and approving it for publication was Yudong Zhang <sup>ID</sup>.

measures can be taken, such as 1) identification of the feet at risk 2) regular examinations. 3) raising awareness in the general public 4) treating risk factors. While it is important to design an early detection intervention, the integration of technology can also be explored to increase the accuracy of the results and the ease of examination procedures [4]. According to the Foot Care Clinic of APSA International, located in Mauritius, approximately 500 individuals undergo amputations each year as a result of type 2 diabetes, with an estimated 88% of these cases being preventable [5]. Annually, it is estimated that 67% of amputations in the United States and 90% of amputations in the United Kingdom are attributed to diabetes [6].

## A. ARTIFICIAL INTELLIGENCE (AI) AND HEALTHCARE

Medical imaging data is one of the best sources of information about patients and helps to see inside the person's

body non-invasively or as least invasively as possible. In the current context of soaring demand for medical imaging and the prevailing challenge of staffing shortages in hospitals, the integration of AI tools holds promise as a potential solution [7]. The integration of digital imaging and AI has had a significant impact on the medical field. The use of AI algorithms has enhanced the accuracy and efficiency of these diagnoses. Research has shown that AI can accurately diagnose conditions such as retinal disorders [8], diabetic retinopathy [9], breast cancer [10], and skin cancer [11] by relying on digital images.

### B. AI, HEALTHCARE AND ETHICS

While the use of AI in the field of healthcare is extremely promising and is progressing at a sustained pace, there are major challenges in terms of ethics and privacy [12]. Collecting healthcare data in a particular country that is stored on a remote server in another country with a different jurisdiction is one of the challenges of AI [13]. The governance of these health data, ensuring thoughtful aggregation and appropriate access to fuel innovation and improve patient outcomes and healthcare system efficiency while protecting the privacy and security of data subjects [14]. However, the World Health Organisation (WHO) acknowledged the potential of AI to enhance diagnosis, treatment, health research, and drug development, as well as support governments in carrying out public health functions such as surveillance and outbreak response, but also proposed strict guidelines that need to be followed [15] among which ethical guidelines are as follows:

- Avoid harming others.
- Promote the well-being of others
- Ensure that all persons are treated fairly.
- Deal with people in ways that respect their interests.

The above ethical considerations were taken into consideration while working on this research.

### C. AIMS AND OBJECTIVES

DFUs are currently assessed by diabetes physicians and podiatrists in foot clinics and hospitals. There have been several research projects based on the application of AI and deep learning for DFU classification and even detection. The work is inspired by the successful implementation of AI in the medical field and takes advantage of the DFU Grand Challenge [16] which provides a labeled dataset with 4 classes that can be used by AI researchers to experiment and test the best model for classifications of DFU.

The DFU2021 Challenge dataset was obtained from the organisers of the DFU challenge. The objective was to experiment with Convolutional Neural Network coupled with latest vision-based transformers model which has achieved state-of-the-art performance on a number of computer vision benchmark including ImageNet classification and COCO object detection and instance segmentation [17]. This paper implements the use of Siamese Neural Network coupled with the K-nearest neighbors algorithm to implement the

classification of images of DFU disease. The Siamese Neural Network architecture was first introduced in the early 1990s for the purpose of solving signature verification as an image matching problem [18].

Our research primarily aims to introduce an improved DFU classification model that outperforms the latest advancements in this field. This marks the initial phase in creating a tool for monitoring Diabetic Foot Ulcer treatment protocols initiated by medical practitioners. For successful integration into such protocols, the model's DFU classification must be accurate. The subsequent step involves using this model as an additional resource for healthcare professionals to validate their treatment approaches. However, we anticipate various challenges before reaching this milestone. These include addressing the limited data accessible to AI researchers and handling the sensitivity of healthcare data, particularly when involving images of body parts.

The structure of the rest of this paper is organized as follows: We first review some important concepts relating in machine learning in Section II. We then expose the related works III on machine learning models used in the medical field, and more specifically, machine learning applied to DFU classification. Section IV gives a detailed presentation of the proposed architecture of the DFU-SIAM. We then give a comprehensive presentation of experimental results and discussions in Section V. We finally conclude and explore further research opportunities in Section VI.

## II. BACKGROUND AND PRELIMINARIES

Prior to taking a deep dive into the use of AI with regard to Diabetic Foot Ulcer we present some important background information on the techniques we will be using in this research.

### A. ARTIFICIAL NEURAL NETWORKS (ANN)

ANN is a supervised learning algorithm that is inspired by the structure and functioning of the human brain [19]. It consists of interconnected nodes, as shown in Figure 1, which are also known as neurons, organized into layers. Each neuron processes input data and passes its output to the next layer, ultimately producing an output. ANNs are widely used for tasks such as pattern recognition, classification, and regression.

ANN consists of numerous neurons, also known as perceptrons, which are organised into layers. The layers communicate through the network's parameters, which are shown as arrows. These parameters encompass weights and biases. The weights control the importance of each input, while biases determine how easily a neuron fires or activates. The outcome generated during forward propagation, known as the predicted value, is matched against the corresponding actual value (ground truth) to evaluate the neural network's effectiveness. This evaluation is facilitated by using the loss function. The loss function is also referred to as the cost function. The aim is to minimize the loss. In the first iteration, the predicted values are far from the ground truth values,

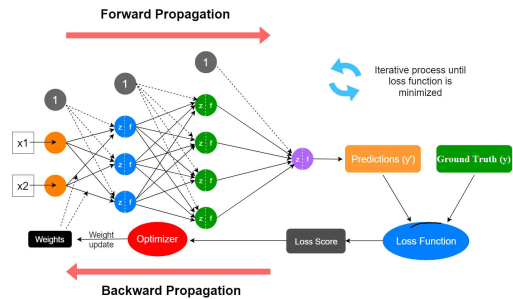


**FIGURE 1.** Graphical representation of an Artificial Neural Network showing the whole learning process, which consists of mainly three steps, which are: 1. Forward propagation; 2. Calculation of the loss function; and 3. Backward propagation [20].

and the loss will be high as weights and biases were initially assigned arbitrary values. The latter need to be updated in order to minimize the loss function, and this process of updating network parameters is called parameter learning or optimization which is done using an optimization algorithm (optimizer) that implements backpropagation. Backpropagation is a key step in training a neural network. It entails using the error from forward propagation to adjust the weights by propagating this loss backward through the network's layers. This goes on for the number of epochs, which is fixed as a hyperparameter. An epoch is an iteration over the entire training dataset, which means the network has considered all the inputs once. An activation function is a function that is applied to the output of a neuron in an artificial neural network to determine whether the neuron will be activated or not. This is an important function as it introduces non-linearity in the network. There are several types of activation functions; among the most widely used are the softmax and sigmoid functions.

### 1) CONVOLUTIONAL NEURAL NETWORKS (CNN)

A CNN is a deep learning algorithm that utilizes convolutional operations to identify patterns within data, specifically image and video data. The convolution operation involves the application of a filter to the input data, through a process of sliding the filter over the data and computing the dot product between the filter and input. This produces a feature map, which summarizes the presence of distinct features within the input data. It was introduced by Lecun et al. [21] and has since achieved state-of-the-art performance in image classification task. CNN leverages the fact that nearby pixels are more strongly related than distant ones. It uses a special technique called convolution. Figure 2 shows a CNN that takes in an input image, assigns importance, learnable weights, and biases to various aspects of the image. The convolutional layers, explained in Figure 3 extract features from input data that are subjected to filters. This produces feature maps, which are passed into further processing layers.

The Max Pooling layer applies a pooling operation, which involves sliding a two-dimensional filter over each channel of

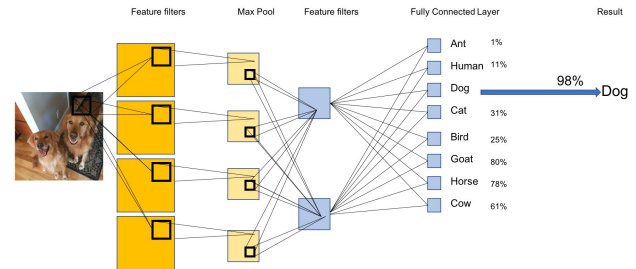


**FIGURE 2.** Simplified graphical representation of an CNN showing the processing of classification of images, including the convolutional layer, Max Pooling, and the Fully Connected layer [22].

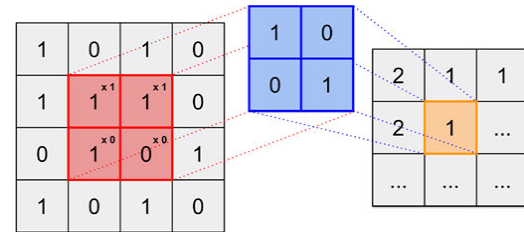


**FIGURE 3.** Illustration of a digital image undergoing convolution with a filter. The image on the left undergoes transformation into a feature map on the right, achieved through the use of a convolutional filter at the center. This specific filter is tailored to detect diagonal lines extending from the top left to the bottom right of the image. As the convolutional filter traverses the image in a predetermined manner, each element in the image (highlighted in red) is multiplied by its corresponding element in the convolutional filter (shown in blue). The sum of these products (depicted in orange) is then generated as output in a new matrix that indicates the presence of a diagonal line. In this feature map, a value of 2 indicates a complete diagonal line is detected, 1 suggests a portion of it is identified, and 0 signifies none of it is detected [23].

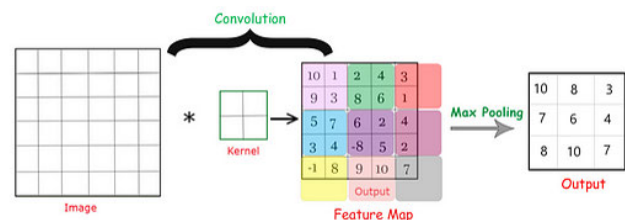


**FIGURE 4.** Illustration of Max Pooling in a CNN Network [24].

the feature map. The pooling layer summarizes the features lying in the region covered by the filter, thereby reducing the dimensions of the feature maps. This decreases the number of parameters to learn and the amount of computation performed in the network. There are different types of pooling layers, including Max pooling, average pooling, and global pooling. Figure 4 show ab example of applying Max pooling.

### 2) SIAMESE NEURAL NETWORK SNN

The Siamese network was presented in the context of signature verification [18] and comprises two identical networks that take in separate inputs, but are connected in the last layer. Siamese architecture aims to model semantic relationships between classes to extract discriminating features [25].

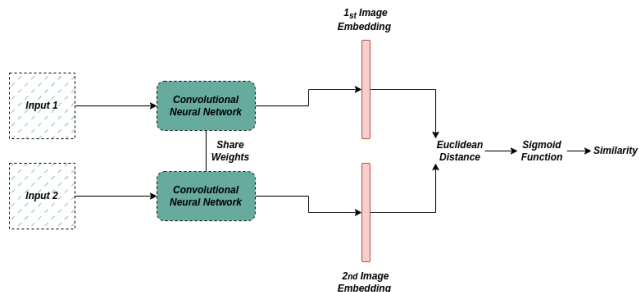


**FIGURE 5.** Illustration of a SNN with each sub-network consisting of a CNN architecture. The final output of the Siamese Network is a similarity score, which indicates how similar or different the two input images are. This score can be used to make a prediction, such as whether two images belong to the same class or not [27].

The twin networks have identical architecture, as shown in Figure 5. They also share weights and work in parallel to create vector representations for the inputs. For instance, we can use ResNet as the twin network if our inputs are images. This parallel CNN architecture allows the model to learn similarity, which can be used for tasks such as similarity measurement or classification. We can think of Siamese neural networks as wrappers for twin networks. They help produce better vector representations by measuring similarities between vectors. The loss function used by the SNN is the contrastive loss [26] which aims to maximise the proximity between positive pairs while simultaneously increasing the dissimilarity between negative pairs. Contrastive loss introduces the concept of margin, which is a minimal distance that dissimilar points need to keep. So it penalizes dissimilar samples for being closer than the given margin.

### 3) VISION IMAGE TRANSFORMERS (ViT)

Transformers are neural network architectures that have had a ground-breaking influence in the field of Natural Language Processing (NLP). Transformer architectures were able to tackle the shortcomings of sequential data tasks that were otherwise processed with Recurrent Neural Networks (RNNs). It came to the forefront in the famous paper “Attention Is All You Need” and uses self-attention mechanisms to capture the context of words in a sentence [28]. ViT was first introduced by the paper “An Image is Worth  $16 \times 16$  Words: Transformers for Image Recognition at Scale” [29]. In ViTs, images are converted into sequences, enabling the models to predict class labels independently and learn image structures effectively. Each input image is treated as a sequence of patches, with each patch flattened into a single vector by concatenating the channels of its pixels. The resulting vectors are then linearly projected to achieve the desired input dimension. This approach allows ViTs to process images as sequences and capture their important features for classification tasks. This is illustrated in Figure 6.

Embedding is a process used in natural language processing for converting raw text into mathematical vectors since computers understand only 0s and 1s. As in any sentence, the exact position where a word is situated in a sentence can alter

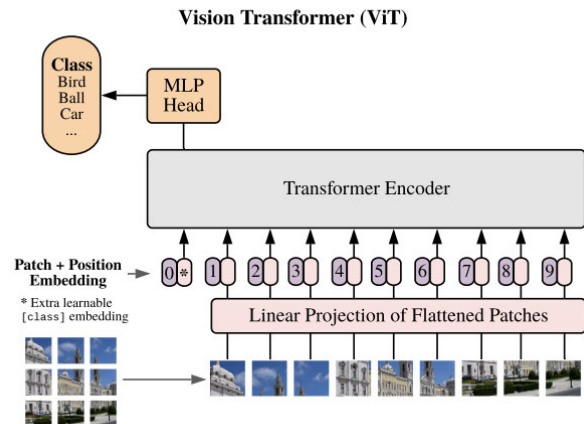


**FIGURE 6.** ViT splits an image into fixed-size patches, linearly embeds each of them, adds position embeddings, and feeds the resulting sequence of vectors to a standard Transformer encoder. In order to perform classification, it uses the standard approach of adding an extra learnable classification token to the sequence [29].

its meaning, so it is important to take this information into consideration. Positional embedding is a technique used in transformer models to add information about the position of a token in a sequence to its embedding.

### B. MACHINE LEARNING PROCESS WORKFLOW

Before explaining the proposed system, we shall explain the workflow when engaging in a machine learning research and development project.

- 1) Historical Data: In supervised learning, labeled data is necessary to acquire the ability to understand features. The initial phase involves ensuring the presence of dependable data. This process encompasses data collection and pre-processing to structure the data appropriately for supervised learning. In summary, we need data that has been accurately labeled and will be used for training the future machine learning model.
- 2) Model building: Depending on the desired objective, construct the model by meticulously selecting a suitable machine learning algorithm adapted for the problem you are looking to solve. Problems may include, for example, regression problems, classification problems, segmentation problems, and detection problems.
- 3) Model Evaluation: In order to enhance the potential for the algorithm to perform well on new, unseen data, it’s common practice to divide the training dataset into a slightly smaller training set and a distinct validation set. The choice of evaluation metrics for assessing a model varies based on the nature of the model and whether it’s being trained or tested. The validation set is designed to resemble the test dataset, aiding data scientists in refining an algorithm by pinpointing instances where the model could potentially generalize effectively and function within a novel population [23].
- 4) Model Optimisation: Machine learning algorithms consist of parameters. This stage focuses on utilizing the

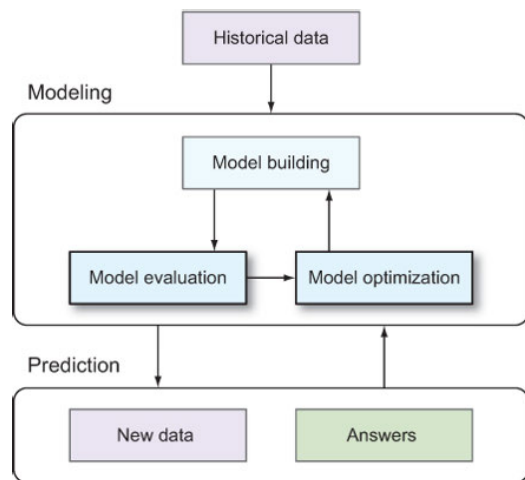


**FIGURE 7.** Workflow of real-world machine learning systems. From historical input data, you can build a model using a machine learning algorithm. You then need to evaluate the performance of the model and optimize its accuracy and scalability to meet your requirements. With the final model, you can make predictions on new data [30].

most suitable parameters to attain the highest level of performance.

### III. RELATED WORKS

The potential AI has garnered attention from researchers who are aware of the risks posed by DFUs. In this section, we first study some recent work in the medical field and the AI algorithms used before taking a deep dive into our investigation of the use of AI in addressing the challenges posed by DFU.

#### A. AI TECHNIQUES AND HEALTHCARE

Electronic Health Record (EHR) systems store data associated with each patient encounter, including demographic information, diagnoses, laboratory tests and results, prescriptions, radiological images, and clinical notes [31]. These data are the raw materials used by researchers in AI and Healthcare. In this section, we look at the various AI algorithms that are used when dealing with this kind of data. Markovic et al. [32] applied a Novel NLP to medical records to create a patient-specific drug profile for diabetic patients. The degree of similarity between clustered profiles was calculated using Euclidean Distance. Yu et al. [33] also exploited transformers-based NLP Models to study social and behavioural determinants of health in Lung cancer patients. The models they used were BERT and RoBERTa, which are pre-trained language models. Furthermore, Soni et al. [34] also takes advantage of the use of Transformers, namely Bidirectional Encoder Representations from Transformers (BERT) for cohort retrieval in EHR.

Medical images have also been widely exploited by AI specialists in research. In their latest work, Yesilkaya et al. [35] tested nine classifiers, namely, nine distinct classifiers: k-nearest neighbors, decision tree, support vector machines,

stochastic gradient descent, random forest, multi-layer perceptron, Naive Bayes, logistic regression, and AdaBoos for the detection of ovarian cancer. They apply feature reduction techniques to simplify their classification algorithms. In recent research, Rabiei et al. [36] tested random forest, neural network, gradient boosting trees, and genetic algorithms to mammographic features for prediction of breast cancer. Sajjad et al. [37] a pre-trained CNN model, VGG-19, is fine-tuned using augmented data for brain tumour grade classification into four classes.

Appiahene et al. [38] use non-invasive palm images to detect iron deficiency anaemia. They tested CNN, K-NN, Naive Bayes, Support Vector Machine, and Decision Tree after augmenting the dataset from 527 to 2635 images. In this case Naive Bayes achieved a 99.96% accuracy, while the Support Vector Machine achieved the lowest accuracy of 96.34%, and the CNN also performed better with an accuracy of 99.92% in detecting anaemia. In another non-invasive method, Al-Karawi et al. [39] experimented with severity-level detection of diabetic retinopathy using an ensemble model of CNN consisting of EfficientNetB7, ResNet50, and VGG19. The classification accuracy achieved using the concatenation ensemble is 96%, which is higher than that obtained via individual CNN models. The use of ensemble techniques is promising and should be explored further.

#### B. AI TECHNIQUES AND DFU

In this section, we provide an in-depth review related to the main objective of this paper, which is the classification of DFU images using AI techniques.

The study by Galdran et al. [40] compares the performance of CNNs and ViTs [29] for the classification of DFUs. The authors investigated the efficacy of the ResNeXt50 [41] architecture from Big Image Transfer (BiT) [42] and EfficientNet [43] for CNNs, as well as the ViT and Data-efficient Image Transformers (DeiT) [44]. In addition, they compared the optimization approaches of Stochastic Gradient Descent [45] and Sharpness-Aware Optimization (SAM) [46] for neural network training. The authors employed various data augmentation techniques during training, including random rotations, horizontal/vertical flipping, and contrast/saturation/brightness adjustments. For testing, four versions of each image were generated, and the predictions were averaged for improved accuracy. Based on the results, the authors found that all pre-trained models performed better with the SAM optimizer. Specifically, the ResNeXt50 architecture demonstrated the highest performance on the test data. Interestingly, the authors achieved the highest scores by combining predictions from both CNN architectures. Through a thorough analysis of the various models, it can be concluded that CNNs outperform ViTs for the task of DFU classification.

Bloch et al. [47] introduced a novel approach for DFU classification using an ensemble of EfficientNets combined with

a semi-supervised training strategy incorporating pseudo-labeling [48]. They address the challenge of class imbalance in the dataset, by using Conditional Generative Adversarial Networks (GANs) [49] to generate synthetic DFU images. They utilized the pix2pixHD [50] framework for conditional image generation. The proposed pipeline consisted of three phases: baseline training, dataset extension, and extension training. In the baseline training phase, the best-performing models were combined into an ensemble model. The baseline model was then employed to train the GAN with pseudo-labeling for both unlabeled and test images. The resulting dataset was subsequently used to retrain the EfficientNet variants, and the best-performing models were merged for ensemble prediction. Notably, the proposed approach demonstrated improved performance of 55.80% compared to the work of Gladran et al. [40] 52.82% for ischaemia class F1 score.

In the study conducted by Ahsan et al. [51], the authors focused on investigating various CNN-based deep learning architectures for binary classification. Specifically, they evaluated the performance of AlexNet, VGG16/19, GoogLeNet, ResNet50.101, MobileNet, SqueezeNet, and DenseNet. Employing a fine-tuning approach, the authors conducted experiments and assessed the accuracy of each architecture. Notably, the results revealed that ResNet50 exhibited the highest accuracy among all the tested architectures. It is important to note that although this research is recent, it lacked comprehensive information regarding the hyperparameters used.

In their work, Goyal et al. introduced an ensemble CNN model that leverages the power of Inception-V3, ResNet50, and InceptionResNetV2 architectures [52], [53], [54]. The model combines bottleneck features extracted from these CNNs. During the training phase, the authors employed a strategy where the weights of the initial layers in the pre-trained networks were frozen to capture common features such as edges and curves. Subsequently, the later layers were unfrozen to focus on learning dataset-specific features. The ensemble-CNN model used the combined bottleneck features as input for binary classification, employing the Support Vector Machine algorithm. Comparative analyses were conducted against traditional machine learning methods, including BayesNet, Random Forest, and CNN-only approaches. Notably, the proposed CNN ensemble model outperformed all traditional machine learning techniques and CNN-only models, showcasing its superior performance in binary classification tasks.

Santos et al. [55] presented DFU-VGG, an innovative approach for the classification of diabetic foot ulcers (DFUs). The authors employed the VGG-19 architecture as the backbone of their CNN. Notably, they introduced batch normalization after each convolutional block. The performance of DFU-VGG was evaluated against fine-tuned versions of VGG-16, VGG-19, InceptionV3, ResNet50, DenseNet201, MobileNetV2, and EfficientNetB0 networks in their original configurations. In a separate study conducted

by Santos et al. [56], an experiment was conducted to investigate the performance of an ensemble model comprising various combinations of VGG-16, VGG-19, InceptionV3, ResNet50, and DenseNet201 architectures. The outcome of the experiment showed that the ensemble model consisting of VGG-16, VGG-19, and DenseNet201 demonstrated the highest performance among the tested combinations. This research sheds light on the effectiveness of ensemble models in improving the classification performance of DFU classification. Thotad et al. [57], also proposed to use a fine-tuned CNN backbone based on EfficientNet [43].

Khandakar et al. [58] approach for DFU classification by combining a CNN-based backbone with traditional machine learning algorithms. The features of DFU are extracted using a pre-trained CNN model. Then unsupervised method of k-mean clustering is used for clustering the images into three categories, namely mild, moderate, and severe.

Qayyum et al. [59] experimented with CNN and ViT. They used transformer-based architectures that were originally trained on the ImageNet dataset. The different vision transformers are fine-tuned by adding a fully connected layer with feature size ( $3072 \times 768$ ), ReLU activation (ReLU), dropout layer for regularization, and another fully connected layer with feature size ( $768 \times 4$ ) at the end layer of the different pre-trained transformers. The features extracted from the last layer of multiple transformers are concatenated pair-wise and applied to a fully connected layer at the end to concatenate the features of individual transformers and then pass to the classifier layer. Table 1 provides a concise overview of the outcomes from the research related to machine learning and DFU classifications.

Based on the findings from above, it is evident that ensemble methods have demonstrated favorable outcomes, as has the use of CNN architectures for image-related tasks. Additionally, promising results have been observed with the application of transformer-based architectures for image classification. In light of this, our research will use these insights and introduce an innovative model for DFU classification, which will be elaborated further in the forthcoming section IV.

#### IV. PROPOSED ARCHITECTURE

This research proposes an innovative architecture for the classification of images of DFU diseases, as illustrated in Figure 8. We use an ensemble of CNN (Section II-A1) and ViT (Section II-A3) as the backbone for the two “identical twins” networks of the SNN (Section II-A2) for feature extraction. A detailed explanation of the model training process can be found in Section IV-C. The training procedure involves utilizing DFU images and employing k-fold validation with K set to 5. A comprehensive description of the dataset used and pre-processing applied in this study is provided in Section V-A. Once the model is trained, it becomes proficient in classifying input images into one of the four classes: none, infection, ischaemia, or both. To generate predictions on the test images, a k-Nearest Neighbors

**TABLE 1.** Summary of related works.

Research Work	Architecture	Type of Classification
Thotad et al. [57]	EfficientNet	Binary Class Abnormal / Normal
F Santos et al. [55]	VGG-16, VGG-19, InceptionV3, ResNet50, DenseNet201, MobileNetV2 EfficientNetB0	Multi-Class None / Infection/ Ischaemia / Both
E Santos et al. [56]	CNN Ensemble [ VGG-16, VGG-19, InceptionV3, ResNet50, DenseNet201, MobileNetV2 ]	Multi-Class None / Infection/ Ischaemia / Both
Galdran et al. [40]	CNN [BIT- ResNeXt50, EfficientNet] ViT[ViT-base ,DeiT-small]	Multi-Class None / Infection/ Ischaemia / Both
Qayyum et al. [59]	ViT[vit_base_patch16_224]	Multi-Class None / Infection/ Ischaemia / Both
Ahmed et al. [60]	EfficientNet B0-B6 Resnet-50	Multi-Class None / Infection/ Ischaemia / Both
Bloch et al. [47]	EfficientNets B0,B1,B2 Pseudo-Labeling GAN	Multi-Class None / Infection/ Ischaemia / Both
Ahsan et al. [51]	AlexNet, VGG16/19, GoogLeNet, ResNet50.101, MobileNet, SqueezeNet, and DenseNet	Binary Class Infection / schaemia
Khandakar et al. [58]	K-Mean Clustering CNN	Multi-Class Mild / Moderate / High
Goyal et al. [61]	Ensemble CNN Support Vector Machine	Binary Class Infection / Ischaemia

(kNN) model is integrated into the approach, conducting neighbourhood analysis to enhance the prediction of the model. A detailed explanation of this process is presented in Section IV-C.

The dataset used in this work was obtained from the DFUC2021 challenge [62], as detailed in Section V-A. Due to the imbalanced nature of the dataset, various image augmentation techniques were employed to enhance the training process of the Siamese model. For both training and classification tasks, the KNN classifier was utilized.

### A. DFU-SIAM

DFU-SIAM is a DFU disease classification model that implements a SNN. Figure 9 shows the ensemble model architecture. For the CNN backbone, we use EfficientNetV2S based on EfficientNet [43] architectures, which have been shown to significantly outperform other networks in classification tasks while having fewer parameters. EfficientNetV2S has fewer parameters, making it more suitable for low-resource settings, and it uses a combination of efficient network design and compound scaling to achieve high accuracy with fewer parameters [63].

The second backbone of the ensemble model is based on ViTs (Section II-A3), more specifically, Bidirectional Encoder representation from Image Transformers (BEiT). BEiT uses a pre-training task called masked image modeling (MIM) and stands for Bidirectional Encoder representation from Image Transformers, which draws inspiration from BERT [64]. MIM uses two views for each image, namely, image patches and visual tokens. The image is split into a grid of patches that are the input representation of the backbone Transformer. The image is “tokenized” into discrete visual tokens. During pre-training, some proportion of image patches are randomly masked, and the corrupted input is fed to Transformer. The model learns to recover the visual tokens of the original image instead of the raw pixels of masked patches.

The vector representation of image 1 is passed into both the EfficientNet model and the ViT model. In the EfficientNet, we remove the last dense layer from the pre-trained model to obtain the features from the last flattened layer (average pool). In the ViT model, we obtain the last hidden states, which contain all the patches from the last attention layer, except the classification token; then we flatten them and use another dense to reduce the shape to make the output

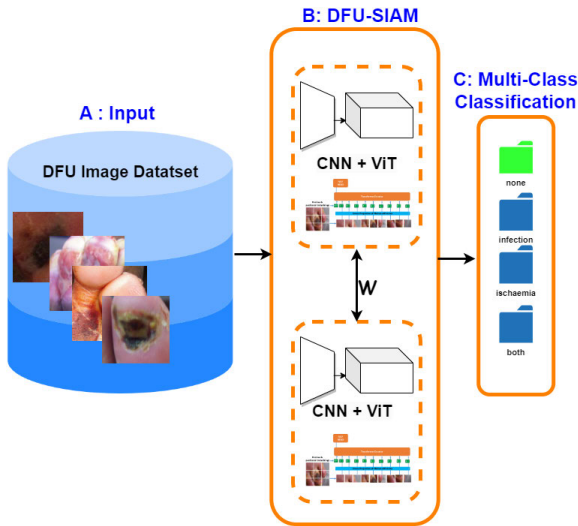


**FIGURE 8.** DFU-SIAM Architecture Overview for DFU Classification. A: Input images were sourced from the DFU2021 Dataset used for initial training and validation. B: The proposed Network, consisting of an ensemble of CNN and ViT within a Siamese Architecture. C: Visualization of the four distinct classes into which the DFU images are accurately classified.

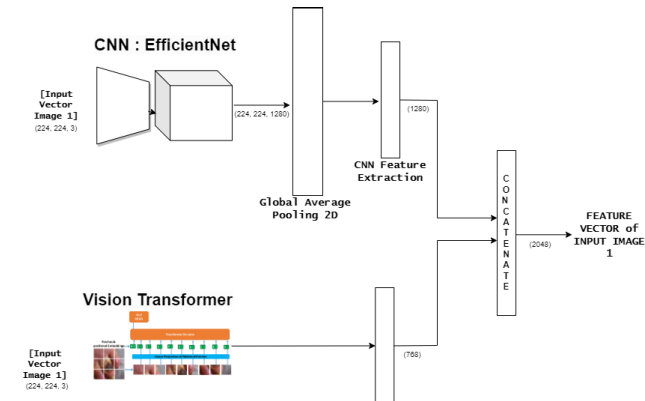


**FIGURE 9.** Block Diagram of the Ensemble Network, illustrating the internal architecture of the individual networks composing the SNN. The CNN utilized is EfficientNet, while the ViT employed is BEiT.

(features) have the same size as the feature extracted from EfficientNet. Finally, we merge the two feature sets.

Traditional Artificial Neural Networks learn by trying to minimise the loss function. Siamese Neural Network uses a different loss function, which is explained in the next section.

## B. LOSS FUNCTION OF DFU-SIAM

While Siamese networks normally use contrastive loss, for DFU-SIAM we chose to implement Large Margin Cotangent Loss (LMCoT). Duong et al. [65] proposed LMCoT as a novel approach for enhancing performance in verification and identification tasks. The LMCoT loss utilizes the cotangent function instead of the cosine function. The cotangent function has a broader range of values, allowing for better optimization. Experimental results demonstrated that LMCoT outperformed

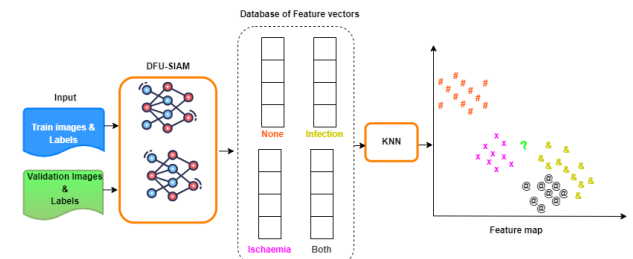


**FIGURE 10.** Illustration of the training process of DFU-SIAM, demonstrating the integrated approach of utilizing the SNN for feature extraction and machine learning for prediction during the training phase.

existing methods in various benchmark datasets and achieved state-of-the-art performance.

Once the chosen loss function has been established, it becomes crucial to outline the model evaluation and optimisation phase as detailed in Section II-B. In the subsequent section, we will provide a comprehensive explanation of how we intend to execute these steps to ensure optimal performance of the model.

## C. DFU-SIAM MODEL EVALUATION AND OPTIMISATION

This section explains the training, validation, and prediction processes of DFU-SIAM. This process is mentioned in Section II-B where we explain the machine learning process workflow. The augmented dataset, consisting of training and validation images along with their respective labels, is loaded into the model. The model leverages the feature extraction capabilities of twin models to obtain the feature vectors of each image and employs the Large Margin Cotangent Loss as loss function. The objective of the learning process is to iteratively update the model parameters in order to minimize the distance between encoded features when the input images belong to similar classes while maximizing the distance when the input images belong to dissimilar classes. This ensures that the model learns to effectively discriminate between different classes by capturing meaningful patterns and representations in the encoded feature space.

During the validation and prediction processes of the model, it is important to mention that the KNN classifier [66], is used as depicted in Figure 11. We iterate through values of K from 1 to 30 to determine the optimal value of K. The metric we use to get the best K is Macro F1 score. KNN is a classifier model based on nearest neighborhood density estimation. For each epoch, an attempt is made to identify the optimal K value based on the Macro F1-score. Once the best K value is determined for an epoch, the corresponding weights are saved, and predictions are made on the test dataset. This iterative process ensures that the best predictions are obtained for each epoch of the test data.

The whole process of how DFU-SIAM classifies a test image is shown in Figure 12. The test image is fed into DFU-SIAM, which performs encoding and generates a compact feature vector within a lower-dimensional space. Within this

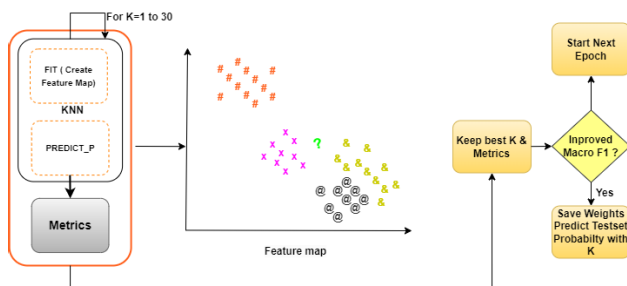


**FIGURE 11.** Schematic representation of the training- process of DFU-SIAM including making predictions using machine learning algorithm KNN to determine the optimal value for K based on the highest macro-F1 score The identified parameters are saved and subsequently employed for predictions on the test data.

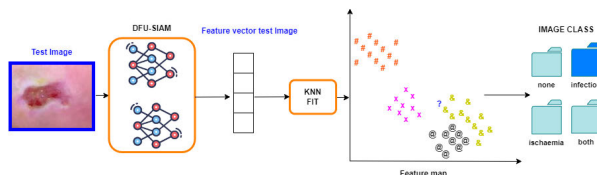


**FIGURE 12.** An overview of the application of DFU-SIAM for Test image classification. Input images are fed into DFU-SIAM, where they are encoded to generate feature vectors. The network then measures the distances between these feature vectors and all the training images. Utilizing the KNN algorithm, the predicted class for the input image is determined based on its proximity to the training samples.

reduced feature space, the encoded representation of the test image is compared to that of all the training samples using suitable distance measures. The classification is then carried out by employing the KNN algorithm.

## V. EXPERIMENTATION AND RESULTS

This section starts by providing a detailed description of the dataset utilized for the experimentation, including details on the preprocessing techniques employed. Additionally, the materials used in the experiments are outlined, and the results obtained are presented alongside a thorough comparison with relevant works in the field.

The quality of the dataset significantly influences the performance of deep learning models in terms of result accuracy. However, ethical reliability of the data source is equally important. In the next section, we will define the characteristics of the dataset employed in DFU-SIAM.

### A. DATASET

In this section, we give an overview of the dataset we will use for this research.

Data quality is a crucial factor that directly affects the performance of supervised learning algorithms. The utilization of a representative and high-quality dataset is critical for achieving optimal accuracy and performance [67]. In this study, we obtained the dataset from the DFUC2021 challenge organized by the Medical Image Computing and Computer-Assisted Intervention (MICCAI) society [62].

The proper licensing was also secured for this research, ensuring that all ethical and legal requirements were met.

Upon initial preprocessing, we observed that the dataset class distribution was imbalanced, with 621, 2555, 227, and 2552 instances belonging to the both, infection, ischaemia, and none categories, respectively, as shown in figure 13. Such an imbalance poses a challenge to the performance of supervised learning algorithms, as they tend to be biased towards the majority class. To address this issue, we applied data augmentation techniques, as discussed in Section V-A1. It should be noted that Siamese networks, when combined with data augmentation techniques, can enhance the performance of various tasks. Data augmentation introduces variations to the training data.

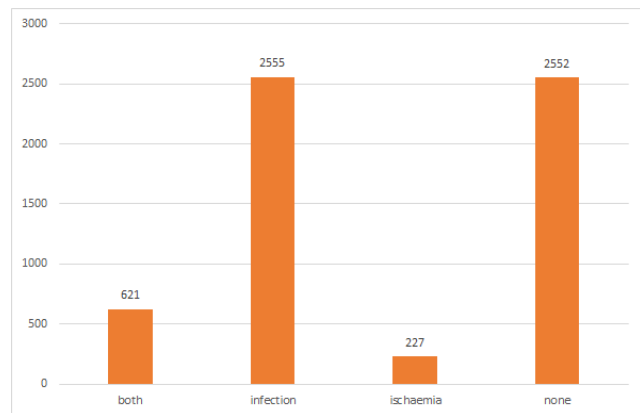


**FIGURE 13.** Class distribution of the DFU2021 Challenge dataset, illustrating the evident imbalance in the dataset.

### 1) DATA AUGMENTATION

Imbalanced data refers to a situation where one class of data examples has much more representation than the other classes [68]. The geometric transformations that were applied to our DFU dataset set images are illustrated in figure 14 and include:

- Colorjitter (brightness = 0.1, contrast = 0.1, Saturation = 0.1, hue = 0.1) Figure 14a
- RandomEqualize( $p = 0.2$ ) Figure 14b
- RandomHorizontalFlip( $p = 0.2$ ) Figure 14c
- RandomVerticalFlip( $p = 0.2$ ) Figure 14d

Prior to executing the model, it is most important to establish a suitable hardware and software setup, as they have an impact on the hyperparameters that will be employed. This setup is elaborated on below.

### B. EXPERIMENTAL SETUP

The experimental setup was conducted on a Windows 10 Pro operating system running on a powerful hardware configuration comprising 64 GB of RAM and an Intel(R) Xeon(R) W-2155 CPU operating at 3.30 GHz. The system was further enhanced with an NVIDIA GeForce RTX 3060 GPU, boasting 12 GB of dedicated memory. To facilitate the

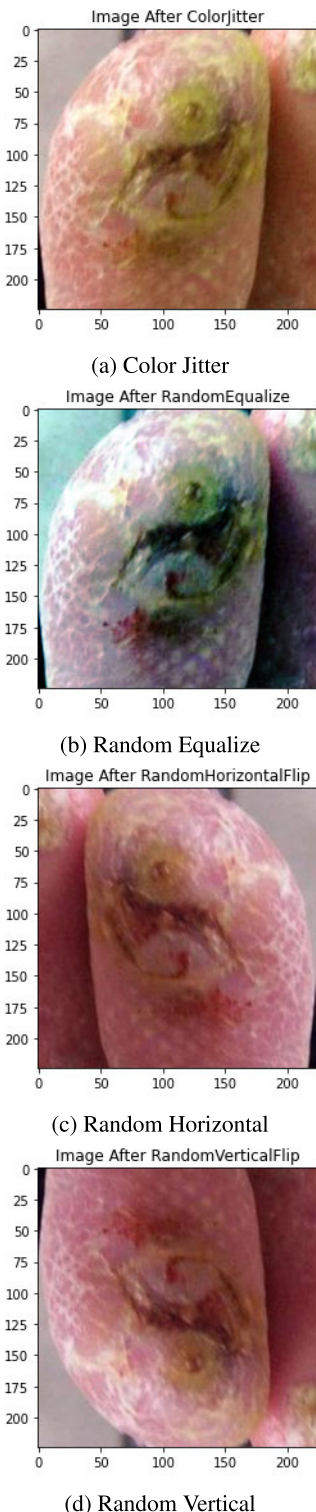


**FIGURE 14.** Demonstration of the application of geometric image transformations (a) Color Jitter, (b)Random Equalize, (c) Random Horizontal Flip, (d) Random Vertical Flip.

experiments, the system was configured with CUDA version 11.7, Tensorflow 2.10.0, and Python 3.10.9.

The selection of hyperparameters in this study was influenced by the computational resources available. The batch

size was set to 8, and the input images were resized to dimensions of 200 by 200 pixels with RGB channels. All models were run for 40 epochs. A fixed learning rate of 10e-6 was employed. To optimize the parameters for prediction on the test data, the KNN algorithm was utilized. Additionally, test time augmentation (TTA) [69] techniques were applied to further enhance the prediction accuracy. TTA introduces random modifications to the test images, enabling the trained model to encounter augmented versions of the images multiple times. The predictions for each corresponding image were averaged, providing a more robust and reliable final prediction.

As explained in the previous section, our intention is to employ an ensemble of CNN and ViT as identical sub-networks of the SNN. The next section will explain the backbone that will be used.

### C. EXPERIMENTAL STRATEGY

For experimental strategy, we tested an ensemble of different combinations of CNN based and ViT based models. For the CNN, we maintained the EFFicientNet. However, for the ViT we experimented with BEiT [64], [70] and SwinTiny(SwinT) [71]. Both will be tested and evaluated against related works.

### D. METRICS

In this study, we used various evaluation metrics to evaluate the performance of our classification algorithms. Commonly used metrics include precision, recall, and F-score, which are essential in quantifying the accuracy and effectiveness of a proposed method and also bench-marking it against other proposed models. This section briefly explains the metrics we used.

The selection among several configurations should be made without subjectivity. Therefore, the following sections will elaborate on the various machine learning metrics that will guide us in determining which model demonstrates the best performance.

#### 1) CONFUSION MATRIX

A confusion matrix is an  $N \times N$  matrix, where  $N$  is the number of classes being predicted. For the DFU problem at hand, we have  $N = 4$ , and hence we get a  $4 \times 4$  matrix. Figure 15 shows an example of a confusion matrix for DFU classification.

#### 2) PRECISION

The precision metric is determined by dividing the number of correctly classified positive samples by the total number of samples classified as positive, including those that were classified incorrectly. This metric serves as an indicator of the model's ability to accurately classify samples as positive. The formula is shown in 1 where TP refers to the True positive and FP represents the False positive.

$$\text{Precision} = \frac{\text{TP}}{\text{TP} + \text{FP}}. \quad (1)$$

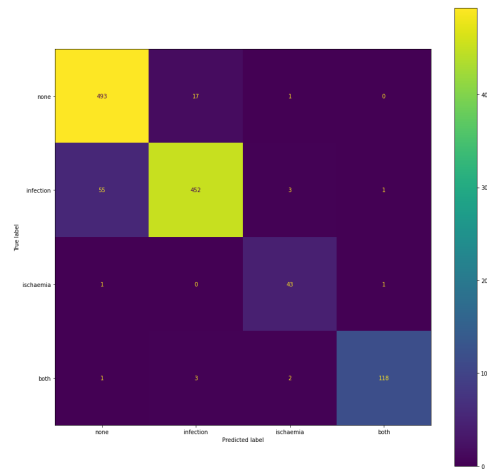
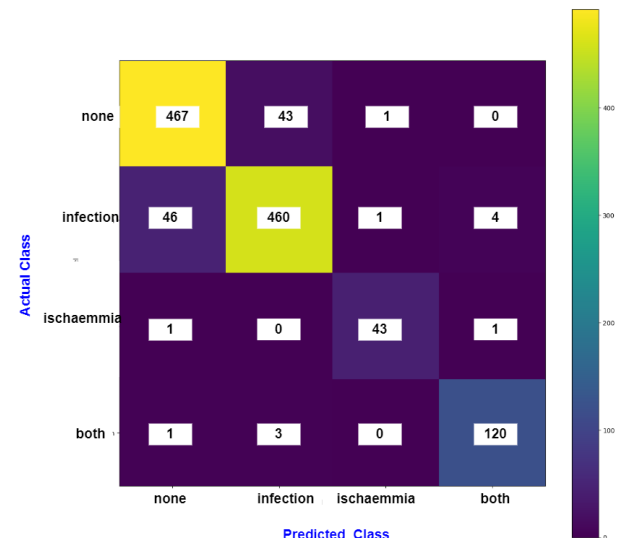
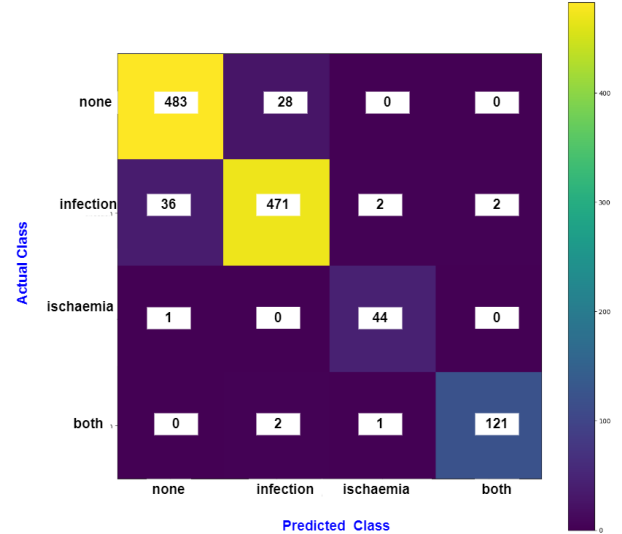


**FIGURE 15.** Example of a Confusion Matrix displaying the True labels and Predicted labels.



(a) CM : EffNet-SwinT



(b) CM: EffNet-BEiT

**FIGURE 16.** Confusion matrix results obtained from applying two different ensembles as identical networks (a) Confusion Matrix with an ensemble of EfficientNet and SwinT. (b) Confusion Matrix with an ensemble of EfficientNet and BeiT.

### 3) RECALL

Recall is derived by dividing the number of positive samples that were correctly classified as positive by the total number of positive samples in the dataset, as illustrated in the formula 2. This metric is used to evaluate the model's capacity to accurately identify positive samples. Higher values of recall indicate that the model is better at detecting positive samples.

$$\text{Recall} = \frac{TP}{TP + FN}. \quad (2)$$

### 4) F1-SCORE

F1-score is the harmonic mean of precision and recall values for a classification problem. F1 score symbolise high precision as well as high recall. It presents a good balance between precision and recall and gives good results on imbalanced classification problems. The following formula: 3

$$\begin{aligned} F1 - Score &= \frac{2 * \text{Precision} * \text{Recall}}{\text{Precision} + \text{Recall}} \\ &= \frac{2 * TP}{2 * TP + FP + FN}. \end{aligned} \quad (3)$$

### 5) MACRO AVERAGE F1-SCORE

In multi-class classification with imbalanced data, the main consideration will be Macro F1-Score. The formula is illustrated with the following formula: 4 where n represents the number of classes involved. In the DFU classification. n is equal to 4.

$$\text{Macro F1 Score} = \frac{\sum_{i=1}^n \text{F1 score}}{n}. \quad (4)$$

## E. RESULTS

### 1) CONFUSION METRICS

The confusion matrix was obtained for the two variations of EfficientNet and ViT transformer, as shown in Figure 16. Figure 16a shows the confusion matrix when the backbone

of our model is run with EfficientNet as the CNN backbone and SwinT( EfficientNEt/SwinT) as the vision Transformer. Figure 16b shows the confusion matrix with EfficientNet and BeiT (EfficientNet/BEiT) as combined backbones. From the overall confusion matrix, the performance metrics are calculated. Table 2 and Table 3 show these metrics. By analysing the confusion matrices, we see that both models are wrongly predicting some instances of none class as infection and some as infection as none.

From Table 2 and Table 3 we can see that EfficientNet and BEiT has a better accuracy of 95% compared to 93% of EfficientNet and SwinT. The Macro F1-score is same at 0.95. EfficientNet and BEiT model has a higher macro F1-score for the classes none and infection.

**TABLE 2.** Metrics from confusion matrix EfficientNet/SwinT.

	Precision	Recall	F1-Score
none	0.92	0.94	0.93
infection	0.93	0.91	0.92
ischaemia	0.96	1	0.98
both	0.98	0.98	0.98
accuracy			0.93
macro avg.	0.95	0.96	0.95
weighted avg.	0.93	0.93	0.93

**TABLE 3.** Metrics from confusion matrix EfficientNet and BEiT.

	Precision	Recall	F1-Score
none	0.93	0.95	0.94
infection	0.94	0.92	0.93
ischaemia	0.94	0.98	0.96
both	0.98	0.98	0.98
accuracy			0.95
macro Avg.	0.95	0.96	0.95
weighted avg.	0.94	0.94	0.94

## 2) LOSS

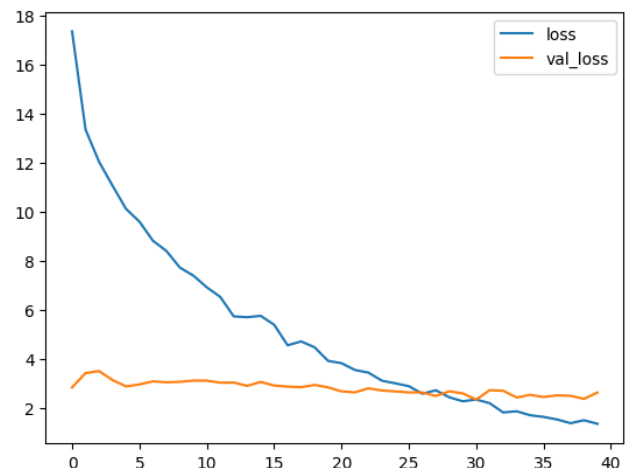
The loss function provides insights into the effectiveness of the models in minimizing errors and improving their predictive performance. By analyzing the loss curves, we can observe the behavior of the models over time and assess their training progress. As far as training loss is concerned, we can see in Figure 17 for both models that training loss decreases at a constant rate. This indicates effective learning and model improvement throughout the training process. Furthermore by analysing validation loss curves, we can assess how well the models are learning and how effectively they are adapting to the validation dataset. The validation loss very quickly stagnates for both models. However, we can witness a constant decrease for the EfficientNet and BEiT model as shown in Figure 17b.

## 3) ACCURACY

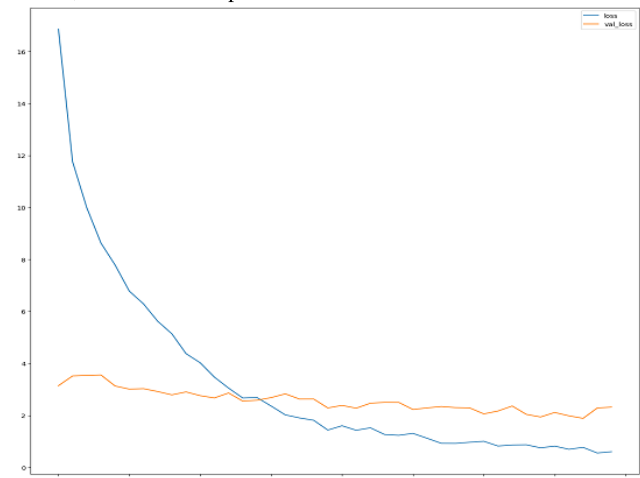
In the best case, for a deep learning model, we would like both curves to increase harmoniously during the training process, indicating that the model is learning and improving its performance on both the training and validation datasets. In Figure 18a training and learning curves intersect at around epoch 30 while in Figure 18b the intersection is earlier at around epoch 13. If the change continues to increase with validation and training accuracy diverging, this will signal that the model is overfitting. In the current case, while there seems to be a discrepancy, we do not believe that the model is overfitting. However, this shows that there is room to further investigate and improve performance.

## 4) MACRO F1-SCORE

In figure 19 we show how the Macro-F1 score varies during the 40 epochs. Figure 19a shows that a high Macro F1 score is obtained very early, at epoch 15. However, a look at



(a) Loss curve of the model with an ensemble of EfficientNet and SwinT, trained for 40 epochs.



(b) Loss curve of the model with an ensemble of EfficientNet and BEiT, trained for 40 epochs.

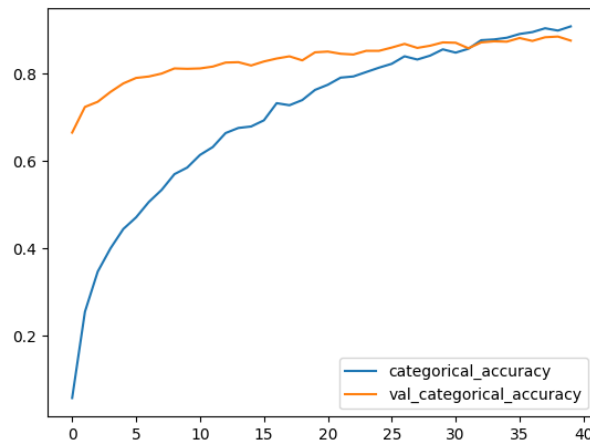
**FIGURE 17.** Loss curves of the two models being experimented.

Figure 19b shows a peak at epoch 17 but it has another peak at epoch 38. This indicated that it is a good idea to investigate both models on unseen test data to have a better indication of which is most suited for the DFU disease classification.

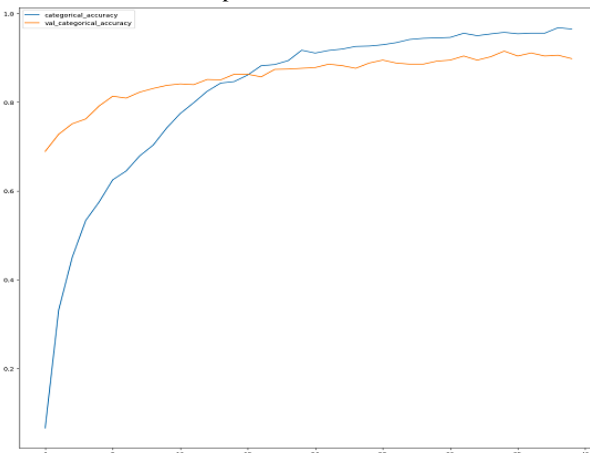
## 5) SUMMARY OF METRIC AND COMPARISON

In this section, a summary of the two models is shown in table 4. For this table it can be seen that based on the main metric on which we are evaluating our model the EfficientNet and SwinT model has a higher macro F1-score compared to the EfficientNet and BEiT model. The class F1-score for none,infection is better for EfficientNet and BEiT while for ischaemia EfficientNet and SwinT is better. For both class they have same class F1-score.

The two models were evaluated on test data provided by the DFU2021 Challenge. This consists of 5734 unlabeled images that are used to make predictions and uploaded on the platform to get the required metrics.



(a) Accuracy of the model with an ensemble of EfficientNet and SwinT, trained for 40 epochs



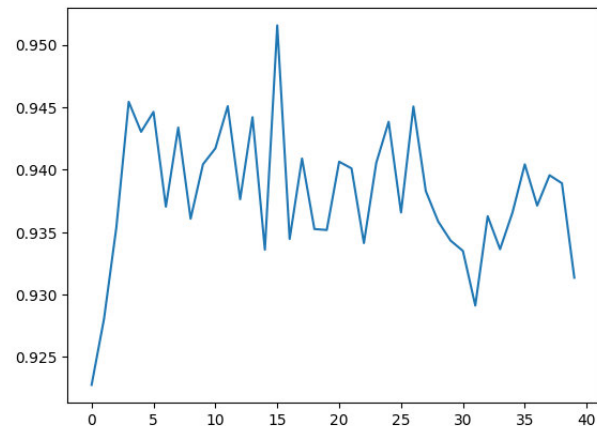
(b) Accuracy of the model with an ensemble of EfficientNet and BEiT, trained for 40 epochs

**FIGURE 18.** Accuracy curves of the two models being experimented.

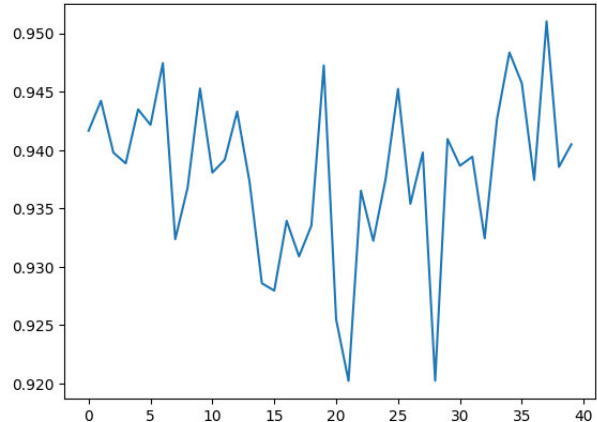
**TABLE 4.** Comparison of CNN and ViT siamese models.

Model	EfficientNet and SwinT	EfficientNet and BEiT
Macro F1-Score	<b>0.9516</b>	0.9510
loss	5.3856	<b>0.6980</b>
categorical_accuracy	0.6922	<b>0.9556</b>
val_loss	2.9078	<b>1.9856</b>
val_categorical_accuracy	0.8270	<b>0.9110</b>
Accuracy	0.9320	<b>0.9395</b>
None F1-Score	0.9265	<b>0.9370</b>
Infection F1-Score	0.9217	<b>0.9308</b>
Ischaemia F1-Score	<b>0.9783</b>	0.9565
Both F1-Score	0.9798	0.9798
Macro Precision	<b>0.9477</b>	0.9472
Macro Recall	<b>0.9558</b>	0.9551
Macro AUC	0.9748	<b>0.9781</b>
Weighted Avg. Precision	0.9322	<b>0.9397</b>
Weighted Avg. Recall	0.9320	<b>0.9395</b>
Micro F1-Score	0.9320	<b>0.9395</b>
Epoch #	<b>15</b>	38

Table 5 presents the performance of the two models on test data which were uploaded on the DFU2021 live challenge board. From the table, it can clearly be observed that the EfficientNet and BEiT model exhibits better overall performance



(a) Macro F1 Score variation over the 40 epochs of training for the model with an ensemble of EfficientNet and SwinT, exhibiting a peak at epoch 15.



(b) Macro F1 Score variation over the 40 epochs of training for the model with an ensemble of EfficientNet and BEiT, exhibiting a peak at epoch 38

**FIGURE 19.** Macro F1-Score variation of the two models being experimented over 40 epochs.

**TABLE 5.** Performance on test data.

Metrics	EfficientNet/SWINt	EfficientNet/BEiT
Macro F1-Score	0.5850	<b>0.6160</b>
None F1-Score	0.7442	<b>0.7478</b>
Infection F1-Score	0.6072	<b>0.6149</b>
Ischaemia F1-Score	0.5367	<b>0.5613</b>
Both F1-Score	0.4520	<b>0.5401</b>
Macro Precision	0.5892	<b>0.6115</b>
Macro Recall	0.6368	<b>0.6570</b>
Macro AUC	0.8043	<b>0.8298</b>
Weighted Avg. Precision	<b>0.6818</b>	0.6728
Weighted Avg. Recall	0.6610	<b>0.6918</b>
epochs	16	7

in almost all the metrics except for the weighted average precision. Hence, the EfficientNet and BEiT model was further optimised. The predictions that showed the highest macro-F1 score were averaged and loaded on the classification liveboard.

**TABLE 6.** DFU-SIAM comparison with related works.

Metrics	DFU-SIAM	Galdran et al. [40]	Bloch et al. [47]	Ahmed et al. [60]	Qayyum et al. [59]
<b>Rank</b>	<b>BEST</b>	1st	2nd	3rd	4th
Macro F1-Score	<b>0.6228</b>	0.6216	0.6077	0.5959	0.5691
None F1-Score	0.7553	<b>0.7574</b>	0.7453	0.7157	0.7466
Infection F1-Score	0.6276	0.6388	0.5917	<b>0.6714</b>	0.6281
Ischaemia F1-Score	0.5495	0.5282	<b>0.558</b>	0.4574	0.467
Both F1-Score	<b>0.5588</b>	0.5619	0.5359	0.539	0.4347
Macro Precision	0.5486	0.614	<b>0.6207</b>	0.5984	0.5814
Macro Recall	<b>0.6554</b>	0.6522	0.6246	0.5979	0.6104
Macro AUC	0.8599	<b>0.8855</b>	0.8616	0.8644	0.8488
W.Avg. Precision	0.6983	<b>0.7009</b>	0.6853	0.6730	0.68
W.Avg Recall	0.6815	<b>0.6856</b>	0.6657	0.6711	0.6636
Micro F1-Score	0.6749	<b>0.6801</b>	0.6532	0.6714	0.6577
epochs	Avg(best epoch)	NA	NA	NA	5(ended)

When compared to the performance of related works, DFU-SIAM which is a model based on a siamese neural network for DFU disease classification, exhibits the best Macro F1-Score as shown in Table 6. Galdran et al. [40] (Galdran 22) were actually the winners of the DFU challenge.

## F. DISCUSSION

DFU classification is implemented using a Siamese Neural Network which is in itself a novel architecture, combined with Large Margin Cotangent Loss (LMCot) as a novel approach for enhancing performance in verification and identification. We further introduce the KNN classifier while iteratively searching for the best K while doing prediction on test data. These are the reasons that explain why our model, DFI-SIAM, performs better than the other model in the related work. While Galdran et al. [40] focused on comparing Convolutional Neural Networks (CNNs) and Vision Transformers (ViTs) and achieved the best macro F1-score, our approach takes a different direction by combining these two architectures. By incorporating the strengths of both CNNs and ViTs, we capitalize on their complementary features and achieve improved results. As far as Bloch et al. [47] they used an ensemble of EfficientNet families with pseudo-labeling. In DFU-SIAM we choose EfficientNet, or more precisely, EfficientNetV2S, which is one of the best performing pre-trained CNN. Qayyum et al. [59] concentrated essentially on vision transformers. They propose the combination of two different pre-trained ViT models for feature extraction. For our proposed model, we chose BEiT, which is one of the best performing pre-trained transformers. However, we decided to make the last 10 layers of the BEiT transformer trainable as our experiments showed a significant increase in performance.

DFU classification in our study used a novel approach of using innovative SNN architecture for classification of DFU. To further enhance its performance, we chose to use a novel approach called the Large Margin Cotangent Loss (LMCot) proposed by Duoung et al. [65]. Our proposed model,

DFI-SIAM, surpasses the performance of other models discussed in related works.

Bloch et al. [47] employed an ensemble of EfficientNet models with pseudo-labeling, which differs from our methodology. Instead, we specifically chose the EfficientNetV2S model, known for its outstanding performance as a pre-trained CNN. We acknowledge, however, that the pseudo-labeling can be used in our model to further improve its performance.

Furthermore Qayyum et al. [59] concentrated on Vision Transformers, proposing the combination of two distinct pre-trained ViT models for feature extraction. In our study, we adopt the BEiT model, which exhibits very good performance as a pre-trained transformer. However, we make a deliberate choice to train only the last 10 layers of the BEiT transformer to strike a balance between fine-tuning and computational efficiency.

By integrating these advancements and tailoring them to the specific requirements of DFU classification, the DFU-SIAM model achieves remarkable accuracy and sets a new benchmark in the field. It should be noted that the model's computational efficiency was not evaluated at this stage. This parameter is important if the model is to be deployed on ubiquitous devices. One limiting factor of the system is the imbalanced data, and this is also acknowledged by other researchers, with Bloch et al. [47] using pseudo-labeling and Generative Adversarial Network to tackle this.

While exploring need for more data, We may have clinics or medical centers that adhere to the idea of using deep learning models but are not willing to share the data with third parties. Ensuring patient privacy while integrating diverse datasets into a model has emerged as a significant limitation in deep learning research [72]. This problem can be addressed by deploying the model using Federated Learning [73]. The notable aspect of Federated Learning lies in its ability to handle data in a decentralized manner, thereby fostering a privacy-preserving environment in AI applications [74] in the

event we require several distant sites to contribute to having even more data, which is an important aspect for the training and implementation of a deep learning model.

#### G. LIMITATIONS

One limitation of our study arises from the substantial class imbalance present within the dataset, particularly evident in the under representation of “both” and the Ischaemia class class. Upon careful inspection of the images, we observed that certain geometric data augmentation techniques were already applied to these classes during the dataset creation process. This imbalance has influenced the overall performance of the models. Nevertheless, it is worth noting that the DFU2021 dataset is currently the most comprehensive resource available for conducting research in this domain. Furthermore, we remain optimistic that with adequate computational resources, there is potential to explore additional variations and employ ensemble modeling techniques to enhance the outcome of our study.

#### VI. CONCLUSION AND FUTURE WORKS

In this paper, we have trained and tested a new model based on an ensemble of EfficientNet and BeIT Transformer in a SNNmodel that has outperformed some of the best results obtained for classification of DFU as detailed in related works III. The dataset limitations can be addressed in future work by investigating the use of GAN which is a type of deep neural network that consists of two components: a generator network and a discriminator network [49]. Another option would be using pseudo labeling which is a technique used in machine learning to improve model performance by using unlabeled data in conjunction with labeled data [48]. The 5734 unlabeled data in the test image can thus be exploited.

This research marks an important step towards tackling the use of machine learning in the field of DFU image classification. Despite our limited processing power, we effectively utilized available resources to achieve significant results. With access to greater computational capabilities, we anticipate that further fine-tuning of our model will lead to even better performance.

As previously specified, there is a need to have a better-quality and more balanced dataset to curb data bias and ensure the model generalises well to unseen data. One possible solution that should be explored is accessing data collected at different geographically located medical facilities. This clearly poses the problem of data privacy, as the owner of the data would not want highly sensitive health-related data to be transferred to a third party. To overcome this barrier, the use of centralized Federated Learning or Peer-to-peer Federated Learning should be explored. Federated Learning, an innovative distributed interactive AI concept, holds exceptional promise in the realm of intelligent healthcare. This approach enables multiple clients, including entities like hospitals, to engage in AI training while upholding stringent data privacy protocols [75], [76], [77]. It entails the

training of machine learning models across datasets dispersed throughout various data centers, such as hospitals and clinical research labs, all while safeguarding data integrity [78].

Incorporating data from a variety of sources will undoubtedly contribute to enhancing the dataset’s imbalance, thereby alleviating the data bias observed in the “both” and “ischaemia” classes. These classes currently exhibit only 621 and 227 occurrences, in contrast to the “infection” and “none” classes which encompass 2555 and 2552 instances, respectively. It’s important to highlight that “both” and “ischaemia”, which are the most serious forms of DFU, are relatively less prevalent in the samples. However, this poses a challenge for machine learning algorithms. One potential approach to addressing this imbalance is to employ GAN [79] for generating synthetic images. This technique has been successfully employed by Kim et al. [80] to augment liver ultrasonic image data using a semi-supervised approach.

This work serves as a stepping stone for future research and development aimed at effectively detecting, treating, and managing diabetic foot ulcers. Our ultimate goal is to contribute to advancements in the medical field, leading to improved patient outcomes and healthcare management. As the machine learning model learns by trying to reduce the loss to a minimum, it is prone to making erroneous predictions. If data bias is present, then there will most certainly be errors in predictions. Hence, from a medical point-of-view, it is mandatory to explainability on top of clinical validation [81]. The critical obstacle to the widespread acceptance of machine learning in healthcare and research relates to the black box nature of machine learning algorithms for the end user [82]. There is presently extensive research concentrating on Explainable AI (XAI), which aims to provide a suite of machine learning techniques that enable human users to understand, appropriately trust, and produce more explainable models [83]. This has to be given priority in any future work. One simple step could be to show a class activation mapping (CAM) approach that highlights the infected section or section with ischaemia and improves the visual interpretability [84]. Techniques like LIME (Local Interpretable Model-Agnostic Explanations) [85] and SHAP (Shapley Additive exPlanations) should be explored [86].

A crucial future direction for our research involves utilizing the Siamese Neural Network to develop a tool that can aid medical practitioners in evaluating the treatment protocols they administer to patients over time. This longitudinal disease evaluation tool would enable practitioners to monitor and adjust treatments as needed. Subsequently, after thorough testing and evaluation of the tool, it can be adapted into a preventive tool for early detection of DFU disease in patients, accessible via a mobile phone platform. In order to advance to the next phase, our plan involves collaborating with experts from public health research labs who possess the necessary expertise in designing protocols for assessing the effectiveness and acceptability of technology adoption in healthcare settings.

## ACKNOWLEDGMENT

The authors would like to thank the Research Team U1094 Inserm U270 IRD EpiMaCT “Épidémiologie des maladies chroniques en zone tropicale” of the University of Limoges, which has contributed to this work by offering the processing power of their server for the GPU processing.

## REFERENCES

- [1] (2021). *IDF Diabetes Atlas, 10th EDN. International Diabetes Federation*. Brussels, Belgium. [Online]. Available: [https://diabetesatlas.org/idfawp/resource-files/2021/07/IDF\\_Atlas\\_10th\\_Edition\\_2021.pdf](https://diabetesatlas.org/idfawp/resource-files/2021/07/IDF_Atlas_10th_Edition_2021.pdf)
- [2] L. Chen, S. Sun, Y. Gao, and X. Ran, “Global mortality of diabetic foot ulcer: A systematic review and meta-analysis of observational studies,” *Diabetes, Obesity Metabolism*, vol. 25, no. 1, pp. 36–45, 2023.
- [3] R. G. Frykberg, “Diabetic foot ulcers: Pathogenesis and management,” *Amer. family physician*, vol. 66, no. 9, p. 1655, 2002.
- [4] I. D. A. Rismayanti, V. N. Farida, N. W. S. Dewi, R. Utami, A. Aris, and N. L. P. I. B. Agustini, “Early detection to prevent foot ulceration among type 2 diabetes mellitus patient: A multi-intervention review,” *J. Public Health Res.*, vol. 11, no. 2, p. jphr.2022.2752, Apr. 2022.
- [5] A. International. (2021). *Foot Care*. [Online]. Available: <https://apsa.mu/foot-care/>
- [6] N. Ahmad, G. N. Thomas, P. Gill, and F. Torella, “The prevalence of major lower limb amputation in the diabetic and non-diabetic population of England 2003–2013,” *Diabetes Vascular Disease Res.*, vol. 13, no. 5, pp. 348–353, Sep. 2016.
- [7] C. McCague, K. MacKay, C. Welsh, A. Constantinou, R. Jena, and M. Crispin-Ortuzar, “Position statement on clinical evaluation of imaging ai,” *Lancet Digital Health*, vol. 5, no. 7, pp. 400–402, 2023.
- [8] F. Li, H. Chen, Z. Liu, X. Zhang, and Z. Wu, “Fully automated detection of retinal disorders by image-based deep learning,” *Graefe's Arch. Clin. Experim. Ophthalmol.*, vol. 257, no. 3, pp. 495–505, Mar. 2019.
- [9] R. Gargaya and T. Leng, “Automated identification of diabetic retinopathy using deep learning,” *Ophthalmology*, vol. 124, no. 7, pp. 962–969, Jul. 2017.
- [10] A. Rodríguez-Ruiz, E. Krupinski, J.-J. Mordang, K. Schilling, S. H. Heywang-Köbrunner, I. Sechopoulos, and R. M. Mann, “Detection of breast cancer with mammography: Effect of an artificial intelligence support system,” *Radiology*, vol. 290, no. 2, pp. 305–314, Feb. 2019.
- [11] A. Esteva, B. Kuprel, R. A. Novoa, J. Ko, S. M. Swetter, H. M. Blau, and S. Thrun, “Dermatologist-level classification of skin cancer with deep neural networks,” *Nature*, vol. 542, pp. 115–118, Jan. 2017.
- [12] I. Bartoletti, “Ai in healthcare: Ethical and privacy challenges,” in *Artificial Intelligence in Medicine*, D. Riano, S. Wilk, and A. ten Teije, Eds. Poznań, Poland: Springer, 2019, pp. 7–10.
- [13] V. N. Shah and S. K. Garg, “Managing diabetes in the digital age,” *Clin. Diabetes Endocrinol.*, vol. 1, no. 1, pp. 1–7, Dec. 2015.
- [14] J. S. Winter, “AI in healthcare: Data governance challenges,” *J. Hospital Manag. Health Policy*, vol. 5, p. 8, Mar. 2020.
- [15] *Ethics and Governance of Artificial Intelligence for Health: WHO Guidance*, World Health Organization, Geneva, Switzerland, 2021.
- [16] M. H. Yap, B. Cassidy, and C. Kendrick, *Diabetic Foot Ulcers Grand Challenge*. Berlin, Germany: Springer, 2022.
- [17] Z. Xie, Y. Lin, Z. Yao, Z. Zhang, Q. Dai, Y. Cao, and H. Hu, “Self-supervised learning with Swin transformers,” 2021, *arXiv:2105.04553*.
- [18] J. Bromley, I. Guyon, Y. LeCun, E. Säckinger, and R. Shah, “Signature verification using a ‘Siamese’ time delay neural network,” in *Proc. Adv. Neural Inf. Process. Syst.*, vol. 6, 1993.
- [19] H. H. Aghdam and E. J. Heravi, *Guide to Convolutional Neural Networks*, vol. 10. New York, NY, USA: Springer, 2017, p. 51.
- [20] R. Pramoditha. (2022). *Overview of a Neural Network’s Learning Process*. Accessed: Aug. 17, 2023. [Online]. Available: <https://medium.com/data-science-365/overview-of-a-neural-networks-learning-process-61690a502fa>
- [21] Y. LeCun, L. Bottou, Y. Bengio, and P. Haffner, “Gradient-based learning applied to document recognition,” *Proc. IEEE*, vol. 86, no. 11, pp. 2278–2324, Nov. 1998.
- [22] P. Lea, *Internet of Things for Architects: Architecting IoT Solutions by Implementing Sensors, Communication Infrastructure, Edge Computing, Analytics, and Security*. Birmingham, U.K.: Packt Publishing, 2018.
- [23] R. Y. Choi, A. S. Coyner, J. Kalpathy-Cramer, M. F. Chiang, and J. P. Campbell, “Introduction to machine learning, neural networks, and deep learning,” *Transl. Vis. Sci. Technol.*, vol. 9, no. 2, p. 14, 2020.
- [24] K. Prasant. (2021). *Max Pooling, Why Use it and Its Advantages*. Accessed: Aug. 21, 2023. [Online]. Available: <https://medium.com/geekculture/max-pooling-why-use-it-and-its-advantages-5807a0190459>
- [25] S. Berlemon, G. Lefebvre, S. Duffner, and C. Garcia, “Class-balanced Siamese neural networks,” *Neurocomputing*, vol. 273, pp. 47–56, Jan. 2018.
- [26] R. Hadsell, S. Chopra, and Y. LeCun, “Dimensionality reduction by learning an invariant mapping,” in *Proc. IEEE Comput. Soc. Conf. Comput. Vis. Pattern Recognit. (CVPR)*, Jun. 2006, pp. 1735–1742.
- [27] N. Georgios. (2023). *How Do Siamese Networks Work in Image Recognition? | Baeldung on Computer Science*. Accessed: Aug. 17, 2023. [Online]. Available: <https://www.baeldung.com/cs/siamese-networks>
- [28] A. Vaswani, N. Shazeer, N. Parmar, J. Uszkoreit, L. Jones, A. N. Gomez, Ł. Kaiser, and I. Polosukhin, “Attention is all you need,” in *Proc. Adv. Neural Inf. Process. Syst.*, vol. 30, 2017, pp. 1–11.
- [29] A. Dosovitskiy, L. Beyer, A. Kolesnikov, D. Weissenborn, X. Zhai, T. Unterthiner, M. Dehghani, M. Minderer, G. Heigold, S. Gelly, J. Uszkoreit, and N. Houlsby, “An image is worth 16×16 words: Transformers for image recognition at scale,” 2020, *arXiv:2010.11929*.
- [30] H. Brink, J. Richards, and M. Fetherolf. (2016). *Real-World Machine Learning*. Simon and Schuster. [Online]. Available: <https://livebook.manning.com/book/real-world-machine-learning/chapter-1/>
- [31] G. S. Birkhead, M. Klompass, and N. R. Shah, “Uses of electronic health records for public health surveillance to advance public health,” *Annu. Rev. Public Health*, vol. 36, no. 1, pp. 345–359, Mar. 2015.
- [32] R. Marković, V. Grubelník, T. Završnik, H. B. Vošner, P. Kokol, M. Perc, M. Marhl, M. Zavrsnik, and J. Zavrsnik, “Profiling of patients with type 2 diabetes based on medication adherence data,” *Frontiers Public Health*, vol. 11, Jul. 2023, Art. no. 1209809.
- [33] Z. Yu, X. Yang, C. Dang, S. Wu, P. Adekkattu, J. Pathak, T. J. George, W. R. Hogan, Y. Guo, and J. Bian, “A study of social and behavioral determinants of health in lung cancer patients using transformers-based natural language processing models,” in *Proc. AMIA Annu. Symp.*, 2021, p. 1225.
- [34] S. Soni and K. Roberts, “Patient cohort retrieval using transformer language models,” in *Proc. AMIA Annu. Symp.*, 2020, p. 1150.
- [35] B. Yesilkaya, M. Perc, and Y. Isler, “Manifold learning methods for the diagnosis of ovarian cancer,” *J. Comput. Sci.*, vol. 63, Sep. 2022, Art. no. 101775.
- [36] R. Rabiei, “Prediction of breast cancer using machine learning approaches,” *J. Biomed. Phys. Eng.*, vol. 12, no. 3, p. 297, Jul. 2022.
- [37] M. Sajjad, S. Khan, K. Muhammad, W. Wu, A. Ullah, and S. W. Baik, “Multi-grade brain tumor classification using deep CNN with extensive data augmentation,” *J. Comput. Sci.*, vol. 30, pp. 174–182, Jan. 2019.
- [38] P. Appiahene, J. W. Asare, E. T. Donkoh, G. Dimauro, and R. Maglietta, “Detection of iron deficiency anemia by medical images: A comparative study of machine learning algorithms,” *BioData Mining*, vol. 16, no. 1, pp. 1–20, Jan. 2023.
- [39] A. Al-Karawi and E. Avşar, “A deep learning framework with edge computing for severity level detection of diabetic retinopathy,” *Multimedia Tools Appl.*, pp. 1–22, Mar. 2023.
- [40] A. Galdran, G. Carneiro, and M. A. G. Ballester, “Convolutional nets versus vision transformers for diabetic foot ulcer classification,” in *Diabetic Foot Ulcers Grand Challenge*. Cham, Switzerland: Springer, 2022, pp. 21–29.
- [41] S. Xie, R. Girshick, P. Dollár, Z. Tu, and K. He, “Aggregated residual transformations for deep neural networks,” in *Proc. IEEE Conf. Comput. Vis. Pattern Recognit. (CVPR)*, Jul. 2017, pp. 1492–1500.
- [42] A. Kolesnikov, L. Beyer, X. Zhai, J. Puigcerver, J. Yung, S. Gelly, and N. Houlsby, “Big transfer (BiT): General visual representation learning,” in *Computer Vision—ECCV*. Glasgow, U.K.: Springer, 2020, pp. 491–507.
- [43] M. Tan and Q. Le, “EfficientNet: Rethinking model scaling for convolutional neural networks,” in *Proc. 36th Int. Conf. Mach. Learn.*, vol. 97, K. Chaudhuri and R. Salakhutdinov, Eds. 2019, pp. 6105–6114.
- [44] H. Touvron, M. Cord, M. Douze, F. Massa, A. Sablayrolles, and H. Jegou, “Training data-efficient image transformers & distillation through attention,” in *Proc. Int. Conf. Mach. Learn.*, 2021, pp. 10347–10357.

- [45] S. H. Haji and A. M. Abdulazeez, "Comparison of optimization techniques based on gradient descent algorithm: A review," *PalArch's J. Archaeol. Egypt/Egyptol.*, vol. 18, no. 4, pp. 2715–2743, 2021.
- [46] P. Foret, A. Kleiner, H. Mobahi, and B. Neyshabur, "Sharpness-aware minimization for efficiently improving generalization," 2020, *arXiv:2010.01412*.
- [47] L. Bloch, R. Brunel, and C. M. Friedrich, "Boosting efficientnets ensemble performance via pseudo-labels and synthetic images by pix2pixHD for infection and ischaemia classification in diabetic foot ulcers," in *Diabetic Foot Ulcers Grand Challenge*. Cham, Switzerland: Springer, 2022, pp. 30–49.
- [48] D.-H. Lee, "Pseudo-label: The simple and efficient semi-supervised learning method for deep neural networks," in *Proc. Int. Conf. Mach. Learn. (ICML)*, 2013, vol. 3, no. 2, p. 896.
- [49] I. J. Goodfellow, J. Pouget-Abadie, M. Mirza, B. Xu, D. Warde-Farley, S. Ozair, A. C. Courville, and Y. Bengio, "Generative adversarial networks," *Commun. ACM*, vol. 63, no. 11, pp. 139–144, 2020.
- [50] T.-C. Wang, M.-Y. Liu, J.-Y. Zhu, A. Tao, J. Kautz, and B. Catanzaro, "High-resolution image synthesis and semantic manipulation with conditional GANs," in *Proc. IEEE Conf. Comput. Vis. Pattern Recognit.*, Jun. 2018, pp. 8798–8807.
- [51] M. Ahsan, S. Naz, R. Ahmad, H. Ehsan, and A. Sikandar, "A deep learning approach for diabetic foot ulcer classification and recognition," *Information*, vol. 14, no. 1, p. 36, Jan. 2023.
- [52] C. Szegedy, V. Vanhoucke, S. Ioffe, J. Shlens, and Z. Wojna, "Rethinking the inception architecture for computer vision," in *Proc. IEEE Conf. Comput. Vis. Pattern Recognit. (CVPR)*, Jun. 2016, pp. 2818–2826.
- [53] K. He, X. Zhang, S. Ren, and J. Sun, "Deep residual learning for image recognition," in *Proc. IEEE Conf. Comput. Vis. Pattern Recognit. (CVPR)*, Jun. 2016, pp. 770–778.
- [54] C. Szegedy, S. Ioffe, V. Vanhoucke, and A. Alemi, "Inception-v4, inception-ResNet and the impact of residual connections on learning," in *Proc. AAAI Conf. Artif. Intell.*, 2017, vol. 31, no. 1, pp. 4278–4284.
- [55] F. Santos, E. Santos, L. H. Vogado, M. Ito, A. Bianchi, J. M. Tavares, and R. Veras, "DFU-VGG, a novel and improved VGG-19 network for diabetic foot ulcer classification," in *Proc. 29th Int. Conf. Syst., Signals Image Process. (IWSSIP)*, Jun. 2022, pp. 1–4.
- [56] E. Santos, F. Santos, J. Dallyson, K. Aires, J. M. R. S. Tavares, and R. Veras, "Diabetic foot ulcers classification using a fine-tuned CNNs ensemble," in *Proc. IEEE 35th Int. Symp. Comput.-Based Med. Syst. (CBMS)*, Jul. 2022, pp. 282–287.
- [57] P. N. Thotad, G. R. Bharamagoudar, and B. S. Anami, "Diabetic foot ulcer detection using deep learning approaches," *Sensors Int.*, vol. 4, 2023, Art. no. 100210.
- [58] A. Khandakar, M. E. H. Chowdhury, M. B. Ibne Reaz, S. H. M. Ali, M. A. Hasan, S. Kiranyaz, T. Rahman, R. Alfkey, A. A. A. Bakar, and R. A. Malik, "A machine learning model for early detection of diabetic foot using thermogram images," *Comput. Biol. Med.*, vol. 137, Oct. 2021, Art. no. 104838.
- [59] A. Qayyum, A. Benzinou, M. Mazher, and F. Meriaudeau, "Efficient multi-model vision transformer based on feature fusion for classification of DFUC2021 challenge," in *Diabetic Foot Ulcers Grand Challenge*, M. H. Yap, B. Cassidy, and C. Kendrick, Eds. Cham, Switzerland: Springer, 2022, pp. 62–75.
- [60] S. Ahmed and H. Naveed, "Bias adjustable activation network for imbalanced data," in *Diabetic Foot Ulcers Grand Challenge*, M. H. Yap, B. Cassidy, and C. Kendrick, Eds. Cham, Switzerland: Springer, 2022, pp. 50–61.
- [61] M. Goyal, N. D. Reeves, S. Rajbhandari, N. Ahmad, C. Wang, and M. H. Yap, "Recognition of ischaemia and infection in diabetic foot ulcers: Dataset and techniques," *Comput. Biol. Med.*, vol. 117, Feb. 2020, Art. no. 103616.
- [62] M. H. Yap, B. Cassidy, J. M. Pappachan, C. O'Shea, D. Gillespie, and N. D. Reeves, "Analysis towards classification of infection and ischaemia of diabetic foot ulcers," in *Proc. IEEE EMBS Int. Conf. Biomed. Health Informat. (BHI)*, Jul. 2021, pp. 1–4.
- [63] M. Tan and Q. V. Le, "EfficientNetV2: Smaller models and faster training," in *Proc. Int. Conf. Mach. Learn.*, M. Meila and T. Zhang, Eds. 2021, pp. 10096–10106.
- [64] H. Bao, L. Dong, S. Piao, and F. Wei, "BEiT: BERT pre-training of image transformers," 2021, *arXiv:2106.08254*.
- [65] A.-K. Duong, H.-L. Nguyen, and T.-T. Truong, "Large margin cotangent loss for deep similarity learning," in *Proc. Int. Conf. Adv. Comput. Analytics (ACOMPA)*, Nov. 2022, pp. 40–47.
- [66] M. A. Jabbar, B. L. Deekshatulu, and P. Chandra, "Classification of heart disease using K-nearest neighbor and genetic algorithm," *Proc. Technol.*, vol. 10, pp. 85–94, Jan. 2013.
- [67] D. Sculley, G. Holt, D. Golovin, E. Davydov, T. Phillips, D. Ebner, V. Chaudhary, M. Young, J.-F. Crespo, and D. Dennison, "Hidden technical debt in machine learning systems," in *Proc. Adv. Neural Inf. Process. Syst.*, vol. 28, 2015, pp. 2503–2511.
- [68] H. Kaur, H. S. Pannu, and A. K. Malhi, "A systematic review on imbalanced data challenges in machine learning: Applications and solutions," *ACM Comput. Surv.*, vol. 52, no. 4, pp. 1–36, Jul. 2020.
- [69] D. Shanmugam, D. Blalock, G. Balakrishnan, and J. Guttag, "Better aggregation in test-time augmentation," in *Proc. IEEE/CVF Int. Conf. Comput. Vis. (ICCV)*, Oct. 2021, pp. 1214–1223.
- [70] Z. Peng, L. Dong, H. Bao, Q. Ye, and F. Wei, "BEiT v2: Masked image modeling with vector-quantized visual tokenizers," 2022, *arXiv:2208.06366*.
- [71] P. Pathak, J. Zhang, and D. Samaras, "Local learning on transformers via feature reconstruction," 2022, *arXiv:2212.14215*.
- [72] L. Kwak and H. Bai, "The role of federated learning models in medical imaging," *Radiol., Artif. Intell.*, vol. 5, no. 3, May 2023, Art. no. e230136.
- [73] N. Rieke, J. Hancox, W. Li, F. Milletari, H. R. Roth, S. Albarqouni, S. Bakas, M. N. Galtier, B. A. Landman, K. Maier-Hein, S. Ourselin, M. Sheller, R. M. Summers, A. Trask, D. Xu, M. Baust, and M. J. Cardoso, "The future of digital health with federated learning," *npj Digit. Med.*, vol. 3, no. 1, p. 119, Sep. 2020.
- [74] M. F. Sohan and A. Basalamah, "A systematic review on federated learning in medical image analysis," *IEEE Access*, vol. 11, pp. 28628–28644, 2023.
- [75] A. Rahman, M. S. Hossain, G. Muhammad, D. Kundu, T. Debnath, M. Rahman, M. S. I. Khan, P. Tiwari, and S. S. Band, "Federated learning-based AI approaches in smart healthcare: Concepts, taxonomies, challenges and open issues," *Cluster Comput.*, vol. 26, no. 4, pp. 2271–2311, Aug. 2023.
- [76] G. A. Kaassis, M. R. Makowski, D. Rückert, and R. F. Braren, "Secure, privacy-preserving and federated machine learning in medical imaging," *Nature Mach. Intell.*, vol. 2, no. 6, pp. 305–311, Jun. 2020.
- [77] M. J. Sheller, B. Edwards, G. A. Reina, J. Martin, S. Pati, A. Kotrotsou, M. Milchenko, W. Xu, D. Marcus, R. R. Colen, and S. Bakas, "Federated learning in medicine: Facilitating multi-institutional collaborations without sharing patient data," *Sci. Rep.*, vol. 10, no. 1, p. 12598, Jul. 2020.
- [78] M. Joshi, A. Pal, and M. Sankarasubbu, "Federated learning for healthcare domain-pipeline, applications and challenges," *ACM Trans. Comput. Healthcare*, vol. 3, no. 4, pp. 1–36, Oct. 2022.
- [79] I. Goodfellow, J. Pouget-Abadie, M. Mirza, B. Xu, D. Warde-Farley, S. Ozair, A. Courville, and Y. Bengio, "Generative adversarial nets," in *Proc. Adv. Neural Inf. Process. Syst.*, vol. 27, Z. Ghahramani, M. Welling, C. Cortes, N. Lawrence, and K. Weinberger, Eds. Red Hook, NY, USA: Curran Associates, 2014, pp. 1–9.
- [80] S. Kim and S. Lee, "Self-supervised augmentation of quality data based on classification-reinforced GAN," in *Proc. 17th Int. Conf. Ubiquitous Inf. Manag. Commun. (IMCOM)*, Jan. 2023, pp. 1–7.
- [81] J. Amann, A. Blasimme, E. Vayena, D. Frey, and V. I. Madai, "Explainability for artificial intelligence in healthcare: A multidisciplinary perspective," *BMC Med. Informat. Decis. Making*, vol. 20, no. 1, pp. 1–9, Dec. 2020.
- [82] L. Rubinger, A. Gazendam, S. Ekhiani, and M. Bhandari, "Machine learning and artificial intelligence in research and healthcare," *Injury*, vol. 54, pp. 69–73, May 2023.
- [83] R. Dwivedi, D. Dave, H. Naik, S. Singhal, R. Omer, P. Patel, B. Qian, Z. Wen, T. Shah, G. Morgan, and R. Ranjan, "Explainable AI (XAI): Core ideas, techniques, and solutions," *ACM Comput. Surveys*, vol. 55, no. 9, pp. 1–33, Sep. 2023.
- [84] D. Saraswat, P. Bhattacharya, A. Verma, V. K. Prasad, S. Tanwar, G. Sharma, P. N. Bokoro, and R. Sharma, "Explainable AI for healthcare 5.0: Opportunities and challenges," *IEEE Access*, vol. 10, pp. 84486–84517, 2022.
- [85] M. T. Ribeiro, S. Singh, and C. Guestrin, "Why should I trust you? Explaining the predictions of any classifier," in *Proc. 22nd ACM SIGKDD Int. Conf. Knowl. Discovery Data Mining*, 2016, pp. 1135–1144.
- [86] E. T. Joa and C. Guan, "A survey on explainable artificial intelligence (XAI): Toward medical XAI," *IEEE Trans. Neural Netw. Learn. Syst.*, vol. 32, no. 11, pp. 4793–4813, Nov. 2021.



**MOHAMMUD SHAAD ALLY TOOFANEE** is currently pursuing the Ph.D. degree in artificial intelligence with the Research Laboratory XLIM, UMR CNRS 7252, University of Limoges, France. He is also a Senior Lecturer with Université des Mascareignes, Mauritius (UDM). He is the co-director of the master's course in artificial intelligence and robotics. His research interests are using machine learning in the field of health and more precisely diabetes prevention, management, and education. He is investigating the use of vision transformer for image and transformers for natural language processing.



**KARIM TAMINE** is an Associate Professor/a Researcher with the XLIM Laboratory, University of Limoges. He is the main resource person in artificial intelligence for the setting up of the master's degree with Université des Mascareignes Mauritius. He has supervised eight Ph.D. thesis and is supervising two Ph.D. students. His research work focuses on the use of artificial intelligence methods in various fields, such as computer graphics, security, and quality of service in dynamic communication networks.



**VINCENT PETIT** is currently pursuing the M.Sc. degree with ESPOIR, Université des Mascareignes, Mauritius. He is also a Software Engineer with Kaizen Solutions, Grenoble, France. He studied data science after a diverse experience in applied mechanics. His research interests include statistics, uncertainty assessment, machine learning, and deep learning, more especially computer vision and NLP, based upon which he strives to run research projects in the field of public health.



**ANH KIET DUONG** received the bachelor's degree (Hons.) from the Ho Chi Minh City University of Science, Vietnam. He is currently pursuing the master's degree with CRYPTIS, University of Limoges. His research interests include similarity learning, artificial intelligence, network security, federated learning, and cryptography.



**MOHAMED HAMROUN** received the Engineering degree from the Higher Institute of Computer Science and Multimedia, University of Sfax, Tunisia, in 2014, and the Ph.D. degree in computer science from the LaBRI Laboratory, University of Bordeaux, in December 2019. He pursued a career in industry before returning to school. He has held three postdoctoral research positions in two different laboratories, such as first with the LISIC Laboratory, University of Littoral; and second with the XLIM Laboratory, University of Limoges. He is an Associate Professor with the 3IL School and a Researcher with the XLIM Laboratory, UMR CNRS 7252, University of Limoges. His research interests are related to image and AI for health, pattern recognition, image and video processing, indexing and information retrieval, information extraction, machine learning, clustering, and deep learning.

**DAMIEN SAUVERON** is a Professor/a Researcher with the XLIM Laboratory, University of Limoges. He is also the Dean of the Faculty of Science and Technology. His research interests are related to smart card applications and security (at hardware and software level), RFID/NFC applications and security, mobile networks (e.g., UAV fleets) applications and security, sensors network applications and security, smart home applications and security, Internet of Things (IoT) security, cyber-physical systems security, security of distributed objects and systems, and security evaluation/certification processes.

• • •

RESEARCH

Open Access



# Diabetic foot ulcer mobile detection system using smart phone thermal camera: a feasibility study

Luay Fraiwan<sup>1,2\*</sup> , Mohanad AlKhodari<sup>1</sup>, Jolu Ninan<sup>1</sup>, Basil Mustafa<sup>1</sup>, Adel Saleh<sup>1</sup> and Mohammed Ghazal<sup>1</sup>

\*Correspondence:  
fraiwan@just.edu.jo

<sup>2</sup> Biomedical Engineering Department, Jordan University of Science and Technology, Irbid 22110, Jordan  
Full list of author information is available at the end of the article

## Abstract

**Background:** Nowadays, the whole world is being concerned with a major health problem, which is diabetes. A very common symptom of diabetes is the diabetic foot ulcer (DFU). The early detection of such foot complications can protect diabetic patients from any dangerous stages that develop later and may require foot amputation. This work aims at building a mobile thermal imaging system that can be used as an indicator for possible developing ulcers.

**Methods:** The proposed system consists of a thermal camera connected to a Samsung smart phone, which is used to acquire thermal images. This thermal imaging system has a simulated temperature gradient of more than 2.2 °C, which represents the temperature difference (in the literature) than can indicate a possible development of ulcers. The acquired images are processed and segmented using basic image processing techniques. The analysis and interpretation is conducted using two techniques: Otsu thresholding technique and Point-to-Point mean difference technique.

**Results:** The proposed system was implemented under MATLAB Mobile platform and thermal images were analyzed and interpreted. Four testing images (feet images) were used to test this procedure; one image with any temperature variation to the feet, and three images with skin temperature increased to more than 2.2 °C introduced at different locations. With the two techniques applied during the analysis and interpretation stage, the system was successful in identifying the location of the temperature increase.

**Conclusion:** This work successfully implemented a mobile thermal imaging system that includes an automated method to identify possible ulcers in diabetic patients. This may give diabetic patients the ability for a frequent self-check of possible ulcers. Although this work was implemented in simulated conditions, it provides the necessary feasibility to be further developed and tested in a clinical environment.

**Keywords:** Ulcer detection, Mobile thermal camera, Thermal imaging, Otsu thresholding, Image registration

## Background

Diabetes Mellitus (DM) is a metabolic chronic disease that is associated with abnormal glucose levels in the blood. There are two causes of Diabetes Mellitus, the first one is the abnormal production of insulin by the pancreas (Type I), while the second cause is

related to inadequate cells action to insulin (Type II). Both types of Diabetes Mellitus can pose a serious threat to patients' health concerning the cardiovascular system, kidneys, and extremities such as the feet [1]. According to the World Health Organization (WHO), this disease has been dramatically spreading and growing worldwide with an estimation of 422 million adults who live with diabetes in 2014, compared to 108 million adults in 1980 [2]. One of the most dangerous symptoms of this disease is foot complications. Around 15 to 25% of diabetic patients are going to suffer from foot complications at a later stage of the disease [3]. These complications occur as a consequence of infection, peripheral ischemia, and ulceration in the foot [4, 5]. Foot ulcer happens mainly because diabetes introduces peripheral neuropathy, which affects the ability of the foot to feel and sense. That being considered, any injury in the foot can go unnoticed [6, 7]. Pre-signs for such complications include fissures, blisters, abundant callus formation, redness, and increased temperature regions [7]. A physician can check and analyze these physical features in order to diagnose the case. Foot complications can severely develop and result in limb amputation within the foot or even death if left untreated (diabetic foot) [8]. In patients with Diabetes Mellitus disease, approximately 85% of all lower extremity amputations are preceded by foot ulcer [5].

Diabetic foot ulcer can be avoided or delayed if adequately treated at an early stage. Currently, the assessment of such foot complications is done frequently by clinicians through analyzing blood circulations, plantar foot pressure, and foot neuropathy [9, 10]. Moreover, specialist clinicians usually assess lower extremity vascular status using Doppler ultrasound. This allows the possibility of getting accurate analysis regarding the current situation of foot ulcers and its risks [11]. However, patients are forced to go for frequent visits to doctors for diabetic foot assessment, which is considered intrusive and costly. In addition, self-assessment is considered difficult because it depends on the knowledge of patients with this disease, and on the usage of medical equipment. The treatments for such complications are commonly associated with therapeutic footwear, foot education, and normal foot care [12]. For example, a modified walking apparatus is used to provide consistent pressure relief at the diabetic patient's foot. Thus, the prevention of more developed stages of current foot complications situation can be maintained and even healed [13].

The occurrence of diabetic foot complications is often related to the plantar region temperature distribution. Increased temperature may be present in the foot a week before a neuropathic ulcer appears [14]. Researchers often use technologies such as the liquid crystal thermography (LCT) and infrared (IR) thermography to demonstrate the temperature variations [15]. LCT is a color representation proportional to the temperature of the in-contact foot surface with the thermochromic liquid crystal [16]. However, the infrared (IR) thermal imaging is much preferable because of being a non-invasive technology that acquires thermal images based on the heat emitted from the body. Infrared radiations are waves from the electromagnetic spectrum with a range of 760 nm to 1 mm [17]. This technology has made it possible to measure any increased temperature that occurs in some regions within the foot. A 1 °C temperature increase within the foot over the normal foot mean temperature requires an accurate assessment in order to decide whether it is a normal increase or an occurrence of foot ulcers [12, 18, 19]. Moreover, temperature differences of more than 2.2 °C between a region on one foot and the same region on the contra-lateral foot are considered Hyperthermia [14, 19]. Monitoring

such differences through thermal images proved to be an efficient way of detecting diabetic foot ulceration.

The aim of this work is to build an ulcer detection/indication system based on a mobile thermal camera and a mobile application. The proposed system would serve as a self-monitoring tool with a mobile app giving diabetic patients the ability to self-check their extremities for any possible ulcer, without the need for frequent visits to the diabetic clinic. The proposed system was implemented using a mobile application where thermal images were acquired, processed, and analyzed for any possible ulceration. Two image-processing techniques were deployed to detect possible ulcers automatically: the Otsu thresholding techniques and the point-to-point difference techniques. Both techniques were tested on thermal images. The implementation of the image processing algorithms was done using MATLAB mobile (Mathworks, Inc.). It was also complied into Java, and a mobile application was built for this purpose.

## Methods

The proposed system consists of a hardware part, which is mainly a mobile thermal image acquisition camera and a smart phone, along with image processing and analysis software. The entire software was run on MATLAB and was later implemented on a mobile phone through MATLAB Mobile Android application. After that, the entire software was compiled into Java code to build a complete and integrated application with user interface.

### Thermal image acquisition system

#### *Thermal imaging system*

The thermal image acquisition system, a Smartphone-based system, consists of an infrared (IR) thermal camera, the FLIR ONE (FLIR Systems), shown in Fig. 1. This camera was connected and running on Samsung Galaxy S6 Edge Plus smart phone. FLIR ONE consists of two cameras; Lepton camera, which has a compact long-wave infrared sensor for acquiring thermal images, and a standard camera that provides standard physical details to the raw thermal image. Considering the specifications of this camera, few parameters should be taken into account before applying further analysis on images: scene temperature range, sensitivity, resolution, and emissivity. As shown in Table 1, this IR camera detects temperatures that fall in the range of  $-20$  to  $120$  °C,



**Fig. 1** FLIR ONE Infrared Thermal Camera

**Table 1** FLIR ONE complete specifications

Cameras	Lepton and standard VGA
Scene temperature range	-20 to 120 °C
Operating temperature	0 to 35 °C
Sensitivity	0.1 °C
Resolution	160 × 120

with sensitivity in detection of 0.1 °C. FLIR ONE images resolution is not considered the best compared to high end FLIR devices designed for the same purpose. However, as a Smartphone thermal camera, it does provide good images with 160 × 120 resolution [20].

Regarding the emissivity of objects, FLIR ONE cameras automatically calibrate the scene temperature in order to provide the highest possible accuracy. In this regard, the camera calculates the emissivity of objects, the distance, and the reflected temperature, and then it returns the actual temperature of the object. The accuracy of the FLIR ONE camera and the calibration process have been tested by researchers through placing a reference object with a known temperature and emissivity, such as a blackbody device (Omega BB701), which has 1.0 emissivity and a pre-assigned temperature, in the field-of-view of the camera while conducting a human subject test. Thus, the actual temperature measurements from the camera could be compared with much more accurate devices such as FLIR E60 and IR thermometer (Omega OSXL450) before and after manual calibration procedures. The results showed that both the FLIR E60 and Omega OSXL450 IR thermometer measurements were close to each other and were improved by the calibration process, while FLIR ONE measurements remained the same. FLIR ONE accuracy resulted in having ≈ 2 °C more temperature compared to the other accurate devices while observing the measurements [21], meaning that it was with around ± 5% accuracy in temperature readings. This can be considered a good background for our proposed techniques and analysis as a smart-phone thermal camera for early detection purposes. The complete system with a test image is shown in Fig. 2. The use of FLIR ONE camera requires an application which is available for free on Google play store.

#### ***Image acquisition and measurement procedure***

The images acquired by FLIR ONE camera were stored in the Smartphone in Joint Photographic Experts Group (JPEG) format. FLIR ONE fused the standard image with the thermal image through Multi Spectral Dynamic Technology (MSX). This was done to provide physical details to the raw thermal image, and therefore, resulted in a better vision as RGB scaled images [20]. In addition, each thermal image was acquired along with a temperature matrix that represents the exact prevalence of temperature within the image. As shown in Fig. 3, a cold towel was held behind the plantar feet to ensure a homogeneous cold background that could be accurately separated from the foreground, which are the plantar feet. Patients are advised to sit and relax for around 3 min in order to maintain stable blood flow within their plantar feet. Furthermore, for accurate analysis, the feet should be placed over a non-reflective surface such as a velvet fabric. Moreover, users are advised to maintain that their feet are located in the center of



**Fig. 2** The complete smartphone system along with FLIR ONE app

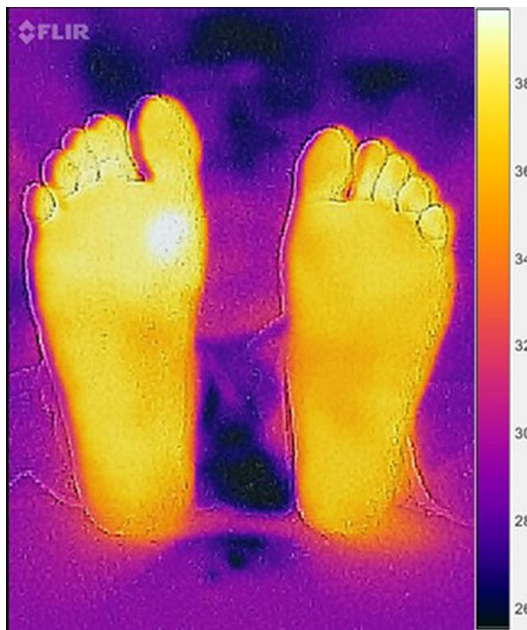


**Fig. 3** Test image acquired by the camera following the acquisition procedure

the field-of-view of the camera for accurate segmentation results. The objects taken to test the algorithms were non-diabetic feet images obtained at room temperature (20–25 °C). To illustrate abnormalities in the feet, we simulated an ulcer by heating coins

and materials with different shapes and sizes to a certain temperature. Heating a coin and placing it near the surface of the foot increased the temperature values of the region by around +2.2 °C higher than the normal plantar feet temperature. As previously discussed, Hyperthermia occurs if there is a temperature increase of more than 2.2 °C in some regions within the foot compared to other regions [14, 19].

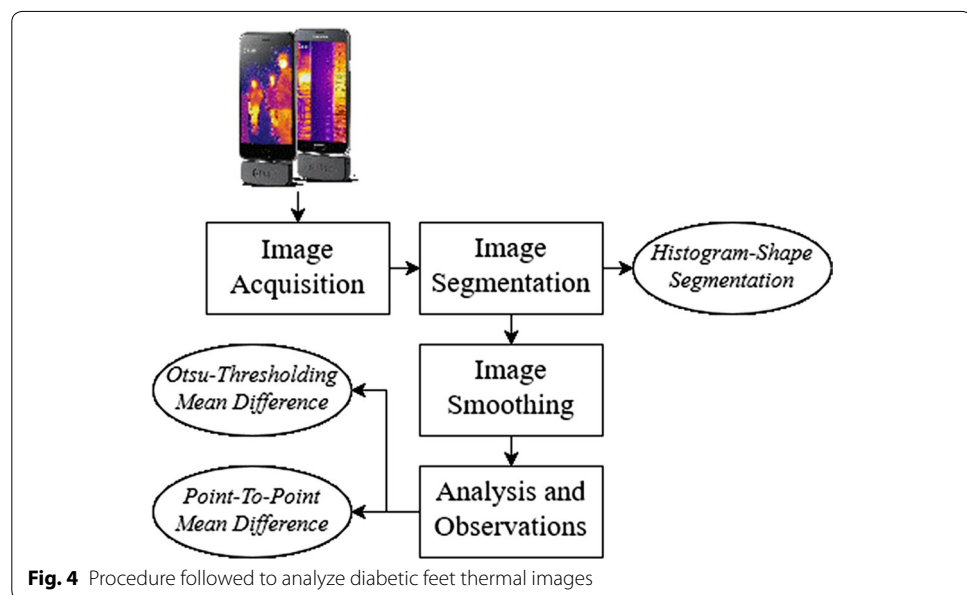
### **Image analysis and interpretation**

The recorded thermal image was a gray scale image and further analysis and interpretation was conducted. As shown in Fig. 4, the proposed system incorporates various image processing steps including image segmentation, image smoothing, and analysis and observation. The last step was implemented using two techniques: Otsu thresholding mean difference and point-to-point mean difference.

### **Image segmentation**

The purpose of image segmentation is the extraction of certain objects or segments from original images. In this work, image segmentation was performed twice. The first one was to extract the object of interest from the thermal image, which are the diabetic feet, while the second one was to extract and identify possible ulcer in the diabetic feet. The first segmentation procedure was applied on the raw thermal image with the purpose of extracting the feet from the background, which was in this case the cold towel behind the feet. The technique used for the segmentation process is called Histogram shape thresholding. This technique was applied indicating that thermal images acquired following the acquisition protocol mentioned above resulted in a bi-modal histogram with two peaks, as shown in Fig. 5. The histogram shape thresholding requires finding the optimum threshold to separate the background (dark or cold region) from the foreground (warm object) [22].

In the histogram representation of a sample image shown in Fig. 5, there are two regions that indicate the presence of two different objects; dark and bright objects [22].



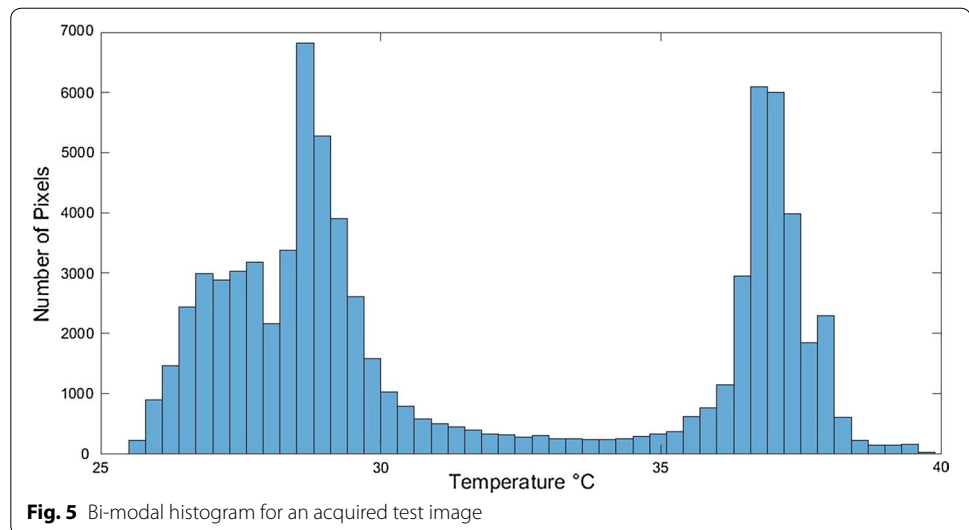


**Fig. 5** Bi-modal histogram for an acquired test image

The optimum threshold was calculated using Otsu methods [23]. The calculated threshold was used to assign labels for the background (below threshold) and the foreground (above threshold) pixels in the image. Moreover, the probability of gray level  $i$  is represented by the following equation:

$$p_i = n_i/N \quad (1)$$

where  $n_i$  is the number of pixels at level  $i$  and  $N$  is the total number of pixels.

Then, the pixels of the images were separated into two regions:  $R_1$  with gray levels  $[0, 1, \dots, t]$  and  $R_2$  with gray levels  $[t + 1, \dots, L - 1]$ , where  $t$  is the threshold value. The means of class  $R_1$  and  $R_2$  are given by

$$u_1 = \sum_{i=0}^t ip_i/w_1 \quad (2)$$

$$u_2 = \sum_{i=t+1}^{L-1} ip_i/w_2 \quad (3)$$

where  $w_1$  and  $w_2$  are the gray level probability distributions for the two regions. The total mean of gray levels is given by

$$u_T = w_1 u_1 + w_2 u_2. \quad (4)$$

The within-region variance is given by:

$$\sigma_W^2 = \sum_{k=1}^M W_k \sigma_k^2 \quad (5)$$

where  $\sigma_k^2$  is each region variance value and given by:

$$\sigma_1^2 = \sum_{k=0}^t (t - u_1)^2 p_i / w_1 \quad (6)$$

$$\sigma_2^2 = \sum_{k=t+1}^{L-1} (t - u_2)^2 p_i / w_2 \quad (7)$$

The between-region variance is given by

$$\sigma_B^2 = w_1(u_1 - u_T)^2 + w_2(u_2 - u_T)^2 \quad (8)$$

Otsu method picks a threshold  $t$  by maximizing the between-region variance or minimizing the within-region variance. The total variance, which is the sum of the within-region variance and the between-region variance, is constant for different partitions.

$$t = \arg \max_{0 \leq t \leq L-1} \sigma_B^2(t) = \arg \min_{0 \leq t \leq L-1} \sigma_W^2(t) \quad (9)$$

In MATLAB, the function graythresh automatically find the parameter needed, which is the optimum threshold values  $t$ , which can separate the two intensity histogram regions. This parameter is given as a normalized value between 0 and 1 of the corresponding scene temperature. The outcome from Otsu thresholding technique was a binary image, with values from 0 to 1, of the segments needed for further analysis, which are the plantar feet.

#### ***Image smoothing***

The technique of Histogram shape segmentation resulted in a binary image of the segmented foreground, which were the plantar feet. However, some images are not easy to segment, especially if there are some parts within the image where the temperature of the background is close to the foreground temperature. As a result, dark objects are marked as bright objects and vice-versa. This affects any further image processing analysis of the plantar feet image. Therefore, image-smoothing techniques were performed to avoid such errors.

At the beginning, borders clearing technique was used to remove any objects that are connected to the border of the image, or even separated in different places within the image. This was done by suppressing any light structures and removing them from the surrounding border of the image. Then, segments' smoothing was performed to erode the resulting image with a diamond-structuring element. The element used had a single pixel distance from the origin of its structure to the points of the diamond. This prepares the feet segment to be smoothed at the edges and ensures that no unconnected objects are taking place in the image. Finally, the binary segment created might include some interior gaps, therefore, these gaps were filled with hole-filling objects [24]. The plantar feet segments were ready to be analyzed for any occurrence of diabetic feet abnormalities.

#### ***Analysis and observation***

After segmenting the plantar feet image, further processing was performed to identify any possible ulcers or occurrence of hyperthermia (a 2.2 °C difference) [12, 18, 19]. Two

techniques were used for this purpose, Otsu thresholding technique (discussed in the previous section) and point-to-point difference technique.

#### Otsu thresholding technique

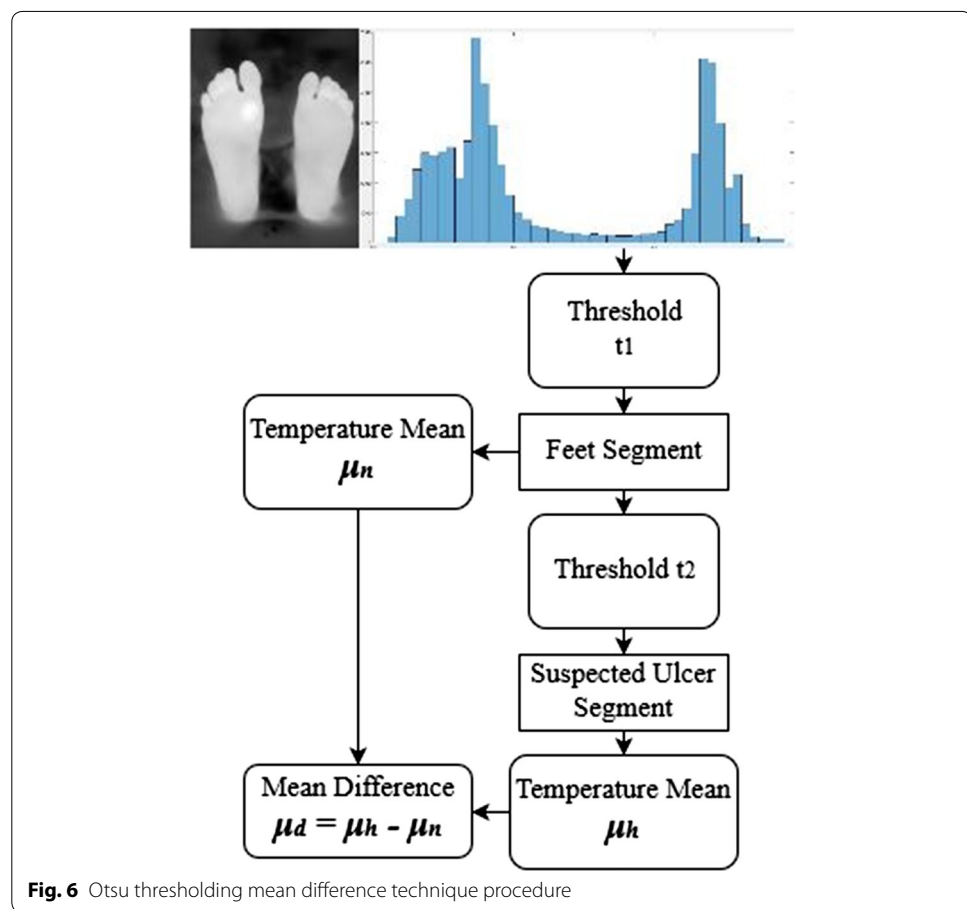
Shown in Fig. 6, this procedure is the same as the thresholding technique applied previously to extract the plantar feet. Here it was performed only on the pixels forming the plantar feet that might have any possible ulceration. Therefore, the feet were now the background and the possible ulcers were the foreground. After thresholding was performed, an independent t test was done to check if the difference between the foreground (suspected ulcer) mean temperature and the background (diabetic feet) mean temperature was greater than 2.2. If the difference was greater than 2.2, then the foreground region was considered as a possible ulcer location.

The complete procedure for the proposed algorithm is illustrated on Fig. 7.

#### Point-to-point mean difference

Another technique was applied for the detection of any possible ulcer, which is called the point-to-point mean difference shown in Fig. 8 [19]. In this technique, the pixel-to-pixel temperature difference between both feet was calculated.

The processed image included both feet; therefore, it was automatically divided into two equal parts; one for the left foot and one for the right foot. As previously mentioned

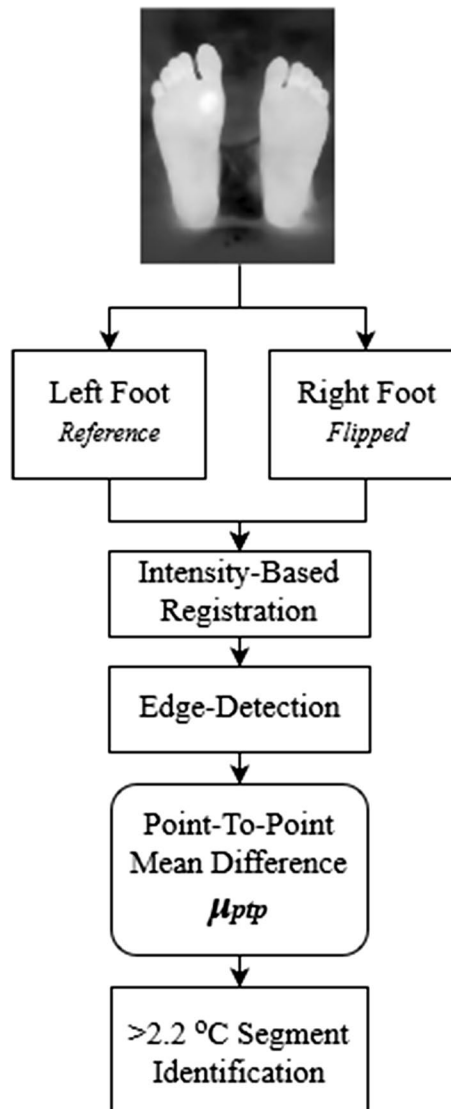


**Algorithm 1 Otsu Thresholding Mean Difference**

```

1: procedure OTSU THRESHOLDING ALGORITHM
2:   Temperature Matrix .m  $\leftarrow$  Loads the temperature matrix file
3:   Normalizing Values  $\leftarrow$  Converting each temperature value to a scale from 0 to 1
4:   graythresh: Threshold t1  $\leftarrow$  Observes the "Level" value of the optimum threshold
5:   imbinarize: Feet Segment  $\leftarrow$  Applies the threshold t1 value
6:   Threshold t2  $\leftarrow$  Uses a specific pre-determined threshold value, always higher than t1
7:   imbinarize: Hot Segment  $\leftarrow$  Applies the threshold t2 value
8:   Smoothing feet segment  $\leftarrow$  Applying "imclearborders", "imerode", and "imfill" commands
9:   Mean Values Observations  $\leftarrow$  Obtaining the mean temperature values for both segments
10:  diffinmeans  $\leftarrow$  Finds the mean difference between the two mean values
11:  if diffinmeans  $\geq 2.2$  then
12:    HighTemperature – Ulceration.
13:  if diffinmeans  $< 2.2$  then
14:    NoRiskOfUlceration.

```

**Fig. 7** The complete algorithm followed using Otsu thresholding technique**Fig. 8** Point-to-point mean difference technique procedure

in the acquisition procedure, users are advised to maintain that their feet are in the center of the camera field-of-view for accurate cutting and analysis results. The left foot segment was chosen as the reference foot (the right foot can also be chosen). The deployed technique requires both feet to be aligned together. Hence, two steps were performed; the first one was flipping the right foot to make both feet look identical and the second step was image registration to align both feet together. The adopted image registration technique was the intensity-based registration [25]. Image registration allows both images (left foot and right foot) to be aligned in a way that makes them spatially corresponding to each other [26].

The next step was implementing an edge detection technique to remove the edges from the left and right feet images. The edge detection was applied using the Sobel operators [27]. The resulting image was the difference between the left and the right foot, and pixels with a temperature difference greater than 2.2 °C were identified using thresholding. The resulting image could identify any possible ulcers.

The complete procedure followed in this technique's algorithm is shown in Fig. 9.

## Results

The proposed techniques were tested by acquiring thermal images from the feet of a healthy subject. The ulcers were simulated by heating a metal object (a coin) with a diameter of around 1.5 cm. The heated object was placed on the skin to raise its temperature and emulate the possible ulcer (hyperthermia). Eight test images were acquired, one without any skin heating (test image 1) and the seven other images with the feet heated into different locations. The thermal camera temperature measurement was used to make sure that the heated region temperature was more than 2.2 °C higher than the normal feet temperature. A test image illustrating the effect of image smoothing techniques is shown on Fig. 10. A hot object (fingers) is shown in the background, which illustrates an error case in the segmentation and analysis of diabetic foot. Further analysis based on the wrongly segmented plantar feet (Fig. 10b) results in missing the accurate true temperature values for feet and hot regions, therefore, wrong indication of the feet abnormalities situation takes place.

---

### Algorithm 1 Point-To-Point Mean Difference

---

```

1: procedure POINT-TO-POINT ALGORITHM
2:   Temperature Matrix .m  $\leftarrow$  Loads the temperature matrix file
3:   Normalizing Values  $\leftarrow$  Converting each temperature value to a scale from 0 to 1
4:   graythresh: Threshold t1  $\leftarrow$  Observes the "Level" value of the optimum threshold
5:   imbinarize: Feet Segment  $\leftarrow$  Applies the threshold t1 value
6:   Smoothing feet segment  $\leftarrow$  Applying "imclearborders", "imerode", and "imfill" commands
7:   Separating feet  $\leftarrow$  Cutting the image into equal halves
8:   fliplr: right foot  $\leftarrow$  Flips the right foot segment
9:   imwarp: intensity-based registration  $\leftarrow$  Aligns the right foot with the left foot segment
10:  edge: sobel operator  $\leftarrow$  Extracts the edges from the two segments
11:  Absolute difference  $\leftarrow$  Finding the absolute difference between each pixel on both feet
12:  Mean difference  $\leftarrow$  Obtaining the mean temperature difference between the segments
13:  if Meandifference  $\geq 2.2$  then
14:    HighTemperature – Ulceration.
15:  if Meandifference  $< 2.2$  then
16:    NoRiskOfUlceration.

```

---

**Fig. 9** The complete algorithm followed using point-to-point technique

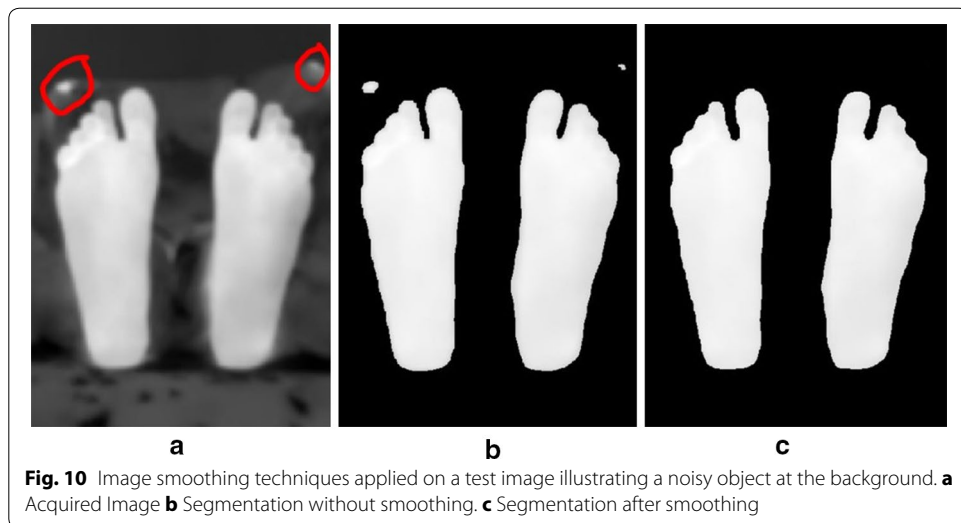


Figure 11 shows the results from the first four test images, chosen for display, using the Otsu thresholding technique for analysis and observation. Table 2 shows the average temperatures recorded in the identified background (Feet) and foreground (Suspected ulcer) regions in test images 2, 3, and 4. Moreover, the other four test images observations are recorded and mentioned on the table.

Furthermore, the algorithm was tested by adding additional six test images with various shapes simulating ulcer. The shapes used were a small coin of 0.5 cm diameter, a rectangle of 2 cm length, a small half-shaped ring, a 3.5 cm length rectangle, a 2.5 cm diameter coin, and a 1 cm diameter coin. Figure 12 shows the detection results following Otsu thresholding procedure.

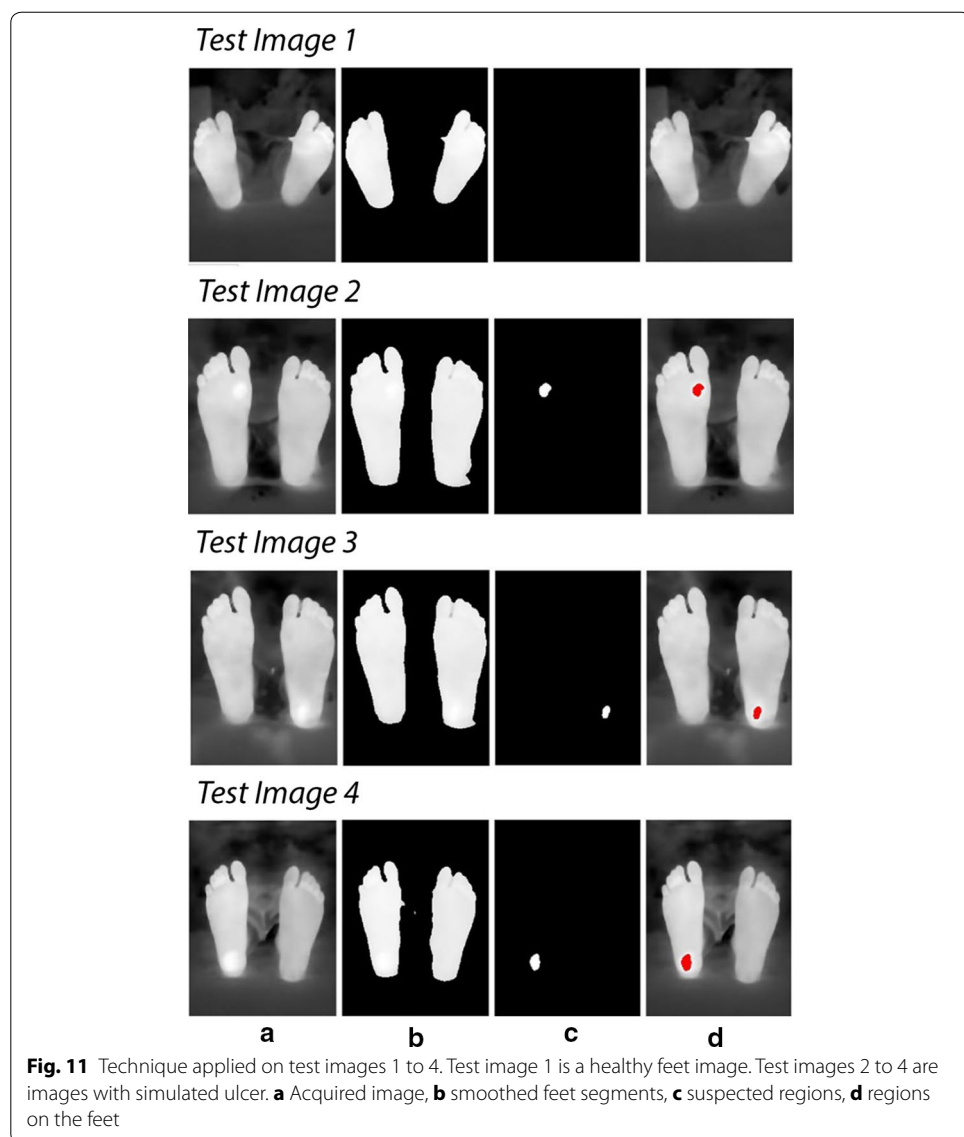
The same test images were used to test the proposed system with the technique of point-to-point difference for image analysis and interpretation. Figure 13 shows an example of the initial steps of this technique which involved image flipping and registration (flipping was done for the right foot). The image splitting and edge detection are shown in Fig. 14.

The results of the point-to-point difference method implemented are shown in Fig. 15 for test images 1 to 4 respectively.

Moreover, the same six test images with the different shapes and sizes were analyzed by the point-to-point algorithm, and the results are shown on Fig. 16.

## Discussion

The main objective of this research was to build a thermal imaging system based on smart phone. The proposed system incorporated the hardware as well as the necessary image processing and interpretation software techniques. According to the obtained results, the proposed system has successfully identified regions with hyperthermia with temperature gradient greater than 2.2 °C which is considered as the value that can be used to identify possible ulcers [14, 19]. The proposed system can also be used to identify temperatures less than this value, but they are not considered as possible ulcers according to the literature. The testing procedure was implemented on four images; one with

**Table 2** Mean temperature values ( $\mu_n$ ,  $\mu_h$ , and  $\mu_d$ ) for test images 1 to 8

Observation	Image 1 (°C)	Image 2 (°C)	Image 3 (°C)	Image 4 (°C)	Image 5 (°C)	Image 6 (°C)	Image 7 (°C)	Image 8 (°C)
Feet mean temperature ( $\mu_n$ )	33.2	36.9	35.5	35.3	36.2	36.3	36.2	34.8
Suspected region mean temperature ( $\mu_h$ )	35.0	39.4	38.0	37.8	38.4	38.5	38.6	37.0
Mean difference ( $\mu_d$ )	1.8 (No Ulcer)	2.5	2.5	2.5	2.2	2.2	2.4	2.2

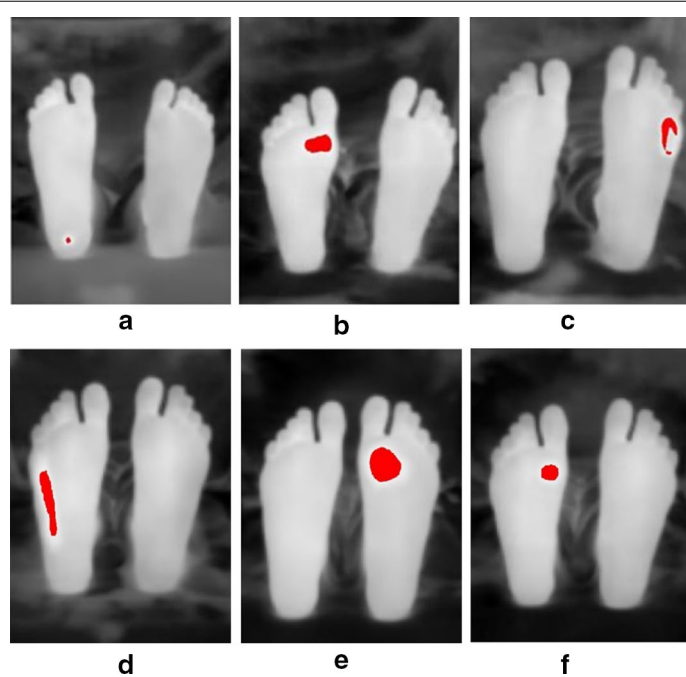


**Fig. 12** Additional six test images with various shapes to illustrate ulcer. **a** 0.5 cm diameter coin. **b** 2 cm rectangle. **c** Half-shaped ring. **d** 3.5 cm rectangle. **e** 2.5 cm diameter coin. **f** 1 cm diameter coin

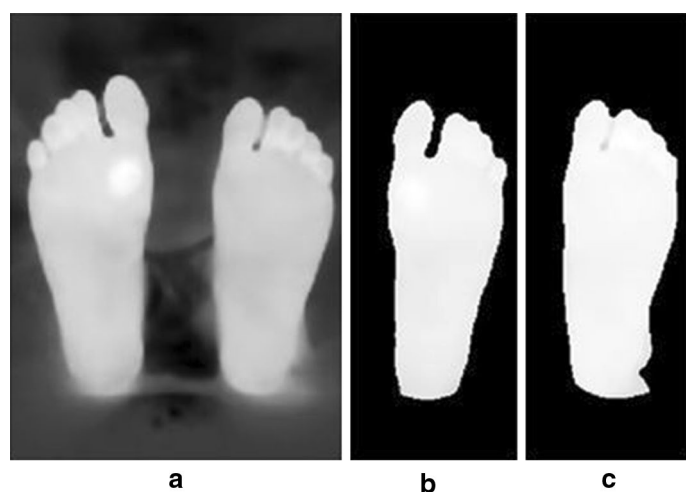


**Fig. 13** Image flipping and registration applied on testi mage 2. **a** Acquired image. **b** Right foot flipped and registered. **c** Left foot (reference)

no temperature gradient introduced and the other three images with thermal gradient at three different locations. The two techniques deployed for image interpretation and analysis were successful in identifying regions with thermal gradient representing possible ulcers. The histogram thresholding techniques used the statistical t-test to verify if the difference between the background and the potential region were statistically different with the mean values listed in Table 2.

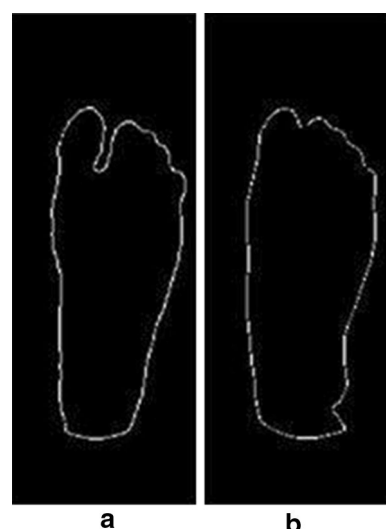
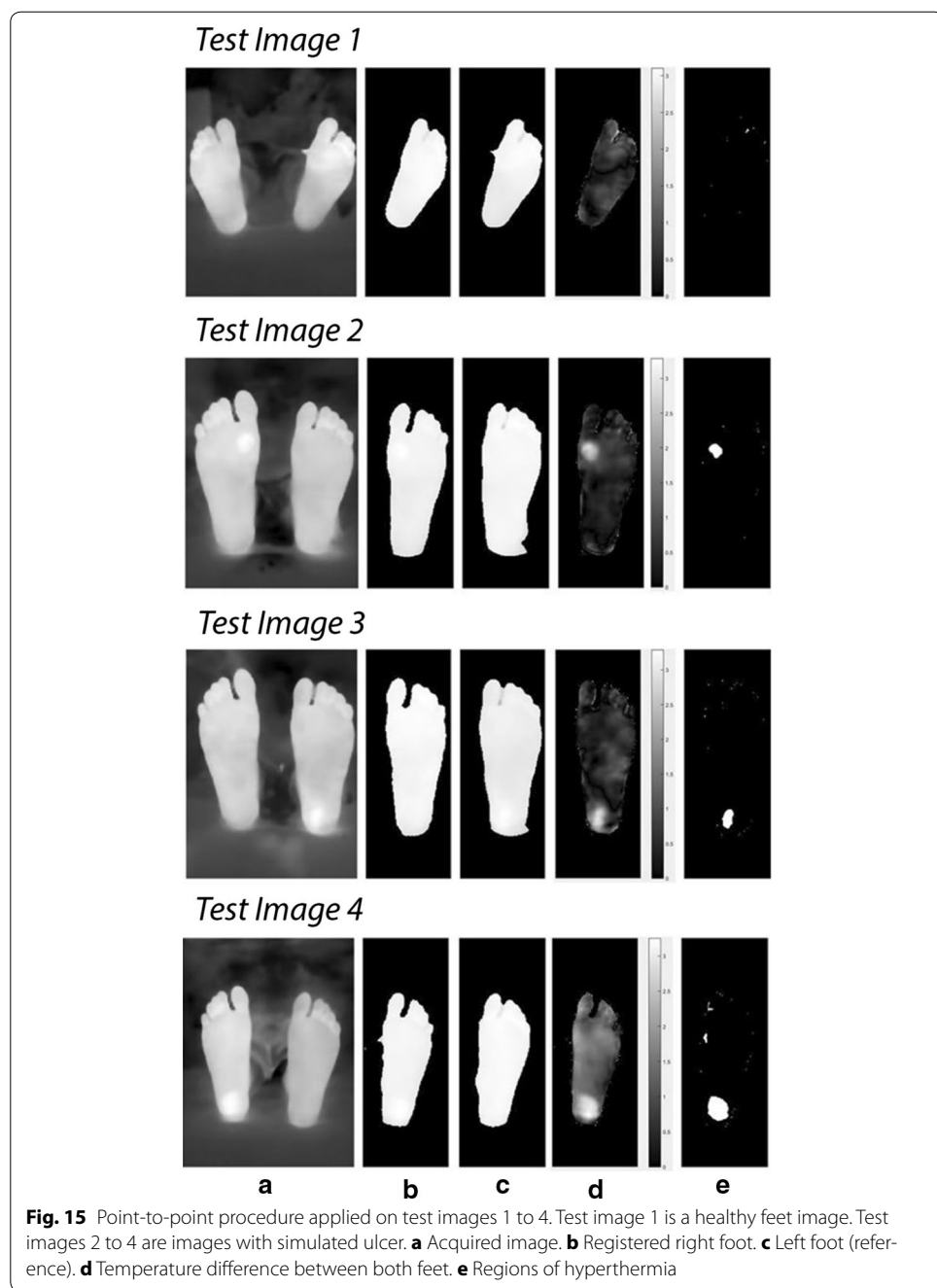


**Fig. 14** Edge detection technique. **a** Registered right foot contours. **b** Left foot contours

The second technique used for analysis and interpretation made use of both legs to be a reference for the background. This technique was used by Vilchuaman et al. [19]. The only difference in this work is that we excluded the edges of the feet using edge detection techniques. This was done because it appeared that the images processed had a high temperature gradient at the edges, which could introduce a kind of false positives. This could be attributed to the processing techniques used, such as image smoothing and image registration. The generated images were for the difference between the two images of the left and right feet as shown in Fig. 14. The average temperature in the difference images generated were 2.4, 2.5, 2.6, 2.2, 2.3, 2.6, and 2.3 °C, for test images 2 to 8, respectively. While in using the Otsu thresholding technique, the average difference between the averages of the background and the foreground were 2.5, 2.5, and 2.5 °C, 2.2, 2.2, 2.4, and 2.2 °C, for test images 2 to 8, respectively. Table 3 shows the complete observations obtained from the actual camera detector, Otsu thresholding, and point-to-point techniques. The actual camera detector values are obtained from the FLIR ONE app direct measurements. Moreover, the six additional test images used illustrated the possibility of detection for various shapes that simulate ulcer. Both algorithms were successful in detecting the shape of the different material used. The current developed techniques do not depend on the shape of ulcer, they depend on the temperature pixels that lies within the suspected region.

The entire system was implemented on a Smartphone under MATLAB mobile with processing on a cloud MATLAB server. The use of MATLAB mobile provides the flexibility to do further processing, store the data on a cloud account, and build the necessary interface.



### Conclusion and future work

The proposed system provides a framework to build a complete mobile system that can help diabetic patients self-check their feet for any possible ulcers. The system provides only an indicative tool, not a diagnostic tool, as the final diagnosis should be done by the physician (the gold standard). The future work requires upgrading the system with an advanced thermal camera with higher image quality that can be connected to a mobile

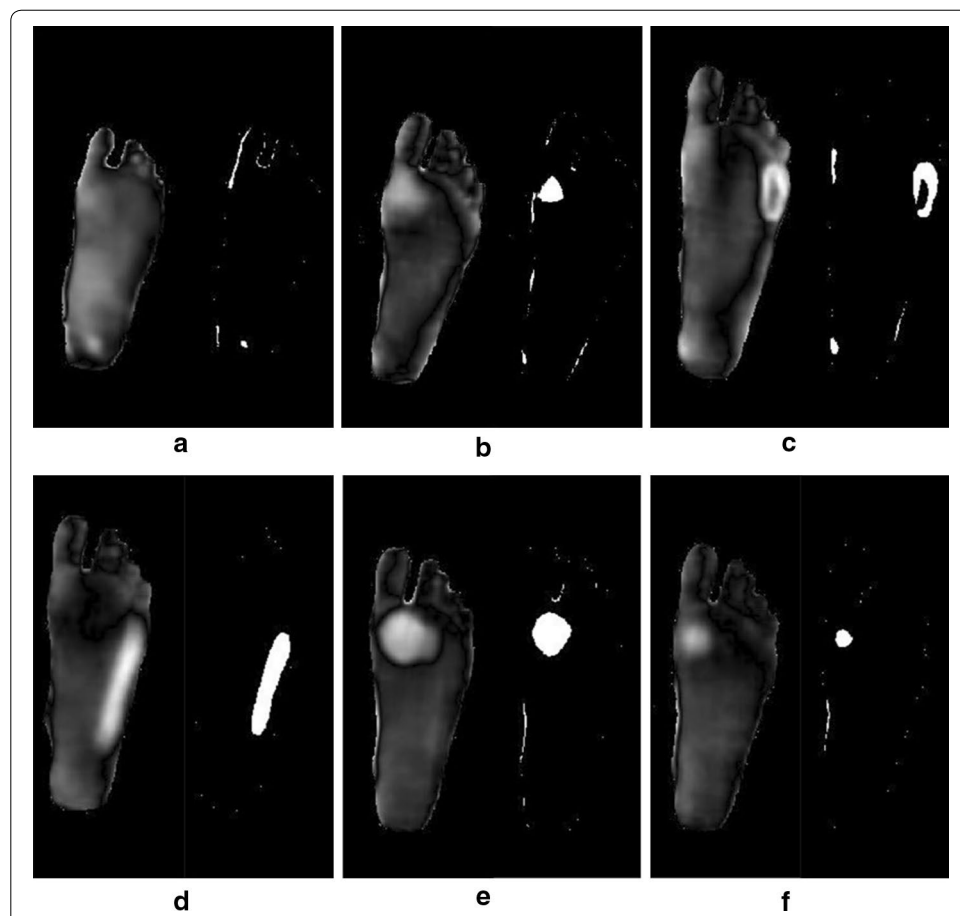


**Fig. 16** Six test images with different shapes to illustrate ulcer. **a** 0.5 cm diameter coin. **b** 2 cm rectangle. **c** Half-shaped ring. **d** 3.5 cm rectangle **e**. 2.5 cm diameter coin. **f** 1 cm diameter coin

**Table 3 Complete observations for test images 1 to 8**

Observations	Image 1 (°C)	Image 2 (°C)	Image 3 (°C)	Image 4 (°C)	Image 5 (°C)	Image 6 (°C)	Image 7 (°C)	Image 8 (°C)
Actual camera measured difference	1.7	2.4	2.4	2.5	2.3	2.2	2.5	2.3
Otsu thresholding mean difference	1.8	2.5	2.5	2.5	2.2	2.2	2.4	2.2
Point-to-point mean difference	0	2.4	2.5	2.6	2.2	2.3	2.6	2.3

in order to perform the necessary processing. Further testing and validation of the system should be performed under clinical environment, which was not possible at this stage due to the strict regulations applied. Moreover, this work can be extended to other possible applications such as wound healing and trauma monitoring.

#### Authors Contributions

LF suggested the idea, the design of the study, and the methodology. He also contributed to the writing of the manuscript. MA did the image processing and image analysis, and manuscript writing. JN did the coding and the mobile interface. AS and BM did the literature survey and conducted the measurements. MG contributed to the image processing part. All the authors read and approved the final manuscript.

#### Author details

<sup>1</sup> Electrical and Computer Engineering Department, Abu Dhabi University, 59911 Abu Dhabi, United Arab Emirates. <sup>2</sup> Biomedical Engineering Department, Jordan University of Science and Technology, Irbid 22110, Jordan.

#### Acknowledgements

This work is supported by Abu Dhabi University's, Office of Research and Sponsored Programs.

#### Competing interests

The authors declare that they have no competing interests.

#### Ethics approval and consent to participate

Not Applicable.

#### Publisher's Note

Springer Nature remains neutral with regard to jurisdictional claims in published maps and institutional affiliations.

Received: 25 May 2017 Accepted: 25 September 2017

Published online: 03 October 2017

#### References

- Chieng M, Chuan O, Wee T, Joseph A, Mun Y, Hejar A. Prevalence of metabolic syndrome in type 2 diabetic patients: a comparative study using WHO, NCEP ATP III, IDF and Harmonized definitions. *Sci Res.* 2013;5(10):1689–96.
- World Health Organization. Global report on diabetes. 2016. <http://www.who.int>.
- Chanjuan L, Van Netten J, Van Baal J, Bus S, van der Heijden F. Automatic detection of diabetic foot complications with infrared thermography by asymmetric analysis. *Biomed Opt.* 2015;20(2):026003.
- Apelqvist J, Larsson J. What is the most effective way to reduce incidence of amputation in the diabetic foot? *Diabetes Metab Res Rev.* 2000;16(1):S75–83.
- Boulton A, Vileikyte L, Tennval G, Apelqvist J. The global burden of diabetic foot disease. *Lancet.* 2005;366:1719–24.
- Rebolledo F, Teran T, Escobedo J. The pathogenesis of the diabetic foot ulcer: prevention and management. In: Dinh T. Global perspective on diabetic foot ulcerations. InTech. 2011. p. 155–182.
- Chanjuan L, van der Heijden F, Klein M, van Baal J, Bus S, van Netten J. Infrared dermal thermography on diabetic feet soles to predict ulcerations: a case study. Advanced biomedical and clinical diagnostic systems XI. SPIE. 2013; doi:10.1117/12.2001807.
- Diabetic foot problems: prevention and management. NICE Guidelines NG19. <https://www.nice.org.uk/guidance/ng19>. Accessed 26 August 2015.
- Bharara M, Schoess J, Armstrong D. Detecting inflammation in the acute diabetic foot and the foot in remission. *Diabetes Metab Res Rev.* 2012;28(S1):15–20. doi: 10.1002/dmrr.2231.
- Schaper N, van Netten J, Apelqvist J, Lipsky B, Bakker K. Prevention and management of foot problems in diabetes: a summary guidance for daily practice, based on the IWGDF guidance documents. *Diabetes Metab Res Rev.* 2016;32(S1):7–15. doi:10.1002/dmrr.2695.
- Singh N, Armstrong D, Lipsky B. Preventing foot ulcers in patients with diabetes. *JAMA.* 2005;293(2):217–28.
- Cajácuri L. Early diagnostic of diabetic foot using thermal images. HAL. <https://tel.archives-ouvertes.fr/tel-01022921/document>. Accessed 11 July 2014.
- Morbach S, Hartmann P. Diagnosis, treatment, and prevention of the diabetic foot syndrome. HARTMANN. Heidenheim D-89522; 2004.
- van Netten J, van Baal J, Chanjuan L, van der Heijden F, Bus S. Infrared thermal imaging for automated detection of diabetic foot complications. *Diabetes Sci Technol.* 2013;7(5):1122–9.
- Hernandez-Conteras D, Peregrina-Barreto H, Rangel-Magdaleno J, Gonzalez-Bernal J. Diabetic foot and infrared thermography. *Infrared Phys Technol.* 2016;78:105–17.
- Bharara M, Cobb JE, Claremont DJ. Thermography and thermometry in the assessment of diabetic neuropathic foot: a case for furthering the role of thermal techniques. *Int J Low Extrem Wounds.* 2006;5(4):250–60.
- Cho S, Shin M, Kyung Y, Seo J, Lee Y, Park C, Chung J. Effects of infrared radiation and heat on human skin aging in vivo. *Invest Dermatol Symp Proc.* 2009;14:15–9.

18. Peregrina-Barreto H, Morales-Hernandez L, Rangel-Magdaleno J, Avina-Cervantes J, Ramirez-Cortes J, Morales-Caporal R. Quantitative estimation of temperature variations in plantar angiosomes: a study case for diabetic foot. *Comput Math Methods Med.* 2014; doi:[10.1155/2014/585306](https://doi.org/10.1155/2014/585306).
19. Vilcahuaman L, Harba R, Canals R, Zequera M, Wilches C, Arista M, Torres L, Arbanil H. Automatic analysis of plantar foot thermal images in at-risk Type II diabetes by using an infrared camera. *IFMBE Proc.* 2015;51:228–31.
20. FLIR Systems. FLIR ONE. <http://www.flir.eu/flirone/ios-android>. Accessed 16 June 2015.
21. Curran A, Klein M, Hepokoski M, Packard C. Improving the accuracy of infrared measurements of skin temperature. *Extreme Physiol Med.* 2015. doi:[10.1186/2046-7648-4-S1-A140](https://doi.org/10.1186/2046-7648-4-S1-A140).
22. Moallem P, Razmjoo N. Optimal Threshold computing in automatic image thresholding using adaptive particle swarm optimization. *J Appl Res Technol.* 2012;10(5):703–12.
23. Dongju L, Jian Y. Otsu method and K-means. *IEEE Comp Soc.* 2009. doi:[10.1109/HIS.2009.74](https://doi.org/10.1109/HIS.2009.74).
24. MATLAB Image processing toolbox. MathWorks. <http://www.mathworks.com/examples>. Accessed 1994.
25. Valsecchi A, Damas S, Santamaria J. Evolutionary intensity-based medical image registration: a review. *Curr Med Imag Rev.* 2013;9(4):283–97.
26. Medha V, Pardeep M, Hemant K. Image registration techniques: an overview. *Int J Sig Process Image Process Pattern Recognit.* 2009;2(3):11–28.
27. Gonzalez R, Woods R. Digital image processing. 3rd ed. London: Pearson Education; 2008.

Submit your next manuscript to BioMed Central  
and we will help you at every step:

- We accept pre-submission inquiries
- Our selector tool helps you to find the most relevant journal
- We provide round the clock customer support
- Convenient online submission
- Thorough peer review
- Inclusion in PubMed and all major indexing services
- Maximum visibility for your research

Submit your manuscript at  
[www.biomedcentral.com/submit](http://www.biomedcentral.com/submit)



See discussions, stats, and author profiles for this publication at: <https://www.researchgate.net/publication/271541388>

# Infrared Dermal Thermography on Diabetic Feet Soles to Predict Ulcerations: a Case Study

Conference Paper in Proceedings of SPIE - The International Society for Optical Engineering · March 2013

DOI: 10.1117/12.2001807

---

CITATIONS

55

READS

1,148

6 authors, including:



Chanjuan Liu

University of Twente

7 PUBLICATIONS 474 CITATIONS

[SEE PROFILE](#)



Jeff G van Baal

Ziekenhuisgroep Twente

32 PUBLICATIONS 1,232 CITATIONS

[SEE PROFILE](#)



Sicco A Bus

Academisch Medisch Centrum Universiteit van Amsterdam

210 PUBLICATIONS 14,456 CITATIONS

[SEE PROFILE](#)

# Infrared Dermal Thermography on Diabetic Feet Soles to Predict Ulcerations: a Case Study

Chanjuan Liu<sup>a</sup>, Ferdi van der Heijden<sup>a</sup>, Marvin E. Klein<sup>c</sup>, Jeff G. van Baal<sup>b</sup>, Sicco A. Bus<sup>b,d</sup>  
and Jaap J. van Netten<sup>b</sup>

<sup>a</sup>SIGNALS AND SYSTEMS GROUP, FACULTY ELECTRICAL ENGINEERING, MATHEMATICS AND COMPUTER SCIENCE, UNIVERSITY OF TWENTE, THE NETHERLANDS

<sup>b</sup>DIABETIC FOOT UNIT, DEPARTMENT OF SURGERY, HOSPITAL GROUP TWENTE, ALMELO, THE NETHERLANDS

<sup>c</sup>DEMCON ADVANCED MECHATRONICS BV, OLDENZAAL, THE NETHERLANDS

<sup>d</sup>DEPARTMENT OF REHABILITATION, ACADEMIC MEDICAL CENTER, UNIVERSITY OF AMSTERDAM, THE NETHERLANDS

## ABSTRACT

Diabetic foot ulceration is a major complication for patients with diabetes mellitus. If not adequately treated, these ulcers may lead to foot infection, and ultimately to lower extremity amputation, which imposes a major burden to society and great loss in health-related quality of life for patients. Early identification and subsequent preventive treatment have proven useful to limit the incidence of foot ulcers and lower extremity amputation. Thus, the development of new diagnosis tools has become an attractive option. The ultimate objective of our project is to develop an intelligent telemedicine monitoring system for frequent examination on patients' feet, to timely detect pre-signs of ulceration.

Inflammation in diabetic feet can be an early and predictive warning sign for ulceration, and temperature has been proven to be a vicarious marker for inflammation. Studies have indicated that infrared dermal thermography of foot soles can be one of the important parameters for assessing the risk of diabetic foot ulceration. This paper covers the feasibility study of using an infrared camera, FLIR SC305, in our setup, to acquire the spatial thermal distribution on the feet soles. With the obtained thermal images, automated detection through image analysis was performed to identify the abnormal increased/decreased temperature and assess the risk for ulceration. The thermography for feet soles of patients with diagnosed diabetic foot complications were acquired before the ordinary foot examinations. Assessment from clinicians and thermography were compared and follow-up measurements were performed to investigate the prediction. A preliminary case study will be presented, indicating that dermal thermography in our proposed setup can be a screening modality to timely detect pre-signs of ulceration.

**Keywords:** Diabetic Foot Ulceration, Pre-Ulceration Detection, Telemedicine, Temperature, Infrared Imaging, Dermal Thermometry

## 1. INTRODUCTION

Diabetes Mellitus (DM) is one of the most common chronic disease worldwide and continues to increase in population and significance. There were 194 million people suffering from DM worldwide in 2004,<sup>1</sup> and this number is expected to grow to 439 million by 2030.<sup>2</sup> Vascular and neurological disorder in lower extremities is one of the common complications with DM. Approximately 15% to 25% of patients with DM eventually develop foot ulcers.<sup>3</sup> If not adequately treated, these ulcers may lead ultimately to total (or partial) lower extremity amputation. Approximately, foot ulceration causes 85% of all lower extremity amputations in patients with DM.<sup>4</sup> The onset of diabetic foot ulcers may be prevented by early identification and subsequent treatment of pre-signs of ulceration, such as callus formation, redness, fissures, and blisters. However, early identification depends on

---

Further author information: (Send correspondence to Chanjuan Liu)  
Chanjuan Liu: E-mail: c.liu@utwente.nl

frequent risk assessment, which is not always possible. Self-examination is difficult or impossible, due to the consequences of DM, and it is costly and not feasible to do frequent examination by health care professionals.

Thus, any initiative that may overcome these limitations, contribute to automated detection of the early warning signs, and be non-invasive, non-interactive and easy in use should be supported and implemented in diabetic foot care.<sup>5</sup> As to the knowledge of the author, there are four different imaging techniques that are used in detecting these pre-signs of ulceration to predict the diabetic foot ulceration, which are thermal imaging, foot sole scanning, photographic imaging, and hyperspectral imaging.<sup>6</sup> Among the four techniques, foot sole scanning requires patients to press the foot against the scanner, which will cause some unwanted pressure on the foot sole. Thus, a non-contact foot scanner is desirable to obtain a better view of the foot skin.

Pre-signs of ulceration in diabetic foot include redness, increased local skin temperature,<sup>5</sup> thickening of the skin, fissures, blisters and abundant callus formation, all of which are physical features that enable a physician to diagnose the foot and to locate risk areas.<sup>7-9</sup> Increased temperature can be obtained by thermal measurement and the physiological parameters, such as thickening of the skin and the skin spectral properties, can be achieved by hyperspectral image analysis. Besides, 3D surface reconstruction is also essential for detecting the pre-signs, which can reveal the local 3D deformations of the skin surface, and then provide the information about the surface textures. These textures are either caused by geometrical variations of the surface (e.g. papillary lines, fissures, abundant callus) or by radiometric variations (i.e. pigment variations).<sup>6</sup>

The ultimate objective of our project is to develop an intelligent telemedicine monitoring system that can be deployed at the patients' home environment for frequent examination of the patients' feet, to detect pre-signs of ulceration in a timely manner. As the first step, an experimental setup consisting three modalities, which are thermal imaging, hyperspectral imaging and photometric imaging was built.

The study presented in this paper will focus on the preliminary analysis on the acquired thermal images with our setup to show the potential of using thermal imaging to detect the local temperature increase. An IR thermal camera, FLIR SC305, is used to record the temperature distribution of patients' foot soles. The acquired thermal images are then analyzed to detect the abnormalities.

The rest of this paper proceeds as follows: in the next section, an overview of thermal measurement in diabetic foot will be given. The experimental setup and the methodology in thermal image analysis will be presented in Section 3. Results and discussion follow in Section 4. Finally, Section 5 presents the conclusions.

## 2. RELATED WORK

Diabetic foot ulcerations are invariably proceeded by inflammation, presence of infection and pain.<sup>10</sup> However, in the early stage of wounds developing, patients with DM can hardly feel pain because of neuropathic sensory loss. On the other hand, inflammation can be easily identified by temperature assessments of the affected foot.<sup>11</sup> Thus, temperature assessment seems to be a useful predictive sign of foot ulceration and subclinical inflammation of the foot.<sup>12</sup>

Researches show that there is a relationship between increased temperature and foot complications in diabetes. Temperature increasing may be detected up to one week before a foot ulceration forms. Foot temperatures vary between patients and depend on ambient temperature and level of activity.<sup>12</sup> Therefore, a standardized reference is required for defining 'increased temperature'. The most common used criterion is as follows: if the temperature difference of the corresponding area of the right and left foot is more than 2.2°C, there is a high risk of infection or ulceration on the diabetic feet.<sup>5,13</sup>

Pilot studies indicate that the incidence of foot ulcerations could be reduced by timely treatment, whereby the lower amputations.<sup>5</sup> The technologies that have been used for temperature assessment to diagnose of foot problems fall in three categories: *a*) dermal infrared (IR) thermometer (local measurement),<sup>5,13</sup> *b*) liquid crystal thermography (LCT),<sup>14,15</sup> and *c*) traditional IR camera systems.<sup>16,17</sup> Among these three categories, only the handheld dermal IR thermometers have been validated by randomized controlled trials for preventing diabetic foot ulceration recurring in the home-based environment.<sup>5,13</sup> However, the demerit of this technology is that the temperature is measured only on specific spots manually, which makes it subjective and impossible to get the temperature distribution of the whole foot. The contact and low-cost LCT has attracted more and more

attention in this area. However, the non-contact traditional IR camera was chosen for our research because of its advantages over LCT as follows. First of all, non-contact of feet is required to prevent un-wanted pressures and the transmission of the pathological organisms.<sup>18</sup> The temperatures of non-contact foot area, such as the medial arch, can be easily measured. Additionally, it is capable of measure the dorsal side of the foot for the future development.

### 3. MATERIALS AND METHODS

An experimental setup, consisting of an IR camera FLIR SC305, was built as shown in Fig. 1. The camera has a resolution of  $320 \times 200$  pixels and is placed at a distance of 860 mm so that it provides a sampling resolution on the foot soles of about 8 pixels per centimeter. A set of six thermal reference elements is mounted in the field-of-view of the thermal camera, above and below the foot positions. These reference elements are heated to different, constant temperatures in the range expected for the foot soles and serve as long-term reference of the absolute temperatures. Within 1 second of acquiring a thermal image their temperatures are measured via built-in calibrated PT1000 resistors are read out by the control software and stored together with the image. Prior to the clinical tests, the uniformity of the thermal camera response was characterized. The minimal temperature difference that can be measured between corresponding locations on the soles of the left and the right foot is  $\pm 0.25\text{K}$  for  $4 \times 4$  pixel areas (circa  $5\text{ mm} \times 5\text{ mm}$ ).

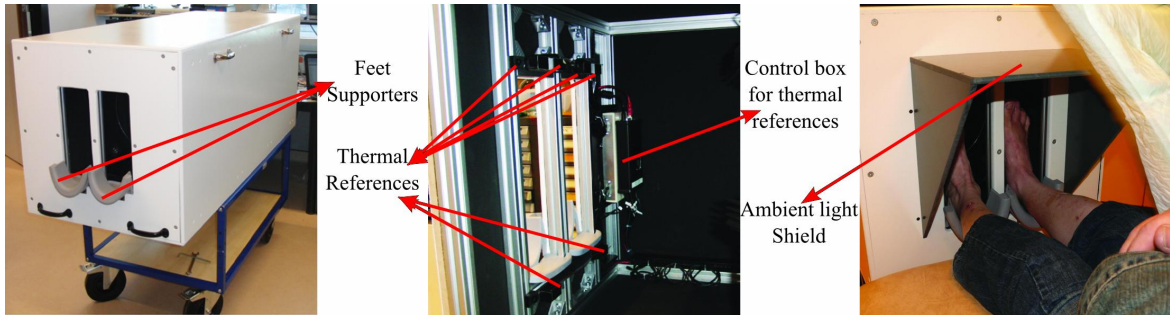


Figure 1: The experimental setup for foot scanning and measurement with it. The blocks on the top and bottom of the images are the thermal references.

Patients were recruited from the multidisciplinary diabetic foot clinic of the Hospital Group Twente, Almelo, the Netherlands. The patients included in this study are all diagnosed with diabetes and showed (pre-signs of) ulceration or have a history of ulceration.

All the patients were asked to remain in a seated position with bare foot for 5 -10 minutes before the measurements. This can help to achieve equilibration with the contrast ambient temperature. The feet are placed into the right position with the help of clinicians. Hospital cloth and black cloth are draped over the shield of the setup and the lower legs to block external light sources and provide a homogeneous background.

For each patient who participated in this project, a live assessment form of the feet soles was filled by clinicians. The live assessment will be used for inspection of the automatic abnormality detection with the thermal images in the post-processing stage.

#### 3.1 Methodology

The acquired thermal images are analysed as shown in Fig. 2 to identify the abnormality. These steps are implemented with MATLAB platform, described as follows:

##### (1) Foot Segmentation

Extract left and right foot from the background in the acquired thermal images.

##### (2) Feet Registration

Register the left and right foot based on the contours of the feet so that corresponding points on left and right foot can be compared.

### (3) Abnormality Detection

Compare the pixel values of the left and right feet to determine whether there is risk of the abnormality .

At this moment, we also added a step for checking whether the resulted segmentation is satisfactory or not. If not (too over segmented or inadequately segmented), the foot contour will be manually labeled to accomplish the segmentation.

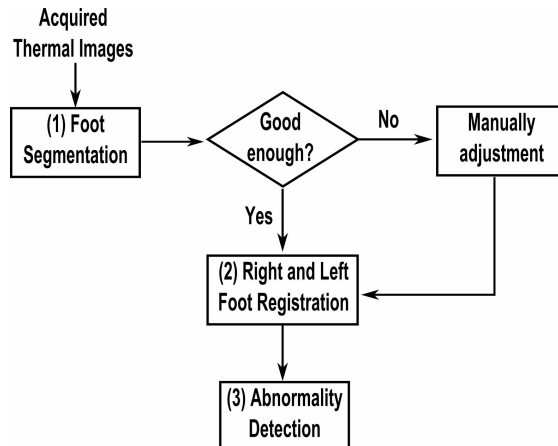


Figure 2: The flowchart of the methodology for thermal image analysis.

### 3.2 Foot Segmentation

Foot segmentation is an important step in the proposed methodology, and presents several challenges. First of all, some patients have feet or parts of the feet with low temperatures, which is close to the ambient temperature (Fig. 3b). Sun et al.<sup>16</sup> indicated that the temperature of the medical arch was the highest and that of the lesser toes was the lowest in healthy and some of the patient population. Thus, for thermal images of such feet, it is difficult to extract the foot area from background, especially for the toes. Second, the radiation from the ankles and legs are visible (Fig. 3c), which also increases the difficulty of segmentation. Besides, these radiation could increase the background temperatures. Although cloth was used to eliminate this affect, the patients always likes to rest their feet onto the supporting bars so the ankles were still visible.

Therefore, it is important to find an appropriate segmentation technique for extracting feet from these thermal images. Kaabouch and colleagues<sup>17</sup> implemented and evaluated five groups of auto-thresholding techniques, which are histogram shape-based methods, clustering-based methods, entropy-based methods, object attribute-based methods and complex genetic algorithms. They found genetic algorithms provided better results than

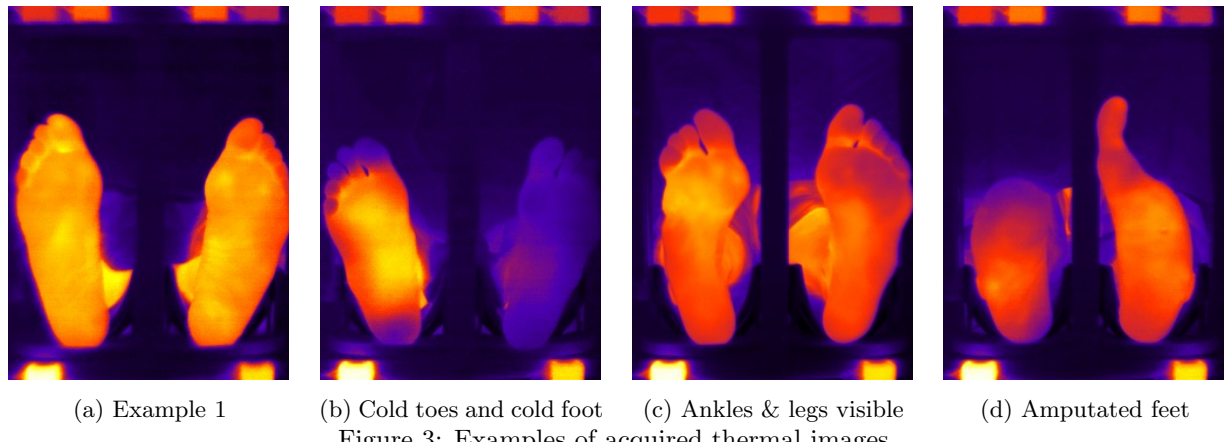


Figure 3: Examples of acquired thermal images.

the other implemented images. We also implemented these methods for our acquired images, yet none of them provides satisfactory results, especially for images like Fig. 3b and Fig. 3c. The reason may be that there is no clear intensity difference between the foot and the surroundings.

In this paper, the segmentation method implemented was active contours without edges (ACWE),<sup>19</sup> which is a region-based method, which will be introduced briefly later.

To make the segmentation easier and eliminate the noise between feet, the images are separated with the help of the bars between the left and right foot. Image segmentation is done separately for each foot. Besides, we also enhance the higher temperatures, before segmentation, with the following equations:

$$I_{inv} = \max(I) - I; \quad I_{en} = I - I_{inv} \quad (1)$$

where  $I$  represents the input image intensities,  $I_{inv}$  is the inverse of the input image intensities, while  $I_{en}$  is the image intensities that has been enhanced.

### 3.2.1 Active Contours Without Edges

Edge detections based on active contour models (ACMs) have been extensively applied for image segmentation. Compared with the conventional edge detection methods, ACM have the following significant advantages: *a*) The ACMs can allow incorporation of various prior knowledge, such as shape and intensity distribution; *b*) the ACMs can achieve sub-pixel accuracy of the object boundaries; *c*) the ACMs can provide smooth and closed contours, which can avoid the post processing in traditional edge detection models.

There are two categories of ACMs, which are edge-based and region-based. The first uses local edge information to guide the contour searching towards the object boundaries, while the other utilizes the image statistical information and has better performance over the edge base ACMs.<sup>20</sup> Nowadays, one of the most popular region-based models is ACWE model. The ACWE model is a simplified piecewise-constant Mumford-Shah model. Let  $\Omega \subset \mathbb{R}^2$  be the image domain and  $I : \Omega \rightarrow \mathbb{R}$  be the given gray level image. The variable  $(x, y)$  in  $I(x, y)$  is a point in  $\Omega$ .  $C = \partial\omega$ , with  $\omega \subset \Omega$  being an open subset. Let  $\Omega_1 = \omega$  (regions outside contour) and  $\Omega_2 = \Omega/\omega$  (regions inside contour), and two unknown constants  $c_1$  and  $c_2$ , which denote the image intensities in  $\Omega_1$  and  $\Omega_2$ , respectively, the contour can be found by minimizing the following energy function:

$$E = \mu L_C(C) + \nu A_{\Omega_2}(C) + \lambda_1 \int_{\Omega_1} |I(x, y) - c_1|^2 dx dy + \lambda_2 \int_{\Omega_2} |I(x, y) - c_2|^2 dx dy \quad (2)$$

where  $\lambda_1, \lambda_2 > 0$ ,  $\mu, \nu \geq 0$  are fixed parameters;  $L_C(C)$  and  $A_{\Omega_2}(C)$  represent the length of the contour and the area of the regions inside the contour, respectively. The last two items in the above equation are called the global data fitting energy.<sup>19</sup>

With level sets,<sup>21</sup> representing the contour  $C$  with zero level set  $C = \{x, y \in \Omega \mid \phi(x, y) = 0\}$ , the solutions obtained by minimizing Eq. 2 is:

$$\begin{cases} c1(\phi) &= \frac{\int_{\Omega} I(x, y) H_{\varepsilon}(\phi(x, y)) dx dy}{\int_{\Omega} H_{\varepsilon}(\phi(x, y)) dx dy} \\ c1(\phi) &= \frac{\int_{\Omega} I(x, y) (1 - H_{\varepsilon}(\phi(x, y))) dx dy}{\int_{\Omega} (1 - H_{\varepsilon}(\phi(x, y))) dx dy} \\ \frac{\partial \phi}{\partial t} &= \delta_{\varepsilon}(\phi) \left[ \mu \operatorname{div} \left( \frac{\nabla \phi}{|\nabla \phi|} \right) - \nu u - \lambda_1 (I(x, y) - c_1)^2 + \lambda_2 (I(x, y) - c_2)^2 \right] \end{cases} \quad (3)$$

where  $H_{\varepsilon}(\phi(x, y))$  and  $\delta_{\varepsilon}(\phi)$  are regularized versions of the Heaviside function and the Dirac function, respectively:

$$\begin{aligned} H_{\varepsilon}(\phi) &= \frac{1}{2} \left[ 1 + \frac{2}{\pi} \arctan \left( \frac{\phi}{\varepsilon} \right) \right] \\ \delta_{\varepsilon}(\phi) &= \frac{1}{\phi} \frac{\varepsilon}{\varepsilon^2 + \phi^2} \end{aligned} \quad (4)$$

### 3.3 Left and Right Foot Registration

The abnormality in the proposed method is identified by comparing the temperatures of the corresponding points on the left and right foot. However, the feet in the thermal images are hardly at symmetric position. And there are usually deformations due to DM or amputations. Therefore, the left and right foot need to be registered with each other.

Image registration is a process for determining the correspondence of features between images collected at different times or using different image modalities. The correspondences can be used to change the appearance of the object by rotating, translating and scaling. The image registration techniques fall into two categories, which are rigid and non-rigid methods. When using the rigid method, the registration between the images are assumed to be achieved by rotating and/or translating with respect to each other. On the other hand, nonrigid method assumed that the correspondences can not be achieved without localised scaling of the images, due to biological differences or imaging acquisition or both.<sup>22</sup>

Suppose we have two images  $I_l(x, y)$  and  $I_r(x, y)$ , The goal of the registration for these two images is to find the transformation  $T$  to make

$$I_r(x, y) \simeq I'_l(x, y) = T(I_l(x, y)) \quad (5)$$

For the study, the B-spline grid, non-rigid point-based registration proposed by Klein et. al<sup>23,24</sup> was implemented.

Based on the segmentation done, 300 corresponding points on each contour of left and right feet are extracted, except for the centroid and the furthest points on the heels. Most of the points are located surrounding the heels to avoid the area where deformation most likely happened. All the extracted contour points are used as landmarks to calculate the displacement and the transformation.

### 3.4 Abnormality Detection

Once the registration is done, geometric transformation will be done to right foot to make the pixels on it are corresponded with pixels on the left foot. The spots at risk will be identified simply by subtraction between the corresponding pixel values from the left and right foot. The threshold we use for abnormality detection is: if the temperature difference of the corresponding area of the right and left foot is more than  $2.2^{\circ}\text{C}$ , there is a high risk of infection or ulceration on the diabetic feet.<sup>5,13</sup> This is the most common and the only criterion which has been clinically validated for determining abnormality on diabetic foot.

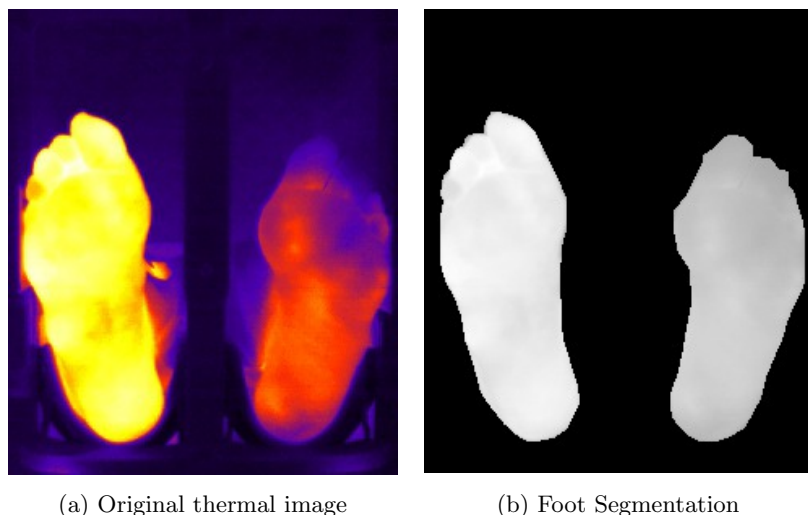


Figure 4: Examples of original thermal images without the thermal references and segmentation results. The left foot was presented in the left of the thermal image.

## 4. RESULTS AND DISCUSSION

An example thermal image (Fig. 4a) and the segmentation result of the example (Fig. 4b) are given. For the thermal images like the left foot in Fig. 4a, where only small part of the ankle are captured and the foot has clear edges from the background, the ACWE model can easily get a satisfactory result. Although the small part of ankles may still be detected, post-processing can easily remove it automatically. However, for images those have the similar temperature distribution as that shown in Fig. 3c (large parts of ankles or legs), and the left feet in Fig. 3b and Fig. 4a (no clear boundaries from the background), some of them (7 among 20 measurements analysed so far) still need the manually segmentation. The segmentation error may result from a intrinsic disadvantages that the algorithm can be easily affected by the initial position of the contours and the noises in the images. To solve this, shape-based segmentation methods might be options, such as Active shape Model and Active Appearance Model, which have advantages over ACWE models in finding contours in noisy images.

The registration results are shown in Fig. 5. We always make the left foot as the static one and try to transform the right foot on to it. As shown in Fig 5b, the B-spline grid, non-rigid point registration method works pretty well, even for foot with large deformation. Thus, we can conclude that this registration technique is suitable to register the feet with whatever shapes, sizes and positions, once the contours are well detected.

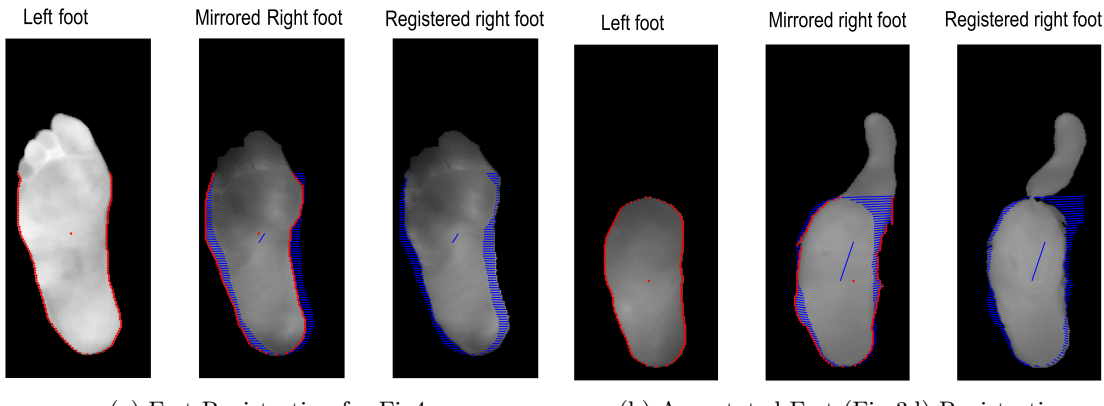
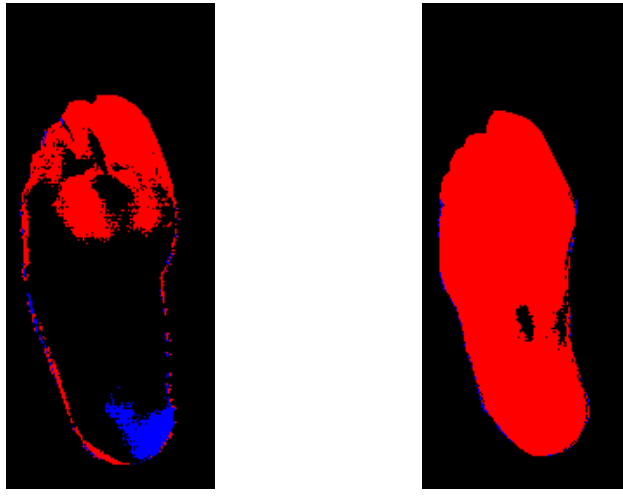


Figure 5: Examples of segmentation results with different techniques. The red dots represents the landmarks on the feet contours and the blue lines illustrate how the displacement moves.

Examples of possible future clinical application of thermal images are shown in Fig. 6. By calculating the temperature difference between the left and the right foot, taking  $2.2^{\circ}\text{C}$  as a clinically relevant difference,<sup>5,13</sup> (pre-)signs of ulceration can be automatically detected. The first example, patient 01 (figure 6a), shows a patient with an infected ulcer on his left foot. This results in a much higher temperature in the infected area, which can be automatically detected by thermal imaging. The second example, patient 02 (figure 6b), is a patient with a diagnosis of an active Charcot foot. This is reflected in the thermal image by the large difference between the left and right foot, more than  $2.2^{\circ}\text{C}$  on any part of the feet. Thermal imaging may be used for this patient in the follow-up, to see if the Charcot foot is still active. When the temperature difference between both feet is smaller than  $2.2^{\circ}\text{C}$ , the next phase of the treatment can start.<sup>4</sup>

## 5. CONCLUSION AND FUTURE WORK

In this contribution, an experimental setup was build with an IR thermographic camera was built. A methodology was proposed for detecting the abnormality on diabetic foot with the acquired thermal images. The left and right foot was extracted with ACWE model from the background. The model works well so far, although manual adjustment is still needed for some feet with cold toes and visible ankle. The registration between left and right foot, based on foot contours, presents fairly good results, no matter the shapes, locations or positions of the feet. Through the preliminary analysis presented here, we have proven the feasibility that the images acquired



(a) Patient 01

(b) Patient 02 (Fig4a)

Figure 6: Examples of abnormalities identification results. According to the live assessment done by clinicians, the red part in Fig. 6a is ulceration and redness. Red color means the temperature on the left foot is  $2.2^{\circ}\text{C}$  is higher than that on the right. The inverse status is presented by blue color.

through our experimental setup can detect the (pre-)signs of ulcerations as well as other complications of the diabetic foot, which is associated with temperature changes.

Due the fact the the foot usually has a lower temperature than the other body part, when the other body parts visible in the thermal images, e.g the legs and ankle, the segmentation work for extracting the feet from the background still remains a difficult task. Besides, the low temperature of the toes also increase the segmentation difficulties. In the future, we can try the shape-based model and also enhance the shielding of these radiations to solve the problem.

## ACKNOWLEDGMENTS

This project is granted by public funding from ZonMw, the Netherlands Organisation for Health Research and Development. The authors are very grateful for the patients who participated in the data collection, and the clinicians in Diabetic Foot Unit, Department of Surgery, Hospital Group Twente, Almelo, the Netherlands. We also appreciate Geert-Jan Laanstra of the Signals and Systems Group, Faculty of EEMCS, University of Twente, who gave us plenty support in building the experimental setup. Moreover, we also appreciate the effort of Tim J.P.M Op 't Root of DEMCON Advanced Mechatronics BV, Oldenzaal, the Netherlands, who has developed the thermal reference elements and characterized the camera for the purpose of these measurements.

## REFERENCES

- [1] Wild, S., Roglic, G., Green, A., Sicree, R., and King, H., "Global prevalence of diabetes: Estimates for the year 2000 and projections for 2030," *Diabetes Care* **27**, 1047–1053 (2004).
- [2] Shaw, J. E., Sicree, R. A., and Zimmet, P. Z., "Global estimates of the prevalence of diabetes for 2010 and 2030," *Diabetes Research and Clinical Practice* **87**, 4–14 (2010).
- [3] Boulton, A. J., Vileikyte, L., Ragnarson-Tennvall, G., and Apelqvist, J., "The global burden of diabetic foot disease," *The Lancet* **366**, 12–18 (2005).
- [4] Apelqvist, J., Bakker, K., van Houtum, W. H., Nabuurs-Franssen, M. H., and Schaper, N. C., "International consensus and practical guidelines on the management and the prevention of the diabetic foot," *Diabetes/Metabolism Research and Reviews* **16**, S84–S92 (2010).
- [5] Lavery, L. A., Higgins, K. R., Lanctot, D. R., Constantinides, G. P., Zamorano, R. G., Athanasiou, K. A., Armstrong, D. G., and Agrawal, C. M., "Preventing diabetic foot ulcer recurrence in high-risk patients: use of temperature monitoring as a self-assessment tool," *Diabetes Care* **30**, 14–20 (2007).

- [6] Liu, C., van der Heijden, F., and van Netten, J. J., "Towards surface analysis on diabetic foot soles to predict ulcerations using photometric stereo," in [*Proceedings of SPIE 8214, Advanced Biomedical and Clinical Diagnostic Systems X*], **82141D**, 82141D–82141D–12, SPIE (2012).
- [7] Singh, N., Armstrong, D. G., and Lipsky, B. A., "Preventing foot ulcers in patients with diabetes," *The Journal of the American Medical Association* **293**, 217–228 (2005).
- [8] Apelqvist, J., Bakker, K., van Houtum, W., and Schaper, N. C., "Practical guidelines on the management and prevention of the diabetic foot," *Diabetes/Metabolism Research and Reviews* **24**, S181–S187 (2008).
- [9] Korzon-Burakowska, A. and Edmonds, M., "Role of the microcirculation in diabetic foot ulceration," *International Journal of Lower Extremity Wounds* **5**, 144–148 (2006).
- [10] Bharara, M., Cobb, J. E., and Claremont, D. J., "Thermography and thermometry in the assessment of diabetic neuropathic foot: A case for furthering the role of thermal techniques," *International Journal of Lower Extremity Wounds* **5**, 250–260 (2006).
- [11] Armstrong, D. G., Holtz-Neiderer, K., Wendel, C., Mohler, M. J., Kimbriel, H. R., and Lavery, L. A., "Skin temperature monitoring reduces the risk for diabetic foot ulceration in high-risk patients," *The American Journal of Medicine* **120**, 1042–1046 (2007).
- [12] Roback, K., "An overview of temperature monitoring devices for early detection of diabetic foot disorders," *Expert Reviews of Medical Devices* **7**, 711–718 (2010).
- [13] Lavery, L. A., Higgins, K. R., Lanctot, D. R., Constantinides, G. P., Zamorano, R. G., Armstrong, D. G., Athanasiou, K. A., and Agrawal, C. M., "Home monitoring of foot skin temperatures to prevent ulceration," *Diabetes Care* **27**, 2642–2647 (2004).
- [14] Roback, K., Johansson, M., and Starkhammar, A., "Feasibility of a thermographic method for early detection of foot disorders in diabetes," *Diabetes Technology & Therapeutics* **11**, 663–337 (2009).
- [15] Frykberg, R. G., Tallis, A., and Tierney, E., "Diabetic foot self examination with the tempstat<sup>TM</sup> as an integral component of a comprehensive prevention program," *The Journal of Diabetic Foot Complications* **1**, 13–18 (2009).
- [16] Sun, P., Lin, H., Jao, S. H. E., Ku, Y. C., Chan, R. C., and Cheng, C. K., "Relationship of skin temperature to sympathetic dysfunction in diabetic at-risk feet," *Diabetes Research and Clinical Practice* **73**, 41–46 (2006).
- [17] Kaabouch, N., Chen, Y., Hu, W.-C., Anderson, J. W., Ames, F., and Paulson, R., "Enhancement of the asymmetry-based overlapping analysis through features extraction," *Journal of Electronic Imaging* **20**(1), 013012–013012–7 (2011).
- [18] Nagase, T., Sanada, H., Takehara, K., Oe, M., Iizaka, S., Ohashi, Y., Oba, M., Kadokami, T., and Nakagami, G., "Variations of plantar thermographic patterns in normal controls and non-ulcer diabetic patients: novel classification using angiosome concept.," *Journal of Plastic, Reconstructive & Aesthetic Surgery* **64**, 860–866 (2011).
- [19] Chan, T. F. and Vese, L. A., "An active contour model without edges," *IEEE transactions on image processing* **10**(2), 266–277 (2001).
- [20] Jing, Y., An, J., and Liu, Z., "A novel edge detection algorithm based on global minimization active contour model for oil slick infrared aerial image," *IEEE transactions on geoscience and remote sensing* **49**(6), 2005–2013 (2011).
- [21] Osher, S. and Sethian, J. A., "Fronts propagating with curvature-dependent speed: algorithms based on hamilton-jacobi formulations," *Journal of Computational Physics* **79**, 12–49 (1988).
- [22] Crum, W. R., Hartkens, T., and Hill, D. L. G., "Non-rigid image registration: theory and practice," *The British Journal of Radiology* **77**, S140–S153 (2004).
- [23] Klein, A., Kroon, D. J., Hoogeveen, Y., Kool, L. J. S., Renema, W. K. J., and Slump, C. H., "Multimodal image registration by edge attraction and regularization using a b-spline grid," in [*Medical Imaging 2011: Image Processing, Lake Buena Vista, Florida, USA*], Dawant, D. M. and Haynor, D. R., eds., *Proceedings of SPIE* **7962**, 796220, SPIE, Bellingham, USA (February 2011).
- [24] Kroon, D.-J., "B-spline grid, image and point based registration." on-Line. Last accessed January 9, 2013.

See discussions, stats, and author profiles for this publication at: <https://www.researchgate.net/publication/257812773>

# Infrared Thermal Imaging for Automated Detection of Diabetic Foot Complications

Article in *Journal of Diabetes Science and Technology* · September 2013

DOI: 10.1177/193229681300700504 · Source: PubMed

---

CITATIONS

147

5 authors, including:



[Jaap J Van Netten](#)  
Academisch Medisch Centrum Universiteit van Amsterdam

177 PUBLICATIONS 8,235 CITATIONS

[SEE PROFILE](#)

---

READS

2,440



[Jeff G van Baal](#)  
Ziekenhuisgroep Twente

32 PUBLICATIONS 1,232 CITATIONS

[SEE PROFILE](#)



[Chanjuan Liu](#)  
University of Twente

7 PUBLICATIONS 474 CITATIONS

[SEE PROFILE](#)

## Infrared Thermal Imaging for Automated Detection of Diabetic Foot Complications

Jaap J. van Netten, Ph.D.,<sup>1</sup> Jeff G. van Baal, M.D., Ph.D.,<sup>1</sup> Chanjuan Liu, M.Sc.,<sup>2</sup> Ferdi van der Heijden, Ph.D.,<sup>2</sup> and Sicco A. Bus, Ph.D.<sup>1,3</sup>

### Abstract

#### Background:

Although thermal imaging can be a valuable technology in the prevention and management of diabetic foot disease, it is not yet widely used in clinical practice. Technological advancement in infrared imaging increases its application range. The aim was to explore the first steps in the applicability of high-resolution infrared thermal imaging for noninvasive automated detection of signs of diabetic foot disease.

#### Methods:

The plantar foot surfaces of 15 diabetes patients were imaged with an infrared camera (resolution, 1.2 mm/pixel): 5 patients had no visible signs of foot complications, 5 patients had local complications (e.g., abundant callus or neuropathic ulcer), and 5 patients had diffuse complications (e.g., Charcot foot, infected ulcer, or critical ischemia). Foot temperature was calculated as mean temperature across pixels for the whole foot and for specified regions of interest (ROIs).

#### Results:

No differences in mean temperature  $>1.5^{\circ}\text{C}$  between the ipsilateral and the contralateral foot were found in patients without complications. In patients with local complications, mean temperatures of the ipsilateral and the contralateral foot were similar, but temperature at the ROI was  $>2^{\circ}\text{C}$  higher compared with the corresponding region in the contralateral foot and to the mean of the whole ipsilateral foot. In patients with diffuse complications, mean temperature differences of  $>3^{\circ}\text{C}$  between ipsilateral and contralateral foot were found.

#### Conclusions:

With an algorithm based on parameters that can be captured and analyzed with a high-resolution infrared camera and a computer, it is possible to detect signs of diabetic foot disease and to discriminate between no, local, or diffuse diabetic foot complications. As such, an intelligent telemedicine monitoring system for noninvasive automated detection of signs of diabetic foot disease is one step closer. Future studies are essential to confirm and extend these promising early findings.

*J Diabetes Sci Technol* 2013;7(5):1122–1129

**Author Affiliations:** <sup>1</sup>Diabetic Foot Unit, Department of Surgery, Hospital Group Twente, Almelo, the Netherlands; <sup>2</sup>Signals and Systems Group, Faculty of Electrical Engineering, Mathematics, and Computer Science, University of Twente, Enschede, the Netherlands; and <sup>3</sup>Department of Rehabilitation Medicine, Academic Medical Center, University of Amsterdam, Amsterdam, the Netherlands

**Abbreviations:** (ROI) region of interest, (SD) standard deviation

**Keywords:** automatic detection, diabetic foot, infrared imaging, prevention, telemedicine, thermography

**Corresponding Author:** Jaap J. van Netten, Ph.D., Zilvermeeuw 1, 7609 PP Almelo, The Netherlands; email address [jv.netten@zgt.nl](mailto:jv.netten@zgt.nl)

## Introduction

**F**oot ulcers are a frequent and costly complication of diabetes, with a lifetime incidence of 15–25% and up to 20% of the total health care expenditure on diabetes attributable to foot ulcers.<sup>1,2</sup> If left untreated, ulcers will become severely infected and ultimately result in amputation of the limb and/or death.<sup>2,3</sup> Diabetic foot ulcers are preventable through the early detection and timely treatment of signs of diabetic foot disease.<sup>2</sup> However, early detection depends on frequent assessment, which may be limited for various reasons. Self-examination can be difficult or impossible due to the health impairments related to diabetes or social impairments. Frequent (e.g. weekly) examination by health care professionals would be too intrusive and costly and is also limited because, for example, the human hand is not an objective means to assess temperature, which is a marker of underlying inflammation.<sup>4</sup> Our ultimate objective is to develop an intelligent telemedicine monitoring system that can be deployed for frequent examination of the patient's feet to timely and automatically detect signs of diabetic foot complications.

Thermal imaging is a promising technology to achieve this objective, as increased plantar foot temperature is a key sign of underlying inflammation. Thermal imaging has been shown to be a useful technique in the clinical management of the diabetic foot.<sup>5,6</sup> Several diabetic foot complications such as neuropathic ulcers,<sup>7,8</sup> osteomyelitis,<sup>9,10</sup> and Charcot foot<sup>7,11</sup> have been identified at increased temperature locations. Increased plantar foot temperature may even be present a week before a neuropathic ulcer appears.<sup>11</sup> Clinical studies on home-monitoring of plantar foot temperature based on that finding have shown that frequent temperature assessments and immediate treatment in case of temporally persistent temperature differences ( $>2.2\text{ }^{\circ}\text{C}$ ) between a foot region and the same region in the contralateral foot can prevent diabetic foot ulcers.<sup>12–14</sup> On the other hand, decreased foot temperatures may indicate vascular insufficiency in the foot.<sup>15,16</sup> Finally, a relationship between a temperature-based wound inflammatory index and wound healing has been proposed as a robust indicator of tissue health with a quicker response time to predict healing versus wound size.<sup>17</sup>

A variety of thermal imaging techniques have been used and tested to date, of which infrared imaging and liquid crystal thermography seem to hold most promise for use in daily clinical practice.<sup>5,15,18</sup> Compared with liquid crystal thermography, infrared imaging has the advantage of being a noninvasive measurement with possibilities for automatic analysis. As such, infrared imaging shows greater potential for telemedical applications and will be the focus of this article. The first clinical application of infrared imaging in the diabetic foot was measurement of plantar foot temperatures using a handheld thermometer as described by Lavery and coauthors<sup>12–14</sup> in their clinical studies. Although being low cost, the disadvantages of such a thermometer are: low spatial resolution (temperature is measured on selected individual spots only), the necessity that patients perform the measurement themselves, and lack of options for automatic analysis. Furthermore, results on sensitivity and specificity of the algorithm used in these clinical studies have not been published to date. With technological advancements in infrared imaging and analysis, it is possible to overcome these limitations. The aim of this study was to explore the first steps in the applicability of high-resolution infrared thermal imaging for noninvasive automated detection of signs of diabetic foot disease.

## Methods

For this pilot study, a convenience sample of 15 patients with diabetes mellitus type 1 or 2 was obtained, equally divided over three groups: 5 patients without present signs of diabetic foot complications, 5 patients with local signs of diabetic foot complications (e.g., abundant callus or neuropathic ulcer), and 5 patients with diffuse complications (e.g., Charcot foot, infected ulcer, or critical ischemia). Screening and diagnosis for presence of signs of diabetic foot complications was done by a certified wound consultant who, in accordance with diagnostic criteria described in the international guidelines, had more than 15 years of experience in diabetic foot care, before treatment started.<sup>2</sup> Patients were included within 2 weeks after first presentation at the outpatient clinic with their foot complications. Neuropathy was assessed with a 10 g Semmes–Weinstein monofilament and peripheral arterial disease by assessment of pedal pulses and toe pressure. Diagnosis of osteomyelitis and Charcot foot was confirmed by the findings of the radiologist on X ray and magnetic resonance imaging. Presence of critical ischemia was confirmed by Doppler toe pressure measurements  $<30\text{ mm Hg}$ . Informed consent was obtained from all patients before the measurements. All research efforts were

in compliance with the World Medical Association's Declaration of Helsinki. The Medical Ethical Committee Twente approved the study protocol.

Patients were seated in supine position on a treatment bench. After shoes, socks, and (if applicable) dressings were removed, patients remained seated for a minimum of 5 min to allow equilibration of foot temperature. Pilot measurements showed no further changes in foot temperature after 5 min of rest. Patients were instructed to place their feet on support bars inside an experimental setup (**Figure 1**) in such a way that their shank and thigh remained supported on the treatment bench. The experimental setup comprised two cameras (one for color images, one for thermal images; specifications in **Table 1**), a light module, thermal reference elements, and foot supports. The light module consisted of eight LZ1-10WW05 light-emitting diodes (LendEngin Inc.), each sized  $4.4 \times 4.4$  mm. Thermal reference elements were six black blocks of  $35 \times 20$  mm, with calibrated PT1000 resistor and heating resistors. The cameras, light module, and thermal references were connected to a desktop computer and a screen.

All parts of the system apart from the desktop computer and the screen were mounted in a wooden box sized  $600 \times 600 \times 1900$  mm, with a light-shielding extension in front. Both shanks and thighs of the patient were covered with a sterile cloth. The entrance of the light-shielding extension of the box was further covered with a black cloth to eliminate any influence of ambient light conditions.

The color image camera was automatically focused during every measurement. The thermal camera was calibrated and focused at the start of each measurement day, using a plate covered with flat black spray paint that was positioned at the location of the feet, with the thermal reference elements above and beneath the plate. Calibration was performed based on the equal thermal distribution of the plate (room temperature). Additionally, temperature of the thermal reference elements was obtained during the measurements to ensure consistency of the thermal measurements during the day by comparing measured temperature values with registered temperature values of the reference elements.

**Table 1.**  
**Specifications of the Two Cameras in the Experimental Setup**

	Color image camera	Thermal camera
Camera type	Canon Eos 40D with EF-s 17–85 mm lens	FLIR SC305 with 16 bit resolution
Resolution	APS-C size ( $22.2 \times 14.8$ mm)	$320 \times 240$ pixels, 1.2 mm per pixel
Sensor	10.5 mega pixel single plate complementary metal-oxide semiconductor sensor	
Angle of view	Horizontal: $68^{\circ}40' - 15^{\circ}25'$ Vertical: $48 - 10^{\circ}25'$ Diagonal: $78^{\circ}30' - 18^{\circ}25'$	$25^{\circ} \times 19^{\circ}$ ; focal length 18 mm
Field of view	$420 \times 280$ mm	$420 \times 315$ mm
Thermal sensitivity	Not applicable	$<0.05 - 30$ °C
Objective temperature range	Not applicable	-20 to 120 °C
Computer interface	USB 2.0 high speed	Ethernet IEEE 802.3

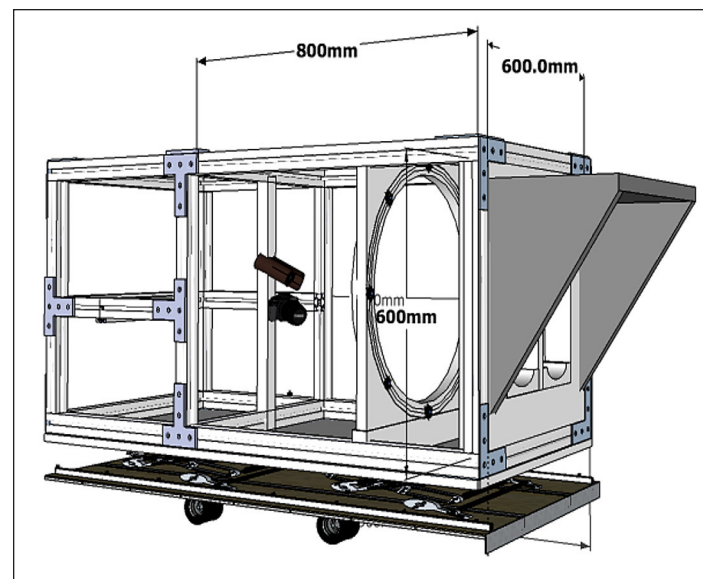


**Figure 1.** Schematic drawing of the interior of the experimental setup. The feet are positioned on the support bars, below the light shield, on the right side of the image. The thermal camera and the color image camera are placed 800 mm from the foot supports, with the thermal camera above the color image camera. The light module is the ring between the cameras and the foot supports, containing eight light-emitting diodes (black dots).

During each measurement, two images were acquired: one color image with all light sources on, followed by an infrared image with all light sources off. Both cameras were driven using custom-made MATLAB software (the Mathworks, MA). Data were processed in MATLAB. For live assessment of the patient's feet, the wound consultant annotated specific regions of interest (ROIs) with signs of diabetic foot complications (e.g., callus, ulcer) using a paper sheet on which the foot boundaries were drawn. In the color image, both the boundaries of the foot and the ROIs were manually annotated with self-designed MATLAB software (see **Figure 2**). This annotation was transferred to the thermal image. From the pixels encapsulated by the boundaries of the foot as well as those encapsulated by the ROIs, the mean temperature and the standard deviation (SD) across pixels were automatically processed using MATLAB.

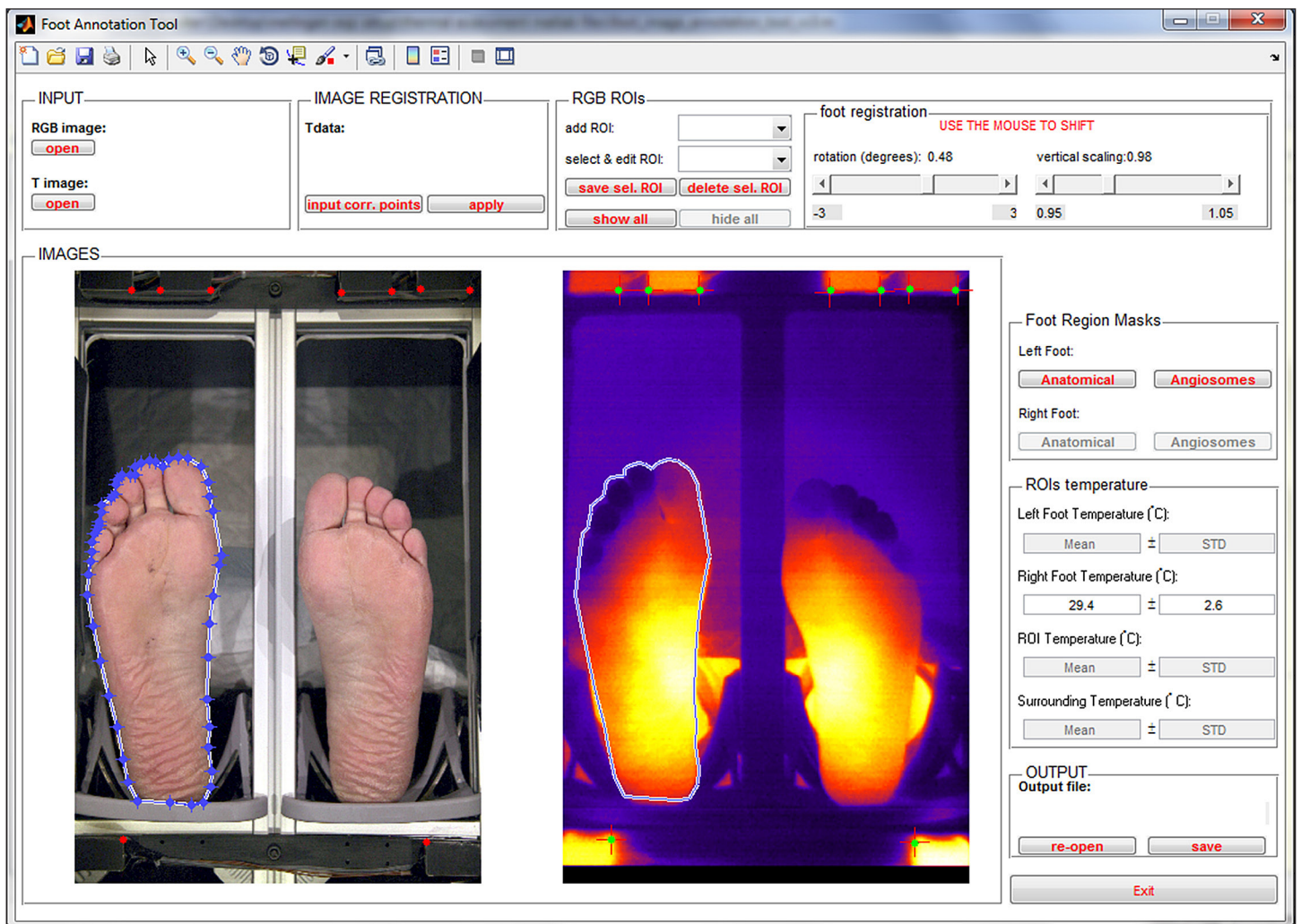


**Figure 2.** Screenshot of the manual annotation of the right foot in the color image and its subsequent transfer to the thermal image.

## Results

Patient characteristics and temperature results from the infrared imaging are shown in **Table 2**. Mean (SD) number of pixels encapsulated by the foot boundary was 11,462 (1492); mean (SD) number of pixels encapsulated by the ROI was 82 (40). Thermal images are shown in **Figure 3** for the three subgroups of patients. Differences in mean temperature between the ipsilateral and contralateral foot in patients with no or local complications were at maximum 1.5 °C. Mean temperature between ipsilateral and contralateral foot of patients with diffuse complications differed at minimum 3 °C, where feet with osteomyelitis and/or Charcot feet were warmer and those with critical ischemia were colder compared with the contralateral foot.

In four out of five patients with local foot complications, temperature at the ROI was  $>2$  °C higher compared with the corresponding region in the contralateral foot, and  $>2$  °C higher compared with the mean temperature of the ipsilateral foot. In four out of five patients with diffuse complications, temperature at the ROI was  $>3$  °C higher compared with the corresponding region in the contralateral foot. In these patients, the temperature difference between the ROI and the mean temperature of the ipsilateral foot was  $<1.5$  °C.

**Table 2.**  
**Patient Characteristics and Temperature Values in Mean (SD) Degrees Celsius<sup>a</sup>**

Patient characteristics							Temperature (°C), mean (SD)							
#	M/F	Age	DM type	Neuropathy	PAD	Complications <sup>b</sup>	Foot	Ipsilateral foot <sup>c</sup>	Contralateral foot	ΔT1	ROI ipsilateral foot <sup>d</sup>	ROI contralateral foot <sup>d</sup>	ΔT2	ΔT3
<b>No complications</b>														
1	M	58	2	Yes	No	—		33.6 (1.4)	33.6 (1.4)	0.0				
2	F	36	1	No	No	—		29.6 (2.7)	29.4 (2.6)	0.2				
3	M	84	2	Yes	Yes	—		29.4 (1.8)	29.7 (1.1)	-0.3				
4	M	79	2	Yes	No	—		28.8 (1.7)	29.6 (1.6)	-0.8				
5	M	81	2	Yes	No	—		33.9 (1.9)	33.8 (1.0)	0.1				
<b>Local complications</b>														
6	M	76	2	Yes	No	Ulcer hallux (1A)	Left	30.8 (2.4)	29.3 (2.0)	1.5	35.0 (0.6)	26.2 (0.7)	8.8	4.2
7	M	69	2	Yes	Yes	Ulcer hallux (1A)	Right	26.1 (1.4)	26.2 (1.4)	-0.1	28.9 (0.6)	24.9 (0.7)	4.0	2.8
8	M	49	2	Yes	No	Ulcer hallux (1A)	Right	29.5 (2.0)	29.1 (1.4)	0.4	32.7 (0.9)	31.5 (0.5)	1.2	3.2
9	M	68	2	Yes	No	Ulcer 2nd ray (1A) <sup>e</sup>	Left	30.8 (1.5)	30.2 (1.1)	0.6	33.1 (0.3)	30.6 (0.3)	2.5	2.3
10	F	67	2	Yes	No	Callus MTP2-4	Left	26.0 (1.1)	24.9 (0.7)	1.1	27.3 (0.1)	25.0 (0.2)	2.3	1.3
<b>Diffuse complications</b>														
11	M	81	2	Yes	Yes	Critical ischemia Ulcer hallux (1C)	Right	25.1 (0.7)	29.0 (2.0)	-3.9	24.0 (0.1)	24.6 (0.1)	-0.6	-1.1
12	M	71	2	Yes	No	Charcot foot Ulcer hallux (1A)	Left Left	33.6 (1.1)	28.1 (1.4)	5.5	34.1 (0.3)	26.4 (0.3)	7.7	0.5
13	F	84	2	Yes	No	Ulcer MTP1 with osteomyelitis (3B)	Left	30.0 (1.5)	27.0 (1.4)	3.0	31.1 (0.5)	26.2 (0.1)	4.9	1.1
14	M	79	2	Yes	No	Charcot foot Ulcer lateral midfoot with osteomyelitis (3B)	Left Left	32.1 (1.9)	26.0 (1.2)	6.1	33.4 (0.3)	25.9 (0.3)	7.5	1.3
15	M	60	2	Yes	No	Ulcer MTP5 with osteomyelitis (3B)	Right	32.3 (1.0)	28.6 (1.0)	3.7	33.0 (0.5)	29.3 (0.3)	3.7	0.7

<sup>a</sup> #, patient number; M, male; F, female; DM, diabetes mellitus; MTP, metatarsophalangeal joint; PAD, peripheral arterial disease; ΔT1, difference between mean temperature of ipsilateral and contralateral foot; ΔT2, difference between mean temperature of ROI and corresponding contralateral ROI; ΔT3, difference between mean temperature of ROI and mean temperature of ipsilateral foot.

<sup>b</sup> Between brackets: Ulcer classification according to University of Texas wound classification.

<sup>c</sup> For patients without complications, left foot was defined as ipsilateral foot.

<sup>d</sup> The ROIs in patients with diffuse complications were their ulcer locations.

<sup>e</sup> Only one complication of patient 9 is shown. In **Figure 3** it can be seen that another ROI (abundant callus on first metatarsophalangeal joint) is present on the right foot. However, as there was no contralateral metatarsophalangeal joint 1 due to amputation, this ROI is not further analyzed.

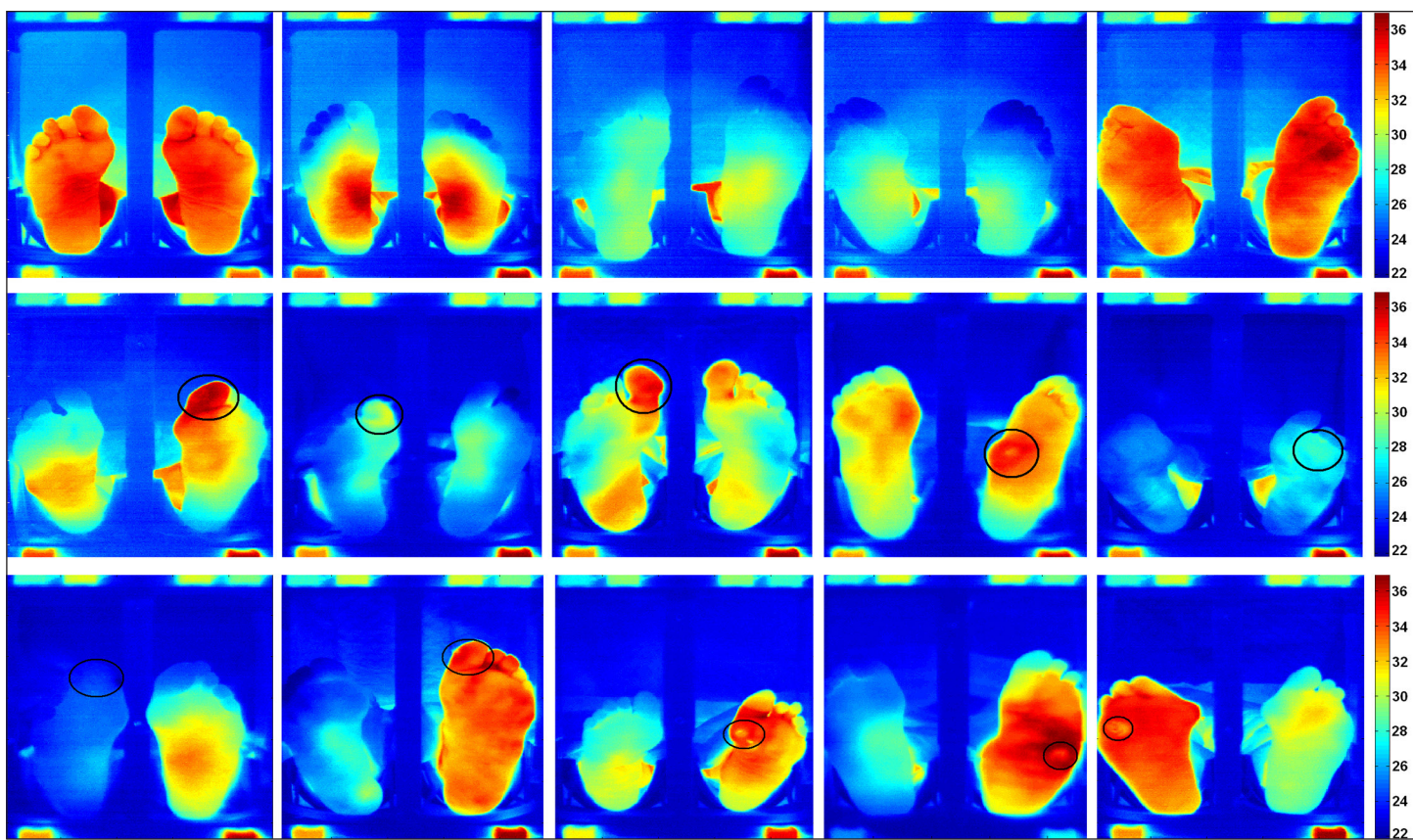


**Figure 3.** Thermal images of both feet of five patients without foot complications (top row, left to right, patients 1 to 5), five patients with local foot complications (middle row, left to right, patients 6 to 10), and five patients with diffuse foot complications (bottom row, left to right, patients 11 to 15). The ROIs are roughly indicated with black circles drawn on top of the image, actual ROIs were smaller and more precisely drawn. The six blocks shown along the perimeter in each image are the thermal references blocks.

## Discussion

Technological advances in infrared imaging, concerning both the speed of assessment and the spatial resolution of image pixels, have increased possibilities to quantify thermal patterns and perform automated analysis on acquired thermal images of patients' feet.<sup>6</sup> In the current study, we explored the first steps in the applicability of high-resolution infrared thermal imaging for noninvasive automated detection of signs of diabetic foot disease. An algorithm was developed for detecting signs of diabetic foot disease by measuring the temperature of the plantar surface of the feet, based solely on parameters that can be captured and analyzed with an infrared camera and a computer. With this algorithm, a good distinction could be made between patients having no diabetic foot complications, local complications, or diffuse complications. Patients without complications showed only small temperature differences between feet. Patients with local complications such as a noninfected and nonischemic foot ulcer or abundant callus showed locally increased temperatures of  $>2^{\circ}\text{C}$  compared with both the contralateral foot and the average temperature of the ipsilateral foot. Patients with diffuse complications such as a foot ulcer with osteomyelitis or a Charcot foot showed an increased mean temperature of  $>3^{\circ}\text{C}$  compared with the contralateral foot. These results indicate that advanced infrared thermal imaging may be applicable as diagnostic tool for noninvasive automated detection of signs of diabetic foot disease. This may be applied for early detection and timely management of diabetic foot complications, which could contribute to the prevention of further, more devastating consequences.

In the only clinical study known to the authors that measured foot temperature in the diabetic foot, Lavery and coauthors<sup>12-14</sup> define a difference of  $4^{\circ}\text{F}$  (or  $2.2^{\circ}\text{C}$ ) between a foot region and the corresponding region in the contralateral foot as clinically significant. The temperature differences measured in the current study confirm this threshold as clinically relevant. However, from the results of this study, it can be seen that more advanced infrared cameras

allow further specification of temperature differences between feet, where temperature difference thresholds of 2 °C apply to local complications such as neuropathic ulcers and abundant callus, and temperature difference thresholds of 3 °C apply to diffuse complications such as Charcot foot, ulcers with osteomyelitis, and critical ischemia. Further testing in larger groups of unselected patients is necessary to confirm the findings of this pilot study, to refine the classification of complications based on measured temperature differences, and to calculate diagnostic accuracy with parameters such as sensitivity and specificity.

The necessity for manual annotation of the boundaries of the foot in the color image was a limitation in this study. It is unlikely that manual annotation of foot boundaries has affected the results, as adequate accuracy could be guaranteed (**Figure 2**). However, automated analysis is not possible when all feet require manual annotation. We are currently working on automated image analysis similar to an already-described method.<sup>20</sup> This method includes automated definition of foot boundaries, calculation of mean temperatures, and comparison of temperatures with contralateral regions. These developments are needed to achieve our goal of an intelligent telemedicine monitoring system based on infrared imaging. Inclusion in this study was limited to patients either with or without existing pathologies. Future studies should follow patients without existing pathologies over time to investigate the diagnostic accuracy of the system in detecting diabetic foot complications as early as possible. Another limitation was the rather rudimentary differentiation in “no,” “local,” and “diffuse” complications. The local complications “neuropathic ulcer” and “abundant callus” have a different clinical significance, and therefore different referral times, but these signs could not be separated from the thermal images obtained in this study. Future studies need to explore if further differentiation is possible between these signs of diabetic foot disease based on thermal images.

Infrared temperature measurements have some limitations when applied for clinical purposes, which have been described earlier.<sup>5,21</sup> The first is the detection of local complications that are bilaterally present in the same foot region at the same time. This is visible, for example, in patient 8, who had an ulcer with local temperature increase at the right hallux but also increased temperature at the left hallux. As a result, the temperature difference between these regions did not exceed 2 °C. As shown in this study, this limitation can be overcome with further optimization of the algorithms based on the comparison of temperature at the ROI with the mean ipsilateral foot temperature. The second limitation is the detection of diffuse complications present in both feet at the same time. Patient 5 had temperature values in both feet that are higher compared with the values measured in other patients. Based on the infrared image only, it is not possible to confirm whether this patient has bilaterally Charcot feet, bilaterally osteomyelitis, or just a pair of warm feet (e.g., due to the presence of autonomic neuropathy). By combining infrared imaging with, for example, photographic imaging, this limitation may be overcome, although it must be noted that the chances of having such severe complications on both feet at the same time are very low. Finally, the value of using absolute foot temperature values for the detection of signs of foot disease is still not clear. Foot temperatures may vary from person to person as a result of age- and sex-related differences, presence of autonomic neuropathy or peripheral vascular disease, and environmental factors such as ambient temperature.<sup>5</sup> Properly controlled studies with advanced infrared imaging in large groups of participants are needed to determine the (additional) value of absolute foot temperature values for diagnostic purposes. Such studies preferably conduct measurements over time within patients to determine intraindividual temperature patterns and changes.

An intelligent telemedicine monitoring system as envisioned in our project is not yet close to being used in daily clinical practice. Technological issues need to be resolved, including patient positioning, camera positioning, the need for adding other imaging modalities, and automated image registration and analysis.<sup>6</sup> Feasibility studies are needed to establish the most optimal requirements for such a system and the most effective application in daily life. Subsequently, the (cost) effectiveness of using such a system for the prevention of diabetic foot disease will have to be assessed. Prices of advanced thermal imaging systems are dropping, but it is not clear whether prices are low enough to implement such a system as a monitoring tool.

## Conclusions

In this study, we explored the first steps in the applicability of infrared thermal imaging for noninvasive automated detection of signs of diabetic foot disease. We have found an algorithm that can detect signs of diabetic foot disease

and discriminate between no, local, or diffuse diabetic foot complications. This algorithm is based solely on parameters that can be captured and analyzed with an infrared camera and a computer. As such, an intelligent telemedicine monitoring system is one step closer. Future studies are essential to confirm and extend these promising early findings.

**Funding:**

This project is supported by public funding from Zon-MW, the Dutch Organisation for Health Research and Development (project ID 40-00812-98-09031).

**Acknowledgments:**

The authors acknowledge Marvin Klein and Tim Op't Root, Demcon Advanced Mechatronics b.v., Enschede, for their assistance in calibrating the thermal camera and the thermal references and Geert Jan Laanstra, University of Twente, for his assistance in building the experimental setup.

**References:**

1. Boulton AJ, Vileikyte L, Ragnarson-Tennvall G, Apelqvist J. The global burden of diabetic foot disease. *Lancet*. 2005;366(9498):1719–24.
2. Bakker K, Apelqvist J, Schaper NC; International Working Group on Diabetic Foot Editorial Board. Practical guidelines on the management and prevention of the diabetic foot 2011. *Diabetes Metab Res Rev*. 2012;28 Suppl 1:225–31.
3. Lepäntalo M, Apelqvist J, Setacci C, Ricco JB, de Donato G, Becker F, Robert-Ebadi H, Cao P, Eckstein HH, De Rango P, Diehm N, Schmidli J, Teraa M, Moll FL, Dick F, Davies AH. Chapter V: diabetic foot. *Eur J Vasc Endovasc Surg*. 2011;42 Suppl 2:S60–74.
4. Murff RT, Armstrong DG, Lanctot D, Lavery LA, Athanasiou KA. How effective is manual palpation in detecting subtle temperature differences? *Clin Podiatr Med Surg*. 1998;15(1):151–4.
5. Bharara M, Cobb JE, Claremont DJ. Thermography and thermometry in the assessment of diabetic neuropathic foot: a case for furthering the role of thermal techniques. *Int J Low Extrem Wounds*. 2006;5(4):250–60.
6. Bharara M, Schoess J, Armstrong DG. Coming events cast their shadows before: detecting inflammation in the acute diabetic foot and the foot in remission. *Diabetes Metab Res Rev*. 2012;28 Suppl 1:15–20.
7. Armstrong DG, Lavery LA, Liswood PJ, Todd WF, Tredwell JA. Infrared dermal thermometry for the high-risk diabetic foot. *Phys Ther*. 1997;77(2):169–77.
8. Armstrong DG, Lavery LA. Monitoring neuropathic ulcer healing with infrared dermal thermometry. *J Foot Ankle Surg*. 1996;35(4):335–73.
9. Harding JR, Wertheim DF, Williams RJ, Melhuish JM, Banerjee D, Harding KG. Infrared imaging in diabetic foot ulceration. *Proc 20th Annual Int Conf IEEE Engineering Med Biol Soc*. 1998;20:916–8.
10. Oe M, Yotsu RR, Sanada H, Nagase T, Tamaki T. Thermographic findings in a case of type 2 diabetes with foot ulcer and osteomyelitis. *J Wound Care*. 2012;21(6):274, 276–8.
11. Armstrong DG, Lavery LA. Monitoring healing of acute Charcot's arthropathy with infrared dermal thermometry. *J Rehabil Res Dev*. 1997;34(3):317–21.
12. Lavery LA, Higgins KR, Lanctot DR, Constantinides GP, Zamorano RG, Armstrong DG, Athanasiou KA, Agrawal CM. Home monitoring of foot skin temperatures to prevent ulceration. *Diabetes Care*. 2004;27(11):2642–7.
13. Armstrong DG, Holtz-Neiderer K, Wendel C, Mohler MJ, Kimbriel HR, Lavery LA. Skin temperature monitoring reduces the risk for diabetic foot ulceration in high-risk patients. *Am J Med*. 2007;120(12):1042–6.
14. Lavery LA, Higgins KR, Lanctot DR, Constantinides GP, Zamorano RG, Athanasiou KA, Armstrong DG, Agrawal CM. Preventing diabetic foot ulcer recurrence in high-risk patients: use of temperature monitoring as a self-assessment tool. *Diabetes Care*. 2007;30(1):14–20.
15. Ring F. Thermal imaging today and its relevance to diabetes. *J Diabetes Sci Technol*. 2010;4(4):857–62.
16. Nagase T, Sanada H, Takehara K, Oe M, Iizaka S, Ohashi Y, Oba M, Kadowaki T, Nakagami G. Variations of plantar thermographic patterns in normal controls and non-ulcer diabetic patients: novel classification using angiosome concept. *J Plast Reconstr Aesthet Surg*. 2011;64(7):860–6.
17. Bharara M, Schoess J, Nouvong A, Armstrong DG. Wound inflammatory index: a “proof of concept” study to assess wound healing trajectory. *J Diabetes Sci Technol*. 2010;4(4):773–9.
18. Roback K. An overview of temperature monitoring devices for early detection of diabetic foot disorders. *Expert Rev Med Devices*. 2010;7(5):711–8.
19. Armstrong DG, Lavery LA, Harkless LB. Validation of a diabetic wound classification system. the contribution of depth, infection, and ischemia to risk of amputation. *Diabetes Care*. 1998;21(5):855–9.
20. Kaabouch N, Hu WC, Chen Y, Anderson JW, Ames F, Paulson R. Predicting neuropathic ulceration: analysis of static temperature distributions in thermal images. *J Biomed Opt*. 2010;15(6):061715.
21. Armstrong DG, Lavery LA. Predicting neuropathic ulceration with infrared dermal thermometry. *J Am Podiatr Med Assoc*. 1997;87(7):336–7.

## Research Article

# Quantitative Estimation of Temperature Variations in Plantar Angiosomes: A Study Case for Diabetic Foot

**H. Peregrina-Barreto,<sup>1</sup> L. A. Morales-Hernandez,<sup>2</sup> J. J. Rangel-Magdaleno,<sup>1</sup> J. G. Avina-Cervantes,<sup>3</sup> J. M. Ramirez-Cortes,<sup>1</sup> and R. Morales-Caporal<sup>4</sup>**

<sup>1</sup> Instituto Nacional de Astrofísica, Óptica y Electrónica, Luis Enrique Erro No. 1, 72840 Tonantzintla, PUE, Mexico

<sup>2</sup> Universidad Autónoma de Querétaro, Cerro de las Campanas S/N, 76010 Querétaro, QRO, Mexico

<sup>3</sup> División de Ingenierías del Campus Irapuato-Salamanca, Universidad de Guanajuato, Carretera Salamanca-Valle de Santiago Km 3.5+1.8, Comunidad de Palo Blanco, 36885 Salamanca, GTO, Mexico

<sup>4</sup> Instituto Tecnológico de Apizaco, Avenida Instituto Tecnológico, 90300 Apizaco, TLAX, Mexico

Correspondence should be addressed to H. Peregrina-Barreto; [peregrina.barreto.hayde@gmail.com](mailto:peregrina.barreto.hayde@gmail.com)

Received 6 October 2013; Accepted 2 January 2014; Published 13 February 2014

Academic Editor: Volkhard Helms

Copyright © 2014 H. Peregrina-Barreto et al. This is an open access article distributed under the Creative Commons Attribution License, which permits unrestricted use, distribution, and reproduction in any medium, provided the original work is properly cited.

Thermography is a useful tool since it provides information that may help in the diagnostic of several diseases in a noninvasive and fast way. Particularly, thermography has been applied in the study of the diabetic foot. However, most of these studies report only qualitative information making it difficult to measure significant parameters such as temperature variations. These variations are important in the analysis of the diabetic foot since they could bring knowledge, for instance, regarding ulceration risks. The early detection of ulceration risks is considered an important research topic in the medicine field, as its objective is to avoid major complications that might lead to a limb amputation. The absence of symptoms in the early phase of the ulceration is conceived as the main disadvantage to provide an opportune diagnostic in subjects with neuropathy. Since the relation between temperature and ulceration risks is well established in the literature, a methodology that obtains quantitative temperature differences in the plantar area of the diabetic foot to detect ulceration risks is proposed in this work. Such methodology is based on the angiosome concept and image processing.

## 1. Introduction

Infrared (IR) technology allows the capture of natural heat radiation from the human body and its representation in a thermal image (thermogram) [1]. Since this heat radiation is produced by a thermal exchange process among skin tissue, inner tissue, local vasculature, and metabolic activity, the resulting temperature distribution could provide information regarding several diseases [1–3]. In diabetes mellitus cases, it is widely known that there is a high risk of complications in the foot; moreover, several studies have been focused in the analysis and characterization of its temperature. Some studies suggest a constant inspection of feet temperature in order to know how it behaves in diabetic patients [4, 5]. In addition, some reports have established that there are

important differences of temperature in the plantar region between healthy and diabetic subjects with and without neuropathic damage [6, 7]. According to several investigations, the presence of hot regions in the plantar area may indicate tissue damage, inflammation, and arteriovenous shunting, which could compromise the nutritive capillary flow and increase the predisposition to cutaneous ulceration [8–10]. For instance, Brånenmark et al. [11] found that diabetic patients present abnormal temperature patterns in feet and hands associated to common ulceration regions in a study made by using IR. Recently, Bharara et al. [12] proposed an analysis based on the thermal profile of a foot wound in order to provide a healing wound index for diabetic subjects. In fact, IR technology application has even been used to determine the required amputation level [13].

In [14], it is reported that nearly 50% of cases with diabetes mellitus have foot complications caused by a decrease of blood supply (vascular disorder) and loss of sensation (neuropathy). In the global scene, the incidence of foot ulceration is 2% in people with diabetes from which approximately the 15% will suffer the amputation of a limb [15]. This represents a major amputation every 30 seconds with over 2500 limbs lost per day [16]. Early detection of ulceration is complicated because diabetes causes a loss of connection between the muscle and the nerves (sensory denervation) and affects thermoreceptors and mechanoreceptors by depriving the patient from feeling any symptom, such as pain or swelling, when some injury has occurred [9, 12]. Diabetic patients require continuous medical care and demand the development of tools that bring reliable information so as to facilitate an early diagnostic [17]. Since the early detection of areas of risk on the diabetic foot is a topic of interest and temperature monitoring could reduce this risk of foot ulcerations and limb amputation [7], the development of methodologies that facilitate an opportune diagnosis turns into a relevant task. Therefore, it can be said that thermography represents an opportunity for early detection of ulcerations risk as well as a noninvasive and reliable method for diabetic foot care.

In this work, a methodology that determines and analyzes temperature differences is proposed to detect abnormal temperature increase in the diabetic foot. The plantar area is analyzed by taking into account the angiosome concept since the blood flow in these regions accurately reflects the temperature variation. In the angiosome, temperature estimation is calculated by identifying the present color regions, which at the same time are characterized and related to a temperature value. Thus, temperature differentiation between corresponding angiosomes can be achieved. Moreover, this process enables the localization of the area that covers each temperature; thereby, it also allows the detection of abnormal hot spots at the interior of the angiosome.

## 2. Materials and Methods

**2.1. Patients Information.** This study was carried out by considering a group of diagnosed patients with diabetes mellitus type 2 in the General Hospital of San Juan del Río, México, with the collaboration of a diabetes expert group in 2012. The focus group included male and female patients, in an age range from 35 to 80, with and without neuropathy. The patients attending a scheduled meeting were invited to participate in the study and they agreed. Exclusion occurred when the patient had an amputated toe, fractures or surgery of the lower limbs, peripheral arterial disease, presence of ulcers, or a history of ulcers. Thermograms were obtained in a conditioned room at controlled temperature of  $25 \pm 1^\circ\text{C}$  where the patient is allowed to rest in supine position, as it is suggested in previous works [5, 13, 18]. The recommendations of the International Academy of Clinical Thermology [19] were followed as well. As underlined in previous works, this preparation allows the detection of skin temperature variations in the range of 0.05 to  $0.1^\circ\text{C}$  [2]. The preparation was done as follows: patient is asked to remove shoes and

socks and to clean his/her feet with a damp towel. After that, patient is placed in supine position on the examination bed (Figure 1(a)), while the medical specialist collects some data (name, age, sex, height, weight, body temperature). At the end of the first 15 to 20 minutes of stabilization, an IR obstructive device is placed on patient feet in order to avoid outer heat radiation to appear in the thermogram (Figure 1(b)). The isolated feet temperature with its respective color palette and temperature scale is obtained by the thermogram.

The thermographic camera sensor is an IR detector, which absorbs the infrared energy emitted by an object and converts it into an electrical signal. IR is a technology that uses the blackbody radiation law, proposed by Max Plank, which establishes that every object with temperature above zero absolute emits electromagnetic radiation, also known as infrared radiation or thermal radiation [3, 20]. Later, Hardy [21, 22] proposed that human skin could be considered as a blackbody radiator, starting the IR use in medicine. In this way, when the surface of the skin changes, the emitted heat radiation is captured by the IR sensor and is translated into a thermogram. When a region of the skin increases/decreases its temperature, this region stands out from the background. Each pixel of a thermogram has a specific temperature value, and the image contrast is derived from the skin surface differences (gradients) in temperature. In this work, the thermograms have a color representation and were captured with an IR camera FLIR A300 with a thermal sensitivity of 0.05 at  $30^\circ\text{C}$ .

**2.2. Color Characterization.** Thermograms are represented in the RGB color space, and a rainbow palette is used for representing a scale of  $25\text{--}35^\circ\text{C}$ . The value range was discretized into ten segments with the aim of representing  $1^\circ\text{C}$  per segment. However, the color palette is blurred and most of the segments have a soft transition between colors at the beginning (Figure 2(a)). This characteristic may complicate the definition of one representative color per segment; therefore, in order to avoid this problem, the median value was extracted from the spatial center of the segment. In this way, the extreme colors are not involved and the representative color is the most predominant among the colors contained in the segment. Figure 2(b) shows the resulting palette with the representative color of each section, as well as their corresponding RGB coordinates.

Since the color identifies the temperature in a thermal image, each segment of the new palette has an associated value in centigrades ( $^\circ\text{C}$ ). The palette of representative colors now is simplified to eight representative color classes. The first three segments, from left to right in Figure 2(b), are taken as one single segment related to the coldest regions or background in the image with an interval of  $[25, 28]^\circ\text{C}$ . The background corresponds to a thermal insulation board used in the capture of images to avoid heat sources unrelated to the feet area (Figure 1(a)). The other segments have an individual representation and are associated with a temperature that varies in the range  $[28, 35]^\circ\text{C}$ , as shown in Table 1. This was determined by taking into account the results reported in [6], where subjects with diabetes risk have a temperature of

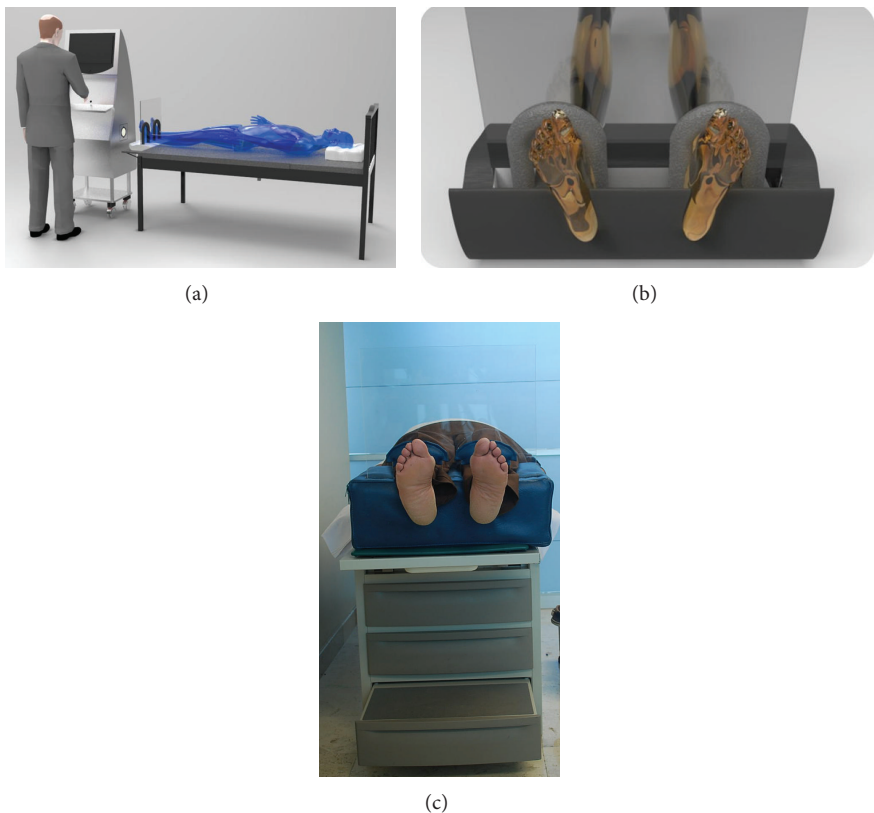


FIGURE 1: (a) The resting supine position for the image acquisition, (b) IR obstructive device, and (c) the preparation of real patient.

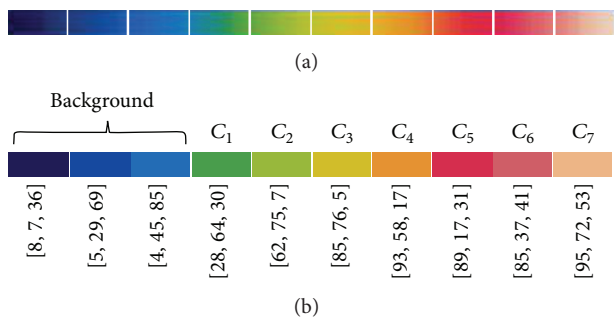


FIGURE 2: (a) Original color palette and (b) palette of representative colors with their respective RGB coordinates.

$30.0 \pm 1.3^\circ\text{C}$ , and healthy subjects have a temperature of  $26.8 \pm 1.8^\circ\text{C}$ , and after verifying that the mean plantar temperature of the patients was consistent with these ranges. In this way, it is possible to separate the feet area from the background. Since each segment of the palette represents an interval of the temperature, a representative classmark is assigned to them as shown in Table 1.

**2.3. Temperature Estimated Difference.** In order to analyze the temperature distribution of the foot, it is necessary to establish a method for this analysis. In a recent study, Nagase et al. [23] suggested the use of the angiosome concept,

TABLE 1: Temperature classes.

Temperature classes	Interval ( $^\circ\text{C}$ )	Classmark ( $^\circ\text{C}$ )
$C_0$	[25, 28)	26.5
$C_1$	[28, 29)	28.5
$C_2$	[29, 30)	29.5
$C_3$	[30, 31)	30.5
$C_4$	[31, 32)	31.0
$C_5$	[32, 33)	32.5
$C_6$	[33, 34)	33.5
$C_7$	[34, 35)	34.5

proposed by Taylor and Palmer [24]. An angiosome in a foot is a region of tissue which has blood supply by a single artery. These regions are important since one of the main causes of diabetic foot ulceration is produced by a decrease of blood supply [5]. In 2006, Attinger et al. [25] proposed four main angiosomes as regions of interest in the plantar area for their temperature analysis (Figure 3): medial plantar artery (MPA), lateral plantar artery (LPA), medial calcaneal artery (MCA), and lateral calcaneal artery (LCA). Therefore, in this work the analysis of the plantar area is made based on the angiosomes concept and using the temperature estimation approach proposed by Peregrina-Barreto et al. [26]. The thermal image of each foot is divided into four subimages, corresponding to the four angiosomes mentioned before, and then all the

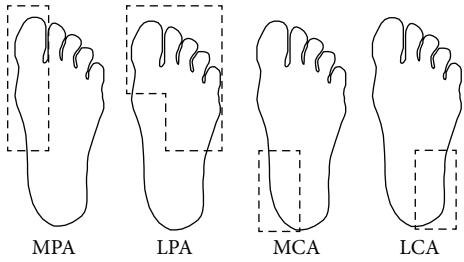


FIGURE 3: Angiosomes suggested by Taylor and Palmer [24] for temperature analysis.

pixels are classified according to their temperature. The image division is manually performed.

Let  $I \in \mathbb{R}^{n \times m}$  be an image corresponding to an angiosome,  $p_{\text{RGB}}(x, y) \in I$  is a pixel in the color space RGB,  $C$  is the set of temperature classes, and  $C_{\text{RGB}}$  is the set of the RGB coordinates of each class. Consequently, the pixel classification is achieved through the following rule:

$$k \in \arg \min_{C_{\text{RGB}}} \|p_{\text{RGB}} - C_{\text{RGB}}\|_2, \quad (1)$$

where  $k$  is the index related to the closest temperature class to  $p$ ; that is, the  $C_k$  is the class assigned to  $p$ . An area value  $A = \{a_0, \dots, a_7\}$  has been assigned to each temperature class. When a pixel is classified with the class  $C_k$ , its corresponding area ( $a_k$ ) is increased. In this way, when the complete image is processed, the area covered by certain class is known. In the case of the background, composed of more than one segment, all pixels are considered belonging to the same class ( $C_0$ ). The foot total area ( $a_{\text{total}}$ ) is composed of the area of all classes in  $C$ , except  $C_0$ :

$$a_{\text{total}} = \sum_{i=1}^7 a_i. \quad (2)$$

In order to approximate the general temperature of an angiosome, it is considered the weighted mean of the largest class and its adjacent classes as the estimated temperature (ET),

$$\text{ET} = \frac{a_{j-1}C_{j-1} + a_jC_j + a_{j+1}C_{j+1}}{a_{j-1} + a_j + a_{j+1}} \quad \text{s.t } j \in \arg \max_A (A), \quad (3)$$

where  $j$  is the index of the element belonging to  $A$  with higher value. Since the estimated temperature of an angiosome is known, it is possible to have the estimated temperature difference (ETD) of the corresponding angiosomes between both feet to determine if the difference is normal [20]

$$\text{ETD} = |\text{ET}_{\text{left Angiosome}} - \text{ET}_{\text{right Angiosome}}|. \quad (4)$$

**2.4. Hot Spots Detection.** Hot spots are considered small regions on the foot with a higher temperature compared to the ET value of the angiosome they belong. Previous works reported that hot spots occur mainly upon the metatarsal

heads, great toe and heel, all of them areas of high foot pressure [8, 11]. Hot spots frequently lead in a high risk of ulceration thus their early detection is important. Considering that ETD value is based on the most representative areas, it does not bring information about the beginning of the temperature increasing (hot spots) that could represent a major risk when they cover a larger area. In order to determine if a hot spot represents an ulceration risk, a deeper analysis of the temperatures in the angiosomes is carried out. First, the higher index is selected ( $l$ ) among the corresponding indexes of the elements of  $A$  with nonzero values,

$$l = \arg \min_X (X) \quad \text{s.t. } X = \{i \mid a_i \in A \neq 0\}. \quad (5)$$

As a result, the higher temperature present in the angiosome ( $C_l$ ) is known regardless the area that it covers. Thereupon, the presence of a hot spot is estimated by obtaining the difference of temperature between  $C_l$  and the ET (6). The hot spot estimator (HSE) provides useful information on whether there are small hot spots and how much they differ from the general temperature of the angiosome:

$$\text{HSE} = |c_l - \text{ET}|. \quad (6)$$

### 3. Experimental Results

According to previous studies, the temperature variation between corresponding regions in both feet usually does not vary beyond  $1^\circ\text{C}$ ; a difference greater than  $2.2^\circ\text{C}$  is considered as abnormal [15, 27]. The ranges established by [6] were considered in order to determine whether the plantar temperature is normal. Moreover, research results presented by Papanas et al. [7] about plantar temperature were taken into account. That study concluded that patients with diabetes type 2 with and without neuropathy have a plantar temperature of  $32.2 \pm 0.94^\circ\text{C}$  and  $30.7 \pm 1.07^\circ\text{C}$ , respectively. The goal in this work is to identify differences between corresponding areas of the right and left foot in order to obtain quantitative information about the plantar temperature distribution. Furthermore, it addressed the early detection of hot spots in an initial phase (small areas) with the aim of preventing their expansion and future complications. Both estimations could be useful for the specialist in early risk detection. The thermal images used in this work correspond to patients diagnosed with diabetes type 2 and neuropathy. Figure 4 shows one of the obtained images, which is divided into two sections corresponding to the right and left foot. These images are processed in order to classify their pixels. All the pixels from each image are processed and classified in order to make the limits among the temperature regions clear. As it was described in Table 1, there are eight classes with a representative temperature and an associated color, and all the pixels are classified according to (1).

The importance of this process lies on the fact that in the original images it is difficult to determine where a color starts or ends due to the large number of colors (Figures 5(a) and 5(c)). The proposed classification process provides an estimated number of pixels (area) for every temperature

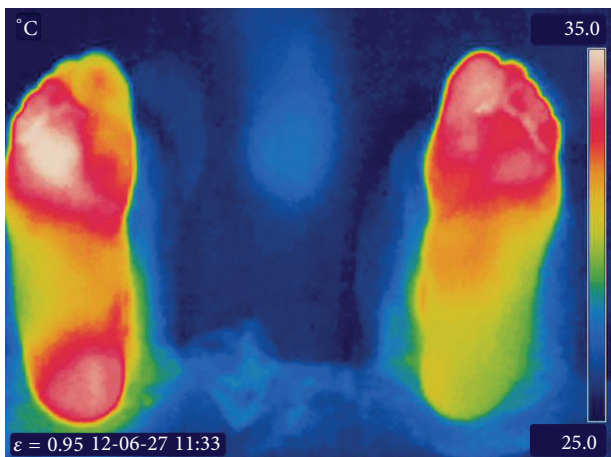


FIGURE 4: Original thermal feet image.

class. Every time a pixel is classified as belonging to a class, the counter associated with that class is increased. Since only the foot area is relevant for the analysis, the remaining temperatures are considered background and they are not taken into account for the measurement. Thus, the classes  $C_1$  to  $C_7$  comprise the total foot area ( $a_{\text{total}}$ ). In this way, the foot is off the background, as it can be observed in Figures 5(b) and 5(d), where the background is uniform and the regions are well defined in their corresponding classes. In this case, the entire feet were processed by way of example and to provide a better perspective of the classification process. For practical purposes, in this methodology the pixel classification is as follows. Once the feet are separated in their corresponding images (Figures 5(a) and 5(c)), they are again divided into four subsections, one per angiosome (Figure 6). Observing the original MPA angiosome image of the left foot (Figure 6(a)), it can be supposed that the color corresponding to the  $C_5$  class has the greatest area. However, it is difficult to establish the limit among the colored regions in a clear way because of the similitude among some colors. A visual comparison between the MPA angiosome of both feet could be even more complicated; therefore, it is important to go beyond the visual perception and make a quantitative comparison of the temperature distribution. Once the pixel classification has been made, it is possible to clearly observe the area that covers certain temperature associated with a class.

The areas of each angiosome in Figure 6(b) are shown in the plot of Figure 7. The areas are translated into percentages and based on this data, it determined which classes have the larger area in the same angiosome of both feet. In the MPA angiosome analysis, it is observed that the majority of the angiosome area is divided among classes  $C_4$ ,  $C_5$ , and  $C_6$  for the left foot (Figure 7(a)), that is, a temperature interval of  $[31, 34]^\circ\text{C}$  according to Table 1. For the right foot, the class  $C_4$  is the predominant one with an interval of  $[31, 32]^\circ\text{C}$ . In the LPA plot (Figure 7(b)), it is observed that the foot temperatures are more distributed, being  $C_5$  and  $C_6$  the largest classes for the left foot, while  $C_4$  is the largest for the right foot. Then, the temperature intervals in the LPA angiosome are  $[32, 34]$

TABLE 2: Temperature analysis of Figure 4.

Angiosome	Foot	$C_j$	ET ( $^\circ\text{C}$ )	ETD ( $^\circ\text{C}$ )
MPA	Left	$C_6$	33.2	1.4
	Right	$C_4$	31.8	
LPA	Left	$C_6$	33.1	1.5
	Right	$C_4$	31.6	
MCA	Left	$C_3$	30.6	2.8
	Right	$C_6$	33.4	
LCA	Left	$C_2$	29.4	2.2
	Right	$C_4$	31.6	

and  $[31, 32]^\circ\text{C}$  for the left and right foot, respectively. For the calcaneal angiosomes (MCA and LCA), the temperature distribution has a more drastic variation respect to MPA and LPA. The MCA angiosome temperature in the left foot with a predominant class  $C_3$  is lower ( $[30, 31]^\circ\text{C}$ ) than in the right foot with a predominant class  $C_6$  ( $[33, 34]^\circ\text{C}$ ), as shown in Figure 7(c). LCA temperature is also very different, being  $C_2$  ( $[29, 30]^\circ\text{C}$ ) in the left foot and,  $C_4$  ( $[31, 32]^\circ\text{C}$ ) the right foot, the predominant classes (Figure 7(d)).

The importance of including the data of the adjacent classes is because they have values closer to the class with larger area and they allow a better estimation of the temperature by (3). For the MPA in the left foot,  $C_j = C_6$  and the adjacent classes are  $C_5$  and  $C_7$  with classmarks 33.5, 32.5 and 34.5 and areas 28, 27 and 10 (percentages), respectively. Thus, the estimated temperature in this region is  $\text{ET}_{\text{leftMPA}} = 33.2^\circ\text{C}$ . Following the same procedure, the MPA for the right foot with  $C_j = C_4$  has an  $\text{ET}_{\text{rightMPA}} = 31.8^\circ\text{C}$ . With these data, it is possible to estimate by (4) that between the MPAs regions there is an  $\text{ET}_{\text{DMPA}} = 1.4^\circ\text{C}$ . Table 2 summarizes the described estimation for all the angiosomes of both feet by (3). In Figure 6(a), it is noted that the biggest visual difference is in the MCAs and LCAs angiosomes, and after computing their data it is known that these regions have a difference of temperature that exceeds the normal difference of  $2^\circ\text{C}$ . In addition, if the mean temperature of the whole feet (ET) is estimated based on the temperatures of each angiosome, then both feet have a temperature of  $31.6^\circ\text{C}$  and  $32.1^\circ\text{C}$ , respectively. The difference between this data suggests a small difference in the temperature condition of the feet. However, after a deeper analysis, it can be observed that there are important differences in some regions that may not be distinguished in a qualitative analysis.

Another example is presented in Figure 8, where it is noticed how the pixel classification could be useful in the improvement of the temperature regions limitation. Figure 8(a) presents a wide red region in which it is difficult to define the limits of a color due to smooth transitions. Some regions even seem to be homogeneous at first sight. However, after the classification process (Figure 8), the regions identification is clearer and their analysis is easier; it is noted the presence of small hot spots. Table 3 summarizes the information obtained from the temperature classes and areas.

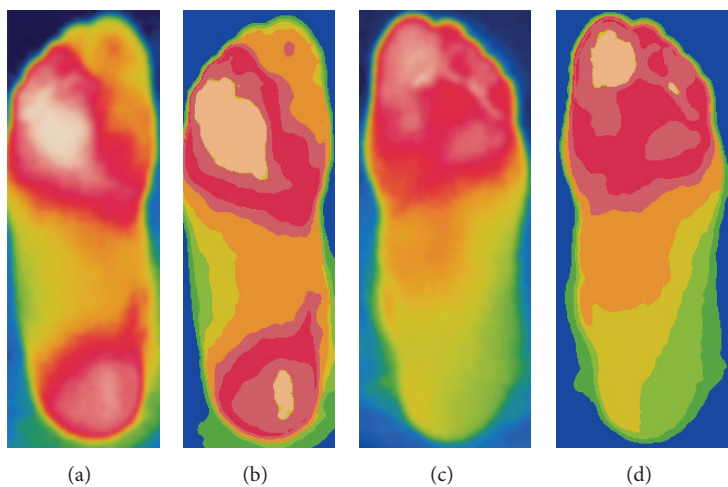


FIGURE 5: ((a), (c)) Feet images extracted from Figure 4 and ((b), (d)) the result of pixel classification.

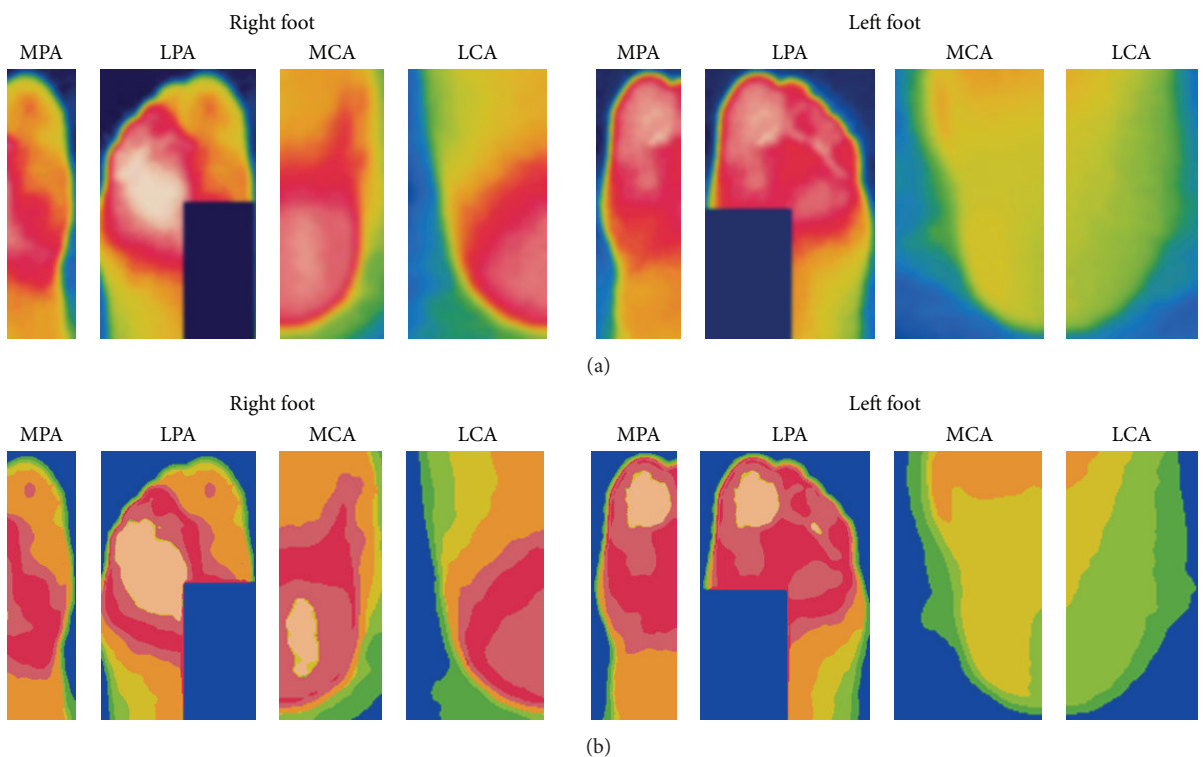


FIGURE 6: (a) Angiosome images of Figure 4 and (b) their color classification.

As it is observed, the most representative temperature classes are similar in some angiosomes in which ETD has lower values. According to the ETD values, there are no abnormal differences between feet; nevertheless, it is important to analyze the temperature differences inside an angiosome with the aim of detecting an additional type of abnormalities: hot spots. Although ETD brings important information, it does not detect abnormalities when the temperatures in the feet are similar because it is based on the values of larger classes. As mentioned before, a hot spot is an area whose temperature is significantly higher respect to its adjacent areas and the

HSE value tries to detect it in an initial phase. Hot spots detection provides information that help to detect suspicious areas where an ulceration process could be starting.

In order to detect hot spots, the HSE value is calculated by (6). First, it is necessary to determine the class associated with higher temperature present in an angiosome ( $C_l$ ). For instance in the MPA angiosome of Figure 8,  $C_l$  corresponds to  $C_6$  for the right foot then, HSE value is  $2.0^\circ\text{C}$  right foot; once again, the differences in more than  $2^\circ\text{C}$  degrees are suspicious. In this angiosome, a small hot spot near the thumb bottom as well as a wider area belonging to  $C_4$  can be observed. The

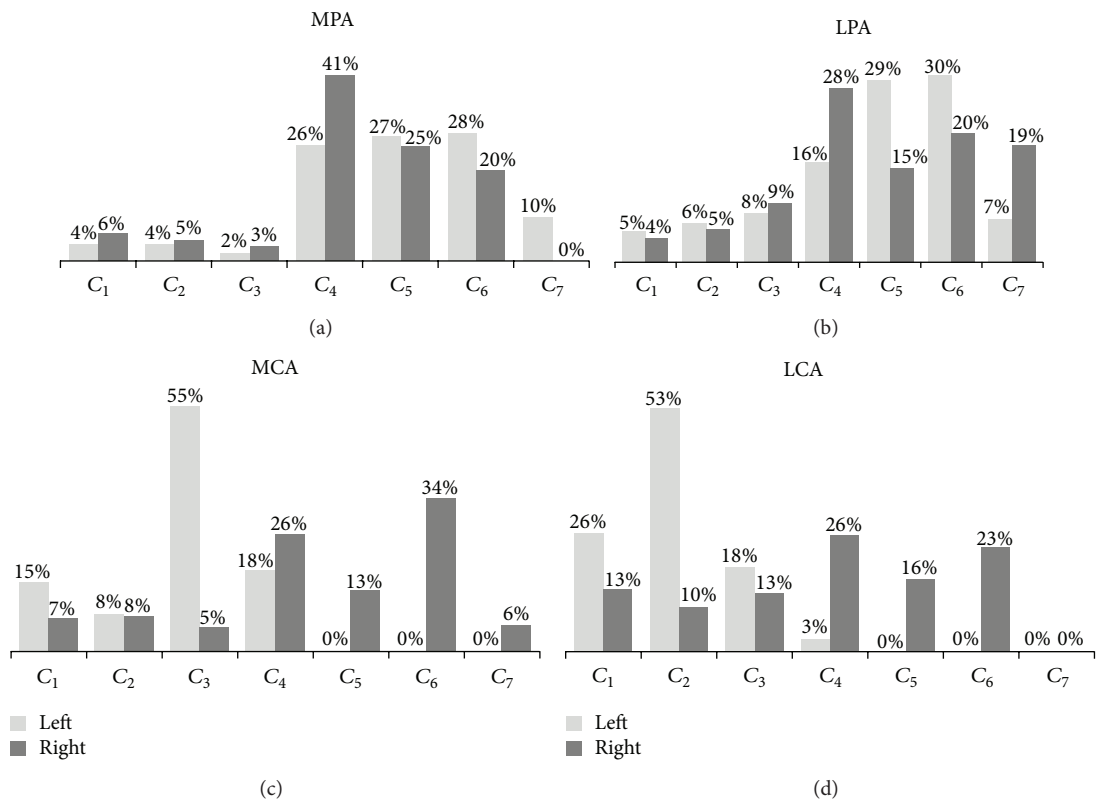


FIGURE 7: Graphical representation of the area (as percentage) that covers each temperature class in the angiosome (a) MPA, (b) LPA, (c) MCA and (d) LCA of the left and right feet of Figure 6(b). The representative temperature of an angiosome is given by the larger class and their two adjacent classes.

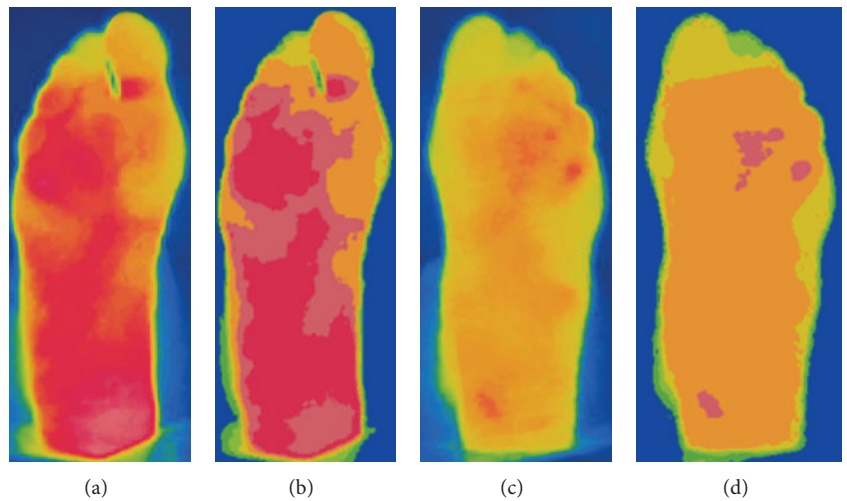


FIGURE 8: Example 2 of thermal feet images ((a), (c)) and their results after pixel classification.

HSE value suggests that there are abnormal areas but it is the expert who should decide which ones must be under observation. This is because an angiosome only shows a segment of the plantar area and one region detected as a hot spot may be part of a larger region and not a hot area in an initial phase. This is the case for the hot spots detected in the right MPA. For the left MPA with  $C_l = C_4$ , the HSE value is

0.2°C. In the analysis of the LPA angiosome (which include the MPA region mentioned above) the HSE does not show abnormal differences in the right foot. For the left LPA the detector indicates a difference of 2.3°C which is associated with three hot spots near each other. In this case, the hot spots neither belong to a larger region nor appear in the respective MPA. Another hot spot was found in the left MCA where

TABLE 3: Temperature analysis of Figure 8.

Angiosome	Foot		ETD (°C)	
	Right	Left		
MPA			$C_j = C_4$ ET = 31.5°C $C_l = C_6$ HSE = 2.0°C $C_j = C_4$ ET = 31.2°C $C_l = C_4$ HSE = 0.2°C	0.3
LPA			$C_j = C_4$ ET = 31.8°C $C_l = C_6$ HSE = 1.7°C $C_j = C_4$ ET = 31.2°C $C_l = C_6$ HSE = 2.3°C	0.6
MCA			$C_j = C_5$ ET = 32.9°C $C_l = C_6$ HSE = 0.6°C $C_j = C_4$ ET = 31.4°C $C_l = C_6$ HSE = 2.1°C	1.5
LCA			$C_j = C_5$ ET = 32.6°C $C_l = C_6$ HSE = 0.9°C $C_j = C_4$ ET = 31.4°C $C_l = C_4$ HSE = 0.4°C	1.2
$\overline{ET} = 32.2^\circ\text{C}$		$\overline{ET} = 31.3^\circ\text{C}$		

$C_l = C_6$  and the HSE = 2.1°C. Although the angiosome differences (ETD) do not indicate abnormal temperatures, the HSE estimator indicates the presence of possible hot spots in the right MPA, and in the left LPA and MCA. The estimator could be suggesting that these angiosomes contain suspicious areas which should be under a continuous revision.

It is observed that the mean temperatures of the feet in Figure 5 (31.6°C and 32.1°C) and Figure 8 (32.2°C and 31.3°C) exceed the normal plantar temperature ( $26.8 \pm 1.8^\circ\text{C}$ ) and both are in the characteristic range classified as neuropathy ( $32.2 \pm 0.94^\circ\text{C}$ ). It can be noticed by observing the temperatures of the angiosomes that most of them are also

in this last range. Both thermographs correspond to patients diagnosed with neuropathy as mentioned before.

## 4. Discussion

While there is an important amount of scientific reports about temperature analysis in the diabetic foot, most of them rely on qualitative analysis. However, it is not always simple to estimate the abnormal temperature differences by visual inspection of the thermogram. The aim of the proposed methodology is to bring precise information about such differences by facilitating the detection of possible risks regions and their evolution to the medical specialist. Although not all the regions with abnormal temperature will become an ulcer, their monitoring is very important as they represent high-risk regions. It is significant to remark that this methodology is not a diagnostic tool but a tool that brings complementary information to be evaluated by the medical specialist in order to facilitate early detection of ulceration risks.

## 5. Conclusions

Thermal imaging and image analysis are useful tools in the medicine field applied to the study of diseases such as diabetes. Temperature distribution in the plantar area contains relevant information about the condition of diabetic foot and ulceration risks. In this work, a methodology was presented aiming at providing quantitative information about abnormal temperature differences in symmetric regions between feet and inside of the same foot. The methodology took into account the temperature differences, their distribution, and area. As a first analysis, differences between symmetric areas in both feet were studied since it is known that symmetric regions in the body have similar temperatures. For this, the plantar area was divided into four main regions (angiosomes) and the temperatures inside those regions were grouped in classes according to a color similitude criterion. An index (ET) based on the relation between the class with larger area and its adjacent classes was proposed in order to estimate a representative temperature for each angiosome. Thus, it was possible to obtain an estimated difference (ETD) between symmetric regions which obtained an accurate measure to determine whether there is an abnormal difference or not. A second analysis was performed to study the temperatures inside the angiosomes with the aim of detecting the presence of small abnormal areas (hot spots). For that reason, it proposed a hot spot estimator (HSE) that relates the representative temperature of the angiosome with the higher temperature on it. This estimator was capable to detect the presence of abnormal regions in initial phase that, for their small area, were not detected by the estimator ETD. In this way, it was possible to analyze the whole plantar area by bringing quantitative information to determine the presence of regions in possible risk of ulceration. The results of the temperature measurement agreed with previous reports about the diabetic foot temperature characterization. Thus, this study provided an approach to bring reliable information

to help the specialist in the early detection of the ulceration risks of the diabetic foot associated with high temperatures.

## Conflict of Interests

The authors declare that there is no conflict of interests regarding the publication of this paper.

## Acknowledgment

The author H. Peregrina-Barreto wants to thank to the Consejo Nacional de Ciencia y Tecnología (CONACYT, México) for the financial support through the postdoctoral residency for the develop of this work.

## References

- [1] N. A. Diakides, "Infrared imaging: an emerging technology in medicine," *IEEE Engineering in Medicine and Biology Magazine*, vol. 17, no. 4, pp. 17–18, 1998.
- [2] S. Sivanandam, M. Anburajan, B. Venkatraman, M. Menaka, and D. Sharath, "Medical thermography: a diagnostic approach for type 2 diabetes based on non-contact infrared thermal imaging," *Endocrine*, vol. 42, no. 2, pp. 434–451, 2012.
- [3] B. B. Lahiri, S. Bagavathiappan, T. Jayakumar, and J. Philip, "Medical applications of infrared thermography: a review," *Infrared Physics and Technology*, vol. 55, no. 4, pp. 221–235, 2012.
- [4] L. A. Lavery, K. R. Higgins, D. R. Lanctot et al., "Home monitoring of foot skin temperatures to prevent ulceration," *Diabetes Care*, vol. 27, no. 11, pp. 2642–2647, 2004.
- [5] S. Bagavathiappan, J. Philip, T. Jayakumar et al., "Correlation between plantar foot temperature and diabetic neuropathy: a case study by using an infrared thermal imaging technique," *Journal of Diabetes Science and Technology*, vol. 4, no. 6, pp. 1386–1392, 2010.
- [6] P. C. Sun, H. D. Lin, S. H. E. Jao, Y. C. Ku, R. C. Chan, and C. K. Cheng, "Relationship of skin temperature to sympathetic dysfunction in diabetic at-risk feet," *Diabetes Research and Clinical Practice*, vol. 73, no. 1, pp. 41–46, 2006.
- [7] N. Papanas, K. Papatheodorou, D. Papazoglou, C. Monastiriotis, and E. Maltezos, "Foot temperature in type 2 diabetic patients with or without peripheral neuropathy," *Experimental and Clinical Endocrinology and Diabetes*, vol. 117, no. 1, pp. 44–47, 2009.
- [8] D. G. Armstrong, L. A. Lavery, P. J. Liswood, W. F. Todd, and J. A. Tredwell, "Infrared dermal thermometry for the high-risk diabetic foot," *Physical Therapy*, vol. 77, no. 2, pp. 169–175, 1997.
- [9] H. I. Lippmann, "Must loss of limb be a consequence of diabetes mellitus?" *Diabetes Care*, vol. 2, no. 5, pp. 432–436, 1979.
- [10] S. J. Benbow, A. W. Chan, D. R. Bowsher, G. Williams, and I. A. Macfarlane, "The prediction of diabetic neuropathic plantar foot ulceration by liquid-crystal contact thermography," *Diabetes Care*, vol. 17, no. 8, pp. 835–839, 1994.
- [11] P. I. Bränemark, S. E. Fagerberg, L. Langer, and J. Säve-Söderbergh, "Infrared thermography in diabetes mellitus a preliminary study," *Diabetologia*, vol. 3, no. 6, pp. 529–532, 1967.
- [12] M. Bharara, J. Schoess, and D. G. Armstrong, "Coming events cast their shadows before: detecting inflammation in the acute diabetic foot and the foot in remission," *Diabetes/Metabolism Research and Reviews*, vol. 28, no. 1, pp. 15–20, 2012.

- [13] S. Ohsawa, Y. Inamori, K. Fukuda, and M. Hirotuji, "Lower limb amputation for diabetic foot," *Archives of Orthopaedic and Trauma Surgery*, vol. 121, no. 4, pp. 186–190, 2001.
- [14] D. S. Sims Jr., P. R. Cavanagh, and J. S. Ulbrecht, "Risk factors in the diabetic foot: recognition and management," *Physical Therapy*, vol. 68, no. 12, pp. 1887–1902, 1988.
- [15] K. Roback, "An overview of temperature monitoring devices for early detection of diabetic foot disorders," *Expert Review of Medical Devices*, vol. 7, no. 5, pp. 711–718, 2010.
- [16] M. Bharara, J. L. Mills, K. Suresh, H. L. Rilo, and D. G. Armstrong, "Editorial: diabetes and landmine-related amputations: a call to arms to save limbs," *International Wound Journal*, vol. 6, no. 1, pp. 2–3, 2009.
- [17] S. O. Skrøvseth and F. Godtliebsen, "Scale space methods for analysis of type 2 diabetes patients' blood glucose values," *Computational and Mathematical Methods in Medicine*, vol. 2011, Article ID 672039, 7 pages, 2011.
- [18] K. S. Cheng, J. S. Yang, M. S. Wang, and S. C. Pan, "The application of thermal image analysis to diabetic foot diagnosis," *Journal of Medical and Biological Engineering*, vol. 22, no. 2, pp. 75–81, 2002.
- [19] "Thermography guidelines," Standards and Protocols in Clinical Thermographic Imaging IACT (International Academy of Clinical Thermology), 2002, <http://www.iact-org.org/professionals/thermog-guidelines.html>.
- [20] M. Glehr, A. Stibor, P. Sadoghi et al., "Thermal imaging as a noninvasive diagnostic tool for anterior knee pain following implantation of artificial knee joints," *International Journal of Thermodynamics*, vol. 14, no. 2, pp. 71–78, 2011.
- [21] J. D. Hardy, "The radiation of heat from the human body. I. An instrument for measuring the radiation and surface temperature of the skin," *Journal of Clinical Investigation*, vol. 13, no. 14, pp. 593–620, 1934.
- [22] J. D. Hardy, "The radiation of heat from the human body. III. The human skin as a black-body radiator," *Journal of Clinical Investigation*, vol. 13, no. 4, pp. 615–620, 1934.
- [23] T. Nagase, H. Sanada, K. Takehara et al., "Variations of plantar thermographic patterns in normal controls and non-ulcer diabetic patients: novel classification using angiosome concept," *Journal of Plastic, Reconstructive and Aesthetic Surgery*, vol. 64, no. 7, pp. 860–866, 2011.
- [24] G. I. Taylor and J. H. Palmer, "The vascular territories (angiosomes) of the body: experimental study and clinical applications," *British Journal of Plastic Surgery*, vol. 40, no. 2, pp. 113–141, 1987.
- [25] C. E. Attinger, K. K. Evans, E. Bulan, P. Blume, and P. Cooper, "Angiosomes of the foot and ankle and clinical implications for limb salvage: reconstruction, incisions, and revascularization," *Plastic and Reconstructive Surgery*, vol. 117, no. 7, pp. 261S–293S, 2006.
- [26] H. Peregrina-Barreto, L. M. Morales-Hernandez, J. J. Rangel-Magdaleno, and P. Vazquez-Rodríguez, "Thermal image processing for quantitative determination of temperature variations in plantar angiosomes," in *Proceedings of the IEEE International Conference on Instrumentation and Measurement*, pp. 816–820, 2013.
- [27] D. G. Armstrong, B. A. Lipsky, A. B. Polis, and M. A. Abramson, "Does dermal thermometry predict clinical outcome in diabetic foot infection? Analysis of data from the SIDESTEP trial," *International Wound Journal*, vol. 3, no. 4, pp. 302–37, 2006.

# Thermographic findings in a case of type 2 diabetes with foot ulcer and osteomyelitis

Using thermography, skin temperature was evaluated in a 76-year-old patient with type II diabetes mellitus, presenting with diabetic foot ulceration on the right hallux and a corn on the left fourth toe. Increased skin temperature was observed in both the right hallux and the left fourth toe, though there were no visible clinical signs of infection. Unexpectedly, the high temperature area was seen to extend from the left fourth toe to the ankle. The patient was later diagnosed with osteomyelitis, due to the presence of a high-intensity area on T2-weighted magnetic resonance imaging, suggesting the elevated skin temperature was due to osteomyelitis. Based on these observations, thermography could prove useful for screening for foot ulcers with osteomyelitis.

**diabetic foot ulcers; osteomyelitis; thermography**

**M. Oe,<sup>1</sup>** PhD, RN;  
**R.R.Yotsu,<sup>2</sup>** MD, MIPH;  
**H. Sanada,<sup>1</sup>** PhD,  
 WOCN, RN;  
**T. Nagase,<sup>1</sup>** MD, PhD;  
**T.Tamaki,<sup>2</sup>** MD, PhD;  
<sup>1</sup> Department of  
 Gerontological Nursing/  
 Wound Care  
 Management, Graduate  
 School of Medicine,  
 University of Tokyo, Japan;  
<sup>2</sup> Department of  
 Dermatology, National  
 Centre for Global Health  
 and Medicine (NCGM)  
 Hospital, Tokyo, Japan.  
 E-mail: yotsurie@hotmail.com

**Declaration of interest:**  
 This study was supported by a grant from the National Centre for Global Health and Medicine (22-120). The authors have no additional conflicts of interest to declare.

**D**iabetic foot ulceration (DFU) severely affects a patient's physical condition, long-term prognosis and quality of life.<sup>1–4</sup> Furthermore, diabetic patients with neuropathy cannot recognise an injury until ulceration and/or infection occurs,<sup>5</sup> therefore, an effective, objective assessment method for identifying developing or progressing DFU is important.

One possible tool for detecting the risk of ulceration in patients with diabetes mellitus is thermography. A number of studies have previously highlighted the usefulness of thermometry in monitoring skin temperature to reduce the risk of ulceration.<sup>6–8</sup> However, compared with conventional devices for measuring skin temperature at local points, such as contact infrared skin thermometers (TempTouch; Xilas Medical, Inc.),<sup>6–8</sup> thermography has the advantage that it can visualise morphological patterns of temperature distribution.<sup>9,10</sup> In a cross-sectional study of patients with foot calluses, latent inflammation was detected by thermography in 10% of patients with diabetes,<sup>11</sup> suggesting the versatility of thermography as a screening tool for the potential risk of DFU.

One of the most serious complications of DFU is osteomyelitis, as its diagnosis and treatment (surgery and/or long-term antibiotics) have been

long-standing controversies.<sup>12–14</sup> Therefore, early detection of osteomyelitis is important. Although magnetic resonance imaging (MRI) is the gold standard for diagnosing osteomyelitis,<sup>12–14</sup> it has disadvantages, such as high cost and non real-time diagnosis. Temperature assessment using non-invasive and easy-to-use thermography could be one consideration in helping identify the presence of osteomyelitis. However, to date, there have been no reports on thermography of DFU with osteomyelitis. Here, we report a case study of patient with both DFU and osteomyelitis, detailing the thermographic findings.

This research was approved by the Ethics Committee at National Centre for Global Health and Medicine Hospital. The patient gave his written informed consent.

## Case report

A 76-year-old man with type 2 diabetes mellitus (disease duration 28 years) was admitted to the Department of Dermatology, National Centre for Global Health and Medicine (NCGM) Hospital, Tokyo, Japan, with DFU located on the right hallux. He had neuropathy (decrease in sensation for 5.07 monofilament) and angiopathy (ankle brachial pressure index=0.63 [right] and 1.09 [left]).

**Table 1. Skin temperature at days 106 and 196**

		Day 106		Day 196	
		Skin temp (°C)	ΔTemp* (°C)	Skin temp (°C)	ΔTemp* (°C)
<b>Right</b>	Hallux	34.2	0.7	32.8	-0.1
	Dorsum	33.8	0.3	31.3	-1.6
	Ankle	33.8	0.3	31.9	-1.6
	Knee	33.5	—	32.9	—
<b>Left</b>	Fourth toe	35.3	1.2	33.4	0.3
	Dorsum	35.2	1.1	33.3	0.2
	Ankle	35.2	1.1	33.5	0.4
	Knee	34.1	—	33.1	—

\*Temperature difference ( $\Delta\text{Temp}$  = temperature of local skin–knee skin temperature) was adopted as the secondary outcome in this study for the parameter of increasing skin temperature, as toe skin temperature is not typically higher than knee skin temperature. Positive values for temperature difference could indicate inflammatory temperature increase at each site

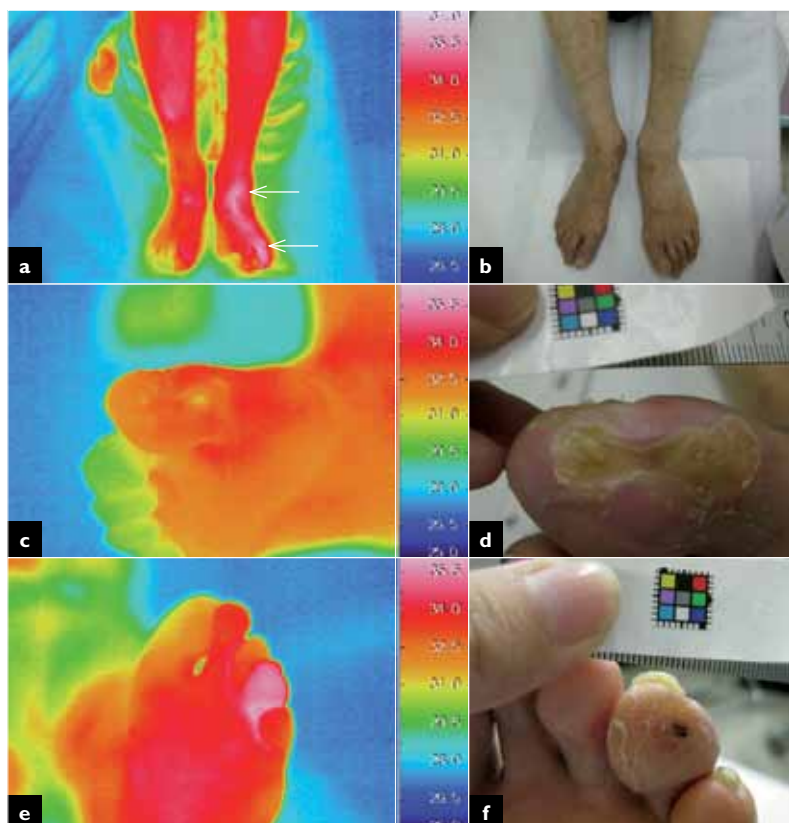


**Fig 1.** Thermal and visual images at day 106 of both legs, (a, b), the ulcer on the right hallux, (c, d), and corn on the left fourth toe, (e, f). Increased skin temperature was observed in both the right hallux and the left fourth toe with corn, though the infection was not observed by visual image, (f). Notably, the area of increasing skin temperature extended to the ankle (arrows)

On admission, he was diagnosed with osteomyelitis in his right hallux, due to a high intensity area on T2-weighted MRI, and was treated by systemic antibiotics (ampicillin and gentamicin) and topical silver sulphadiazine cream. The ulcer was not offloaded due to the patient's non-concordance, although the necessity of offloading was explained. Cleansing of the wound, and dressing change, were conducted once a day, and necrotic tissue was debrided, if necessary. His HbA1c level was 8.7%, and he was treated by subcutaneous insulin infusion. Wound size gradually decreased.

On day 106, a thermographic image of both his feet was taken using a Thermotracr TH7800N (NEC Avio Co. Ltd.); it was the first time that thermography was applied to a patient with DFU, in this setting. Thermographic images, after 15min of equilibration<sup>9,11</sup> were used to evaluate skin temperature. The temperature difference between the knee and each site was also evaluated, as foot skin temperature is not typically higher than knee skin temperature.

Thermography on day 106 confirmed that skin temperature was still increased in the right hallux. Unexpectedly, a greater increase in temperature was thermographically detected in the left fourth toe with a corn, although no macroscopic signs of infection were observed (Fig 1).

Notably, the area of increased skin temperature extended from the fourth toe to the ankle (arrows in Fig 1a, and Table 1), implying that latent inflammation could be associated with the corn.<sup>11</sup> On day 121, the patient was diagnosed with osteomyelitis in the left fourth toe by MRI (Fig 2), suggesting that the elevated skin temperature from the fourth toe to the ankle was due to osteomyelitis. Following diagnosis, systemic antibiotic therapy was restarted. No macroscopic signs of infection of the corn on the left fourth toe were observed following therapy. On day 106, the corn was treated through debridement, revealing a small ulcer underneath.

By day 195, the high intensity area on the right hallux was no longer visible on MRI; however, it was still observed on the left fourth toe (Fig 3). Increased skin temperature again extended from the left fourth toe to the ankle (arrows in Fig 4a); however, only a minimal increase in skin temperature was observed in the right hallux (Fig 4, Table 1).

These data might suggest that thermographic findings can reflect the time course of the osteomyelitis identified by MRI. The osteomyelitis could have been mostly healed in the right hallux, whereas it was clearly prolonged in the left fourth toe, even without visual inflammatory symptoms.

## Discussion

To our knowledge, this is the first report of thermography in a DFU patient with osteomyelitis. Notably, the area of increased skin temperature was seen

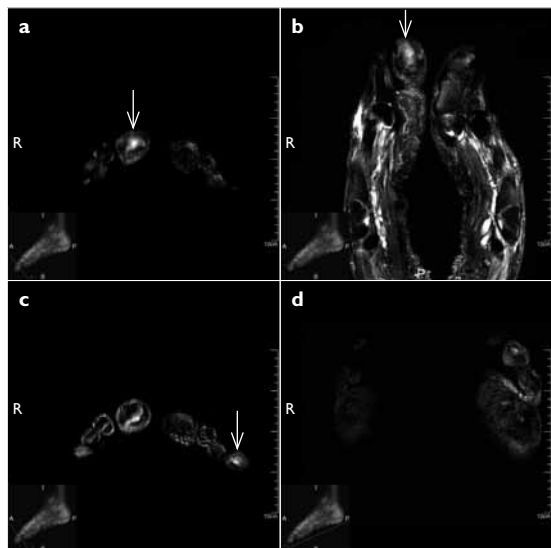


**Fig 2.** MRI on day 121 revealed a corresponding focus of increased T2 signal in the left fourth toe, (a, b), and right hallux, (c, d) (arrows)

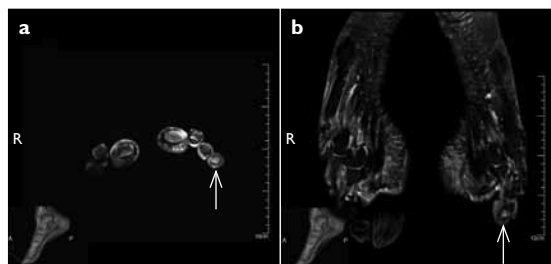


**Fig 3.** MRI at day 195 revealed a corresponding focus of increased T2 signal in the left fourth toe (a, b; arrows); prolonged osteomyelitis is suspected

to extend to the ankle, in a diabetic patient presenting with, previously undiagnosed, osteomyelitis of the left fourth toe.

In this case, increased skin temperature was observed exceeding the affected area of osteomyelitis. Swelling and/or the redness is sure to be macroscopically observed, if it is due to phlebitis or cellulitis, therefore, this result might suggest that fever of osteomyelitis can extend beyond the infected bone. More detailed analyses will be needed to confirm whether extension of increased skin temperature is a specific sign of osteomyelitis.

It is also of note that the corn without inflammatory signs was associated with prolonged osteomyelitis. It is reported that inflammatory subcutaneous changes are occasionally found underneath asymptomatic, seemingly dry, corns or calluses in patients with diabetes mellitus.<sup>11,15,16</sup> Such minimal skin changes should not be underestimated in the diabetic population.

While the importance of thermometry for lower extremities has been emphasised as a method for

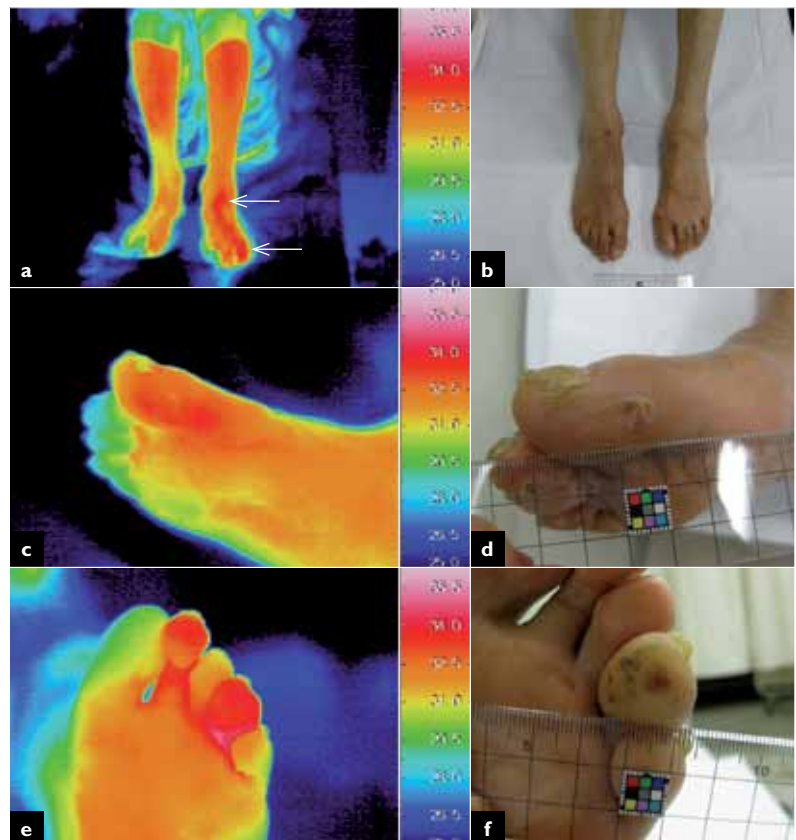


**Fig 4.** Thermal and visual images at day 196 of both legs, (a, b), the ulcer on the right hallux, (c, d), and corn on the left fourth toe, (e, f). Increased skin temperature was observed in the left fourth toe, and the area of increasing skin temperature was still extended to the ankle (a). On the other hand, increasing skin temperature in the right hallux was hardly observed. Note the absence of visual inflammatory signs in the left fourth toe, (f)

detecting risk of DFU,<sup>16,17</sup> only the local skin temperatures were measured in most of the previous reports. Here, thermography was used to visualise temperature distribution as the primary outcome, with the thermographic area of increased skin temperature found to extend to the ankle in this patient with osteomyelitis. This type of temperature evaluation may only be possible with thermography. Therefore, thermography could be a useful screening tool for DFU with osteomyelitis.

### Conclusion

Using thermography, skin temperature was evaluated in a patient with DFU. A high temperature area was observed, not only in the wounds, but also in the ankles. The patient was later diagnosed with osteomyelitis, due to the presence of a high-intensity area on MRI. Moreover, the high temperature was not observed in the wound after osteomyelitis had resolved. Based on these findings, thermography could prove useful for screening for DFU with osteomyelitis. ■

**References**

- 1** Lehto, S., Rönnemaa, T., Pyörälä, K., Laakso, M. Risk factors predicting lower extremity amputations in patients with NIDDM. *Diabetes Care.* 1996; 19: 6, 607–612.
- 2** Boyko, E.J., Ahroni, J.H., Smith, D.G., Davignon, D. Increased mortality associated with diabetic foot ulcer. *Diabet Med.* 1996; 13: 11, 967–972.
- 3** Ragnarson Tennvall, G., Apelqvist, J. Health-related quality of life in patients with diabetes mellitus and foot ulcers. *J Diabetes Complications.* 2000; 14: 5, 235–241.
- 4** Nabuurs-Franssen, M.H., Huijberts, M.S., Nieuwenhuijzen Kruseman, A.C. et al. Health-related quality of life of diabetic foot ulcer patients and their caregivers. *Diabetologia.* 2005; 48: 9, 1906–1910.
- 5** Pecoraro, R.E., Reiber, G.E., Burgess, E.M. Pathways to diabetic limb amputation. Basis for prevention. *Diabetes Care.* 1990; 13: 5, 513–521.
- 6** Armstrong, D.G., Holtz-Neiderer, K., Wendel, C. et al. Skin temperature monitoring reduces the risk for diabetic foot ulceration in high-risk patients. *Am J Med.* 2007; 120: 12, 1042–1046.
- 7** Lavery, L.A., Higgins, K.R., Lanctot, D.R. et al. Preventing diabetic foot ulcer recurrence in high-risk patients: use of temperature monitoring as a self-assessment tool. *Diabetes Care.* 2007; 30: 1, 14–22.
- 8** Lavery, L.A., Higgins, K.R., Lanctot, D.R. et al. Home monitoring of foot skin temperatures to prevent ulceration. *Diabetes Care.* 2004; 27: 11, 2642–2647.
- 9** Nagase, T., Sanada, H., Takehara, K. et al. Variations of plantar thermographic patterns in normal controls and non-ulcer diabetic patients: Novel classification using angiosome concept. *J Plast Reconstr Aesthet Surg.* 2011; 64: 7, 860–866.
- 10** Roback, K., Johansson, M., Starkhammar, A. Feasibility of a thermographic method for early detection of foot disorders in diabetes. *Diabetes Technol Ther.* 2009; 11: 10, 663–667.
- 11** Nishide, K., Nagase, T., Oba, M. et al. Ultrasonographic and thermographic screening for latent inflammation in diabetic foot callus. *Diabetes Res Clin Pract.* 2009; 85: 3, 304–309.
- 12** Jeffcoate, W.J., Lipsky, B.A. Controversies in diagnosing and managing osteomyelitis of the foot in diabetes. *Clin Infect Dis.* 2004; 39: (Suppl. 2), S115–122.
- 13** Berendt, A.R., Peters, E.J., Bakker, K. et al. Diabetic foot osteomyelitis: a progress report on diagnosis and a systematic review of treatment. *Diabetes Metab Res Rev.* 2008; 24: (Suppl. 1), S145–161.
- 14** Game, F. Management of osteomyelitis of the foot in diabetes mellitus. *Nat Rev Endocrinol.* 2010; 6: 1, 43–47.
- 15** Edmonds, M.E., Foster, A.V. Diabetic foot ulcers. *BMJ.* 2006; 332: 7538, 407–410.
- 16** Nagase, T., Sanada, H., Oe, M. et al. Screening of foot inflammation in diabetic patients by non-invasive imaging modalities. In: Dinh, T. (ed). *Global Perspective on Diabetic Foot Ulcerations.* InTech, 2011.
- 17** Bharara, M., Cobb, J.E., Claremont, D.J. Thermography and thermometry in the assessment of diabetic neuropathic foot: a case for furthering the role of thermal technique. *Int J Low Extrem Wounds.* 2006; 5: 4, 250–260.

Systematic Review

# Update on the Use of Infrared Thermography in the Early Detection of Diabetic Foot Complications: A Bibliographic Review

Marina Faus Camarena <sup>1</sup>, Marta Izquierdo-Renau <sup>1</sup>, Iván Julian-Rochina <sup>1,2,\*</sup>, Manel Arrébola <sup>3</sup> and Manuel Miralles <sup>3,4,5</sup>

<sup>1</sup> Nursing Department, University of Valencia, 46010 Valencia, Spain; marinafauscama@gmail.com (M.F.C.); marta.izquierdo-renau@uv.es (M.I.-R.)

<sup>2</sup> Frailty Research Organized Group (FROG), University of Valencia, 46010 Valencia, Spain

<sup>3</sup> Department Angiology and Vascular Surgery, La Fe University and Polytechnic Hospital, 46026 Valencia, Spain; manelarrebola@gmail.com (M.A.); mirallesmanher@gva.es (M.M.)

<sup>4</sup> Department of Surgery, University of Valencia, 46010 Valencia, Spain

<sup>5</sup> Haemostasis, Thrombosis, Arteriosclerosis and Vascular Biology Research Group, Medical Research Institute, Hospital La Fe, 46026 Valencia, Spain

\* Correspondence: ivan.julian@uv.es; Tel.: +34-961625679

**Abstract:** Foot lesions are among the most frequent causes of morbidity and disability in the diabetic population. Thus, the exploration of preventive control measures is vital for detecting early signs and symptoms of this disease. Infrared thermography is one of the complementary diagnostic tools available that has proven to be effective in the control of diabetic foot. The last review on this topic was published in 2015 and so, we conducted a bibliographic review of the main databases (PubMed, the Web of Science, Cochrane library, and Scopus) during the third quarter of 2023. We aimed to identify the effectiveness of infrared thermography as a diagnostic element in pre-ulcerous states in diabetic patients and to detect diabetic foot ulcer complications. We obtained a total of 1199 articles, 26 of which were finally included in the present review and published after 2013. After analyzing the use of infrared thermography in diabetic patients both with and without ulcers, as well as in healthy individuals, we concluded that it is an effective tool for detecting early-stage ulcers in diabetic foot patients.

**Keywords:** infrared thermography; thermal imaging; diabetic foot ulcer; diabetic neuropathy; diabetic patients; peripherical arterial disease; foot at risk



**Citation:** Faus Camarena, M.; Izquierdo-Renau, M.; Julian-Rochina, I.; Arrébola, M.; Miralles, M. Update on the Use of Infrared Thermography in the Early Detection of Diabetic Foot Complications: A Bibliographic Review. *Sensors* **2024**, *24*, 252. <https://doi.org/10.3390/s24010252>

Academic Editors: Weiting Liu and Georg Fischer

Received: 13 October 2023

Revised: 29 November 2023

Accepted: 22 December 2023

Published: 31 December 2023



**Copyright:** © 2023 by the authors. Licensee MDPI, Basel, Switzerland. This article is an open access article distributed under the terms and conditions of the Creative Commons Attribution (CC BY) license (<https://creativecommons.org/licenses/by/4.0/>).

## 1. Introduction

Foot lesions are among the most frequent causes of morbidity and disability in the population with diabetes and are the most common reason for hospital admission and decreased patient quality of life. Indeed, in this population, there is a 40–70% probability of requiring a lower limb amputation [1]. Exploration and preventive control of this pathology are vital to detect early signs and symptoms that, in the long term, can promote the appearance of ulcers. This exploration must be performed at least once in the absence of risk factors and once every six months if there is any risk of ulcers [2]. Therefore, it is especially important to follow a protocol for these patients, in which the anamnesis and clinical history play a substantial role.

Different complementary telemedical methods are available to aid the diagnosis of diabetic foot, of which infrared thermography is one of the most important [3]. This technique was first used for military applications at the beginning of the 20th century. However, infrared thermography soon transferred to biomedical fields and started being used for the non-invasive diagnosis of vascular disease, fever, breast cancer, and in the analysis of inflammatory arthritis, osteoarthritis, and other pathologies [4].

Infrared thermography is a safe, repeatable, contactless, and non-invasive procedure that measures and maps the temperature distribution radiating from body surfaces [5]. An infrared camera identifies and monitors the amount of radiation emitted and translates this value into a temperature. These projections allow identification of the heat radiating away from the body [3,6] and produce images with specific physiological thermal patterns that can be collected according to specific standards, thereby allowing the quality of this technique to increase in the future [6].

Feet temperature variation in neuropathic patients is a predictive element of the ulcer appearance, so infrared thermography, due to its characteristics and easy use, is a good tool to detect this temperature difference [7].

The aim of this systematic review was to define the effectiveness of infrared thermography as a diagnosis tool for pre-ulcerous states in patients with type-2 diabetic mellitus and to detect ulcer complications in patients with diabetic foot.

Based on the results obtained, we will try to provide relevant information for health professionals who use this technique, speeding up and helping in decision-making in patients who may develop an ulcer or its reappearance. However, there is some controversy in generalizing these statements, so more studies are needed to generalize the findings.

## 2. Materials and Methods

Following the preferred reporting items for systematic review and meta-analysis descripts (PRISMA) guidelines, we conducted a systematic review of the academic literature on infrared thermography as a tool for diagnosing diabetic foot. We followed the population, intervention, control, and outcomes (PICO) format (Table 1) to formulate the basis of this research.

**Table 1.** PICO research questions.

P	Patient	Healthy or diabetic patients with or without ulcers.
I	Intervention	Diagnosis of diabetic foot complications.
C	Comparison	Use of thermography as a diagnostic tool for complications versus not using this technology.
O	Outcomes	Early detection of complications.

We consulted the Descriptors in Health Science (DeCS) and Medical Subject Headings (MeSH) terms to devise the following PubMed search strategy: (((("Diabetic Foot"[Title/Abstract]) OR (diabetic foot[MeSH Terms])) OR ("Diabetic Neuropat hies"[Title/Abstract]) OR (diabetic neuropathies[MeSH Terms]))) AND (((("thermal imaging"[Title/Abstract]) OR (differential thermal analysis[MeSH Terms])) OR (analyses, differential thermal[MeSH Terms])). The results were subsequently summarized in databases, as shown in Table 2.

We searched the main health science databases including PubMed, the Web of Science (WoS), Scopus, and the Cochrane library during the third quarter of 2023. The inclusion criteria were articles about infrared thermography conducted in humans with and without diabetes and ulcers, published from 2013 to 2023 in English or Spanish. Some publications such as editorials, editor's letters, reviews, systematic reviews, meta-analyses, books or books chapters and conference reports were excluded. Of note, no Cochrane reviews were included because none met the inclusion criteria. Once the screened publications were obtained, we read the publications and reviewed their quality by employing the PEDro scale [8].

**Table 2.** Bibliographical database search strategy.

Database	Search Strategies	Data	Results
PubMed	((("Diabetic Foot"[Title/Abstract]) OR (diabetic foot[MeSH Terms])) OR (("Diabetic Neuropathies"[Title/Abstract]) OR (diabetic neuropathies[MeSH Terms]))) AND (((thermal imaging"[Title/Abstract]) OR (differential thermal analysis[MeSH Terms])) OR (analyses, differential thermal[MeSH Terms])))	September 2023	30
WoS	("Diabetic Foot" OR "Diabetic Neuropathies") AND ("thermal imaging" OR "differential thermal analysis")	September 2023	61
Cochrane	((diabetic foot) OR (neuropathy)) and ((thermal imaging) OR (infrared thermography) OR (temperature monitoring) or (infrared image) OR (skin temperature) OR (thermal imaging) OR (infrared sensor technology))	September 2023	224
SCOPUS	((diabetic AND foot) OR (neuropathy)) AND ((thermal imaging") OR ("infrared thermography") OR ("temperature monitoring") OR ("infrared image") OR ("skin temperature") OR ("thermal imaging") OR ("infrared sensor technology")))	September 2023	884

### 3. Results

Our search strategy obtained a total of 1199 publications (30 in PubMed, 61 in the WoS, 224 in the Cochrane library, and 884 in Scopus). After applying the inclusion criteria, 26 valid citations were reviewed, as reflected in the PRISMA flowchart (Figure 1). A brief description of the main features of the 26 articles found is provided in Table 3 (Table 3).

All the articles included were assessed according to the PEDro scale which assigned a score of 0 if the criterion is absent and 1 if it is present in the article [9]. The first criterion on this scale, reporting eligibility criteria, was not recorded because it considered the external validity of the articles. The conduct and design of study are evaluated by eight items (item 2–9). Item 10 involves reporting between-group statistical comparisons, and item 11 involves measures of variability [10]. On this scale, studies with scores higher than 9 points are considered to have excellent methodological quality, those with scores between 6 and 8 points are deemed good, those from 4 to 5 points are considered to have regular quality and those below 4 are regarded as having poor methodological quality.

**Table 3.** Description of articles included in the systematic review.

Author	Year	Type	Sample	Objectives	Results	Conclusions
1. Automatic detection of diabetic foot complications with infrared thermography by asymmetric analysis						
Liu, C.; van Netten, J.J.; van Baal, J.G.; Bus, S.A.; van der Heijden, F. [3]	2015	Asymmetric analysis.	76 patients with DM and diabetic foot complications.	Perform simple asymmetric analysis between the left and right foot combined with foot segmentation based on color images and non-rigid registration according to landmarks.	A segmentation of the feet was performed and infrared and color images were obtained.	Comparison of color and thermal images allowed the identification of common points between both materials.

**Table 3.** *Cont.*

Author	Year	Type	Sample	Objectives	Results	Conclusions
2. Infrared thermography and vascular disorders in diabetic feet						
Ilo, A.; Romsi, P.; Mäkelä, J. [5]	2020	Case-controlled study.	118 patients with DM and 93 healthy individuals.	Evaluate the diagnostic potential of a novel non-invasive diagnostic method, IRT, compared with the conventional non-invasive method (ankle-brachial index and pressure on the 1st finger) in 5 study areas.	Patients with DM generally had warmer feet with a significantly higher temperature. IRT revealed differences between angiosomal areas, subclinical infections, and high-pressure plantar areas.	IRT revealed local temperature differences in high-risk diabetic feet. However, it is important to combine its use with other traditional screening methods.
3. A medical thermal imaging device for the prevention of diabetic foot ulceration						
Machin, G.; Whittam, A.; Ainarkar, S.; Allen, J.; Bevans, J.; Edmonds, M.; Kluwe, B.M.A.; Petrova, N.; Plassmann, P.; Ring, F.; et al. [11]	2019	Descriptive, observational study.	103 healthy volunteers (50 men and 53 women).	Describe the development, characterization, and initial results of a thermal imaging device aimed at significantly reducing the incidence of DRFUs.	Healthy feet are thermally symmetrical. In some participants, there were differences of $>2.2^{\circ}\text{C}$ between the same site on both feet. After 10 min, these differences had significantly reduced.	These thermal imaging devices were shown to be fit for purpose and could identify areas of concern in the foot. This device could also be beneficial in other clinical settings such as in the study and prevention of pressure ulcers.
4. Reliability of a novel thermal imaging system for temperature assessment of healthy feet						
Petrova, N.L.; Whittam, A.; MacDonald, A.; Ainarkar, S.; Donaldson, A.N.; Bevans, J.; Allen, J.; Plassmann, P.; Kluwe, B.; Ring, F.; et al. [12]	2018	Multicenter clinical trial.	52 men and 53 women aged 18 to 69 years.	Explore the reliability of this device for assessing the temperature of healthy feet.	There was substantial-to-perfect inter-instrument agreement between the handheld thermometer and thermal imaging device, with the intra-class correlation coefficients in the 5 regions of interest ranging from 0.94 to 0.97.	The thermal imaging device showed exceptionally good agreement over repeated evaluations. Additionally, it could provide an instantaneous thermal image of all the sites on the feet.

**Table 3.** *Cont.*

Author	Year	Type	Sample	Objectives	Results	Conclusions
5. Reproducibility of thermal images: some healthy examples						
Macdonald, A.; Petrova, N.; Ainarkar, S.; Allen, J.; Plassmann, P.; Whittam, A.; Bevans, J.; Ring, F.; Kluwe, B.; Simpson, R.; et al. [13]	2017	Comparative, observational study.	30 healthy participants.	Investigate the use of thermal imaging in the treatment of patients at a high risk of developing DRFUs.	The feet were thermally symmetrical, although the absolute temperature varied between visits. Temperature differences at specific locations on the foot exceeded the threshold of 2.2 °C.	These studies provide a basic understanding of thermal symmetry in the feet of healthy participants that can be used when interpreting images of the feet of patients with DM and DPN.
6. Validation of low-cost smartphone-based thermal camera for diabetic foot assessment						
Van Doremalen, R.F.M.; van Netten, J.J.; van Baal, J.G.; Vollenbroek-Hutten, M.M.R.; van der Heijden, F. [14]	2019	Simple study.	32 participants.	Validate a smartphone-based high-end infrared camera for the assessment of diabetic foot.	Near-perfect agreement for the temperature measurements, both throughout the plantar foot and in pre-specified regions.	The validity of the smartphone-based infrared camera was excellent for assessing diabetic foot.
7. Infrared thermography and ulcer prevention in the high-risk diabetic foot: data from a single-blind multicentre controlled clinical trial						
Petrova, N.L.; Donaldson, N.K.; Tang, W.; MacDonald, A.; Allen, J.; Lomas, C.; Leech, N.; Ainarkar, S.; Bevans, J.; Plassmann, P. [15]	2020	Single-blinded, multicenter clinical trial.	110 patients with diabetes mellitus (DM), diabetic peripheral neuropathy (DPN), and a history of diabetes-related foot ulcers (DRFUs).	Evaluate the usefulness of thermography and standard foot care in reducing DRFU recurrence.	After 12 months, 62% of the participants in the intervention group and 56% in the control group were ulcer-free.	Monthly intervention with thermal imaging did not result in a significant reduction in the ulcer recurrence rate or increased ulcer-free survival. However, a refined study with a longer follow-up and group stratification was planned.

**Table 3.** Cont.

Author	Year	Type	Sample	Objectives	Results	Conclusions
8. Infrared thermal imaging for automated detection of diabetic foot complications						
Van Netten, J.J.; Van Baal, J.G.; Liu, C.; Van Der Heijden, F.; Bus, S.A. [16]	2013	Pilot study.	15 diabetic patients.	Explore the applicability of infrared thermal imaging for non-invasive automated systems.	Differences in the average temperature between the ipsilateral and contralateral foot were a maximum of 1.5 °C. The difference in patients with complications was at least 3 °C, with the feet of patients with Charcot–Marie–Tooth disease or osteomyelitis being warmer, and those with critical ischemia being colder compared to the contralateral foot.	An algorithm that could detect signs of diabetic foot disease and discriminate between non-local or diffuse diabetic foot complications was found. This algorithm was based solely on parameters that can be captured and analyzed with an infrared camera and a computer.
9. Infrared 3D thermography for inflammation detection in diabetic foot disease: a proof of concept						
Van Doremalen, R.F.M.; van Netten, J.J.; van Baal, J.G.; Vollenbroek-Hutten, M.M.R.; van der Heijden, F. [17]	2020	Single-center, prospective, cross-sectional study.	8 diabetic patients with a DRFU.	Explore the importance of 3D viewing of thermal imaging models for the detection of inflammation in diabetic foot disease.	Color definition maps were combined with thermal infrared images to create the first 3D infrared thermography (IRT) images of diabetic feet. Validity was evaluated +– 6 and +– in 2 cases.	3D viewing of thermographic images was clinically useful for the detection of inflammation.
10. Is thermal imaging a useful predictor of the healing status of diabetes-related foot ulcers? A pilot study						
Aliahmad, B.; Tint, A.N.; Arjunan, S.P.; Rani, P.; Kumar, D.K.; Miller, J.; Zajac, J.D.; Wang, G.; Ekinci, E.I. [18]	2018	Prospective, observational study.	Thermal and color images of 26 neuropathic DRFUs in people with type-1 or 2 DM.	Predict the healing of DRFUs using thermal imaging within the first 4 weeks of ulceration.	For the cases that healed, the ratio of wound bed area to baseline wound area measured by thermal imaging was significantly lower at 2 weeks compared to cases that did not heal.	This demonstrated that the change in the isothermal area of DRFUs can predict their healing status. DRFU thermal imaging has the advantage of incorporating both area and temperature, allowing the early prediction of healing of these ulcers.

**Table 3.** *Cont.*

Author	Year	Type	Sample	Objectives	Results	Conclusions
11. Between visit variability of thermal imaging of feet in people attending podiatric clinics with DPN at high risk of developing foot ulcers						
Macdonald, A.; Petrova, N.; Ainarker, S.; Allen John Lomas, C.; Tang, W.; Plassmann, P.; Ehittam, A.; Bevans, J.; Ring, F.; Kluwe, B. [19]	2019	Observational, prospective study.	96 patients DRFUs.	Quantify the inter-and intra-patient thermal variations presented in diabetic feet with a high risk of ulceration.	The variation in right/left temperature differences for patients between visits was comparable to the variation observed between patients.	Thresholds that depend on thermal differences from one visit to another are unlikely to be sufficiently specific to effectively target treatments designed to prevent the development of DRFUs.
12. The application of medical thermography to discriminate neuroischemic toe ulceration in the diabetic foot						
Gatt, A.; Falzon, O.; Cassar, K.; Camilleri, K.P.; Gauci, J.; Ellul, C.; Mizzi, S.; Mizzi, A.; Papanas, N.; Sturgeon, C.; et al. [20]	2018	Prospective study.	12 patients with type-2 DM recruited from a hospital.	Determine if thermography can detect temperature differences between healthy feet, non-ulcerated neuroischemic feet, and neuroischemic feet with toe ulcers in patients with type-2 DM.	There was a significant difference in toe temperature between these 3 groups.	First study to examine the thermographic patterns related to the toe temperature of patients with neuroischemic ulceration compared to non-ulcerated neuroischemic and healthy feet in patients with type-2 DM.
13. Comparison of thermal foot maps between diabetic patients with neuropathic, vascular, neurovascular, and no complications						
Astasio-Picado, Á.; Martínez, E.E.; Gómez-Martin, B. [21]	2019	Descriptive, cross-sectional, observational study.	277 patients with a diabetic pathology.	Use IRT to analyze temperature differences between the feet of users with DM with DPN, vasculopathy, neurovascular disease, or none of the above, by segmenting the sole of the foot into 4 areas for the purposes of the study.	Lower temperatures under the ball of the big and little toes, heel, and pulp of the big toe in patients with DM compared to the healthy group.	IRT may be useful in evaluating the foot at risk in order to reveal temperature variability depending on the area under study.

**Table 3.** Cont.

Author	Year	Type	Sample	Objectives	Results	Conclusions
14. Thermal map of the diabetic foot using infrared thermography						
Astasio-Picado, A.; Martinez, E.E.; Nova, A.M.; Rodriguez, R.S.; Gomez-Martin, B. [22]	2018	Descriptive, cross-sectional, observational study.	277 diabetic patients.	Study the use of IRT in the analysis of foot temperature variability in diabetic patients by segmenting the sole of the foot into 4 areas of interest.	The technique distinguishes any temperature variability between the different study areas of the soles of each foot.	IRT can provide useful clinical information to aid in the early diagnosis and prevention of lesions to compromised areas of the foot.
15. Morphological pattern classification system for plantar thermography of patients with diabetes						
Mori, T.; Nagase, T.; Takehara, K.; Oe, M.; Ohashi, Y.; Amemiya, A.; Noguchi, H.; Ueki, K.; Kadokawa, T.; Sanada, H. [23]	2013	Cross-sectional, observational study.	32 healthy individuals and 129 patients with DM.	Evaluate individual thermographic variations and compare them with angiosome results obtained in previous studies.	Different thermographic patterns (whole pattern and butterfly pattern) were compared between diabetic and non-diabetic patients.	The system, which was based on IRT, was useful for screening the circulatory status in patients with DM.
16. Early diagnosis of DPN based on infrared thermal imaging technology						
Zhou, Q.; Qian, Z.; Wu, J.; Liu, J.; Ren, L.; Ren, L. [24]	2021	Case-controlled study.	60 patients with mild DPN and 60 healthy volunteers.	Detect and compare the surface temperature of the plantar vessels in patients with mild DPN and healthy controls.	Excellent test-retest reliability, with differences in skin temperature between patients with mild DPN and healthy controls.	They provided a convenient, non-invasive, in vivo approach and methods for the early diagnosis of DPN.
17. Plantar temperature and vibration perception in patients with diabetes: a cross-sectional study						
Bhargavi, A.; Anantha, K.; Janarthan, K. [25]	2020	Case-controlled study.	50 healthy individuals and 50 patients with DM.	Correlate the temperature and vibration sensitivity values obtained from the same patient to reduce false positive results in the diagnosis of DRFUs.	The perception of vibration was compared with the points with the highest temperature on the contralateral feet.	More variables need to be compared to obtain better results for the classification of lesions in pre-ulcerative stages.
18. Early detection of foot ulceration in type II diabetic patient using registration method in infrared images and descriptive comparison with deep learning methods						
Rai, M.; Maity, T.; Sharma, R.; Yadav, R.K. [26]	2022	Observational, comparative study.	60 people (37 men and 23 women).	Early diagnosis and minimization of the appearance of DRFUs with the use of IRT.	The results clearly distinguished the foot region which showed a temperature difference higher than the assumed threshold value.	This analysis clearly classified the foot as at risk of ulceration and it was quite easy to understand compared to existing deep learning techniques.

**Table 3.** Cont.

Author	Year	Type	Sample	Objectives	Results	Conclusions
19. Morphological foot model for temperature pattern analysis proposed for diabetic foot disorders						
Arteaga-Marrero, N.; Bodson, L.C.; Hernandez, A.; Villa, E.; Ruiz-Alzola, J. [27]	2021	Comparative, observational study.	9 healthy women and 13 healthy men.	Provide a methodology to explore all the plantar aspects of both feet, based on IRT, for the evaluation of diabetic foot anomalies.	Comparison of both feet to register patterns; differences were observed between men and women.	A quick and easy monitoring tool was provided for diagnostic use in patients with diabetic foot disorders.
20. Plantar thermogram database for the study of diabetic foot complications						
Hernandez-Contreras, D.A.; Peregrina-Barreto, H.; Rangel-Magdaleno, J.D.; Reniero-Carrillo, F.J. [28]	2019	Descriptive, observational study.	334 plantar thermograms.	Use thermograms to collect images corresponding to the 4 plantar angiosomes in order to create a database.	Describes the plantar thermogram acquisition protocol, including the acquisition system and proper preparation of patients.	It was hoped that the database would become a valuable resource to promote research into the potential of IRT for the early diagnosis of diabetic foot problems.
21. Thermographic characteristics of the diabetic foot with peripheral arterial disease using the angiosome concept						
Carabott, M.; Formosa, C.; Mizzi, A.; Papanas, N.; Gatt, A. [29]	2021	Comparative study.	27 participants.	Compare temperature changes in 3 forefoot angiosomes after a limb elevation challenge between type-2 DM patients with and without peripheral arterial disease (PAD).	The mean resting temperature for all the angiosomes of participants with PAD were higher than for those without PAD. There was a significant difference in the initial mean temperature between the groups in the medial and lateral forefoot angiosomes.	Patients with PAD exhibited significantly higher forefoot temperatures, according to the analysis applying the angiosome concept.
22. Use of smartphone attached mobile thermography assessing subclinical inflammation: a pilot study						
Kanazawa, T.; Nakagami, G.; Goto, T.; Noguchi, H.; Oe, M.; Miyagaki, T.; Hayashi, A.; Sasaki, S.; Sanada, H. [30]	2016	Pilot study.	16 images.	Verify the reliability and validity of the FLIR ONE® camera for evaluating inflammation based on the relative temperature increase compared to thermography when routinely used in the evaluation of pressure ulcers and diabetic foot.	An analysis of 16 thermal images.	This study suggested that FLIR ONE® may function as an alternative device for the evaluation of subclinical inflammation in pressure ulcers and diabetic foot in clinical settings.

**Table 3.** *Cont.*

Author	Year	Type	Sample	Objectives	Results	Conclusions
23. Prevention of diabetic foot ulcers using a smartphone and mobile thermography: a case study						
Oe, M.; Tsuruoka, K.; Ohashi, Y.; Takehara, K.; Noguchi, H.; Mori, T.; Yamauchi, T.; Sanada, H. [31]	2021	Case study.	2 patients.	Evaluate the effects of a self-monitoring device to prevent diabetic foot ulcers using a thermographic camera connected to a smartphone.	One patient is able to detect an increase in temperature when walking while the other one cannot.	This device can be used for self-care, although it is important to modify it for use in high-risk situations.
24. Evaluation of the surface temperature distribution in the feet of patients with type 2 diabetes using the thermal imaging method						
Dębiec-Bąk, A.; Skrzek, A.; Ptak, A.; Majerski, K.; Uiberlayová, I.; Stefańska, M. [32]	2023	Case-control.	52 diabetic subjects and 33 controls.	Superficial dorsal and plantar temperature of both feet was measured in all participants using a thermal imaging device.	On average, diabetic patients dorsal and plantar temperature were 2.2 °C and 1.5 °C higher, respectively.	Thermography in diabetic patients can be a useful tool to detect neurotrophic changes in the feet.
25. Mobile Application for Ulcer Detection						
Fraiwan, L.; Ninan, J.; Al-Khodari, M. [33]	2018	Cross-sectional study.	4 images were analyzed: one healthy foot and the other 3 were ulcer-simulated situations	Develop a mobile application to detect potential ulcers using a smartphone connected to a thermal camera. A mean temperature difference greater than 2.2 °C was considered as an indicator of possible ulcer development.	The app detected one image with a mean temperature difference lower than 2.2 °C and the other three greater, as expected.	Temperature monitoring of the feet in diabetic patients can help in the diabetic foot ulcer prevention. This app is a promising tool.
26. Monitoring of pH and temperature of neuropathic diabetic and nondiabetic foot ulcers for 12 weeks: An observational study						
Gethin, G.; O'Connor, G.M.; Abedin, J.; Newell, J.; Flynn, L.; Watterson, D.; O'Loughlin, A. [34]	2018	Case-control.	50 neuropathic patients: (34 with diabetes).	Determine baseline date regarding pH, size and temperature of non-infected neuropathic foot ulcer surfaces. Survey changes for 12 weeks looking for the changes in these characteristics related to the healing of the ulcer.	62.5% of the cases where the ulcer was healed had a reduction in the central temperature of the wound.	Reference values of the thermal variation are given and can be used in greater cohort studies.

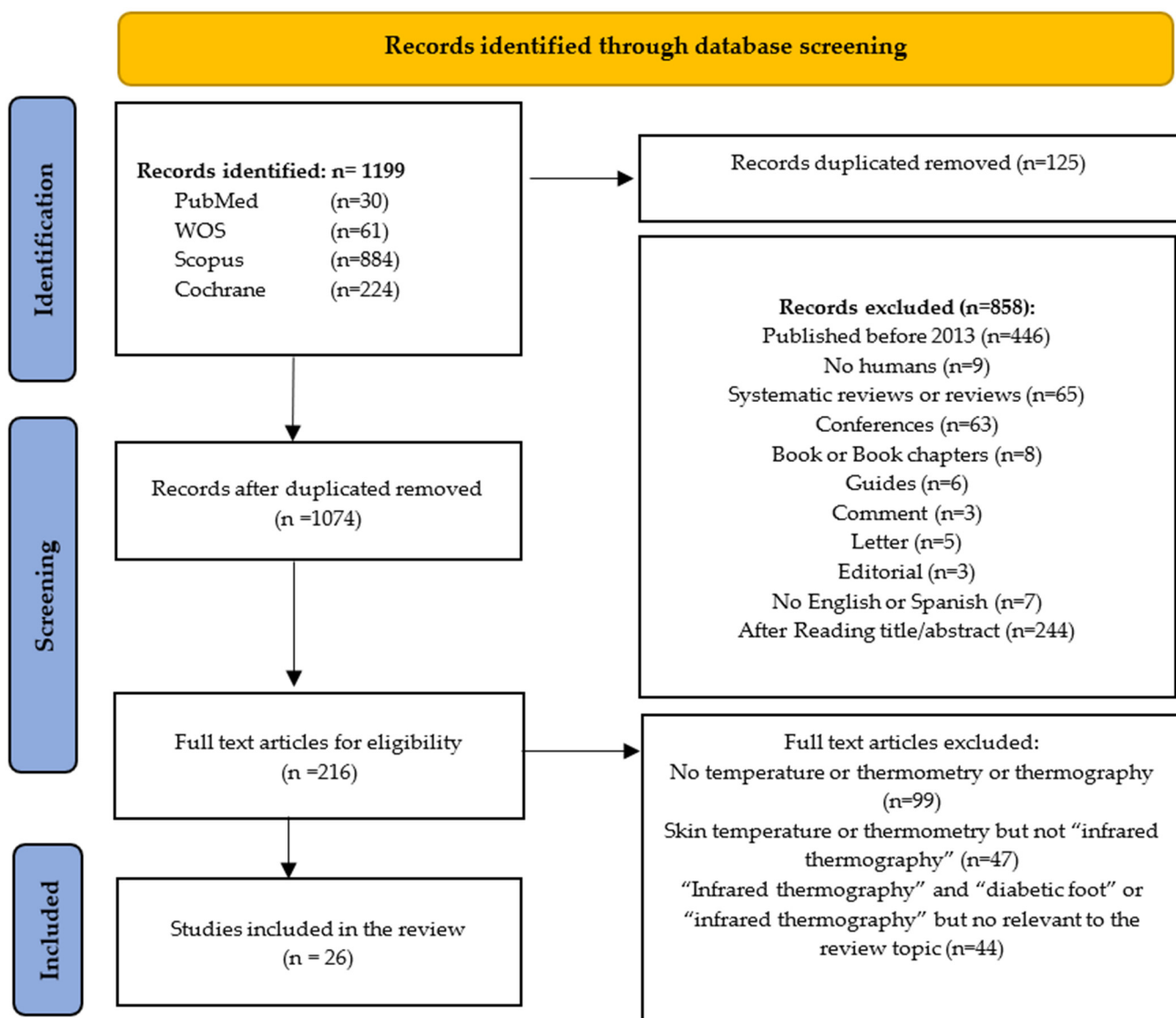


**Figure 1.** PRISMA study selection flowchart.

In this review, only one paper was considered to have excellent methodological quality, and three studies were rated as having a good quality. The majority fell within the range of 5–4 points. Only four references scored below 4 points, indicating poor methodological quality (Table 4).

**Table 4.** Articles' methodology quality scores according to the PEDro scale. “✓” Meet requirement and “✗” do not meet requirement.

	Inclusion and Source	Random Assign	Hidden Assign	Baseline Comparability	Blinded Subjects	Blinded Therapists	Blinded Raters	Results above 85%	Analysis by “Intention to Treat”	Statistical Comparisons between Groups	Measurement and Variability Data	SCORE
Liu, C.; van Netten, J.J.; van Baal, J.G.; Bus, S.A.; van der Heijden, F. (2015) [3]	✓	✗	✗	✗	✗	✗	✗	✓	✓	✓	✓	4
Ilo, A.; Romsí, P.; Mäkelä, J. (2020) [5]	✓	✗	✗	✓	✗	✗	✗	✓	✓	✓	✓	5
Machin, G.; Whittam, A.; Ainarkar, S.; Allen, J.; Bevans, J.; Edmonds, M.; Kluwe, B.M.A.; Petrova, N.; Plassmann, P.; Ring, F.; et al. (2019) [11]	✓	✗	✗	✓	✗	✗	✗	✓	✓	✓	✓	5
Petrova, N.L.; Whittam, A.; MacDonald, A.; Ainarkar, S.; Donaldson, A.N.; Bevans, J.; Allen, J.; Plassmann, P.; Kluwe, B.; Ring, F.; et al. (2018) [12]	✓	✗	✗	✓	✗	✗	✗	✓	✓	✓	✓	5
Macdonald, A.; Petrova, N.; Ainarkar, S.; Allen, J.; Plassmann, P.; Whittam, A.; Bevans, J.; Ring, F.; Kluwe, B.; Simpson, R.; et al. (2017) [13]	✓	✗	✗	✓	✗	✗	✗	✓	✓	✓	✓	5
Van Doremalen, R.F.M.; van Netten, J.J.; van Baal, J.G.; Vollenbroek-Hutten, M.M.R.; van der Heijden, F. (2019) [14]	✓	✗	✗	✓	✗	✗	✗	✓	✓	✓	✓	5
Petrova, N.L.; Donaldson, N.K.; Tang, W.; MacDonald, A.; Allen, J.; Lomas, C.; Leech, N.; Ainarkar, S.; Bevans, J.; Plassmann, P. (2020) [15]	✓	✓	✓	✓	✓	✗	✗	✓	✓	✓	✓	8
Van Netten, J.J.; Van Baal, J.G.; Liu, C.; Van Der Heijden, F.; Bus, S.A. (2013) [16]	✓	✗	✓	✓	✗	✗	✗	✓	✓	✓	✓	6
Van Doremalen, R.F.M.; van Netten, J.J.; van Baal, J.G.; Vollenbroek-Hutten, M.M.R.; van der Heijden, F. (2020) [17]	✓	✗	✓	✗	✓	✗	✗	✗	✓	✓	✓	5

**Table 4.** Cont.

	Inclusion and Source	Random Assign	Hidden Assign	Baseline Comparability	Blinded Subjects	Blinded Therapists	Blinded Raters	Results above 85%	Analysis by "Intention to Treat"	Statistical Comparisons between Groups	Measurement and Variability Data	SCORE
Aliahmad, B.; Tint, A.N.; Arjunan, S.P.; Rani, P.; Kumar, D.K.; Miller, J.; Zajac, J.D.; Wang, G.; Ekinci, E.I. (2018) [18]	✓	✓	✗	✓	✗	✓	✗	✓	✓	✓	✓	7
Macdonald, A.; Petrova, N.; Ainarker, S.; Allen John Lomas, C.; Tang, W.; Plassmann, P.; Ehittam, A.; Bevans, J.; Ring, F.; Kluwe, B (2019) [19]	✓	✓	✓	✓	✓	✗	✗	✓	✓	✓	✓	8
Gatt, A.; Falzon, O.; Cassar, K.; Camilleri, K.P.; Gauci, J.; Ellul, C.; Mizzi, S.; Mizzi, A.; Papanas, N.; Sturgeon, C.; et al. (2018) [20]	✓	✗	✗	✗	✗	✗	✗	✗	✓	✓	✓	4
Astasio-Picado, Á.; Martínez, E.E.; Gómez-Martín, B. (2019) [21]	✓	✗	✗	✓	✗	✗	✗	✗	✓	✓	✓	4
Astasio-Picado, A.; Martinez, E.E.; Nova, A.M.; Rodriguez, R.S.; Gomez-Martin, B. (2018) [22]	✓	✗	✗	✓	✗	✗	✗	✓	✓	✓	✓	5
Mori, T.; Nagase, T.; Takehara, K.; Oe, M.; Ohashi, Y.; Amemiya, A.; Noguchi, H.; Ueki, K.; Kadowaki, T.; Sanada, H. (2013) [23]	✓	✗	✗	✗	✗	✗	✗	✓	✓	✓	✓	4
Zhou, Q.; Qian, Z.; Wu, J.; Liu, J.; Ren, L.; Ren, L (2021) [24]	✓	✓	✓	✓	✓	✗	✗	✓	✓	✓	✓	8
Bhargavi, A.; Anantha, K.; Janarthan, K (2020) [25]	✓	✗	✗	✓	✓	✗	✗	✓	✓	✓	✓	6
Rai, M.; Maity, T.; Sharma, R.; Yadav, R.K. (2022) [26]	✓	✗	✗	✗	✗	✗	✗	✓	✓	✓	✓	4
Arteaga-Marrero, N.; Bodson, L.C.; Hernandez, A.; Villa, E.; Ruiz-Alzola, J. (2021) [27]	✓	✗	✗	✗	✗	✗	✗	✗	✓	✓	✓	3

**Table 4.** *Cont.*

	Inclusion and Source	Random Assign	Hidden Assign	Baseline Comparability	Blinded Subjects	Blinded Therapists	Blinded Raters	Results above 85%	Analysis by "Intention to Treat"	Statistical Comparisons between Groups	Measurement and Variability Data	SCORE
Hernandez-Contreras, D.A.; Peregrina-Barreto, H.; Rangel-Magdaleno, J.D.; Renero-Carrillo, F.J (2019) [28]	✓	✗	✗	✗	✗	✗	✗	✗	✓	✓	✓	3
Carabott, M.; Formosa, C.; Mizzi, A.; Papanas, N.; Gatt, A. (2021) [29]	✓	✗	✗	✗	✗	✗	✗	✗	✓	✓	✓	3
Kanazawa, T.; Nakagami, G.; Goto, T.; Noguchi, H.; Oe, M.; Miyagaki, T.; Hayashi, A.; Sasaki, S.; Sanada, H. (2016) [30]	✓	✓	✓	✓	✓	✗	✓	✓	✓	✓	✓	9
Oe, M.; Tsuruoka, K.; Ohashi, Y.; Takehara, K.; Noguchi, H.; Mori, T.; Yamauchi, T.; Sanada, H. (2021) [31]	✓	✗	✗	✗	✗	✗	✗	✗	✓	✓	✓	3
Dębiec-Bąk, A.; Skrzek, A.; Ptak, A.; Majerski, K.; Uiberlayová, I.; Stefańska, M. (2023) [32]	✓	✗	✗	✓	✗	✗	✗	✓	✓	✓	✓	5
Fraiwan, L.; Ninan, J.; Al-Khodari, M. (2018) [33]	✓	✗	✗	✓	✗	✗	✗	✗	✓	✓	✓	4
Gethin, G.; O'Connor, G.M.; Abedin, J.; Newell, J.; Flynn, L.; Watterson, D.; O'Loughlin, A. (2018) [34]	✓	✗	✗	✓	✗	✗	✗	✓	✓	✓	✓	5

#### 4. Discussion

To assess if infrared thermography was a useful tool for diagnosing pre-ulcerous states and detecting the complications of ulcers in diabetic patients, we performed an exhaustive review of the relevant available literature. We found elements that made this comparison difficult, such as the differences in the samples and methodology used in each study, including the infrared camera employed and the protocol followed to capture the images. In spite of these challenges, we have emphasized the lack of evidence for the use of thermography in preventing complications, the absence of consensus in the use of angiosomes and temperature distribution patterns, as well as the need to establish thermographic standards that facilitate the comparison of obtained data.

Our search highlighted articles that had analyzed and compared foot temperature using infrared thermography in healthy [11–14] and diabetic patients [3,5,14–23], although other studies had directly analyzed both types of patients [24–34]. This type of comparison had confirmed the difference between the temperature of both groups, registering lower temperatures in the healthy group as compared with the diabetic one [3,5,24–27,32,33]. However, it is important to consider the results obtained depend on the protocol used. Indeed, studies such as those by Machin et al. [11] and Rai et al. [26] observed an increase in plantar temperature in healthy patients that could be indicative of the presence of inflammation. The previous publication of benchmark values in healthy people [11–13] allowed us to define standardized results that could be used to refine the methodology to achieve satisfactory results when taking samples.

Studies in diabetic patients have highlighted the fact that thermography can be used as a method of temperature control (which is approximately 2 °C higher in infected wounds) useful to help patients in avoiding pressure zones, thereby favoring the prevention of lesions and their complications [16,34]. However, other authors such as Petrova et al. [15] found no difference in ulcer appearance in diabetic patients allocated in a randomized control trial where one group was blinded to the results of the thermography and the other was not (both receiving also standard care and follow-up). Therefore, there is insufficient evidence to support the use of thermography to prevent complications because the values it detects do not always significantly differ from normality and studies with larger sample sizes are still required. Databases such as the one published by Hernández-Contreras et al. [28] which contain both healthy and diabetic patient thermograms could be created. This database contains 167 patients and so could serve as a useful baseline for the comparison of results with those of future studies. Although different types of voluntary subjects were included in the different studies considered in this review, these results could be addressed together because they all suggest that thermography is a suitable tool to detect foot temperature changes. If they are detected sufficiently early, this technology may help to prevent the appearance of pre-ulcerous complications and could favor ulcer healing and avoiding infections through early treatment [15,18,25,34].

Even though one of the exclusion criteria for this current work was not being exposed to other pathologies that could result in temperature changes, it was very difficult to isolate diabetic foot from other pathologies such as peripheral vascular disease because many of these coexist [25,28,29,31]. Indeed, some authors observed that temperatures in the fifth metatarsal and hallux were lower in patients with associated pathologies [5,21].

Furthermore, Mori et al. [23] suggest that temperature distribution patterns must be identified by collecting and classifying these images according to maps of heat distribution so that they can be compared without relying on the angiosome divisions proposed by other authors [5,23]. Other authors suggest that patients with diabetic foot present a significantly higher temperature in the fifth metatarsal area and hallux compared to healthy individuals [20,22,27]. These variations represent different pattern distributions of temperature. For example, diabetic patients have notably higher temperature asymmetry and hot spots on the sole of the foot that indicate a heat increase [11,26]. Regardless, the lack of consensus in the use of angiosomes and temperature distribution patterns make it difficult to generalize the results published up to date. Moreover, it is important to highlight the differences

in thermographic images from studies comparing the affected and contralateral limbs in diseased or healthy patients. According to Van Netten et al. [16], there was no difference between the limbs of the same patient, while Macdonald et al. [20] or Mori et al. [23] suggested that intra-patient variability is comparable with that of other patients, with a difference of up to 2 °C between both feet. Nonetheless, infrared thermography is the most common method used to compare contralateral limbs in these patients [13,15,16,19,22]. The work by Gatt et al. [20] indicated that there were differences between patients with or without lesions. This increased temperature may be altered in pre-ulcerous states, although once the wound is present it is difficult to predict the development of complications using thermography alone, because no difference between ulcerated and healthy toes of the same foot can be detected. However, Gethin [34] is able to show a progressive core temperature reduction along with the healing of the wound.

As previously mentioned, not only the study population is variable in the studies reported, but also the characteristics of the thermal imaging device and methods of image acquisition. A wide range of different infrared cameras are used for these types of study. On average, it can be assumed that a standard spatial resolution of  $320 \times 240$  pixels [15,20,22,26] confers a thermal resolution of up to 0.1 °C [16,19,20,25] with a temperature range of 0–100 °C [30]. Although the use of standard infrared cameras is quite common, some studies have proposed using infrared smartphone cameras [14,30,31,33] to make this technique even more accessible. Indeed, some studies have even proposed merging 3D and thermography images to obtain more realistic results [16], as well as developing mobile apps able to detect temperature changes. [31,33]. However, phone cameras have a lower ( $160 \times 120$  pixels) resolution [14,17] and these devices cannot obtain specific data like absolute temperature. Despite this limitation, Kanazawa et al. [30] suggest that images are obtained much faster and are sufficient for data comparison. In fact, Van Doremalen et al. [14] stated that cameras connected to smartphones showed excellent validity for studying diabetic foot and therefore, such studies with smartphone cameras should be increased. Of note, although working at room temperature, some studies use a black background to dampen the influence of light [3,14,22,25,26] because environmental variations can alter the results, as shown by Bhargavi et al. [25].

As it has been observed during the development of this current study, there are some limitations to comparing the use of infrared thermography in patients with diabetic foot. First, very few studies have individually tackled this technique, comparing it with other techniques or in other pathologies associated with diabetic foot. Second, a wide range of cameras can be used to record sample images, leading to the misconception that accuracy is unreliable, but actually, images are not necessarily comparable, depending on many factors, especially their spatial resolution. Furthermore, the decision to use a black background in the images can significantly alter the results and no algorithms have yet been developed that can unify all these criteria.

In addition, it is to be highlighted that working with healthy or diabetic individuals with or without an ulcer or underlying pathologies can result in very disparate sample images. Thus, it has been proposed by other authors, the generation of a large thermographic image database could help to create thermographic standards and to make the comparison of results more feasible. Homogenous criteria that can help to unify results must be developed so that this technique can be used to help prevent complications or promote ulcer healing in diabetic patients.

## 5. Conclusions

Infrared thermography represents a potentially effective tool for detecting pre-ulcerous states in diabetic foot patients. However, further research is still required to investigate its applications for preventing diabetic foot ulcer complications. It is very important to highlight that these thermographic studies must consider the sample type (healthy or diabetic patients, with or without an ulcer), protocol used to obtain the images (e.g., with or without a black background), and results analysis (software used). It is essential to continue

research into infrared thermography, especially with the aim of clarifying whether the use of angiosomes or patterns of plantar temperature distribution is better; the influence of peripheral vascular disease on variations in plantar temperature in the diabetic population; and the reliability of cameras connected to smartphones. Infrared thermography is a cheap, non-invasive, and painless technique that can provide useful data for the development of new methods to further prevent and palliate diabetic foot complications.

**Author Contributions:** M.F.C. participated in the conception and design of the study, completed the literature research, was involved in the analysis and interpretation of the results and drafted the article. I.J.-R. and M.I.-R. participated in the conception and the design of the study, were involved in the analysis and interpretation of the results and reviewed the article critically for important intellectual content. M.M. and M.A. reviewed the article critically for important intellectual content and gave final approval of the version to be published. All authors have read and agreed to the published version of the manuscript.

**Funding:** This research received no funding.

**Institutional Review Board Statement:** Not applicable.

**Informed Consent Statement:** Not applicable.

**Data Availability Statement:** Data are contained within the article.

**Conflicts of Interest:** The authors declare no conflicts of interest.

## References

1. Enciso Rojas, Á.D. Risk factors associated with diabetic foot. *Rev. Virtual Soc. Paraguaya Med. Interna* **2016**, *3*, 58–70. [CrossRef]
2. Rincón, Y.; Gil, V.; Pacheco, J.; Benítez, I.; Sánchez, M. Evaluación y tratamiento del pie diabético. *Rev. Venez. Endocrinol. Metab.* **2012**, *10*, 176–187.
3. Liu, C.; van Netten, J.J.; van Baal, J.G.; Bus, S.A.; van der Heijden, F. Automatic detection of diabetic foot complications with infrared thermography by asymmetric analysis. *J. Biomed. Opt.* **2015**, *20*, 026003. [CrossRef]
4. Ramírez-Arbeláez, L.M.; Jiménez-Díaz, K.T.; Correa-Castañeda, A.C.; Giraldo-Restrepo, J.A.; Fandiño-Toro, H.A. Protocolo de adquisición de imágenes diagnósticas por termografía infrarroja. *Med. Lab.* **2015**, *21*, 161–178. [CrossRef]
5. Ilo, A.; Romsi, P.; Mäkelä, J. Infrared Thermography and Vascular Disorders in Diabetic Feet. *J. Diabetes Sci. Technol.* **2019**, *14*, 28–36. [CrossRef]
6. Hidalgo Salvador, E.; Álvarez González, F.; Salvador Luna, A. Application of Infrared thermography in legal medicine. Is it a valid test for an objective assessment. *Cuad. Med. Forense* **2014**, *20*, 77–84. [CrossRef]
7. Chicharro-Luna, E.; Portabales Botana, I.; Ramírez Monreal, L.; Torrent Ivorra, E. Monitorización de la temperatura del pie como herramienta en la neuropatía diabética. *Rev. Int. Cienc. Podol.* **2015**, *10*, 9–16. [CrossRef]
8. da Franciele, C.S.; Beatriz Angélica, V.A.; da Rodrigo, R.I.; Paulo Jose, B.G.F.; da Rudney, S. Escalas y listas de evaluación de la calidad de estudios científicos. *Rev. Cuba Inf. Cienc. Salud* **2013**, *24*, 295–312. Available online: [http://scielo.sld.cu/scielo.php?script=sci\\_arttext&pid=S2307-21132013000300007&lang=pt](http://scielo.sld.cu/scielo.php?script=sci_arttext&pid=S2307-21132013000300007&lang=pt) (accessed on 12 April 2023).
9. Albanese, E.; Bütkofer, L.; Armijo-Olivio, S.; Ha, C.; Egger, M. Construct validity of the Physiotherapy Evidence Database (PEDro) quality scale for randomized trials: Item response theory and factor analyses. *Res. Synth. Methods* **2020**, *11*, 227–236. [CrossRef]
10. Escala PEDro—PEDro. Available online: <https://pedro.org.au/spanish/resources/pedro-scale/> (accessed on 12 April 2023).
11. Machin, G.; Whittam, A.; Ainarkar, S.; Allen, J.; Bevans, J.; Edmonds, M.; Kluwe, B.M.A.; Petrova, N.; Plassmann, P.; Ring, F.; et al. A medical thermal imaging device for the prevention of diabetic foot ulceration. *Iopscience* **2019**, *6*, 125337. [CrossRef]
12. Petrova, N.L.; Whittam, A.; MacDonald, A.; Ainarkar, S.; Donaldson, A.N.; Bevans, J.; Allen, J.; Plassmann, P.; Kluwe, B.; Ring, F.; et al. Reliability of a novel thermal imaging system for temperature assessment of healthy feet. *J. Foot Ankle Res.* **2018**, *11*, 22. [CrossRef]
13. Macdonald, A.; Petrova, N.; Ainarkar, S.; Allen, J.; Plassmann, P.; Whittam, A.; Bevans, J.; Ring, F.; Kluwe, B.; Simpson, R.; et al. Reproducibility of Thermal Images: Some Healthy Examples. In *Application of Infrared to Biomedical Sciences*; Ng, E.Y.K., Etehad tavakol, M., Eds.; Springer: Singapore, 2017; pp. 265–276. [CrossRef]
14. Van Doremalen, R.F.M.; van Netten, J.J.; van Baal, J.G.; Vollenbroek-Hutten, M.M.R.; van der Heijden, F. Validation of low-cost smartphone-based thermal camera for diabetic foot assessment. *Diabetes Res. Clin. Pract.* **2019**, *149*, 132–139. [CrossRef]
15. Petrova, N.L.; Donaldson, N.K.; Tang, W.; MacDonald, A.; Allen, J.; Lomas, C.; Leech, N.; Ainarkar, S.; Bevans, J.; Plassmann, P.; et al. Infrared thermography and ulcer prevention in the high-risk diabetic foot: Data from a single-blind multicentre controlled clinical trial. *Diabet. Med.* **2020**, *37*, 95–104. [CrossRef]
16. Van Netten, J.J.; Van Baal, J.G.; Liu, C.; Van Der Heijden, F.; Bus, S.A. Infrared thermal imaging for automated detection of diabetic foot complications. *J. Diabetes Sci. Technol.* **2013**, *7*, 1122–1129. [CrossRef]

17. Van Doremalen, R.F.M.; van Netten, J.J.; van Baal, J.G.; Vollenbroek-Hutten, M.M.R.; van der Heijden, F. Infrared 3D Thermography for Inflammation Detection in Diabetic Foot Disease: A Proof of Concept. *J. Diabetes Sci. Technol.* **2020**, *14*, 46–54. [[CrossRef](#)]
18. Aliahmad, B.; Tint, A.N.; Arjunan, S.P.; Rani, P.; Kumar, D.K.; Miller, J.; Zajac, J.D.; Wang, G.; Ekinci, E.I. Is Thermal Imaging a Useful Predictor of the Healing Status of Diabetes-Related Foot Ulcers? A Pilot Study. *J. Diabetes Sci. Technol.* **2019**, *13*, 561–567. [[CrossRef](#)]
19. Macdonald, A.; Petrova, N.; Ainarker, S.; Allen John Lomas, C.; Tang, W.; Plassmann, P.; Ehittam, A.; Bevans, J.; Ring, F.; Kluwe, B.; et al. Between visit variability of thermal imaging of feet in people attending podiatric clinics with diabetic neuropathy at high risk of developing foot ulcers. *Physiol. Meas.* **2019**, *40*, 084004. [[CrossRef](#)]
20. Gatt, A.; Falzon, O.; Cassar, K.; Camilleri, K.P.; Gauci, J.; Ellul, C.; Mizzi, S.; Mizzi, A.; Papanas, N.; Sturgeon, C.; et al. The Application of Medical Thermography to Discriminate Neuroischemic Toe Ulceration in the Diabetic Foot. *Int. J. Low. Extrem. Wounds* **2018**, *17*, 102–105. [[CrossRef](#)]
21. Astasio-Picado, Á.; Martínez, E.E.; Gómez-Martín, B. Comparison of Thermal Foot Maps between Diabetic Patients with Neuropathic, Vascular, Neurovascular, and No Complications. *Curr. Diabetes Rev.* **2019**, *15*, 503–509. [[CrossRef](#)]
22. Astasio-Picado, A.; Martinez, E.E.; Nova, A.M.; Rodriguez, R.S.; Gomez-Martin, B. Thermal map of the diabetic foot using infrared thermography. *Infrared Phys. Technol.* **2018**, *93*, 59–62. [[CrossRef](#)]
23. Mori, T.; Nagase, T.; Takehara, K.; Oe, M.; Ohashi, Y.; Amemiya, A.; Noguchi, H.; Ueki, K.; Kadokawa, T.; Sanada, H. Morphological pattern classification system for plantar thermography of patients with diabetes. *J. Diabetes Sci. Technol.* **2013**, *7*, 1102–1112. [[CrossRef](#)]
24. Zhou, Q.; Qian, Z.; Wu, J.; Liu, J.; Ren, L.; Ren, L. Early diagnosis of diabetic peripheral neuropathy based on infrared thermal imaging technology. *Diabetes Metab. Res. Rev.* **2021**, *37*, e3429. [[CrossRef](#)]
25. Bhargavi, A.; Anantha, K.; Janarthan, K. Plantar temperature and vibration perception in patients with diabetes: A cross-sectional study. *Biocybern. Biomed. Eng.* **2020**, *40*, 1600–1610. [[CrossRef](#)]
26. Rai, M.; Maity, T.; Sharma, R.; Yadav, R.K. Early detection of foot ulceration in type II diabetic patient using registration method in infrared images and descriptive comparison with deep learning methods. *J. Supercomput.* **2022**, *78*, 13409–13426. [[CrossRef](#)]
27. Arteaga-Marrero, N.; Bodson, L.C.; Hernandez, A.; Villa, E.; Ruiz-Alzola, J. Morphological Foot Model for Temperature Pattern Analysis Proposed for Diabetic Foot Disorders. *Appl. Sci.* **2021**, *11*, 7396. [[CrossRef](#)]
28. Hernandez-Contreras, D.A.; Peregrina-Barreto, H.; Rangel-Magdaleno, J.D.; Renero-Carrillo, F.J. Plantar Thermogram Database for the Study of Diabetic Foot Complications. *IEEE Access* **2019**, *7*, 161296–161307. [[CrossRef](#)]
29. Carabott, M.; Formosa, C.; Mizzi, A.; Papanas, N.; Gatt, A. Thermographic Characteristics of the Diabetic Foot with Peripheral Arterial Disease Using the Angiosome Concept. *Exp. Clin. Endocrinol. Diabetes* **2021**, *129*, 93–98. [[CrossRef](#)]
30. Kanazawa, T.; Nakagami, G.; Goto, T.; Noguchi, H.; Oe, M.; Miyagaki, T.; Hayashi, A.; Sasaki, S.; Sanada, H. Use of smartphone attached mobile thermography assessing subclinical inflammation: A pilot study. *J. Wound Care* **2016**, *25*, 177–182. [[CrossRef](#)]
31. Oe, M.; Tsuruoka, K.; Ohashi, Y.; Takehara, K.; Noguchi, H.; Mori, T.; Yamauchi, T.; Sanada, H. Prevention of diabetic foot ulcers using a smartphone and mobile thermography: A case study. *J. Wound Care* **2021**, *30*, 116–119. [[CrossRef](#)]
32. Dębiec-Bąk, A.; Skrzek, A.; Ptak, A.; Majerski, K.; Uiberlayová, I.; Stefańska, M. Evaluation of the surface temperature distribution in the feet of patients with type 2 diabetes using the thermovision method. *Physiother. Q.* **2023**, *31*, 92–97. [[CrossRef](#)]
33. Fraiwan, L.; Ninan, J.; Al-Khodari, M. Mobile application for ulcer detection. *Open Biomed. Eng. J.* **2018**, *12*, 16–26. [[CrossRef](#)] [[PubMed](#)]
34. Gethin, G.; O'Connor, G.M.; Abedin, J.; Newell, J.; Flynn, L.; Watterson, D.; O'Loughlin, A. Monitoring of pH and temperature of neuropathic diabetic and nondiabetic foot ulcers for 12 weeks: An observational study. *Wound Repair Regen.* **2018**, *26*, 251–256. [[CrossRef](#)] [[PubMed](#)]

**Disclaimer/Publisher's Note:** The statements, opinions and data contained in all publications are solely those of the individual author(s) and contributor(s) and not of MDPI and/or the editor(s). MDPI and/or the editor(s) disclaim responsibility for any injury to people or property resulting from any ideas, methods, instructions or products referred to in the content.